The lasting health toll of chemical warfare p. 20

Hidden impacts of air pollution p. 39

Flying through Saturn's ionosphere p. 66

Science

$15
5 JANUARY 2018
sciencemag.org
AAAS

GUT MICROBES AND CANCER

The microbiome influences patient response to immunotherapy

pp. 32, 91, 97, & 104

CONTENTS

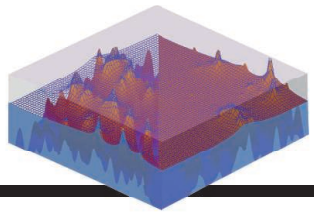

38
Testing surface adhesion

5 JANUARY 2018 • VOLUME 359 • ISSUE 6371

NEWS

IN BRIEF

IN DEPTH

FEATURES

INSIGHTS

LETTERS

PERSPECTIVES

POLICY FORUM

BOOKS *ET AL.*

Published by AAAS

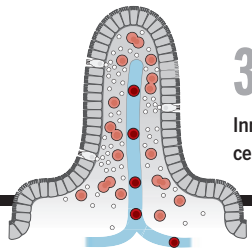

36 & 114
Innate lymphoid cell migration

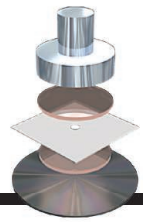

72
Mending under pressure

RESEARCH

IN BRIEF

REVIEW

RESEARCH ARTICLES

REPORTS

DEPARTMENTS

ON THE COVER

Illustration of gut microbial species assembling into the shape of a cancer awareness ribbon. Cancer patients with an abundance of different gut bacteria have better survival outcomes after checkpoint inhibitor immunotherapy, whereas patients with depleted gut flora respond poorly to this treatment. Thus, modulating the microbiome may provide hope for improved cancer patient responses. See pages 32, 91, 97, and 104. *Illustration: V. Altounian/*Science

SCIENCE (ISSN 0036-8075) is published weekly on Friday, except last week in December, by the American Association for the Advancement of Science, 1200 New York Avenue, NW, Washington, DC 20005. Periodicals mail postage (publication No. 484460) paid at Washington, DC, and additional mailing offices. Domestic Individual membership, including subscription (12 months): $165 ($74 allocated to subscription). Domestic institutional subscription (51 issues): $1808; Foreign postage extra: Mexico, Caribbean (surface mail) $55; other countries (air assist delivery): $89 First class, airmail, student, and emeritus rates on request. Canadian rates with GST available upon request, GST #125488122. Publications Mail Agreement Number 1069624. **Printed in the U.S.A.** **Change of address:** Allow 4 weeks, giving old and new addresses and 8-digit account number. **Postmaster:** Send change of address to AAAS, P.O. Box 96178, Washington, DC 20090–6178. **Single-copy sales:** $15 each plus shipping and handling; bulk rate on request. **Authorization to reproduce** material for internal or personal use under circumstances not falling within the fair use provisions of the Copyright Act is granted by AAAS to libraries and others who use Copyright Clearance Center (CCC) Pay-Per-Use services provided that $35.00 per article is paid directly to CCC, 222 Rosewood Drive, Danvers, MA 01923. The identification code for *Science* is 0036-8075. *Science* is indexed in the *Reader's Guide to Periodical Literature* and in several specialized indexes.

Science
AAAS
1200 New York Avenue, NW, Washington, DC 20005
Clarendon House, Clarendon Road, Cambridge, UK CB2 8FH

SUBSCRIPTION SERVICES For change of address, missing issues, new orders and renewals, and payment questions: 866-434-AAAS (2227) or 202-326-6417, FAX 202-842-1065. Mailing addresses: AAAS, P.O. Box 96178, Washington, DC 20090-6178 or AAAS Member Services, 1200 New York Avenue, NW, Washington, DC 20005

INSTITUTIONAL SITE LICENSES 202-326-6730 **REPRINTS:** Author Inquiries 800-635-7181 **COMMERCIAL INQUIRIES** 803-359-4578 **PERMISSIONS** 202-326-6765, permissions@aaas.org **AAAS Member Central Support** 866-434-2227 www.aaas.org/membercentral.

INFORMATION FOR AUTHORS See pages 624 and 625 of the 5 February 2016 issue or access www.sciencemag.org/authors/science-information-authors

Published by AAAS

EDITORIAL

Progress on reproducibility

Ideas supported by well-defined and clearly described methods and evidence are one of the cornerstones of science. After several publications indicated that a substantial number of scientific reports may not be readily reproducible, the scientific community and public began engaging in discussions about mechanisms to measure and enhance the reproducibility of scientific projects. In this context, several innovative steps have been taken in recent years. The results of these efforts confirm that improving reproducibility will require persistent and adaptive responses, and as we gain experience, implementation of the best possible practices.

A framework has been developed to promote transparency and openness in scientific publications—the Transparency and Openness Promotion (TOP) guidelines (http://science.sciencemag.org/content/348/6242/1422.full). They cover key principles that apply to many scientific fields, although they were developed primarily by social scientists. The editors at *Science* have adjusted practices based on these policies and have gained experience with many of these issues. We fully support the principles behind these guidelines, including the centrality and benefits of transparency, as captured in our editorial principle that "all data and materials necessary to understand, assess, and extend the conclusions of the manuscript must be available to any reader" of *Science* and the *Science* family of journals. Our editorial policies now contain specific statements for each TOP guideline category. In some cases, we include the possibility of granting specific exceptions but insist that these circumstances be discussed with our editors early in the manuscript evaluation process to allow for thoughtful examination.

Another approach to assess reproducibility involved an experimental program that attempted to replicate selected findings in cancer biology by groups not involved with the original studies (see https://elifesciences.org/collections/9b1e83d1/reproducibility-project-cancer-biology). Although some findings were largely reproduced, in at least one case (which was published in *Science*), the key finding was not. Yet, the initial results have been utilized and extended in published studies from several other laboratories. This case reinforces the notion that reproducibility, certainly in cancer biology, is quite nuanced, and considerable care must be taken in evaluating both initial reports and reported attempts at extension and replication. Clear description of experimental details is essential to facilitate these efforts. The increased use of preprint servers such as bioRxiv by the biological and biomedical communities may play a role in facilitating communication of successful and unsuccessful replication results.

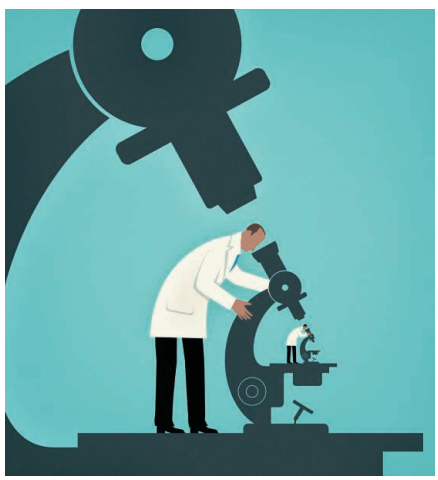

"...improving reproducibility will require...the best possible practices."

Over the past year, we have retracted three papers previously published in *Science*. The circumstances of these retractions highlight some of the challenges connected to reproducibility policies. In one case, the authors failed to comply with an agreement to post the data underlying their study. Subsequent investigations concluded that one of the authors did not conduct the experiments as described and fabricated data. Here, the lack of compliance with the data-posting policy was associated with a much deeper issue and highlights one of the benefits of policies regarding data transparency. In a second case, some of the authors of a paper requested retraction after they could not reproduce the previously published results. Because all authors of the original paper did not agree with this conclusion, they decided to attempt additional experiments to try to resolve the issues. These reproducibility experiments did not conclusively confirm the original results, and the editors agreed that the paper should be retracted. This case again reveals some of the subtlety associated with reproducibility. In the final case, the authors retracted a paper over extensive and incompletely described variations in image processing. This emphasizes the importance of accurately presented primary data.

As this new year moves forward, the editors of *Science* hope for continued progress toward strong policies and cultural adjustments across research ecosystems that will facilitate greater transparency, research reproducibility, and trust in the robustness and self-correcting nature of scientific results.

–Jeremy Berg

Editor-in-Chief, Science *Journals.*
jberg@aaas.org

10.1126/science.aar8654

NEWS

IN BRIEF

Edited by **Jeffrey Brainard**

AREAS TO WATCH

What's coming up in 2018

Tumultuous political change will shape the course of science in the new year. U.S. President Donald Trump's administration is expected to continue working to dismantle science-based environmental regulations. The United Kingdom's decision to leave the European Union has posed unresolved questions about research funding and migration of scientists. And China's push to become a scientific and economic leader is sure to affect how, and where, research is done. As these broad trends play out, *Science*'s news staff predicts specific areas of research and policy likely to be in the news this year.

A look at a monster black hole

ASTRONOMY | An international team of astronomers took a snapshot in April 2017 of the supermassive black hole at the heart of our galaxy. In the coming months, they hope to discover how well the picture came out. The Event Horizon Telescope team marshaled the forces of six radio observatories—a total of 80 dishes stretching from Hawaii to Spain to the South Pole. This multitude was needed to get sufficient resolution to image the black hole, which, though huge in mass (the equivalent of 4 million suns), is surprisingly small in volume (with a diameter less than half the distance from Mercury to the sun). After processing and correlating the data, they will obtain either a glorious silhouette of the black hole against the brilliant matter swirling around it or, as in earlier attempts using fewer telescopes, a tantalizing blur.

New clues from ancient DNA

HUMAN ORIGINS | New sources of ancient DNA should amplify the power of this molecular relic to shed light on human ancestors. Bones are the usual source of ancient human DNA, but last spring, scientists announced that they had managed to pick it up from cave sediments. That achievement may power a boom in studies tracing Neandertal, Denisovan, or modern human DNA to particular sites and artifacts, further detailing our ancestors' interactions with other archaic humans. And although most ancient DNA has come from cold climates, where it degrades slowly, results from warmer spots are emerging thanks to better sampling and analytic techniques. Ancient DNA from Africa may reveal new clues to our species's origin and diversity, and data from South America and Asia could uncover the paths humans took as they settled the globe. Other studies will zero in on the origins of Italians, Jews, Palestinians, and people from India.

A test for quantum computing

COMPUTER SCIENCE | Physicists may soon reach a major milestone in the decades-long quest to build a quantum computer, which instead of flipping ordinary bits would rely on subtler phenomena, such as the interference of quantum waves, to perform calculations. Researchers at Google and other laboratories are racing to build a quantum computer big enough to solve a test problem that would overwhelm ordinary computers. Such a demonstration of "quantum supremacy" would prove that the devices can do things that conventional computers cannot. But it will be years before quantum computers have enough power and reliability to achieve some of the much-hyped practical applications of such machines—including cracking current internet encryption schemes.

A big health study gets rolling

BIOMEDICINE | This spring, the U.S. National Institutes of Health will hit the launch button on one of its most ambitious projects ever: a long-term study of at least 1 million Americans that will explore the interplay among genes, lifestyle, the environment, and health. The projected 10-year, $4 billion All of Us study, proposed by then-President Barack Obama in 2015 as part of a push for personalized medicine, has already enrolled more than 15,000 participants for pilot testing. By the end of this year, study leaders aim to sharply increase that number

Telescopes including the Atacama Large Millimeter/ submillimeter Array in Chile will gaze at a massive black hole.

and ensure that at least 50% of volunteers are from groups underrepresented in biomedical research. Persuading large numbers of people from minority groups that have been ignored or even mistreated historically in biomedical studies to share their medical records and genetic data with researchers may be a tall order.

Epidemics make a return

PUBLIC HEALTH | Epidemics are hard to predict, but recent years have seen a resurgence of old foes, and it is likely the world will witness more in 2018. Wherever conflicts or other crises lead to a breakdown of sanitation, vaccination, or the health system generally, defeated diseases return. There are fears of a yellow fever outbreak in Nigeria, where widely scattered cases have popped up, suggesting transmission is already taking place across a large area. Diphtheria is staging a comeback among the Rohingya refugees in Bangladesh and sickening hundreds in war-torn Yemen, which had not seen cases in a quarter-century. The cholera outbreak in Yemen is the biggest in modern history, with 1 million suspected cases in 2017 alone. Stockpiles of cholera and yellow fever vaccine are limited, but a new cholera vaccine manufacturer may help ease the shortage.

Next steps for Brexit

POLICY | The United Kingdom's decision to leave the European Union in 2019 has raised so many unanswered questions, including its effects on the research world, that we're highlighting it for the second year in a row. Negotiations with Brussels in the coming year will be critical in resolving issues such as trade, immigration, and the terms under which the United Kingdom might participate in EU research funding programs. December brought some good news for U.K. research: EU scientists already living in the United Kingdom can remain there post-Brexit, and the United Kingdom will remain in Horizon 2020, the EU research program, until it ends in 2020.

War in Yemen has unleashed a large epidemic of cholera.

PHOTO: ABDULJABBAR ZEYAD/REUTERS

Europe crafts research megaplan

FUNDING | The European Commission's next large funding program for research and innovation will start taking shape this year. The 7-year program, to begin in 2021, replaces Horizon 2020, which provided €77 billion between 2014 and 2020. National governments, industry, and academia have begun lobbying for what they want to see in the plan. But after decades of steady increases, the research budget now faces fallout from Brexit: When the United Kingdom leaves the European Union in 2019, some EU programs will see their budgets shaved as the bloc's revenues decline.

Shots may treat HIV

PUBLIC HEALTH | More than 30 antiretroviral (ARV) drugs have come to market to treat HIV, and many combinations enable infected people to live near-normal life spans. But the pills work only if taken, and many infected people have difficulty adhering to their daily regimens. Later this year, several large studies are expected to report whether injectable, long-lasting ARVs given once every 4 weeks work as well as pills taken daily. Studies of monkeys suggest injected ARVs might last 3 months, and human studies also are now examining long-acting monoclonal antibodies that target HIV. These injections could be a game changer for prevention, too, as ARVs taken by uninfected people—so-called pre-exposure prophylaxis—derail transmissions.

A rush to the moon

SPACE FLIGHT | President Donald Trump directed NASA to return U.S. astronauts to the moon, but it may be crowded by the time they get there. Both India and China are planning to put down robotic landers on the moon this year (the Chandrayaan-2 and Chang'e 4 missions, respectively) and five companies are vying to deposit rovers there before the end of March to claim the Google Lunar XPRIZE. Launch company SpaceX may even shoot two space tourists around the moon before NASA's giant rocket, the Space Launch System, makes its first uncrewed flight, in December at the earliest.

A court ruling on gene editing

BIOTECHNOLOGY | This year, the European Union's Court of Justice is expected to decide how to regulate crops modified with

CRISPR and similar gene-editing tools. The United States moved ahead in this field in 2016 when it green-lighted one such crop: a humble white mushroom that scientists modified by removing a short DNA sequence to prevent browning. Regulators decided the mushroom was not subject to rules on genetically modified organisms (GMOs) because, unlike previous genetic engineering techniques, gene editing does not insert foreign DNA from viruses or bacteria to alter a plant's function. The court case in Europe, where public opposition to GMOs runs high, will determine whether an existing EU regulation permits a similar exception for CRISPR-edited crops.

RNA treatments move forward

CLINICAL RESEARCH | Scientists aiming to turn RNA molecules into therapies are entering this year with new optimism, after years of frustration. RNA-based drugs could treat a host of genetic diseases by intervening in the cellular process that turns DNA's messages into proteins. But it has proved tricky to sneak these delicate RNA payloads past the body's defenses and into the desired tissue while avoiding toxic effects from their delivery vehicles. In September 2017, Alnylam Pharmaceuticals announced that its small RNA molecules silenced the gene that causes the progressive disease hereditary ATTR amyloidosis in a successful phase III trial. Ionis Pharmaceuticals recently announced that an RNA approach called antisense reduced toxic brain proteins in a phase I trial to treat Huntington disease. And several ongoing clinical trials will test messenger RNA molecules that could turn cells into factories of therapeutic proteins.

Scientists are using double-stranded RNA, shown here, to block the expression of specific genes.

One of the Large Hadron Collider's detectors could yield evidence of new kinds of particles.

FDA targets stem cell clinics

DRUG OVERSIGHT | Last year, the U.S. Food and Drug Administration (FDA) signaled that it would crack down on clinics that offer unproven stem cell treatments for conditions ranging from knee injuries to neurological disease. In 2017, the agency finalized guidelines about which products must go through its premarket approval process. FDA also issued a warning letter to one stem cell company and seized unauthorized vaccines from another. Advocates for greater oversight are now watching whether other clinics flying under the regulatory radar—which potentially number in the hundreds—will face any consequences.

Scientists run for office

POLITICS | Energized by their opposition to the science and environmental policies of President Donald Trump and the Republican-controlled Congress, many U.S. researchers have decided to take their activism to the next level by running for office. Mostly novice politicians, and almost all Democrats, they are hoping their scientific credentials will be an asset with voters. A science-friendly political action committee has already raised $2 million for national, state, and local races—a record amount for such a cause—and helped train the candidates in the basics of running a campaign. Many will likely be derailed in crowded primaries, and none is a favorite to win in November. But their commitment to electoral politics adds a new element to the 2018 election season.

In pursuit of new particles

PARTICLE PHYSICS | Keep an eye out for clues to new particles from the world's largest atom smasher, the Large Hadron Collider (LHC) in Switzerland. In 2012, physicists there first glimpsed the Higgs boson, the last missing piece in the standard model of particles and forces. But so far, scientists haven't spotted what they want even more: new particles beyond those in the standard model. Instead of trying to see new particles directly, researchers working with the LHC beauty experiment study the decays of familiar particles called B mesons, which contain a massive bottom quark and lighter antiquark. Rates of certain decays don't quite match those predicted by the standard model. The anomalies could point indirectly to new particles flitting in and out of existence within the B mesons—a hint that scientists are eager to pursue.

IMAGES: (TOP TO BOTTOM) EQUINOX GRAPHICS/SCIENCE SOURCE; CERN/SCIENCE SOURCE

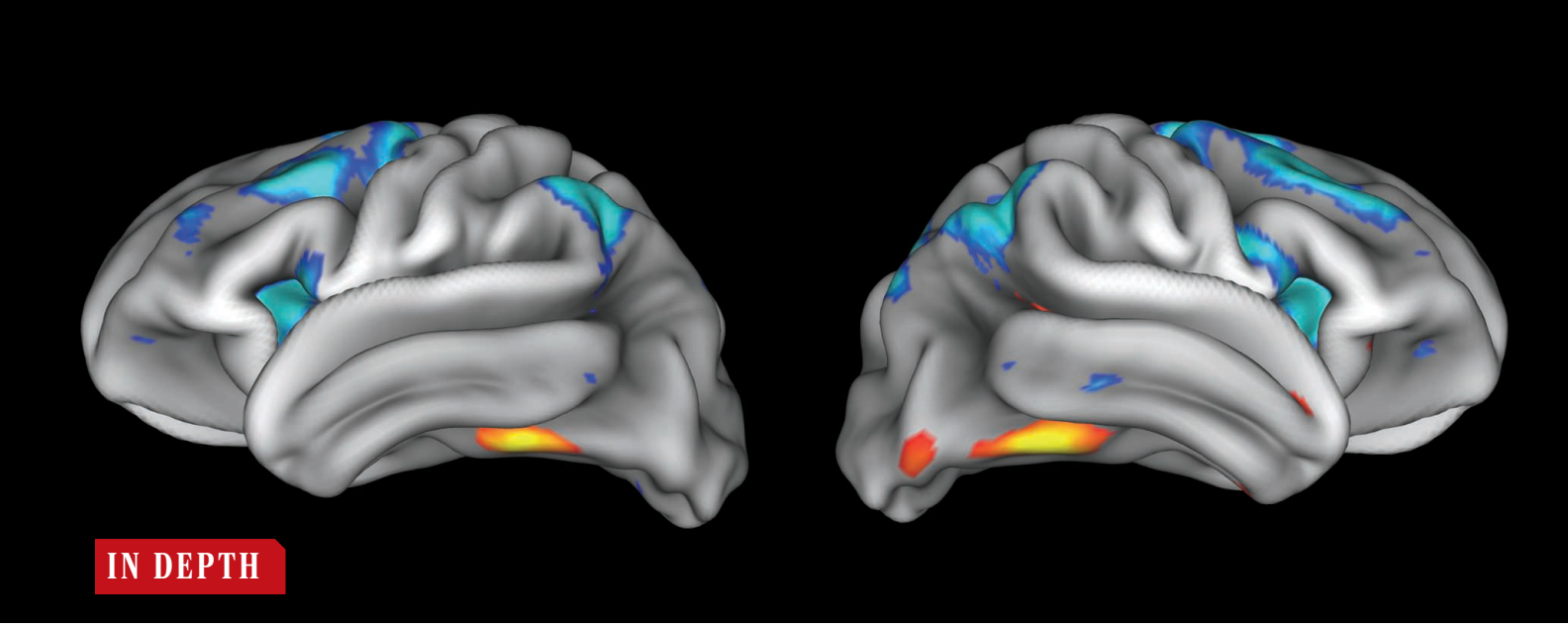

IN DEPTH

NEUROSCIENCE

Watching the teen brain grow

Over a decade, researchers aim to follow 10,000 children through the challenges of adolescence

By **Meredith Wadman**

Chya* (pronounced SHY-a), who is not quite 10 years old, recently spent an unusual day at the University of Maryland School of Medicine in Baltimore. Part of the time she was in a "cool" brain scanner while playing video games designed to test her memory and other brain-related skills. At other points, she answered lots of questions about her life and health on an iPad.

A slender Baltimore third grader who likes drawing, hip hop, and playing with her pet Chihuahua, Chya is one of more than 6800 children now enrolled in an unprecedented examination of teenage brain development. The Adolescent Brain Cognitive Development Study—or ABCD Study—will complete its 2-year enrollment period in September, and this month will release a trove of data from 4500 early participants into a freely accessible, anonymized database. Ultimately, the study aims to follow 10,000 children for a decade as they grow from 9- and 10-year-olds into young adults.

Supported by the first chunk of $300 million pledged by several institutes at the National Institutes of Health (NIH) in Bethesda, Maryland, teams at 21 sites around the United States are regularly using MRI machines to record the structure and activity of these young brains. They're also collecting reams of psychological, cognitive, and environmental data about each child, along with biological specimens such as their DNA. In addition to providing the first standardized benchmarks of healthy adolescent brain development, this information should allow scientists to probe how substance use, sports injuries, screen time, sleep habits, and other influences may affect—or be affected by—a maturing brain.

"A lot of studies in this area are plagued by the fact that we tend to capture teenagers after they have already started to misbehave in various ways. So, the fact that we are following kids from … before they engage in a lot of risk-taking behavior—it's going to be an incredibly rich data set," says clinical neuroscientist Monica Luciana of the University of Minnesota in Minneapolis, an ABCD Study site where she is a principal investigator (PI).

Clarifying the impacts of alcohol and drug use is a key goal for the study's leading funders: the National Institute on Drug Abuse (NIDA) and the National Institute on Alcohol Abuse and Alcoholism (NIAAA), both in Bethesda. "There is an urgency to try to address these questions," says NIDA Director Nora Volkow, the prime mover behind the study. The recent legalization of recreational marijuana in several states makes the study especially timely, she argues.

Other studies have used MRI to follow teen brain development. Europe's IMAGEN enrolled 2000 14-year-olds and scanned them at intervals over the past decade.

Combining results from 628 children's brains, this MRI scan shows regions activated as faces are viewed (yellow and orange) and other areas (blue and cyan) activated during a demanding working memory task.

And NIAAA has been funding a study of alcohol's impacts, imaging the brains of more than 800 youths once a year for 4 years. But ABCD "is going to be by far the largest," Volkow says. "It's [also] longer-lasting, starts younger, and is much more comprehensive" in terms of testing.

Every 2 years, researchers will image the brain structures of Chya and other subjects, and record their neural activity as they perform tasks involving memory, rewards, and face recognition. Every year, the participants will have their height, weight, and waist measured, and answer questions designed to assess psychological symptoms. They will also be asked annually about environmental influences—things like family conflict and neighborhood crime.

The study aims to describe a normal trajectory of adolescent brain development—similar to the height and weight charts in pediatricians' offices—and use that to begin to answer the many chicken-and-egg questions that correlational studies can't. For instance, people who smoke marijuana heavily beginning in adolescence or young adulthood show markedly less connectivity between the neuronal axons of the hippocampus, a brain region important to long-term memory formation and learning, than do nonusers. But were the users' brains wired differently to begin with, leading them to smoke cannabis heavily? Or did the smoking cause the changes?

"At age 9 and 10 you can get a nice clean baseline assessment on these kids," says Hugh Garavan, a neurobiologist who is the PI at the ABCD Study site at the University of Vermont (UVM) in Burlington. "Then, when someone develops psychosis at 16,

The ABCD Study keeps participants anonymous; the families of the kids in this article allowed the use of their first names.

IMAGES: RICHARD WATTS AND HUGH GARAVAN

we can go back and look at their brains and psychological assessments at 9, 10, 11, and 12. Were there markers of risk there?"

Such markers, it's hoped, will ultimately allow much earlier diagnosis, treatment, or prevention of substance abuse, mental illness, and other conditions. A key strength of the study is that it will enroll enough children—including 800 pairs of twins—to answer questions that require large numbers of subjects, such as whether there are age windows when the brain is particularly vulnerable to use of a given drug.

The study intends to reflect the United States's socioeconomic, geographical, racial, and ethnic diversity. Planners want the study pool to be 6% Asian-American, 16% black, and 24% Hispanic. As of early January, with 8 months left in recruitment, they are falling short on Asian-American and black enrollment, at 2% and 12%, respectively, but were close to meeting the Hispanic target, at 22%. And the "other" category, which includes mixed-race kids and Native Americans, accounts for fully 11% of enrollees, more than double the organizers' 5% target.

The ABCD Study crystallized at an inauspicious time. In May 2014, when its planners held their first meeting, the National Children's Study, an NIH effort to follow 100,000 children from the womb to age 21, was collapsing as a result of daunting logistics, overambitious objectives, and a projected cost of more than $3 billion (*Science*, 19 December 2014, p. 1441). "We were very, very aware, because of the Children's Study, that we didn't want to load up the Christmas tree with too many ornaments," recalls George Koob, NIAAA director since 2014.

By September 2016, under a tightly designed protocol dictated by the attention spans and wiggles of 9- and 10-year-old children, the ABCD Study was enrolling. The organizers are assuming 15% of the planned 11,500 enrollees will drop out over the decade, leaving the desired 10,000 participants. Some fear that may be optimistic, but Garavan is bullish. "Because it's a longitudinal study, we have to make sure the kids enjoy the experience," he says.

Garavan has succeeded with at least one recruit. "You had to drool into two vials, not spit. And it was fun," recalls Afton, who had his brain scanned at UVM last September, a day before his 10th birthday. "Eventually they are going to learn how to track if someone has depression or something else, or not, by just looking at their brain in an MRI machine. I thought that was cool. And I wanted to help."

Chya, for her part, left the Baltimore study site last month with a picture of her brain and an ABCD T-shirt. She plans to return at the same time next year. ■

ARCHAEOLOGY

Americas peopled in a single wave, ancient genome reveals

DNA from Alaskan infant suggests a long arctic sojourn

By **Michael Price**

A rare smidgen of ancient DNA has sharpened the picture of one of humanity's greatest migrations. Some 15,000 to 25,000 years ago, people wandered from Asia to North America across a now-submerged land called Beringia, which once connected Siberia and Alaska. But exactly when these ancient settlers crossed and how many migrations occurred are hotly debated. Now, the oldest full genome to be sequenced from the Americas suggests that some settlers stayed in Beringia while another group headed south and formed the population from which all living Native Americans descend.

"This is an important study that significantly narrows the subset of possibilities [for how the Americas were peopled]," says David Reich, a geneticist at Harvard Medical School in Boston. "It's very exciting."

> ***"Because they have the whole nuclear genome, you can really tell a lot about when and where this migration happened."***
>
> **Connie Mulligan**, University of Florida

The genome comes from an 11,500-year-old infant found in 2013 at the site of Upward Sun River in central Alaska's Tanana River Basin, a part of Beringia that's still above sea level. The infant, one of two from the site, belonged to a population that likely numbered in the low thousands, who hunted Beringia's abundant herds and gathered plants (*Science*, 28 February 2014, p. 961).

A team led by geneticist Eske Willerslev of the University of Copenhagen and the University of Cambridge in the United Kingdom isolated DNA from bone powder taken from the infant's skull. The researchers sequenced the DNA repeatedly to get a virtually complete copy of the genome. They compared it to that of modern Native Americans, as well as to other ancient and living people across Eurasia and the Americas. By looking at genetic similarities and estimating how long it would take for key mutations to pop up, the researchers assembled a family tree with rough dates.

The infant's group was most closely related to modern Native Americans—but it wasn't a direct ancestor. Instead, it and modern Native Americans shared common ancestors who must have entered Beringia some 25,000 years ago, the researchers report this week in *Nature*. Perhaps 21,000 years ago, those ancient settlers branched into at least two groups: one that included the infant and another that gave rise to Native Americans.

That supports the idea that Asian migrants lingered in Beringia and became genetically isolated—the so-called Beringian standstill model—says anthropologist Connie Mulligan of the University of Florida in Gainesville. "Because they have the whole nuclear genome, you can really tell a lot about when and where this migration happened," she says. But Reich cautions that date estimates from a single genome are necessarily rough.

The researchers also found that the ancient Beringian infant is equally related to both the northern and southern genetic subgroups of Native Americans, implying that both descend from a single migration. The team suggests that a group headed south into North America about 20,000 years ago and only afterward split into distinct subpopulations, perhaps between 14,500 and 17,000 years ago, dates that fit with previous studies.

Why did one group linger and thrive in Beringia while another took off to explore the Americas? A search for fresh resources could have spurred the migrants, Willerslev says, but so could sheer curiosity. "There were people who were happy with what they had, and there were others who looked out at the great ice caps and wanted to see what was on the other side," he says.

That's a compelling speculation, Mulligan says. "Once they got into North America, they really high-tailed it through the continent and down into South America within just a few thousand years," she says. A cultural or genetic penchant for exploration "could help explain why they were in such a hurry." ■

Michael Price is a freelance writer in San Diego, California.

Physician-scientist Norman "Ned" Sharpless will lead the largest NIH institute.

PHOTO: DARR BEISER/NATIONAL CANCER INSTITUTE

BIOMEDICINE

Cancer institute head touts big data and basic research

NCI's new director compares progress against cancer today to early strides against infectious disease

By **Jocelyn Kaiser**

Cancer researchers had worried that President Donald Trump might choose an unconventional candidate to replace Harold Varmus as director of the National Cancer Institute (NCI) in Bethesda, Maryland. But his choice, announced in June 2017, allayed their fears. Norman "Ned" Sharpless, who was then director of the Lineberger Comprehensive Cancer Center at the University of North Carolina (UNC) in Chapel Hill, checked all the right boxes for the community: He is a physician-scientist who treats patients, he has started two biotech companies, and he runs a basic research lab focused on p16, a protein important to cell division and aging.

Sharpless, 51, who started work at NCI in October 2017, takes over from Doug Lowy, who had been acting director since Varmus's departure in March 2015. In an interview last month, Sharpless declined to lay out specific plans for the $5.7 billion institute. But he stressed three areas: big data, basic research, and translating discoveries into devices and treatments. He's also been thinking of ways to bolster the careers of young investigators, a perennial issue for NCI's parent agency, the National Institutes of Health. This interview has been edited for brevity and clarity.

Q: Why did you want to be NCI director?
A: My old boss Ron DePinho [Sharpless's postdoctoral adviser, now at MD Anderson Cancer Center in Houston, Texas], who nominated me for the job, actually called to convince me why I should consider doing it. And I sort of stopped him in mid-sentence and said, "Wait, Ron, you had me at 'NCI director.'"

I really believe it's a special time in cancer research. We have this basic biological understanding and the notion that cancer is thousands of different diseases, and that has really allowed us to speed progress. We're going to remember the cancer researchers of the day the way we talk about [Louis] Pasteur and [Robert] Koch and antibiotics.

Q: Critics of IBM's use of the Watson supercomputer to guide cancer care say it merely compiles existing knowledge without producing new insights. What do you think about big data?
A: I am 100% convinced that the area of artificial intelligence and machine learning will have a huge impact on cancer research and cancer care. [At UNC], we used Watson to organize the literature related to novel therapeutics for [our] molecular tumor board that was trying to decide what drug to give a patient based on [their tumor] mutation. When you start doing a thousand patients a year, the allocation of therapy decisions gets very hard.

Q: How can machine learning help make sense of cancer patient data?
A: The clinical data are the hard part. Genomic data are black-and-white compared to the clinical data in electronic health records. Having med students reading charts and abstracting them is just too slow, and so these tools that use natural language processing to extract the records are very useful. That's going to get us a million patients that are clinically annotated and aggregated with genomic data sets.

Q: Where should NCI be going with immunotherapy?
A: Around 6 years ago, one of the senior leaders of the immunotherapy movement was complaining to me about how NCI's portfolio for immunotherapy research was small and didn't have enough basic science or clinical trials. I don't think anyone could make that statement about the NCI portfolio today. … [But] we just don't understand cell biology well enough to make full therapeutic use of immunotherapies.

Q: Are you worried about the drastic cuts to the 2018 NIH budget that the Trump administration has proposed?
A: I am obligated to support the president's budget. I will say that the congressional commitment to [NIH] has been good. The budget has gone up significantly in the last 2 years, and the [preliminary congressional] budget for 2018 looks promising as well. I think the budgetary challenges are real. Because if you consider the burden of cancer or what it costs society, even $5.7 billion is not really enough.

Q: What are your thoughts on NIH's efforts to help young researchers?
A: One idea we've been kicking around is to give some subset of new, young investigators an extended period of R01-like funding. [R01s are NIH's standard research grants.] So instead of stopping the grant at 5 years, they would submit a slightly more significant package than a standard noncompeting renewal. And if that's approved they would get 2 years extra funding.

We realize there are intense pressures on young faculty to get data together before they can get their second grant and get tenure. I'm a little worried that young investigators are becoming demoralized. We are committed to their success.

Q: Are you planning to have a lab at NIH?
A: Most of the people who worked for me at [UNC] have now gotten their own jobs. But I have some knock-in mice that I produced in my lab that I'm trying to import to the NCI so that I can start a lab effort here. It's very important to me. It's just nice to think about science. It's nice to understand the problems of a working scientist. ■

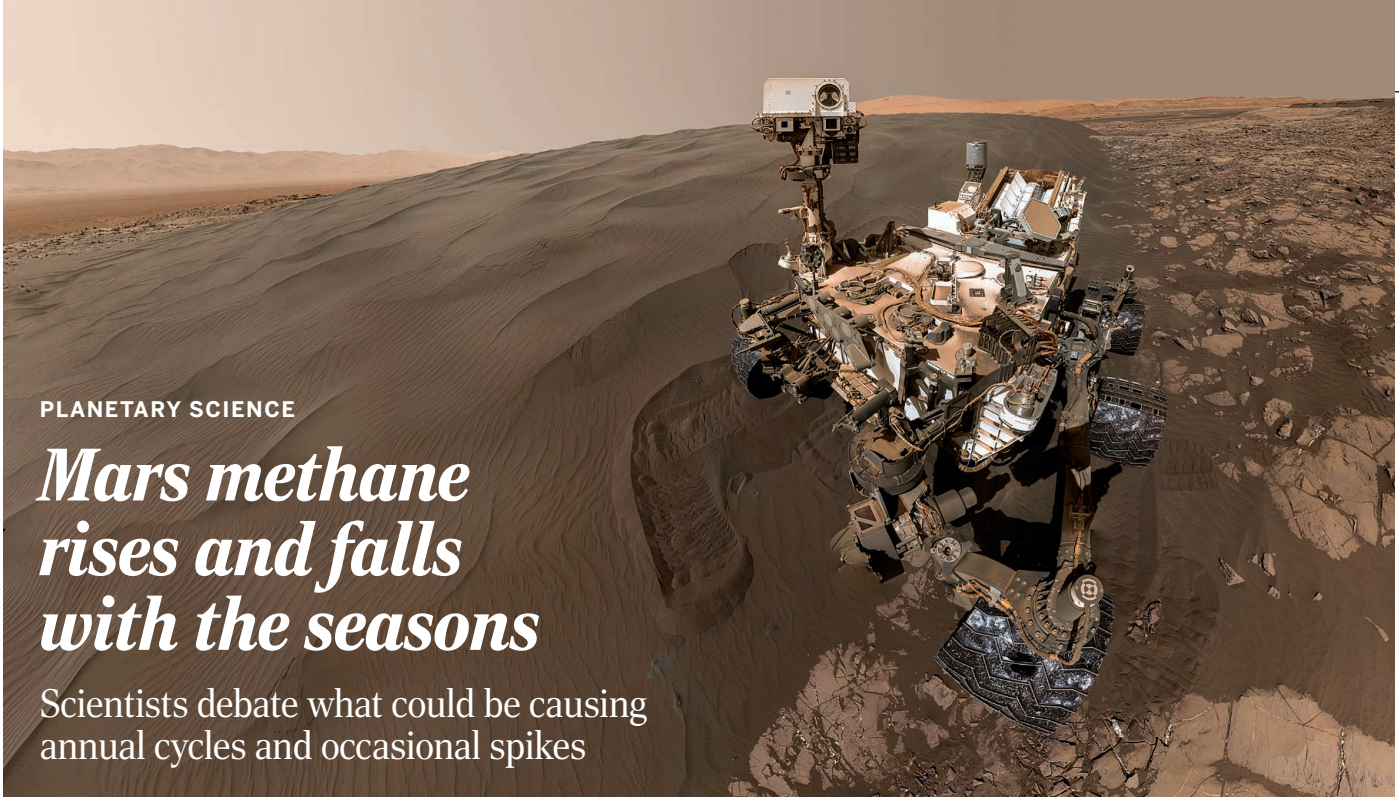

PLANETARY SCIENCE

Mars methane rises and falls with the seasons

Scientists debate what could be causing annual cycles and occasional spikes

By **Eric Hand**

From the pasture to the swamp, methane emissions on Earth are the effluvia of life. So what are whiffs of the gas doing on barren Mars? Trace detections of the stuff, alongside glimpses of larger spikes, have fueled debates about biological and nonbiological sources of the gas. Last month, at a meeting of the American Geophysical Union (AGU) in New Orleans, Louisiana, NASA scientists announced a new twist in the tale: a seasonal cycle in the abundance of martian methane, which regularly rises to a peak in late northern summer.

"The thing that's so shocking here is this large variation," said Chris Webster, who leads the methane-sensing instrument on NASA's Curiosity rover. "We're left trying to imagine how we can create this seasonal variation," says Webster, who is at the Jet Propulsion Laboratory in Pasadena, California.

It is a variation on a very faint theme. Since landing in 2012, Curiosity has on 30 occasions opened a few valves to the martian night and taken a sniff of the thin, frigid air. In a small, mirrored chamber, it shines a laser through the air sample and measures the absorption at specific wavelengths that indicate methane. At the meeting, Webster reported vanishingly small background levels of the gas: 0.4 parts per billion (ppb), compared with Earth's 1800 ppb.

Where that whiff comes from is the heart of the mystery. Microbes (including those that live in the guts of cows and sheep) are responsible for most of Earth's methane, and Mars's could conceivably come from microbes as well—either contemporary microbes or ancient ones, if the methane they produced was trapped underground. But methane can also be made in ways that have nothing to do with biology. Hydrothermal reactions with olivine-rich rocks underground can generate it, as can reactions driven by ultraviolet (UV) light striking the carbon-containing meteoroids and dust that constantly rain down on the planet from space.

Now, add to the methane puzzle the seasonal variation Curiosity has detected, with levels cycling between about 0.3 ppb and 0.7 ppb over more than two martian years.

> ***"We're left trying to imagine how we can create this seasonal variation."***
>
> **Chris Webster**, Jet Propulsion Laboratory

Some seasonality is expected in an atmosphere that is mostly carbon dioxide (CO_2), says François Forget, who models the climate of Mars at the Laboratory of Dynamical Meteorology in Paris. In the southern winter, some of that CO_2 freezes out onto the large southern polar cap, making the overall atmosphere thinner. That boosts the concentration of any residual methane, which doesn't freeze, and by the end of northern summer this methane-enriched air makes its way north to Curiosity's location, Forget says. Seasonal variations in dust storms and levels of UV light could also affect the abundance of methane, if interplanetary dust is its primary source.

But, Webster said at the meeting, the seasonal signal is some three times larger than those mechanisms could explain. Maybe the methane—whatever its source—is absorbed and released from pores in surface rocks at rates that depend on temperature, he said. Another explanation, "one that no one talks about but is in the back of everyone's mind," is biological activity, says Mike Mumma, a planetary scientist at Goddard Space Flight Center in Greenbelt, Maryland. "You'd expect life to be seasonal."

The seasonal wiggles are a mystery within a larger mystery: claims of occasional methane spikes an order of magnitude or two higher than the background. Mumma and his colleagues reported one of the largest in 2009, when they detected spectral signs of a 45-ppb methane plume through a telescope in Hawaii. Curiosity, too, has detected a handful of spikes, to about 7 ppb. For these events, Webster favors the idea of a sudden release from a deep underground source.

Other scientists are looking skyward. Marc Fries, the cosmic dust curator at Johnson Space Center in Houston, Texas, says the source of methane spikes could be the hail of tiny meteors that falls when a planet crosses a comet's orbit and sweeps up carbon-rich dust and debris shed by the comet. Fries says that as the dust particles vaporize at altitudes of tens of kilometers, the same chemical reaction that produces methane from interplanetary dust at the surface would take place more quickly, driven by the stronger UV light at high altitudes. All the claimed methane spikes over the past 2 decades occurred within about 2 weeks of a known martian meteor shower, Fries and

PHOTO: NASA/JPL-CALTECH/MSSS

During its 5-year sojourn on Mars, the Curiosity rover has repeatedly sniffed the air for methane.

his colleagues found. "It could be a cause, and it could be a coincidence," he says.

Skeptics say the atmospheric reactions may not occur quickly enough and that meteor showers don't deposit much more material than the background flux of interplanetary dust. In 2014, when Mars nearly collided with comet Siding Spring, NASA's Mars Atmosphere and Volatile Evolution Mission (MAVEN) spacecraft was watching, monitoring magnesium ions as a proxy for dust dumped in the upper atmosphere. The MAVEN team reckons the encounter put 16 tons of material into the martian atmosphere—not much more than the 3 tons of interplanetary dust estimated to fall daily, and much less than the tens of thousands of tons that Fries says are needed to make a large methane plume. "I don't see how it's possible to produce the methane abundance he needs," says Matteo Crismani, a MAVEN science team member and postdoctoral researcher at the Laboratory for Atmospheric and Space Physics at the University of Colorado in Boulder. But Fries contends that meteor showers are highly variable, and just because the Siding Spring encounter was close does not mean it was rich in dust and debris.

It happens that Fries will have a chance to test the hypothesis. On 24 January, Mars will have a close brush—less than a tenth of the Earth-moon distance—with the orbit of comet C/2007 H2 Skiff. Mumma is skeptical about Fries's idea, but he will nevertheless be watching for methane with his telescope in Hawaii in the days after the encounter. The MAVEN and Curiosity teams also plan to watch. "This is a great opportunity to test this hypothesis," Crismani says.

One spacecraft won't quite be ready to participate—even though it is best positioned overall to resolve the methane debate. In April, the European Space Agency's ExoMars Trace Gas Orbiter (TGO) will settle into its final orbit and begin science observations, mapping concentrations of methane across the planet. Atmospheric dust will probably prevent the orbiter from reaching its originally advertised sensitivity of several tens of parts per trillion, says Geronimo Villanueva, a science team member at Goddard. But he expects the TGO to approach Curiosity's sensitivity—and its ability to hunt for methane sources in space and time will be unrivaled. The "TGO will allow us to search for this molecule with new eyes," he says. ■

With additional reporting by Paul Voosen from the AGU meeting.

CREDITS: (GRAPHIC) ADAPTED FROM I. KICKBUSCH *ET AL*., *THE LANCET* 390, 898 (2017) BY V. ALTOUNIAN/*SCIENCE*; (DATA) OECD DAC AND CRE DATABASE

EUROPE

Germany steps up to the plate in global health

A country long held back by its past emerges as a new leader, but its own research output is still lagging

By **Kai Kupferschmidt**, *in Berlin*

When health ministers and other top health officials from 19 of the world's largest economies were ushered into a meeting room here in May 2017, they walked right into an unfolding international crisis. A video screen showed news reports of a mystery disease, apparently a cousin of severe acute respiratory syndrome, causing respiratory illness and death. What began as a local outbreak soon engulfed multiple countries, and the officials faced difficult choices about how to respond.

The scenario was fictitious; it began in a nation named Anycountry and was designed primarily to raise awareness about the threat of emerging diseases. But the event marked a real-world shift. It was the first-ever gathering of the G-20's health ministers, and it was organized by Germany—one of many signs that the nation's role in global health is growing rapidly.

"For a long time there was a sense that Germany wasn't contributing as much as it could," says Jeremy Farrar, director of the Wellcome Trust in London, a major private funder of medical research. But recently, the German government has embarked on several international health initiatives and has doubled its financial contributions to global health aid. As a result, the country has become a destination for major players in the field, including the Bill & Melinda Gates Foundation, headquartered in Seattle, Washington, which plans to set up an office here next year. Berlin will also host a new, international center focused on the rising threat of antimicrobial resistance (AMR), and its World Health Summit, an annual meeting here, is drawing an increasingly influential crowd.

For decades, Germany's past made it wary of taking the lead on the global stage, especially in public health, or *Volksgesundheit*, a label used by Nazi doctors to justify sterilizing and killing people with mental illness and epilepsy. German research in public health has long languished as well. Today, "Germany is getting rid of its post–World War II inhibitions to finally play a role that is commensurate with

Healthy growth

In addition to spearheading initiatives such as a new center to combat antimicrobial resistance, Germany has doubled its global health aid budget. It still lags far behind the United States and the United Kingdom, however.

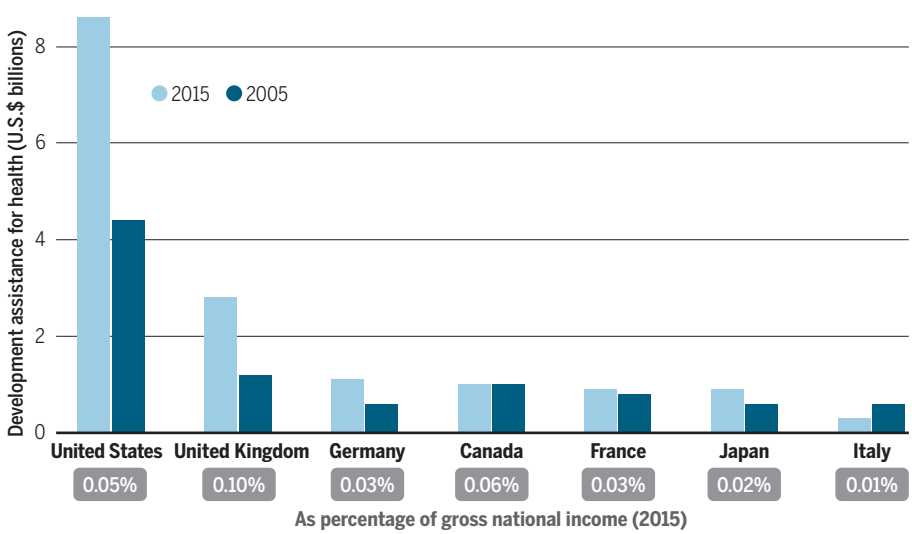

its economic weight and its intellectual leadership," says Peter Piot, director of the London School of Hygiene & Tropical Medicine (LSHTM).

German Chancellor Angela Merkel has been a driving force. She put global health at the top of the agenda as host of the G-7 summit in 2015 and at last year's gathering of the G-20. In 2015, Merkel also became the first German chancellor to speak at the World Health Assembly, the World Health Organization's (WHO's) annual member meeting. "I have no doubt that she is committed on a personal level to this," says Farrar, who has met Merkel.

Germany's spending on development assistance for health is still below WHO's goal of 0.1% of gross national income, and far behind that of the United States and the United Kingdom. But at $1.1 billion, it now surpasses spending by Japan, France, and Canada (see graphic, p. 17). The country has championed raising WHO membership dues and is the largest contributor to WHO's new Contingency Fund for Emergencies, set up in response to the West African Ebola outbreak.

German Chancellor Angela Merkel, who takes a personal interest in global health, welcomed Bill Gates in 2014.

Antimicrobial resistance is a focus because it is by nature an international problem, Hermann Gröhe, Germany's minister of health since 2013, tells *Science*. "We can make all the effort we want in Germany, but it's all for nothing if there aren't similar efforts happening around the world." The new AMR hub will be supported by the G-20, but Germany's leadership in securing their commitment was "indispensable," says Keith Klugman, who leads AMR strategy at the Gates Foundation: "I really can't overstate the importance of this hub."

Germany has also been instrumental in setting up the Coalition for Epidemic Preparedness Innovations, a public-private coalition that aims to develop vaccines for possible future pandemics. "Germany is a latecomer, but it has been catching up fast," says Ilona Kickbusch, director of The Graduate Institute's Global Health Centre in Geneva, Switzerland. (Farrar, Kickbusch, and four other experts recently agreed to serve on an international advisory board to help the German government draw up a new international health policy strategy.)

As worries grow that the United Kingdom and the United States are becoming more inward-looking, public health leaders are happy Germany is stepping up. Whether London will remain a magnet for international talent after Brexit remains to be seen, Piot says. Gates Foundation CEO Sue Desmond-Hellmann says she is "deeply concerned" about dramatic cuts in the budget of some global health programs proposed by U.S. President Donald Trump. "We're extremely positive about having wealthy nations like Germany or China emerge as government spenders in this area," she adds.

Yet Gröhe is quick to point out that Germany can't make up for a retreat by other nations. "I would warn against any expectation that Germany could somehow replace the U.S. engagement," he says. "But we can complement it." And although Merkel's Christian Democrats won the biggest share of the vote in October 2017's federal elections, attempts to form a coalition with the Liberal Democrats and the Greens fell apart in late November 2017; it's unclear what the next government will look like and whether it will continue the country's newfound leadership.

Meanwhile, Germany's own research output in global health is still lagging. Piot says that in tallies of joint authorship, LSHTM researchers "publish more with the Netherlands, Belgium, Switzerland, or France than with Germany." A 2015 assessment by the German National Academy of Sciences also noted that countries with far smaller populations such as Canada, Sweden, and the Netherlands produced more papers on public health than Germany. "Although there are excellent individuals and institutions working in public and global health in Germany," it said, "they need increased political support, improved structures, and significant research investment." Germany's next big effort in global health may well be at home. ■

ASTRONOMY

Earth-based planet finders power up

Increases in precision put Earth twins in reach

By **Daniel Clery**

When it comes to finding new worlds, NASA's Kepler spacecraft hogs the headlines, having racked up thousands of exoplanet discoveries since its launch in 2009. But before Kepler, the workhorses of exoplanet identification were ground-based instruments that measure tiny stellar wobbles caused by the gravity of an orbiting planet. They are now undergoing a quiet renaissance. The new generation of these devices may be precise enough to find a true Earth twin: a planet with the same mass as ours, orbiting a sunlike star once a year. That's something Kepler—sensitive to planet size, but not mass—can't do.

On 9 December 2017, the Extreme Precision Spectrometer (EXPRES) took its first view of the sky on the Discovery Channel Telescope in Arizona. And in October 2017, the Echelle Spectrograph for Rocky Exoplanet and Stable Spectroscopic Observations (ESPRESSO) began operating at the European Southern Observatory's (ESO's) Very Large Telescope in Chile. Nearly two dozen other instruments are either under construction or have recently begun service. "It's now clear that exoplanets are a major part of astronomy," says astronomer Jason Wright of Pennsylvania State University in State College. "So every major observatory needs a high-resolution spectrograph."

Such spectrographs spread starlight out into its array of spectral colors, which contains dark lines at wavelengths where gases in the star's atmosphere absorb light. Astronomers then look for tiny oscillating Doppler shifts in these lines over time, caused by planetary tugging.

The technique works best for a massive planet orbiting close to its star, because its gravitational tug will be stronger. As a result, early discoveries—such as the first exoplanet to be found, in 1995—were usually "hot Jupiters," giant planets in tight

The Discovery Channel Telescope hunts for exoplanets by sensing the stellar wobbles they cause.

PHOTO: JEREMY PEREZ

orbits. Then came the High Accuracy Radial velocity Planet Searcher (HARPS) at ESO's La Silla Observatory in Chile in 2003, a second-generation spectrograph that enabled astronomers to find smaller planets in wider orbits. (It has spotted about 130 to date.)

In recent years, however, a new "transit" technique, led by Kepler, began to dominate. Kepler stared at 145,000 stars in one part of the sky and looked for dips in stellar brightness when a planet passed in front. Although Kepler has been prolific, identifying thousands of exoplanets and gauging their sizes, the planets and their stars are mostly too far away for ground-based spectrographs to determine their masses. Over the coming year, the launch of Kepler's successor, the Transiting Exoplanet Survey Satellite (TESS), along with Europe's Characterising Exoplanets Satellite (CHEOPS), will change all that. They will scour the sky for transits of nearby bright stars—perfect for ground-based follow-up. "To understand them we have to know their mass, that's absolutely fundamental," says René Doyon of the University of Montreal in Canada.

The new spectrographs should be able to weigh many of the planets found by TESS and CHEOPS. Astronomers boosted the instruments' precision in part by isolating them from mechanical and thermal noise—mounting them inside vacuum vessels that are separated from the telescope and piping in light through optical fibers. They also improved the reference spectrum against which the slow shifts in the spectral lines are gauged.

Instruments such as HARPS rely on reference spectra produced by a thorium-argon lamps. But these produce a jumble of spectral lines of varying brightness. The new wave of spectrographs, including ESPRESSO and EXPRES, instead use laser frequency combs, which duplicate a single spectral line from a laser to form an ultra-precise reference grid, with lines of equal brightness spaced at regular intervals.

> ***"To understand [exoplanets] we have to know their mass, that's absolutely fundamental."***
>
> **René Doyon**, University of Montreal

With these improvements, says lead scientist Francesco Pepe of the University of Geneva in Switzerland, ESPRESSO aims to measure stellar movements as slow as 10 centimeters per second (roughly the speed of a giant tortoise). That would be a factor of 10 better than HARPS, and is exactly the motion expected to be caused by an Earth twin in an Earth-size orbit around a sunlike star.

At this sort of precision, pulsing gases in the star's atmosphere can swamp the signal of any wobble. With some of the new spectrographs, researchers hope to disentangle the wobble from the noise by comparing spectral shifts across a range of wavelengths. But Pepe expects the noise to limit ESPRESSO to planets that are about three or four times as heavy as Earth. Only if the star is much less massive and more susceptible to a planet's tug might ESPRESSO see Earth-size planets.

Other spectrographs aim for increased sensitivity to small planets by focusing on some of the smallest stars: red dwarfs. Red dwarfs emit most of their light in the infrared. Yet Earth's atmosphere allows only a narrow range of near-infrared wavelengths to reach the ground, posing a challenge for instrument builders. "There is a big push to develop instruments," says Doyon, who leads a team building the Near-InfraRed Planet Searcher to work alongside HARPS on ESO's 3.6-meter telescope in Chile.

The new instruments could even enhance transit studies. Besides searching for the spectral wobbles, they might see additional spectral lines caused by starlight passing through the atmosphere of a transiting planet. Transit spectroscopy with existing instruments has already revealed gases such as water and carbon dioxide in exoplanet atmospheres, and astronomers are now using it to look for signs of life (*Science*, 3 November 2017, p. 578). If the new spectrographs can characterize planets as well as find them, the renaissance could become a revolution. ■

Halabja, 17 March 1988: Iraq attacked its own citizens with nerve agents. During its war with Iran, enemy soldiers and civilians were frequent targets.

CHEMICAL MARTYRS

Three decades after Iraq unleashed chemical weapons on Iran, scientists there are unraveling the long-term effects

By **Richard Stone**, *in Tehran*

On a chilly morning in September 1987, in the waning days of the Iran-Iraq War, an 18-year-old Iranian soldier named Seyed Naser Emadi drove from a battlefield in northwestern Iran to a hospital in Nagadeh, a city a couple hours away. Crammed in the back of his Land Rover were four soldiers, moaning, vomiting, and coughing. "I'll never forget the sound of their breathing," Emadi says. "It was rattling, raspy." The terrified young men did not know what was happening, and Emadi had no idea how to help them.

They complained about the cold, so Emadi rolled up his window. The air in the vehicle became stifling, and a strong chemical odor wafted from the men's uniforms. Emadi grew nauseous and dizzy, but he made it to the hospital. There, he tried to rouse the nearest victim, whose face and hands had large blisters. The young man would not wake up. As Emadi and a hospital aide carried the victim out of the vehicle, a blister on the man's arm burst, and fluid splattered on the back of Emadi's hand. A couple hours later, he felt a burning sensation and his own hand began to blister.

The experience set Emadi on the path to becoming a medical researcher. (He is now a dermatologist at Tehran University of Medical Sciences and a volunteer with Doctors Without Borders.) It also highlighted one of the cruelest practices in the 1980–88 conflict, which also featured child soldiers and trench warfare. For the first time ever on a battlefield, nerve agents including sarin and tabun were unleashed by Iraqi forces. "These are the most toxic chemical warfare agents ever developed," says Jonathan Newmark, a neurologist in Burke, Virginia, who has helped develop countermeasures against such weapons at the U.S. Army Medical Research Institute of Chemical Defense (USAMRICD) in Edgewood, Maryland, and other agencies. And on scores of occasions, Iraq shelled soldiers and villagers with sulfur mustard—the chemical that afflicted Emadi and his passengers.

After the war, Iraq—pressured to own up to the attacks—acknowledged that it had "consumed" 1800 tons of mustard, 600 tons of sarin, and 140 tons of tabun. All told, according to Iran's Foundation of Martyrs and Veterans Affairs (FMVA), the chemical onslaught killed nearly 5000 Iranians and sickened more than 100,000. That doesn't include Iraqi victims: In March 1988, Iraq's forces attacked its own citizens with mustard and nerve agents in Halabja, killing as many as 5000 and wounding 7000.

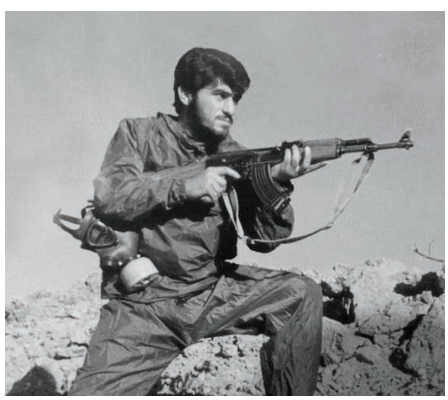

Seyed Naser Emadi as a teenage soldier in the Iran-Iraq War, where he witnessed chemical attacks, and at a meeting of survivors in Tehran last October.

PHOTOS: (TOP TO BOTOM) SEYED NASSER EMADI; EBRAHIM MIRMALEK; (OPPOSITE PAGE) SAEED SADEGHI/COURTESY ABBAS FOROUTAN

Sulfur mustard, a family of compounds first used in World War I, left the deepest and most visible scars on survivors of the war. Three decades later, about 56,000 Iranians are coping with lingering health effects from the blistering agent, ranging from skin lesions and failing corneas to chronic obstructive lung disease and possibly cancer, says Tooba Ghazanfari, an immunologist at Shahed University here.

The scale of the atrocities means that Iran has a unique opportunity to study the long-term effects of chemical weapons. Ghazanfari is leading an effort at a dozen research centers across Iran to uncover how wartime mustard exposures wreaked molecular mayhem that, decades later, triggers illnesses and death. "I'm pretty amazed about the scale of exposures and how many people have been followed," says neuroscientist David Jett, director of the Countermeasures Against Chemical Threats (CounterACT) Program at the U.S. National Institutes of Health in Bethesda, Maryland, which is spearheading R&D on several promising methods of neutralizing such agents (see sidebar, p. 23).

The data, some of which are beginning to appear in Western journals, have unavoidable limitations. The Iranian researchers can only estimate the doses that victims absorbed, and complicating the picture is the fact that Iraqi forces sometimes attacked with mustard and nerve agents simultaneously. "That makes it really difficult to determine what's going on," says James Madsen, a physician and lead clinical consultant in USAMRICD's Chemical Casualty Care Division. Still, U.S. researchers say the Iranian findings are pointing to new molecular targets for treating mustard's long-term effects.

So far, Iran has not undertaken a similar study of nerve agent survivors, who also number in the thousands. Based on Japanese victims of sarin attacks by the Aum Shinrikyo doomsday cult in the mid-1990s and U.S. soldiers possibly exposed to sa-

rin in Iraq, researchers suspect that nerve agents leave a legacy of neurological damage. But chemical weapons experts have struggled to link sarin to specific chronic symptoms; they are hoping for some clarity from a U.S. review that is about to be released. And Iranian researchers say they may start their own probe of nerve agents' long-term health effects. "We want to get the knowledge out," says Mohammad-Reza Soroush, a physician here at the Janbazan Medical and Engineering Research Center.

Ali Reza Yazdanpanah holds up a photo of himself after he was exposed to sulfur mustard during the Iran-Iraq War. Now a docent at the Tehran Peace Museum, he calls the repeated use of chemical weapons against his nation "Iran's Hiroshima."

WITH HIS BEARISH FRAME and thick black beard, Ali Cherchi would be an imposing figure—if he weren't propped up in a hospital bed with an oxygen tube in his nose and an intravenous line plying him with antibiotics. His infection-riddled lungs are giving out.

Like many teenage boys filled with patriotic fervor during the war, Cherchi lied about his age, saying he was 18 instead of 17 so he could enlist in the army. One day in 1986, near the Persian Gulf in southern Iran, the Iraqis shelled his 200-strong platoon with mustard and tabun. Many of the young men had beards, so their gas masks did not fit tightly. "I felt like I was suffocating," Cherchi says. Only a few dozen survived the attack, and since then most of the rest have died. "I'm the champion for having lasted so long," he says with an ironic laugh.

For years, Cherchi indeed considered himself fortunate: He studied law, married, and had children. But now, a short stroll can leave him gasping for breath. Lung infections land him for weeks at a stretch here at Sasan Hospital, Iran's premier facility for chemical weapons victims, which treats as many as 150 such patients on any given day. As Cherchi tells his life story in a hospital ward, his confident voice falters and, eyes widening, he reaches for an inhaler. "Chemical weapons are not fair," he says.

An old scourge ruined Cherchi's lungs. Called mustard because of its odor and the enormous yellowish blisters, or bullae, that it forms on the skin, bis(2-chloroethyl) sulfide—the primary member of a family of noxious compounds—debuted on the battlefield in July 1917, when Germany used it against U.K. and Canadian soldiers near Ypres, Belgium. After a mustard-filled artillery shell detonates, the chemical is dispersed as fine droplets that settle to the ground. In hot and dry climates, mustard can vaporize and is more likely to be inhaled. A mere 7 grams—a teaspoonful—is a lethal dose, Madsen says.

How the mustards produce their acute effects is well known. The oily liquid dissolves readily in fat, allowing it to penetrate skin. Inside cells, the chemical corrupts DNA and proteins. Recovery from the tissue damage can take months, and some World War I mustard survivors succumbed years later to respiratory failure.

Countries stockpiled sulfur mustard during World War II, but it saw limited use in battle. However, thousands of workers in a weapons factory on Ōkunoshima, an island in Japan, were exposed to mustard on the job. Studies flagged an elevated lung cancer risk, but failed to shed light on the mechanism of sulfur mustard's long-term effects, says pharmacologist Jeffrey Laskin, who directs a CounterACT center on chemical weapons countermeasures at Rutgers University's Robert Wood Johnson Medical School in Piscataway, New Jersey.

Iranian scientists are seeking answers. A decade ago, Ghazanfari and colleagues launched the Sardasht-Iran cohort study, named after a town in the northwest part of the country that was the site of one of the war's more reprehensible acts.

On 28 June 1987, Iraqi aircraft dropped four 250-kilogram bombs filled with mustard on residential areas of Sardasht. "It was a completely innocent city," says Mohammad-Reza Vaez Mahdavi, a Shahed University physiologist who studies the survivors. Records show that 8025 of the 12,000-odd residents were exposed. A few dozen—mostly children and elderly—died within hours or days. About 1500 people suffered moderate to severe symptoms, and at least 100 have since succumbed to respiratory failure, Ghazanfari says.

With funding from FMVA, Ghazanfari's team is tracking the health of 850 male victims, now aged 30 to 70. Most still reside in Sardasht. For a control group, the scientists recruited 150 men of equivalent age in Rabat, a village 15 kilometers from Sardasht. During the war, Rabat was shelled often—but never with chemical weapons. "Both populations endured a lot of stress," Ghazanfari says. In principle, that allows her team to zero in on illnesses in Sardasht that can't be chalked up to stress or factors such as diet and economic status, which are similar in Sardasht and Rabat.

The Sardasht survivors have much higher rates of eye and skin disorders. A few have also developed cutaneous T-cell lymphoma at the site of old mustard burns. Emadi says the uncommon skin cancer may also explain mysterious lesions that doctors in the early 20th century noted in World War I mustard victims. But he says that benign skin lesions are far more common in the victims: patches that lack sweat glands or the ability to secrete sebum, resulting in intensely itchy, dry skin that's susceptible to infection.

PHOTO: EBRAHIM MIRMALEK

How to defeat a nerve agent

Even 3 decades later, Seyed Naser Emadi's first encounter with nerve agents haunts him. In 1987, as a soldier fighting for Iran in its war with Iraq, he came across a hillside strewn with comrades killed by an Iraqi nerve agent, perhaps tabun or sarin. Unable to breathe, the victims had clawed at their necks to try to open a hole in their throats, recalls Emadi, now a dermatologist in Tehran. In fact, their windpipes were clear; the nerve agent had shut down control of breathing in the central nervous system. They "had no choice except death," he says.

The long-term effects of nerve agents remain uncertain (see main story, p. 21), but with the right antidotes, these poisons need not be an immediate death sentence. A few years after Emadi's experience, U.S. soldiers in 1991's Gulf War carried autoinjectors filled with drugs that—in principle—would keep them breathing and protect them from seizures if Iraqi forces again unleashed nerve agents. They never did, most historians agree, but the threat remains real today, as chemical attacks in Syria's ongoing civil war make clear. It is spurring urgent efforts to find better countermeasures, with several promising compounds in the pipeline.

First synthesized by German chemists on the eve of World War II, nerve agents kill by binding to acetylcholinesterase (AChE), an enzyme that dismantles the neurotransmitter acetylcholine when it is released into synapses. One of the most efficient enzymes known, a single AChE molecule can hydrolyze 600,000 acetylcholine molecules per minute, says Palmer Taylor, a pharmacologist at the University of California, San Diego.

Nerve agents slot right into AChE's active center, a narrow gorge. Once one nestles there and forms a covalent bond with a serine group, AChE "can't spit it out," says James Madsen of the U.S. Army Medical Research Institute of Chemical Defense (USAMRICD) in Edgewood, Maryland. As acetylcholine builds up in the synapses, victims may develop chorea and dance ghoulishly before collapsing and writhing in seizures. Without medical intervention, the brain stops sending signals to the muscles that control respiration and maintain blood pressure: Victims drift into a coma and will probably stop breathing. Milligram amounts of nerve agents are enough to kill.

For defense against seizures, U.S. soldiers carry an anticonvulsant. Diazepam has been the treatment of choice, but the U.S. National Institutes of Health (NIH) in Bethesda, Maryland, and the U.S. Department of Defense have thrown their weight behind a faster-acting compound, midazolam. "We think it's going to be a much better drug in mass casualty situations," NIH neuroscientist David Jett says.

Other remedies take aim at the cause of the symptoms: excess acetylcholine. Atropine, a compound derived from the belladonna plant, blocks acetylcholine receptors and was used to treat nerve agent victims in the Iran-Iraq War. But it can't prevent nerve agent molecules that do latch onto AChE from forming an irreversible bond with the enzyme, a process measured by the nerve agent's "aging" time. Sarin's aging time is about 5 hours. Soman, a less known but much-feared nerve agent, ages AChE in just 2 minutes.

Given only atropine, nerve agent survivors need weeks for their bodies to regenerate AChE. That's why victims are also given—as soon as possible after exposure—what Madsen calls the "true antidote" for nerve agent poisoning: oximes. Like a molecular crowbar, these chemicals jimmy the nerve agent off AChE before the complex ages.

In the United States, the only oxime approved for use against nerve agents is 2-pralidoxime chloride, or 2-PAM. But because 2-PAM is positively charged, little if any crosses the blood-brain barrier, Taylor says. That's a serious drawback, because nerve agents exert their most destructive effects in the brain.

In 2001, Taylor teamed up with K. Barry Sharpless, a chemist at the Scripps Research Institute in San Diego, to create oximes that lose protons to become a neutral species; the compounds were screened for those that, once inside the brain, can regain a positive charge, which is crucial for the molecular jimmying to work. Taylor's team has tested its front-runner in mice and in macaques exposed to sarin, and in August 2017 reported that it rapidly reversed symptoms.

A group led by Carlos Valdez, a chemist at the Lawrence Livermore National Laboratory in Livermore, California, has also developed a potent neutral oxime that readily enters the brain of guinea pigs. And Janice Chambers, a biologist at Mississippi State University in Starkville, together with her late husband, Howard Chambers, created a novel oxime with a fat-loving group that should help it traverse the blood-brain barrier. It alleviated symptoms in rats exposed to nerve agent surrogates and is undergoing further testing.

The likeliest nerve agent to be used in future attacks, defense experts say, is sarin. It's as volatile as water, disperses widely in the air, and doesn't linger, so attacking troops could enter a battlefield soon after its release. But soman, too, is a formidable threat. It evaporates only a fifth as quickly as sarin and therefore persists longer in the environment. Soman's tactical value "would be to deny the use of key terrain" by contaminating it, says Jonathan Newmark, a neurologist formerly with USAMRICD.

Soman's lightning-fast aging time means that oximes won't work against it. During the Gulf War, soldiers deemed at a risk of exposure out in the field proactively took pyridostigmine bromide, a drug used to treat a neuromuscular disorder called myasthenia gravis. It lodges temporarily in the AChE gorge, thwarting nerve agent binding. A countermeasure that has to be taken before exposure has obvious limitations: If terrorists were to get their hands on soman, they would almost certainly give no warning. —*Richard Stone*

A deadly grasp

Nerve agents bind to acetylcholinesterase (AChE), an enzyme that controls levels of the neurotransmitter acetylcholine. Each agent's "aging time," listed here, indicates how long it takes for the bond to become irreversible.

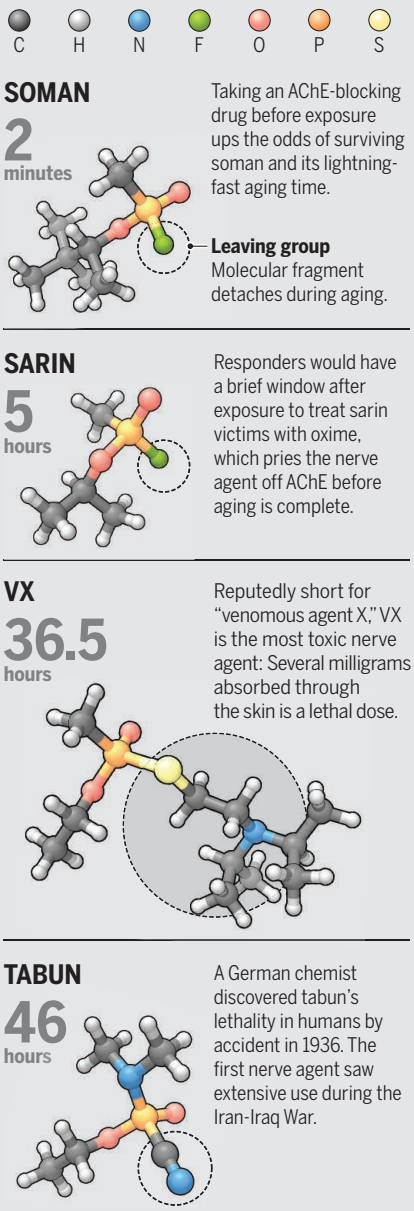

GRAPHIC: K. SUTLIFF/*SCIENCE*

IT'S IN THE LUNGS where mustard wreaks the most havoc. "Many soldiers on the battlefield don't have symptoms, but years later they come to us with problems," says Mostafa Ghanei, a physician at Baqiyatallah University of Medical Sciences here who consults for the Organisation for the Prohibition of Chemical Weapons (OPCW) in The Hague, Netherlands. Mustard creates what he calls a "unique pathology": peribronchial fibrosis—a thickening in tissues surrounding the bronchi—coupled with an airway obstruction called bronchiolitis obliterans.

To get at the roots of these symptoms, the Iranian team is probing a complex cascade of biochemical perturbations that persists in mustard survivors. They have detected, for example, revved up signaling molecules involved in inflammation, such as tumor necrosis factor α (TNFα) and other cytokines; skewed populations of natural killer cells and other immune cells; imbalances in the protein-destroying enzymes called proteases; and a shortening of the telomeres, the "end caps" on chromosomes, which indicates prematurely aged cells.

"They're doing a really good job documenting what's going on," Laskin says. But why the cellular dysfunction occurs decades after exposure is still a puzzle, he adds.

DNA methylation and other epigenetic alterations—chemical changes to DNA that can alter a gene's expression without affecting its protein-coding sequence—may underlie some of the lasting biochemical havoc, Ghanei says. He and colleagues have found evidence, for example, that methylation of tumor suppressor genes may inactivate them and help explain the development of peribronchial fibrosis as well as slightly elevated rates of certain cancers, in particular blood cancers.

In the past, Ghanei says, mustard victims with chronic symptoms were given standard treatments for chronic pulmonary disorders such as asthma: corticosteroids to tamp down inflammation and β2-agonists for smooth muscle relaxation. He and his colleagues now view oxidative stress as a prime target, because levels of an important antioxidant and an enzyme that scavenges destructive free radicals are suppressed in mustard victims. Iranian doctors now treat chronic mustard patients with antioxidants such as N-acetylcysteine, which alleviates the frequency and severity of bronchiolitis attacks, Ghanei has found.

Researchers in the United States are exploring other potential treatments. Drugs that neutralize TNFα might help, Laskin says. Another promising lead came when pediatric pulmonologist Livia Veress of the University of Colorado in Denver and colleagues zeroed in on fibrin clots in rats exposed to mustard. When she dissected the animals, she pulled out of their lungs white clots called casts that looked like "tree branches," she says. "I realized I'd seen that before"—in children with plastic bronchitis, a rare complication of surgery to repair congenital heart defects. Veress tested a clot-busting drug, tissue plasminogen activator (tPA), in rats exposed to normally lethal mustard doses—they all survived. Her team has since given tPA to seven children with plastic bronchitis, which normally has a mortality rate of up to 60%. "These are really sick kids," she says. All survived; other hospitals have treated 22 children, all of whom recovered, too. "It's pretty darn cool," Veress says. Her team is working toward U.S. Food and Drug Administration (FDA) approval for tPA's use for plastic bronchitis and next month, they will start testing the drug in pigs to further demonstrate its potential as a sulfur mustard treatment.

Those prospects, although tantalizing, are still on the horizon, and mustard remains a grave concern: In March 2016, the Islamic State group shelled a village in Iraq near Kirkuk with rockets filled with mustard. "It is just as much of a threat now as it was in the Iran-Iraq War," Madsen says.

THAT IS EQUALLY TRUE for the nerve agents, which many nations still stockpile and which were used as recently as last April against civilians and rebel soldiers in Syria.

Syed Abbas Foroutan remembers their grim debut. In March 1984, he was a young army doctor running a unit for treating mustard victims when some soldiers with unusual symptoms were brought in. They were coughing and short of breath, and some were vomiting and drifting in and out of consciousness. It was clear to the doctors that they weren't dealing with mustard. "We could only say it was not this, not that," Foroutan says—until he found a symptom common to all the victims: "Their pupils were constricted to pinholes."

That pointed to a nerve agent. Such weapons form a covalent bond to and inactivate acetylcholinesterase (AChE), an enzyme that breaks down acetylcholine in synapses, thereby regulating levels of the neurotransmitter. A few days later, comatose victims started arriving to the clinic. Foroutan checked their AChE levels—they were near zero. The clincher was that the ill soldiers responded to atropine, which binds to and blocks acetylcholine receptors, reducing the effects of excess levels of the neurotransmitter. That realization was the beginning of a grave challenge for a young doctor fresh out of medical school, says Newmark, who has studied Foroutan's experiences. "He was the

Weapons in waiting

On the night of 26 October 2002, Russian special forces raided the Dubrovka Theater in Moscow, where terrorists were holding several hundred hostages. They had pumped a narcotic aerosol into the hall, aiming to incapacitate the terrorists. But the vapor was so potent that many hostages lapsed into a coma, and 124 of them died. In a nifty bit of detective work, the Defence Science and Technology Laboratory in Porton Down, U.K., analyzed clothing and urine from three survivors and revealed in 2012 that the narcotic was a combination of two fentanyl derivatives, carfentanil and remifentanil, both far more powerful than morphine.

The botched raid marked the debut of a new chemical weapon, one of many that worry experts. The U.S. Department of Homeland Security has a list of about 100 chemicals that pose a serious risk of being weaponized. Some were tested on animals decades ago, as the United States and other nations raced to acquire new chemical arms. Others are natural toxins that have long entranced weaponeers but are hard to disperse: tetrodotoxin from puffer fish, for example, and botulinum toxin, one of the most poisonous known compounds. (Sarin's lethal dose in mice is 100 micrograms per kilogram; botulinum toxin's is 0.001 micrograms per kilogram.) These days, the huge availability of synthetic opioids "is worrying a lot of folks," says David Jett, a neuroscientist at the U.S. National Institutes of Health (NIH) in Bethesda, Maryland.

The potential threats are spurring a search for new countermeasures. NIH is backing studies on whether opioid overdose therapies such as naloxone could be used if opioids are ever weaponized again. But Jett notes that "it's an arduous task to develop an antidote for every single threat agent." Instead, NIH has categorized chemicals of concern according to their toxidrome, or the broad set of symptoms they trigger. (Nerve agents, for example, have their own toxidrome, as do blistering agents such as sulfur mustard.) The aim, Jett says, is to develop antidotes "that work for most, if not all, chemicals in a toxidrome." —*Richard Stone*

world's first physician to care for battlefield nerve agent casualties."

Undeterred by charges that it was engaging in a war crime, Iraq repeatedly shelled Iranian forces with tabun, sarin, and a binary form of the agent, cyclosarin. As Iraqi chemists learned to synthesize nerve agents with fewer contaminants and the military became more adroit at delivering them, the attacks were deadlier. Some casualties went "from fully functioning to seizing and comatose in seconds," Newmark says. Emadi, who witnessed such deaths, calls the victims "chemical martyrs."

To cope with the more potent threat, Foroutan pumped afflicted patients with massive doses of atropine—up to 10 times the amount that the United States and the North Atlantic Treaty Organization advise, near the threshold where the drug itself becomes toxic. "Foroutan was doing the best he could with what he had," Madsen says.

The radical treatment paid off, Newmark says. In most nerve agent fatalities, death occurs after the agent binds to enough AChE to block signal transmission from the brain's respiratory center to the diaphragm, paralyzing the muscle that's vital for breathing. "It takes fairly high doses of atropine to get into the brain," Madsen says. "What Foroutan did was intuitive. He gave so much atropine, we think that it started to take care of the [central nervous system] effects." Newmark puts it this way: "If a soldier got a snoot full of nerve agent, he was lucky to get to Foroutan's unit."

But what happened in later years to Foroutan's patients—and to thousands of others who survived nerve agent attacks—is largely unknown. That frustrates researchers, who would like to follow up on hints that exposure takes a long-term toll.

One clue comes from an episode in the United States, during Prohibition, when doctors started seeing patients with muscle spasms, tingling and numbness in the legs, and, in some cases, paralysis. The cause turned out to be an adulterant, triorthocresyl phosphate, in a bootleg ginger liquor. That compound, like nerve agents, is an organophosphate, and the symptoms that afflicted the "Ginger Jake" drinkers—some 30,000 documented cases—are now known as organophosphate-induced delayed neurotoxicity (OPIDN). The same syndrome affected one victim of the Aum Shinrikyo cult's sarin terrorism, says Bahie Abou-Donia, a neurobiologist at Duke University in Durham, North Carolina. "It would not surprise me to see OPIDN in the Iranian survivors," Madsen says.

There's firmer evidence, he says, that nerve agents mess with the mind. Studies of the Aum Shinrikyo survivors link exposure "even at really low doses" to symptoms such as nightmares, headaches, drowsiness, confusion, memory deficits, irritability, and depression—a syndrome called organophosphorus-ester-induced chronic neurotoxicity (OPICN). In March 1991, during the Gulf War, tens of thousands of U.S. soldiers may have been exposed to low doses of sarin after the destruction of an Iraqi ammunition dump, says Abou-Donia, a sarin expert. An unknown percentage of cases of the still-controversial Gulf War Syndrome, he says, may in fact be OPICN.

Female volunteers learning to use gas masks in a Tehran mosque in May 1988. In the waning days of the war, Iraq resorted more frequently to bombarding soldiers and civilians with sulfur mustard and nerve agents.

PHOTO: KAVEH KAZEMI/GETTY IMAGES

More clarity on the long-term effects of nerve agents will come from a U.S. National Toxicology Program report on sarin. The draft review concludes that sarin's chronic effects include AChE inhibition, vision and memory problems in people, as well as nerve pathology detailed in animal studies.

The Iranian veterans could yield a more definitive picture. "Whatever comes out of Iran on this," Newmark says, "will be the best human data that exists." But so far, no one is gathering it. After the war, Foroutan became a professor—he's now at Shahid Beheshti University of Medical Sciences here—and has not tracked his former patients. And zeroing in on late nerve agent effects is not simple. "We don't have reliable information on who was exposed solely to nerve agents," says Janbazan medical researcher Batool Mousavi, because of the Iraqi practice of bombarding troops with nerve agents and mustard simultaneously or on consecutive days.

Foroutan believes that it's not too late to delve into the long-term consequences. "We need a Sardasht cohort for nerve cases," he says. It could even be an international effort, Newmark suggests, if Iran were to set up a collaboration under OPCW's auspices. "It's important to know if neuropathology and resultant long-term effects actually occur in humans," Jett adds, "before we approach the FDA for approval of a neuroprotectant drug."

In the heart of Tehran, a modest one-story building is a living memorial to Iran's chemical weapons victims. Inside the Tehran Peace Museum, exhibits recount the global history of chemical warfare. Chemical victims of the Iran-Iraq War volunteer as docents. One is named Ali Reza Yazdanpanah.

When he was 15 years old, Yazdanpanah tricked his mother into signing his enlistment papers. Several weeks later, he and 31 other young men in his regiment were exposed to mustard near Khorramshahr, a port city on the Persian Gulf, near the Iraq border. Some of the blistering agent got in his eyes. "I lost my sight for some time," he says. It came back, but he has had to endure four cornea transplantations, and is on a waiting list for a new pair of lungs. He says he has never felt completely well.

Yazdanpanah is keeping the memory alive. And as a subject in Iran's research efforts, he hopes his experience will benefit future victims of these ghoulish weapons. "The best years of my life," he says, "were stolen from me." ■

Reporting for these stories was supported by the Pulitzer Center on Crisis Reporting.

NEXTGEN VOICES

Research resolutions

We asked young scientists this question: **What is your New Year's resolution for your field? Describe one thing that your field's research community could do better in the coming year.** We received responses from scientists around the world representing a variety of fields. Excerpts of their responses are printed below. —**Jennifer Sills**

Communication and outreach

Environmental scientists should connect with people who depend on natural resources, such as farmers, fishermen, and hunters. This year, we should strive to start a dialogue, build trust, and ultimately create collaborative research projects for more sustainable use and management of natural resources.

Felicia Olmeta-Schult
Environmental and Natural Resource Sciences, Washington State University, Vancouver, WA 98686, USA. Email: folmeta@wsu.edu

In a world where fact checking is at an all-time low and the positive public perception of science is dwindling, scientists must learn to effectively communicate. Plant pathologists are in an ideal position to address this issue—they are centered between farmers, scientists, and the public. This year, it is imperative that our field works toward meaningful and targeted collaboration.

Lauren Massa Segal
Department of Plant Pathology, University of Nebraska–Lincoln, Lincoln, NE 68583, USA. Email: lsegal3@gmail.com

Forensic statisticians need to do a better job of communicating with lawyers, judges, and other practitioners. Poor communication in the forensic and legal fields can lead to miscarriages of justice. It is our responsibility to work with practitioners to improve forensic science techniques and the discussion of such techniques in the courtroom.

Sam Tyner
Center for Statistics and Applications in Forensic Evidence, Iowa State University, Ames, IA 50014, USA. Email: sctyner@iastate.edu

Earth scientists should resolve to talk more publicly about what we do know. Traditionally, scientists emphasize uncertain results that require more research. But taking this tack with the public invites confusion. Instead, we should be talking about our well-established findings. For example, we are certain that Earth's ice is melting, with substantial consequences for coastal erosion and flooding, saltwater inundation, and water security. We are also certain that human action can postpone the arrival of the most dire effects.

Twila Alexandra Moon
National Snow and Ice Data Center, University of Colorado, Boulder, CO 80309, USA. Email: twila.science@gmail.com

In the current U.S. political climate, science is under attack. Our representatives circulate falsehoods that blatantly contradict scientific literature. This year, the medical research community's

PHOTO: JOCHEN TACK/ALAMY STOCK PHOTO

A natural historian resolves to better explain the value of museum collections to the public.

engagement in politics must expand beyond matters pertaining to the NIH budget. We can begin by pressuring our representatives and making our voices heard. But to initiate the path toward systemic change, we must ultimately cultivate challengers of the political status quo from within our research communities. It is time to bring our passion from the lab bench to the podium.

Ryan Dz-Wei Chow
Yale School of Medicine, New Haven, CT 06510, USA.
Email: ryan.chow@yale.edu

My New Year's resolution for biologists: Do a better job explaining to the public why natural history museum collections are important. Natural historians are sometimes misunderstood as hunters or stamp collectors, but their collections, when curated ethically and legally, can open up a world of knowledge about our planet.

Prosanta Chakrabarty
Museum of Natural Science, Louisiana State University, Baton Rouge, LA 70803, USA.
Email: prosanta@lsu.edu

Deep sequencing and genome-editing technologies make personalized medicine, gene therapies, and transgenic livestock possible. Yet manipulation of genetic material carries a social stigma, due to ethical and ecological concerns. To overcome this stigma, the gene-editing community needs to better communicate the implications (good or bad) of our research to the public.

Martin Pacesa
Department of Biochemistry, University of Zurich, 8057 Zurich, Switzerland.
Email: m.pacesa@bioc.uzh.ch

Interdisciplinary collaboration

In 2018, I hope that human genetics researchers will increase our understanding of the biological mechanisms underlying genome-wide association study data by collaborating with computational and experimental scientists.

Anna Igorevna Podgornaia
Merck Research Labs, Boston, MA 02115, USA.
Email: anna.podgornaia@merck.com

When infectious diseases strike, serum from survivors can be administered to others to confer passive immunity. However, serum-based therapy is inefficient and expensive. Moving forward, immunologists and public health officials should strengthen their pipelines to identify such survivors and sequence their antibodies, thereby enabling mass production of the protective antibodies.

Jennifer Chen
Yale School of Medicine, New Haven, CT 06510, USA.
Email: jennifer.s.chen@yale.edu

I hope that computational biologists can take part in more multi-institutional projects that involve both computational and experimental researchers from academia and industry. Such collaboration could help us solve real-life practical problems.

Bipin Singh
School of Engineering and Technology, BML Munjal University, Gurgaon, Haryana 122413, India.
Email: bipin.singh@bmu.edu.in

For kidney disease researchers, interdisciplinary collaboration between scientists focusing on renal diseases, cell reprogramming, 3D printing, and biomechanics is urgently needed this year to push forward the development of artificial organs.

Bo Cao
Core Research Laboratory, The Second Affiliated Hospital, School of Medicine, Xi'an Jiaotong University, Xi'an Shaanxi, 710004, China.
Email: bocao@vip.qq.com

A kidney researcher hopes that collaborations will lead to artificial kidneys similar to this bladder.

Neuromorphic engineers try to create circuits and algorithms that function like the human brain. However, once a basic biological model is implemented, most efforts focus on algorithmic efficiency, which makes the system less realistic. We need more input from neuroscientists. My New Year's resolution is to create a close-knit community of engineers and scientists.

Rishi Raj Singh Sidhu
Electrical Engineering, Centre of Excellence in IC Design (VIRTUS), Nanyang Technological University, Singapore, 639798, Singapore.
Email: rishirajsidhu@gmail.com

Data sharing and analysis

In an era of next-generation sequencing and artificial intelligence processing of large amounts of biological data, the field of molecular biology should go beyond statistical power and fulfill three criteria: statistical, biological, and clinical significance. Often, statistically significant associations in the laboratory do not have significant clinical utility. We should adopt a clinical perspective that allows clinicians and scientists to harness the power of big data to improve the lives of patients.

Bryce W. Q. Tan
Department of Physiology, National University of Singapore, Singapore 117456, Singapore.
Email: brycetan03@hotmail.com

The life sciences community should resolve to generate and interpret data more responsibly. We need to dispel myths and fears surrounding data analytics, adequately train our scientific workforce, and encourage open data and protocol sharing. We need to prevent data dredging, encourage complete and transparent reporting, avoid financial and nonfinancial conflicts, and reward reproducibility as much as novelty.

Prashant Sood
MRC Centre for Medical Mycology, Institute of Medical Sciences, University of Aberdeen, Aberdeen AB25 2ZD, UK. Email: drprashantsood@gmail.com

This year, geologists should emphasize observation-driven over model-driven science. Our models may speak to physically possible hypotheses, but they often fail to be predictive.

Stuart Parker
Idaho State University, Pocatello, ID 83204, USA.
Email: parkstua@isu.edu

My New Year's resolution for psychology and neuroscience is to move beyond a "one-size-fits-all" approach to mental health treatments. We could improve treatment effectiveness by taking individual variability into account. In the next year, I hope that the field works to identify neurological, genetic, and psychological markers of who will best respond to specific interventions or combinations of interventions.

Matthew A. Scult
Department of Psychology and Neuroscience, Duke University, Durham, NC 27708, USA.
Email: matthew.scult@duke.edu

In 2018, I think my field of cancer nanotechnology could benefit from more complete reporting of experimental details, particularly nanoparticle concentrations, animal experiment details, and cell experiment details. Most publications

PHOTO: WAKE FOREST INSTITUTE FOR REGENERATIVE MEDICINE

provide minimum explanation in these areas, which can make reproducing the findings difficult.

Desiree Van Haute
Jefferson, AR 72114, USA.
Email: desireevanhaute@gmail.com

My 2018 resolution would involve a community effort by biologists to integrate data from various sources in databases, which would become available to everyone as fast as possible. Analysis of these data by research labs with diverse interests would lead to an explosion of scientific discoveries.

Nikos Konstantinides
Department of Biology, New York University, New York, NY 10003, USA. Email: nk1845@nyu.edu

I wish that the field of education research could come together to (finally) agree upon a common core. Without agreement on the foundations of learning and teaching, the field remains divided and of limited use to practitioners and decision-makers.

Beat A. Schwendimann
Berkeley, CA 94720, USA.
Email: beat.schwendimann@gmail.com

Affordable research benefits

Arsenic in rice is a huge problem in Southeast Asia. My New Year's resolution for environmental scientists is to come up with low-cost and easily applicable solutions that allow local farmers to grow safe rice crops.

Sudhakar Srivastava
Institute of Environment and Sustainable Development, Banaras Hindu University, Varanasi, Uttar Pradesh 221005, India.
Email: sudhakar.srivastava@gmail.com

At its current cost, there is no hope that next-generation sequencing will be accessible enough to affect medical diagnosis. Sequencing has become a profit-driven business. This year, biotechnology companies should take seriously the task of creating a $100 genome, a cost directly controlled by reagent pricing. A lower price tag would make personalized medicine a global possibility, give better data sets for population studies, and make academic research more feasible.

Raffaele Fiorenza
Sequencing Operations Lab, New York Genome Center, New York, NY 10013, USA.
Email: ralphie.fiorenza@gmail.com

This year, we need to discuss how we will achieve sustainable and affordable oncology with relevant stakeholders, from consumers, researchers, and clinicians to leaders in industry and government. Exploring new funding models and financial structures that continue to incentivize discovery and innovation will be critical for our continued success in treating late-stage cancer.

Ken Dutton-Regester
QIMR Berghofer Medical Research Institute, Brisbane, QLD 4006, Australia.
Email: ken.dutton-regester@qimrberghofer.edu.au

Diversity in science

My research resolution for ecology would be to ensure that those who have the chance to research biodiversity are as diverse as the communities we study. Ecologists need to do more to recognize the contributions of women and minority researchers and to break down systemic barriers to their inclusion, such as the prevalence of unpaid "voluntary" field experience positions. We study behavior and species interactions in the field; let's be as aware of our own biases.

Rachel Hale
Ocean and Earth Science, National Oceanography Centre Southampton, University of Southampton Waterfront Campus, Southampton, Hampshire SO14 3ZH, UK. Email: r.hale@soton.ac.uk

In 2018, instead of focusing on postdoc positions, physics advisers at research institutions should customize career plans for their Ph.D. candidates that take into account each individual's goals, interests, and abilities.

Emre Ozan Polat
ICFO-The Institute of Photonic Sciences, 08860 Barcelona, Spain. Email: emre-ozan.polat@icfo.es

Postdoctoral fellows are a major driving force of biomedical research, but many postdocs are undercompensated and underrecognized. Our field should remedy this by acknowledging their role as intellectually independent scientists. More invitations could be directly extended to postdocs to pen commentaries, serve as panelists, review grant proposals, and referee manuscripts. Many postdocs already assist their lab heads in review tasks; inviting them to formally serve as reviewers will be a major step toward better postdoc recognition.

Edward Lau
School of Medicine, Stanford University, Palo Alto, CA 94305, USA. Email: lau1@stanford.edu

My New Year's resolution for ecologists: Pay more attention to the science produced by women and underrepresented minorities. Ensure diversity of keynote speakers, panels, journal editors, and awards. Insist upon field excursions and labs that are supportive and inclusive so that all trainees can thrive.

Audrey L. Mayer
SFRES, Michigan Technological University, Houghton, MI 49931, USA. Email: almayer@mtu.edu

Although biology graduate programs now have a balance of men and women, the leaky pipeline persists. One challenge to increasing diversity is ongoing sexual harassment on campus, at conferences, and during field work. Such a hostile environment prevents us from creating an inclusive community. Everyone, men in particular, must step up to combat sexual harassment.

Easton R. White
University of California, Davis, Davis, CA 95616, USA.
Email: eawhite@ucdavis.edu

An environmental scientist hopes to help farmers, such as this one in Thailand, affordably grow safe rice crops.

PHOTO: EDUARDO PRIM/UNSPLASH

10.1126/science.aar7504

Genomic characteristics influence the ability of yellow warbler populations to adapt to climate change.

PHOTO: ISTOCK.COM/PAUL REEVES PHOTOGRAPHY

EVOLUTION

The genomics of climate change

A study of yellow warblers identifies genomic regions involved in climate change adaptation

By **Mark J. Fitzpatrick** *and* **Allan H. Edelsparre**

Human-induced climate change is causing rapidly changing global temperatures and extreme fluctuations in precipitation. These changes force organisms to adapt and evolve or face extinction. Understanding and predicting the evolutionary responses to climate change is critical for preserving biodiversity, but predictions are challenging because they involve interactions between adaptive plasticity (such as altered breeding times) and evolved responses (such as increased metabolism). On page 83 of this issue, Bay *et al*. (*1*) combine high-resolution genomic sequencing with population trends and global climate predictions to estimate the adaptive potential (that is, the genetic variation necessary for adaptation) of yellow warblers (see the photo) to climate change and predict future population declines. In doing so, they produce a powerful tool for estimating genomic vulnerability to climate change and locate candidate genes that are key for climate change adaptation.

Yellow warblers are migratory birds with a wide distribution across North America. They occupy a rich set of habitats that range from marshes and forests to urbanized areas. They can be found in lowlands as well as at high altitudes, such as in the Rocky Mountains in the west and the Appalachian Mountains in the east. Given their wide distribution and general abundance, recent declines of some populations have raised concerns that yellow warblers may be negatively affected by climate change (*2*).

Bay *et al.* initially obtained DNA samples from 229 birds, representing 21 populations that span the yellow warbler breeding range. They used more than 100,000 nucleotide markers [single-nucleotide polymorphisms (SNPs)] to characterize the statistical associations between current population-level genetic variation and 25 environmental variables associated with climate change. The variables included factors associated with precipitation, temperature, elevation, tree cover, and vegetation. The strongest associations between genomic and environmental variation were those related to precipitation. This makes sense, because changes in precipitation directly influence biomass, which in turn affects other factors, such as shelter and food availability. Extreme changes in precipitation remain among the most important, but least understood, consequences of rising temperatures across the globe (*3*).

By extracting information from their assembly of the yellow warbler genome, the authors assessed the adaptive potential of each population by piecing together a portrait of genomic regions that respond to climate-related changes and then searched for traces of selection in those regions. One

Integrative Behaviour and Neuroscience Group, Department of Biological Sciences, University of Toronto Scarborough, Toronto ON, M1C 1A4, Canada. Email: mark.fitzpatrick@utoronto.ca

major advantage to teasing out the adaptive potential from standing genetic variation is that it gives us the ability to ask whether such information can be used to forecast climate-related declines. By comparing the genomically determined adaptive potential of each population with local climate-related variables, Bay *et al*. were able to determine which populations have the greatest mismatch with their environment (as determined by the degree to which their genomic variation matches the environmental variation they experience), a metric they refer to as genomic vulnerability.

The most vulnerable populations largely reside along the Rocky Mountains, a region particularly affected by droughts over the past decade (*4*). The authors determined that these vulnerable populations coincide with recent population declines reported in the literature (*5*). This link between genomic vulnerability scores and realized population trends strongly suggests that genomic vulnerability accurately forecasts which populations may be at risk of declining. This allows conservation efforts to target these identified areas and populations before environmental conditions become unsustainable.

"...behavioral genes may represent 'first responders' to climate change adaptation."

The estimates of adaptive potential within species can be used to identify the traits and genes influenced by climate change. To do so, Bay *et al*. took a closer look within the important genomic regions discussed above. They found a strong association between climate (e.g., precipitation) and a SNP marker on chromosome 5, located very close to *DRD4* and *DEAF1*; these two genes were previously linked with migration and exploratory behavior in several species, including birds (*6*) and humans (*7*). Initial responses to climate change likely involve highly plastic traits like behavior, where individuals themselves can act to better match their current environmental conditions; examples include avoidance behavior, retreating or reclaiming new habitats, diet modifications, dispersal, and migration.

Although the direct involvement of *DRD4/DEAF1* needs to be established, their potential role in climate change adaptation is intriguing and raises the possibility that behavioral genes may represent "first responders" to climate change adaptation. If these adaptations involve dietary changes, dispersal, and migration, then additional candidate genes may include *Pgi* (*8*), *npr-1* (*9*), and *foraging* (*10*), all of which have been associated with food search and dispersal.

Identifying general features of evolutionary responses to climate change is a crucial, but intricate, mission. Climate-driven adaptations will necessarily involve the genome, but time- and context-dependent factors will likely influence the specific pathway that any given population takes (including extinction). Some scenarios will directly lead to the evolution of new/modified alleles, whereas other scenarios may exist without any traditional genomic responses but instead be regulated by factors such as adaptive plasticity and epigenetics. The latter is particularly interesting, because both *DRD4* (*11*) and *foraging* (*12*) can be regulated epigenetically to produce variations in behavioral tendencies that underlie food-searching and exploratory strategies within populations.

Climate change is happening and, despite growing global concern, is predicted to progress (*13*). Bay *et al*.'s study of the yellow warbler shows that, although populations can evolve in response to climate change, this response is limited by the adaptive potential and genomic vulnerability found among populations. A critical next step will be to determine how broadly these findings apply to other species and communities, especially those that are highly threatened. Time is of the essence. The widespread impact of climate change on our ecosystems and biodiversity has occurred over a relatively short time scale (about 50 years). According to the global forecasts of future climate change, the pervasive impact and strain on biodiversity will only intensify (*3*). ■

REFERENCES

1. R. A. Bay *et al.*, *Science* **359**, 83 (2018).
2. W. D. Shuford, T. Gardali, Eds., *California Bird Species of Special Concern: A Ranked Assessment of Species, Subspecies, and Distinct Populations of Birds of Immediate Conservation Concern in California* (Western Field Ornithologists, 2008), pp. 332–339.
3. K. Marvel, C. Bonfils, *Proc. Natl. Acad. Sci. U.S.A.* **110**, 19301 (2013).
4. J. Funk, S. Saunders, *Rocky Mountain Forests at Risk* (Union of Concerned Scientists and Rocky Mountain Climate Organization, 2014).
5. J. R. Sauer *et al.*, The North American Breeding Bird Survey, Results and Analysis 1966–2012, Version 02.19. 2014 (U.S. Geological Survey, 2014).
6. J. C. Mueller *et al.*, *Mol. Ecol.* **22**, 2797 (2013).
7. L. J. Matthews, P. M. Butler, *Am. J. Phys. Anthropol.* **145**, 382 (2011).
8. C. R. Haag, M. Saastamoinen, J. H. Marden, I. Hanski, *Proc. R. Soc. Lond. B* **272**, 2449 (2005).
9. A. Gloria-Soria, R. B. R. Azevedo, *Curr. Biol.* **18**, 1694 (2008).
10. A. H. Edelsparre, A. Vesterberg, J. H. Lim, M. Anwari, M. J. Fitzpatrick, *Ecol. Lett.* **17**, 333 (2014).
11. E. C. Verhulst *et al.*, *Mol. Ecol.* **25**, 1801 (2016).
12. I. Anreiter, J. M. Kramer, M. B. Sokolowski, *Proc. Natl. Acad. Sci. U.S.A.* **114**, 12518 (2017).
13. C. P. Nadeau, M. C. Urban, J. R. Bridle, *Trends Ecol. Evol.* **32**, 786 (2017).

10.1126/science.aar3920

CELL BIOLOGY

A new mitotic activity comes into focus

The ATR kinase has a role in mitosis to promote chromosome segregation

By **Joshua C. Saldivar** *and* **Karlene A. Cimprich**

During mitosis, each duplicated chromosome must be accurately attached to the microtubule spindle, which pulls the chromosomes to opposite poles of the cell, where they are segregated to daughter cells. A number of mitotic kinases orchestrate mitosis to ensure accurate segregation, including cyclin-dependent kinase 1 (CDK1), the Polo-like kinases, and the Aurora kinases (*1*). The kinase ATR (ataxia telangiectasia and Rad3-related), which is involved in DNA damage responses during interphase of the cell cycle, has also been shown to prevent chromosome segregation errors (*2*). However, this role of ATR was presumed to be an indirect effect. On page 108 of this issue, Kabeche *et al*. (*3*) unveil a mitosis-specific ATR activity that ensures proper chromosome segregation and that this activity is dependent on a specific three-stranded nucleic acid structure known as an R loop.

ATR is a master regulator of the cellular responses to DNA damage and DNA replication stress by controlling cell-cycle progression, replication origin firing, replication fork stability, and DNA repair (*4*). These functions are mediated by the kinase activity of ATR and safeguard genome integrity. Kabeche *et al*. found that ATR is localized to and active at mitotic centromeres, the chromosomal region where the microtubule spindle attaches (see the figure). Because no mitosis-specific function of ATR was previously known, this is an intriguing observation.

Microtubules of the mitotic spindle attach to kinetochores at centromeres to facilitate chromosome segregation (*5*). Given the local activation of ATR at the centromeres of mitotic chromosomes, the authors assessed chromosome segregation

Department of Chemical and Systems Biology, Stanford University School of Medicine, 318 Campus Drive, Stanford, CA 94305-5441, USA. Email: cimprich@stanford.edu

when ATR was inactivated in mitosis and observed "lagging" chromosomes in anaphase (a stage of mitosis). A lagging chromosome is observed when it is not accurately attached to the mitotic spindle as the spindle pulls chromosomes to opposite spindle poles (see the figure). Failure to properly segregate chromosomes can lead to aneuploidy (an abnormal number of chromosomes in a cell) (*5*). Importantly, mitotic inactivation of ATR resulted in aneuploidy, suggesting that the mitosis-specific activity of ATR promotes accurate chromosome segregation.

On the surface, this specific ATR activity appears counterproductive. Throughout interphase, ATR suppresses the activity of multiple CDKs, which controls DNA replication and cell-cycle progression. However, mitosis is a period of high CDK1 activity. It is unknown why ATR activation in mitosis does not suppress CDK1 activity and delay mitotic progression. One possibility is that the pathways that link the ATR pathway to CDK1 inactivation are rewired in mitosis. Alternatively, the focal activity of ATR at centromeres may spatially separate ATR and CDK1 throughout mitosis.

R loops activate ATR in mitosis

ATR activity at the centromere of mitotic chromosomes is induced by R loops and requires Aurora A and CENP-F. ATR phosphorylates CHK1, which phosphorylates Aurora B, which promotes kinetochore-microtubule attachments and accurate chromosome separation.

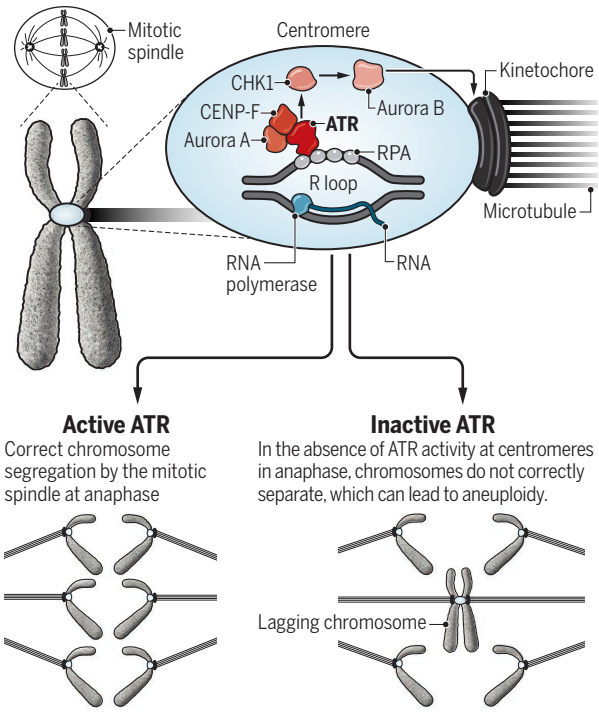

Kabeche *et al.* investigated how ATR is activated in mitosis at centromeres. In interphase, ATR is activated by specific DNA structures that form during DNA replication (S phase) or at DNA damage sites. Minimally, these structures consist of single-stranded DNA (ssDNA) and a 5′-ended ssDNA–double-stranded DNA junction (*4*). Because mitotic chromosomes are highly condensed and residual replication structures are processed by mitotic nucleases, it is unlikely that these structures would be abundant and specific to centromeres to activate ATR. Moreover, in S phase, centromeric repeat regions form structures that attenuate ATR activation (*6*).

Kabeche *et al.* speculated that R loops may be the centromere-specific ATR-activating structures. R loops are RNA-DNA hybrids with a displaced ssDNA loop [which is bound by replication protein A (RPA)] that could serve as a platform for ATR recruitment. Indeed, they showed that mitotic centromeres are enriched for RNA-DNA hybrids. Disruption of these hybrids prevented ATR recruitment and kinase activity at centromeres and increased the frequency of lagging chromosomes. The recruitment of ATR to centromeric R loops is complex because it depends on Aurora A and centromere protein F (CENP-F), which may bring ATR to the centromere. Once recruited, exactly how ATR is activated at centromeres remains unclear. In other contexts, ssDNA is only sufficient to recruit ATR to chromatin; activation requires a second factor to stimulate kinase activity. Understanding ATR activation at R loops will be an interesting area for future investigation.

How does centromeric ATR promote chromosome segregation? Inhibition of ATR kinase activity decreased Aurora B activity at centromeres, where Aurora B normally ensures that sister kinetochores are attached to microtubules from opposite spindle poles. Loss of this Aurora B function leads to lagging chromosomes (*7*), which is in agreement with a mitotic role of ATR to increase Aurora B activity. Kabeche *et al.* also showed that the main downstream effector of ATR, checkpoint kinase 1 (CHK1), is needed for full activation of Aurora B, which is consistent with a previous study (*8*).

One of the intriguing findings is the involvement of R loops in ATR–Aurora B signaling. R loops can be harmful and induce DNA breaks and genome instability (*9*), but they are also known to have important regulatory roles in transcription (*10*). Kabeche *et al.* show that in the context of mitotic centromeres, R loops serve as a signaling hub for the ATR pathway and are critical for chromosome stability. Whether other processes and signaling pathways intersect at and depend on R loops remains to be explored.

How R loops form at centromeres during mitosis is also a mystery. Although most transcription is downregulated in mitosis, there is active transcription at centromeres (*11*, *12*). Whether this transcription leads to R loop formation is unclear. In fact, previous work concluded that single-stranded long noncoding RNAs (lncRNAs) are formed and required for the centromeric localization of the chromosomal passenger complex, which includes Aurora B, potentiation of Aurora B kinase activity, and accurate chromosome segregation (*12*). The functional similarities of R loops and lncRNAs are striking and raise numerous questions, including whether these nucleic acids have distinct functions at centromeres or whether they are somehow related.

Kabeche *et al.* conclude that centromeric R loops serve as a focus for mitotic ATR signaling, promoting full activation of Aurora B and ensuring accurate chromosome segregation. This finding may prompt consideration of ATR as a peer of the classic mitotic kinases. Many aspects of this story are surprising, not least being why cells need such a complex response involving transcription, R loop formation, ATR recruitment, and consequent CHK1 phosphorylation to induce a moderate increase in Aurora B activity. Perhaps it allows the spatiotemporal modulation of Aurora B, preventing excessive Aurora B activity away from centromeres? It will also be interesting to learn whether centromeric R loops signal to proteins other than ATR and whether centromeric ATR has other downstream targets. Undoubtedly, Kabeche *et al.* will motivate new investigations into the importance of ATR during mitosis. ■

REFERENCES AND NOTES

1. E. A. Nigg, *Nat. Rev. Mol. Cell Biol.* **2**, 21 (2001).
2. J. K. Eykelenboom *et al.*, *Cell Rep.* **5**, 1095 (2013).
3. L. Kabeche *et al.*, *Science* **359**, 108 (2018).
4. J. C. Saldivar *et al.*, *Nat. Rev. Mol. Cell Biol.* **18**, 622 (2017).
5. D. Cimini, F. Degrassi, *Trends Cell Biol.* **15**, 442 (2005).
6. A. Aze *et al.*, *Nat. Cell Biol.* **18**, 684 (2016).
7. M. A. Lampson, I. M. Cheeseman, *Trends Cell Biol.* **21**, 133 (2011).
8. E. Petsalaki *et al.*, *J. Cell Biol.* **195**, 449 (2011).
9. J. Sollier, K. A. Cimprich, *Trends Cell Biol.* **25**, 514 (2015).
10. J. M. Santos-Pereira, A. Aguilera, *Nat. Rev. Genet.* **16**, 583 (2015).
11. F. Ferri *et al.*, *Nucleic Acids Res.* **37**, 5071 (2009).
12. M. D. Blower, *Cell Rep.* **15**, 1624 (2016).

ACKNOWLEDGMENTS

K.A.C. is supported by grants from the NIH (ES016486 and GM119334). J.C.S. is supported by a Postdoctoral Fellowship (PF-15-165-01-DMC) from the American Cancer Society and holds a Postdoctoral Enrichment Program Award from the Burroughs Wellcome Fund.

10.1126/science.aar4799

GRAPHIC: A. KITTERMAN/*SCIENCE*

CANCER THERAPY

Precision medicine using microbiota

Intestinal microbiota influence cancer patient responses to immunotherapy

By **Christian Jobin**

Accumulating evidence indicates that dysregulation of microbiota-host interactions associates with various diseases, including inflammatory bowel diseases (IBDs), colorectal cancer, diabetes, and liver cirrhosis (*1*). Recently, research has generated paradigm shifts in concepts about the interactions between bacteria and cancer therapeutic drugs. For example, bacteria modulate the antitumor efficacy in preclinical models of various chemotherapies (*2*–*4*) and immunotherapeutic agents (*5*, *6*). Conceptually, these findings suggest that bacteria-mediated interactions with the immune system are essential for optimal drug efficacy. However, there is limited information regarding the functional impact of the composition of the human microbiome and therapeutic outcomes in cancer patients. On pages 91, 97, and 104 of this issue, Routy *et al.* (*7*), Gopalakrishnan *et al.* (*8*), and Matson *et al.* (*9*), respectively, address this important issue and demonstrate that patients can be stratified into responders and nonresponders to immunotherapy on the basis of the composition of their intestinal microbiomes, suggesting that microbiota should be considered when assessing therapeutic intervention.

Effector T lymphocytes represent a critical branch of the adaptive immune response to antigens, and controlling the length and strength of this activation is necessary to preserve healthy tissues from the destructive potential of these cells. A series of coinhibitory molecules, called immune checkpoints, expressed by antigen presenting cells are responsible for switching off T cell activation and terminating the immune response. Although this regulatory system is essential for a measured immune response, and thus for host homeostasis, expression of immune checkpoint molecules by tumor cells leads to inactivation of cytotoxic $CD8^+$ T cells (a type of effector T lymphocyte) and, as a result, evasion of the antitumor immune response. Unleashing the power of adaptive immune responses by targeting immune checkpoints, such as the programmed cell death protein 1 (PD-1)–PD-1 ligand 1 (PD-L1) axis has emerged as a promising approach for cancer therapy in solid tumors. However, patient responses to immune checkpoint therapies are heterogeneous and transient, a phenomenon related to limited immune cell infiltration of tumors and an immunosuppressive tumor microenvironment. Because microbiota have a pronounced modulatory effect on the immune system, they may enhance responses to immune checkpoint therapies.

In an effort to identify microbes associated with treatment responsiveness, Gopalakrishnan *et al.* surveyed the oral and intestinal microbiota of patients with metastatic melanoma undergoing anti–PD-1 therapy. Interestingly, patients responding to this therapy had a high relative abundance of bacteria of the *Faecalibacterium* genus, whereas nonresponding patients displayed a high relative abundance of bacteria of the order Bacteroidales in their feces (indicating the presence of these bacteria in the intestines). They observed that the strongest fecal microbial predictors of anti–PD-1 therapy response were bacterial diversity and abundance of *Faecalibacterium* and Bacteroidales. No such microbial correlations were observed in the oral cavity, suggesting that the intestinal community is the source of bacterial-immune synergy for response to anti–PD-1 therapy. By also analyzing patients with metastatic melanoma undergoing this therapy, Matson *et al.* found responding patients had an increased abundance of eight microbial species, including *Bifidobacterium longum*. The presence of this species in the intestines of tumor-bearing mice was previously found to improve anti–PD-L1 therapy (*6*). Interestingly, two species were also associated with nonresponsiveness (*Ruminococcus obeum* and *Roseburia intestinalis*).

Routy *et al.* studied interactions between microbiota and response to anti–PD-1 treatment in patients with non–small cell lung cancer, renal cell carcinoma, and urothelial carcinoma. They observed that antibiotic exposure, taken during the course of cancer therapy to treat various infections, negatively correlates with patients' response to anti–PD-1 treatment. This suggests that disruption of microbial networks and loss of specific bacterial clades interfere with the efficacy of immune checkpoint blockade. Comparing the fecal microbiota of responders to nonresponders revealed increased relative abundance of *Akkermansia muciniphila* in patients showing favorable outcomes to anti–PD-1 treatment. Routy *et al.* surmised that microbial diversity and composition are a predictor of anti–PD-1 treatment response for these types of cancer. If the microbiota of responding patients containing immunoregulatory bacteria (for example, *Akkermansia*, *Faecalibacterium*, and *Bifidobacterium*) functionally drive

Department of Medicine, Department of Infectious Diseases and Immunology, and Department of Anatomy and Cell Biology, University of Florida, Gainesville, FL 32611, USA. Email: christian.jobin@medicine.ufl.edu

anti–PD-1 efficacy, then it is expected that germ-free mice implanted with human tumor cells and transplanted with feces from these patients [a technique known as fecal microbiota transplantation (FMT)] would display better responses to treatment. Routy *et al.* and Gopalakrishnan *et al.* observed an improved response to anti–PD-1 therapy in mice receiving FMT from responsive patients compared to that in mice colonized with feces from nonresponsive patients. Gopalakrishnan *et al.* showed this improved response correlated with a higher abundance of *Faecalibacterium* in the feces of the mice. Matson *et al.* observed that anti–PD-L1 treatment was only effective in mice receiving FMT from responding patients, with five out of the eight strains originally found to be associated with anti–PD-1 response in patients detected in the feces of the mice, including *Bifidobacterium*. In all three studies, tumors of mice receiving FMT from responsive patients displayed a higher density of $CD8^+$ T cells compared to that in tumors in mice that received nonresponder FMT. This suggests that immune checkpoint therapy targets the repertoire and activity of host immune cells and induces antitumor responses mediated both by $CD8^+$ T cells and a decrease in $CD4^+$ regulatory T (T_{reg}) cells, which are immunosuppressive.

An important and clinically relevant issue is whether manipulation of the intestinal microbiome could turn patients that are nonresponsive to immune checkpoint blockade into responders. Routy *et al.* found that introduction of *A. muciniphila* to mice receiving human nonresponder FMT reversed the low response to PD-1 blockade, improving antitumor immune cell infiltration and activity in tumors. Overall, these studies report a fascinating interaction between intestinal bacteria and antitumor efficacy of PD-1 blockade in patients, suggesting that precision medicine strategies should include the intestinal microbiota as a potential treatment modifier (see the figure).

What is the evidence that microbiota-derived research could translate to new therapeutics? The most celebrated medical success targeting microbiota came from the field of infectious diseases, with FMT-mediated treatment of recurrent *Clostridium difficile* infection (CDI), a leading cause of antibiotic-associated diarrhea with an alarming increased incidence in Europe, Asia, and the United States. Patients with recurrent CDI showed a 90% clinical response rate after FMT with feces from healthy donors (*10*). This resulted in considerable effort from both academic and private enterprises to design synthetic microbial communities to treat various microbiota-associated diseases such as CDI and IBDs. A similar route could be envisioned for cancer treatment, where synthetic microbial communities could be assembled to optimize patient responses to immunotherapy. Intestinal microbial communities have the capacity to modulate health status by engaging various immune and nonimmune cell types through microbial-derived structures (RNA, DNA, and membrane components) and by generating an impressive network of metabolites. In addition to having individualized microbiota, patients responding to immune checkpoint therapy could be predisposed to intestinal bacterial translocation into secondary lymphoid organs, where they could mount a specific antitumor immune response to allow better synergy with treatment. Untangling components that regulate the complex interaction between microbiota and host could also lead to the generation of targeted therapy, rather than nonspecific FMT.

Although these studies collectively agreed on the critical role of bacteria in defining responsiveness to anti–PD-1 therapy, no universal bacterial species define this response. The divergence in microbial communities associated with the same therapeutic agent (anti–PD-1) may be related to the type of cancer (for example, metastatic melanoma with *Faecalibacterium* and non–small cell lung cancer, renal cell carcinoma, and urothelial carcinoma with *Akkermansia*) or patient population (U.S. versus European cohorts). However, both Matson *et al.* and Gopalakrishnan *et al.* conducted their studies using U.S.-based patient populations with metastatic melanoma, yet observed different PD-1 immunoregulatory bacterial species. The reason for this microorganism specificity is unclear, but it is likely that a convergent mechanism, which is yet to be identified, unifies them. Detailed mechanistic studies into how bacteria reenergize tumor immune microenvironments will be necessary to fully comprehend this phenomenon. Another intriguing observation is that strains of *Akkermansia*, *Faecalibacterium*, and *Bifidobacterium* have been associated with anti-inflammatory responses, a regulatory arm of the immune system that aims to prevent overactivation of the immune response and restores host homeostasis. For example, decreased relative abundance of *A. muciniphila* in the intestine associates with many diseases, including IBDs, type 2 diabetes, and liver diseases (*11*). Similarly, *Faecalibacte-*

The intestinal microbiota influences the efficacy of PD-1 blockade

The enrichment of specific microbial taxa in intestines correlates with response to PD-1 blockade in cancer patients. FMT from responders into tumor-bearing mice improved responses to anti–PD-1 therapy and correlated with increased antitumor $CD8^+$ T cells in the tumors. Mice receiving FMT from nonresponders did not respond to anti–PD-1 therapy, and tumors had a high density of immunosuppressive $CD4^+$ T_{reg} cells.

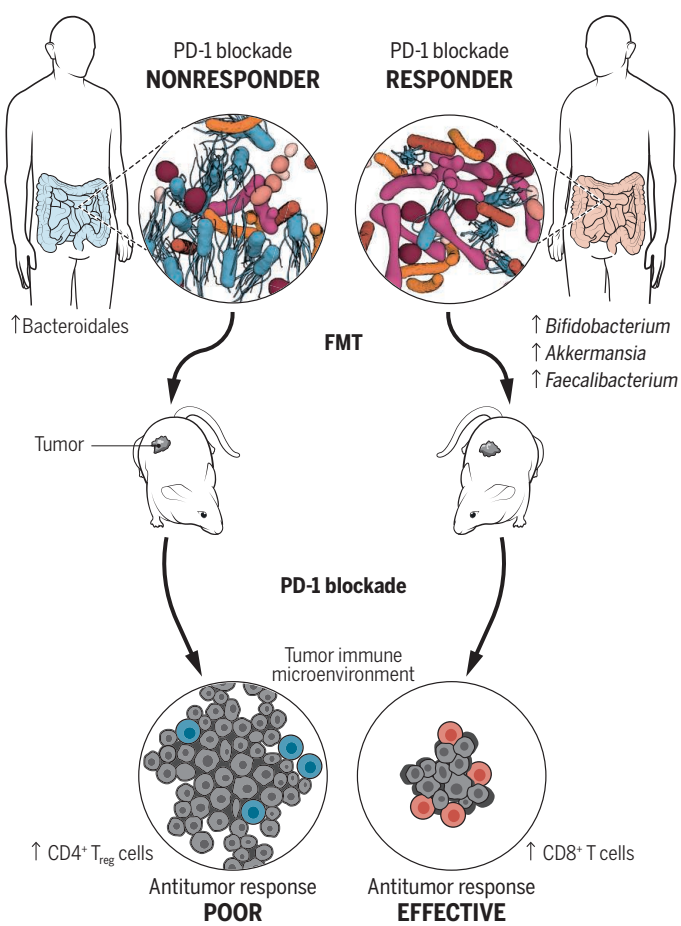

GRAPHIC: V. ALTOUNIAN/*SCIENCE*

rium prausnitzii down-regulates intestinal inflammation, which is associated with the production of specific metabolites, such as butyrate and salicylic acid derived from host cells or bacteria in the intestine and peripheral blood (*12*). Clearly, molecular characterization of intestinal *Akkermansia*, *Faecalibacterium*, and *Bifidobacterium* strains from cancer patients is needed to fully understand how they influence the tumor microenvironment and synergize with immune checkpoint blockade. These studies could lead to the isolation and characterization of microbial components that are responsible for the beneficial effects. For example, administration of Amuc_1100, a protein isolated from the outer membrane of *A. muciniphila*, reproduces the beneficial effect of the bacterium on diabetes in preclinical models (*13*).

The relationship between microbial communities and antitumor drug responses are complex. On the one hand, depletion of selective bacterial taxa by means of antibiotic exposure or other stressor conditions may diminish immunotherapy responses. On the other hand, the presence of specific microorganisms in local or distant sites may interfere with treatment through metabolic activities (*14*). For example, bacteria of the Enterobacteriaceae family, such as *Escherichia coli* strains, decrease efficacy of the chemotherapeutic agent gemcitabine by metabolizing and deactivating the active form of the drug, thereby negatively interfering with tumor response (*15*). Therefore, the presence of specific strains of bacteria may be able to modulate cancer progression and therapeutics, raising the possibility that precision medicine directed at the microbiota could inform physicians about prognosis and therapy. One could view the microbiota as a treasure trove for next-generation medicine, and tapping into this network may produce new therapeutic insights. ■

REFERENCES AND NOTES

1. E. Pasolli *et al.*, *PLOS Comput. Biol.* **12**, e1004977 (2016).
2. S. Viaud *et al.*, *Science* **342**, 971 (2013).
3. N. Iida *et al.*, *Science* **342**, 967 (2013).
4. R. Daillère *et al.*, *Immunity* **45**, 931 (2016).
5. M. Vétizou *et al.*, *Science* **350**, 1079 (2015).
6. A. Sivan *et al.*, *Science* **350**, 1084 (2015).
7. B. Routy *et al.*, *Science* **359**, 91 (2018).
8. V. Gopalakrishnan *et al.*, *Science* **359**, 97 (2018).
9. V. Matson *et al.*, *Science* **359**, 104 (2018).
10. C. R. Kelly *et al.*, *Gastroenterology* **149**, 223 (2015).
11. P. D. Cani, W. M. de Vos, *Front. Microbiol.* **8**, 1765 (2017).
12. S. Miquel *et al.*, *mBio* **6**, e00300-15 (2015).
13. H. Plovier *et al.*, *Nat. Med.* **23**, 107 (2017).
14. N. Koppel *et al.*, *Science* **356**, eaag2770 (2017).
15. L. T. Geller *et al.*, *Science* **357**, 1156 (2017).

ACKNOWLEDGMENTS

C.J. is supported by National Institutes of Health grant R01 DK73338 and by the University of Florida, Department of Medicine Gatorade Fund.

10.1126/science.aar2946

OCEANS

Mind the seafloor

Research and regulations must be integrated to protect seafloor biota from future mining impacts

By **Antje Boetius**[1,2,3] *and* **Matthias Haeckel**[4]

As human use of rare metals has diversified and risen with global development, metal ore deposits from the deep ocean floor are increasingly seen as an attractive future resource. Japan recently completed the first successful test for zinc extraction from the deep seabed, and the number of seafloor exploration licenses filed at the International Seabed Authority (ISA) has tripled in the past 5 years. Seafloor-mining equipment is being tested, and industrial-scale production in national waters could start in a few years. We call for integrated scientific studies of global metal resources, the fluxes and fates of metal uses, and the ecological footprints of mining on land and in the sea, to critically assess the risks of deep-sea mining and the chances for alternative technologies. Given the increasing scientific evidence for long-lasting impacts of mining on the abyssal environment, precautionary regulations for commercial deep-sea mining are essential to protect marine ecosystems and their biodiversity.

"To be economical, any single operation would have to mine several hundred square kilometers of deep seafloor per year..."

REMOTE AND UNKNOWN

The seabed covers 70% of Earth's surface and is home to a virtually uncharted diversity of marine life. The ocean floor, at an average depth of 4 km, is characterized by pressures of several hundred bars, temperatures around the freezing point of water, and no sunlight for photosynthetic productivity. For humans, this environment is inhabitable, barely accessible, and extreme. et, the relatively stable environmental conditions of the deep sea have promoted a vast biodiversity of taxa that are not found in shallow waters or on land.

Because of its remoteness and the technical challenges associated with reaching the deep seabed, much less than one-thousandth of its area has been studied (*1*). As a result, little is known about how much deep-sea species contributed to the evolution of life and biodiversity on Earth, how they can tap into unusual energy sources, how the sparse populations maintain enough standing stock in this vast realm, and how they adapt to perturbations. No country sustains the necessary amount of deep-sea observations required to answer such questions. The lack of long-term ecological time series is particularly problematic, making it difficult to decipher natural dynamics and anthropogenic perturbations (*2*). Recent findings suggest a tight coupling between the dynamics of surface and deep-sea processes and confirm that effects of climate change and pollution propagate quickly. But little is known about the resilience and recovery of deep-sea communities in the context of activities such as mining (*3*).

HAZARDS OF DEEP-SEA MINING

Critical metal resources in the deep sea include arsenic, copper, cobalt, nickel, lithium, platinum, tellurium, zinc, and many rare earth elements (*4*). The exploitable resources of the potentially prolific, 40-million-km^2 deep-sea area (*5*) could be worth $20 trillion to $30 trillion, considering current metal prices. However, these resources are not renewable, because polymetallic nodules and crusts grow very slowly over millions of years. Furthermore, mining is highly invasive, damaging the surface seafloor and entailing considerable risks for deep-sea life (*6*, *7*). Even in shallow seas, there is no efficient governance for monitoring, managing, and protecting the oceans. The extensive seafloor damage caused by benthic trawling or by accidents such as the 2010 *Deepwater Horizon* oil spill in the Gulf of Mexico shows that ecological impacts on the deep sea remain literally out of sight in ocean resource management. Even in national waters, no system is in place to repair, restore, and compensate for loss of seafloor habitat.

On land, metal mining is highly destructive to the environment and can put the

[1]*Alfred Wegener Institute Helmholtz Center for Polar and Marine Research, Bremerhaven, Germany.* [2]*Max Planck Institute for Marine Microbiology, Bremen, Germany.* [3]*MARUM Center for Marine Environmental Sciences, University of Bremen, Bremerhaven, Germany.* [4]*GEOMAR Helmholtz Centre for Ocean Research Kiel, Kiel, Germany. Email: antje.boetius@awi.de; mhaeckel@geomar.de*

health of miners and local communities at risk, if not carefully regulated and managed. Mitigation actions such as habitat compensation, restoration, and adaptive management are expensive, but can minimize the damage to biodiversity and help to restore terrestrial landscapes within a few decades. However, it remains questionable whether any land-based mitigation mechanisms can serve as a blueprint for regulations of deep-sea mining (*8*). The high economic costs of ecological impact on land (*9*) are often used as an argument for deep-sea mining. Yet, such a "not-in-my-backyard" drive toward seafloor uses would violate the internationally affirmed precautionary approach, as reflected in principle 15 of the 1992 Rio Declaration on Environment and Development.

The ISA, which is responsible for controlling the exploitation of mineral resources in international waters, adopts this principle in its draft regulation, published on 8 August 2017 (*10*). However, concrete environmental objectives for protecting and conserving the deep-sea environment, including its biological diversity and ecological integrity, have not been agreed upon yet. To be economical, any single operation would have to mine several hundred square kilometers of deep seafloor per year, but this estimate does not include the costs of environmental management. At the anticipated scale of seafloor damage, monitoring, compensation, and restoration techniques would be extremely expensive to implement. But without such measures, the use of deep-sea mineral resources to sustain further global economic growth would endanger the deep sea's genetic resources, which are a long-term target for biotechnology and medicine (*11*).

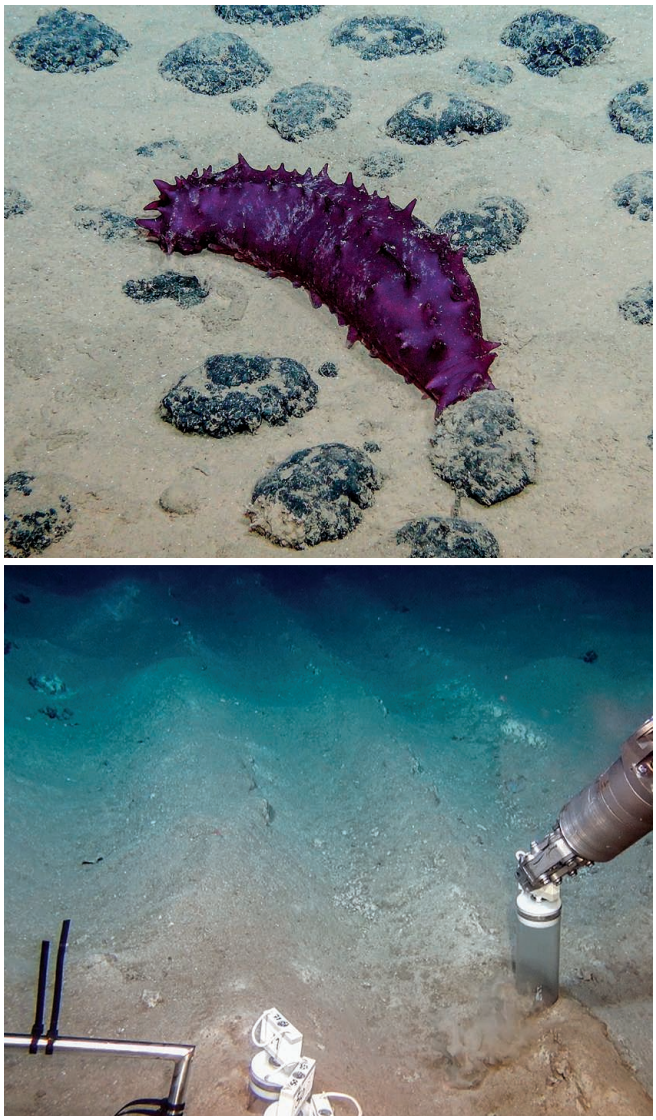

(Top) Holothurian in a polymetallic nodule field of the Clarion-Clipperton Fracture Zone of the Pacific Ocean. (Bottom) ROV Kiel 6000 push coring disturbed surface sediment of the 26-year old plow track of the DISCOL experiment in the Pacific Peru Basin.

PHOTOS: GEOMAR, KIEL

THE RESEARCH BASIS

Several countries are currently funding a range of activities connected to deep-sea mining, from developing technologies for deep-sea raw materials extraction to researching the ecological consequences of deep-sea mining, but there is no central synthesis platform to bring together arising knowledge.

The MiningImpact project (a part of the Joint Programming Initiative Healthy and Productive Seas and Oceans) has brought together 11 European countries to study the environmental impacts of seafloor mining, with a focus on polymetallic nodules. The researchers revisited benthic impact experiments in the Pacific Peru Basin and in ISA contract areas in the Clarion-Clipperton Fracture Zone in the Pacific Ocean (see the photos). Some of these experiments were initiated up to 40 years ago and have now been studied with state-of-the-art methods (*12*). Key conclusions were that deep-sea ecosystems associated with polymetallic resources support a diverse fauna with high spatial and temporal variability and largely unknown connectivity; that the loss of seafloor integrity by mining reduces population densities and ecosystem functions for many decades; and that sediment plumes will likely blanket the seafloor up to several tens of kilometers outside the mined area (*13*). On the basis of current scientific knowledge, the long-term risks of industrial-scale deep-sea mining to the marine environment seem unmanageable from both the economical and the ecological perspective.

However, predicting impacts on the basis of small-scale benthic impact experiments is associated with many uncertainties. Benthic trawling provides a rough analog for large-scale impact on seafloor integrity. In shelf seas, recovery of seafloor communities from benthic trawling can take less than a decade depending on the substrate (*14*), but decades to centuries are needed in deep-water habitats (*15*). In 2016, the European Union banned seabed trawling on continental slopes below 800 m to reduce risks for deep-sea life.

Dark, cold, energy-poor deep-sea ecosystems are particularly vulnerable to mechanical disruption of the surface seafloor, which contains most of the food and microbial communities on which benthic fauna depend. Biogeochemical investigations as part of the MiningImpact experiments confirm that even the soft sediment seafloor would take many decades to hundreds of years to recover from the disturbance caused by nodule removal (*13*). The nodules and crusts themselves, which provide habitats to many deep-sea species, would need millions of years to grow back (*4*).

CAREFUL OCEAN GOVERNANCE

Strict environmental regulations need to be formulated by the ISA as they finalize their regulations (*10*). Before any industrial activities could begin, long-term studies with realistic analogs to mining technologies would be needed. Conservation areas must closely match ecosystem characteristics of mined areas to safeguard abyssal biodiversity. Technologies for baseline studies and monitoring need to be standardized and regularly revised to reflect state-of-the-art science. Indicator sets for deep-sea ecosystem status and threshold values for harmful effects must be defined. Environmental management plans need to address uncertainties of sediment-plume dispersal. Finally, transparent and independent international scientific assessment of environmental management plans needs to be in place before any deep-sea mining

operations can start. Transparency also needs to be increased in the ISA's decision-making process for issuing contracts, as has become obvious by the latest approval of a 10,000-km^2 claim at the Mid-Atlantic Ridge (*16*) that includes the hydrothermal-vent systems of Lost City, Trans-Atlantic Geotraverse, and Broken Spur, which are key scientific research sites.

Before taking any risk to destroy deep-sea habitats and endanger marine species, metal resources on land could be fully mapped and explored. Technological and social innovations could improve the way metals are used and recycled, and international politics could foster metal-market stability. In all of this, holistic science projects and stakeholder dialogue could help in finding solutions to the development of metal resources, uses, and fates. This would also provide the necessary time to valorize ocean life and its genetic resources (*11*). A new kind of international deep-sea science and policy, in which knowledge and governance of mineral and genetic resources as well as other ocean ecosystem services are integrated and channeled into international policy, would allow humanity to sustain the full range of options for the deep sea. ■

REFERENCES AND NOTES

1. E. Ramirez-Llodra *et al.*, *Biogeosciences* **7**, 2851 (2010).
2. K. L. Smith *et al.*, *Eos* 10.1029/2015EO038095 (2015).
3. S. Gollner *et al.*, *Marine Environ. Res.* **129**, 76 (2017).
4. J. R. Hein, A. Koschinsky, *Deep-Ocean Ferromanganese Crusts and Nodules, Treatise on Geochemistry* (Elsevier, ed. 2, 2014), pp. 273–291.
5. S. Petersen *et al.*, *Mar. Policy* **70**, 175 (2016).
6. L. M. Wedding *et al.*, *Science* **349**, 144 (2015).
7. C. L. Van Dover *et al.*, *Nat. Geosci.* **10**, 464 (2017).
8. J. M. Durden *et al.*, *Mar. Policy* **84**, 193 (2017).
9. J. R. Wakefield, K. Meyers, *Mar. Policy* 10.1016/j.marpol.2016.06.018 (2016).
10. www.isa.org.jm/files/documents/EN/Regs/DraftExpl/ISBA23-LTC-CRP3-Rev.pdf
11. Royal Society, Future ocean resources: Metal-rich minerals and genetics, Evidence pack (2017); https://royalsociety.org/topics-policy/projects/future-ocean-resources.
12. A. Vanreusel, A. Hilario, P. A. Ribeiro, L. Menot, P. M. Arbizu, *Sci. Rep.* **6**, 26808 (2016).
13. Announced to stakeholders at the project's final conference at the Natural History Museum in London on 18 to 20 October 2017.
14. J. G. Hiddink *et al.*, *Proc. Natl. Acad. Sci. U.S.A.* **114**, 8301 (2017).
15. V. A. I. Huvenne, B. J. Bett, D. G. Masson, T. P. Le Bas, A. J. Wheeler, *Biol. Conserv.* **200**, 60 (2016).
16. www.isa.org.jm/sites/default/files/files/documents/isba-23c-14_1.pdf

ACKNOWLEDGMENTS

We acknowledge funding by Joint Programming Initiative Healthy and Productive Seas and Oceans (JPI Oceans) "MiningImpact" (Fkz 03F0707A) of the Federal Ministry of Education and Research (BMBF), the EU project Managing Impacts of Deep Sea Resource Exploitation (MIDAS) (GA 603418), and by the German Research Foundation (DFG) Excellence Clusters "Future Ocean" and "MARUM—The Ocean in the Earth System."

10.1126/science.aap7301

IMMUNOLOGY

Lung inflammation originating in the gut

Parasite infection in the intestine can lead to inflammatory immune cells in the lung

By **Jenny Mjösberg**[1,2] *and* **Anna Rao**[1]

Innate lymphoid cells (ILCs) are a type of immune cell that are considered to be tissue-resident gatekeepers situated in mucosal membranes, where they contribute to both homeostasis and pathology (*1*). In healthy individuals, ILCs are involved in tissue repair, but ILCs have also been shown to participate in several types of inflammation, including allergy and asthma. Whereas ILCs can be found at low frequencies in the blood circulation, mucosal barriers such as the intestine and airways are enriched for ILCs (*1*). However, whether ILCs are in fact tissue resident in the sense that they self-renew without substantial replenishment from other organs has been a topic of debate. The mechanisms of ILC circulation are important for understanding various types of inflammatory conditions and how they can be treated. On page 114 of this issue, Huang *et al.* (*2*) demonstrate that ILC2s are not obligate tissue-resident cells because they can be recruited from the gut to the lung and other organs in response to inflammatory signaling.

"...ozanimod and related drugs might interfere with the ILC gut-lung axis and be beneficial in chronic lung inflammation..."

ILC2s contribute to so-called "type 2 immunity" in which they are typically activated by the cytokines interleukin-25 (IL-25) and IL-33 to produce large amounts of IL-5 and IL-13, which are key players in this type of inflammation. In 2015, Huang *et al.* (*3*) described a population of lung ILC2s characterized by high expression of killer cell lectin-like receptor subfamily G member 1 (KLRG1) and the IL-25 receptor, IL-17 receptor-β (IL-17Rβ), but low expression of the IL-33 receptor, ST2 (KLRG1^{high} ST2^{low} ILC2s). In contrast to natural ILC2s (nILC2s), which reside in the lungs during homeostatic conditions, KLRG1^{high} ST2^{low} ILC2s were termed inflammatory ILC2s (iILC2s) as they arise in the lungs only after type 2 immunity induced by IL-25 exposure or gastrointestinal infection with the parasitic worm *Nippostrongylus brasiliensis*. Now Huang *et al.* (*2*) extend their observations using a model to study circulation of blood-borne cells between two surgically connected (parabiotic) mice to show that iILC2s accumulate in the lungs during these conditions because they are rapidly recruited within 3 to 5 days. These data challenge the existing view established following the seminal paper by Gasteiger *et al.* (*4*), who did not observe replenishment of ILC2s until day 15 after *N. brasiliensis* infection in parabiotic mice. The discrepancy in timing of ILC2 recruitment between these two studies might be due to different conditions in which mice were housed. Gasteiger *et al.* kept their mice on antibiotic treatment, whereas Huang *et al.* (*2*) did not. It is therefore possible that the intestinal microbiota might play an important role in ILC2 circulation.

Huang *et al.* (*2*) identify the intestine as the critical origin of iILC2s recruited to the lung upon IL-25 administration, revealing a striking ILC2 gut-lung recruitment axis (see the figure). Supporting the intestine as the major source of iILC2s in the lung, transcriptional analysis demonstrates that lung iILC2s are more similar to small intestine ILC2s (siILC2s) than to lung nILC2s.

The recruitment of iILC2s in the lung is a transient phenomenon. Twelve days after IL-25 administration, iILC2s are undetectable in the lung. However, parabiosis experiments reveal that 10% of nILC2s in the lung and 40% of ILC2s in the intestine originate from the donor mouse, suggesting that lung iILC2s can return to the intestine or display plasticity and convert into nILC2-like cells in the lung (see the figure). Because these nILC2-like cells in the lung are derived from activated iILC2s, it is possible that they make up tissue-resident

[1]*Center for Infectious Medicine, Department of Medicine, Karolinska Institutet, Stockholm, Sweden.* [2]*Department of Clinical and Experimental Medicine, Linköping University, Sweden. Email: jenny.mjosberg@ki.se*

epigenetically poised "memory" ILC2s, as previously reported in mice exposed to allergens (*5*). Memory ILC2s would enable a rapid and more efficient immune response following a repeated immune challenge. In addition to developing into nILC2-like cells, iILC2s express *IL17A* transcripts (*2*), indicative of transdifferentiation to ILC3s. It is interesting to note that nILC2s, which expand locally in the lung, express receptors for IL-1β and IL-18, raising the possibility that nILC2s are prone to transdifferentiate to ILC1s, as occurs in human chronic obstructive pulmonary disease (COPD) (*6*, *7*). Hence, iILC2s and nILC2s serve distinct and important purposes in the lung: iILC2s are recruited from the intestine for rapid and transient type 2 immunity, whereas nILC2s are largely tissue resident and potentially give rise to immunity against viral infections, for example.

Huang *et al*. also describe the mechanism of IL-25–induced gut-lung recruitment. iILC2s are found in lymphatic vessels in the gut as well as in peripheral blood, suggesting that they circulate via the lymphatic system into the blood. In support of this, IL-25–activated iILC2s in the lung express sphingosine 1-phosphate (S1P) receptors S1P1 and S1P4 (*2*), indicating that iILC2s can cross lymphatic endothelial barriers, similar to T cells (*8*). Furthermore, like tissue-resident T cells (*9*), siILC2s in healthy mice lack expression of S1P1, reflecting their inability to egress from the gut in the absence of immune activation. Blocking S1P signaling with an inhibitor dramatically reduced the frequency of iILC2s in the lung and concordantly reduced the survival of mice following *N. brasiliensis* infection (*2*). As Gasteiger *et al*. observed a delay in the recruitment of ILC2s to the lung following *N. brasiliensis* infection in antibiotic-treated mice (*4*), it is possible that the gut microbiota regulates S1P receptor expression on ILC2s. This, however, is unexplored.

Importantly, Huang *et al*. (*2*) show that S1P receptor–mediated egress is a conserved phenomenon that occurs both in innate (for example, ILCs) and adaptive (for example, T cells) lymphoid cells. However, it remains unclear if and by which mechanisms other ILC populations circulate during inflammation. It is also unknown how intestinal ILC2s enter the lung tissue from the blood. In addition to recruitment of activated ILC2s, as described by Huang *et al*. (*2*), it was recently shown that circulating human blood ILC precursors can seed tissues and differentiate to form all known ILC subtypes (*10*). However, it remains unclear how much recruitment of circulating precursors and local ILC generation contribute to the total ILC pool in an organ, relative to local proliferation (as observed for nILC2s) and plasticity and recruitment of differentiated ILCs (as seen for iILC2s) (*2*).

The ILC2 gut-lung axis identified by Huang *et al*. (*2*) is interesting in the context of the link between disturbances in the intestinal microbiota and lung diseases such as asthma and COPD (*11*). Considering that the S1P1 inhibitor ozanimod is currently in clinical trials for treatment of multiple sclerosis (*12*) and inflammatory bowel disease (*13*), perhaps ozanimod and related drugs might interfere with the ILC gut-lung axis and be beneficial in chronic lung inflammation, such as asthma and COPD. ■

Model for ILC2 gut-lung circulation

ILCs are involved in tissue repair, but ILCs have also been shown to participate in several types of inflammation, including allergy and asthma. Whereas ILCs can be found at low frequencies in the blood circulation, mucosal barriers such as the intestine and airways are enriched for ILCs. Huang *et al*. (*2*) demonstrate that ILC2s can be recruited from the gut to the lung in response to inflammatory signals.

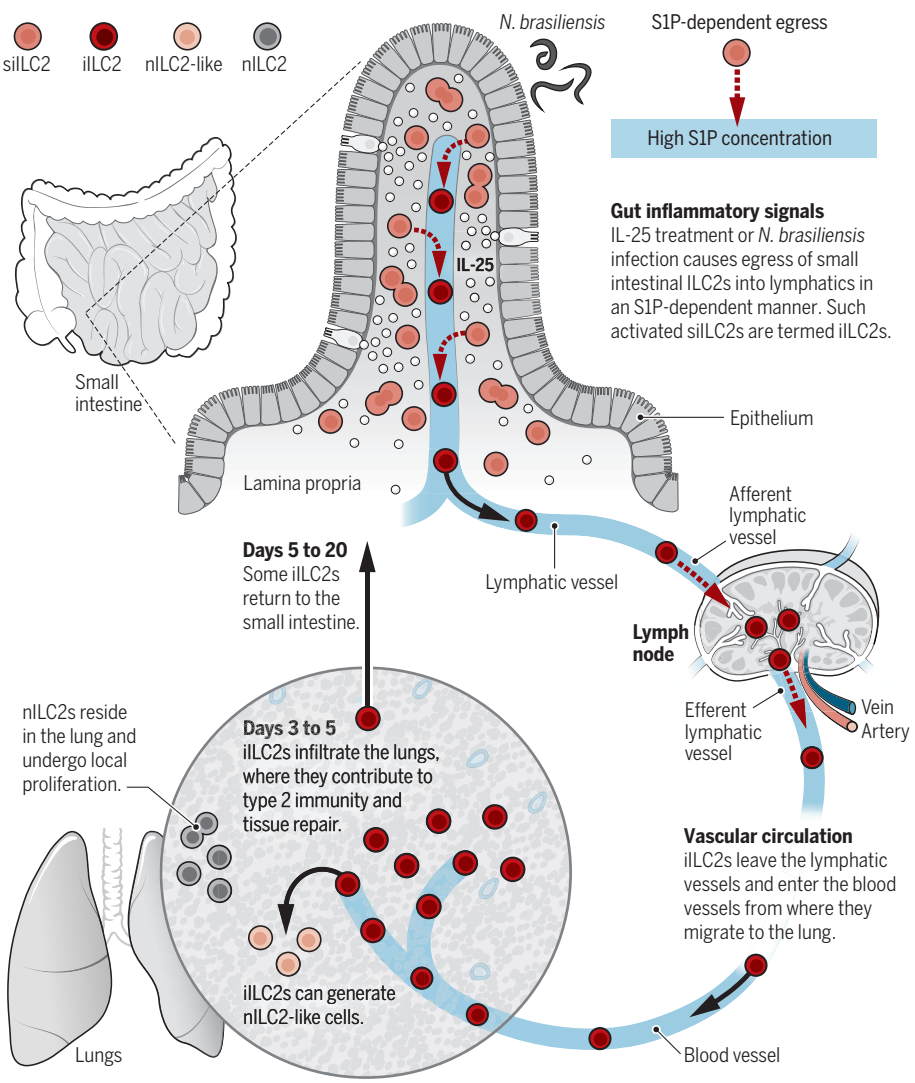

GRAPHIC: K. SUTLIFF/*SCIENCE*

REFERENCES

1. M. Ebbo, A. Crinier, F. Vély, E. Vivier, *Nat. Rev. Immunol.* **17**, 665 (2017).
2. Y. Huang *et al.*, *Science* **359**, 114 (2018).
3. Y. Huang *et al.*, *Nat. Immunol.* **16**, 161 (2015).
4. G. Gasteiger, X. Fan, S. Dikiy, S. Y. Lee, A. Y. Rudensky, *Science* **350**, 981 (2015).
5. I. Martinez-Gonzalez *et al.*, *Immunity* **45**, 198 (2016).
6. S. M. Bal *et al.*, *Nat. Immunol.* **17**, 636 (2016).
7. J. S. Silver *et al.*, *Nat. Immunol.* **17**, 626 (2016).
8. S. Mandala *et al.*, *Science* **296**, 346 (2002).
9. C. N. Skon *et al.*, *Nat. Immunol.* **14**, 1285 (2013).
10. A. I. Lim *et al.*, *Cell* **168**, 1086 (2017).
11. K. F. Budden *et al.*, *Nat. Rev. Microbiol.* **15**, 55 (2017).
12. B. Z. Chaudhry, J. A. Cohen, D. S. Conway, *Neurotherapeutics* **14**, 859 (2017).
13. M. Vetter, M. F. Neurath, *Therap. Adv. Gastroenterol.* **10**, 773 (2017).

10.1126/science.aar4301

TRIBOLOGY

The contact sport of rough surfaces

Approximate models of interacting surfaces competed against a supercomputer solution

By **Robert W. Carpick**

Describing the way two surfaces touch and make contact may seem simple, but it is not. Fully describing the elastic deformation of ideally smooth contacting bodies, under even low applied pressure, involves second-order partial differential equations and fourth-rank elastic constant tensors. For more realistic rough surfaces, the problem becomes a multiscale exercise in surface-height statistics, even before including complex phenomena such as adhesion, plasticity, and fracture. A recent research competition, the "Contact Mechanics Challenge" (*1*), was designed to test various approximate methods for solving this problem. A hypothetical rough surface was generated, and the community was invited to model contact with this surface with competing theories for the calculation of properties, including contact area and pressure. A supercomputer-generated numerical solution was kept secret until competition entries were received. The comparison of results (*2*) provides insights into the relative merits of competing models and even experimental approaches to the problem.

Understanding contact and friction fascinated da Vinci, Coulomb, Prandtl, and de Gennes, among others (*3*). In 1881, Hertz solved the problem of two smooth, elastic spheres coming into contact, launching the field of "contact mechanics" (*4*) and leading to the development of equations for contact area, contact pressure, stresses, strains, and deformations for smooth, loaded contact geometries. However, real surfaces are rarely smooth. Even finely polished metals retain peaks and valleys with wavelengths ranging from nanometers to micrometers, leading to a seemingly random distribution of asperity contacts separated by stress-free noncontact zones (see the figure). Solving such contact problems is fundamental to understanding how gears turn, tires roll, and geckos climb (*5*), as well as for engineering any device with moving or contacting parts. It also underpins theories of friction, adhesion, lubrication, and wear, which can be empirical and highly system-specific.

Department of Mechanical Engineering and Applied Mechanics, University of Pennsylvania, Philadelphia, PA 19104-6315, USA. Email: carpick@seas.upenn.edu

Just over 50 years ago, an elegant analysis of contacting rough surfaces assumed that surface summit heights, all with the same radii, had an approximately Gaussian distribution (*6*). This Greenwood-Williamson (GW) model is the most common approach to modeling rough surfaces and has since spawned a plethora of other models. These approaches involve both analytical extensions to the GW model as well as numerical approaches, with different degrees of complexity that account for effects such as plastic flow, adhesive forces, and anisotropic properties.

This wide variety of models not only makes it difficult for experimentalists and engineers to decide which approach to adopt but also throws into question their accuracy. Predictions from different models disagree strongly (as do their authors), and

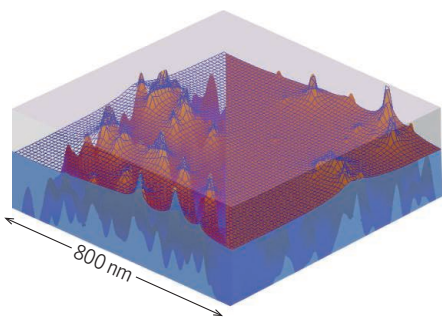

The contacting surfaces like those used in the competition. The blue grid shows the deformations of the lowermost surface of an elastic solid (the left half is rendered more transparent) pressed against a rigid substrate with fractal roughness. The color range of the lower surface corresponds to height, enlarged ~30 times versus the in-plane directions. [Adapted from (*10*).]

experimental validations are scant. In late 2015 (*1*), Müser formulated a contact problem and, along with Spencer and Tysoe, invited researchers to partake in the Contact Mechanics Challenge. Müser used a supercomputer to conduct brute-force numerical simulations of a rough surface contacting a flat plate with a moderate amount of adhesion. The topography and material properties were shared on the internet, but the solution was held secret. The scientific community was challenged to share results from their preferred models for properties including the total contact area, the contact spot distribution, stresses, and deformations.

The response was impressive: 12 groups involving more than 30 authors from Austria, England, France, Germany, Italy, Iran, the Netherlands, Taiwan, and the United States submitted entries that ranged from analytical solutions based on GW-inspired models to more recent fractal-based theories (*7*) and numerical solutions. One group even three-dimensionally printed a model of the rough surface and measured the resulting contact properties with a frustrated total-internal-reflection method (*8*).

Müser and Greenwood compared and summarized the results (*2*). The multiscale approaches had the winning score, with an honorable mention for the experimental method, which matched the solution extremely well. Multiscale approaches based on Persson's theory (*7*) fitted much better than those based on GW for two reasons. First, ignoring small-scale roughness neglects high-pressure zones, whereas ignoring large-scale roughness neglects substantial overall deformation as surfaces conform together. Second, with elastic solids, pushing down on one asperity creates a long-range elastic field that affects the neighbors by pushing them down as well. This effect renders summits near another summit less likely to make contact themselves, thus breaking up the contact area into smaller patches.

The importance of multiscale roughness has long been recognized (*9*), but the Contact Mechanics Challenge results signal that the time has come to standardize multiscale descriptions with elastic coupling, to develop next-generation models to account for behavior beyond the elastic limit, and to confront the next frontier in contact modeling—namely, describing rough surface contact during sliding. This last step would help fulfill da Vinci's dream of understanding what causes friction. ■

REFERENCES

1. N. D. Spencer, W. T. Tysoe, *Trib. Lubr. Technol.* **71**, 96 (2015).
2. M. H. Müser *et al.*, *Tribol. Lett.* **65**, 118 (2017).
3. D. Dowson, *History of Tribology* (Wiley-Blackwell, ed. 2, 1998).
4. K. L. Johnson, *Contact Mechanics* (Cambridge Univ. Press, 1987).
5. C. M. Mate, *Tribology on the Small Scale: A Bottom Up Approach to Friction, Lubrication, and Wear* (Oxford Univ. Press, 2008).
6. J. A. Greenwood, B. P. Williamson, *Proc. R. Soc. Lond. A* **295**, 300 (1966).
7. B. N. J. Persson, *J. Chem. Phys.* **115**, 3840 (2001).
8. A. I. Bennett *et al.*, *Tribol. Lett.* **65**, 123 (2017).
9. J. Archard, *Proc. R. Soc. Lond. A* **243**, 190 (1957).
10. C. Campañá, M. H. Müser, *Phys. Rev. B.* **74**, 075420 (2006).

10.1126/science.aaq1814

Air pollution, seen here over Mexico City, has many effects that are detrimental to the economy.

POLICY FORUM

ENVIRONMENTAL ECONOMICS

Air pollution's hidden impacts

Exposure can affect labor productivity and human capital

By **Joshua Graff Zivin**[1] *and* **Matthew Neidell**[2]

Nearly every country in the world regulates air pollution. But how much pollution control is enough? Answering that question requires considerable information about the costs as well as the benefits of regulation. Historically, efforts to measure benefits have focused on averting major health insults, such as respiratory or cardiovascular events that result in hospitalizations or death, which typically only afflict the most vulnerable segments of the population. These health episodes are clearly consequential—e.g., the U.S. Clean Air Act Amendments of 1990 avert an estimated 160,000 deaths and 86,000 hospitalizations annually (*1*)—but may only represent the tip of the proverbial iceberg, compared to the number of cases of respiratory impairment and other health insults that affect many healthy people every day but do not require hospitalizations or even formal health care encounters. The ubiquity of these less lethal impacts, revealed by emerging economic research on labor productivity and human capital accumulation, suggests that even modest impacts at the individual level can add up to considerable, society-wide impacts across the globe.

[1]*Department of Economics and School of Global Policy and Strategy, University of California, San Diego, La Jolla, CA 92093, USA.* [2]*Department of Health Policy and Management, Mailman School of Public Health, Columbia University, New York, NY 10032. USA. Email: jgraffzivin@ucsd.edu*

Our understanding of these less-severe health impacts is hampered by two factors. First, the number of potential channels through which pollution could affect human functioning is large, as pollution can alter the function of several organ systems and even genetic expression (*2*). Because these are difficult to assess, only a relatively small number have been well studied, leaving large gaps in our understanding of basic physiological relationships. Second, among channels that have been studied, it is often difficult to discern how the physiological and cognitive impacts that have been identified translate into meaningful effects outside of the controlled laboratory setting in which they were assessed. Does a 10% drop in forced expiratory volume, for example, influence the performance of daily life activities?

An emerging literature has begun to overcome these challenges with a new focus on the effects of acute exposure on measures of great economic importance, which, in turn, can easily be monetized for regulatory purposes.

LABOR MARKET PERFORMANCE

Although hospitalized individuals are unable to attend work, and others who are severely ill may also miss workdays, the impacts from less-severe pollution-induced illness on work hours are less well known. Research in Mexico City found that reductions in sulfur dioxide pollution led to sizable increases in work hours per week by individuals in the local labor market (*3*). Of course, the degree of infirmity that necessitates a shortened workday is still nontrivial. It may require some type of health care encounter and at a minimum is obvious to the person experiencing it.

A handful of recent studies attempt to capture even subtler health impacts by focusing on the productivity of workers while they work. The premise behind these studies is that even minor impairments of respiratory and cardiovascular function can increase fatigue, decrease focus, and impair cognition (*4*), even in seemingly healthy populations, thus diminishing the ability to perform one's job. For example, agricultural workers in the Central Valley of California produce less as ozone increases, even though daily pay directly depends on how much fruit they harvest (*5*). These effects arise at ambient concentrations of ozone that are well below regulatory standards and at levels at which obvious health symptoms are not generally present in healthy populations.

Although agricultural employment is important in developing countries, it represents a small fraction of the labor force in more developed ones. Moreover, because agricultural work takes place outdoors, it is not a priori obvious that these results are germane to indoor work, which contributes most of the value in most economies. But a recent study and some preliminary findings suggest impacts of particulate matter pollution on indoor worker productivity in the manufacturing sector (*6*, *7*).

The aforementioned studies focus on physically demanding work, and thus perhaps represent the most logical place for the impacts of minor respiratory and cardiovascular insults to manifest themselves. But findings from a study in China suggest that the information economy is not inoculated against these effects (*8*). Productivity of call center workers in two Chinese cities is negatively affected by fine particulate matter (particles with diameters less than 2.5 μm). These impacts are not limited to extreme pollution days, but emerge at pollution levels that regularly obtain in several major cities within the United States.

HUMAN CAPITAL ACCUMULATION

Human capital, a measure of the intangible resources an individual possesses, such as knowledge, skills, and judgment, plays a fundamental role in labor market outcomes and other aspects of life, including health, civic participation, and criminal activities. A fairly new body of literature focuses on latent impacts of in utero and early-childhood exposure to pollution on later-life outcomes. Although health insults from pollution may indirectly affect human capital accumulation through channels like school attendance and

other educational investments, this focus is motivated by the "fetal origins hypothesis" and literature that documents impacts of stimuli during these critical periods of human development (*9*).

Recent studies provide compelling evidence that early-life exposure to pollution can have lasting impacts on cognitive abilities later in life. Children born in Texas when airborne total suspended particulates (TSPs) were atypically low (due to decreases in industrial production during a brief economic recession) went on to have higher high school test scores (*10*). Children born in Santiago, Chile, with higher exposure to fetal pollution, such as carbon monoxide and particulate matter, went on to perform worse on high-stakes national exams that determine access to secondary schools (*11*). Another study makes the linkage between the labor productivity and human capital literatures more transparent, demonstrating that higher TSP levels in the year of birth lead to lower labor force participation and lower earnings in adulthood (*12*).

INCENTIVES AND DESIGN

Much of what is currently known about benefits from environmental protection in the United States is a result of measurement incentives embodied in Section 812 of the 1990 Clean Air Act amendments and other executive orders that require cost-benefit analyses. U.S. Environmental Protection Agency (EPA) procedures virtually ensure that those incentives remain focused on nationally representative evidence of impacts on high-visibility health endpoints, leaving the investigation of a wide range of other impacts to the idiosyncratic curiosities of the research community. These new forms of evidence could be incorporated into the formal structure of EPA cost-benefit analyses (*13*), while recognizing that forgone earnings due to diminished labor productivity or human capital attainment will not capture all the welfare losses experienced.

More can be done to transform opportunistic study of individual firms into systematic study of productivity impacts. Existing national surveillance systems can be augmented to collect data from industries in which productivity measures are standardized, such as local, state, and national employment data collected from the U.S. Bureau of Labor Statistics. Such data will facilitate calculations of benefits, play a critical role in assessing the generalizability of the results thus far uncovered, and provide a database through which new channels of influence can be explored. For industries in which productivity measures are not standardized, national data on worker hours and absences that could be matched to environmental data could prove useful in uncovering morbidity impacts and how they affect labor markets.

The ideal data collection effort would provide rich spatial and temporal resolution at the level of individual workers. Because such data would provide valuable intelligence on the state of the economy more generally, it would naturally fall in the United States under the jurisdiction of the Departments of Labor or Commerce. Absent resources for substantial new data collection efforts, some of these data could be collected through supplements to existing efforts by the Census Bureau, including the Annual Survey of Manufacturers and the every-5-year Economic Census for industries outside of manufacturing.

The impacts of pollution on labor markets and human capital suggest that policy implications extend beyond the EPA, transforming part of this problem into an occupational safety issue. As such, the Occupational Safety and Health Administration, both in the United States and European Union and in similar agencies in many other countries, may have a role to play in improving indoor air-quality monitoring in the workplace and fostering solutions to mitigate these impacts. If made public, these indoor air-quality measures could help overcome an important obstacle in current research and help deepen our understanding of the relationships between pollution, health, and worker productivity.

> ***"The impacts of pollution on labor markets and human capital suggest that policy implications extend beyond the EPA..."***

The long-lived impacts of pollution exposure during a brief window in early life also suggest a potential role for public health interventions that target pregnant mothers and underscore the need for more epigenetic research to uncover the mechanisms through which these impacts manifest themselves. Although the science is not completely settled, this relatively brief and well-identified period of vulnerability appears particularly ripe for small-scale interventions that can minimize exposure with large-scale returns. Health care providers and public health officials can play a more prominent role in disseminating relevant information and in facilitating access to technologies, such as home air filters, designed to eliminate harm.

Advances in information technology and measurement have allowed examination of a wide range of pollution impacts that were not visible even a decade ago. Yet, in many respects, these studies just begin to scratch the surface. Much is still unknown about how far these impacts might reach. If pollution can affect reasoned judgment and decision-making, as some recent preliminary findings suggest (*14*), then perhaps every aspect of daily living may be altered by our contaminated environment. Whether these effects of acute exposure to pollution are compounded by chronic exposure is also of great importance and is largely unknown.

Deepening our scientific understanding of these relationships is constrained by the nature of the exercise, which tends to fall between the conventional silos of major research funding agencies. The EPA spends relatively little money on external research. The health-centric focus of the National Institute of Environmental Health Science (NIEHS) has generally viewed this more expansive view of health with a skeptical eye. The Dynamics of Coupled Natural and Human Systems Program at the National Science Foundation (NSF) remains focused on a much broader scale than the studies outlined above. Broadening the scope of what constitutes health at the NIEHS, a more human-scale focus on environmental impacts at the NSF, and a more robust extramural research program at the EPA could help advance scientific understanding of these relationships.

The societal harm generated by these more subtle and pervasive impacts should be reflected in the calculus that helps to determine regulatory standards. Whether they are large enough to justify further revisions to those standards is an important question worthy of more effort and attention. ■

REFERENCES

1. U.S. EPA, "The Benefits and Costs of the Clean Air Act from 1990 to 2020: Final Report" (Office of Air and Radiation, March 2011).
2. A. Petronis, *Nature* **465**, 721 (2010).
3. R. Hanna, P. Oliva, *J. Public Econ.* **122**, 68 (2015).
4. R. Nelesen, Y. Dar, K. Thomas, J. E. Dimsdale, *Arch. Intern. Med.* **168**, 943 (2008).
5. J. Graff Zivin, M. Neidell, *Am. Econ. Rev.* **102**, 3652 (2012).
6. T. Chang, J. Graff Zivin, T. Gross, M. Neidell, *Am. Econ. J. Econ. Policy* **8**, 141 (2016).
7. A. Adhvaryu, N. Kala, A. Nyshadham, "Management and shocks to worker productivity," Mimeograph, University of Michigan Working Paper; www.achadhvaryu.com/#papers, 2016.
8. T. Chang, J. Graff Zivin, T. Gross, M. Neidell, "The Effect of Pollution on Worker Productivity: Evidence from Call-Center Workers in China," WP 22328, National Bureau of Economic Research (2016); www.nber.org/papers/w22328 (*Am. Econ. J. Appl. Econ.* 10.1257/app.20160436, forthcoming).
9. D. Almond, J. Currie, *J. Econ. Perspect.* **25**, 153 (2011).
10. N. J. Sanders, *J. Hum. Resour.* **47**, 826 (2012).
11. P. Bharadwaj, M. Gibson, J. G. Zivin, C. Neilson, *J. Assoc. Environ. Resour. Econ.* **4**, 505 (2017).
12. A. Isen, M. Rossin-Slater, W. R. Walker, *J. Polit. Econ.* **125**, 848 (2017).
13. A. McGartland *et al.*, *Science* **357**, 457 (2017).
14. A. Heyes, M. Neidell, S. Saberian, "The Effect of Air Pollution on Investor Behavior: Evidence from the S&P 500," no. w22753. National Bureau of Economic Research (2016).

10.1126/science.aap7711

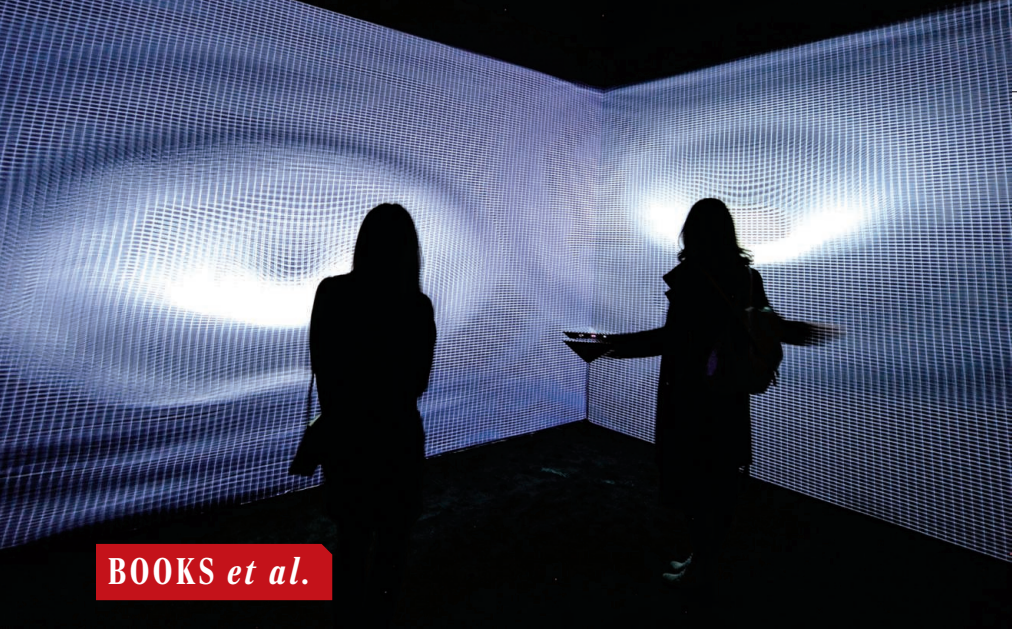

BOOKS *et al.*

An interactive video installation allows visitors to deform space-time and generate gravitational waves.

PHOTO: © MAURIZIO PERCIBALLI, INFN, SEZIONE DI ROMA SAPIENZA

PHYSICS

The art of space-time

An ambitious exhibition explores the intersection of the cosmos and contemporary artistry

By **Edwin Cartlidge**

When it comes to sparking the public's interest in science, no individual, living or dead, can rival Albert Einstein. His name and face, if not his ideas, are known the world over, and headline writers cite him eagerly to pull in readers. So perhaps it is no surprise that the Museo Nazionale delle Arti del XXI Secolo (MAXXI; National Museum of 21st Century Arts) in Rome has chosen the famous physicist as the figurehead of its latest exhibition, entitled *Gravity. Imaging the Universe After Einstein.*

Einstein's theory of gravity, known as general relativity, marks a fundamental break in our conception of the universe. Whereas Newton envisaged gravity as a force of attraction between two objects in empty space, relativity instead tells us that gravity is a distortion of space (and time) itself. The theory was published in 1915 and since then has been confirmed experimentally time and again, including the spectacular, if expected, discovery in 2015 of ripples in space-time known as gravitational waves.

The MAXXI exhibition, running until 29 April 2018, is designed to study "the meeting point of the current understanding of the cosmos and contemporary art and thinking." Or, in the words of MAXXI president Giovanna Melandri, who dreamt up the event, to show that art and science are "two lenses giving a single vision." Co-organizer Fernando Ferroni, president of Italy's National Institute of Nuclear Physics, echoes that sentiment. "Specialization in itself doesn't resolve anything," he says. "You need a big vision of society."

Whether the exhibition gives visitors that vision is debatable. The centerpiece of the show is an installation by Argentine artist Tomás Saraceno entitled "Cosmic Concert" that cleverly portrays how we influence the space-time structure of the universe just as space-time affects us. It consists of a spider slowly weaving its web, which quivers ever so slightly in response to changing sounds and other vibrations in the environment while its tiny movements are themselves picked up by sensors that in turn modify the output from an array of loudspeakers overhead.

Gravity. Imaging the Universe After Einstein
National Museum of the 21st Century Arts
Rome, Italy.
Through 29 April 2018.

Elsewhere, however, art seems thin on the ground. In one corner of the exhibition gallery sits a model of the New Jersey radio antenna that in 1965 provided the first evidence of the cosmic microwave background, very faint but ubiquitous radiation emitted just after the universe exploded into life during the Big Bang. Accompanied by a mildly hypnotic soundtrack and projection showing what appear to be bats flying through a forest, the strangely shaped device, alternately illuminated by the video and in shade, is intriguing but inert. More entertaining is footage showing an interlinked series of things (e.g., bottles, tires, candles, and balloons) rolling down planks, spilling, burning, and exploding—an "endless chain reaction of apparently insignificant events" that is thought-provoking but slightly at odds with the other items on display.

Much of the exhibition consists of scientific instruments illuminated within the otherwise almost total darkness of the gallery. These artifacts include a mirror from the Virgo detector near Pisa, which, along with the Laser Interferometer Gravitational-Wave Observatory (LIGO) facility in the United States, uses laser beams as extremely precise rulers to measure the miniscule stretching and compression of space caused by passing gravitational waves. Also on display is a model of the Laser Relativity Satellite (LARES), a 36-centimeter-diameter tungsten sphere launched by the Italian Space Agency (ASI) to measure how a rotating body distorts space-time. There is even one of Galileo's telescopes, as well as a 17th-century armillary sphere showing the orbits of planets and moons in the solar system.

These objects have considerable scholarly and historical value, and their geometry and craftsmanship confer them with undoubted beauty. But they very much lie in the scientific, rather than the artistic, realm, as do the various explanations of scientific concepts dotted around the gallery, be they in the form of written text or in animations and interactive exhibits.

Some of those explanations will make more sense to the layman than others. One video graphic, illustrating how someone on a moving train measures space and time differently from someone standing still, is a brave stab at explaining the counterintuitive effects of special relativity in a simple way. But even this is likely to be beyond the conceptual ability of most museumgoers.

Surely the aim of an exhibition like this is to pique people's curiosity and give them a very broad sense of the mind-bending concepts that underlie modern physics. The art, if well done, could whet their appetite and, as ASI's Roberto Battiston put it, "expand their horizons." But too much detail is likely to turn them off and reinforce their impression that physics is only for the eggheads, not for them. Pulling off a true synthesis of art and science is always hard, and unfortunately, with *Gravity*, MAXXI has fallen some way short. ■

The reviewer is a journalist based in Rome, Italy.
Email: edwin.cartlidge@yahoo.com

10.1126/science.aar6576

RESEARCH METHODS

Social science, today

A breezy, personal guide provides a road map to solid computational social science research

By **David Lazer**

Subatomic particle physics has CERN. Astronomy has the Hubble telescope. Social science has the Internet, smartphones, email, social media, satellites, and a myriad of other ways to follow human behavior. The gods of the information age have produced a whole panoply of technologies for social research along the journey to other destinations.

Generally, social scientists have been poorly equipped to deal with the 21st-century deluge of large-scale complex data. Computer scientists, well equipped to handle the data, are often ignorant of social theory and of foundational research methods in the social sciences. What is needed is an articulation of core principles of designing research that are accessible to multiple disciplines.

Into this breach steps Matthew Salganik. Salganik is one of the first natural-born computational social scientists, a sociologist whose doctoral work was one of the early landmark projects in the field (*1*). *Bit by Bit* is 90% textbook, 10% biography, putting into personal context issues that Salganik was among the first to wrestle with.

The volume fits solidly into a genre of textbooks in the social sciences, inaugurated in 1963 by Donald Campbell and Julian Stanley (*2*), that might be termed "practical epistemology." That is, they address such questions as these: How do we create knowledge in the social sciences? How do we measure things? What's the basis for statements like "20% of the population is X", or "X causes Y"?

In a sense, this type of textbook is about the architecture of research, the structure that will be necessary to support potential assertions. However, the range of social science research activities has changed dramatically, with profound implications for potential design.

Much as a steel frame enables the construction of buildings that reach toward the heavens and transform city skylines, the pervasive instrumentation of human behavior should likewise transform social science research. *Bit by Bit* is the first—and quite worthy—successor to the Campbell volume, aimed at informing students how to design those blueprints in the emerging field of computational social science.

Other than the introduction and conclusion, there are five core chapters to *Bit by Bit*. The first, "Observing behavior," is focused on the massive, passive data collection that occurs in everyday life, identifying key opportunities and challenges in using big data for research. "Asking questions" adapts lessons learned from survey methodology to big data: Core concerns about representativeness and measurement are amplified when recycling big data collected for other purposes.

"Running experiments" discusses the scientific potential to run heretofore inconceivably large-scale experiments. The Internet, in particular, argues Salganik, enables the facilitation of large group experiments as well as the evaluation of heterogeneity of treatment effects. "Creating mass collaboration" discusses the harnessing of the small efforts of many people for large-scale scientific applications.

The final chapter, "Ethics," is a thoughtful exposition on the core principles around ethical research generally, with a particular focus on the challenges that large-scale data collection poses. Privacy and security concerns, for example, are magnified with scale and consentless third-party data collection.

Bit by Bit
Social Research in the Digital Age
Matthew J. Salganik
Princeton University Press, 2017. 445 pp.

The text is clearly written—even breezy, in parts. It puts the reader in the shoes of the researcher: What decisions were made, why, and were those the best choices? It is suitable for an advanced undergraduate or graduate class in methodology, with a rigorous, mathematical appendix and a range of useful problems at the conclusion of each chapter.

This book is not the place to learn about cutting-edge computational techniques. However, if you want to reflect on the potential value of, say, deep learning to understanding human behavioral data, there are relevant lessons. Despite the rapid evolution of the domain, this book will likely have staying power.

It is telling that my only complaint is that I would have liked to see more topics covered. How, for example, do we translate more quasi-experimental approaches to the big data world? How do we rethink the power of panel data when there may be thousands or millions of observations per individual? How do we manage the complex workflow of a computational social science project? How do we deal with the issue of replication with data that often cannot be shared?

It may be, however, that the field more generally must advance before these chapters can be written. In the interim, *Bit by Bit* will be required reading for my students. ■

The reviewer is at the Department of Political Science and the College of Computer and Information Science, Northeastern University, Boston, MA 02115, USA, and the Institute for Quantitative Social Science, Harvard University, Cambridge, MA 02138, USA. Email: d.lazer@northeastern.edu

A deluge of digital data is transforming the way we collect and interpret social research.

PHOTO: TZIDO/ISTOCKPHOTO

REFERENCES

1. M. J. Salganik, P. S. Dodds, D. J. Watts, *Science* **311**, 854 (2006).
2. D. Campbell, J. Stanley, *Experimental and Quasi-Experimental Designs for Research* (Houghton Mifflin, Boston, 1963).

10.1126/science.aaq0679

RESEARCH

Vivax malaria uses transferrin receptor to gain entry

Gruszczyk et al., *p. 48*

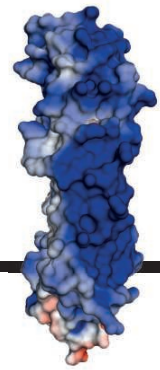

IN *SCIENCE* JOURNALS

Edited by **Stella Hurtley**

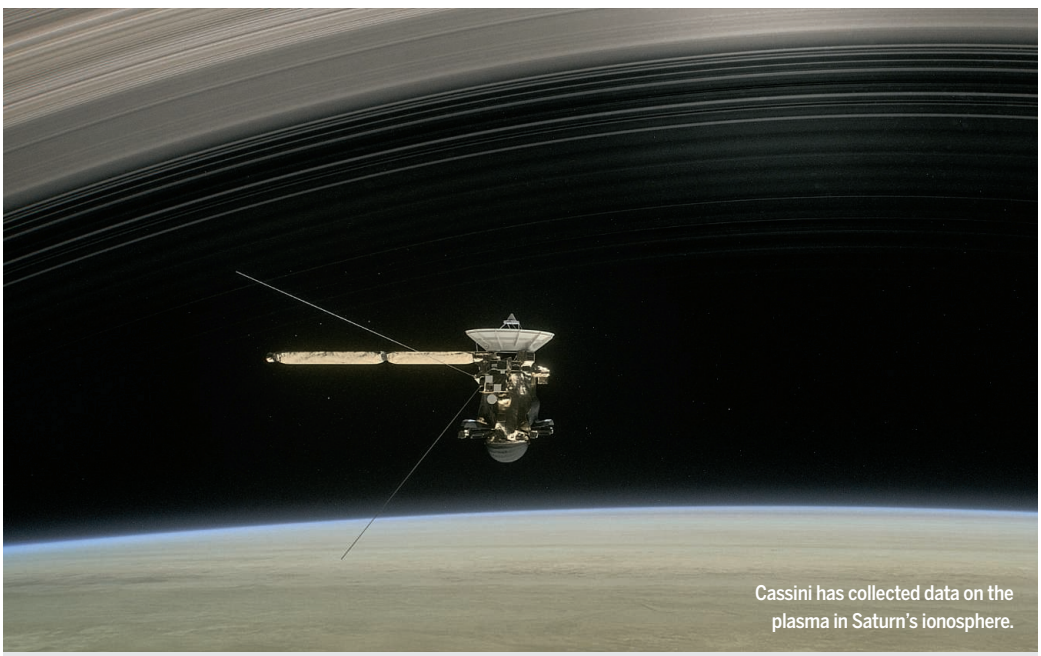

Cassini has collected data on the plasma in Saturn's ionosphere.

GAS GIANT PLANETS

Cassini enters Saturn's ionosphere

The upper reaches of most planetary atmospheres contain a layer that is ionized by incoming solar radiation—the ionosphere. As it went through its final orbits around Saturn, the Cassini spacecraft dipped close enough to the planet to pass directly through the ionosphere. Wahlund *et al*. examined the plasma data collected in situ and found that Saturn's ionosphere is highly variable and interacts with the planet's inner ring. They also observed decreases in ionization within regions shaded from the Sun by the rings. —KTS

Science, this issue p. 66

MATERIALS SCIENCE

Liquids show their strength

Dielectric elastomer actuators are electrically powered muscle mimetics that offer high actuation strain and high efficiency but are limited by failure caused by high electric fields and aging. Acome *et al*. used a liquid dielectric, rather than an elastomeric polymer, to solve a problem of catastrophic failure in dielectric elastomer actuators. The dielectric's liquid nature allowed it to self-heal—something that would not be possible with a solid dielectric. The approach allowed the authors to exploit electrostatic and hydraulic forces to achieve muscle-like contractions in a powerful but delicate gripper. —MSL

Science, this issue p. 61

TOPOLOGICAL MATTER

Heating up the quantum spin Hall effect

Taking practical advantage of the topologically protected conducting edge states of topological insulators (TIs) has proven difficult. Semiconductor systems that have been identified as two-dimensional TIs must be cooled down to near liquid helium temperatures to bring out their topological character. Wu *et al*. fabricated a heterostructure consisting of a monolayer of WTe_2 placed between two layers of hexagonal boron nitride and found that its topological properties persisted up to a relatively high temperature of 100 K. Engineering this so-called quantum spin Hall effect in a van der Waals heterostructure makes it possible to apply many established experimental tools and functionalities. —JS

Science, this issue p. 76

CANCER IMMUNOTHERAPY

Good bacteria help fight cancer

Resident gut bacteria can affect patient responses to cancer immunotherapy (see the Perspective by Jobin). Routy *et al*. show that antibiotic consumption is associated with poor response to immunotherapeutic PD-1 blockade. They profiled samples from patients with lung and kidney cancers and found that nonresponding patients had low levels of the bacterium *Akkermansia muciniphila*. Oral supplementation of the bacteria to antibiotic-treated mice restored the response to immunotherapy. Matson *et al*. and Gopalakrishnan *et al*. studied melanoma patients receiving PD-1 blockade and found a greater abundance of "good" bacteria in the guts of responding patients. Nonresponders had an imbalance in gut flora composition, which correlated with impaired immune cell activity. Thus, maintaining healthy gut flora could help patients combat cancer. —PNK

Science, this issue p. 91, p. 104, p. 97; see also p. 32

CREDITS: (TOP TO BOTTOM) GRUSZCZYK *ET AL.*; NASA/JPL-CALTECH

Published by AAAS

MOLECULAR BIOLOGY

Mitosis-specific role of ATR

The ATR (ataxia telangiectasia mutated and Rad3-related) kinase plays important roles in the S phase and during the DNA damage response to safeguard genome integrity. Kabeche *et al.* identified a distinct ATR activation pathway in mitosis that is also critical for suppressing genome instability (see the Perspective by Saldivar and Cimprich). ATR is recruited by Aurora A and activated by R loops at centromeres of mitotic chromosomes; this leads to Aurora B activation, which is necessary for accurate chromosome segregation. This mitotic, R loop–driven ATR signaling pathway could potentially be exploited in the search for cancer therapeutics. —SYM

Science, this issue p. 108; see also p. 30

CORAL REEFS

Not enough time for recovery

Coral bleaching occurs when stressful conditions result in the expulsion of the algal partner from the coral. Before anthropogenic climate warming, such events were relatively rare, allowing for recovery of the reef between events. Hughes *et al.* looked at 100 reefs globally and found that the average interval between bleaching events is now less than half what it was before. Such narrow recovery windows do not allow for full recovery. Furthermore, warming events such as El Niño are warmer than previously, as are general ocean conditions. Such changes are likely to make it more and more difficult for reefs to recover between stressful events. —SNV

Science, this issue p. 80

In a warming world, corals struggle to recover between bleaching events.

SOCIAL SCIENCES

Global reciprocity drives cooperation

Cooperation among nations promotes international trade, law, peace, and environmental protection. But how does cooperation emerge and persist among independent, self-interested, and often competing nations? Frank *et al.* applied powerful causal inference techniques to a detailed global data set of country interactions from 1995 to 2015 to map international cooperation, influence, and reciprocity. In agreement with predictions from evolutionary game theory, reciprocity among nations, including powerful countries, is pervasive and leads to stable cooperation, even in the face of minor transgressions. —AC

Sci. Adv. 10.1126/sciadv.aao5348 (2018).

TINNITUS

The sound of silence

Tinnitus reduces the quality of life for millions of sufferers worldwide. Using a guinea pig model of tinnitus induced by noise trauma, Marks *et al.* delivered precisely timed bimodal auditory-somatosensory stimulation to induce long-term depression (LTD) in the cochlear nucleus. Twenty minutes of treatment per day reduced physiological and behavioral evidence of tinnitus in the animals. The same bimodal protocol reduced tinnitus loudness in human subjects in a double-blind, sham-controlled, crossover clinical study. Unimodal stimulation did not reduce tinnitus in the animals or the humans. This approach thus holds promise for suppressing chronic tinnitus in patients. —OMS

Sci. Transl. Med. **10**, eaal3175 (2018).

SIGNAL TRANSDUCTION

Unconventional thyroid hormone signals

Thyroid hormone canonically signals through thyroid hormone receptors to enhance transcription of target genes. There is also evidence that thyroid hormone can activate nontranscriptional signaling mechanisms. To sort out the relative importance of canonical and noncanonical signaling, Hones *et al.* generated mice in which thyroid hormone receptors were altered to prevent DNA binding and transcriptional effects (but noncanonical signaling remained) and compared thyroid hormone action in these animals with that in wild-type mice or mice lacking thyroid hormone receptors entirely. They found that in vivo, several physiological actions of thyroid hormone—including regulation of body temperature, glucose and triglyceride concentrations in the blood, and heart rate—all appear to be mediated by noncanonical or nontranscriptional mechanisms. —LBR

Proc. Natl. Acad. Sci. U.S.A. 10.1073/pnas.1706801115 (2017).

BIOCATALYSIS

Guiding an enzyme all around a ring

Most compounds of interest for pharmaceuticals, agrochemicals, and cosmetics have many C–H bonds, interspersed with a few carbon bonds to heavier elements that give them their distinct properties. Chemists therefore prize methods that let them selectively modify a variety of C–H bonds. Gilbert *et al.* report a versatile strategy that relies on a tethered amine to steer an engineered cytochrome P450 enzyme around 11- or 12-membered rings, transforming specific C–H bonds into C–O bonds. Subtle structural variation of the tether through click chemistry tunes the site selectivity. —JSY

ACS Cent. Sci. 10.1021/acscentsci.7b00450 (2017).

MINOR PLANETS

An object from beyond the solar system

Gravitational interactions occasionally eject small bodies from the solar system, and this process is thought to have been

PHOTOS: (LEFT TO RIGHT) ACRO_PHUKET/SHUTTERSTOCK.COM; DENNIS KUNKEL MICROSCOPY/SCIENCE SOURCE

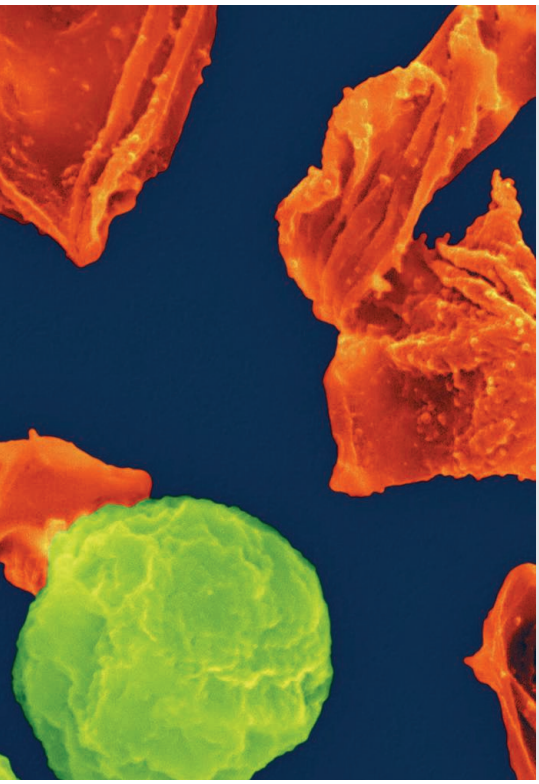

PARASITE GENOMICS

Single-cell sequencing of malarial genomes

Infection with the parasite *Plasmodium falciparum* causes malaria. Individuals may be infected with multiple strains of *P. falciparum*, some of which may be drug-resistant. Understanding the complexity of these infections may provide information about the diversity of the parasite population and aid in drug-targeting strategies. Overcoming the difficulties caused by AT bias in the *Plasmodium* genome, Trevino *et al.* optimized single-cell sequencing for late-stage *P. falciparum* parasites within infected individuals. From this analysis, they documented at least seven distinct parasitic haplotypes, traced meiotic events and hence relatedness among parasitic lineages, and found distinct single-nucleotide variants that could be used for bulk analysis. —LMZ

Genome Biol. Evol. 10.1093/gbe/evx256 (2017).

Single-cell sequencing of *Plasmodium*, here released from lysed red blood cells, allows for tracking of variation in the host.

particularly common while the system was first forming. The same thing should have occurred around other stars, casting comets and asteroids into interstellar space, but no such interstellar objects have been identified. Meech *et al.* discovered a small object, now formally designated 1I/2017 U1 ('Oumuamua), whose trajectory indicates that it arrived from interstellar space. Changes in its brightness demonstrate that 'Oumuamua is rotating and is several times longer than it is wide. 'Oumuamua is quickly passing through the solar system and soon will resume its interstellar journey. —KTS

Nature 10.1038/nature25020 (2017).

MICROBIOTA

Eats leaves and grooms

The gut microbiota influences many aspects of mammalian development and physiology. Yet we have a poor understanding of how the gut microbiota is acquired and assembled. We know that social networks are important for the transmission of pathogens, but are they also implicated in transmission of symbionts? Perofsky *et al.* investigated the microbiota of a social primate, a lemur species called Verreaux's sifaka, living in the wild in Madagascar. These lemurs eat leaves and have a distinctive microbiota capable of digesting and detoxifying plant matter. The authors found that sex, dominance, and age influenced gut microbial composition, but social group membership explained 58% of the variation. Grooming and scent-marking are essential for lemur social cohesion, and commensal microbes are transferred between individuals through this type of intimate contact, rather than being regulated by genetics or diet. —CA

Proc. R. Soc. B **284**, 20172274 (2017).

Social interaction among Verreaux's sifaka is responsible for transmission of gut microbes that are essential for digestion of their leaf-based diet.

PHOTO: HAJAKELY/SHUTTERSTOCK.COM

BIOLOGY

Cytoplasmic transfer to tumor cells

Macrophages are innate immune cells that, when recruited to tumors, can promote tumor progression. Macrophage activity and phenotype can be influenced by molecules secreted by tumor cells. To monitor macrophage behavior, Roh-Johnson *et al.* used time-lapse imaging of a zebrafish model of melanoma. Unexpectedly, macrophages not only bound to but also transferred their cytoplasm into melanoma cells, which promoted metastasis. Macrophage cytoplasmic transfer to melanoma cells also correlated with metastasis in mice. This unusual mechanism of cell-cell signaling raises questions about how such intercellular communication is regulated and what molecules are transferred to melanoma cells to promote their metastasis. —GKA

Dev. Cell **43**, 549 (2017).

TRANSLATION

Ribosomes ignore the stop sign

Aminoglycoside antibiotics bind to bacterial ribosomes and inhibit protein synthesis. Eukaryotic ribosomes, in contrast, are not strongly inhibited by these molecules but show errors such as inaccurate translation and read-through of stop codons. Prokhorova *et al.* determined structures of the eukaryotic ribosome in complex with aminoglycoside antibiotics and investigated how these molecules alter the conformation of the ribosome. They found distinct binding sites for different classes of aminoglycosides and multiple possible binding sites on each ribosome. The conformational changes induced by these molecules suggest multiple mechanisms by which the antibiotics interfere with eukaryotic translation. —MAF

Proc. Natl. Acad. Sci. U.S.A. 10.1073/pnas.1715501114 (2017).

ALSO IN *SCIENCE* JOURNALS

Edited by **Stella Hurtley**

OCEANS

Beneath the waves, oxygen disappears

As plastic waste pollutes the oceans and fish stocks decline, unseen below the surface another problem grows: deoxygenation. Breitburg *et al*. review the evidence for the downward trajectory of oxygen levels in increasing areas of the open ocean and coastal waters. Rising nutrient loads coupled with climate change—each resulting from human activities—are changing ocean biogeochemistry and increasing oxygen consumption. This results in destabilization of sediments and fundamental shifts in the availability of key nutrients. In the short term, some compensatory effects may result in improvements in local fisheries, such as in cases where stocks are squeezed between the surface and elevated oxygen minimum zones. In the longer term, these conditions are unsustainable and may result in ecosystem collapses, which ultimately will cause societal and economic harm. —CA

Science, this issue p. 46

CELL BIOLOGY

Biophysical responses of proteins to stress

Much recent work has focused on liquid-liquid phase separation as a cellular response to changing physicochemical conditions. Because phase separation responds critically to small changes in conditions such as pH, temperature, or salt, it is in principle an ideal way for a cell to measure and respond to changes in the environment. Small pH changes could, for instance, induce phase separation of compartments that store, protect, or inactivate proteins. Franzmann *et al*. used the yeast translation termination factor Sup35 as a model for a phase separation–induced stress response. Lowering the pH induced liquid-liquid phase separation of Sup35. The resulting liquid compartments subsequently hardened into gels, which sequestered the termination factor. Raising the pH triggered dissolution of the gels, concomitant with translation restart. Protecting Sup35 in gels could provide a fitness advantage to recovering yeast cells that must restart the translation machinery after stress. —SMH

Science, this issue p. 47

MALARIA

Vivax malaria host receptor

Human malaria is caused by half a dozen species of *Plasmodium* protozoan parasites, each with distinctive biology. *P. vivax*, which causes relapsing malaria, specifically parasitizes immature red blood cells called reticulocytes. Gruszczyk *et al*. identified TfR1 (host transferrin receptor 1) as an alternative receptor for *P. vivax*. TfR1 binds to a specific *P. vivax* surface protein. However, the parasite that causes cerebral malaria, *P. falciparum*, does not share TfR1 as a receptor: *P. falciparum* could still infect cells in which TfR1 expression was knocked down, but *P. vivax* could not. Monoclonal antibodies to the *P. vivax* protein successfully hindered *P. vivax* infection of red blood cells. –CA

Science, this issue p. 48

COMPARATIVE GENOMICS

Examining the consequences of selfing

The *Caenorhabditis* genus of nematodes includes a mix of closely related outcrossing and self-fertilizing (selfing) species. Genome size differs widely among these different species. Yin *et al*. generated a genome assembly for the outcrossing nematode *C. nigoni* and compared it with that of its close relative, the selfing *C. briggsae*. *C. briggsae* has experienced a substantial decrease in genome size since the two species' recent divergence. The underlying causes of this size difference appear to involve a decrease in protein-coding genes and changes in other types of sequences that have homology with RNAs expressed primarily in *C. nigoni* males. One of the implicated gene families, the mss family, compromises sperm competitiveness. Thus, in nematodes, selfing appears to result in a decrease in genome size owing to selection to reduce male reproductive function. —LMZ

Science, this issue p. 55

STELLAR ASTROPHYSICS

Observing more massive stars

The number of stars that form at each mass is known as the initial mass function (IMF). For most masses, the IMF follows a power-law distribution, first determined by Edwin Salpeter in 1955. Schneider *et al*. used observations of the nearby star-forming region 30 Doradus (also known as the Tarantula Nebula) and combined these with stellar modeling to determine its IMF. They found more stars above 30 solar masses than predicted by the Salpeter distribution. Because the most massive stars also have the biggest influence on their surroundings—for instance, through ultraviolet radiation, stellar winds, supernova explosions, and production of heavy elements—this excess will have wide-ranging implications. —KTS

Science, this issue p. 69

POLYMERS

A healing squeeze

The very long molecules found in synthetic polymers, and their tendency to entangle and partially crystallize, impart many of the polymers' useful properties. However, these same characteristics also mean that chain dynamics are slow, which impedes potential self-healing. Yanagisawa *et al*. developed a family of ether-thiourea linear polymers that form hydrogen-bonded networks and still manage to stay amorphous. The polymers are stiff, showing the strength of the hydrogen bonding; however, because these bonds can easily reform, the polymer is also able to self-heal when compressed. —MSL

Science, this issue p. 72

HIV SUSCEPTIBILITY

Inhibiting natural killer cells in AIDS

The human leukocyte antigen (HLA) gene complex varies enormously among individuals and helps explain individual variation in immunity to infectious diseases. Ramsuran *et al*. examined data from almost 10,000 HIV infections. Expression of the *HLA-A* and *-B* alleles was associated with higher viral load, reduced $CD4^+$ T cell counts, and accelerated progression to AIDS. Higher levels of *HLA-A* expression increased expression of *HLA-E*, which blocks a specific receptor (NKG2A) on the immune cells that normally eliminate virus-infected cells. Thus, targeting NKG2A might provide a therapeutic avenue for HIV treatment. —CA

Science, this issue p. 86

ECOLOGICAL GENOMICS

Yellow warblers already in decline

As the climate changes, species' ability to adapt to changing conditions may relate directly to their future persistence. Determining whether and when this will happen is challenging, however, because it is difficult to tease apart the causes of decline or maintenance. Bay *et al*. looked at the relationship

between genomic variation and the environment in North American populations of the yellow warbler (see the Perspective by Fitzpatrick and Edelsparre). Genes linked to exploratory and migratory behavior were important for successful climate adaptation. Furthermore, populations identified as "genetically vulnerable" because of limited climate-associated genomic variation were already declining. —SNV

Science, this issue p. 83; see also p. 29

IMMUNOLOGY

Inflammatory ILC2s are itinerant sentinels

Group 2 innate lymphoid cells (ILC2s) are a population of immune cells that play important roles in tissue homeostasis and barrier immunity to helminths. Recent work has suggested that ILC2s are primarily long-term residents of tissues that do not readily recirculate. Huang *et al*. now demonstrate, however, that these findings do not necessarily hold true for the interleukin-25 (IL-25)–responsive KLRG1^{hi} "inflammatory" ILC2 (iILC2) subset (see the Perspective by Mjösberg and Rao). In response to exogenous IL-25 or helminth infection, iILC2 precursors in the small intestinal lamina propria proliferate and alter their expression of sphingosine 1-phosphate (S1P) receptors. They then traffic to both lymphatic and nonlymphatic organs in a partly S1P-dependent manner, participating in vital anti-helminth and tissue repair responses. —STS

Science, this issue p. 114; see also p. 36

OCEANS

To mine or not to mine

The seafloor contains large amounts of valuable minerals that are increasingly seen as viable mining targets. In a Perspective, Boetius and Haeckel argue that such mining would carry large environmental risks—for example, to little-known ecological communities in the deep sea. Mining impacts in such environments would be difficult and expensive to remediate, and research knowledge from small-scale experiments is difficult to extrapolate to the commercial scale. The authors call for an integrated research and regulatory framework that protects the seafloor. —JFU

Science, this issue p. 34

CANCER IMMUNOTHERAPY

Taking aim at regulatory T cells

Cancer immunotherapy attempts to stimulate the patient's immune system against a tumor, but it can be limited by the suppressive effects of the patient's own regulatory T (T_{reg}) cells. Nie *et al*. showed that coinhibiting a TNF (tumor necrosis factor) receptor reduced T_{reg} cell activity and proliferation, stimulated antitumor immune memory, and even shrank colon and breast tumors in mice that were unresponsive to common single-agent immunotherapies. Thus, adding anti-TNF therapeutics may help to increase and broaden the efficacy of immunotherapy for cancer patients. —LKF

Sci. Signal. **10**, eaan0790 (2018).

HUMAN IMMUNOLOGY

Taking a look at lipid surveillance

Human group 2 innate lymphoid cells (ILC2s) play roles in maintaining homeostasis and defending against pathogens, but dysregulated ILC2 responses have been linked to asthma and allergic responses. Hardman *et al*. used an in vivo human skin challenge model to show that ILC2s express CD1a, which is regulated by the cytokine TSLP. CD1a$^+$ ILC2s can present endogenous lipid antigens to CD1a-reactive T cells and induce inflammatory responses. CD1a$^+$ ILC2s expressed the phospholipase PLA2G4A, contributing to CD1a-mediated T cell activation. This pathway was involved in sensing *Staphylococcus aureus*–associated skin inflammation. Thus, lipid sensing by skin-resident ILC2s may contribute to atopic skin inflammation and pathogen surveillance. —CNF

Sci. Immunol. **2**, eaan5918 (2017).

REVIEW SUMMARY

OCEANS

Declining oxygen in the global ocean and coastal waters

Denise Breitburg,* Lisa A. Levin, Andreas Oschlies, Marilaure Grégoire, Francisco P. Chavez, Daniel J. Conley, Véronique Garçon, Denis Gilbert, Dimitri Gutiérrez, Kirsten Isensee, Gil S. Jacinto, Karin E. Limburg, Ivonne Montes, S. W. A. Naqvi, Grant C. Pitcher, Nancy N. Rabalais, Michael R. Roman, Kenneth A. Rose, Brad A. Seibel, Maciej Telszewski, Moriaki Yasuhara, Jing Zhang

BACKGROUND: Oxygen concentrations in both the open ocean and coastal waters have been declining since at least the middle of the 20th century. This oxygen loss, or deoxygenation, is one of the most important changes occurring in an ocean increasingly modified by human activities that have raised temperatures, CO_2 levels, and nutrient inputs and have altered the abundances and distributions of marine species. Oxygen is fundamental to biological and biogeochemical processes in the ocean. Its decline can cause major changes in ocean productivity, biodiversity, and biogeochemical cycles. Analyses of direct measurements at sites around the world indicate that oxygen-minimum zones in the open ocean have expanded by several million square kilometers and that hundreds of coastal sites now have oxygen concentrations low enough to limit the distribution and abundance of animal populations and alter the cycling of important nutrients.

ADVANCES: In the open ocean, global warming, which is primarily caused by increased greenhouse gas emissions, is considered the primary cause of ongoing deoxygenation. Numerical models project further oxygen declines during the 21st century, even with ambitious emission reductions. Rising global temperatures decrease oxygen solubility in water, increase the rate of oxygen consumption via respiration, and are predicted to reduce the introduction of oxygen from the atmosphere and surface waters into the ocean interior by increasing stratification and weakening ocean overturning circulation.

In estuaries and other coastal systems strongly influenced by their watershed, oxygen declines have been caused by increased loadings of nutrients (nitrogen and phosphorus) and organic matter, primarily from agriculture; sewage; and the combustion of fossil fuels. In many regions, further increases in nitrogen discharges to coastal waters are projected as human populations and agricultural production rise. Climate change exacerbates oxygen decline in coastal systems through similar mechanisms as those in the open ocean, as well as by increasing nutrient delivery from watersheds that will experience increased precipitation.

Expansion of low-oxygen zones can increase production of N_2O, a potent greenhouse gas; reduce eukaryote biodiversity; alter the structure of food webs; and negatively affect food security and livelihoods. Both acidification and increasing temperature are mechanistically linked with the process of deoxygenation and combine with low-oxygen conditions to affect biogeochemical, physiological, and ecological processes. However, an important paradox to consider in predicting large-scale effects of future deoxygenation is that high levels of productivity in nutrient-enriched coastal systems and upwelling areas associated with oxygen-minimum zones also support some of the world's most prolific fisheries.

ON OUR WEBSITE

Read the full article at http://dx.doi.org/10.1126/science.aam7240

OUTLOOK: Major advances have been made toward understanding patterns, drivers, and consequences of ocean deoxygenation, but there is a need to improve predictions at large spatial and temporal scales important to ecosystem services provided by the ocean. Improved numerical models of oceanographic processes that control oxygen depletion and the large-scale influence of altered biogeochemical cycles are needed to better predict the magnitude and spatial patterns of deoxygenation in the open ocean, as well as feedbacks to climate. Developing and verifying the next generation of these models will require increased in situ observations and improved mechanistic understanding on a variety of scales. Models useful for managing nutrient loads can simulate oxygen loss in coastal waters with some skill, but their ability to project future oxygen loss is often hampered by insufficient data and climate model projections on drivers at appropriate temporal and spatial scales. Predicting deoxygenation-induced changes in ecosystem services and human welfare requires scaling effects that are measured on individual organisms to populations, food webs, and fisheries stocks; considering combined effects of deoxygenation and other ocean stressors; and placing an increased research emphasis on developing nations. Reducing the impacts of other stressors may provide some protection to species negatively affected by low-oxygen conditions. Ultimately, though, limiting deoxygenation and its negative effects will necessitate a substantial global decrease in greenhouse gas emissions, as well as reductions in nutrient discharges to coastal waters. ■

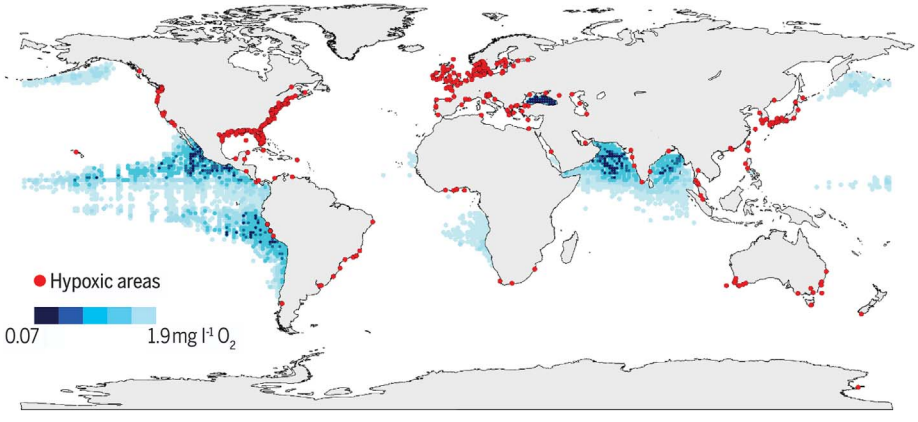

Low and declining oxygen levels in the open ocean and coastal waters affect processes ranging from biogeochemistry to food security. The global map indicates coastal sites where anthropogenic nutrients have exacerbated or caused O_2 declines to <2 mg liter^{-1} (<63 μmol liter^{-1}) (red dots), as well as ocean oxygen-minimum zones at 300 m of depth (blue shaded regions). [Map created from data provided by R. Diaz, updated by members of the GO$_2$NE network, and downloaded from the World Ocean Atlas 2009].

The list of author affiliations is available in the full article online.
*Corresponding author. Email: breitburgd@si.edu
Cite this article as D. Breitburg *et al.*, *Science* **359**, eaam7240 (2018). DOI: 10.1126/science.aam7240

REVIEW

OCEANS

Declining oxygen in the global ocean and coastal waters

Denise Breitburg,[1]* Lisa A. Levin,[2] Andreas Oschlies,[3] Marilaure Grégoire,[4] Francisco P. Chavez,[5] Daniel J. Conley,[6] Véronique Garçon,[7] Denis Gilbert,[8] Dimitri Gutiérrez,[9,10] Kirsten Isensee,[11] Gil S. Jacinto,[12] Karin E. Limburg,[13] Ivonne Montes,[14] S. W. A. Naqvi,[15]† Grant C. Pitcher,[16,17] Nancy N. Rabalais,[18] Michael R. Roman,[19] Kenneth A. Rose,[19] Brad A. Seibel,[20] Maciej Telszewski,[21] Moriaki Yasuhara,[22] Jing Zhang[23]

Oxygen is fundamental to life. Not only is it essential for the survival of individual animals, but it regulates global cycles of major nutrients and carbon. The oxygen content of the open ocean and coastal waters has been declining for at least the past half-century, largely because of human activities that have increased global temperatures and nutrients discharged to coastal waters. These changes have accelerated consumption of oxygen by microbial respiration, reduced solubility of oxygen in water, and reduced the rate of oxygen resupply from the atmosphere to the ocean interior, with a wide range of biological and ecological consequences. Further research is needed to understand and predict long-term, global- and regional-scale oxygen changes and their effects on marine and estuarine fisheries and ecosystems.

Oxygen levels have been decreasing in the open ocean and coastal waters since at least the middle of the 20th century (*1*–*3*). This ocean deoxygenation ranks among the most important changes occurring in marine ecosystems (*1*, *4*–*6*) (Figs. 1 and 2). The oxygen content of the ocean constrains productivity, biodiversity, and biogeochemical cycles. Major extinction events in Earth's history have been associated with warm climates and oxygen-deficient oceans (*7*), and under current trajectories, anthropogenic activities could drive the ocean toward widespread oxygen deficiency within the next thousand years (*8*). In this Review, we refer to "coastal waters" as systems that are strongly influenced by their watershed, and the "open ocean" as waters in which such influences are secondary.

The open ocean lost an estimated 2%, or 4.8 ± 2.1 petamoles (77 billion metric tons), of its oxygen over the past 50 years (*9*). Open-ocean oxygen-minimum zones (OMZs) have expanded by an area about the size of the European Union (4.5 million km^2, based on water with <70 μmol kg^{-1} oxygen at 200 m of depth) (*10*), and the volume of water completely devoid of oxygen (anoxic) has more than quadrupled over the same period (*9*). Upwelling of oxygen-depleted water has intensified in severity and duration along some coasts, with serious biological consequences (*11*).

Since 1950, more than 500 sites in coastal waters have reported oxygen concentrations ≤2 mg $liter^{-1}$ (=63 μmol $liter^{-1}$ or ≅61 μmol kg^{-1}), a threshold often used to delineate hypoxia (*3*, *12*) (Fig. 1A). Fewer than 10% of these systems were known to have hypoxia before 1950. Many more water bodies may be affected, especially in developing nations where available monitoring data can be sparse and inadequately accessed even for waters receiving high levels of untreated human and agricultural waste. Oxygen continues to decline in some coastal systems despite substantial reductions in nutrient loads, which have improved other water quality metrics (such as levels of chlorophyll a) that are sensitive to nutrient enrichment (*13*).

Oxygen is naturally low or absent where biological oxygen consumption through respiration exceeds the rate of oxygen supplied by physical transport, air-sea fluxes, and photosynthesis for sufficient periods of time. A large variety of such systems exist, including the OMZs of the open ocean, the cores of some mode-water eddies, coastal upwelling zones, deep basins of semi-enclosed seas, deep fjords, and shallow productive waters with restricted circulation (*14*, *15*). Whether natural or anthropogenically driven, however, low oxygen levels and anoxia leave a strong imprint on biogeochemical and ecological processes. Electron acceptors, such as Fe(III) and sulfate, that replace oxygen as conditions become anoxic yield less energy than aerobic respiration and constrain ecosystem energetics (*16*). Biodiversity, eukaryotic biomass, and energy-intensive ecological interactions such as predation are reduced (*17*–*19*), and energy is increasingly transferred to microbes (*3*, *16*). As oxygen depletion becomes more severe, persistent, and widespread, a greater fraction of the ocean is losing its ability to support high-biomass, diverse animal assemblages and provide important ecosystem services.

But the paradox is that these areas, sometimes called dead zones, are far from dead. Instead they contribute to some of the world's most productive fisheries harvested in the adjacent, oxygenated waters (*20*–*22*) and host thriving microbial assemblages that utilize a diversity of biogeochemical pathways (*16*). Eukaryote organisms that use low-oxygen habitats have evolved physiological and behavioral adaptations that enable them to extract, transport, and store sufficient oxygen, maintain aerobic metabolism, and reduce energy demand (*23*–*26*). Fishes, for example, adjust ventilation rate, cardiac activity, hemoglobin content, and O_2 binding and remodel gill morphology to increase lamellar surface area (*27*). For some small taxa, including nematodes and polychaetes, high surface area–to–volume ratios enhance diffusion and contribute to hypoxia tolerance (*26*). Metabolic depression (*23*, *25*, *28*) and high H_2S tolerance (*24*) are also key adaptations by organisms to hypoxic and anoxic environments.

Causes of oxygen decline

Global warming as a cause of oxygen loss in the open ocean

The discovery of widespread oxygen loss in the open ocean during the past 50 years depended on repeated hydrographic observations that revealed oxygen declines at locations ranging from the northeast Pacific (*29*) and northern Atlantic (*30*) to tropical oceans (*2*). Greenhouse gas–driven global warming is the likely ultimate cause of this ongoing deoxygenation in many parts of the open

[1]Smithsonian Environmental Research Center, Edgewater, MD 21037, USA. [2]Center for Marine Biodiversity and Conservation and Integrative Oceanography Division, Scripps Institution of Oceanography, University of California, San Diego, CA 92093, USA. [3]GEOMAR Helmholtz Centre for Ocean Research Kiel, 24105 Kiel, Germany. [4]Department of Astrophysics, Geophysics and Oceanography, MAST-FOCUS Research Group, Université de Liège, 4000 Liège, Belgium. [5]Monterey Bay Aquarium Research Institute, Moss Landing, CA 95039, USA. [6]Department of Geology, Lund University, Sölvegatan 12, SE-223 62 Lund, Sweden. [7]CNRS/Laboratoire d'Etudes en Géophysique et Océanographie Spatiales, 31401 Toulouse, CEDEX 9, France. [8]Maurice-Lamontagne Institute, Fisheries and Oceans Canada, Mont-Joli, Québec G5H 3Z4, Canada. [9]Instituto del Mar del Perú (IMARPE), Esquina Gamarra y General Valle s/n, Callao, Peru. [10]Facultad de Ciencias y Filosofía, Programa de Maestría en Ciencias del Mar, Universidad Peruana Cayetano Heredia, Lima 31, Peru. [11]Intergovernmental Oceanographic Commission of UNESCO, 75732 Paris, CEDEX 7, France. [12]The Marine Science Institute, University of the Philippines, Diliman, Quezon City, Philippines. [13]State University of New York College of Environmental Science and Forestry, Syracuse, NY 13210, USA. [14]Instituto Geofísico del Perú, Lima, Perú. [15]Environment and Life Sciences Research Center, Kuwait Institute for Scientific Research, Salmiya, 22017 Kuwait. [16]Fisheries Research and Development, Department of Agriculture, Forestry and Fisheries, Cape Town, South Africa. [17]Department of Biological Sciences, University of Cape Town, South Africa. [18]Department of Oceanography and Coastal Sciences, Louisiana State University, Baton Rouge, LA 70803, USA. [19]University of Maryland Center for Environmental Science, Horn Point Laboratory, Cambridge, MD 21613, USA. [20]College of Marine Science, University of South Florida, St. Petersburg, FL 33701, USA. [21]International Ocean Carbon Coordination Project, Institute of Oceanology of Polish Academy of Sciences, Ul. Powstancow Warszawy 55, 81-712 Sopot, Poland. [22]School of Biological Sciences and Swire Institute of Marine Science, University of Hong Kong, Hong Kong SAR, China. [23]State Key Laboratory of Estuarine and Coastal Research, East China Normal University, Shanghai 200062, China.
***Corresponding author. Email: breitburgd@si.edu** †Present address: Council of Scientific and Industrial Research, Rafi Marg, New Delhi, India.

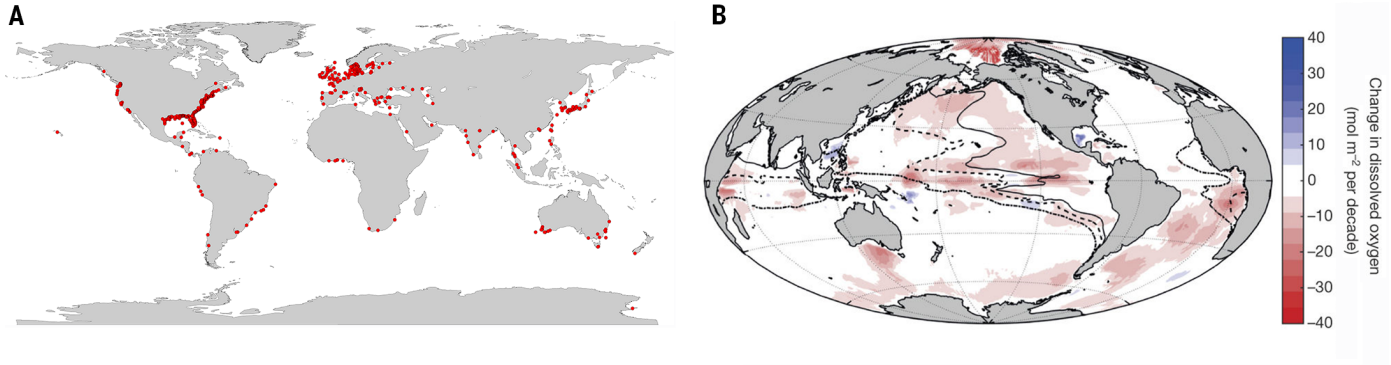

Fig. 1. Oxygen has declined in both the open ocean and coastal waters during the past half-century. (**A**) Coastal waters where oxygen concentrations ≤61 μmol kg^{-1} (63 μmol liter^{-1} or 2 mg liter^{-1}) have been reported (red) (*8*, *12*). [Map created from data in (*8*) and updated by R. Diaz and authors] (**B**) Change in oxygen content of the global ocean in mol O_2 m^{-2} decade^{-1} (*9*). Most of the coastal systems shown here reported their first incidence of low oxygen levels after 1960. In some cases, low oxygen may have occurred earlier but was not detected or reported. In other systems (such as the Baltic Sea) that reported low levels of oxygen before 1960, low-oxygen areas have become more extensive and severe (*59*). Dashed-dotted, dashed, and solid lines delineate boundaries with oxygen concentrations <80, 40, and 20 μmol kg^{-1}, respectively, at any depth within the water column (*9*). [Reproduced from (*9*)]

ocean (*31*). For the upper ocean over the period 1958–2015, oxygen and heat content are highly correlated with sharp increases in both deoxygenation and ocean heat content, beginning in the mid-1980s (*32*).

Ocean warming reduces the solubility of oxygen. Decreasing solubility is estimated to account for ~15% of current total global oxygen loss and >50% of the oxygen loss in the upper 1000 m of the ocean (*9*, *33*). Warming also raises metabolic rates, thus accelerating the rate of oxygen consumption. Therefore, decomposition of sinking particles occurs faster, and remineralization of these particles is shifted toward shallower depths (*34*), resulting in a spatial redistribution but not necessarily a change in the magnitude of oxygen loss.

Intensified stratification may account for the remaining 85% of global ocean oxygen loss by reducing ventilation—the transport of oxygen into the ocean interior—and by affecting the supply of nutrients controlling production of organic matter and its subsequent sinking out of the surface ocean. Warming exerts a direct influence on thermal stratification and indirectly enhances salinity-driven stratification through its effects on ice melt and precipitation. Increased stratification alters the mainly wind-driven circulation in the upper few hundred meters of the ocean and slows the deep overturning circulation (*9*). Reduced ventilation, which may also be influenced by decadal to multidecadal oscillations in atmospheric forcing patterns (*35*), has strong subsurface manifestations at relatively shallow ocean depths (100 to 300 m) in the low- to mid-latitude oceans and less pronounced signatures down to a few thousand meters at high latitudes. Oxygen declines closer to shore have also been found in some systems, including the California Current and lower Saint Lawrence Estuary, where the relative strength of various currents have changed and remineralization has increased (*36*, *37*).

There is general agreement between numerical models and observations about the total amount of oxygen loss in the surface ocean (*38*). There is also consensus that direct solubility effects do not explain the majority of oceanic oxygen decline (*31*). However, numerical models consistently simulate a decline in the total global ocean oxygen inventory equal to only about half that of the most recent observation-based estimate and also predict different spatial patterns of oxygen decline or, in some cases, increase (*9*, *31*, *39*). These discrepancies are most marked in the tropical thermocline (*40*). This is problematic for predictions of future deoxygenation, as these regions host large open-ocean OMZs, where a further decline in oxygen levels could have large impacts on ecosystems and biogeochemistry (Fig. 2A). It is also unclear how much ocean oxygen decline can be attributed to alterations in ventilation versus respiration. Mechanisms other than greenhouse gas–driven global warming may be at play in the observed ocean oxygen decline that are not well represented in current ocean models. For example, internal oscillations in the climate system, such as the Pacific Decadal Oscillation, affect ventilation processes and, eventually, oxygen distributions (*35*).

Models predict that warming will strengthen winds that favor upwelling and the resulting transport of deeper waters onto upper slope and shelf environments in some coastal areas (*41*, *42*), especially at high latitudes within upwelling systems that form along the eastern boundary of ocean basins (*43*). The predicted magnitude and direction of change is not uniform, however, either within individual large upwelling systems or among different systems. Upwelling in the southern Humboldt, southern Benguela, and northern Canary Eastern Boundary upwelling systems is predicted to increase in both duration and intensity by the end of the 21st century (*43*). Where the oxygen content of subsurface source waters declines, upwelling introduces water to the shelf that is both lower in oxygen and higher in CO_2. Along the central Oregon coast of the United States in 2006, for example, anoxic waters upwelled to depths of <50 m within 2 km of shore, persisted for 4 months, and resulted in large-scale mortality of benthic macro-invertebrates (*11*). There are no prior records of such severe oxygen depletion over the continental shelf or within the OMZ in this area (*11*).

Nutrient enrichment of coastal waters

Sewage discharges have been known to deplete oxygen concentrations in estuaries since at least the late 1800s (*44*), and by the mid 1900s the link to agricultural fertilizer runoff was discussed (*45*). Nevertheless, the number and severity of hypoxic sites has continued to increase (Fig. 2B). The human population has nearly tripled since 1950 (*46*). Agricultural production has greatly increased to feed this growing population and meet demands for increased consumption of animal protein, resulting in a 10-fold increase in global fertilizer use over the same period (*47*). Nitrogen discharges from rivers to coastal waters increased by 43% in just 30 years from 1970 to 2000 (*48*), with more than three times as much nitrogen derived from agriculture as from sewage (*49*).

Eutrophication occurs when nutrients (primarily N and P) and biomass from human waste and agriculture, as well as N deposition from fossil fuel combustion, stimulate the growth of algae and increase algal biomass. The enhanced primary and secondary production in surface waters increases the delivery rate of degradable organic matter to bottom waters where microbial decomposition by aerobic respiration consumes oxygen. Once oxygen levels are low, behavioral and biogeochemical feedbacks can hinder a return to higher-oxygen conditions (*50*). For example, burrowing invertebrates that introduce oxygen to sediments die or fail to recruit, and sediment phosphorus is released, fueling additional biological production in the water column and eventual increased oxygen consumption.

Coastal systems vary substantially in their susceptibility to developing low oxygen concentrations. Low rates of vertical exchange within the water

column reduce rates of oxygen resupply (51), and long water-retention times favor the accumulation of phytoplankton biomass (14) and its eventual subsurface degradation. Chesapeake Bay develops hypoxia and anoxia that persist for several months during late spring through early autumn and cover up to 30% of the system area. In contrast, the nearby Delaware Bay, which has weaker stratification and a shorter retention time, does not develop hypoxia, in spite of similar nutrient loads (52). Manila Bay is adjacent to a megacity and also receives similar loads on an annual basis, but it becomes hypoxic principally during the wet southwest monsoon period, when rainfall increases nutrient loads and stratification (53).

Low oxygen in coastal waters and semi-enclosed seas can persist for minutes to thousands of years and may extend over spatial scales ranging from less than one to many thousands of square kilometers. Both local and remote drivers lead to temporal and spatial variations in hypoxia. Local weather can influence oxygen depletion in very shallow water through wind mixing and the effect of cloud cover on photosynthesis (54). At larger spatial scales, variations in wind direction and speed (55), precipitation and nutrient loads (56), sea surface temperature (57), and nutrient content of water masses transported into bottom layers of stratified coastal systems contribute to interannual and longer-period variations in hypoxic volume, duration, and rate of deoxygenation (14).

Climate change in coastal waters

Warming is predicted to exacerbate oxygen depletion in many nutrient-enriched coastal systems through mechanisms similar to those of the open ocean: increased intensity and duration of stratification, decreased oxygen solubility, and accelerated respiration (4, 58, 59). The current rate of oxygen decline in coastal areas exceeds that of the open ocean (60), however, likely reflecting the combined effects of increased warming of shallow water and higher concentrations of nutrients. Higher air temperatures can result in earlier onset and longer durations of hypoxia in eutrophic systems through effects on the seasonal timing of stratification and the rate of oxygen decline (58). An ensemble modeling study of the Baltic Sea projects declining oxygen under all but the most aggressive nutrient-reduction plans, owing to increased precipitation and consequent nutrient loads, decreased flux of oxygen from the atmosphere, and increased internal nutrient cycling. Even aggressive nutrient reduction is projected to yield far less benefit under climate change than under current conditions (61).

Because of regional variations in the effects of global warming on precipitation and winds, the rate and direction of change in oxygen content is expected to vary among individual coastal water bodies (4, 58). Where precipitation increases, both stratification and nutrient discharges are expected to increase, with the reverse occurring in regions where precipitation decreases. Changes in seasonal patterns of precipitation and rates of evaporation can also be important. Coastal wetlands that remove nutrients before they reach open water are predicted to be lost as sea levels rise, decreasing capacity to remove excess nitrogen, but the rate of wetland inundation and the ability of wetlands to migrate landward will vary.

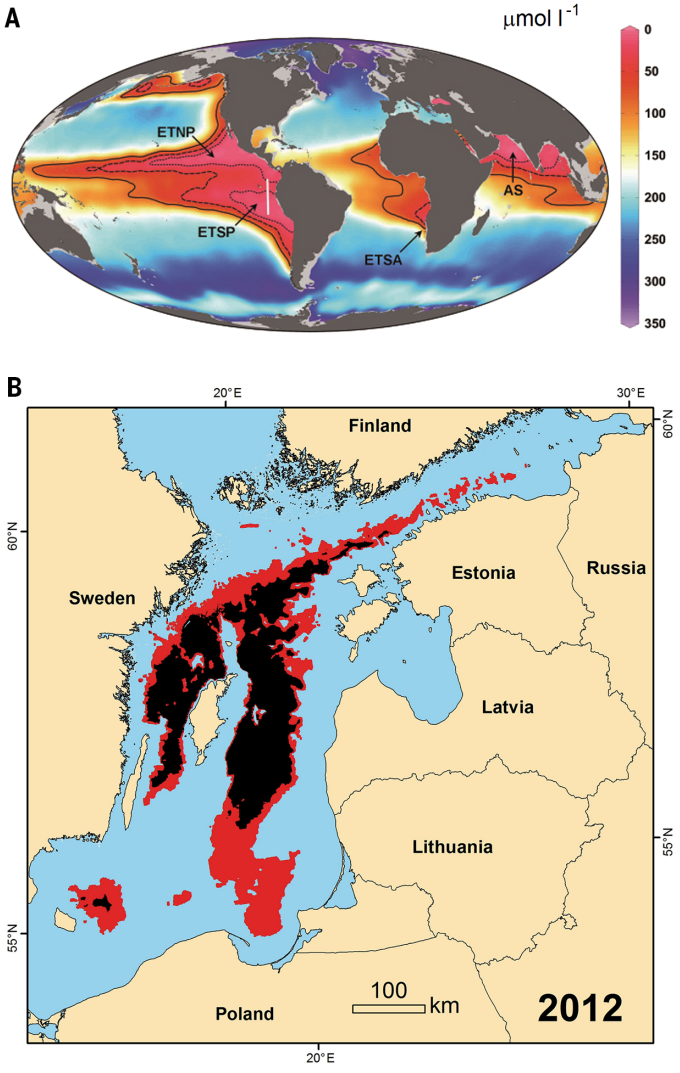

Fig. 2. Dissolved oxygen concentrations in the open ocean and the Baltic Sea. (**A**) Oxygen levels at a depth of 300 m in the open ocean. Major eastern boundary and Arabian Sea upwelling zones, where oxygen concentrations are lowest, are shown in magenta, but low oxygen levels can be detected in areas other than these major OMZs. At this depth, large areas of global ocean water have O_2 concentrations <100 µmol liter^{-1} (outlined and indicated in red). ETNP, eastern tropical North Pacific; ETSP, eastern tropical South Pacific; ETSA, eastern tropical South Atlantic; AS, Arabian Sea. [Max Planck Institute for Marine Microbiology, based on data from the World Ocean Atlas 2009] (**B**) Oxygen levels at the bottom of the Baltic Sea during 2012 (59). In recent years, low-oxygen areas have expanded to 60,000 km^2 as a result of limited exchange, high anthropogenic nutrient loads, and warming waters (59) (red, O_2 concentration ≤63 µmol liter^{-1} [2 mg liter^{-1}]; black, anoxia). [Reproduced from (59)]

Effects of ocean deoxygenation

Oxygen influences biological and biogeochemical processes at their most fundamental level (Fig. 3). As research is conducted in more habitats and using new tools and approaches, the range of effects of deoxygenation that have been identified, and the understanding of the mechanisms behind those effects, has increased substantially. Although 2 mg liter^{-1} (61 µmol kg^{-1}) is a useful threshold for defining hypoxia when the goal is to quantify the number of systems or the spatial extent of oxygen-depleted waters, a more appropriate approach when considering biological and ecological effects is to simply define hypoxia as oxygen levels sufficiently low to affect key or sensitive processes. Organisms have widely varying oxygen tolerances, even in shallow coastal systems (19). In addition, because temperature affects not only oxygen supply (through its effect on solubility and diffusion) but also the respiratory demand by organisms, oxygen limitation for organisms is better expressed as a critical oxygen partial pressure below which specific organisms exhibit reduced metabolic functions than in terms of oxygen concentration (62, 63).

Biological responses

Ocean deoxygenation influences life processes from genes to emergent properties of ecosystems (Fig. 4). All obligate aerobic organisms have limits to the severity or duration of oxygen depletion for which they can compensate. Low oxygen levels can reduce survival and growth and alter behavior of individual organisms (3, 4, 26, 64). Reproduction can be impaired by reduced energy allocation to gamete production, as well as interference with gametogenesis, neuroendocrine function, and hormone production, and can ultimately affect populations and fisheries (65–67). Exposure to hypoxia can trigger epigenetic changes expressed in future generations, even if these generations are not exposed to hypoxia (68). Brief, repeated exposure to low oxygen can alter immune

responses, increase disease, and reduce growth (69, 70).

In both oceanic and coastal systems, vertical and horizontal distributions of organisms follow oxygen gradients and discontinuities, and migratory behavior is constrained in response to both oxygen availability and the ways that oxygen alters the distributions of predators and prey (64, 71). Because oxygen tolerances and behavioral responses to low oxygen levels vary among species, taxa, trophic groups, and with mobility (19), encounter rates, feeding opportunities, and the structure of marine food webs change. Movement to avoid low oxygen can result in lost feeding opportunities on low-oxygen–tolerant prey and can increase energy expended in swimming (19, 70). Hypoxia effects on vision, a function that is highly oxygen intensive, may contribute to these constraints, in part through changing light requirements (72).

The presence and expansion of low–water column oxygen reduces diel migration depths, compressing vertical habitat and shoaling distributions of fishery species and their prey (73–75). For pelagic species, habitat compression can increase vulnerability to predation as animals are restricted to shallower, better-lit waters and can increase vulnerability to fishing by predictably aggregating individuals at shallower or lateral edges of low-oxygen zones (71, 76–78). For demersal species, hypoxia-induced habitat compression can lead to crowding and increased competition for prey (73), potentially resulting in decreased body condition of important fishery species such as Baltic cod (79).

In contrast, migration into and out of hypoxic waters can allow some animals to utilize oxygen-depleted habitats for predator avoidance or to feed on hypoxia-tolerant prey, and then to return to more highly oxygenated depths or locations (23, 80). Habitat compression may also enhance trophic efficiency in upwelling regions, contributing to their extraordinary fish productivity (20, 21). Some hypoxia-tolerant fish and invertebrate species expand their ranges as OMZs expand (28, 81), and their predators and competitors are excluded.

Multiple stressors

Deoxygenation is mechanistically linked to other ocean stressors, including warming (82) and acidification (83), and thus it is often their combined effects that shape marine ecosystems (84, 85). Because hypoxia limits energy acquisition, it is especially likely to exacerbate effects of co-occurring stressors that increase energy demands (65). The thermal tolerance of ectotherms is limited by their capacity to meet the oxygen demands of aerobic metabolism (62). Increased temperature elevates oxygen demand while simultaneously reducing oxygen supply, thus expanding the area of the oceans and coastal waters where oxygen is insufficient. Through this mechanism, ocean warming is predicted to result in shifts in the distribution of fishes and invertebrates poleward by tens to hundreds of kilometers per decade, shifts into deeper waters, and local extinctions (63, 86). Models project that warming combined with even modest O_2 declines (<10 μmol kg^{-1}) can cause declines in important fishery species that are sensitive to low oxygen levels (87). Physiological oxygen limitation in warming waters is also predicted to reduce maximum sizes of many fish species, including some that support important fisheries (88).

Increased respiration that causes deoxygenation also amplifies the problem of ocean acidification because the by-product of aerobic respiration is CO_2. Temporal and spatial variations in oxygen in subpycnocline and shallow eutrophic waters are accompanied by correlated fluctuations in CO_2. In highly productive estuarine, coastal, and upwelling regions, oxygen concentrations and pH can exhibit extreme fluctuations episodically and on diel, tidal, lunar, and seasonal cycles (83, 89). Elevated CO_2 can sometimes decrease the oxygen affinity of respiratory proteins (90), reduce tolerance to low oxygen by increasing the metabolic cost of maintaining acid-base balance (91), and reduce responses to low oxygen that would otherwise increase survival (92). Neither the occurrence nor the magnitude of cases in which acidification exacerbates the effects of low oxygen are currently predictable (83).

Other covarying factors, such as nutrients and fisheries dynamics, can mask or compensate for effects of deoxygenation, complicating management decisions. Fisheries management is designed to adjust effort and catch as population abundance changes (93). Thus, direct and indirect effects of deoxygenation on a harvested population may not be easily traceable in monitoring or catch data because management actions adjust for the loss in abundance. In addition, high nutrient loads can stimulate production in a habitat that remains well oxygenated, at least partially offsetting lost production within a hypoxic habitat (52). Total landings of finfish, cephalopods, and large mobile decapods are positively correlated with nitrogen loads (22), in spite of hypoxia in bottom waters (52). The conflation of habitat loss and nutrient enrichment is prominent in upwelling zones, as well as eutrophic coastal waters. Increased upwelling of nutrient-rich, oxygen-depleted waters from the 1820s to the 20th century has increased primary and fish productivity off the coast of Peru, for example (94). However, there are limits to the extent of hypoxia that can form before total system-wide fishery landings decline. In addition, individual species dependent on a degraded habitat may decline, whereas other species able to use more highly oxygenated habitats within the same system thrive (52).

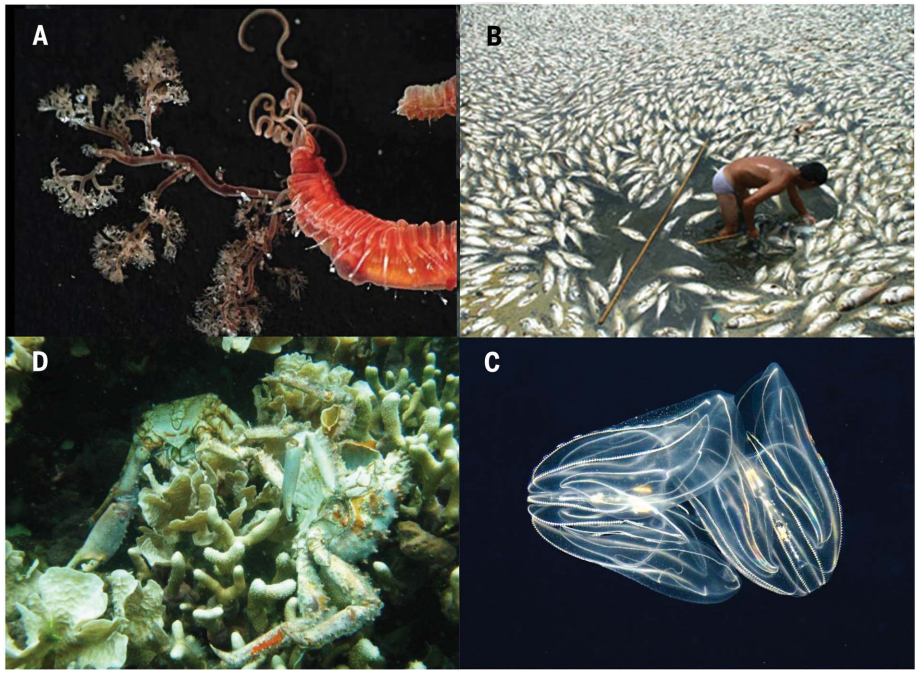

Fig. 3. Life and death at low oxygen levels. (**A**) Animals using low-oxygen habitats exhibit a range of physiological, morphological, and behavioral adaptations. For example, teribellid worms (*Neoamphitrite* sp., Annelida) with large branchaea and high hemoglobin levels can survive in the extremely low oxygen levels found at 400 m depth in the Costa Rica Canyon. (**B**) Fish kills in aquaculture pens in Bolinao, Philippines, had major economic and health consequences for the local population. (**C**) The ctenophore *Mnemiopsis leidyi* is more tolerant of low oxygen than trophically equivalent fishes in its native habitat in the Chesapeake Bay and can use hypoxic areas from which fish are excluded. (**D**) A low-oxygen event caused extensive mortality of corals and associated organisms in Bocas del Toro, Panama. These events may be a more important source of mortality in coral reefs than previously assumed.

PHOTOS: (CLOCKWISE FROM TOP LEFT) GREG ROUSE/SCRIPPS INSTITUTION OF OCEANOGRAPHY; PHILIPPINE DAILY INQUIRER/OPINION/MA. CERES P. DOYO; PETRA URBANEK/WIKIMEDIA COMMONS/HTTPS://CREATIVECOMMONS.ORG/LICENSES/BY-SA/4.0/; ARACDIO CASTILLO/SMITHSONIAN INSTITUTION

Biogeochemistry

Oxygen availability affects remineralization processes and associated sources and sinks of important nutrient elements, such as nitrogen, phosphorus, and iron. Even when occurring in relatively small, low-oxygen regions, the effects of oxygen-dependent nutrient-cycling processes are communicated to the wider ocean by circulation. Hence, local changes within OMZs can influence nutrient budgets, biological productivity, and carbon fixation on regional to global scales, and changes in oxygen-depleted bottom waters of coastal systems can affect entire water bodies.

In addition to nitrogen, phosphorus, and iron, which are discussed in more detail below, a wide range of other elements are affected by oxygen conditions. Hydrogen sulfide, which is toxic to most aerobic organisms, is produced in anoxic sediments and can be released to the overlying water column, especially during upwelling events (*16*). Methane, a potent greenhouse gas, is also produced in anoxic sediments, but methanotrophic activity limits its release to the atmosphere (*95*). Hypoxia increases conversion of As(V) to the more toxic As(III) (*96*). Cadmium, copper, and zinc form sulfide precipitates in the presence of anoxic or extremely oxygen-deficient waters and sulfides (*97*). This process may affect the global distribution of trace metals, some of which serve as micronutrients for plankton growth, but the importance of such controls is yet to be fully evaluated.

Where oxygen levels are extremely low or absent, anaerobic remineralization of organic matter by denitrification and anaerobic ammonium oxidation (anammox) leads to a net loss of bioavailable nitrogen through the formation of dinitrogen gas (N_2). Recent investigations have reported functionally anoxic conditions within open-ocean OMZs (*98*) and have shown that traces of oxygen at nanomolar levels can inhibit anaerobic processes, such as denitrification (*99*). Total loss of bioavailable nitrogen from the open ocean is currently estimated to be 65 to 80 Tg year^{-1} from the water column and 130 to 270 Tg year^{-1} from sediments (*100*). Analysis and modeling of global benthic data also indicate that denitrification in sediments underlying high-nutrient and low-oxygen areas (such as OMZs) removes around three times as much nitrogen per unit of carbon deposited as sediments underlying highly oxygenated water and accounts for ~10% (i.e., 15 Tg year^{-1}) of global benthic denitrification (*101*). Similarly enhanced benthic denitrification has been observed at very low bottom-water oxygen concentrations in eutrophic coastal systems (*102*, *103*) and in the oxycline of the water column, comparable to OMZs (*104*). Certainly, there is genetic potential for water column denitrification to occur once anoxic conditions are reached.

A by-product of both nitrification and denitrification is nitrous oxide, N_2O, a potent greenhouse gas (*105*). The amount of N_2O produced is strongly dependent on prevailing oxygen conditions. Production of N_2O is enhanced at the oxic-suboxic boundaries of low-oxygen waters, but N_2O is further reduced to N_2 in anoxic conditions (*95*), so small differences in oxygen concentration determine whether there is net production or consumption of this gas. Low-oxygen zones (including shelf and coastal areas) contribute a large fraction of the total oceanic N_2O emission to the atmosphere, and expansion of these systems may substantially enhance oceanic N_2O emissions (*95*). Record air-sea N_2O fluxes have recently been observed above the OMZ in the eastern tropical South Pacific (*106*).

Although our understanding of the relationships among oxygen, remineralization of bioavailable N, and production of N_2O has greatly increased, the consequences of a shift in these relationships in a warming world with increased O_2-depleted waters are less well understood. Continued deoxygenation of OMZ waters is expected to increase the volume of water where denitrification and anammox occur and may lead to increased marine nitrogen loss (*99*). This could alter the ocean's nitrogen inventory and, eventually, biological production on millennial time scales if nitrogen losses are not compensated for by increases in nitrogen

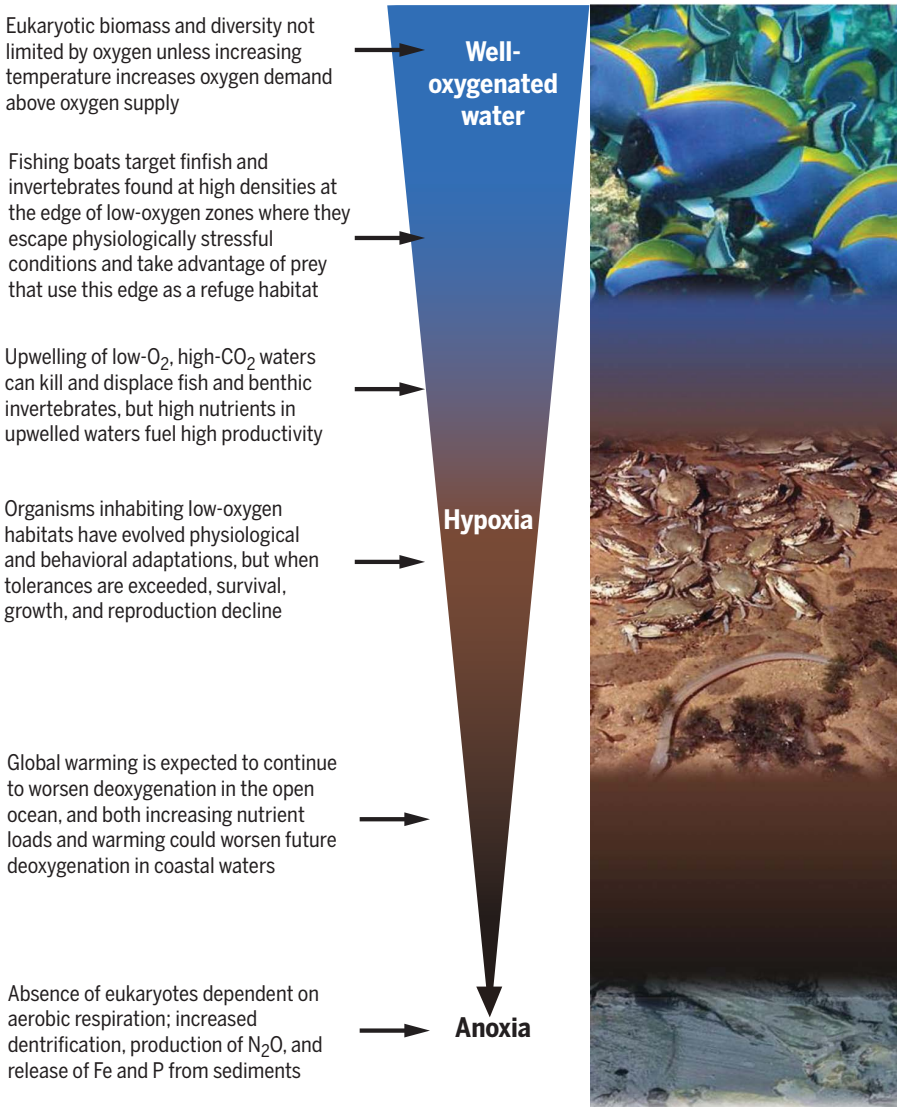

Fig. 4. Oxygen exerts a strong control over biological and biogeochemical processes in the open ocean and coastal waters. Whether oxygen patterns change over space, as with increasing depth, or over time, as the effects of nutrients and warming become more pronounced, animal diversity, biomass, and productivity decline with decreasing levels of oxygen. At the edge of low-oxygen zones, where nutrients are high and predators and their prey are concentrated into an oxygenated habitat, productivity can be very high, but even brief exposures to low oxygen levels can have strong negative effects. (**Top**) Well-oxygenated coral reef with abundant fish and invertebrate assemblages. (**Middle**) Low-oxygen event in Mobile Bay, United States, in which crabs and fish crowd into extreme shallows where oxygen levels are highest. (**Bottom**) Anoxic mud devoid of macrofauna.

PHOTOS: (TOP) UXBONA/WIKIMEDIA COMMONS/HTTPS://CREATIVECOMMONS.ORG/LICENSES/BY/3.0/; (BOTTOM) B. FERTIG/COURTESY OF THE INTEGRATION AND APPLICATION NETWORK, UNIVERSITY OF MARYLAND CENTER FOR ENVIRONMENTAL SCIENCE

fixation (107). However, the feedbacks that link nitrogen loss and nitrogen fixation remain enigmatic (101). The direction and magnitude of change in the N_2O budget and air-sea N_2O flux are also unclear because increased stratification could reduce the amount of N_2O that reaches the surface ocean and escapes to the atmosphere (108).

The supply of phosphorus and iron released from the sediments is generally enhanced under anoxic conditions (109, 110). These nutrients have the potential to further stimulate biological production if they reach well-lit surface waters, such as above the OMZs associated with coastal upwelling regions and the surface layer of coastal waters. Elevated dissolved inorganic phosphorus and chlorophyll are found in surface waters when anoxia occurs in fjords and estuaries (111), and, in some systems, deep waters supply as much phosphorus to productive surface layers as do watershed discharges (112). Increased productivity will tend to increase oxygen consumption, may increase the sediment area in contact with low-oxygen waters, and may eventually lead to further release of phosphorus and iron from the sediment. There is evidence for this positive feedback in enclosed seas such as the Baltic Sea, where enhanced nitrogen fixation in response to deoxygenation has led to the recent proliferation of undesirable cyanobacterial blooms that can be toxic and have adverse effects on ecosystems and society (102). Enhanced phosphate and iron levels may generally favor nitrogen fixation by diazotrophs, especially in the presence of nitrogen loss when ordinary plankton are driven toward nitrogen limitation.

Predicting oxygen decline

Sound management of marine ecosystems is based on reliable predictions under a range of future scenarios and an understanding of associated uncertainties. Numerical models that can project effects of climate change and eutrophication on oxygen availability in the open ocean and in coastal systems can offer these predictions. Current state-of-the-art global models generally agree that the total amount of oxygen loss will be a few percent by the end of the century (31), a decline that could have substantial biogeochemical and ecological effects. However, there is little agreement among models about the spatial distribution of future low-oxygen zones having <100 μmol O_2 kg^{-1} (113) or the spatial patterns of O_2 changes that have occurred over the past several decades (40). This uncertainty currently limits our ability to reliably predict the regional impact of climate warming on open-ocean OMZs and, hence, on oxygen-sensitive biogeochemical processes, including the nitrogen budget. More realistic and detailed inclusion of mechanisms other than CO_2-driven global warming—such as atmospheric nutrient deposition and decadal- to multidecadal-scale climate variability (especially fluctuations in wind patterns)—may improve agreement among models and, therefore, their ability to predict the spatial distribution of past and future low-oxygen areas.

Predicting oxygen levels in individual coastal water bodies requires modeling the variability in these systems, which is tightly governed by interactions with the land, atmosphere, sediment, and offshore waters at small space and time scales. This can be achieved by current estuary-specific and regional three-dimensional coupled hydrodynamic–water quality models (67); these and other state-of-the-art modeling approaches deserve broader implementation. However, model performance can be hampered by the use of forcing data, such as river discharges and atmospheric conditions, that lack sufficiently resolved spatial and temporal detail. Projections of future deoxygenation also require reliable information on changes in key parameters and interactions under a range of climate change and nutrient management scenarios and benefit from the use of approaches that explicitly model connections along the river–estuary–adjacent ocean or sea continuum. Projections of local changes in timing and magnitude of precipitation and warming are especially important. Future characteristics of human populations, such as rates of population growth, the effect of climate change on the geography of population centers, and the effects of education and income on demands for improved sanitation and animal protein are also needed because of their influence on nutrient discharges at both local and global scales.

Improving predictions critical for management in both the open ocean and coastal systems will require increased observations from field measurements and experiments to constrain and refine models. Ideally, such data should include representations of future environmental conditions. An improved mechanistic understanding of feedbacks that limit or exacerbate oxygen depletion and alter oxygen-sensitive biogeochemical cycles is especially important. In the open ocean, information is needed on transport mechanisms—such as small-scale mixing processes (114), stirring, and transport by mesoscale structures (115)—that influence oxygen distributions.

Advanced observation networks can provide data to underpin the development of an improved mechanistic understanding and the refinement of current models. Drifters and autonomous platforms ranging from Argo floats to tethered arrays provide real-time data and have the potential to increase knowledge of oxygen dynamics at the small spatial and temporal scales that are ultimately needed for both regional and global models. High-resolution measurements have revealed the small-scale patchiness of oxygen-sensitive processes in space and time (99, 106) and have provided new insight into the biogeochemistry of OMZs (98). Optical oxygen sensors mounted on Argo floats or gliders can now use atmospheric oxygen to perform ongoing, in situ calibrations throughout the float (116) or glider lifetime. The accuracy of autonomous measurements of in situ oxygen concentrations ≤1 μmol kg^{-1} has been improved by the development of STOX (switchable trace amount oxygen) sensors (117), and novel trace-oxygen optical sensors can now provide precise oxygen quantification in OMZs and detect oxygen concentrations as low as ~5 nmol kg^{-1} (118). The new platforms and sensors facilitate the implementation of regional and global oxygen observatories targeted toward the much-improved monitoring and, eventually, modeling and management of deoxygenation. For coastal waters, it is also important to develop sensors that are affordable for use in low-income developing countries (LIDCs) and that can be used to generate reliable data from citizen science.

Predicting effects at large scales of space, time, and ecological organization

Improved management and conservation of open-ocean and coastal systems requires predictions of the effects of deoxygenation at spatial, temporal, and ecological scales most relevant to the ecosystem services provided by these waters. Although research has clearly shown that low-oxygen zones reduce habitat for species dependent on aerobic respiration and that exposure to suboptimal oxygen levels leads to a host of negative effects on individuals, identifying effects of expanding deoxygenation at the scale of populations or fisheries stocks has been difficult, particularly for mobile species (52, 119). A similar problem applies to scaling up oxygen-sensitive biogeochemical processes to predict feedbacks on global ocean nutrient inventories and Earth's climate.

Scaling to predict effects on food webs and fisheries is confounded by compensatory mechanisms; examples include increased production of planktonic prey under high nutrient loads and increased encounter rates between predators and their prey when they are squeezed into smaller oxygenated habitat space (52, 119, 120). In addition, populations maintained below their habitat-dependent carrying capacity by fisheries or other factors may not be as strongly affected by the loss of habitat as species nearer their carrying capacity. In these cases, habitats suitable for feeding and other life functions may remain sufficient, even when their size is reduced by low oxygen.

The most promising approaches to scaling employ a suite of methods ranging from detailed mechanistic studies to large-scale field efforts, as well as new and increasingly sophisticated analyses and modeling tools that address spatial processes (120), temporal fluctuations (121, 122), and the role of co-occurring stressors. Consideration of the effects of early hypoxia exposure on later life stages after organisms migrate to more highly oxygenated habitats can indicate the large spatial scales over which even spatially limited hypoxia can have impacts (123). Paleoecological approaches are critical for gaining a long-term perspective beyond the time scale of biological and oceanographic observation (94, 124). Even sophisticated approaches will not always provide support for large-scale negative effects of deoxygenation, but eliminating deoxygenation as a major cause of population declines is also important to effective management.

Increased research is most needed in locations where deoxygenation is likely to affect local economies and food security. Place-based, artisanal fisheries with little capacity to relocate as local

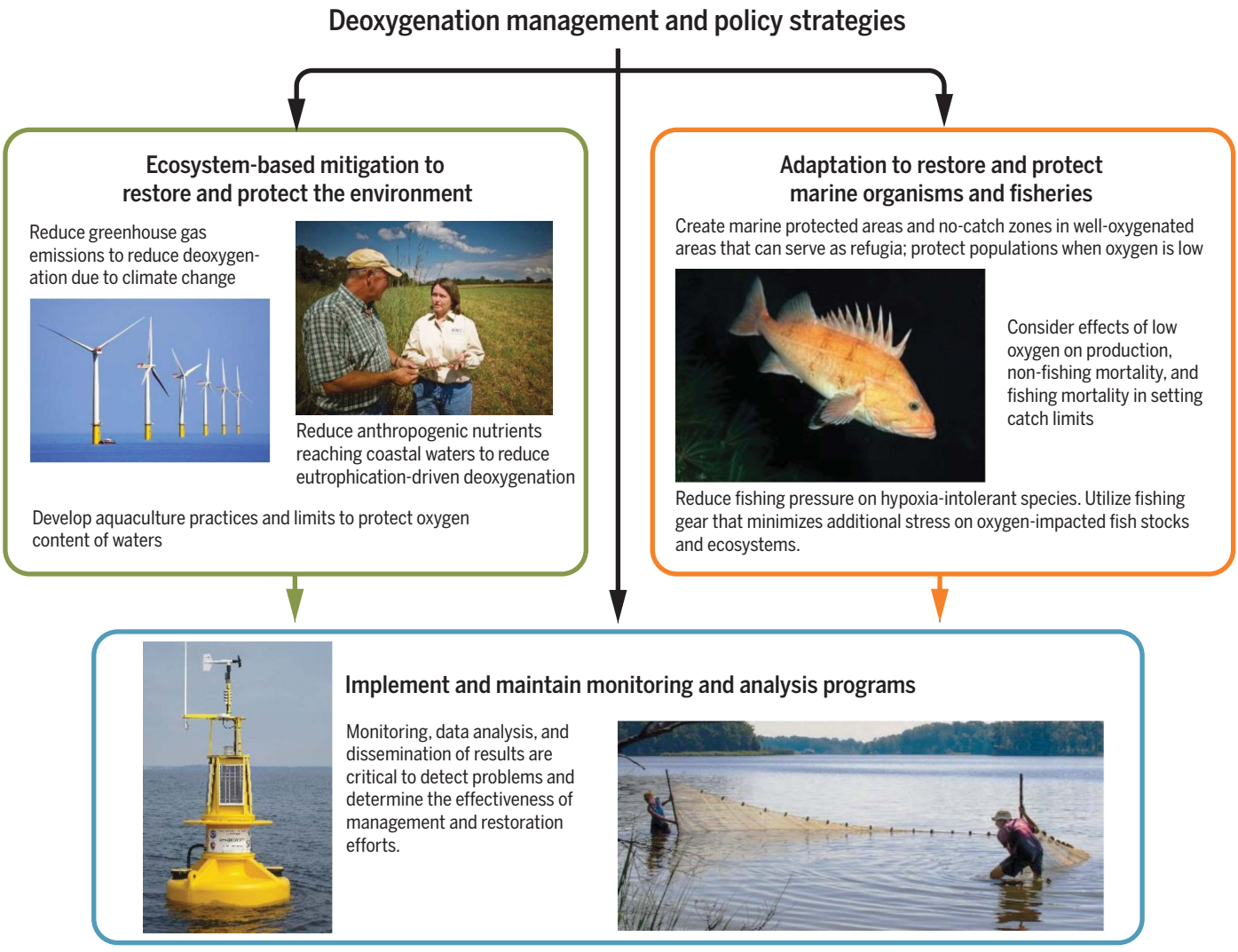

Fig. 5. Strategies for deoxygenation management and policy-making. (**Left**) Multiple management actions can help to mitigate deoxygenation. Key among these are reductions in (i) anthropogenic nutrient inputs from land, which will reduce algal blooms and subsequent oxygen drawdown; (ii) greenhouse gas emissions, which will slow warming; and (iii) waste production from aquaculture, which will contribute to oxygen consumption. (**Right**) Adaptive measures can reduce stress and may increase resilience of marine ecosystems that face deoxygenation. Examples include creating protected areas that can serve as refugia in hypoxic areas or during hypoxic events; incorporating oxygen effects on population distribution and dynamics into catch limits and closures, as has been done for rockfish; and adopting gear regulations that reduce stress on vulnerable fisheries or ecosystems. (**Bottom**) Both types of actions benefit from enhanced oxygen and biological monitoring, including access to real-time data that can elicit quick management responses, as well as more synthetic analyses that might reveal spatial and temporal trends.

habitat degrades are more likely to suffer from deoxygenation than industrialized fisheries with highly mobile fishing fleets. Aquaculture, in particular, can be a critical intersection between deoxygenation and societal effects because aquaculture itself can cause deoxygenation (*125*), and animals restrained in nets and cages are unable to escape harmful oxygen conditions. But critically, much of the world's marine aquaculture is done in LIDCs. Fish kills in aquaculture pens (*125*) can compromise livelihoods and can directly harm human health when low incomes and food insecurity lead to consumption of fish killed by low-oxygen conditions (*126*). Coral reefs contribute to food security and local economies through their value to tourism and storm protection, as well as food production. Recent research indicates that low oxygen may be an increasingly important factor in the mortality of corals and associated fauna in some regions and that low-oxygen problems on coral reefs are likely underreported (*127*).

Reducing deoxygenation and its negative effects

Local, national, and global efforts are required to limit further oxygen declines, restore oxygen to previously well-oxygenated environments, and enhance the resilience of ecosystems affected by deoxygenation. At their most basic level, the actions needed to address deoxygenation—reducing nutrient loads to coastal waters and reducing greenhouse gas emissions globally—have substantial benefits to society above and beyond improving oxygen conditions. Improved sanitation can benefit human health directly while also reducing coastal nutrient loads. Eliminating excess and inefficiently applied fertilizer can reduce costs to farmers (*128*) and emissions of N_2O (*129*) and may decrease nitrogen loads to waterways. Eliminating emissions from combustion of fossil fuels can reduce greenhouse gas production and may result in decreased atmospheric deposition

of nitrogen that stimulates primary production in coastal waters (*130*). Reducing or eliminating greenhouse gas emissions can, more generally, lower the threats from global warming and ocean acidification and, simultaneously, reduce ocean deoxygenation. Improved management of fisheries and marine habitats that are sensitive to the development and effects of low oxygen helps to protect economies, livelihoods, and food security (Fig. 5).

Failure to reduce nutrient loads, at all or sufficiently, is the primary reason that oxygen levels have not improved in most coastal systems. But some of the reasons for slow progress are inherent in the problem itself. High sedimentary oxygen demand can continue for decades as accumulated organic matter degrades (*57*), phosphorus may continue to be released from sediments once oxygen thresholds have been crossed (*102*), and nitrogen leached from soils and dissolved in groundwater continues to enter waterways for decades (*131*). Increasing temperatures can require greater reductions in nutrients to meet the same oxygen goals (*57*, *61*). Because of changing conditions and the nonlinearity of ecological processes, ecosystems may not return to their predisturbed state even if conditions that caused the initial deoxygenation are eased (*132*).

To maintain the current conditions, per capita reductions in nutrient discharges and greenhouse gas emissions will need to increase as the global population continues to grow. Nevertheless, considerable improvements have been observed in some coastal systems through implementation of a wide range of strategies to reduce the input of nutrients and biomass (*133*). Some of the most notable improvements have occurred in systems such as the Thames and Delaware River estuaries, where steps to keep raw sewage out of the rivers and, eventually, to treat wastewater substantially decreased biological oxygen demand (*133*). In the Maryland portion of the Chesapeake Bay, where both point- and nonpoint-source nutrient reduction strategies have been implemented, oxygen concentrations <0.1 mg liter^{-1} (<3 μmol kg^{-1}) have rarely been measured since 2014—a marked contrast to the first 30 years of frequent monitoring (1984–2013) (*134*). In one Chesapeake tributary, the Potomac River, nitrogen reductions due to better air quality have played the major role in water quality improvements (*135*). Additionally, better understanding of deoxygenation may enable a range of adaptive, protective actions for fisheries and the habitats that sustain them (Fig. 5).

An integrated framework that combines modeling, observations, and experiments in a multiple-stressor environment and involves the full range of stakeholders (e.g., scientists, local governments, intergovernmental bodies, industrial sectors, and the public) will facilitate the development and implementation of the most ecologically and economically effective plans to reverse deoxygenation (Fig. 6). Networks of research scientists, such as the Intergovernmental Oceanographic Commission (IOC)–UNESCO Global Ocean Oxygen Network (www.unesco.org/new/en/natural-sciences/ioc-oceans/sections-and-programmes/ocean-sciences/global-ocean-oxygen-network/), as well as groups with more limited geographic and disciplinary scope, can help to keep the process updated and to build capacity in parts of the world where improved technology and training are needed. The key to effective management is raised awareness of the phenomenon of deoxygenation, as well as its causes, consequences, and remediation measures.

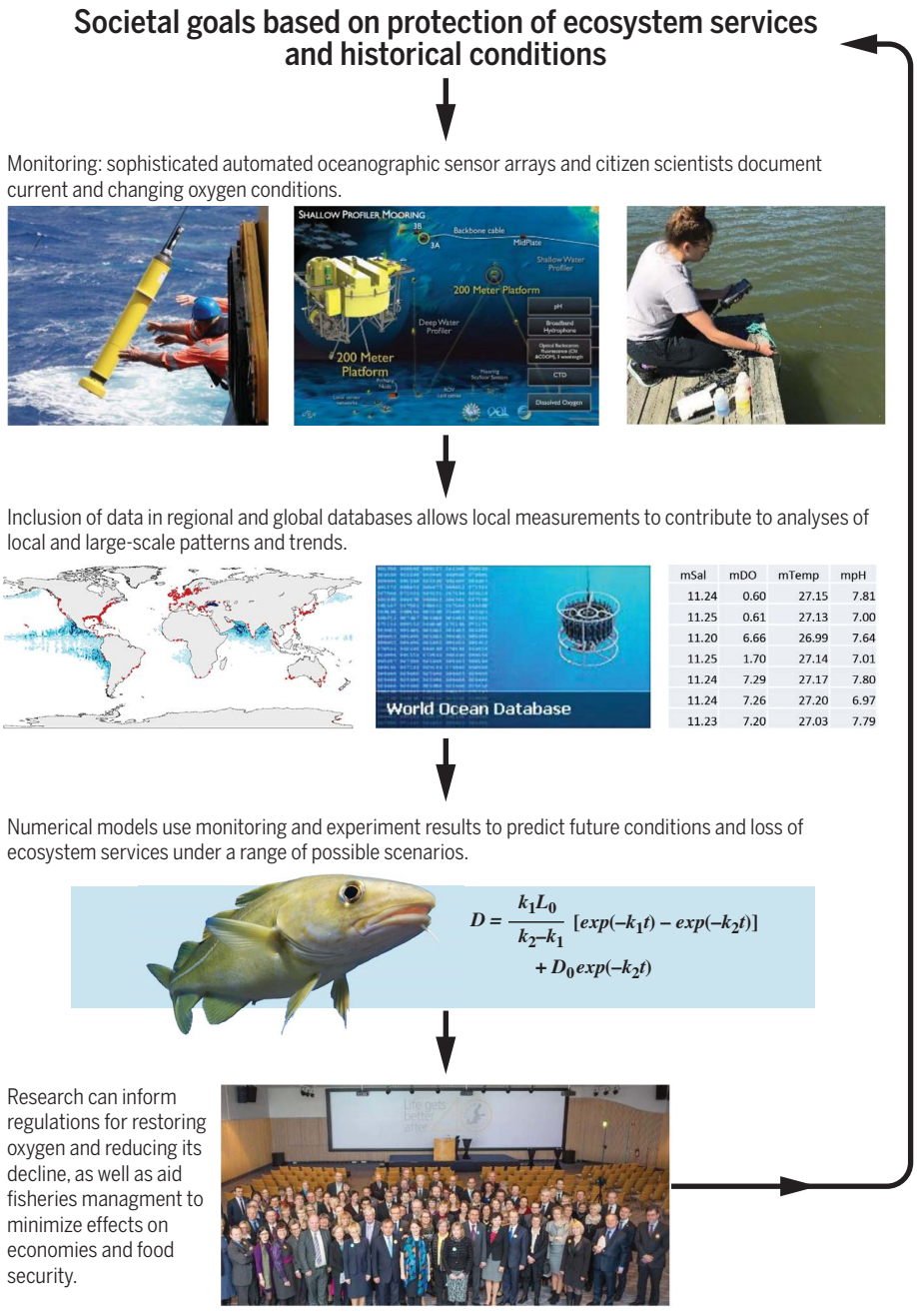

Fig. 6. Monitoring in coastal waters and the open ocean enables documentation of deoxygenation and, in some cases, improved oxygen conditions. In shallow water, handheld, continuous, and shipboard sensors are used worldwide. In the open ocean and nearshore waters, global arrays of sensors (such as the Argo floats), shipboard measurements, and deep platforms and profilers provide data to validate global models. Archiving data in well-documented databases accessible by all stakeholders facilitates scientific and management advances and public engagement. Experiments and field studies at scales ranging from genes to ecosystems provide information to predict the effects of low oxygen levels on ecological processes and services and are also used to develop fisheries and ecosystem models. Model projections and analyses of deoxygenation and its effects inform management and policy at both local and multinational scales and provide the basis for strategies to combat deoxygenation.

REFERENCES AND NOTES

1. R. E. Keeling, A. Körtzinger, N. Gruber, Ocean deoxygenation in a warming world. *Annu. Rev. Mar. Sci.* **2**, 199–229 (2010). pmid: 21141663
2. L. Stramma, G. C. Johnson, J. Sprintall, V. Mohrholz, Expanding oxygen-minimum zones in the tropical oceans. *Science* **320**, 655–658 (2008). doi: 10.1126/science.1153847; pmid: 18451300
3. R. J. Diaz, R. Rosenberg, Spreading dead zones and consequences for marine ecosystems. *Science* **321**, 926–929 (2008). doi: 10.1126/science.1156401; pmid: 18703733
4. N. N. Rabalais *et al*., Eutrophication-driven deoxygenation in the coastal ocean. *Oceanography* **27**, 172–183 (2014). doi: 10.5670/oceanog.2014.21
5. L. A. Levin, D. L. Breitburg, Linking coasts and seas to address ocean deoxygenation. *Nat. Clim. Chang.* **5**, 401–403 (2015). doi: 10.1038/nclimate2595
6. J. Zhang *et al*., Natural and human-induced hypoxia and consequences for coastal areas: Synthesis and future development. *Biogeosciences* **7**, 1443–1467 (2010). doi: 10.5194/bg-7-1443-2010
7. R. D. Norris, S. K. Turner, P. M. Hull, A. Ridgwell, Marine ecosystem responses to Cenozoic global change. *Science* **341**, 492–498 (2013). doi: 10.1126/science.1240543; pmid: 23908226
8. A. J. Watson, Oceans on the edge of anoxia. *Science* **354**, 1529–1530 (2016). doi: 10.1126/science.aaj2321; pmid: 28008026
9. S. Schmidtko, L. Stramma, M. Visbeck, Decline in global oceanic oxygen content during the past five decades. *Nature* **542**, 335–339 (2017). doi: 10.1038/nature21399; pmid: 28202958
10. L. Stramma, S. Schmidtko, L. A. Levin, G. C. Johnson, Ocean oxygen minima expansions and their biological impacts. *Deep-Sea Res. Part I* **57**, 587–595 (2010). doi: 10.1016/j.dsr.2010.01.005
11. F. Chan *et al*., Emergence of anoxia in the California current large marine ecosystem. *Science* **319**, 920 (2008). doi: 10.1126/science.1149016; pmid: 18276882
12. K. Isensee *et al*., "The ocean is losing its breath" in *Ocean and Climate Scientific Notes*, ed. 2 (2016), pp. 20–32; www.ocean-climate.org.
13. B. Riemann *et al*., Recovery of Danish coastal ecosystems after reductions in nutrient loading: A holistic ecosystem approach. *Estuaries Coasts* **39**, 82–97 (2016). doi: 10.1007/s12237-015-9980-0
14. N. Rabalais *et al*., Dynamics and distribution of natural and human-caused hypoxia. *Biogeosciences* **7**, 585–619 (2010). doi: 10.5194/bg-7-585-2010
15. J. Karstensen *et al*., Open ocean dead-zone in the tropical North Atlantic Ocean. *Biogeosciences* **12**, 2597–2605 (2015). doi: 10.5194/bg-12-2597-2015
16. J. J. Wright, K. M. Konwar, S. J. Hallam, Microbial ecology of expanding oxygen minimum zones. *Nat. Rev. Microbiol.* **10**, 381–394 (2012). pmid: 22580367
17. A. J. Gooday *et al*., Habitat heterogeneity and its influence on benthic biodiversity in oxygen minimum zones. *Mar. Ecol.* **31**, 125–147 (2010). doi: 10.1111/j.1439-0485.2009.00348.x
18. E. A. Sperling *et al*., Oxygen, ecology, and the Cambrian radiation of animals. *Proc. Natl. Acad. Sci. U.S.A.* **110**, 13446–13451 (2013). doi: 10.1073/pnas.1312778110; pmid: 23898193
19. R. Vaquer-Sunyer, C. M. Duarte, Thresholds of hypoxia for marine biodiversity. *Proc. Natl. Acad. Sci. U.S.A.* **105**, 15452–15457 (2008). doi: 10.1073/pnas.0803833105; pmid: 18824689
20. A. Bertrand *et al*., Oxygen: A fundamental property regulating pelagic ecosystem structure in the coastal southeastern tropical Pacific. *PLOS ONE* **6**, e29558 (2011). doi: 10.1371/journal.pone.0029558; pmid: 22216315
21. F. P. Chavez, A. Bertrand, R. Guevara-Carrasco, P. Soler, J. Csirke, The northern Humboldt current system: Brief history, present status and a view towards the future. *Prog. Oceanogr.* **79**, 95–105 (2008). doi: 10.1016/j.pocean.2008.10.012
22. S. W. Nixon, B. A. Buckley, "A strikingly rich zone"—Nutrient enrichment and secondary production in coastal marine ecosystems. *Estuaries* **25**, 782–796 (2002). doi: 10.1007/BF02804905
23. B. A. Seibel, Critical oxygen levels and metabolic suppression in oceanic oxygen minimum zones. *J. Exp. Biol.* **214**, 326–336 (2011). doi: 10.1242/jeb.049171; pmid: 21177952
24. A. C. Utne-Palm *et al*., Trophic structure and community stability in an overfished ecosystem. *Science* **329**, 333–336 (2010). doi: 10.1126/science.1190708; pmid: 20647468
25. R. S. Wu, Hypoxia: From molecular responses to ecosystem responses. *Mar. Pollut. Bull.* **45**, 35–45 (2002). doi: 10.1016/S0025-326X(02)00061-9; pmid: 12398365
26. L. Levin, Oxygen minimum zone benthos: Adaptation and community response to hypoxia. *Oceanogr. Mar. Biol.* **41**, 1–45 (2003).
27. J. G. Richards, Metabolic and molecular responses of fish to hypoxia. *Fish Physiol.* **27**, 443–485 (2009). doi: 10.1016/S1546-5098(08)00010-1
28. N. D. Gallo, L. A. Levin, Fish ecology and evolution in the world's oxygen minimum zones and implications of ocean deoxygenation. *Adv. Mar. Biol.* **74**, 117–198 (2016). doi: 10.1016/bs.amb.2016.04.001; pmid: 27573051
29. F. A. Whitney, H. J. Freeland, M. Robert, Persistently declining oxygen levels in the interior waters of the eastern subarctic Pacific. *Prog. Oceanogr.* **75**, 179–199 (2007). doi: 10.1016/j.pocean.2007.08.007
30. I. Stendardo, N. Gruber, Oxygen trends over five decades in the North Atlantic. *J. Geophys. Res.* **117**, C11004 (2012).
31. L. Bopp *et al*., Multiple stressors of ocean ecosystems in the 21st century: Projections with CMIP5 models. *Biogeosciences* **10**, 6225–6245 (2013). doi: 10.5194/bg-10-6225-2013
32. T. Ito, S. Minobe, M. C. Long, C. Deutsch, Upper ocean O_2 trends: 1958–2015. *Geophys. Res. Lett.* **44**, 4214–4223 (2017). doi: 10.1002/2017GL073613
33. K. P. Helm, N. L. Bindoff, J. A. Church, Observed decreases in oxygen content of the global ocean. *Geophys. Res. Lett.* **38**, L23602 (2011). doi: 10.1029/2011GL049513
34. P. G. Brewer, E. T. Peltzer, Depth perception: The need to report ocean biogeochemical rates as functions of temperature, not depth. *Philos. Trans. R. Soc. London Ser. A* **375**, 20160319 (2017). doi: 10.1098/rsta.2016.0319; pmid: 28784710
35. C. Deutsch *et al*., Centennial changes in North Pacific anoxia linked to tropical trade winds. *Science* **345**, 665–668 (2014). doi: 10.1126/science.1252332; pmid: 25104384
36. S. Nam, Y. Takeshita, C. A. Frieder, T. Martz, J. Ballard, Seasonal advection of Pacific Equatorial Water alters oxygen and pH in the Southern California Bight. *J. Geophys. Res. Oceans* **120**, 5387–5399 (2015). doi: 10.1002/2015JC010859
37. D. Gilbert, B. Sundby, C. Gobeil, A. Mucci, G.-H. Tremblay, A seventy-two-year record of diminishing deep-water oxygen in the St. Lawrence estuary: The northwest Atlantic connection. *Limnol. Oceanogr.* **50**, 1654–1666 (2005). doi: 10.4319/lo.2005.50.5.1654
38. A. Oschlies *et al*., Patterns of deoxygenation: Sensitivity to natural and anthropogenic drivers. *Philos. Trans. R. Soc. London Ser. A* **375**, 20160325 (2017). doi: 10.1098/rsta.2016.0325; pmid: 28784715
39. A. Oschlies, K. G. Schulz, U. Riebesell, A. Schmittner, Simulated 21st century's increase in oceanic suboxia by CO_2-enhanced biotic carbon export. *Global Biogeochem. Cycles* **22**, GB4008 (2008). doi: 10.1029/2007GB003147
40. L. Stramma, A. Oschlies, S. Schmidtko, Mismatch between observed and modeled trends in dissolved upper-ocean oxygen over the last 50 yr. *Biogeosciences* **9**, 4045–4057 (2012). doi: 10.5194/bg-9-4045-2012
41. W. J. Sydeman *et al*., Climate change and wind intensification in coastal upwelling ecosystems. *Science* **345**, 77–80 (2014). doi: 10.1126/science.1251635; pmid: 24994651
42. R. A. Feely, C. L. Sabine, J. M. Hernandez-Ayon, D. Ianson, B. Hales, Evidence for upwelling of corrosive "acidified" water onto the continental shelf. *Science* **320**, 1490–1492 (2008). doi: 10.1126/science.1155676; pmid: 18497259
43. D. Wang, T. C. Gouhier, B. A. Menge, A. R. Ganguly, Intensification and spatial homogenization of coastal upwelling under climate change. *Nature* **518**, 390–394 (2015). doi: 10.1038/nature14235; pmid: 25693571
44. D. Galton, 10th Meeting: Report of the royal commission on metropolitan sewage. *J. Soc. Arts* **33**, 290 (1884).
45. A. D. Hasler, Cultural eutrophication is reversible. *Bioscience* **19**, 425–431 (1969). doi: 10.2307/1294478
46. United Nations Department of Economic and Social Affairs/Population Division, "World Population Prospects: The 2015 Revision," DVD Edition (2015); https://esa.un.org/unpd/wpp/DataQuery/.
47. International Fertilizer Association, IFADATA (2016); http://ifadata.fertilizer.org/ucSearch.aspx.
48. S. Seitzinger *et al*., Global river nutrient export: A scenario analysis of past and future trends. *Global Biogeochem. Cycles* **24**, GB0A08 (2010). doi: 10.1029/2009GB003587
49. A. F. Bouwman, G. Van Drecht, J. M. Knoop, A. H. W. Beusen, C. R. Meinardi, Exploring changes in river nitrogen export to the world's oceans. *Global Biogeochem. Cycles* **19**, GB1002 (2005). doi: 10.1029/2004GB002314
50. A. Steckbauer, C. M. Duarte, J. Carstensen, R. Vaquer-Sunyer, D. J. Conley, Ecosystem impacts of hypoxia: Thresholds of hypoxia and pathways to recovery. *Environ. Res. Lett.* **6**, 025003 (2011). doi: 10.1088/1748-9326/6/2/025003
51. D. C. Reed, J. A. Harrison, Linking nutrient loading and oxygen in the coastal ocean: A new global scale model. *Global Biogeochem. Cycles* **30**, 447–459 (2016). doi: 10.1002/2015GB005303
52. D. L. Breitburg, D. W. Hondorp, L. A. Davias, R. J. Diaz, Hypoxia, nitrogen, and fisheries: Integrating effects across local and global landscapes. *Annu. Rev. Mar. Sci.* **1**, 329–349 (2009). pmid: 21141040
53. L. P. A. Sotto, G. S. Jacinto, C. L. Villanoy, Spatiotemporal variability of hypoxia and eutrophication in Manila Bay, Philippines during the northeast and southwest monsoons. *Mar. Pollut. Bull.* **85**, 446–454 (2014). doi: 10.1016/j.marpolbul.2014.02.028; pmid: 24655947
54. R. M. Tyler, D. C. Brady, T. E. Targett, Temporal and spatial dynamics of diel-cycling hypoxia in estuarine tributaries. *Estuaries Coasts* **32**, 123–145 (2009). doi: 10.1007/s12237-008-9108-x
55. M. E. Scully, The importance of climate variability to wind-driven modulation of hypoxia in Chesapeake Bay. *J. Phys. Oceanogr.* **40**, 1435–1440 (2010). doi: 10.1175/2010JPO4321.1
56. M. Li *et al*., What drives interannual variability of hypoxia in Chesapeake Bay: Climate forcing versus nutrient loading? *Geophys. Res. Lett.* **43**, 2127–2134 (2016). doi: 10.1002/2015GL067334
57. A. Capet, J.-M. Beckers, M. Grégoire, Drivers, mechanisms and long-term variability of seasonal hypoxia on the Black Sea northwestern shelf–is there any recovery after eutrophication? *Biogeosciences* **10**, 3943–3962 (2013). doi: 10.5194/bg-10-3943-2013
58. A. H. Altieri, K. B. Gedan, Climate change and dead zones. *Global Change Biol.* **21**, 1395–1406 (2015). doi: 10.1111/gcb.12754; pmid: 25385668
59. J. Carstensen, J. H. Andersen, B. G. Gustafsson, D. J. Conley, Deoxygenation of the Baltic Sea during the last century. *Proc. Natl. Acad. Sci. U.S.A.* **111**, 5628–5633 (2014). doi: 10.1073/pnas.1323156111; pmid: 24706804
60. D. Gilbert, N. N. Rabalais, R. J. Díaz, J. Zhang, Evidence for greater oxygen decline rates in the coastal ocean than in the open ocean. *Biogeosciences* **7**, 2283–2296 (2010). doi: 10.5194/bg-7-2283-2010
61. H. M. Meier *et al*., Hypoxia in future climates: A model ensemble study for the Baltic Sea. *Geophys. Res. Lett.* **38**, L24608 (2011). doi: 10.1029/2011GL049929
62. H.-O. Pörtner, Integrating climate-related stressor effects on marine organisms: Unifying principles linking molecule to ecosystem-level changes. *Mar. Ecol. Prog. Ser.* **470**, 273–290 (2012). doi: 10.3354/meps10123
63. C. Deutsch, A. Ferrel, B. Seibel, H.-O. Pörtner, R. B. Huey, Climate change tightens a metabolic constraint on marine habitats. *Science* **348**, 1132–1135 (2015). doi: 10.1126/science.aaa1605; pmid: 26045435
64. D. Breitburg, Effects of hypoxia, and the balance between hypoxia and enrichment, on coastal fishes and fisheries. *Estuaries Coasts* **25**, 767–781 (2002). doi: 10.1007/BF02804904
65. I. M. Sokolova, Energy-limited tolerance to stress as a conceptual framework to integrate the effects of multiple stressors. *Integr. Comp. Biol.* **53**, 597–608 (2013). doi: 10.1093/icb/ict028; pmid: 23615362
66. P. Thomas, M. S. Rahman, M. E. Picha, W. Tan, Impaired gamete production and viability in Atlantic croaker collected throughout the 20,000 km^2 hypoxic region in the northern Gulf of Mexico. *Mar. Pollut. Bull.* **101**, 182–192 (2015). doi: 10.1016/j.marpolbul.2015.11.001; pmid: 26547103
67. K. A. Rose *et al*., "Numerical modeling of hypoxia and its effects: Synthesis and going forward" in *Modeling Coastal Hypoxia* (Springer, ed. 1, 2017), pp. 401–421.
68. S. Y. Wang *et al*., Hypoxia causes transgenerational impairments in reproduction of fish. *Nat. Commun.* **7**, 12114 (2016). doi: 10.1038/ncomms12114; pmid: 27373813

69. A. G. Keppel, D. L. Breitburg, G. H. Wikfors, R. B. Burrell, V. M. Clark, Effects of co-varying diel-cycling hypoxia and pH on disease susceptibility in the eastern oyster *Crassostrea virginica*. *Mar. Ecol. Prog. Ser.* **538**, 169–183 (2015). doi: 10.3354/meps11479
70. K. L. Stierhoff, T. E. Targett, J. H. Power, Hypoxia-induced growth limitation of juvenile fishes in an estuarine nursery: Assessment of small-scale temporal dynamics using RNA: DNA. *Can. J. Fish. Aquat. Sci.* **66**, 1033–1047 (2009). doi: 10.1139/F09-066
71. W. F. Gilly, J. M. Beman, S. Y. Litvin, B. H. Robison, Oceanographic and biological effects of shoaling of the oxygen minimum zone. *Annu. Rev. Mar. Sci.* **5**, 393–420 (2013). doi: 10.1146/annurev-marine-120710-100849; pmid: 22809177
72. L. R. McCormick, L. A. Levin, Physiological and ecological implications of ocean deoxygenation for vision in marine organisms. *Philos. Trans. R. Soc. London Ser. A* **375**, 20160322 (2017). doi: 10.1098/rsta.2016.0322; pmid: 28784712
73. L. A. Eby, L. B. Crowder, Hypoxia-based habitat compression in the Neuse River Estuary: Context-dependent shifts in behavioral avoidance thresholds. *Can. J. Fish. Aquat. Sci.* **59**, 952–965 (2002). doi: 10.1139/f02-067
74. M. Roman, J. J. Pierson, D. G. Kimmel, W. C. Boicourt, X. Zhang, Impacts of hypoxia on zooplankton spatial distributions in the northern Gulf of Mexico. *Estuaries Coasts* **35**, 1261–1269 (2012). doi: 10.1007/s12237-012-9531-x
75. K. F. Wishner *et al*., Vertical zonation and distributions of calanoid copepods through the lower oxycline of the Arabian Sea oxygen minimum zone. *Prog. Oceanogr.* **78**, 163–191 (2008). doi: 10.1016/j.pocean.2008.03.001
76. J. A. Koslow, R. Goericke, A. Lara-Lopez, W. Watson, Impact of declining intermediate-water oxygen on deepwater fishes in the California Current. *Mar. Ecol. Prog. Ser.* **436**, 207–218 (2011). doi: 10.3354/meps09270
77. L. Stramma *et al*., Expansion of oxygen minimum zones may reduce available habitat for tropical pelagic fishes. *Nat. Clim. Chang.* **2**, 33–37 (2012). doi: 10.1038/nclimate1304
78. J. K. Craig, S. H. Bosman, Small spatial scale variation in fish assemblage structure in the vicinity of the northwestern Gulf of Mexico hypoxic zone. *Estuaries Coasts* **36**, 268–285 (2013). doi: 10.1007/s12237-012-9577-9
79. M. Casini *et al*., Hypoxic areas, density-dependence and food limitation drive the body condition of a heavily exploited marine fish predator. *R. Soc. Open Sci.* **3**, 160416 (2016). doi: 10.1098/rsos.160416; pmid: 27853557
80. W. Ekau, H. Auel, H.-O. Pörtner, D. Gilbert, Impacts of hypoxia on the structure and processes in pelagic communities (zooplankton, macro-invertebrates and fish). *Biogeosciences* **7**, 1669–1699 (2010). doi: 10.5194/bg-7-1669-2010
81. K. N. Sato, L. A. Levin, K. Schiff, Habitat compression and expansion of sea urchins in response to changing climate conditions on the California continental shelf and slope (1994–2013). *Deep-Sea Res. Part II* **137**, 377–389 (2017). doi: 10.1016/j.dsr2.2016.08.012
82. A. P. Farrell, Pragmatic perspective on aerobic scope: Peaking, plummeting, pejus and apportioning. *J. Fish Biol.* **88**, 322–343 (2016). doi: 10.1111/jfb.12789; pmid: 26592201
83. C. J. Gobler, H. Baumann, Hypoxia and acidification in ocean ecosystems: Coupled dynamics and effects on marine life. *Biol. Lett.* **12**, 20150976 (2016). doi: 10.1098/rsbl.2015.0976; pmid: 27146441
84. D. L. Breitburg *et al*., And on top of all that… Coping with ocean acidification in the midst of many stressors. *Oceanography* **28**, 48–61 (2015). doi: 10.5670/oceanog.2015.31
85. S. C. Doney, The growing human footprint on coastal and open-ocean biogeochemistry. *Science* **328**, 1512–1516 (2010). doi: 10.1126/science.1185198; pmid: 20558706
86. W. W. Cheung, J. Dunne, J. L. Sarmiento, D. Pauly, Integrating ecophysiology and plankton dynamics into projected maximum fisheries catch potential under climate change in the Northeast Atlantic. *ICES J. Mar. Sci.* **68**, 1008–1018 (2011). doi: 10.1093/icesjms/fsr012
87. C. H. Stortini, D. Chabot, N. L. Shackell, Marine species in ambient low-oxygen regions subject to double jeopardy impacts of climate change. *Global Change Biol.* **23**, 2284–2296 (2017). doi: 10.1111/gcb.13534; pmid: 27753179
88. D. Pauly, W. W. L. Cheung, Sound physiological knowledge and principles in modeling shrinking of fishes under climate change. *Global Change Biol.* 10.1111/gcb.13831 (2017). doi: 10.1111/gcb.13831; pmid: 28833977
89. L. A. Levin *et al*., Comparative biogeochemistry–ecosystem–human interactions on dynamic continental margins. *J. Mar. Syst.* **141**, 3–17 (2015). doi: 10.1016/j.jmarsys.2014.04.016
90. B. A. Seibel, The jumbo squid, *Dosidicus gigas* (Ommastrephidae), living in oxygen minimum zones II: Blood–oxygen binding. *Deep-Sea Res. Part II* **95**, 139–144 (2013). doi: 10.1016/j.dsr2.2012.10.003
91. J. R. Hancock, S. P. Place, Impact of ocean acidification on the hypoxia tolerance of the woolly sculpin, *Clinocottus analis*. *Conserv. Physiol.* **4**, cow040 (2016). doi: 10.1093/conphys/cow040; pmid: 27729981
92. S. H. Miller, D. L. Breitburg, R. B. Burrell, A. G. Keppel, Acidification increases sensitivity to hypoxia in important forage fishes. *Mar. Ecol. Prog. Ser.* **549**, 1–8 (2016). doi: 10.3354/meps11695
93. R. Hilborn, C. J. Walters, *Quantitative Fisheries Stock Assessment: Choice, Dynamics and Uncertainty* (Springer, 2013).
94. D. Gutiérrez *et al*., Rapid reorganization in ocean biogeochemistry off Peru towards the end of the Little Ice Age. *Biogeosciences* **6**, 835–848 (2009). doi: 10.5194/bg-6-835-2009
95. S. Naqvi *et al*., Marine hypoxia/anoxia as a source of CH_4 and N_2O. *Biogeosciences* **7**, 2159–2190 (2010). doi: 10.5194/bg-7-2159-2010
96. L. Li *et al*., Revisiting the biogeochemistry of arsenic in the Baltic Sea: Impact of anthropogenic activity. *Sci. Total Environ.* 10.1016/j.scitotenv.2017.09.029 (2017). pmid: 28926810
97. D. J. Janssen *et al*., Undocumented water column sink for cadmium in open ocean oxygen-deficient zones. *Proc. Natl. Acad. Sci. U.S.A.* **111**, 6888–6893 (2014). doi: 10.1073/pnas.1402388111; pmid: 24778239
98. L. Tiano *et al*., Oxygen distribution and aerobic respiration in the north and south eastern tropical Pacific oxygen minimum zones. *Deep-Sea Res. Part I* **94**, 173–183 (2014). doi: 10.1016/j.dsr.2014.10.001
99. L. A. Bristow *et al*., N_2 production rates limited by nitrite availability in the Bay of Bengal oxygen minimum zone. *Nat. Geosci.* **10**, 24–29 (2017). doi: 10.1038/ngeo2847
100. C. J. Somes, A. Oschlies, A. Schmittner, Isotopic constraints on the pre-industrial oceanic nitrogen budget. *Biogeosciences* **10**, 5889–5910 (2013). doi: 10.5194/bg-10-5889-2013
101. L. Bohlen, A. W. Dale, K. Wallmann, Simple transfer functions for calculating benthic fixed nitrogen losses and C:N:P regeneration ratios in global biogeochemical models. *Global Biogeochem. Cycles* **26**, GB3029 (2012). doi: 10.1029/2011GB004198
102. D. J. Conley, J. Carstensen, R. Vaquer-Sunyer, C. M. Duarte, Ecosystem thresholds with hypoxia. *Hydrobiologia* **629**, 21–29 (2009). doi: 10.1007/s10750-009-9764-2
103. M. J. McCarthy, S. E. Newell, S. A. Carini, W. S. Gardner, Denitrification dominates sediment nitrogen removal and is enhanced by bottom-water hypoxia in the Northern Gulf of Mexico. *Estuaries Coasts* **38**, 2279–2294 (2015). doi: 10.1007/s12237-015-9964-0
104. T. Dalsgaard, L. De Brabandere, P. O. J. Hall, Denitrification in the water column of the central Baltic Sea. *Geochim. Cosmochim. Acta* **106**, 247–260 (2013). doi: 10.1016/j.gca.2012.12.038
105. H. W. Bange *et al*., "Marine pathways to nitrous oxide" in *Nitrous Oxide and Climate Change* (Earthscan, 2010), pp. 36–62.
106. D. L. Arévalo-Martínez, A. Kock, C. R. Löscher, R. A. Schmitz, H. W. Bange, Massive nitrous oxide emissions from the tropical South Pacific Ocean. *Nat. Geosci.* **8**, 530–533 (2015). doi: 10.1038/ngeo2469
107. N. Gruber, Elusive marine nitrogen fixation. *Proc. Natl. Acad. Sci. U.S.A.* **113**, 4246–4248 (2016). doi: 10.1073/pnas.1603646113; pmid: 27071128
108. J. Martinez-Rey, L. Bopp, M. Gehlen, A. Tagliabue, N. Gruber, Projections of oceanic N_2O emissions in the 21st century using the IPSL Earth system model. *Biogeosciences* **12**, 4133–4148 (2015). doi: 10.5194/bg-12-4133-2015
109. E. Ingall, R. Jahnke, Evidence for enhanced phosphorus regeneration from marine sediments overlain by oxygen depleted waters. *Geochim. Cosmochim. Acta* **58**, 2571–2575 (1994). doi: 10.1016/0016-7037(94)90033-7
110. F. Scholz, J. McManus, A. C. Mix, C. Hensen, R. R. Schneider, The impact of ocean deoxygenation on iron release from continental margin sediments. *Nat. Geosci.* **7**, 433–437 (2014). doi: 10.1038/ngeo2162
111. D. J. Conley *et al*., Long-term changes and impacts of hypoxia in Danish coastal waters. *Ecol. Appl.* **17**, S165–S184 (2007). doi: 10.1890/05-0766.1
112. K. Eilola, E. Almroth-Rosell, H. M. Meier, Impact of saltwater inflows on phosphorus cycling and eutrophication in the Baltic Sea: A 3D model study. *Tellus Ser. A* **66**, 23985 (2014). doi: 10.3402/tellusa.v66.23985
113. A. Cabré, I. Marinov, R. Bernardello, D. Bianchi, Oxygen minimum zones in the tropical Pacific across CMIP5 models: Mean state differences and climate change trends. *Biogeosciences* **12**, 5429–5454 (2015). doi: 10.5194/bg-12-5429-2015
114. O. Duteil, A. Oschlies, Sensitivity of simulated extent and future evolution of marine suboxia to mixing intensity. *Geophys. Res. Lett.* **38**, L06607 (2011). doi: 10.1029/2011GL046877
115. J. H. Bettencourt *et al*., Boundaries of the Peruvian oxygen minimum zone shaped by coherent mesoscale dynamics. *Nat. Geosci.* **8**, 937–940 (2015). doi: 10.1038/ngeo2570
116. S. Bushinsky, S. R. Emerson, S. C. Riser, D. D. Swift, Accurate oxygen measurements on modified Argo floats using in situ air calibrations. *Limnol. Oceanogr. Methods* **14**, 491–505 (2016). doi: 10.1002/lom3.10107
117. N. Revsbech *et al*., Determination of ultra-low oxygen concentrations in oxygen minimum zones by the STOX sensor. *Limnol. Oceanogr. Methods* **7**, 371–381 (2009). doi: 10.4319/lom.2009.7.371
118. M. Larsen *et al*., In situ quantification of ultra-low O_2 concentrations in oxygen minimum zones: Application of novel optodes. *Limnol. Oceanogr. Methods* **14**, 784–800 (2016). doi: 10.1002/lom3.10126
119. K. A. Rose *et al*., Does hypoxia have population-level effects on coastal fish? Musings from the virtual world. *J. Exp. Mar. Biol. Ecol.* **381**, S188–S203 (2009). doi: 10.1016/j.jembe.2009.07.022
120. K. de Mutsert *et al*., Exploring effects of hypoxia on fish and fisheries in the northern Gulf of Mexico using a dynamic spatially explicit ecosystem model. *Ecol. Model.* **331**, 142–150 (2016). doi: 10.1016/j.ecolmodel.2015.10.013
121. K. E. Limburg *et al*., Tracking Baltic hypoxia and cod migration over millennia with natural tags. *Proc. Natl. Acad. Sci. U.S.A.* **108**, E177–E182 (2011). doi: 10.1073/pnas.1100684108; pmid: 21518871
122. R. Miller Neilan, K. Rose, Simulating the effects of fluctuating dissolved oxygen on growth, reproduction, and survival of fish and shrimp. *J. Theor. Biol.* **343**, 54–68 (2014). doi: 10.1016/j.jtbi.2013.11.004; pmid: 24269807
123. B. B. Hughes *et al*., Climate mediates hypoxic stress on fish diversity and nursery function at the land-sea interface. *Proc. Natl. Acad. Sci. U.S.A.* **112**, 8025–8030 (2015). doi: 10.1073/pnas.1505815112; pmid: 26056293
124. M. Yasuhara, G. Hunt, D. Breitburg, A. Tsujimoto, K. Katsuki, Human-induced marine ecological degradation: Micropaleontological perspectives. *Ecol. Evol.* **2**, 3242–3268 (2012). doi: 10.1002/ece3.425; pmid: 23301187
125. M. A. Rice, Extension programming in support of public policy for the management of aquaculture in common water bodies. *Aquacultura Indonesiana* **15**, 26–31 (2014).
126. R. R. Cayabyab *et al*., "Histamine fish poisoning following massive fishkill in Bolinao, Pangasinan, February 2002" (Regional Epidemiology and Surveillance Unit I Report 3, Department of Health, Philippines, 2002).
127. A. H. Altieri *et al*., Tropical dead zones and mass mortalities on coral reefs. *Proc. Natl. Acad. Sci. U.S.A.* **114**, 3660–3665 (2017). doi: 10.1073/pnas.1621517114; pmid: 28320966
128. S. S. Rabotyagov *et al*., Cost-effective targeting of conservation investments to reduce the northern Gulf of Mexico hypoxic zone. *Proc. Natl. Acad. Sci. U.S.A.* **111**, 18530–18535 (2014). doi: 10.1073/pnas.1405837111; pmid: 25512489
129. E. A. Davidson, D. Kanter, Inventories and scenarios of nitrous oxide emissions. *Environ. Res. Lett.* **9**, 105012 (2014). doi: 10.1088/1748-9326/9/10/105012
130. S. P. Seitzinger, L. Phillips, Nitrogen stewardship in the Anthropocene. *Science* **357**, 350–351 (2017). doi: 10.1126/science.aao0812; pmid: 28751593
131. K. Van Meter, N. Basu, P. Van Cappellen, Two centuries of nitrogen dynamics: Legacy sources and sinks in the Mississippi and Susquehanna River Basins. *Global Biogeochem. Cycles* **31**, 2–23 (2017). doi: 10.1002/2016GB005498
132. C. M. Duarte, D. J. Conley, J. Carstensen, M. Sánchez-Camacho, Return to Neverland: Shifting baselines affect eutrophication restoration targets. *Estuaries Coasts* **32**, 29–36 (2009). doi: 10.1007/s12237-008-9111-2

133. W. M. Kemp, J. M. Testa, D. J. Conley, D. Gilbert, J. D. Hagy, Temporal responses of coastal hypoxia to nutrient loading and physical controls. *Biogeosciences* **6**, 2985–3008 (2009). doi: 10.5194/bg-6-2985-2009
134. Chesapeake Bay Program DataHub (2017); http://data.chesapeakebay.net/WaterQuality.
135. K. N. Eshleman, R. D. Sabo, Declining nitrate-N yields in the Upper Potomac River Basin: What is really driving progress under the Chesapeake Bay restoration? *Atmos. Environ.* **146**, 280–289 (2016). doi: 10.1016/j.atmosenv.2016.07.004

ACKNOWLEDGMENTS

We thank IOC-UNESCO for financial support and for initiating and supporting the Global Ocean Oxygen Network. We also thank R. Diaz for help with updating the list of coastal sites that have reported hypoxia (Fig. 1A); B. Michael and M. Trice of the Maryland Department of Natural Resources for help with the Maryland water quality database; and our many current and past collaborators on deoxygenation research in coastal systems, OMZs, the Black Sea, and elsewhere. Funding was provided by National Oceanic and Atmospheric Administration (NOAA)–Center for Sponsored Coastal Ocean Research grant NA10NOS4780138 and Maryland Sea Grant SA75281450-P (to D.B.), NSF-EAR grant 1324095 (to L.A.L.), the Deutsche Forschungsgemeinschaft via grant SFB754 (to A.O.), and the Fonds National de la Recherche Scientifique and the BENTHOX program grant T.1009.15 (to M.G.). This study was partly supported by the BONUS COCOA project (grant 2112932-1), funded jointly by the European Union and the Swedish Research Council for Environment, Agricultural Sciences and Spatial Planning.

10.1126/science.aam7240

RESEARCH ARTICLE SUMMARY

CELL BIOLOGY

Phase separation of a yeast prion protein promotes cellular fitness

Titus M. Franzmann, Marcus Jahnel, Andrei Pozniakovsky, Julia Mahamid, Alex S. Holehouse, Elisabeth Nüske, Doris Richter, Wolfgang Baumeister, Stephan W. Grill, Rohit V. Pappu, Anthony A. Hyman,* Simon Alberti*

INTRODUCTION: The formation of dynamic, membraneless compartments using intracellular phase transitions such as phase separation and gelation provides an efficient way for cells to respond to environmental changes. Recent work has identified a special class of intrinsically disordered domains enriched for polar amino acids such as glycine, glutamine, serine, or tyrosine as potential drivers of phase separation in cells. However, more traditional work has highlighted the ability of these domains to drive the formation of fibrillar aggregates. Such domains are also known as prion domains. They have first been identified in budding yeast proteins that form amyloid-like aggregates. Because these aggregates are heritable and change the activity of the prion-domain–containing protein, they are thought to be a common mechanism for phenotypic inheritance in fungi and other organisms. However, the aggregation of prion domains has also been associated with neurodegenerative diseases in mammals. Therefore, the relationship between the role of these domains as drivers of phase separation and their ability to form prion-like aggregates is unknown.

RATIONALE: The budding yeast translation termination factor Sup35 is an archetypal prion-domain–containing protein. Sup35 forms irreversible heritable aggregates, and these aggregates have been proposed to be either a disease or an adaptation that generates heritable phenotypic variation in populations of budding yeast. Despite having been described almost 25 years ago, the physiological functions of the Sup35 prion domain and other prion-like domains remain unclear. Uncovering these functions is a prerequisite for understanding the evolutionary pressures shaping prion-like sequences and how their physiological and pathological transitions affect cellular fitness.

RESULTS: Here, we show that the prion domain of Sup35 drives the reversible phase separation of the translation termination factor into biomolecular condensates. These condensates are distinct and different from fibrillar amyloid-like prion particles. Combining genetic analysis in cells with in vitro reconstitution protein biochemistry and quantitative biophysical methods, we demonstrate that Sup35 condensates form by pH-induced liquid-like phase separation as a response to sudden stress. The condensates are liquid-like initially but subsequently solidify to form protective protein gels. Cryo–electron tomography demonstrates that these gel-like condensates consist of cross-linked Sup35 molecules forming a porous meshwork. A cluster of negatively charged amino acids functions as a pH sensor and regulates condensate formation. The ability to form biomolecular condensates is shared among distantly related budding yeast and fission yeast. This suggests that condensate formation is a conserved and ancestral function of the prion domain of Sup35. In agreement with an important physiological function of the prion domain, the catalytic guanosine triphosphatase (GTPase) domain of the translation termination factor Sup35 readily forms irreversible aggregates in the absence of the prion domain. Consequently, cells lacking the prion domain exhibit impaired translational activity and a growth defect when recovering from stress. These data demonstrate that the prion domain rescues the essential GTPase domain of Sup35 from irreversible aggregation, thus ensuring that the translation termination factor remains functional during harsh environmental conditions.

ON OUR WEBSITE

Read the full article at http://dx.doi.org/10.1126/science.aao5654

CONCLUSION: The prion domain of Sup35 is a highly regulated molecular device that has the ability to sense and respond to physiochemical changes within cells. The N-terminal prion domain provides the interactions that drive liquid phase separation. Phase separation is regulated by the adjacent stress sensor. The synergy of these two modules enables the essential translation termination factor to rapidly form protective condensates during stress. This suggests that prion domains are protein-specific stress sensors and modifiers of protein phase transitions that allow cells to respond to specific environmental conditions. ■

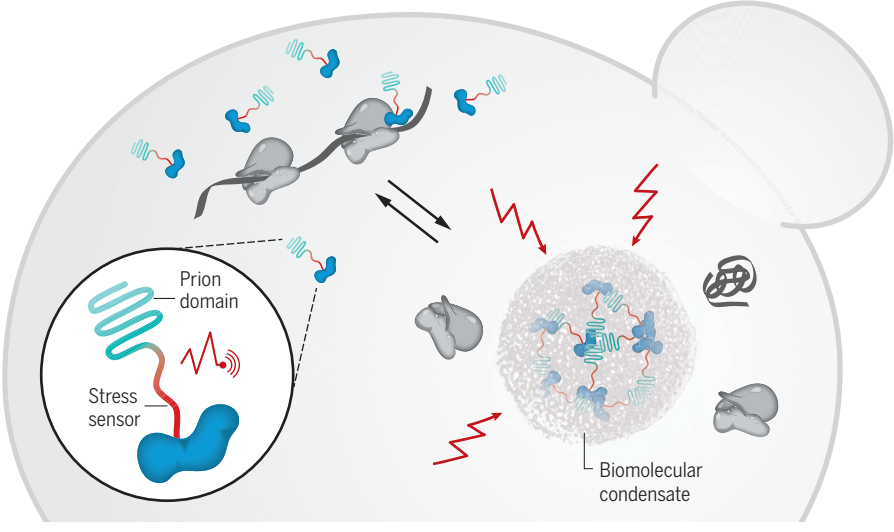

The Sup35 prion domain regulates phase separation of the translation termination factor Sup35 during cellular stress. The translation termination factor Sup35 (depicted in the magnifying glass) consists of a disordered prion domain (cyan) a disordered stress sensor domain (red) and a folded catalytic domain (blue). During growth, Sup35 catalyzes translation termination. During cell stress, the prion domain and the sensor domain act together to promote phase separation into protective and reversible biomolecular condensates.

The list of author affiliations is available in the full article online.
*Corresponding author. Email: alberti@mpi-cbg.de (S.A.); hyman@mpi-cbg.de (A.A.H.)
Cite this article as T. M. Franzmann *et al.*, *Science* **359**, eaao5654 (2018). DOI: 10.1126/science.aao5654

RESEARCH ARTICLE

CELL BIOLOGY

Phase separation of a yeast prion protein promotes cellular fitness

Titus M. Franzmann,[1] Marcus Jahnel,[1,2] Andrei Pozniakovsky,[1] Julia Mahamid,[3] Alex S. Holehouse,[4] Elisabeth Nüske,[1] Doris Richter,[1] Wolfgang Baumeister,[5] Stephan W. Grill,[1,2] Rohit V. Pappu,[4] Anthony A. Hyman,[1]* Simon Alberti[1]*

Despite the important role of prion domains in neurodegenerative disease, their physiological function has remained enigmatic. Previous work with yeast prions has defined prion domains as sequences that form self-propagating aggregates. Here, we uncovered an unexpected function of the canonical yeast prion protein Sup35. In stressed conditions, Sup35 formed protective gels via pH-regulated liquid-like phase separation followed by gelation. Phase separation was mediated by the N-terminal prion domain and regulated by the adjacent pH sensor domain. Phase separation promoted yeast cell survival by rescuing the essential Sup35 translation factor from stress-induced damage. Thus, prion-like domains represent conserved environmental stress sensors that facilitate rapid adaptation in unstable environments by modifying protein phase behavior.

The formation of dynamic, membraneless compartments via intracellular phase transition provides an efficient way for cells to respond to metabolic changes (*1*, *2*). This is because phase transitions are sensitive to small changes in physiochemical conditions, such as the cytosolic pH, which are a readout of metabolic state. Recent work has identified prion-like sequences as drivers of phase separation of protein compartments in cells (*3*–*6*). However, more traditional work has highlighted the ability of prion-like domains to form fibrillar assemblies that are thought to drive heritable phenotypic variation (*7*–*9*). Studies in humans and other mammals have implicated fibrillar assemblies of prion-like proteins in age-related neurodegeneration (*10*). Despite having been described almost 25 years ago (*11*), the physiological functions of prion-like sequences remain unclear. Uncovering this physiological function is an essential and important prerequisite for understanding whether the fibrillar assemblies are purely pathological or whether they have functional relevance.

Cells respond to stress by arresting the cell cycle, shutting down metabolism, and inducing stress-protective pathways. Upon cessation of stress, they must rapidly reprogram their metabolism and restart growth and division. When cells are stressed, they stop translation and release translation factors and mRNAs from polysomes that are subsequently sequestered in granules (*12*, *13*). After removal of stress, mRNAs reassociate with ribosomes, and translation factors ensure proper restart of protein synthesis.

The prion protein Sup35 forms reversible biomolecular condensates in stressed yeast cells

One of the key factors of protein synthesis is the protein Sup35, a translation termination factor. Sup35 is an archetypal prion domain–containing protein. Numerous studies over the past 25 years have shown that the prion domain of Sup35 forms heritable, mainly fibrillar aggregates. Consistent with this idea, when we depleted yeast of energy (see the supplementary materials), Sup35 assembled into submicrometer-scaled particles (Fig. 1A). Particle formation coincided with arrested cell growth, and cells persisted in the arrested state for as long as particles were present (Fig. 1B and movie S1).

However, a number of observations suggested that Sup35 did not actually form amyloid-like prion aggregates. First, Sup35 particles dissolved within a few minutes of removing energy stress when cells started growing (Fig. 1, A and B, and movie S1). Sup35 particles also formed in stationary phase yeast and dissolved after cells were supplied with fresh medium (Fig. 1C and fig. S1A). Neither formation nor dissolution of Sup35 particles depended on the molecular chaperone Hsp104, which is required for propagation of Sup35 prion particles (*14*) (fig. S1B). Furthermore, the stress-induced Sup35 particles did not have any of the biochemical features of amyloid-like aggregates (fig. S1, C and D). This suggests that stress-inducible Sup35 assemblies were not bona fide prion particles but may instead be biomolecular condensates (*1*, *15*) that formed reversibly upon stress.

Starved and energy-depleted yeast experience a reduction in cytosolic pH (*16*). Likewise, the cytosolic pH of stationary phase cells was acidic (fig. S1, E and F). By manipulating the cytosolic pH with the proton carrier 2,4-dinitrophenol (DNP) (*16*–*18*), we found that acidification was sufficient to induce Sup35 condensates (Fig. 1E). The condensates did not colocalize with the stress granule protein Pab1 in stationary phase cells, and partial colocalization was found in pH stressed cells (fig. S1A and G). Thus, physiological pH changes regulate the formation of reversible Sup35 condensates.

Sup35 condensates form by pH-dependent phase separation and gelation

To provide a mechanistic understanding of pH-regulated condensation, we purified Sup35 and reconstituted the condensates in vitro. When 2 μM of purified Sup35 was incubated in physiological buffer, the protein remained diffuse (Fig. 2, A and B, and fig. S2A). However, when the pH was reduced from 7.5 to 6.0, condensates of Sup35 formed (Fig. 2, A and B, and fig. S2, B to D). Sup35 condensates adopted spherical shapes in solution and deformed when contacting the microscope slide (fig. S2B), suggesting that they are liquid-like. Supporting this idea, two Sup35 drops fused when brought together with an optical tweezer (Fig. 2C and movie S2), and photobleached regions within a Sup35 condensate quickly recovered fluorescence (Fig. 2D).

Using fluorescence recovery after photobleaching, we found that Sup35 was mobile in growing cells; it became immobile when sequestered into condensates, upon stress (Fig. 1D). We confirmed this behavior in vitro, where Sup35 initially phase-separated to form liquid droplets but then solidified into a gel-like state as suggested by fusion and photobleaching experiments (Fig. 2D and fig. S2, E to G). Cryo–electron tomography of Sup35 droplets revealed that gel-like droplets consisted of an amorphous, yet well-defined, meshwork with an average mesh size of ~10 nm (Fig. 2E; fig. S2, H to K; and movie S3). Such meshwork has not been seen in droplets formed by well-described stress and P granule proteins (*3*, *19*). Gel-like condensates dissolved when the salt concentration or pH was raised or in the presence of small amounts of detergents, demonstrating reversibility in vitro (fig. S3, A to E). Thus, changes in pH regulate the formation of Sup35 into liquid droplets, which subsequently solidify.

The disordered M domain is a stress sensor that regulates phase separation of Sup35

The N-terminal region of Sup35 is intrinsically disordered and can be divided into two parts: an N-terminal prion domain (N) and a charged middle domain (M) (*20*, *21*) (Fig. 2F). The conserved C-terminal guanosine triphosphatase (GTPase)

[1]Max Planck Institute of Molecular Cell Biology and Genetics, Pfotenhauerstrasse 108, 01307 Dresden, Germany. [2]Biotec, Technische Universität Dresden, Tatzberg 47/48, 01307 Dresden, Germany. [3]European Molecular Biology Laboratory, Heidelberg, Meyerhofstrasse 1, 69117 Heidelberg, Germany. [4]Department of Biomedical Engineering and Center for Biological Systems Engineering, Washington University in St. Louis, St. Louis, Missouri, USA. [5]Max Planck Institute of Biochemistry, Department of Molecular Structural Biology, Am Klopferspitz 18, 82152 Martinsried, Germany.
***Corresponding author. Email: alberti@mpi-cbg.de (S.A.); hyman@mpi-cbg.de (A.A.H.)**

domain (C) is essential and catalyzes termination of protein synthesis. The N and M domains are dispensable, but conservation of the NM domain (*22*–*25*) indicates that they form a bipartite functional unit with an important function, which to date remains undefined.

A minimal module consisting only of the prion (N) and the M domain (NM) formed droplets in a reversible and pH-dependent manner in vitro (Fig. 2I, fig. S3F, and movie S4). The sequence of the M domain has a linear cluster of ionizable groups, specifically glutamic acid residues, located at the C-terminal end (Figs. 2F and 3A). Removing the charges within the negative cluster (Sup35M3 variant) yields a fully functional Sup35 variant (fig. S3, G and H) but with altered phase behavior, such that protein-rich droplets formed at pH 7.5 and the pH dependence of droplet formation was discernibly reduced in vitro (Fig. 2G) and in vivo (Fig. 2H and fig. S3I). Thus, pH sensing of Sup35 is facilitated by its charged M domain through protonation of glutamates. We propose that the high density of acidic residues in the M domain causes an upshift in the pK_a value of glutamic acid (where K_a is the acid dissociation constant), which is normally ~4.1 (*26*). This is consistent with recent studies demonstrating up-shifted pK_a values in acidic tracts of disordered proteins (*27*)

We next dissected the role of the individual Sup35 domains. The isolated C domain formed interconnected irreversible aggregates at all tested pH conditions (*28*) (Fig. 2I and fig. S3, J to L). In the presence of the M domain, the extent of irreversible aggregation was strongly reduced, in agreement with a solubilizing role of M (fig. S3L). The presence of M also partially restored condensate formation, but the amount of condensate formed was an order of magnitude lower than for the wild-type protein (Fig. 2I and fig. S3, L and M). Thus, the NM domain helps maintain the solubility of, and provides the pH sensitivity for, the C-terminal termination factor, in which the N domain provides the cohesiveness required for condensation. In other words, the disordered NM domain alters the phase behavior of the C domain by promoting the formation of reversible gels instead of irreversible aggregates. This phenomenon is consistent with the ideas of Semenov and Rubinstein, who predicted that gelation is driven by phase separation for so-called associative polymers (*29*). This phenomenon has been predicted to be relevant for linear multivalent proteins (*30*), and it appears to apply to Sup35 as well.

Phase separation of Sup35 but not prion formation is conserved among distantly related yeast

The charge distribution, but not the sequence within the Sup35 M domain, is conserved across diverse fungi (Fig. 3A, fig. S4A, and table S1). Indeed, Sup35 from *Schizosaccharomyces pombe* exhibited similar behavior compared with that of *Saccharomyces cerevisiae*; in vivo, it formed stress-dependent intracellular condensates (Fig. 3, B and C, and fig. S4B), and in vitro, it formed reversible liquid droplets at low pH (Fig. 3, D to G; fig. S4, C to G; and movie S5) that cross-link into a meshwork that was indistinguishable from the one of Sup35 from *S. cerevisiae* (Fig. 3H; figs. S4, H to J; and movie S6). Importantly, and in contrast to *S. cerevisiae*, *Sc. pombe* is unable to induce and propagate the prion state of Sup35 (*25*). Thus, condensate formation, but not prion formation, is conserved among distantly related yeast that diverged more than

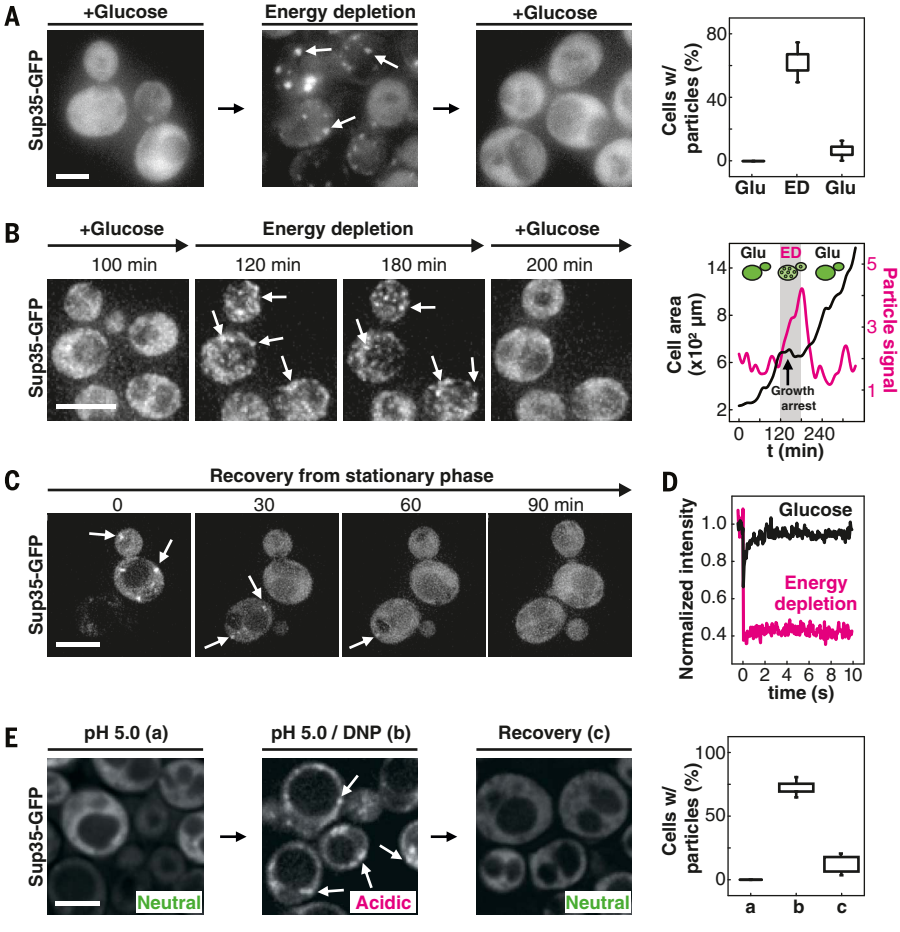

Fig. 1. Sup35 forms reversible condensates in *S. cerevisiae*. (**A**) Fluorescence images of *S. cerevisiae* expressing green fluorescent protein (GFP)–labeled Sup35 during exponential growth (left), during energy depletion (middle), and after recovery from energy depletion (right). Energy depletion causes reversible condensation of Sup35 into intracellular puncta. White arrows point toward Sup35 condensates. The graph on the right shows a quantification of the cells with particles. About 150 to 200 cells per condition were used for quantification. (**B**) Fluorescence images taken from a time-lapse movie (see movie S1) of *S. cerevisiae* growing in a microfluidic device (CellAsic). Cells were grown in synthetic complete media for 2 hours. After 120 min, cells were energy-depleted to form Sup35 condensates. Condensates persisted during energy depletion and dissolved when the cells were recovered by being supplied with fresh synthetic medium. White arrows point toward Sup35 condensates. Cell growth was measured as the total increase in occupied area (cell area) as a function of time (t) (black). For particle signal, the maximum fluorescence signal was divided by the minimum fluorescence signal (magenta). Energy depletion coincides with growth arrest and Sup35 condensation. (**C**) Fluorescence images of *S. cerevisiae* expressing GFP-labeled Sup35 during recovery from stationary phase. Cells were grown to stationary phase for 2 days. White arrows point toward Sup35 particles. Supplying cells with growth medium (t_0) caused dissolution of intracellular condensates and restart of cell growth. (**D**) The intracellular mobility of Sup35 was accessed by fluorescence recovery after photobleaching. The recovery of fluorescence of GFP-labeled Sup35 was measured in exponentially growing (black) and energy-depleted (magenta) cells. (**E**) Fluorescence images of *S. cerevisiae* expressing GFP-labeled Sup35 in 100 mM phosphate, pH 5 (left), 100 mM phosphate buffer, 2 mM DNP, pH 5 (middle), and after 60 min of recovery with synthetic complete medium (right). About 150 to 200 cells were used for quantification of each condition. Box indicates intracellular pH as described by Munder *et al*. (*16*). Scale bar, 5 µm.

400 million years ago and suggests that condensate formation may be the ancestral function of the prion domain of Sup35.

Taken together, our data show that Sup35 forms condensates by pH-dependent phase separation and subsequent gelation into a porous polymer meshwork. The intrinsic disorder of the prion domain likely provides the necessary flexibility for the formation of the meshwork, whereas the precise interactions that cross-link the gel remain to be elucidated (*31*).

Phase separation rescues the catalytic domain of Sup35 from stress-induced damage

To look at the role of the NM domain during the stress response in yeast, we compared the fitness of cells expressing similar levels of full-length Sup35 and the C domain alone (Sup35C) (fig. S5A). We also monitored the aggregation state of the proteins. Cells expressing only the C domain grew without a noticeable growth defect in the absence of stress (Fig. 4, A and B), and at the same time the protein was diffuse and soluble (Fig. 4C). Thus, the C domain is not aggregation-prone in the cellular environment, presumably because of the presence of ligands such as guanosine 5′-triphosphate (GTP) (*28*) (fig. S2A). After stress, the C domain aggregated in a manner that was similar to that of the full-length protein (Fig. 4D). However, after removal of stress, Sup35 condensates dissolved within minutes in wild-type cells. In contrast, in Sup35C cells, dissolution of aggregates could take several hours (Fig. 4, C and D, and fig. S5B). This suggests that the NM domain determines the material properties (reversible gel versus irreversible aggregate) of Sup35 in vivo. Concomitantly, Sup35C cells took longer to restart growth (Fig. 4, A and C, and movies S7 and S8) and exhibited reduced fitness when recovering from stationary phase (Fig. 4B).

Sup35 catalyzes an essential step during protein synthesis, namely translation termination. Indeed, translation was shut down upon energy depletion, as indicated by polysome disassembly (fig. S5, C and D). This coincided with Sup35 condensation. Conversely, dissolution of Sup35 condensates coincided with polysome reformation (fig. S5, C and D). Importantly, translation activity was specifically impaired after energy depletion in recovering Sup35C cells but not in control cells (Fig. 4E).

The prion state interferes with Sup35 condensate formation and impairs recovery of yeast from stress

How does the prion state of Sup35 affect the ability of cells to recover from stress? To investigate this, we compared prion-containing [*PSI*+] with prion-free [*psi*–] cells for their ability to regrow from the stationary phase (*32*). [*PSI*+] cells grew without a noticeable defect under normal conditions, but they showed a growth delay after recovery from stationary phase that was similar to that of Sup35C cells (Fig. 4F and fig. S5E). This suggests that the formation

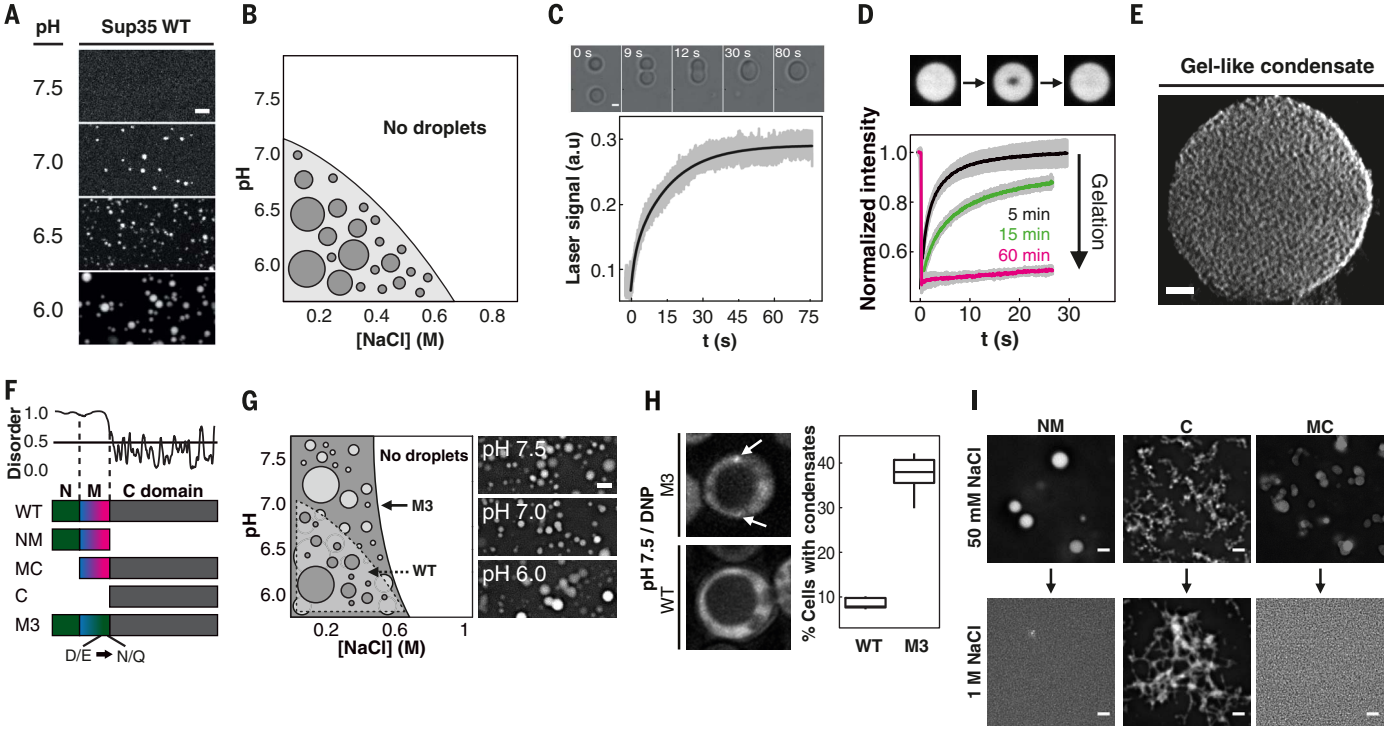

Fig. 2. The Sup35 prion domain synergizes with a pH sensor to drive phase separation into biomolecular condensates. (**A**) Fluorescence images of 2 μM GFP-labeled wild-type (WT) Sup35 at indicated pH. Scale bar, 2 μm. (**B**) Phase diagram of 2 μM WT Sup35 with pH and salt concentration as order parameters. Phase separation was scored by the presence or absence of droplets in the samples. (**C**) Fusion of two Sup35 droplets at pH 6.0. Still images are shown on top. A force curve is shown at the bottom. Scale bar, 2 μm. (**D**) Internal rearrangement of Sup35 molecules was assayed by fluorescence recovery after photobleaching as a function of gelation time. A single pixel spot was bleached, and the change in the fluorescence was analyzed as a function of time. Still images are shown before and after bleaching. The drop size was ~3 μm. Analysis of the fluorescence recovery of 5-min-old (black; N = 19), 15-min-old (green; N = 9), and 60-min-old (magenta; N = 11) drops are shown. SD depicted as gray shadow. (**E**) Three-dimensional (3D)–rendered volume of WT Sup35 gel-like droplet imaged with cryo–electron tomography. Scale bar, 50 nm. (**F**) Disorder analysis (top) and schematic of the *S. cerevisiae* Sup35 domain structure. N (N) and middle (M) domain are disordered. The C-terminal domain is folded. Color gradient in M depicts the net charge along the sequence (blue, positive; magenta, negative; green, neutral). (**G**) Phase diagram of 2 μM Sup35M3 variant with pH and salt concentration as order parameters. Dashed line indicates the phase diagram of Sup35 WT as shown in (B). Representative images of 2 μM Sup35M3-GFP at indicated pH shown. Scale bar, 2 μm. (**H**) Fluorescence images and quantification of *S. cerevisiae* expressing Sup35M3 (top) and Sup35 WT (bottom) in 40 mM PIPES, pH 7.5, 2 mM DNP. Sup35M3 forms condensates at neutral pH, whereas WT stays diffuse. (**I**) Phase separation of Sup35 variants was probed at 2 μM final protein concentration (top). Dissolution was tested by increasing the salt concentration from 50 to 1000 mM NaCl (bottom). Scale bar, 2 μm.

of stress-protective Sup35 condensates is impaired in the presence of the prion and that [*PSI*+] cells have a reduced fitness when recovering from stress. This demonstrates that the ribosome critically depends on the availability of Sup35 after stress. Taken together, these experiments show that the NM domain provides the catalytic C domain of Sup35 with the ability to recover rapidly from stress, and thus ensures a critical step in restarting translation (Fig. 5).

Discussion

Sup35 is a prominent member of a class of proteins with prion-like domains. These are low-complexity protein domains that consist primarily of polar and aromatic amino acids. They are called prion-like domains because they have been associated with the ability of proteins to spread through yeast populations in a prion-like manner (*33*). Indeed, numerous studies have highlighted the aggregation potential of prion-like domains when studied in isolation. Our data suggest that the prion domain, in the context of the full-length protein, adopts a benign role by increasing the solubility of the C-terminal catalytic domain at neutral pH and promoting Sup35 phase separation and gelation under stress. Thus, reversible gel formation, but not prion formation, is likely the ancestral function of the prion domain of Sup35. In agreement, many de novo formed variants of Sup35 prions cause cellular toxicity, suggesting that the prion state could be a sporadically occurring disease (*34*–*37*). Prion states may thus be a frequently occurring epiphenomenon of condensate-forming domains, which may or may not have adaptive value.

More generally, organisms must adapt to sudden changes in the environment, independent of transcriptional and translational regulation. In agreement with previous conjectures (*38*), we suggest that prion domains are protein-specific stress sensors and modifiers of phase transitions that allow cells to respond to specific environmental conditions. In the case of Sup35, this condition is the lowering of the cytosolic pH under energy stress. However, yeast contains more than 200 proteins with predicted prion-like domains, and *Dictyostelium* contains more than 1000 such proteins (*39*, *40*). It seems likely that organisms deploy prion-like domains to generate protein-specific environmental responses. In agreement, another prion-like domain has recently been shown to tune the phase behavior of the yeast stress granule protein Pab1 (*5*). Prion domains are therefore crucial stress-adaptive regions that allow organisms to explore and persist in stressful and unstable environments.

Materials and methods

Strains and culture conditions

S. cerevisiae was grown at 30°C in yeast extract peptone dextrose (YPD), synthetic complete (SC) or synthetic dropout (SD) medium. *Sc. pombe*

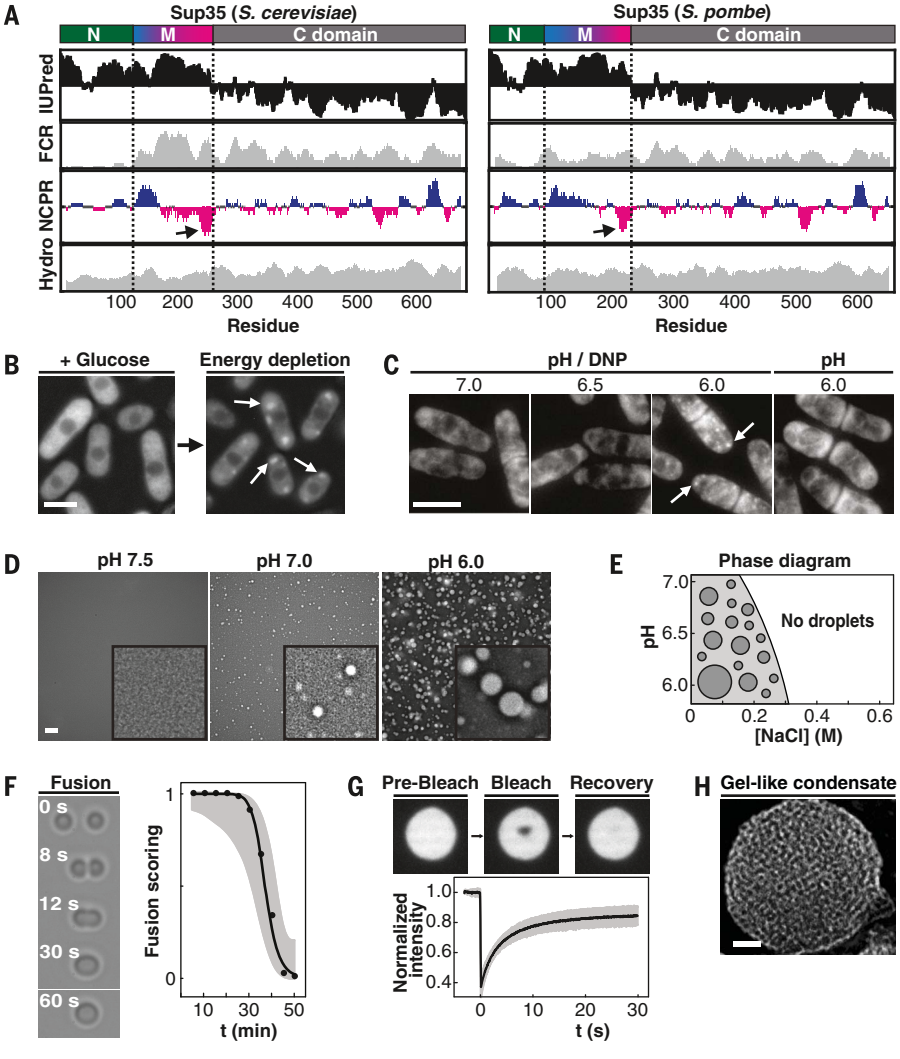

Fig. 3. Phase separation of Sup35 is conserved in the evolutionarily distant fission yeast *Sc. pombe*. (**A**) Comparative bioinformatic analysis of Sup35 from *S. cerevisiae* (left) and *Sc. pombe* (right). Sup35 has three domains. The N (green) and M (blue-magenta) domains are predicted to be disordered, and the C domain (gray) is a folded and conserved GTPase domain (degree of predited disorder; IUPred). FCR, fraction of charged residues; NCPR, net charge per residue; Hydro, hydrophobicity. M is disordered and contains a high density of charged residues with a blocky architecture. It carries an overall net negative charge with a net positive charge at the N-terminal half and a strong net negative charge at the end of M. Arrows point toward the M3 charge cluster. (**B**) Fluorescence images of *Sc. pombe* expressing mCherry-labeled Sup35 grown in medium (left) and after 30 min of energy depletion (right). Scale bar, 5 μm. (**C**) Fluorescence images of *Sc. pombe* expressing mCherry-labeled Sup35 exposed to 100 mM phosphate buffer in the presence or absence of DNP at indicated pH. Scale bar, 5 μm. (**D**) Fluorescence images of 2 μM *Sc. pombe* Sup35 in 20 mM PIPES; 3% polyethylene glycol (PEG), 50 mM NaCl at indicated pH. Scale bar, 2 μm. (**E**) Phase diagram of Sup35 WT from *Sc. pombe* with pH and salt concentration as order parameters. Phase separation of 2 μM Sup35 was scored by the presence or absence of droplets in the respective sample. (**F**) Controlled fusion experiment of two *Sc. pombe* Sup35 droplets using a dual-trap optical tweezer. Still images show fusion of two Sup35 WT droplets (left). Upon contact, Sup35 droplets fuse and coalesce into one spherical droplet. Size of droplets ~3 μm. Solidification of *Sc. pombe* Sup35 WT was assayed by their ability to fuse with each other as a function of time. Successful fusion was scored 1, when droplets coalesced into a new spherical droplet within 30 s (right). (**G**) Internal rearrangement of *Sc. pombe* Sup35 WT molecules was assayed by fluorescence recovery after photobleaching experiments. Sup35-GFP (2 μM) was incubated with 20 mM PIPES, 50 mM NaCl, 3% PEG20K pH 6.0. A single pixel bleach spot was placed in the center of the drop, and the change in the local fluorescence was analyzed as a function of time. Size of droplets ~3 μm. (**H**) Three-dimensional volume rendering of a *Sc. pombe* Sup35 droplet in 20 mM PIPES, 50 mM NaCl, 3% PEG20K pH 6.0 imaged with cryo–electron tomography. Scale bar, 50 nm.

was grown at 30°C in YE5 or EMM5 medium. A list of yeast strains is in table S2.

Plasmids and cloning

A list of plasmids used here can be found in table S2. Gateway cloning (Invitrogen) was carried out as described previously (*41*). *Sc. pombe* Sup35-mCherry was generated according to (*42*) using standard primers for amplification of the linear tagging cassette carrying the fluorescence protein tag. *Sc. pombe* was transformed with purified PCR product (*43*) and selected clones were verified using standard primers (*42*).

Energy depletion of cells

S. cerevisiae and *Sc. pombe* cells were energy depleted as described previously (*16*, *17*). In short: Exponentially growing yeast were transferred to and incubated in liquid SC medium or EMM medium, respectively, without glucose containing 20 mM 2-deoxyglucose (2-DG, inhibition of glycolysis) and 10 μM antimycin A (inhibition of mitochondrial ATP production). Treatment causes about 95% reduction in cellular ATP (*44*). Recovery of cells from energy depletion was by replacing energy depletion media with media containing 2% glucose. In a microfluidic setup (CellAsic), cells were grown for 2-3 hours with media prior to treatment. Medium was pumped with 2 PSI. Exchange of medium was carried out with 4 PSI for 2 min.

pH stress

Exponentially growing *S. cerevisiae* and *Sc. pombe* cells were transferred to 100 mM phosphate buffer of different pH containing 2 mM 2,4-dinitrophenol (DNP). Control samples were treated equally, but DNP was omitted. Cell recovery was by replacing buffer with medium containing 2% glucose. In a microfluidic setup (CellAsic), cells were grown for 2-3 hours prior to treatment. Medium was pumped with 2 PSI. Exchange of medium was at 4 PSI for 2 min.

Microscopy of yeast

Samples were prepared as described above. Imaging was with a DeltaVision (Applied Precision) microscope (Olympus IX70 stand, Osram Mercury short arc HBO light source, Olympus UPlanSApo 100x oil objective, CoolSnap HQ2 camera). Z stacks with 6 planes were collected. Imaging settings were: 5% excitation intensity, 0.15 s exposure time, 512x512 pixels, 2x2 binning.

FRAP measurements

In vivo and in vitro fluorescence recovery after photobleaching (FRAP) experiments were carried out with an Andor spinning disc microscope (Nikon TiE inverted stand, Nikon Apo 100x, NA 1.49 Oil objective, Andor iXon+ camera, EM gain 200, imaging laser intensity of 0.3% for reconstituted protein droplets and 5% for cells) equipped with a FRAPPA unit (Andor). A single pixel was bleached with a 405-nm laser pulse (1 repeat, 10% intensity, dwell time 10 ms). Recovery from photobleaching was recorded in a single focal plane. Image analysis was carried out in Fiji.

Ratiometric pH measurements

Cytosolic pH measurements were carried out as described in (*16*, *17*). In short: pHluorin2 (*45*) was expressed in W303 ADE+ under control of a GPD promoter. pH calibration was obtained as described previously (*16*, *46*). Imaging was carried out using DAPI/FITC (Excitation: DAPI; Emission: FITC) and FITC/FITC (Excitation and emission: FITC) filter sets on a DeltaVision (Applied Precision) microscope (Olympus IX70 stand, Osram Mercury short arc HBO light source, 100x Olympus UPlanSApo objective, CoolSnap HQ2

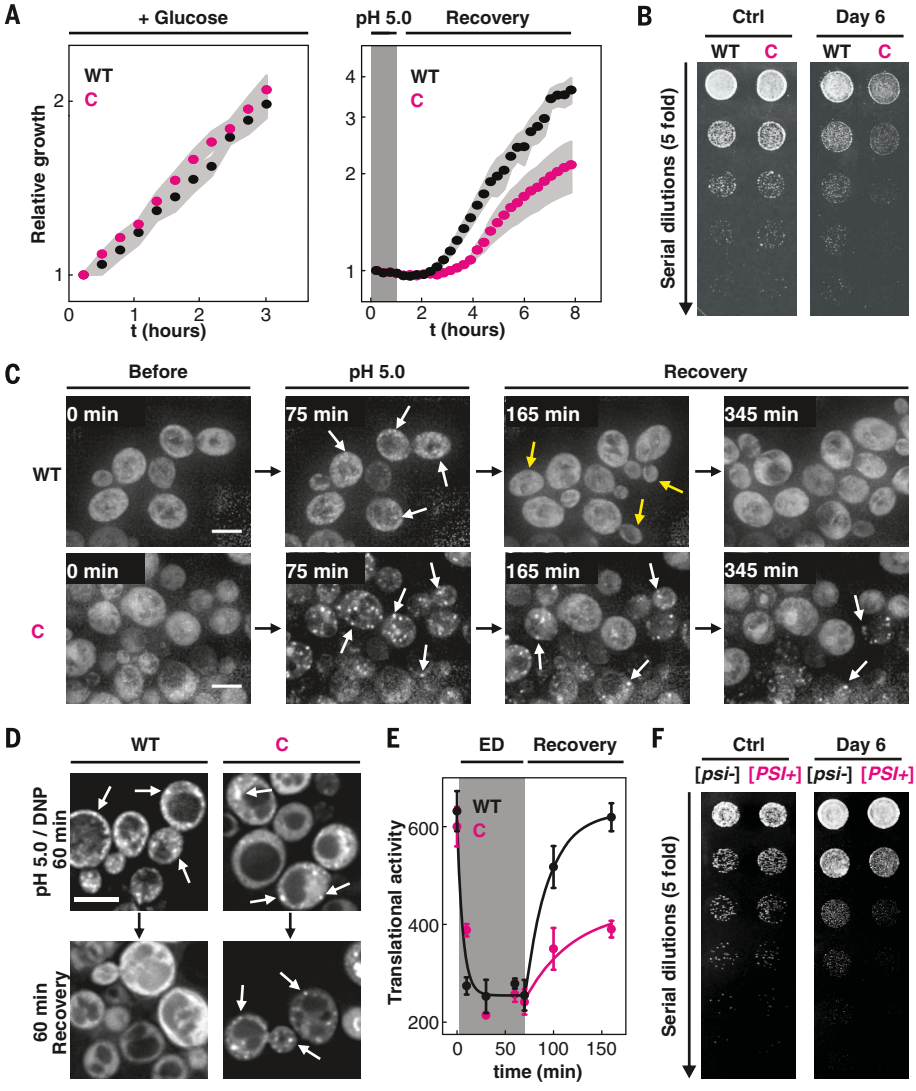

Fig. 4. The prion domain and a pH sensor work in synergy to protect the C domain from stress-induced damage. (**A**) Growth analysis of *S. cerevisiae* expressing WT Sup35 (black) or Sup35C (magenta) growing in synthetic complete medium in a microfluidic setup for 3 hours (left) and upon exposure to and recovery from pH 5.0/DNP for one hour (indicated in gray). SEM is shown in gray. *N* = 9 fields of view. (**B**) Spot-titer growth assay of *S. cerevisiae* expressing WT Sup35 (WT) and Sup35C (C) (Ctrl; exponentially growing cells were spotted) (left) and after recover from stationary phase. (**C**) Fluorescence images of *S. cerevisiae* expressing WT Sup35-GFP (top) and Sup35C-GFP (bottom) before (Before), during pH 5.0/DNP (pH 5.0), and during recovery (Recovery). WT Sup35-GFP particles dissolve rapidly during recovery, and cells grow and divide. Yellow arrows point toward newly formed yeast buds. Particles formed by Sup35C-GFP persist, and cells remain in an arrested state for a long time. Scale bars, 5 μm. (**D**) Fluorescence images of *S. cerevisiae* expressing WT Sup35-GFP (left) and Sup35C-GFP (right) after exposure to pH 5.0/DNP for 60 min (top) and after 60 min of recovery (bottom). Arrows point toward Sup35 condensates. (**E**) Translational activity was determined for cells expressing WT Sup35 and Sup35C during exponential growth (first data point), during 60 min of energy depletion (ED; highlighted in gray) and during the recovery (Recovery). SD is shown; *N* = 500 to 700 cells per data point. (**F**) Spot-titer growth assay of the exponentially grown [*psi*-] and [*PSI*+] yeast (Ctrl) and cells that were grown to stationary phase cells for 6 days (Day 6).

camera). The mean DAPI/FITC to FITC/FITC ratio per cell was calculated from the intensity readouts and compared to the pH calibration.

Yeast growth assays

S. cerevisiae were grown overnight in YPD, diluted to OD600 ~0.1 the next morning and regrown for two days. Stationary phase samples were taken every 24 hours over 20 days, spotted on YPD agar plates as five-fold serial dilutions. Plates were photographed 28 hours after spotting.

Semi-denaturing agarose-gel electrophoresis (SDD-AGE)

Yeast cells were grown to mid exponential phase in liquid rich medium at 30°C. Cells were washed with water and then subjected to the following treatments: 2 hours 100 mM phosphate buffer pH 5.7, 2 mM DNP, 2 hours 100 mM phosphate buffer pH 7.5, 2 mM DNP, 2 hours energy depletion (20 mM 2-Deoxyglucose, 10 µM Antimycin A) and 10 min heat shock at 46°C. Cells were harvested by centrifugation and resuspended in 50 mM Tris, pH 7.5, 150 mM NaCl, 5 mM EDTA, 1% (v/v) Triton X-100, 30 mM NEM, 1 x Complete Protease Inhibitor (Roche). The cells were then lysed using glass beads (TissueLyser II from Qiagen, settings: 15 min, 25/sec) and were briefly spun at 2,000 rpm to sediment debris. 90 µl of supernatant were mixed with 4 × sample buffer (2 x TAE, 20% (v/v) glycerol, 4% (w/v) SDS, bromophenol blue). Samples were incubated at room temperature for 10 min and 50 µL were loaded onto a 1.5% agarose gel containing 1 x TAE and 0.1% SDS. The gel was run in 1 x TAE, 0.1% SDS at 100 V, followed by blotting onto a nitrocellulose membrane (GE Healthcare Life Sciences), as described in (*47*). Detection was with ECL plus solution (GE Healthcare Life Sciences) and a primary antibody against the C-terminal domain of Sup35 (Sup35C antibody kindly provided by R. Halfmann) and a secondary anti-mouse antibody.

Polysome profiling

Polysome profiling was adapted as described in (*48*). In short: 250 mL yeast cultures were grown to OD600 nm = 0.5. 100 mL were treated as untreated control sample, 150 mL were energy depleted as described above. After energy depletion, cycloheximide was added at a final concentration of 0.1 mg/ml to arrest polysomes and the samples were incubated on ice for 5 min. Cells were centrifuged 5 min at 3000 rpm and washed with 5 mL ice-cold polysome extraction buffer (PEB: 20 mM Tris-HCl pH7.4, 140 mM KCl, 5 mM MgCl2, 0.1 mg/ml cycloheximide, 0.5 mM DTT, DECP treated H2O). Cells were resuspended in 800 µL PEB, supplemented with 500 µL glass beads and lysed using a bead beater for 5 min at 30 Hz. The lysate was cleared by centrifugation for 5 min at 8000 × g, the absorbance at 260 nm was determined and an OD260 nm of 20 of the supernatant were layered onto the sucrose gradient. The samples were subjected to ultracentrifugation for 2.5 hours at 35 krpm in an SW40 Ti rotor (Beckman). The gradients were subjected to UV 260 nm readings using a peristaltic pump.

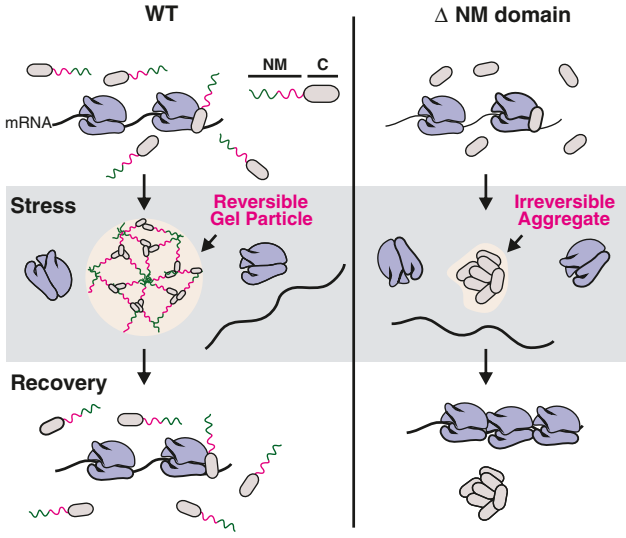

Fig. 5. The role of the Sup35 prion domain in stress adaptation. Sup35 is soluble and catalyzes translation termination during growth. This function is independent of the N-proximal domain (NM) that comprises a prion domain (N, green) and a pH sensor domain (M, magenta). Stress, such as energy depletion, causes a decrease in intracellular pH (middle). The Sup35M domain senses changes in pH by protonation of negatively charged residues. This regulates interactions of the N-terminal prion domain to form biomolecular condensates (left). The Sup35 condensates subsequently solidify into a protective gel-like meshwork sequestering the translation termination factor. In the absence of the disordered NM domain, the C domain undergoes irreversible aggregation (right). Upon cessation of stress, Sup35 gels readily dissolve, releasing the translation termination factor (bottom). The C domain persists in an aggregated state in the absence of the prion domain, thereby impairing protein translation.

Translation activity assay

Cells were grown to mid-log phase in SC medium. Samples were taken before, during after energy depletion at indicated time points. Newly synthesized proteins were labeled by resuspending the cells in SD medium depleted for methionine and supplemented with the methionine analog HPG (Invitrogen) for a 10-min pulse. Samples were fixed with 3.7% formaldehyde, washed twice with PBS and the cell wall was digested with Zymolyase (ZymoReseach). Cells were washed twice with PBS, 3% v/v BSA and permeabilized with 0.5% Triton X-100. Samples were mounted in 4-well dishes treated with polylysine. Click chemistry for HPG labeling was carried out according to the manufacture protocol (Click-iT, Invitrogen). Samples were imaged with a DeltaVision Elite as described above. Image analysis was carried out with Fiji.

Protein purification

Recombinant Sup35 and variants were expressed as N-terminal MBP-fusion proteins with a C-terminal His-Tag. Expression was by baculovirus expression in SF9 insect cells (*3*). Cells were lysed in buffer A (50 mM Tris-HCl, 1 M KCl, 2 mM EDTA, 1 mM DTT, pH 7.5) supplemented with cOmplete Protease Inhibitor Cocktail (Roche) using an Emulsiflex C5 (Avestin). Lysates was cleared by centrifugation (20,000 rpm, JA-25.50 rotor (Beckman Coulter), 60 min, 4°C). Supernatant was applied to MBP resin and washed with 20 column volumes buffer A. Elution was with 20 mM Maltose in buffer A. Samples were pooled and GST-tagged precision protease was added to cleave off the MBP- and His-tag and dialyzed against buffer A overnight at 4°C. The sample was cleared by centrifugation and subjected to size exclusion chromatography using a Superdex-200 26/60 column (GE Healthcare Life Sciences) equilibrated with buffer A running on a BioCad 60 (Applied Biosystems) at RT. Pooled samples were concentrated and frozen in liquid nitrogen.

Reconstitution and microscopy of protein-rich droplets

Protein-rich droplets of Sup35 were formed by dilution of the protein from a stock solution into 20 mM PIPES, 2% Polyethlenglycol 20K. pH was adjusted with NaOH and the respective pH of the buffer is denoted in the figures and figure legends. Sup35 phase separation was tested at concentrations ranging from 0.1-20 µM. Phase diagrams were obtained at 2 µM Sup35. Samples were mixed in low-binding PCR vials and imaged on PEG-silane pacified microscopy slides and/or in 384 low-binding multi-well microscopy plates (Greiner Bio-One). Phase separation was scored yes or no, depending on the presence or absence of protein droplets. Samples for phase diagrams were imaged with a DeltaVision Elite (GE Healthcare Life Sciences), equipped with a multi-well plate holder using an Olympus UPlan SApochromat 100x, NA 1.4 Oil objective. Excitation of GFP labeled samples was at 488 nm and emission was at 520 nm. 20 µm z-stacks with 1 µm spacing were taken. For statistical representation and analysis 16 fields of views with a 50 µm spacing were recorded per sample. Enrichment measurements were carried out on an Andor spinning disc confocal microscope using a Nikon Apo 100x, NA 1.49 Oil objective on a Nikon TiE, inverted stand. Excitation was with a 488 nm DPSS laser.

Emission was recorded at 520 nm and detected with an Andor iXon EM+ DU-897 BV back illuminated EMCCD camera. 10 μm z-stacks with a spacing of 0.5 μm were taken. 9-16 field of views per sample were recorded. Image analysis was carried out with FIJI.

Cryo–electron microscopy and tomography

Copper Quantifoil grids (R2/1, Cu 200 mesh grid, Quantifoil Micro Tools) were glow discharged for 45 s and incubated with BSA-coated 15 nm gold nanoparticles. The solution was allowed to dry to adhere gold particles to the grid support and serve as fiducials for the alignment of tilt series. Phase separation was carried out immediately prior to the application of samples to the grids. 4 μl from each sample were deposited on grids and allowed to settle 30 s. Grids were plunge-frozen into liquid ethane/propane mixture at close to liquid nitrogen temperature using a Vitrobot Mark 4 (FEI). The blotting conditions were set to blot force 0.5-5 s blot time and 2 s drain time. Grids were stored in liquid nitrogen until usage. The blotting chamber conditions were set to 22°C, 90% humidity. Cryo–electron microscopy observations were performed on a Titan Krios operated at 300 kV (FEI), equipped with a field-emission gun, a Quantum post-column energy filter (Gatan) operated in the zero-loss mode, and a special heated phase plate holder (FEI). Data was recorded on a K2 Summit (Gatan) direct detector camera operated in dose fractionation mode. Electron micrographs were recorded under low-dose conditions (10-15 e/Å^2) at EFTEM magnification of 42000 x, corresponding to a pixel size 0.342 nm with target defocus of 4 μm. Individual frames acquired by K2 camera were aligned using an in-house implementation following procedures developed by Li *et al.* (*49*). Tilt-series were collected using SerialEM software (*50*). Tomography acquisition parameters were as follows: EFTEM magnification 42000 x; tilt range was ±60°; tilt increment 2°; total dose ~60 e/Å^2; pixel size 0.342 nm. Data was acquired at target defocus of -0.5 μm with a Volta phase plate. Alignment of tilt-series projection images was performed with gold nanoparticles as fiducials with IMOD software. Final alignment of the tilt-series images was performed using the linear interpolation option in IMOD and a low pass filter (cut off, 0.35; sigma, 0.05). No CTF correction was performed. Filtered volumes were generated in Matlab (Mathworks 2015) using TOM Toolbox and 3D rendered based on intensity threshold with the UCSF Chimera package (http://www.cgl.ucsf.edu/chimera).

Optical tweezer measurements

Controlled droplet fusion experiments were performed in a custom-built dual-trap optical tweezer microscope with two movable traps (*51*). At t = 0, phase separation of Sup35 droplets was induced. 10 μl of the reaction volume were applied and sealed in a static flow chamber (coverslip–double-sided tape–coverslip sandwich). Sample preparation and mounting was carried out within 2-3 min. Protein droplets were trapped due to a mismatch in the index of refraction between droplets and buffer. The laser power of the 1064 nm trapping laser was kept at minimum (<70 mW) to prevent heating artifacts. Keeping one optical trap stationary, the other optical trap was moved until droplets touched, after which droplet fusion was recorded with a temporal resolution of 1 ms (1 kHz). Apparent fusion times were derived from exponential fitting of the fusion traces and normalizing the apparent fusion time by the geometric radii of the droplets. Time of gelation at different conditions was measured by scoring successful and unsuccessful fusion events according to the following criteria: Fused droplet must relax to spherical shape within 30 s. Logistic regression was performed on the resulting curves.

Bioinformatics

Sequence analysis of Sup35 from *S. cerevisiae* and *Sc. pombe* was performed using localCIDER (*52*), IUPred (*53*), and the SuperFamily database (*54*). For each protein, six analysis tracks were generated. SupFam defines the functionally annotated domains, identifying the three well-characterized folded regions in the C-terminal domain. IUpred describes the degree of predicted disorder; the N and M domains are predicted to be disordered while the C domain is predicted to be folded. The remaining four tracks use a 20-residue sliding window to compute local sequence properties of relevance to disordered regions. FCR describes the fraction of charged residues and shows the N domain has relatively few charged residues while the M domain is substantially enriched. NCPR describes the net charge per residue. Despite substantial sequence divergence, the M domains have a characteristic charge distribution of a positively charged N-terminal region and a negatively charged C-terminal region. Hydro describes the local hydrophobicity using the Kyte-Doolite hydrophobicity scale. Comparative charge distribution of various yeast species was also carried out using the emboss explorer charge module with a sliding window of 20-residues. Sequence identify analysis was carried out with ClustalOmega.

REFERENCES AND NOTES

1. S. F. Banani, H. O. Lee, A. A. Hyman, M. K. Rosen, Biomolecular condensates: Organizers of cellular biochemistry. *Nat. Rev. Mol. Cell Biol.* **18**, 285–298 (2017). doi: 10.1038/nrm.2017.7; pmid: 28225081
2. C. P. Brangwynne *et al.*, Germline P granules are liquid droplets that localize by controlled dissolution/condensation. *Science* **324**, 1729–1732 (2009). doi: 10.1126/science.1172046; pmid: 19460965
3. A. Patel *et al.*, A liquid-to-solid phase transition of the ALS protein FUS accelerated by disease mutation. *Cell* **162**, 1066–1077 (2015). doi: 10.1016/j.cell.2015.07.047; pmid: 26317470
4. A. Molliex *et al.*, Phase separation by low complexity domains promotes stress granule assembly and drives pathological fibrillization. *Cell* **163**, 123–133 (2015). doi: 10.1016/j.cell.2015.09.015; pmid: 26406374
5. J. A. Riback *et al.*, Stress-triggered phase separation is an adaptive, evolutionarily tuned response. *Cell* **168**, 1028–1040 (2017). doi: 10.1016/j.cell.2017.02.027; pmid: 28283059
6. M. Kato *et al.*, Cell-free formation of RNA granules: Low complexity sequence domains form dynamic fibers within hydrogels. *Cell* **149**, 753–767 (2012). doi: 10.1016/j.cell.2012.04.017; pmid: 22579281
7. D. M. Garcia, D. F. Jarosz, Rebels with a cause: Molecular features and physiological consequences of yeast prions. *FEMS Yeast Res.* **14**, 136–147 (2014). doi: 10.1111/1567-1364.12116; pmid: 25667942
8. R. Halfmann, S. Lindquist, Epigenetics in the extreme: Prions and the inheritance of environmentally acquired traits. *Science* **330**, 629–632 (2010). doi: 10.1126/science.1191081; pmid: 21030648
9. R. Halfmann, S. Alberti, S. Lindquist, Prions, protein homeostasis, and phenotypic diversity. *Trends Cell Biol.* **20**, 125–133 (2010). doi: 10.1016/j.tcb.2009.12.003; pmid: 20071174
10. A. F. Harrison, J. Shorter, RNA-binding proteins with prion-like domains in health and disease. *Biochem. J.* **474**, 1417–1438 (2017). doi: 10.1042/BCJ20160499; pmid: 28389532
11. R. B. Wickner, [URE3] as an altered URE2 protein: Evidence for a prion analog in *Saccharomyces cerevisiae*. *Science* **264**, 566–569 (1994). doi: 10.1126/science.7909170; pmid: 7909170
12. P. Anderson, N. Kedersha, Stress granules. *Curr. Biol.* **19**, R397–R398 (2009). doi: 10.1016/j.cub.2009.03.013; pmid: 19467203
13. J. R. Buchan, R. Parker, Eukaryotic stress granules: The ins and outs of translation. *Mol. Cell* **36**, 932–941 (2009). doi: 10.1016/j.molcel.2009.11.020; pmid: 20064460
14. J. Shorter, S. Lindquist, Hsp104 catalyzes formation and elimination of self-replicating Sup35 prion conformers. *Science* **304**, 1793–1797 (2004). doi: 10.1126/science.1098007; pmid: 15155912
15. Y. Shin, C. P. Brangwynne, Liquid phase condensation in cell physiology and disease. *Science* **357**, eaaf4382 (2017). doi: 10.1126/science.aaf4382; pmid: 28935776
16. M. C. Munder *et al.*, A pH-driven transition of the cytoplasm from a fluid- to a solid-like state promotes entry into dormancy. *eLife* **5**, 59–69 (2016). doi: 10.7554/eLife.09347; pmid: 27003292
17. I. Petrovska *et al.*, Filament formation by metabolic enzymes is a specific adaptation to an advanced state of cellular starvation. *eLife* **2014**, (2014). doi: 10.7554/eLife.02409; pmid: 24771766
18. B. R. Parry *et al.*, The bacterial cytoplasm has glass-like properties and is fluidized by metabolic activity. *Cell* **156**, 183–194 (2014). doi: 10.1016/j.cell.2013.11.028; pmid: 24361104
19. S. Saha *et al.*, Polar positioning of phase-separated liquid compartments in cells regulated by an mRNA competition mechanism. *Cell* **166**, 1572–1584 (2016). doi: 10.1016/j.cell.2016.08.006; pmid: 27594427
20. T. R. Serio *et al.*, Nucleated conformational conversion and the replication of conformational information by a prion determinant. *Science* **289**, 1317–1321 (2000). doi: 10.1126/science.289.5483.1317; pmid: 10958771
21. S. Alberti, R. Halfmann, O. King, A. Kapila, S. Lindquist, A systematic survey identifies prions and illuminates sequence features of prionogenic proteins. *Cell* **137**, 146–158 (2009). doi: 10.1016/j.cell.2009.02.044; pmid: 19345193
22. I. Stansfield *et al.*, The products of the SUP45 (eRF1) and SUP35 genes interact to mediate translation termination in *Saccharomyces cerevisiae*. *EMBO J.* **14**, 4365–4373 (1995). pmid: 7556078
23. M. D. Ter-Avanesyan *et al.*, Deletion analysis of the SUP35 gene of the yeast *Saccharomyces cerevisiae* reveals two non-overlapping functional regions in the encoded protein. *Mol. Microbiol.* **7**, 683–692 (1993). doi: 10.1111/j.1365-2958.1993.tb01159.x; pmid: 8469113
24. Y. O. Chernoff *et al.*, Evolutionary conservation of prion-forming abilities of the yeast Sup35 protein. *Mol. Microbiol.* **35**, 865–876 (2000). doi: 10.1046/j.1365-2958.2000.01761.x; pmid: 10692163
25. H. K. Edskes *et al.*, Sporadic distribution of prion-forming ability of Sup35p from yeasts and fungi. *Genetics* **198**, 605–616 (2014). doi: 10.1534/genetics.114.166538; pmid: 25081567
26. T. K. Harris, G. J. Turner, Structural basis of perturbed pKa values of catalytic groups in enzyme active sites. *IUBMB Life* **53**, 85–98 (2002). doi: 10.1080/15216540211468; pmid: 12049200
27. F. Ruggeri *et al.*, Single-molecule electrometry. *Nat. Nanotechnol.* **12**, 488–495 (2017). doi: 10.1038/nnano.2017.26; pmid: 28288117

28. J. R. Glover *et al*., Self-seeded fibers formed by Sup35, the protein determinant of [PSI+], a heritable prion-like factor of *S. cerevisiae*. *Cell* **89**, 811–819 (1997). doi: 10.1016/S0092-8674(00)80264-0; pmid: 9182769
29. M. Rubinstein, A. N. Semenov, Thermoreversible gelation in solutions of associating polymers. 2. Linear dynamics. *Macromolecules* **31**, 1386–1397 (1998). doi: 10.1021/ma970617+
30. T. S. Harmon, A. S. Holehouse, M. K. Rosen, R. V. Pappu, Intrinsically disordered linkers determine the interplay between phase separation and gelation in multivalent proteins. *eLife* **6**, e30294 (2017). doi: 10.7554/eLife.30294; pmid: 29091028
31. M.-T. Wei *et al*., Phase behaviour of disordered proteins underlying low density and high permeability of liquid organelles. *Nat. Chem.* **9**, 1118–1125 (2017). doi: 10.1038/nchem.2803; pmid: 29064502
32. L. Z. Osherovich, J. S. Weissman, Multiple Gln/Asn-rich prion domains confer susceptibility to induction of the yeast [PSI$^+$] prion. *Cell* **106**, 183–194 (2001). doi: 10.1016/S0092-8674(01)00440-8; pmid: 11511346
33. S. V. Paushkin, V. V. Kushnirov, V. N. Smirnov, M. D. Ter-Avanesyan, Propagation of the yeast prion-like [psi$^+$] determinant is mediated by oligomerization of the SUP35-encoded polypeptide chain release factor. *EMBO J.* **15**, 3127–3134 (1996). pmid: 8670813
34. R. P. McGlinchey, D. Kryndushkin, R. B. Wickner, Suicidal [PSI$^+$] is a lethal yeast prion. *Proc. Natl. Acad. Sci. U.S.A.* **108**, 5337–5341 (2011). doi: 10.1073/pnas.1102762108; pmid: 21402947
35. R. B. Wickner, D. C. Masison, H. K. Edskes, [PSI] and [URE3] as yeast prions. *Yeast* **11**, 1671–1685 (1995). doi: 10.1002/yea.320111609; pmid: 8720070
36. T. Nakayashiki, C. P. Kurtzman, H. K. Edskes, R. B. Wickner, Yeast prions [URE3] and [PSI$^+$] are diseases. *Proc. Natl. Acad. Sci. U.S.A.* **102**, 10575–10580 (2005). doi: 10.1073/pnas.0504882102; pmid: 16024723
37. R. B. Wickner, H. K. Edskes, D. Bateman, A. C. Kelly, A. Gorkovskiy, The yeast prions [PSI$^+$] and [URE3] are molecular degenerative diseases. *Prion* **5**, 258–262 (2011). doi: 10.4161/pri.17748; pmid: 22052353
38. Y. O. Chernoff, Stress and prions: Lessons from the yeast model. *FEBS Lett.* **581**, 3695–3701 (2007). doi: 10.1016/j.febslet.2007.04.075; pmid: 17509571
39. L. Malinovska, S. Alberti, Protein misfolding in *Dictyostelium*: Using a freak of nature to gain insight into a universal problem. *Prion* **9**, 339–346 (2015). doi: 10.1080/19336896.2015.1099799; pmid: 26529309
40. L. Malinovska, S. Palm, K. Gibson, J.-M. Verbavatz, S. Alberti, *Dictyostelium discoideum* has a highly Q/N-rich proteome and shows an unusual resilience to protein aggregation. *Proc. Natl. Acad. Sci. U.S.A.* **112**, E2620–E2629 (2015). doi: 10.1073/pnas.1504459112; pmid: 25941378
41. S. Alberti, A. D. Gitler, S. Lindquist, A suite of Gateway cloning vectors for high-throughput genetic analysis in *Saccharomyces cerevisiae*. *Yeast* **24**, 913–919 (2007). doi: 10.1002/yea.1502; pmid: 17583893
42. J. Bähler *et al*., Heterologous modules for efficient and versatile PCR-based gene targeting in *Schizosaccharomyces pombe*. *Yeast* **14**, 943–951 (1998). doi: 10.1002/(SICI)1097-0061(199807)14:10<943::AID-YEA292>3.0.CO;2-Y; pmid: 9717240
43. S. L. Forsburg, N. Rhind, Basic methods for fission yeast. *Yeast* **23**, 173–183 (2006). doi: 10.1002/yea.1347; pmid: 16498704
44. R. Serrano, Energy requirements for maltose transport in yeast. *Eur. J. Biochem.* **80**, 97–102 (1977). doi: 10.1111/j.1432-1033.1977.tb11861.x; pmid: 21792
45. M. J. Mahon, pHluorin2: An enhanced, ratiometric, pH-sensitive green florescent protein. *Adv. Biosci. Biotechnol.* **2**, 132–137 (2011). doi: 10.4236/abb.2011.23021; pmid: 21841969
46. C. L. Brett, D. N. Tukaye, S. Mukherjee, R. Rao, The yeast endosomal Na+K+/H+ exchanger Nhx1 regulates cellular pH to control vesicle trafficking. *Mol. Biol. Cell* **16**, 1396–1405 (2005). doi: 10.1091/mbc.E04-11-0999; pmid: 15635088
47. R. Halfmann, S. Lindquist, Screening for amyloid aggregation by semi-denaturing detergent-agarose gel electrophoresis. *J. Vis. Exp.* **17**, e838 (2008). pmid: 19066511
48. T. Mašek, L. Valášek, M. Pospíšek, in *RNA: Methods in Molecular Biology (Methods and Protocols), vol. 703*, H. Nielsen, Ed. (Humana Press, 2011), pp. 293–309.
49. X. Li *et al*., Electron counting and beam-induced motion correction enable near-atomic-resolution single-particle cryo-EM. *Nat. Methods* **10**, 584–590 (2013). doi: 10.1038/nmeth.2472; pmid: 23644547
50. D. N. Mastronarde, Automated electron microscope tomography using robust prediction of specimen movements. *J. Struct. Biol.* **152**, 36–51 (2005). doi: 10.1016/j.jsb.2005.07.007; pmid: 16182563
51. M. Jahnel, M. Behrndt, A. Jannasch, E. Schäffer, S. W. Grill, Measuring the complete force field of an optical trap. *Opt. Lett.* **36**, 1260–1262 (2011). doi: 10.1364/OL.36.001260; pmid: 21479051
52. A. S. Holehouse, R. K. Das, J. N. Ahad, M. O. G. Richardson, R. V. Pappu, CIDER: Resources to analyze sequence-ensemble relationships of intrinsically disordered proteins. *Biophys. J.* **112**, 16–21 (2017). doi: 10.1016/j.bpj.2016.11.3200; pmid: 28076807
53. Z. Dosztányi, V. Csizmok, P. Tompa, I. Simon, IUPred: Web server for the prediction of intrinsically unstructured regions of proteins based on estimated energy content. *Bioinformatics* **21**, 3433–3434 (2005). doi: 10.1093/bioinformatics/bti541; pmid: 15955779
54. J. Gough, K. Karplus, R. Hughey, C. Chothia, Assignment of homology to genome sequences using a library of hidden Markov models that represent all proteins of known structure. *J. Mol. Biol.* **313**, 903–919 (2001). doi: 10.1006/jmbi.2001.5080; pmid: 11697912

ACKNOWLEDGMENTS

We thank the following Services and Facilities of the Max Planck Institute of Molecular Cell Biology and Genetics (MPI-CBG) for their support: We thank B. Borgonovo and R. Lemaitre (Protein Expression Purification and Characterization) for help with protein expression and purification; B. Nitzsche and B. Schroth-Diez (Light Microscopy Facility) for help with light microscopy; F. Friedrich for support with visualization (Media Technologies and Outreach); and C. Iserman for a yeast strain BY4742 coexpressing Sup35-GFP and Pab1-mCherry. We thank members of the MPI-CBG and C. Weber from the Max Planck Institute for the Physics of Complex systems for discussion and comments on the manuscript. R. Halfmann is acknowledged for providing the antibody against Sup35C domain. We gratefully acknowledge funding from the German Federal Ministry of Research and Education (BMBF 031A359A to T.M.F and A.A.H.). This work is supported by the MaxSynBio consortium, jointly funded by the Federal Ministry of Education and Research of Germany and the Max Planck Society. We further acknowledge the U.S. National Institutes of Health for grant 5RO1NS056114 to R.V.P., The Human Frontiers Program for grant RGP0034/2017 to S.A. and R.V.P, the Volkswagen "Life?" initiative for a grant to S.A., and the German Research Foundation (DFG) for a grant to S.A. All the data relevant to this study are included in the main paper or the supplementary materials.

SUPPLEMENTARY MATERIALS

www.sciencemag.org/content/359/6371/eaao5654/suppl/DC1
Figs. S1 to S5
Tables S1 and S2
Movies S1 to S8

3 August 2017; accepted 27 November 2017
10.1126/science.aao5654

RESEARCH ARTICLE

MALARIA

Transferrin receptor 1 is a reticulocyte-specific receptor for *Plasmodium vivax*

Jakub Gruszczyk,[1] Usheer Kanjee,[2] Li-Jin Chan,[1,3] Sébastien Menant,[1] Benoit Malleret,[4,5] Nicholas T. Y. Lim,[1] Christoph Q. Schmidt,[6] Yee-Foong Mok,[7] Kai-Min Lin,[8] Richard D. Pearson,[9,10] Gabriel Rangel,[2] Brian J. Smith,[11] Melissa J. Call,[1,3] Michael P. Weekes,[8] Michael D. W. Griffin,[7] James M. Murphy,[1,3] Jonathan Abraham,[12] Kanlaya Sriprawat,[13] Maria J. Menezes,[14] Marcelo U. Ferreira,[14] Bruce Russell,[15] Laurent Renia,[5] Manoj T. Duraisingh,[2] Wai-Hong Tham[1,3]*

Plasmodium vivax shows a strict host tropism for reticulocytes. We identified transferrin receptor 1 (TfR1) as the receptor for *P. vivax* reticulocyte-binding protein 2b (PvRBP2b). We determined the structure of the N-terminal domain of PvRBP2b involved in red blood cell binding, elucidating the molecular basis for TfR1 recognition. We validated TfR1 as the biological target of PvRBP2b engagement by means of TfR1 expression knockdown analysis. TfR1 mutant cells deficient in PvRBP2b binding were refractory to invasion of *P. vivax* but not to invasion of *P. falciparum*. Using Brazilian and Thai clinical isolates, we show that PvRBP2b monoclonal antibodies that inhibit reticulocyte binding also block *P. vivax* entry into reticulocytes. These data show that TfR1-PvRBP2b invasion pathway is critical for the recognition of reticulocytes during *P. vivax* invasion.

Of the hundreds of *Plasmodium* species, only *P. falciparum*, *P. vivax*, *P. ovale curtisi*, *P. ovale wallikeri*, *P. malariae*, and *P. knowlesi* are known to infect humans. Within the human host, malaria parasites invade liver and red blood cells for replication and transmission. Blood stage infection is the major cause of all clinical symptoms in malaria, and therefore the therapeutic prevention of parasite entry into red blood cells could alleviate malarial disease. Entry into red blood cells depends on the interactions between parasite invasion ligands and their cognate red blood cell receptors, of which only a handful have been identified (*1*–*7*). These ligand-receptor interactions initiate a cascade of molecular events that progress from initial attachment, recognition, commitment, and last, penetration of the parasite into red blood cells (*8*, *9*).

P. vivax is the most widely distributed human malaria parasite. This parasite has a strict preference for invasion into reticulocytes, which are very young red blood cells that are formed in the bone marrow after enucleation and released into the circulation. The reticulocyte-specific receptor involved in *P. vivax* entry has not been identified (*10*). Most studies have focused on the interaction between the *P. vivax* Duffy binding protein (PvDBP) and the red blood cell Duffy antigen receptor for chemokines (DARC) because individuals from western and central Africa lacking DARC are resistant to *P. vivax* invasion (*11*). However, recent reports have highlighted the presence of *P. vivax* in apparently DARC-negative individuals, suggesting that *P. vivax* may enter reticulocytes by binding to other receptors (*12*–*14*). Furthermore, DARC is present on both normocytes and reticulocytes, and therefore this ligand-receptor interaction cannot govern selective entry into reticulocytes (*15*). To identify other parasite proteins involved in reticulocyte recognition, we focused on the *P. vivax* reticulocyte-binding protein family (PvRBP). This protein family comprises 11 members, of which several have been shown to bind reticulocytes; however, their cognate receptors have not been identified (*16*–*19*).

PvRBP2b binds transferrin receptor 1 to mediate recognition of reticulocytes

P. vivax preferentially invades reticulocytes that express high levels of transferrin receptor 1 (TfR1 or CD71) (*20*). TfR1 is an essential housekeeping protein involved in cellular transport of iron into cells through binding of iron-loaded transferrin (Tf) (*21*). On circulating red blood cells, TfR1 is expressed only on reticulocytes and is progressively lost from their membranes as they mature into erythrocytes (*22*, *23*). TfR1 is a type II transmembrane glycoprotein that forms a dimer, and its ectodomain consists of three subdomains: a "protease-like domain" resembling the structure of zinc metalloproteinases, an "apical domain," and a "helical domain" responsible for dimerization (*24*). TfR1 is also a cellular receptor for New World hemorrhagic fever arenaviruses, including Machupo (MACV), Junin, Guanarito, and Sabiá viruses (*25*, *26*). Residues 208 to 212 of the TfR1 apical domain provide a critical recognition site for these viruses (*25*, *26*).

PvRBP2b is expressed in late-stage *P. vivax* parasites, and recombinant PvRBP2b (residues 161 to 1454; $PvRBP2b_{161–1454}$) binds preferentially to reticulocytes that express TfR1 (*19*, *27*). We observed that binding by recombinant PvRBP2b was abolished when reticulocytes were treated with trypsin and chymotrypsin (fig. S1, A and B). We confirmed that the combination of these proteases cleaves TfR1 and complement receptor 1 (CR1) from the surface of reticulocytes, with other known malaria receptors—including glycophorin A, basigin, and DARC—being susceptible to different sets of protease treatment (fig. S1, A and B). The profile of PvRBP2b binding is strikingly similar to the TfR1 surface expression on reticulocytes (Fig. 1A, bottom), and we show that the level of PvRBP2b binding is directly correlated with the levels of TfR1 on the surface of reticulocytes (fig. S1, C and D).

To determine whether $PvRBP2b_{161–1454}$ binds to the population of reticulocytes that express TfR1 on their surfaces, we tested a panel of commercially available anti-TfR1 monoclonal antibodies (mAbs) for their ability to block recombinant PvRBP2b binding. Indeed, anti-TfR1 mAbs 23D10, L01.1, LT71, M-A712, MEM-189, and OKT9 inhibited PvRBP2b binding to reticulocytes by 78, 76, 33, 75, 92, and 90%, respectively (Fig. 1A). M-A712 also prevents MACV pseudovirus entry (*25*, *28*). Anti-TfR1 mAbs 2B6, 13E4, and MEM-75 did not inhibit PvRBP2b binding; although their epitopes have not been mapped, we propose that these three antibodies may bind to a site on TfR1 that is not involved in the PvRBP2b interaction (Fig. 1A). To determine whether this inhibition was specific to $PvRBP2b_{161–1454}$ binding, we analyzed the binding of *P. falciparum* reticulocyte binding protein-like homolog 4 (PfRh4) to its cognate receptor CR1 (*4*). Whereas addition of the first three

[1]The Walter and Eliza Hall Institute of Medical Research, Parkville, Victoria 3052, Australia. [2]Department of Immunology and Infectious Diseases, Harvard T. H. Chan School of Public Health, Boston, MA 02115, USA. [3]Department of Medical Biology, The University of Melbourne, Melbourne, Victoria 3010, Australia. [4]Department of Microbiology and Immunology, Yong Loo Lin School of Medicine, National University of Singapore, 117597 Singapore. [5]Singapore Immunology Network, A*STAR, 138648 Singapore. [6]Institute of Pharmacology of Natural Products and Clinical Pharmacology, Ulm University, Germany. [7]Department of Biochemistry and Molecular Biology, Bio21 Molecular Science and Biotechnology Institute, The University of Melbourne, Melbourne, Victoria 3010, Australia. [8]Cambridge Institute for Medical Research, Cambridge CB2 OXY, UK. [9]Wellcome Trust Sanger Institute, Hinxton, Cambridge, UK. [10]Big Data Institute, Li Ka Shing Centre for Health Information and Discovery, Oxford, UK. [11]La Trobe Institute for Molecular Science, La Trobe University, Melbourne, Victoria 3086, Australia. [12]Department of Microbiology and Immunobiology, Harvard Medical School, Boston, MA 02115, USA. [13]Shoklo Malaria Research Unit, Mahidol-Oxford Tropical Medicine Research Unit, Faculty of Tropical Medicine, Mahidol University, Mae Sot, Thailand. [14]Department of Parasitology, Institute of Biomedical Sciences, University of São Paulo, São Paulo, Brazil. [15]Department of Microbiology and Immunology, University of Otago, Dunedin 9054, New Zealand.
***Corresponding author. Email: tham@wehi.edu.au**

complement control protein modules of CR1 (CCP 1–3) inhibited PfRh4$_{28–766}$ binding as expected (*29*), addition of anti-TfR1 mAb OKT9 did not significantly reduce PfRh4 binding (Fig. 1B). Because anti-TfR1 did not affect PfRh4 binding, these results show that TfR1 is a specific reticulocyte receptor for PvRBP2b.

To evaluate whether PvRBP2b$_{161–1454}$ interacts directly with TfR1, we performed immunoprecipitation experiments using purified recombinant TfR1, Tf, and PvRBP2b$_{161–1454}$ proteins (Fig. 1C) (*30*). Using an anti-PvRBP2b mAb, we immunoprecipitated PvRBP2b in complex with TfR1 and Tf. PvRBP2b and TfR1 also formed a binary complex in the absence of Tf, demonstrating that PvRBP2b binds directly to TfR1 (Fig. 1C). The interaction between PvRBP2b and TfR1 is specific; immunoprecipitation of PvRBP1a, PvRBP1b, or PvRBP2a did not show evidence of complex formation with TfR1 (fig. S2A).

We developed a fluorescence resonance energy transfer (FRET)–based assay to monitor PvRBP2b-TfR1 complex formation in which TfR1 labeled with DyLight-594 could be shown to interact with PvRBP2b$_{161–1454}$ labeled with DyLight-488 (fig. S2B). The addition of 10-fold molar excess of unlabeled PvRBP2b$_{161–1454}$ and TfR1 competed out the labeled proteins and reduced the signal of the PvRBP2b-TfR1 FRET pair. By contrast, proteins that were unable to bind TfR1, such as PfRh4, had no effect on the FRET signal. Using this assay, we observed that anti-TfR1 mAbs 23D10, M-A712, MEM-189, and OKT9 that

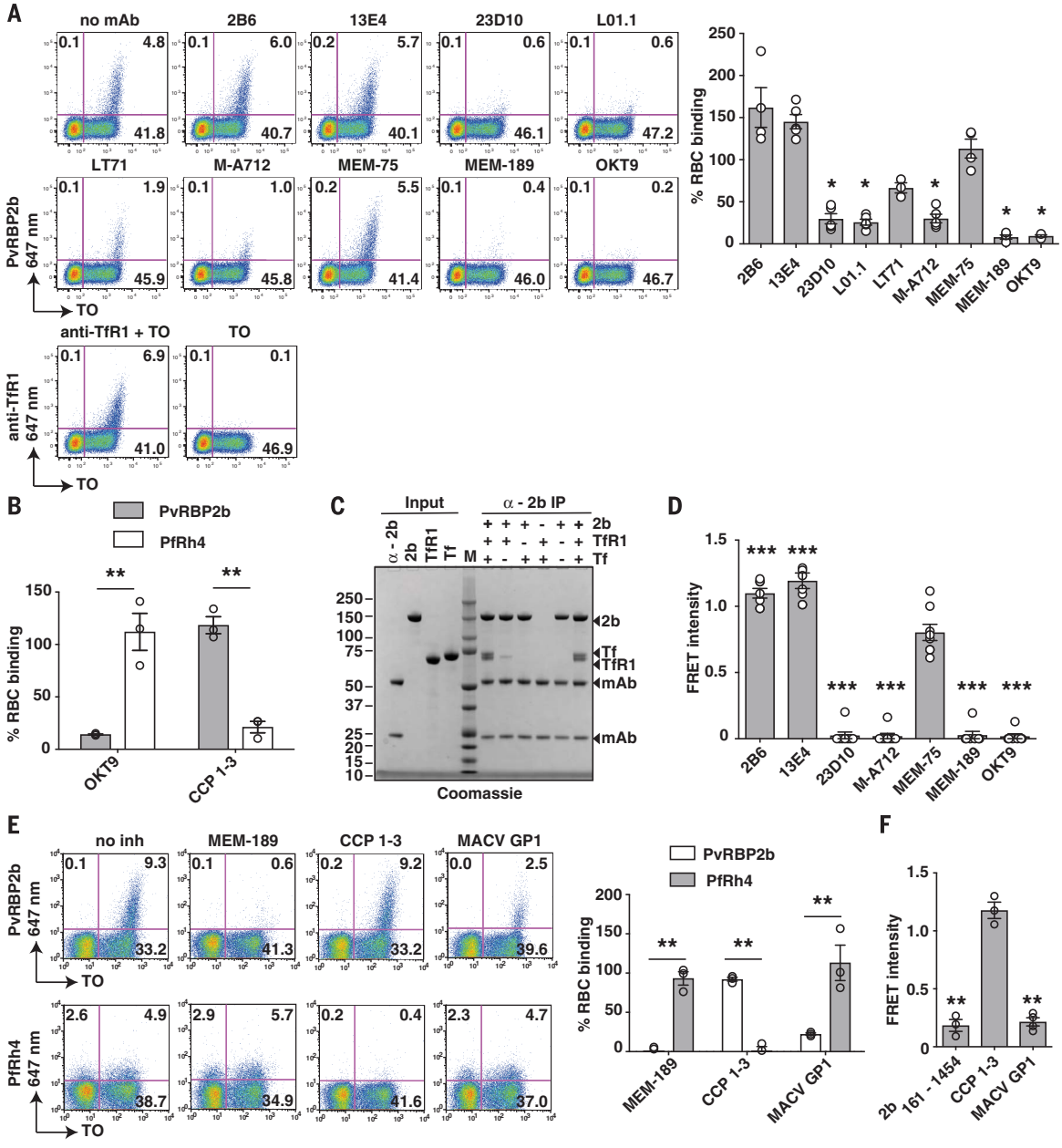

Fig. 1. PvRBP2b binds TfR1 on the reticulocyte surface. (**A**) PvRBP2b$_{161–1454}$ binding in the presence of anti-TfR1 mAbs analyzed by means of flow cytometry. (Left) Dot plots of PvRBP2b$_{161–1454}$ binding (*y* axis) to reticulocytes stained with thiazole orange (TO; *x* axis). (Right) Normalized binding results in which PvRBP2b$_{161–1454}$ binding in the absence of mAbs was arbitrarily assigned to be 100%. (**B**) PvRBP2b$_{161–1454}$ and PfRh4$_{28–766}$ binding were evaluated by means of flow cytometry with the addition of anti-TfR1 mAb OKT9 or CCP 1–3. PvRBP2b$_{161–1454}$ and PfRh4 binding in buffer were arbitrarily assigned to be 100%. (**C**) Eluates of individual or mixtures of proteins immunoprecipitated with anti-PvRBP2b mAb analyzed by means of SDS-PAGE. Plus and minus signs indicate protein present and absent, respectively. M, molecular weight marker. (**D**) Anti-TfR1 mAbs inhibit PvRBP2b-TfR1 complex formation in the FRET-based assay. The FRET signal was relative to "no mAb" control. (**E**) Binding of PvRBP2b$_{161–1454}$ and PfRh4$_{28–766}$ in the presence of anti-TfR1 mAb MEM-189, CCP 1–3, and MACV GP1. (Left) Dot plots showing PvRBP2b$_{161–1454}$ (top) and PfRh4$_{28–766}$ binding (bottom). (Right) Normalized binding results in which PvRBP2b$_{161–1454}$ and PfRh4$_{28–766}$ binding in the presence of buffer was arbitrarily assigned to be 100%. (**F**) MACV GP1 inhibits PvRBP2b$_{161–1454}$–TfR1 complex formation monitored by means of FRET assay. For (A), (B), (D), (E), and (F), mean ± SEM, $n \geq 3$ biological replicates; open circles represent biological replicates. Mann-Whitney test was used for (A) and (D), where MEM-75 was considered noninhibitory, and *t* tests were used for (B), (E), and (F). $^*P \leq 0.05$, $^{**}P \leq 0.001$.

inhibited PvRBP2b$_{161–1454}$ reticulocyte binding also blocked PvRBP2b-TfR1 complex formation (Fig. 1D).

MACV GP1 and PvRBP2b bind to the apical domain of TfR1

The arenavirus envelope glycoprotein is the only protein on the virion surface and, during maturation, is processed into three subunits: the stable signal peptide, GP1, and GP2. The GP1 subunit interacts with cellular receptors, and the structure of a MACV GP1–TfR1 complex shows that MACV GP1 binds to the apical domain of TfR1 (*31*, *32*). To determine whether PvRBP2b interacts with a similar surface on TfR1, we examined whether soluble MACV GP1 competes with PvRBP2b$_{161–1454}$ for binding to TfR1 on reticulocytes (Fig. 1E). Indeed, the addition of MACV GP1 reduced PvRBP2b$_{161–1454}$ binding to reticulocytes, albeit at a lower level of inhibition as compared with the addition of anti-TfR1 mAb MEM-189. This inhibition was specific; PfRh4 binding was unaffected by addition of MACV GP1 or MEM-189 but clearly reduced with the addition of CCP 1–3 (Fig. 1E). The addition of MACV GP1 inhibited PvRBP2b-TfR1 complex formation and reduced the FRET signal to a similar extent as unlabeled PvRBP2b$_{161–1454}$, whereas addition of CCP 1–3 had negligible effect (Fig. 1F). These results indicate that MACV GP1 and PvRBP2b$_{161–1454}$ bind to an overlapping site on TfR1.

Crystal structure of the N-terminal domain of PvRBP2b

PvRBP2b is a 326-kDa protein with a putative red blood cell–binding domain and a C-terminal transmembrane region (Fig. 2). We determined the crystal structure of the N-terminal domain of PvRBP2b (residues 169 to 470; PvRBP2b$_{169–470}$), refined to 1.71-Å resolution (Fig. 2A; fig. S3, A to D; and table S1). The surface of the domain is mostly positively charged (Fig. 2B). It is predominantly an α-helical protein, comprising 10 α-helices and two very short antiparallel β-sheets, each comprising two β-strands. The crystal structure of PvRBP2b$_{169–470}$ has two disulfide bonds: one between Cys^{312} and Cys^{316} and the other between Cys^{240} and Cys^{284}. This structure closely resembles the homologous domain of PvRBP2a and PfRh5, with a root mean square deviation of 1.7 and 3.7 Å over 268 and 225 aligned Cα atoms, respectively (Fig. 2C and fig. S4) (*18*, *33*, *34*). The theoretical x-ray solution scattering pattern calculated from the PvRBP2b$_{169–470}$ crystal structure coordinates shows excellent agreement with the experimental small-angle x-ray scattering (SAXS) data (χ = 0.35) (fig. S5, A to F, and table S2), with concordance between the crystal and solution conformations apparent from the overlay

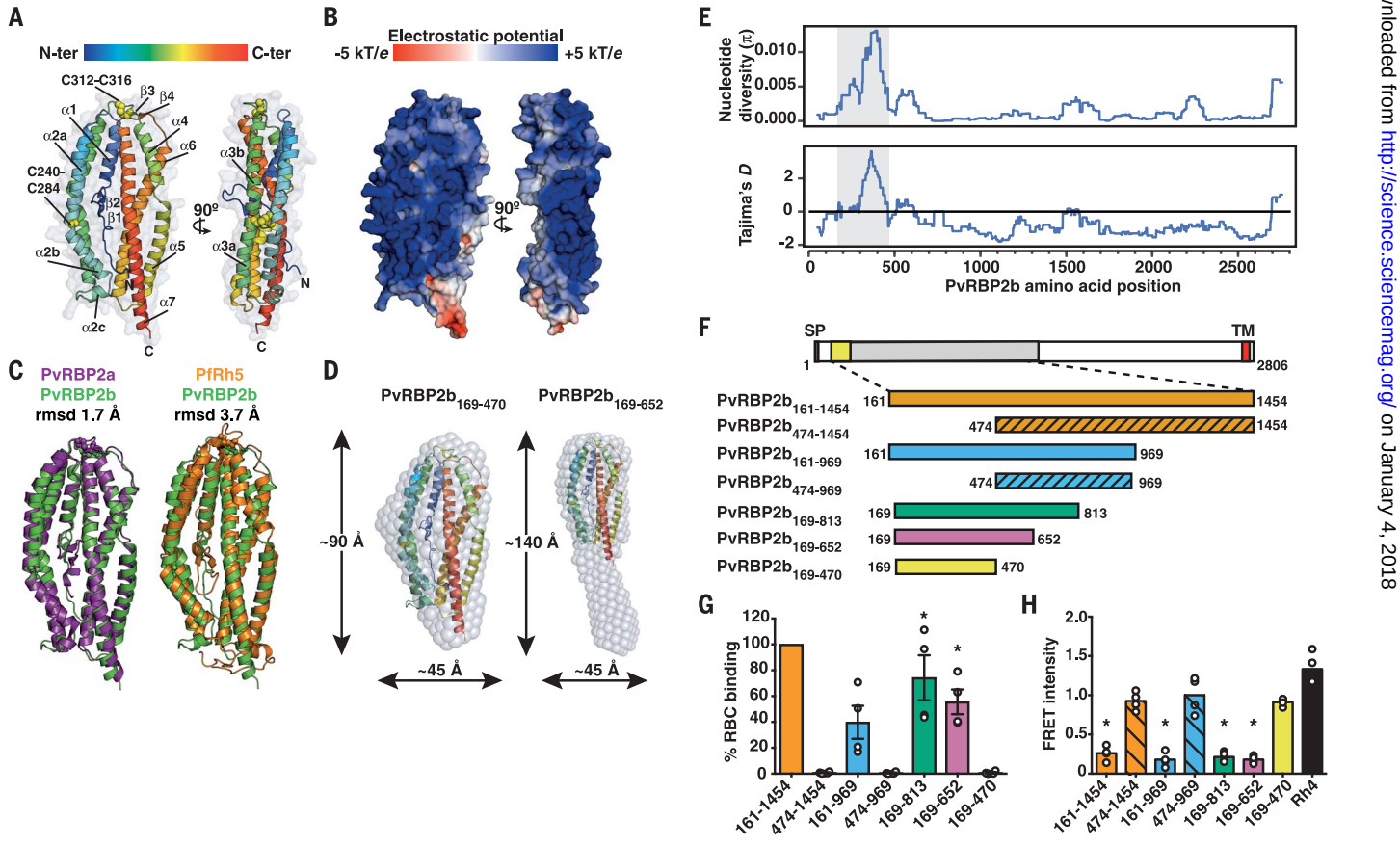

Fig. 2. Crystal structure of the N-terminal domain of PvRBP2b and its functional requirement. (**A**) Structure of the N-terminal domain of PvRBP2b from amino acid 169 to 470 shown in two orthogonal views. (**B**) Electrostatic surface potential on the PvRBP2b structure. (**C**) Superimposition of the PvRBP2b structure (green) with PvRBP2a (purple) and PfRh5 (orange). The Protein Data Bank (PDB) ID codes for PfRh5 and PvRBP2a are 4WAT and 4Z8N, respectively. (**D**) Crystal structure of the N-terminal domain superimposed with SAXS ab initio bead model of PvRBP2b$_{169–470}$ (left) and PvRBP2b$_{169–652}$ (right). (**E**) Sliding window analysis showing nucleotide diversity (π) values and Tajima's *D* statistic in PvRBP2b. The gray boxes refer to a highly polymorphic region at amino acid positions 169 to 470 that appears to be under balancing selection. (**F**) Schematic representation of full-length PvRBP2b and recombinant protein fragments (left). Signal peptide (SP), transmembrane domain (TM), and N-terminal domain (yellow) are indicated. (**G**) PvRBP2b binding results by means of flow cytometry, in which PvRBP2b$_{161–1454}$ binding was arbitrarily assigned to be 100%. (**H**) Unlabeled recombinant PvRBP2b fragments or PfRh4 were mixed at 10-fold molar excess relative to the labeled PvRBP2b$_{161–1454}$–TfR1 FRET pair. The FRET intensity was relative to buffer control. For (G) and (H), mean ± SEM, n = 4 biological replicates; open circles represent biological replicates. The Mann-Whitney test was used to calculate the *P* value by using the binding of 2b$_{474–1454}$ that was considered no binding. *$P \le 0.05$, **$P \le 0.001$.

of the crystal structure and the ab initio calculated molecular envelope (Fig. 2D, left). We also obtained SAXS data for a longer fragment of PvRBP2b including residues 169 to 652 (fig. S6 and table S2). The reconstructed molecular envelope has a rodlike shape, with a C-terminal part forming a continuous extension of the N-terminal domain (Fig. 2D, right). SAXS data for a larger fragment of PvRBP2b encompassing residues 161 to 969 indicate that the molecule adopts an elongated, boomerang-like shape, similar to that previously reported for PvRBP2a (figs. S6, A to F, and S7, A to D, and table S2) (*18*).

We calculated nucleotide diversity (π) and Tajima's D within PvRBP2b using data from

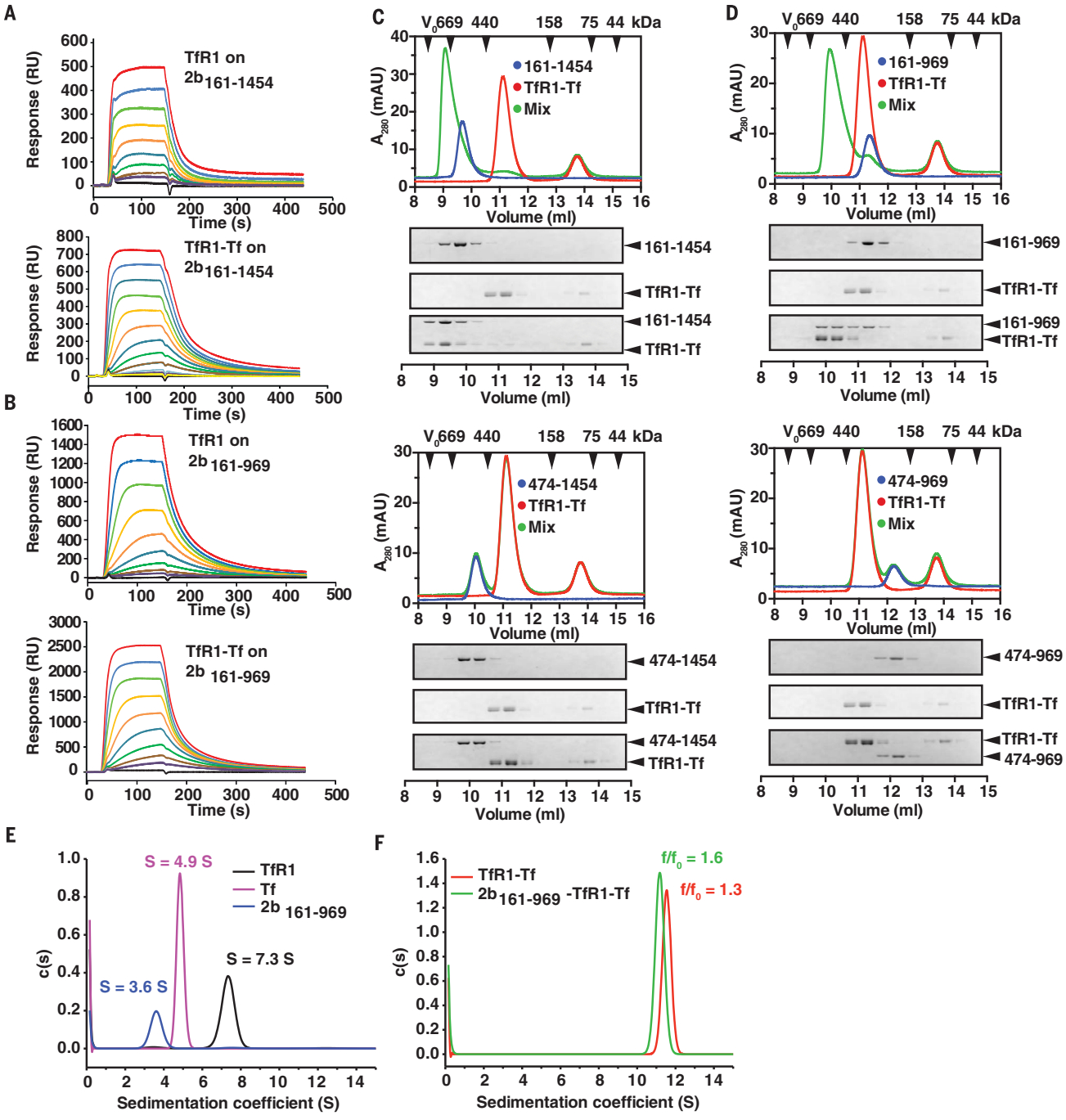

Fig. 3. PvRBP2b binds to TfR1-Tf to form a stable ternary complex. (**A**) PvRBP2b$_{161–1454}$ and (**B**) PvRBP2b$_{161–969}$ were coupled covalently to a biosensor chip to probe binding of TfR1 (concentration range assayed, 2 μM to 7.5 nM, top) and TfR1-Tf complexes [concentration range of TfR1-Tf complexes assayed, 2:4 μM to 1.8:3.9 nM (A) and 2:4 μM to 7.5:15 nM (B), bottom]. (**C** and **D**) Complex formation between PvRBP2b, TfR1, and Tf analyzed by means of analytical SEC. PvRBP2b-TfR1-Tf ternary complex can be observed for PvRBP2b$_{161–1454}$ [(C), top] and PvRBP2b$_{161–969}$ [(D), top]. Two corresponding truncations of the N-terminal domain, PvRBP2b$_{474–1454}$ [(C), bottom] and PvRBP2b$_{474–969}$ [(D), bottom], do not interact with the TfR1-Tf binary complex. The exclusion volume (V_0) of the columns and the elution volumes of selected marker proteins are indicated with black arrowheads. (Bottom) Coomassie blue–stained SDS-PAGE gels of the fractions obtained from SEC. (**E** and **F**) Continuous sedimentation coefficient distributions derived from fitting sedimentation velocity data to a $c(s)$ sedimentation model. (E) $c(s)$ distributions for TfR1 (black line), Tf (magenta line), and PvRBP2b$_{161–969}$ (blue line). (F) $c(s)$ distributions for the TfR1-Tf complex (red line) and PvRBP2b$_{161-969}$–TfR1-Tf complex (green line).

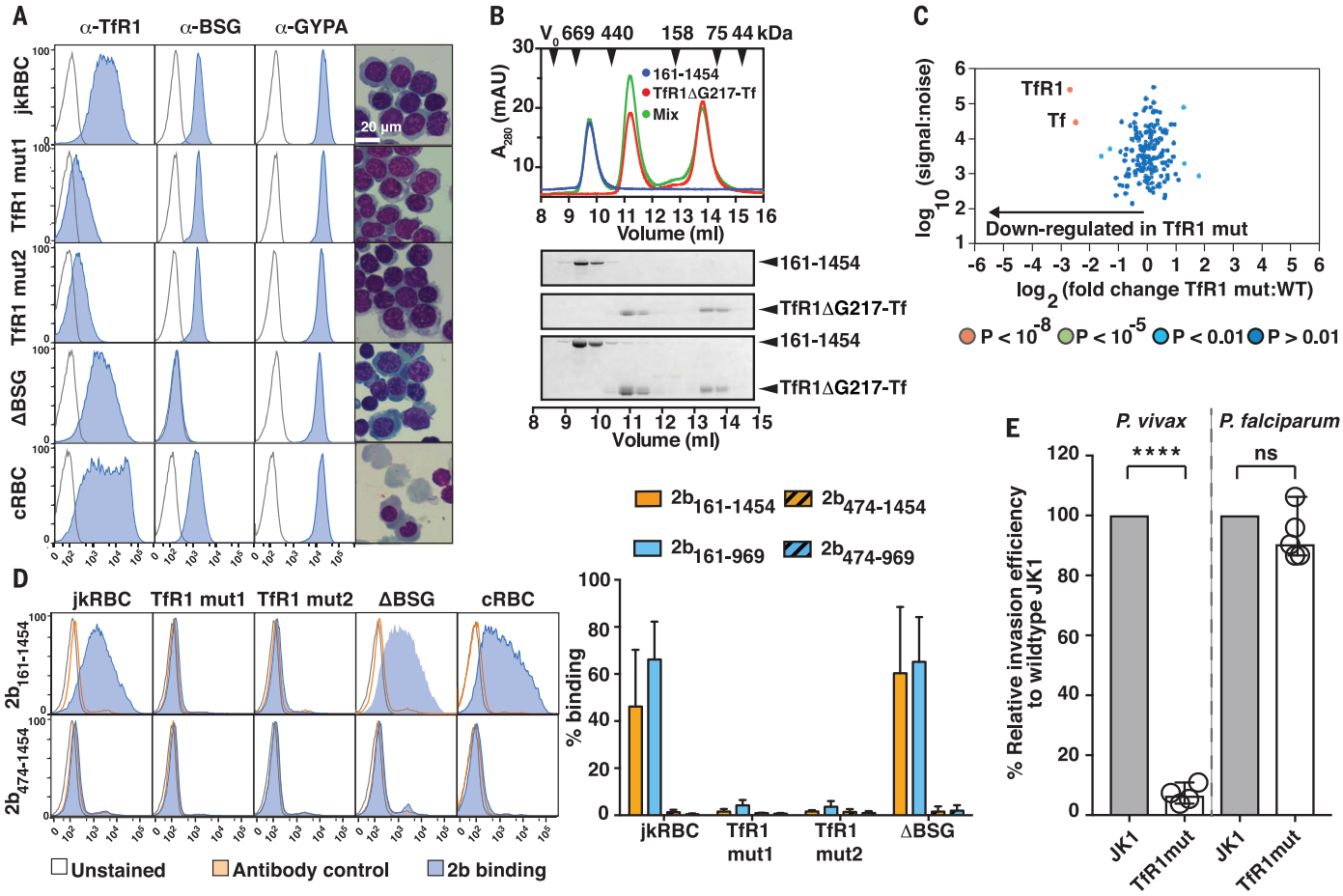

Fig. 4. Deletions in *TFRC* reduce TfR1 surface expression, abolish PvRBP2b binding, and inhibit *P. vivax* invasion. (**A**) Expression of TfR1, BSG, and GypA on the surface of jkRBCs, TfR1 mutants, ΔBSG null, and cultured erythrocytes (cRBCs) as measured with flow cytometry. (Right) Cytospin analysis of cells stained with May-Grünwald Giemsa staining technique. (**B**) TfR1ΔG217 mutation in TfR1 abrogates PvRBP2b binding as observed by using analytical SEC. (**C**) Quantitative surface proteomics demonstrate specific reduction in TfR1 protein levels in TfR1 mutants compared with wild-type jkRBCs. Levels of Tf, the binding partner for TfR1, are similarly reduced. Significance A was used to estimate *P* values, and a minimum of two peptides were required for protein quantitation. (**D**) Binding of recombinant PvRBP2b fragments to jkRBCs, TfR1 mutants, ΔBSG, and cRBCs are shown in blue. Negative controls of unstained cells and isotype control stained cells are shown in the gray and orange lines, respectively. (Right) Compilation of results from PvRBP2b fragment binding to jkRBCs, TfR1 mutants, ΔBSG, and cRBCs. Mean ± SEM, $n = 3$ biological replicates. (**E**) Comparison of invasion efficiency between jkRBCs and TfR1 mutant cell lines with either *P. vivax* or *P. falciparum*. The data shown are averages and SEM from between four to five biological replicates shown as open circles. *P* value was calculated by using a paired, two-tailed *t* test. ****$P \leq 0.0001$; ns, nonsignificant.

the MalariaGEN *P. vivax* Genome Variation project (*35*). There was a peak in both metrics between amino acid positions 169 and 470, suggesting balancing selection within the N-terminal domain (Fig. 2E). Such signatures of balancing selection are often associated with genes or proteins expressed on the surface of merozoites and are likely due to interaction with the immune system.

To determine the importance of the N-terminal domain for PvRBP2b function, we generated a series of purified recombinant PvRBP2b protein fragments (Fig. 2F and tables S3 and S4). All proteins were soluble and properly folded as indicated by high α-helical content in CD spectra, which is in agreement with the secondary structure predictions (fig. S8, A to D). We observed that all fragments with the N-terminal domain bound reticulocytes ($PvRBP2b_{161–1454}$, $PvRBP2b_{161–969}$, $PvRBP2b_{169–813}$, and $PvRBP2b_{169–652}$), whereas their corresponding fragments without the domain did not ($PvRBP2b_{474–1454}$ and $PvRBP2b_{474–969}$) (Fig. 2G). However, the isolated N-terminal domain $PvRBP2b_{169–470}$ was unable to bind reticulocytes on its own (Fig. 2G), indicating that this fragment of PvRBP2b is necessary but not sufficient for reticulocyte binding. The shortest PvRBP2b fragment that showed binding to reticulocytes encompasses residues 169 to 652 (Fig. 2G). Our FRET-based assay showed that unlabeled recombinant fragments that bind reticulocytes inhibited PvRBP2b-TfR1 complex formation, whereas recombinant fragments that did not bind reticulocytes had a negligible effect (Fig. 2H). Collectively, our structural and functional analyses indicate that the N-terminal domain is necessary for binding but requires the presence of the elongated C-terminal fragment to form a fully functional binding site.

PvRBP2b, TfR1, and Tf form a stable complex at nanomolar concentrations

Using surface plasmon resonance, we found that $PvRBP2b_{161–1454}$ interacts with TfR1 alone or with the binary complex of TfR1-Tf (Fig. 3A, top and bottom, respectively). We also observed similar results for the $PvRBP2b_{161–969}$ fragment with TfR1 and TfR1-Tf (Fig. 3B, top and bottom, respectively). These results indicate that Tf was

not required for the PvRBP2b-TfR1 complex formation because the addition of Tf resulted in similar binding responses than for TfR1 alone. We analyzed a PvRBP2b, TfR1, and Tf ternary complex using analytical size exclusion chromatography (SEC) and used SDS–polyacrylamide gel electrophoresis (SDS-PAGE) analyses to confirm comigration of complex components. The ternary complex was detected for PvRBP2b$_{161–1454}$ and PvRBP2b$_{161–969}$ (Fig. 3, C and D, top, respectively, and table S5). By contrast, their corresponding fragments without the N-terminal domain (PvRBP2b$_{474–1454}$ and PvRBP2b$_{474–969}$) did not form any observable ternary complexes (Fig. 3, C and D, bottom). The interaction between PvRBP2b and TfR1-Tf binary complex is similar in the presence of either the iron-depleted or iron-loaded form of human transferrin (fig. S2C). Furthermore, the homologous member of the same protein family, PvRBP2a, did not form a ternary complex with TfR1-Tf (fig. S2D).

Sedimentation velocity analyses of TfR1, Tf, and PvRBP2b$_{161–969}$ indicated that the isolated proteins are homogenous, with weight-average sedimentation coefficients of 7.3, 4.9, and 3.6 *S*, respectively (Fig. 3E). These values are consistent with a stable dimer of TfR1 and monomeric forms of both Tf and PvRBP2b$_{161–969}$. The empirically fitted shape parameter value (frictional ratio) calculated for PvRBP2b$_{161–969}$ was ~1.8, which is consistent with a highly elongated structure in solution. Mixtures of TfR1-Tf and PvRBP2b$_{161–969}$–TfR1-Tf yielded single symmetrical peaks with weight-average sedimentation coefficients of 11.5 and 11.2 *S*, respectively, with no peaks observed for the individual components in these samples (Fig. 3F and fig. S9). These results indicate that Tf and TfR1 form a stable binary complex in solution and that PvRBP2b$_{161–969}$ binds to this binary complex. The frictional ratio (f/f_0) for the ternary PvRBP2b$_{161–969}$–TfR1-Tf was higher than for the binary TfR1-Tf complex, resulting in a reduction in the sedimentation coefficient on formation of the ternary complex and indicating that it has an elongated structure in solution.

Deletions in TfR1 generated via CRISPR/Cas9 abolishes PvRBP2b binding and *P. vivax* invasion

To investigate whether loss of TfR1 surface expression on red blood cells would affect PvRBP2b protein binding, we attempted to generate a knockout of the *TFRC* gene using CRISPR/Cas9 genome editing of the JK-1 erythroleukemia cell line. We obtained single-cell clones that displayed reduced expression of TfR1 and validated the mutation in two independent clones (TfR1 mut1 and TfR1 mut2) (fig. S10, A to C). Both clones contained an identical –3-bp deletion that resulted in the loss of amino acid Gly^{217} in the TfR1 apical domain but left the rest of the protein in-frame. TfR1 mut1 was homozygous for this deletion, whereas TfR1 mut2 has a –3-bp deletion, as described above, on one allele and a –11-bp deletion on the other allele, the latter leading to a premature stop codon. Deletion of *TFRC* in a mouse model is embryonic lethal and leads to severe

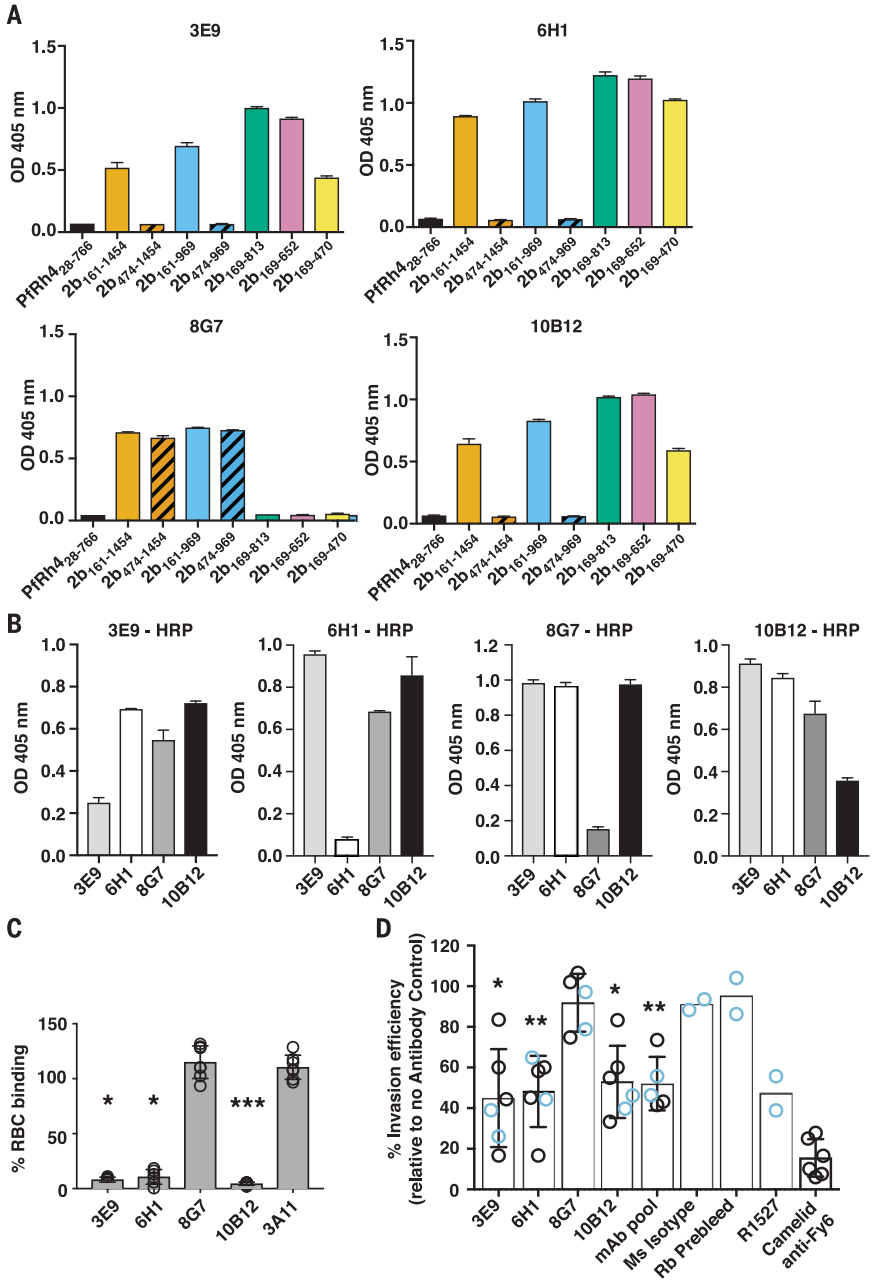

Fig. 5. Anti-PvRBP2b mAbs inhibit reticulocyte binding and *P. vivax* invasion in Brazilian and Thai clinical isolates. (**A**) ELISA plates were coated with equimolar concentrations of each recombinant fragment, and detection with anti-PvRBP2b mAbs 3E9, 6H1, 8G7, and 10B12 are shown. (**B**) Competition ELISA by using immobilized PvRBP2b incubated with unconjugated anti-2b mAbs (*x* axis) and detected with 3E9-HRP, 6H1-HRP, 8G7-HRP, and 10B12-HRP as indicated. For (A) and (B), error bars represent range showing the variability of duplicate measures. (**C**) PvRBP2b$_{161–1454}$ binding in the presence of anti-PvRBP2b mAbs 3E9, 6H1, 8G7, and 10B12 was analyzed by means of flow cytometry. Normalized binding results in which PvRBP2b$_{161–1454}$ binding in the absence of mAbs was arbitrarily assigned to be 100%. The anti-PvRBP2a mAb 3A11 was used as a negative antibody control. Mean ± SEM, $n = 5$ biological replicates, open circles represent biological replicates. The Kruskal-Wallis test was used to calculate the *P* value by using 8G7 binding as no inhibition. $^*P \le 0.05$, $^{***}P \le 0.0001$. (**D**) Invasion of *P. vivax* in Brazilian (blue open circles) and Thai (black open circles) clinical isolates in the presence of anti-PvRBP2b 3E9, 6H1, 8G7, and 10B12, pooled mAbs (each mAb at one-third of final concentration), mouse isotype control, purified rabbit prebleed IgG, purified total IgG of anti-PvRBP2b polyclonal antibody R1527, and camelid anti-Fy6 mAb. Antibodies were added in concentrations from 25 to 125 μg/ml, except for the camelid anti-Fy6 mAb, which was used at 25 μg/ml. Mean ± SD, $n = 2$ to 6 biological replicates; open circles represent biological replicates. For experiments with $n > 2$ biological replicates, we used the Kolmogorov-Smirnov test to compare 8G7 with 3E9, 6H1, and 10B12. $^*P \le 0.05$, $^{**}P \le 0.001$.

disruption of erythropoiesis (*36*), suggesting that complete deletion of *TFRC* in erythroid-lineage cells, such as JK-1, may not be possible.

Differentiated polychromatic JK-1 cells (termed jkRBCs) express surface proteins (including TfR1) at levels comparable with those of differentiated $CD34^+$ bone marrow–derived cultured red blood cells (cRBCs) (*37*). The jkRBCs, cRBCs, and differentiated jkRBCs with a knockout within the basigin receptor (ΔBSG) show normal levels of TfR1, whereas TfR1 mutant clones displayed an intermediate level of TfR1 surface staining, with a panel of anti-TfR1 mAbs (Fig. 4A and fig. S11). Levels of glycophorin A (GypA) and basigin (BSG) on these TfR1 mutant clones were similar to all control cells, showing that only TfR1 surface expression is affected on these cells (Fig. 4A). To determine whether deletion of Gly^{217} affects PvRBP2b binding, we generated a recombinant TfR1 protein that lacks this amino acid (TfR1ΔG217). Using SEC, we show that although TfR1ΔG217 was still able to bind Tf, its binding to PvRBP2b was completely abolished (Fig. 4B). Gly^{217}, which resides on the lateral surface of the TfR1 apical domain, is close to the MACV GP1 interaction surface (fig. S10D) (*31*).

To confirm that the mutation in *TFRC* did not result in changes in expression of other red blood cell proteins, we compared the abundance of cell surface proteins between wild-type jkRBCs and the two TfR1 mutants using tandem mass tag–based quantitative surface proteomics (Fig. 4C). Out of 237 quantified surface proteins, only TfR1 and Tf were significantly modified, confirming the specificity of the *TFRC* mutations.

We next wanted to determine whether PvRBP2b binding was affected in the TfR1 mutant clones. $PvRBP2b_{161–1454}$ and $PvRBP2b_{161–969}$ bound jkRBCs and cRBCs, whereas recombinant fragments $PvRBP2b_{474–1454}$ and $PvRBP2b_{474–969}$ that lacked the N-terminal domain did not (Fig. 4D). By contrast, we did not detect any $PvRBP2b_{161–1454}$ and $PvRBP2b_{161–969}$ binding to TfR1 mutant cells. This abolition of binding was specific to deletions in *TFRC* because PvRBP2b binding was unaffected on ΔBSG null cells or on cRBCs (Fig. 4D, right). We also compared the invasion efficiency between jkRBCs and TfR1 mutant cell lines with either Brazilian *P. vivax* isolates or *P. falciparum* 3D7 (fig. S10E). A significant (>10-fold) reduction in invasion efficiency was observed in the TfR1 mutant line compared with the jkRBCs line with *P. vivax*, whereas no significant difference was observed with *P. falciparum* (Fig. 4E). These results validate TfR1 as the cognate receptor for PvRBP2b and that TfR1 is an essential host factor for *P. vivax* invasion.

Antibodies to PvRBP2b block reticulocyte binding and *P. vivax* invasion

To examine whether PvRBP2b antibodies could inhibit *P. vivax* invasion, we raised mouse monoclonal antibodies to $PvRBP2b_{161–1454}$ and obtained four mAbs. 3E9, 6H1, and 10B12 bound epitopes within the N-terminal domain present in $PvRBP2b_{169–470}$ with high affinities (Fig. 5A; fig. S12, A to C; and table S6), whereas mAb 8G7 recognized an epitope outside the N-terminal domain within amino acids 813 to 969 (Fig. 5A). Competition enzyme-linked immunosorbent assay (ELISA) experiments using mAbs directly conjugated to horseradish peroxidase (HRP) show that each mAb only competed with itself for binding to PvRBP2b, showing that 3E9, 6H1, and 10B12 bind to distinct epitopes in the N-terminal domain (Fig. 5B). Neither polyclonal nor monoclonal antibodies to PvRBP2b recognize recombinant PfRh4 and five other recombinant PvRBPs, indicating that these antibodies are specific to PvRBP2b (fig. S12B) (*19*). Using flow cytometry, we show that addition of anti-PvRBP2b mAbs 3E9, 6H1, and 10B12 abolished the $PvRBP2b_{161–1454}$ binding to reticulocytes, whereas anti-PvRBP2b mAb 8G7 and anti-PvRBP2a mAb 3A11 had no effect (Fig. 5C).

We tested the ability of the antibodies to PvRBP2b to inhibit *P. vivax* invasion into human reticulocytes, using a short-term *P. vivax* ex vivo assay with Brazilian and Thai clinical isolates (Fig. 5D, blue and black open circles, respectively). As a control, we used a camelid antibody to Fy6, which is a single monovalent VHH domain (15 kDa) (*38*, *39*) that targets a surface-exposed epitope on DARC and blocks its interaction with PvDBP. The addition of the 25 μg/ml camelid antibody to Fy6 in ex vivo assays by using Thai isolates resulted in 85% inhibition of *P. vivax* invasion (Fig. 5D). Using four Thai isolates, the addition of inhibitory anti-PvRBP mAbs 3E9, 6H1, and 10B12 at 25 μg/ml resulted in 49, 45, and 42% inhibition of *P. vivax* invasion, respectively. To determine whether inhibition could be improved by increasing the concentration of anti-PvRBP2b mAbs to match the molarity and valency of the single VHH domain, we used 125 μg/ml of inhibitory anti-PvRBP2b mAbs. Under these conditions, we tested the invasion efficiency of two Brazilian isolates. We observed that addition of inhibitory anti-PvRBP mAbs 3E9, 6H1, and 10B12 at 125 μg/ml resulted in 68, 45, and 57% inhibition of *P. vivax* invasion in Brazilian isolates, respectively (Fig. 5D). To enable quantitative analyses of the ex vivo assays, we combined our initial results of Thai and Brazilian isolates at their respective mAb concentrations. Increased concentration of the inhibitory anti-PvRBP2b mAbs resulted in an equivalent or small increase in inhibition of *P. vivax* invasion (Thai at 25 μg/ml versus Brazilian at 125 μg/ml). Thus, our combined sample set underestimates the level of inhibition for antibody concentrations of 125 μg/ml. As additional controls, we included the noninhibitory anti-PvRBP2b mAb 8G7 and an immunoglobulin G1 (IgG1) mouse isotype control, which displayed only 8 and 9% inhibition of *P. vivax* invasion, respectively (Fig. 5D). These results show that addition of anti-PvRBP2b inhibitory mAbs 3E9, 6H1, and 10B12 resulted in significant reduction of *P. vivax* invasion compared with the noninhibitory anti-PvRBP2b mAb 8G7 (Fig. 5D).

We show that the inhibitory anti-PvRBP2b mAbs target a domain that appears to be under balancing selection (Figs. 2E and 5A), which may result in differences in inhibition between clinical isolates owing to the presence of polymorphic epitopes. To circumvent inter-isolate differences, we further tested the combination of all three inhibitory mAbs, 3E9, 6H1, and 10B12 pooled together (mAb pool) and polyclonal antibodies to PvRBP2b. The mAb pool resulted in significant 48% reduction in *P. vivax* invasion in both Thai and Brazilian isolates compared with that of anti-PvRBP2b mAb 8G7 (Fig. 5D). Addition of purified total IgG of polyclonal antibodies to PvRBP2b R1527 resulted in 53% reduction in *P. vivax* invasion, whereas the rabbit prebleed IgG showed only 5% inhibition (Fig. 5D). A previous study using rabbit antibodies to PvDBP shows that *P. vivax* invasion was reduced up to 64% (*40*), a level of inhibition comparable with what has been observed with our antibodies to PvRBP2b (Fig. 5D). These results show that anti-PvRBP2b mAbs that block binding to reticulocytes also inhibit *P. vivax* invasion and highlight the important role of the PvRBP2b-TfR1 invasion pathway in *P. vivax* field isolates.

Our results reveal a stable interaction between PvRBP2b and TfR1 and that antibodies to PvRBP2b that block binding to reticulocytes also inhibit *P. vivax* invasion into human reticulocytes. *P. vivax* invasion is significantly inhibited in the presence of TfR1 mutant cells, showing that TfR1 is a critical host factor for entry into reticulocytes. We propose that the PvRBP2b-TfR1 interaction is important for the initial recognition of the target reticulocyte cells, which results in the commitment of *P. vivax* parasites for reticulocyte invasion and the subsequent engagement of PvDBP-DARC in tight junction formation, leading to the successful completion of the invasion process. Identification of the molecular entities required for *P. vivax* invasion offer the possibility to target multiple invasion pathways for synergistic inhibition of *P. vivax* blood stage infection.

REFERENCES AND NOTES

1. A. G. Maier *et al.*, *Nat. Med.* **9**, 87–92 (2003).
2. C. Crosnier *et al.*, *Nature* **480**, 534–537 (2011).
3. B. K. Sim, C. E. Chitnis, K. Wasniowska, T. J. Hadley, L. H. Miller, *Science* **264**, 1941–1944 (1994).
4. W.-H. Tham *et al.*, *Proc. Natl. Acad. Sci. U.S.A.* **107**, 17327–17332 (2010).
5. L. H. Miller, S. J. Mason, J. A. Dvorak, M. H. McGinniss, I. K. Rothman, *Science* **189**, 561–563 (1975).
6. J. H. Adams *et al.*, *Cell* **63**, 141–153 (1990).
7. R. Horuk *et al.*, *Science* **261**, 1182–1184 (1993).
8. A. F. Cowman, B. S. Crabb, *Cell* **124**, 755–766 (2006).
9. G. E. Weiss *et al.*, *PLOS Pathog.* **11**, e1004670 (2015).
10. I. Mueller *et al.*, *Lancet Infect. Dis.* **9**, 555–566 (2009).
11. L. H. Miller, S. J. Mason, D. F. Clyde, M. H. McGinniss, *N. Engl. J. Med.* **295**, 302–304 (1976).
12. T. G. Woldearegai, P. G. Kremsner, J. F. J. Kun, B. Mordmüller, *Trans. R. Soc. Trop. Med. Hyg.* **107**, 328–331 (2013).
13. C. Mendes *et al.*, *PLOS Negl. Trop. Dis.* **5**, e1192 (2011).
14. D. Ménard *et al.*, *Proc. Natl. Acad. Sci. U.S.A.* **107**, 5967–5971 (2010).
15. B. Malleret *et al.*, *PLOS ONE* **8**, e76062 (2013).
16. J. M. Carlton *et al.*, *Nature* **455**, 757–763 (2008).
17. M. R. Galinski, C. C. Medina, P. Ingravallo, J. W. Barnwell, *Cell* **69**, 1213–1226 (1992).
18. J. Gruszczyk *et al.*, *Proc. Natl. Acad. Sci. U.S.A.* **113**, E191–E200 (2016).
19. C. T. França *et al.*, *PLOS Negl. Trop. Dis.* **10**, e0005014 (2016).
20. B. Malleret *et al.*, *Blood* **125**, 1314–1324 (2015).

21. Y. Cheng, O. Zak, P. Aisen, S. C. Harrison, T. Walz, *Cell* **116**, 565–576 (2004).
22. B. T. Pan, R. M. Johnstone, *Cell* **33**, 967–978 (1983).
23. C. Harding, J. Heuser, P. Stahl, *J. Cell Biol.* **97**, 329–339 (1983).
24. C. M. Lawrence *et al.*, *Science* **286**, 779–782 (1999).
25. S. R. Radoshitzky *et al.*, *Nature* **446**, 92–96 (2007).
26. J. Abraham *et al.*, *PLOS Pathog.* **5**, e1000358 (2009).
27. Z. Bozdech *et al.*, *Proc. Natl. Acad. Sci. U.S.A.* **105**, 16290–16295 (2008).
28. G. Helguera *et al.*, *J. Virol.* **86**, 4024–4028 (2012).
29. W.-H. Tham *et al.*, *Blood* **118**, 1923–1933 (2011).
30. M. J. Bennett, J. A. Lebrón, P. J. Bjorkman, *Nature* **403**, 46–53 (2000).
31. J. Abraham, K. D. Corbett, M. Farzan, H. Choe, S. C. Harrison, *Nat. Struct. Mol. Biol.* **17**, 438–444 (2010).
32. S. R. Radoshitzky *et al.*, *Proc. Natl. Acad. Sci. U.S.A.* **105**, 2664–2669 (2008).
33. K. E. Wright *et al.*, *Nature* **515**, 427–430 (2014).
34. L. Chen *et al.*, *eLife* 10.7554/eLife.04187 (2014).
35. R. D. Pearson *et al.*, *Nat. Genet.* **48**, 959–964 (2016).
36. J. E. Levy, O. Jin, Y. Fujiwara, F. Kuo, N. C. Andrews, *Nat. Genet.* **21**, 396–399 (1999).
37. A. K. Bei, C. Brugnara, M. T. Duraisingh, *J. Infect. Dis.* **202**, 1722–1727 (2010).
38. D. Smolarek *et al.*, *Cell. Mol. Life Sci.* **67**, 3371–3387 (2010).
39. J. S. Cho *et al.*, *Int. J. Parasitol.* **46**, 31–39 (2016).
40. B. T. Grimberg *et al.*, *PLOS Med.* **4**, e337 (2007).

ACKNOWLEDGMENTS

We thank J. Newman from the Commonwealth Scientific and Industrial Research Organization Collaborative Crystallization Centre for assistance with setting up the crystallization screens, the Walter and Eliza Hall Institute's Monoclonal Antibody Facility for production of antibodies, J. Williamson for assistance with mass spectrometry, and MX and SAXS beamline staff at the Australian Synchrotron for their assistance during data collection. We thank F. Nosten, the staff and patients attending the Mae Sot Malaria Clinic in Thailand, and clinics associated with the Shoklo Malaria Research Unit (SMRU), Tak Province, Thailand. We also thank Y. Colin and O. S. Bertrand (INSERM/University Paris 7) for the generous gift of the antibodies to DARC. W.-H.T. is a Howard Hughes Medical Institute–Wellcome Trust International Research Scholar (208693/Z/17/Z). This work was supported in part by the Australian Research Council Future Fellowships to W.-H.T. and M.D.W.G., a Speedy Innovation Grant to W.-H.T., and a National Health and Medical Research Council fellowship (1105754) to J.M.M. U.K. was supported by a Canadian Institutes of Health Research Postdoctoral Fellowship. R.D.P. is funded by Wellcome Trust 090770. M.P.W. was supported by a Wellcome Trust Senior Clinical Research Fellowship (108070/Z/15/Z). This study received funding from Singapore National Medical Research Council (NMRC) (NMRC/CBRG/0047/2013) and the Agency for Science, Technology and Research (A*STAR, Singapore). SMRU is sponsored by The Wellcome Trust of Great Britain as part of the Oxford Tropical Medicine Research Programme of Wellcome Trust–Mahidol University. Work in the M.T.D. laboratory was supported by National Institutes of Health grant 1R01HL139337. We also acknowledge the support of the B.R. laboratory from the Marsden Fund 17-UOO-241.The authors acknowledge the Victorian State Government Operational Infrastructure Support and Australian Government National Health and Medical Research Council Independent Research Institute Infrastructure Support Scheme. All data and code to understand and assess the conclusions of this research are available in the main text, supplementary materials, and via the following repositories: The atomic coordinates and structure factors for PvRBP2b have been deposited in PDB with accession number 5W53. Genotypes were derived from sequence data generated at the Wellcome Trust Sanger Institute (Wellcome Trust 206194 and 098051).

SUPPLEMENTARY MATERIALS

www.sciencemag.org/content/359/6371/48/suppl/DC1
Materials and Methods
Figs. S1 to S12
Tables S1 to S6
References (*41*–*83*)
Data Set S1

6 March 2017; resubmitted 29 September 2017
Accepted 16 November 2017
10.1126/science.aan1078

COMPARATIVE GENOMICS

Rapid genome shrinkage in a self-fertile nematode reveals sperm competition proteins

Da Yin,[1] Erich M. Schwarz,[2]* Cristel G. Thomas,[1,3] Rebecca L. Felde,[1] Ian F. Korf,[4] Asher D. Cutter,[3] Caitlin M. Schartner,[5] Edward J. Ralston,[5] Barbara J. Meyer,[5] Eric S. Haag[1]*

To reveal impacts of sexual mode on genome content, we compared chromosome-scale assemblies of the outcrossing nematode *Caenorhabditis nigoni* to its self-fertile sibling species, *C. briggsae*. *C. nigoni*'s genome resembles that of outcrossing relatives but encodes 31% more protein-coding genes than *C. briggsae*. *C. nigoni* genes lacking *C. briggsae* orthologs were disproportionately small and male-biased in expression. These include the *male secreted short* (*mss*) gene family, which encodes sperm surface glycoproteins conserved only in outcrossing species. Sperm from *mss*-null males of outcrossing *C. remanei* failed to compete with wild-type sperm, despite normal fertility in noncompetitive mating. Restoring *mss* to *C. briggsae* males was sufficient to enhance sperm competitiveness. Thus, sex has a pervasive influence on genome content that can be used to identify sperm competition factors.

Sex between individuals is nearly ubiquitous in eukaryotic life (*1*). However, in multicellular organisms, the costs of sex and scarcity of mates sometimes favor the evolution of uniparental reproduction through asexual parthenogenesis or self-fertilization (*2*). Such changes in sexual reproduction have consequences for both sexual traits and genome content. Comparative genomics using closely related species with different modes of sexual reproduction can reveal sex-related factors that might otherwise remain cryptic. In the nematode species *C. elegans*, *C. briggsae*, and *C. tropicalis*, animals with two X chromosomes that would normally be female have evolved into self-fertilizing hermaphrodites (Fig. 1A) (*3*). Nearly all progeny of these selfing XX hermaphrodites are themselves XX. Rare haplo-X (XO) male progeny experience weaker sexual selection than males from outcrossing species, exhibit atrophy of traits required for efficient mating (*4*–*7*), and are hypersensitive to pheromone-induced mortality (*8*). Sexually antagonistic sperm-female interactions have also been relaxed in self-fertile *Caenorhabditis* (*9*).

Self-fertile *Caenorhabditis* have smaller genomes and transcriptomes than outcrossing *Caenorhabditis* (*10*, *11*), as also observed in the selfing plant *Arabidopsis thaliana* (*12*). However, comparisons of self-fertilizing to outcrossing *Caenorhabditis* have involved species as divergent at the nucleotide level as humans are from mice (*10*, *13*), so it remains unclear how quickly genomic shrinkage occurs. We hypothesized a direct link between the degradation of sexual traits and genome contraction in selfing species. Here, we describe genomic resources and functional experiments that confirm its existence.

[1]Department of Biology, University of Maryland, College Park, MD 20742, USA. [2]Department of Molecular Biology and Genetics, Cornell University, Ithaca, NY 14853, USA. [3]Department of Ecology and Evolutionary Biology, University of Toronto, Toronto, Ontario M5S 3B2, Canada. [4]Department of Molecular and Cellular Biology and Genome Center, University of California, Davis, CA 95616, USA. [5]Howard Hughes Medical Institute and Department of Molecular and Cell Biology, University of California, Berkeley, CA 94720, USA.
*Corresponding author. Email: ems394@cornell.edu (E.M.S.); ehaag@umd.edu (E.S.H.)

Comparison of *C. nigoni* and *C. briggsae* genomes

Of the ~50 known *Caenorhabditis* species, the most closely related pair with different sexual modes are the outcrossing *C. nigoni* and the selfing *C. briggsae* (*14*–*16*). They remain partially interfertile, yet they have numerous genetic and reproductive incompatibilities (*9*, *15*, *17*–*19*). To compare their genomes, we assembled the *C. nigoni* genome from 20-kb Pacific Biosciences (PacBio) and Illumina short-read libraries (table S1) (*20*). The final *C. nigoni* chromosome-scale genome assembly totaled 129 Mb with a size-weighted median (N50) contig length of 3.3 Mb; it was estimated as 99.6% complete (*21*). The genome was 19% larger than that of *C. briggsae* (108 Mb) but was similar in size to genomes of the more distantly related outcrossing species *C. remanei*, *C. sinica*, *C. brenneri*, and *C. japonica*, which range from 131 to 135 Mb (Fig. 1A) (*10*). Therefore, larger genome sizes were probably the ancestral condition, and genomic shrinkage occurred in the *C. briggsae* lineage after it diverged from *C. nigoni*. More than 90% (118 Mb) of the assembly can be aligned to the chromosomes of *C. briggsae* without large translocations or inversions, despite megabase-sized contigs (fig. S1). Thus, the two genomes are essentially colinear but differ in many small species-specific segments. *C. nigoni*'s six chromosomes are 6.6 to 16.6% larger than their *C. briggsae* homologs (table S2).

We used whole-genome alignment to identify species-specific genomic segments (*20*). In *C. nigoni*, 47.7 Mb (36.9%) did not align with *C. briggsae*, and *C. briggsae* had 27.7 Mb (25.6% of 108.4 Mb) that did not align with *C. nigoni*. This 20.0-Mb difference accounted for 95% of the difference in genome sizes. Nonalignable genomic regions were concentrated on the distal arms of all six holocentric chromosomes, where small inversions and repetitive sequences were abundant and gene densities were low (Fig. 1B). These regions were mostly small (median ~500 base pairs; Fig. 2A), but larger (1 to 65 kb) insertions or deletions accounted for 17 Mb (81%) of the genome size difference (Fig. 2B). In both assemblies, nonalignable sequences were most common in intergenic regions and introns (fig. S2). *C. nigoni* harbored 5.4 Mb more species-specific protein-coding sequences than *C. briggsae*, consistent with a net loss of genes in *C. briggsae* (see below). For orthologous genes in both species, exon lengths were highly correlated (Fig. 2C and table S3). In contrast, ortholog intron content was weakly correlated and was significantly larger in *C. briggsae*. Because both genomes had similar repetitive DNA fractions (*C. nigoni* 27% versus *C. briggsae* 25%), disproportionate loss of repetitive sequences (seen in plants) did not contribute to different genome sizes (table S1) (*10*, *12*, *22*).

Impact of genome shrinkage on *C. briggsae* gene content

We predicted 29,167 protein-coding genes for *C. nigoni* (table S4), with 88.9% (25,929) being expressed in adults [≥0.1 transcripts per million (TPM)]. By equivalent methods, we predicted 22,313 genes in *C. briggsae* (*20*), 23.5% less than *C. nigoni*. The published gene annotations for *C. briggsae* (*23*) were even fewer (21,814 genes).

This 6854-gene difference could have several causes, including gene family contraction and loss of sequence classes in *C. briggsae*, as well as *C. nigoni*–biased gain of novel sequences. We compared genes of *C. briggsae* and *C. nigoni* to genes of the outgroups *C. remanei*, *C. brenneri*, and *C. elegans* (*20*). In *C. nigoni*, 24,341 genes (83.5%) were orthologous to 21,124 *C. briggsae* genes, reflecting larger multigene families in *C. nigoni* versus *C. briggsae* (Fig. 3A and table S4) (*24*). Another 2949 *C. nigoni* genes without *C. briggsae* orthologs (10.1%) represent losses in *C. briggsae* based on homologs in *Caenorhabditis* outgroups (fig. S3). Finally, 1877 *C. nigoni* genes (6.4%) lacked homologs entirely and were classed as orphans. These genes could be exceptionally divergent, recently arisen in *C. nigoni*, or arisen shortly before the *C. nigoni*–*C. briggsae* split but then lost in *C. briggsae*. Overall, gene loss in *C. briggsae* appears to be the primary driver of the gene number difference.

To characterize genes lost in *C. briggsae*, we first compared Pfam protein domains encoded by *C. nigoni* versus *C. briggsae*. We found 26 Pfam domains that were overrepresented in *C. nigoni* (fig. S4 and table S5); of these, seven were consistently overrepresented in outcrossing *C. nigoni*, *C. remanei*, and *C. brenneri* relative to the selfing species *C. briggsae* and *C. elegans*. Three of these

domains (F-box, FBA_2/F-box associated, and BTB) are predicted to mediate protein-protein interactions. Male-female *Caenorhabditis* had 272 to 1074 genes in these families, whereas hermaphroditic *Caenorhabditis* had only 101 to 258 genes per family. Two other domains (Peptidase_A17 and DNA_pol_B_2) are associated with repetitive DNA. The final two overrepresented domains were Asp_protease_2 (possibly associated with retroelements) and DUF3557 (a nematode-specific domain, currently of unknown function). One overrepresented domain specific to *C. nigoni* was zf.RING2_finger; the RING domain gene *spe-42* is important for sperm-egg interactions in *C. elegans* (*25*).

Because *C. nigoni*–specific genes might encode fast-evolving proteins that lack known domains, we compared other gene properties. We found that although genes encoding medium to large proteins (≥200 residues) are similar in frequency in both species, *C. nigoni* encodes disproportionately more small proteins (<200 residues) than *C. briggsae* (Fig. 3B and table S6). As seen in other *Caenorhabditis* (*11*), genes with male-biased expression outnumber female-biased genes (Fig. 3C and table S7). However, even against this background, *C. nigoni* genes without *C. briggsae* homologs are disproportionately male-biased in expression. Preferential loss of small and fast-evolving proteins thus occurred in *C. briggsae* after the adoption of selfing.

mss genes encode sperm glycoproteins lost in hermaphrodites

We hypothesized that genes with highly male-biased expression that are present in outcrossing species, but lost in selfing species, might function in sexual selection. Among such genes we identified the *mss* (*male secreted short*) family. We

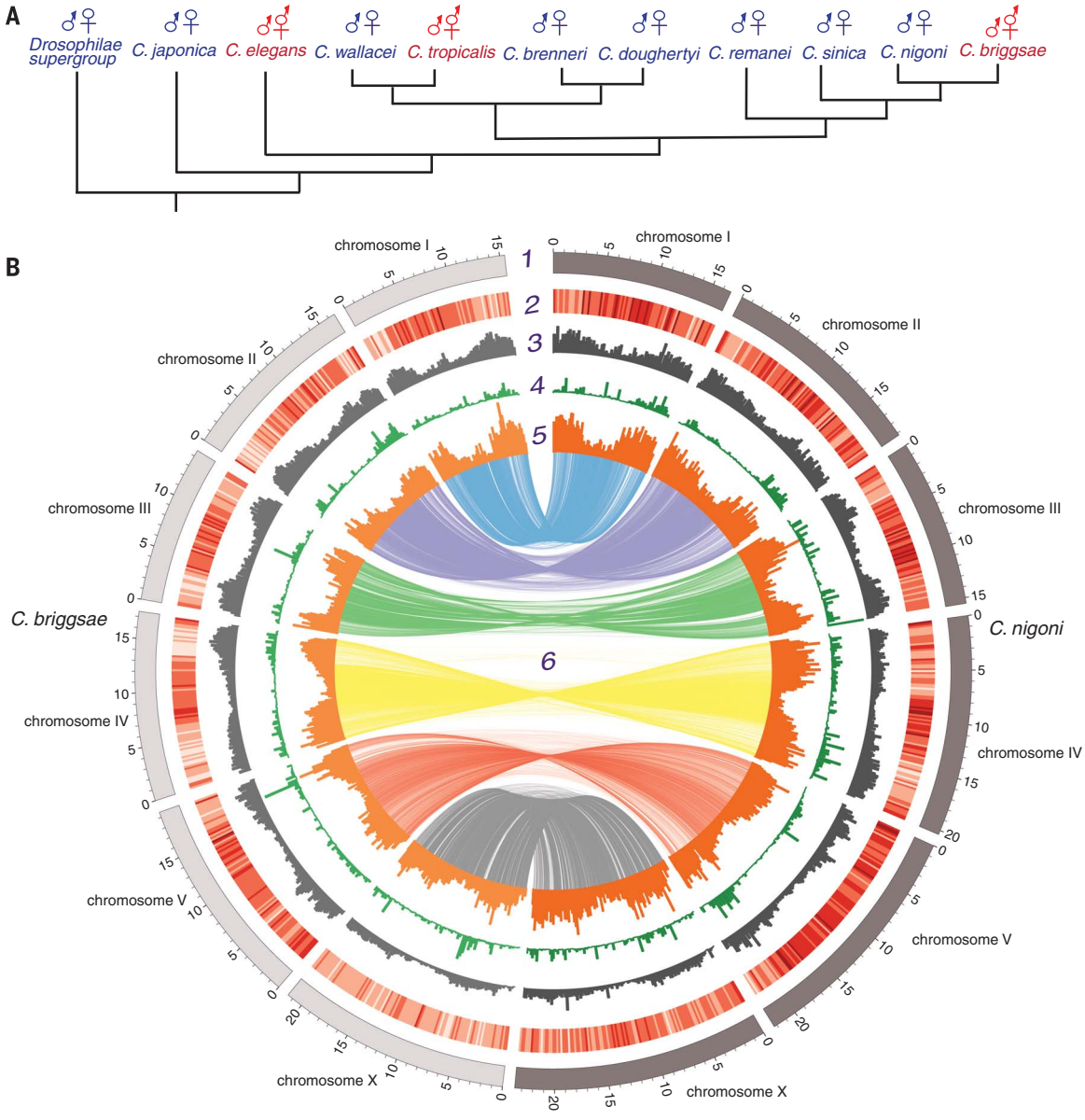

Fig. 1. The phylogenetic relationship of *Caenorhabditis* and comparison of the *C. nigoni* and *C. briggsae* genome assemblies. (**A**) Phylogeny of Elegans supergroup *Caenorhabditis* [adapted from (*3*)] with outcrossing species producing XX females indicated in blue, and self-fertile lineages with XX hermaphrodites indicated in red. (**B**) Chromosomal alignments and genomic features over 200-kb chromosomal intervals. Tracks from outside to inside: **1**, positions (in Mb) of the six chromosomes of *C. nigoni* and *C. briggsae*; **2**, gene density heat map (darker shade indicates higher density); **3**, repeat frequency; **4**, inversion frequencies; **5**, percentage of sequence lacking homology in the other assembly (representing either deletions or species-specific gains); **6**, DNA sequence synteny.

found one to four *mss* genes in the outcrossing species *C. nigoni*, *C. sinica*, *C. remanei*, *C. brenneri*, *C.* sp. 34, *C. japonica*, and *C. afra*, but found none in the selfing *C. elegans*, *C. briggsae*, and *C. tropicalis*. The *mss* family encodes small proteins (median 111 residues) with N-terminal signal sequences, rapidly evolving central domains with several predicted O-glycosylation sites, and C-terminal glycosylphosphatidylinositol (GPI) anchor membrane attachment signals (Fig. 3D). Enzyme treatments confirmed that MSS proteins were heavily glycosylated (fig. S5).

Although we failed to detect *mss* genes in selfing species, we did discover a larger family of *mss*-related protein (*msrp*) genes, within which *mss* forms a monophyletic clade (fig. S6) (*20*). Notably, *msrp* genes are found both in outcrossing *Caenorhabditis* and in the hermaphroditic *C. elegans*, *C. briggsae*, and *C. tropicalis* (fig. S6). Like MSS proteins, MSRP proteins are small and are predicted to be secreted, O-glycosylated, and (often) GPI-anchored. Both *mss* and *msrp* genes show male-biased expression in *C. nigoni* and other species (table S8). In cases where their chromosomal loci can be identified, *mss* and *msrp* genes are autosomal; this linkage fits a general pattern in heterogametic male species of male-biased genes being autosomal rather than X-chromosomal [(*26*) and references therein].

Because we observed *mss* genes in two *C. elegans* outgroups (*C. japonica* and *C. afra*; fig. S6 and table S8), their absence from hermaphrodites most likely reflects independent gene losses rather than phylogenetic restriction to close relatives of *C. nigoni*. Examination of the *C. briggsae* genomic region syntenic to the *C. nigoni mss* locus revealed fragments of *mss-1* and *mss-2* coding sequences and a nearly complete *mss-3* pseudogene (Fig. 3E) (*20*). Mutations that ablate *Cbr-mss-3-ps* function in the AF16 reference strain also occur in 11 wild isolates that span the known diversity of *C. briggsae* (fig. S7) (*20*, *27*). Orthologs of all three *C. nigoni mss* genes were therefore present in the common ancestor of *C. nigoni* and *C. briggsae* but were lost in *C. briggsae* before its global diversification.

In the outcrossing species *C. remanei*, *mss* transcripts were expressed only in adult males (Fig. 4A), with strongest expression in spermatocytes during mid-pachytene of meiosis I (Fig. 4B). To determine subcellular localization of MSS peptides, we used CRISPR/Cas9 editing to tag the *Cre-mss-1* gene of *C. remanei* with the hemagglutinin (HA) epitope. *Crem*-MSS-1::HA expression was first detected in large vesicles and on the plasma membrane of spermatocytes, with intensity increasing and localization restricted to secretory vesicles in mature spermatids (Fig. 4, C to E). The secretory vesicles of nematode sperm, known as membranous organelles (MOs), fuse with the plasma membrane upon ejaculation and sperm activation (*28*).

MSS peptides might be processed by a signal peptidase to release a soluble fragment into the MO lumen, which could then be dumped into seminal fluid upon sperm activation. However, their transient plasma membrane localization in spermatocytes and predicted C-terminal GPI attachment signals (Fig. 3D and table S8) suggested that MSS peptides might instead be attached to membranes. Consistent with this latter hypothesis, *Crem*-MSS::HA remained associated with activated sperm dissected from inseminated females (Fig. 4F). We observed staining of the plasma membrane and of MO-derived punctae

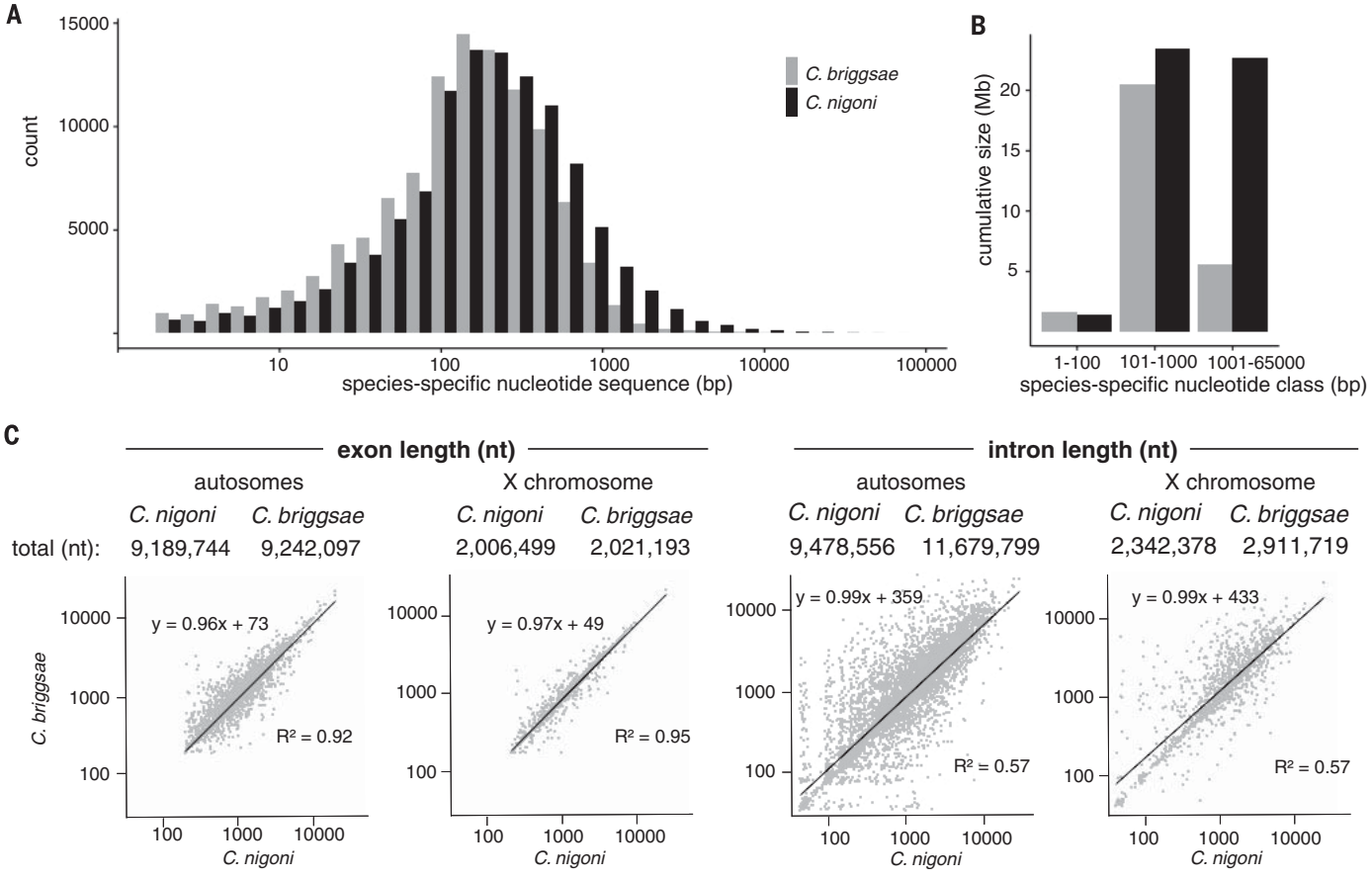

Fig. 2. Size distributions of insertion-deletion variants. (**A**) Size distribution of species-specific sequences in the *C. briggsae*–*C. nigoni* whole-genome alignment. Black, sequences present in *C. nigoni* alone; gray, sequences present in *C. briggsae* alone. (**B**) Contribution of different species-specific sequence types to genome size. (**C**) Regression analysis of total exon and intron lengths for 6404 one-to-one *C. briggsae*–*C. nigoni* orthologs on autosomes and 1394 orthologs on the X chromosome. Interspecies differences were insignificant for either exon set ($P = 0.378$ for autosomes, $P = 0.668$ for X), but introns on autosomes ($P = 1.53 \times 10^{-10}$) and on the X chromosome ($P = 1.2 \times 10^{-5}$) were significantly larger in *C. briggsae* (all *P* values: Wilcoxon rank-sum test with Bonferroni correction).

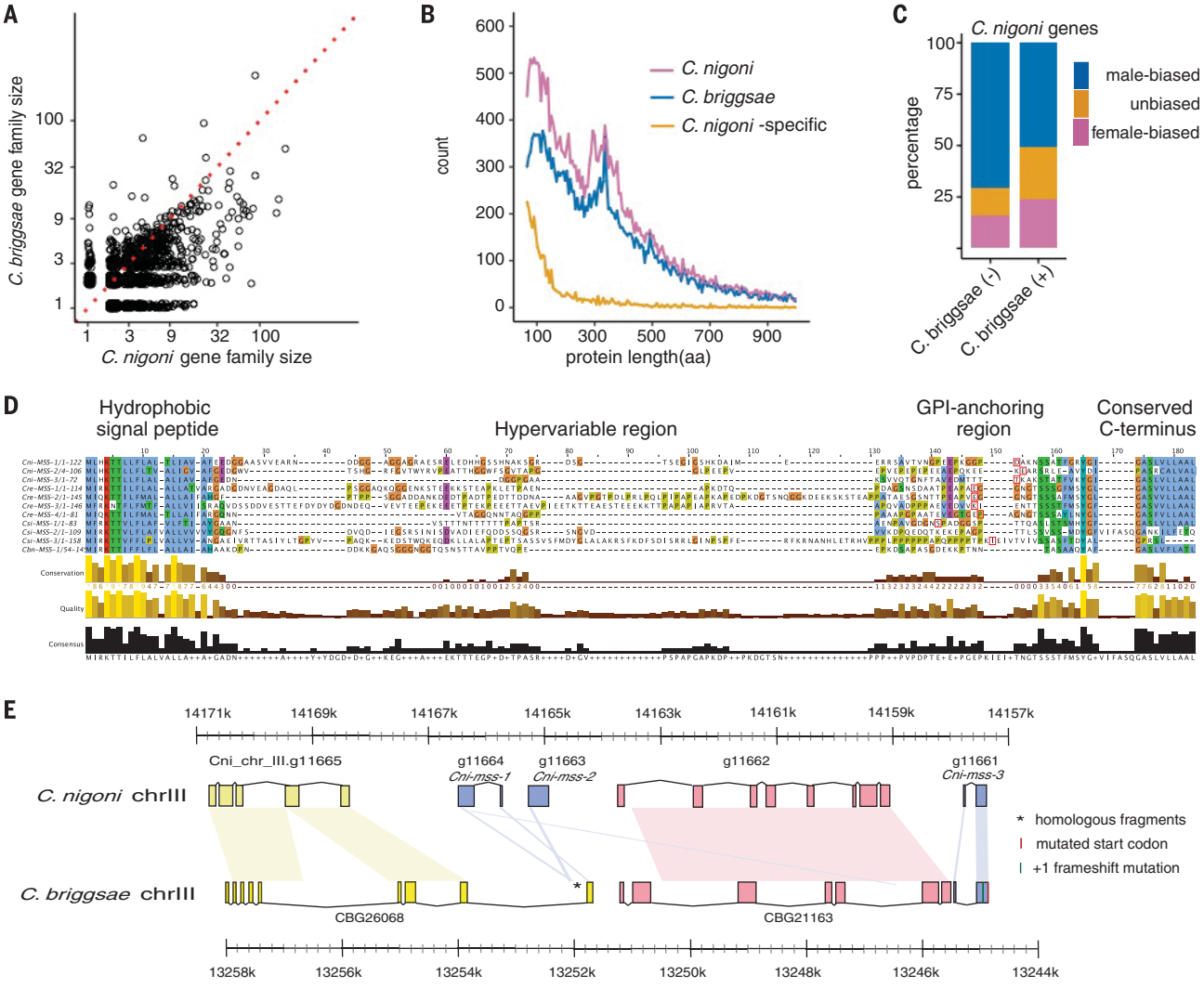

Fig. 3. Comparison of the *C. nigoni* and *C. briggsae* proteomes. (**A**) Scatterplot of sizes of OrthoFinder gene families, excluding one-to-one orthologs (table S4). Of 2367 families with unequal numbers of *C. nigoni* and *C. briggsae* genes, the majority (1624) were larger in *C. nigoni* than in *C. briggsae* ($P < 2.2 \times 10^{-16}$, Wilcoxon signed-rank test). Dotted line indicates equal family sizes. (**B**) Length distributions of *C. nigoni* and *C. briggsae* proteins and of *C. nigoni* proteins that lack *C. briggsae* homologs. (**C**) For genes with sex-biased expression, male bias was seen for 50.9% of 6804 genes with *C. briggsae* homologs ["*C. briggsae* (+)"] but was significantly overrepresented (70.9%) among 605 genes lacking *C. briggsae* homologs ["*C. briggsae* (−)"; $P < 0.0001$, Fisher exact test; table S9]. (**D**) Alignment of predicted MSS homologs from outcrossing *C. nigoni*, *C. sinica*, *C. remanei*, and *C. brenneri* (table S8) (*20*), with protein domains indicated above. Amino acid abbreviations: A, Ala; C, Cys; D, Asp; E, Glu; F, Phe; G, Gly; H, His; I, Ile; K, Lys; L, Leu; M, Met; N, Asn; P, Pro; Q, Gln; R, Arg; S, Ser; T, Thr; V, Val; W, Trp; Y, Tyr. (**E**) Comparison of *mss* gene regions in *C. nigoni* and *C. briggsae*. Pastel shapes connect homologous sequences. Except for *Cni-mss-3*, all genes are transcribed from left to right. Genes surrounding the three *C. nigoni mss* paralogs are conserved in *C. briggsae*, but only fragments and a pseudogene (*Cbr-mss-3-ps*) of the *mss* genes remain. The pseudogene has a lost start codon and a +1 frameshift. CBG26068 has a novel 3′ exon derived from part of the *Cni-mss-1* second exon. See fig. S7 and (*20*) for details.

(Fig. 4G), which may be fused vesicles that remain as cup-like invaginations (*29*). Persistence of MSS on the surface of sperm after activation suggested that MSS acts cell-autonomously, rather than through the seminal fluid.

mss genes mediate sperm competition and affect sex ratios

Because the four *C. remanei mss* paralogs form a 7-kb tandem array (fig. S8A), we deleted the entire *mss* cluster via CRISPR/Cas9 editing. To avoid inbreeding depression associated with homozygosity of entire chromosomes (*30*) (fig. S8B), we generated the *mss* deletion in two different *C. remanei* strains and crossed them to create hybrid *mss*-null mutants. The resulting males showed no intrinsic fertility defects, as judged by overall brood size (fig. S8C). However, when competing against heterozygous *mss*(null/+) males, *mss* mutants sired fewer progeny than nonmutants in both offense (mutant male second) and defense (mutant male first) scenarios (Fig. 5, A and B). The *mss* family is therefore required for male sperm competitiveness in multiple mating situations, but not for fertility itself. Sperm lacking MSS compete poorly even when the female reproductive tract is conditioned by wild-type sperm. Thus, MSS proteins probably do not function as a secreted signal, but instead act cell-autonomously.

We then introduced *mss-1* and *mss-2* genes from *C. nigoni* into *C. briggsae* via a low-copy, germline-expressed MSS transgene; this transgene was strongly expressed in *C. briggsae* males, while also being detectable in hermaphrodites (fig. S9). Remarkably, sperm from transgenic *mss*(+) *C. briggsae* males outcompeted those of wild-type males (Fig. 5, C and D). After *mss*(+) sperm were exhausted, however, wild-type *mss* (null) sperm were still fertilization-competent

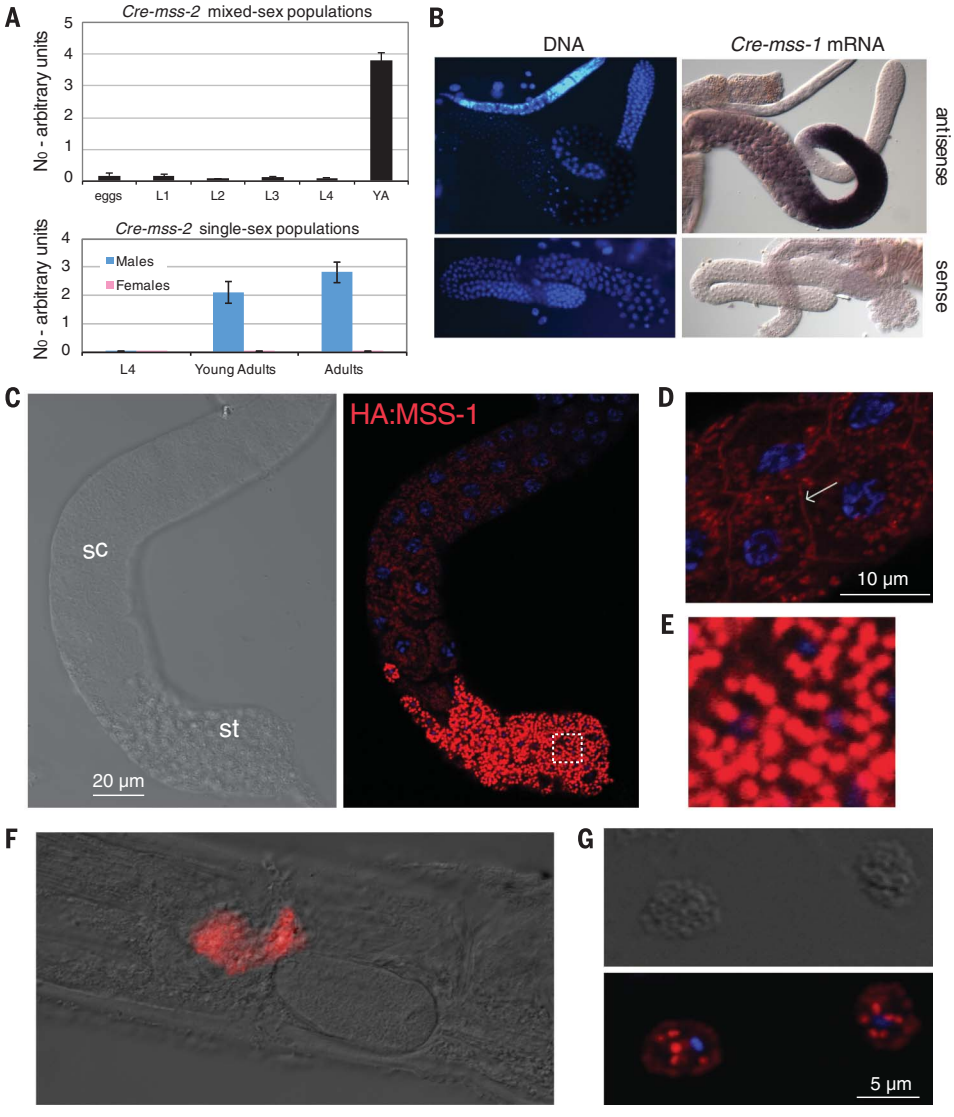

Fig. 4. *C. remanei* MSS is a male-specific protein localized to the surface of activated sperm. (**A**) Quantitative reverse transcription polymerase chain reaction (for *Cre-mss-2*) of mixed-sex populations (top) versus larval and adult sex-specific populations (bottom), showing that *mss* expression is specific to adult males. Data are means ± SEM. Female data are two to three orders of magnitude below male data. (**B**) *Cre-mss-1* transcripts are detected in pachytene-stage primary spermatocytes. (**C**) Dissected testis expressing HA-tagged *Cre*-MSS-1, viewed with differential interference contrast (DIC, left) or anti-HA confocal fluorescence (right) microscopy. *Cre*-HA-MSS-1 is first detectable in spermatocytes (sc) and becomes enriched in spermatids (st). (**D**) Some *Cre*-HA-MSS-1 is localized to the plasma membrane of spermatocytes, as indicated by the arrow. Blue fluorescence: Hoechst-stained DNA. (**E**) Enlarged view of the boxed region in (C), showing complete restriction to membranous organelles (MOs). (**F**) *Cre*-HA-MSS-1 remains attached to sperm after activation and transfer to the female. (**G**) *Cre*-HA-MSS-1 sperm cells dissected from a female and stained with anti-HA immunohistochemistry, imaged with DIC (top) and confocal (bottom) microscopy. *Cre*-HA-MSS-1 is visible in the plasma membrane and fused MO remnants.

(Fig. 5, C and D). In addition, *mss*(+) males were more consistently able to suppress use of a hermaphrodite mate's self-sperm (Fig. 5E).

Because 50% of outcross progeny are male whereas selfed progeny are almost exclusively hermaphrodites, we examined the effect of transgenic *mss* on long-term sex ratios in *C. briggsae* populations. We started both wild-type and *mss*(+) *C. briggsae* populations with a 1:1 male-to-hermaphrodite sex ratio and examined them over time. Wild-type *C. briggsae* showed a rapid decline of males, as previously seen in *C. elegans* (*7*, *31*). However, male frequency remained elevated in the *mss*(+) strain (Fig. 5F), only declining after 12 generations. The expression of MSS proteins was thus sufficient to shift population sex ratios toward parity.

Discussion

Comparison of the *C. nigoni* and *C. briggsae* genomes revealed that *C. briggsae* experienced rapid contraction of chromosomes and loss of protein-coding genes. However, loss of ancestral genomic content in *C. briggsae* does not fully explain their genomic divergence; the ongoing birth of novel sequences in both species, along with loss of ancestral DNA in *C. nigoni*, is also important. Net shrinkage of the *C. briggsae* genome therefore resulted from a substantial increase in the ratio of losses to gains. These losses included many coding sequences, reducing the *C. briggsae* gene count by nearly one-quarter.

Multiple observations implicate the evolution of selfing as the cause of genome shrinkage in *C. briggsae*. Reduced genome and transcriptome sizes are observed in all three selfing *Caenorhabditis* species (*10*, *11*). Continued interfertility of *C. briggsae* and *C. nigoni* (*15*) indicates that self-fertility and genome shrinkage evolved in quick succession. Genes with male-biased expression, such as the *mss* family, are disproportionately and consistently lost from selfing species (*11*). This suggests that genes with male reproductive functions that are either dispensable or maladaptive in the new sexual mode are purged from the genome. Finally, the net genome shrinkage we observed has been predicted to arise from a partially selfing mating system coupled with transmission distortion of autosomal deletion alleles (*32*, *33*). Such distortion is driven by imbalanced chromatin during meiosis I of XO males, and causes preferential inheritance of shorter alleles by hermaphrodite progeny and their increased fixation in the population.

Larger autosomal deletions, influenced most by the deletion segregation distortion mechanism, are primarily responsible for the smaller genome of *C. briggsae* (Fig. 2). However, such deletions and net shrinkage were also found on the X chromosome (table S2), which should be unaffected. Moreover, orthologous genes have larger introns in *C. briggsae* than in *C. nigoni* (Fig. 2), and introns constitute a greater fraction of the *C. briggsae* genome (fig. S2). X-chromosomal *C. briggsae* introns are also larger than those of the outgroup *C. remanei* (10) (fig. S2C), which suggests that introns of many genes expanded in *C. briggsae*. Thus, additional processes must also contribute to shrinkage of the *C. briggsae* genome. Spontaneous short (1- to 5-nucleotide) mutations in *C. elegans* are biased toward insertions rather than deletions

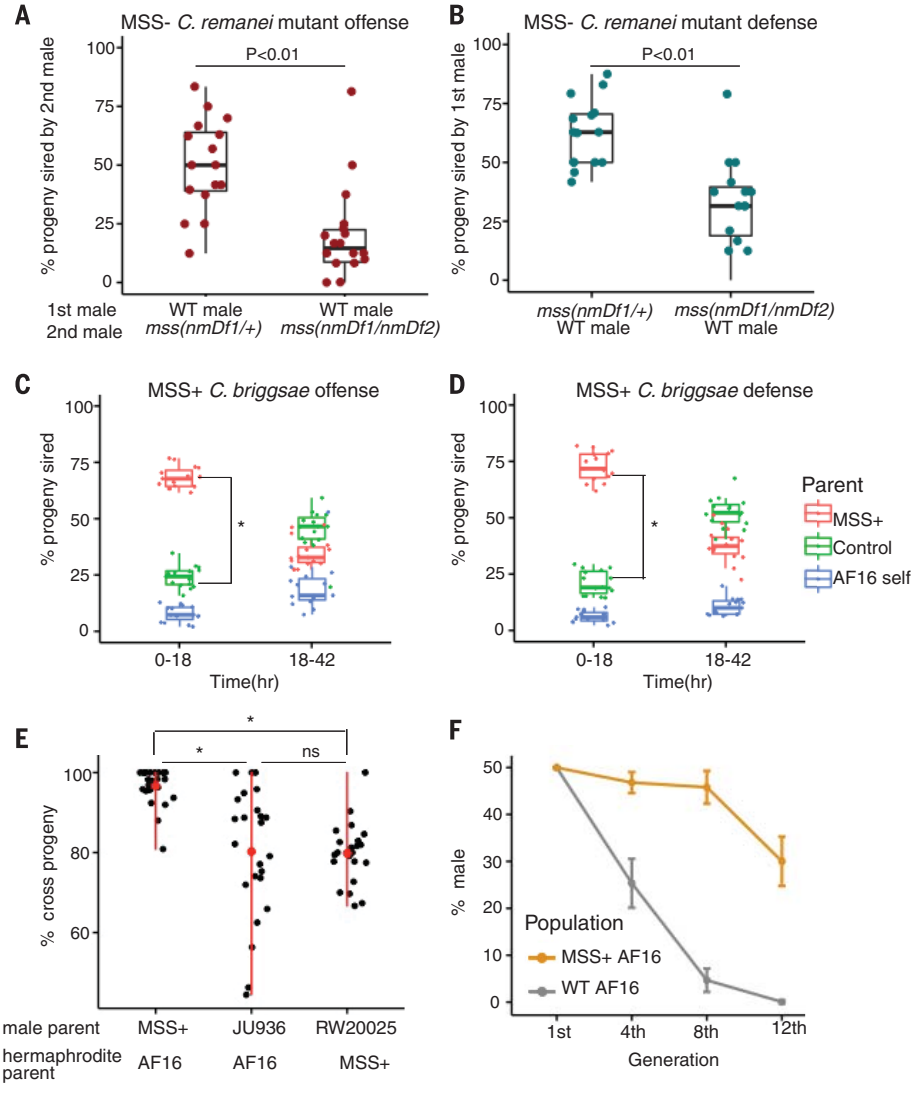

Fig. 5. *mss* genes are necessary for sperm competitiveness in an outcrossing species, and sufficient to enhance it in a selfing species. (**A**) When mated after a wild-type male ("offense"), *C. remanei mss* (*nmDf1/+*) males sire more than twice the progeny of *nmDf1/nmDf2 mss*-null mutants (N = 16 for both). (**B**) When allowed to mate first ("defense"), heterozygous *C. remanei mss*(*nmDf1/+*) males have a slight advantage over wild-type males; *mss*-null mutants, in contrast, do not (N = 15 for both). Heterozygote success is assumed to be double the observed *nmDf1* frequency in their progeny. For both defense and offense, $P < 0.01$ (two-sample Kolmogorov-Smirnov test). (**C** and **D**) Wild-type young *C. briggsae* hermaphrodites were mated sequentially (4 hours each) with conspecific males carrying either a *C. nigoni mss*(+) transgene or a control mCherry::histone reporter (RW0025). Progeny laid 0 to 18 hours and 18 to 42 hours after the second mating were scored for green (MSS+), red (RW0025), or no (self) fluorescent markers. In both offense (C) and defense (D), MSS+ males sire several times as many progeny as control males in the first laying window. *$P < 0.001$. (**E**) MSS+ *C. briggsae* males suppress selfing more effectively than do control AF16 (wild-type) males. Strain JU936 is a second control strain bearing two transcriptional GFP reporters in the AF16 background. *$P < 0.001$ (Kolmogorov-Smirnov test); ns, not significant. (**F**) Male frequency in MSS+ and wild-type AF16 *C. briggsae* populations in which male frequency was artificially elevated to 50% at the start of the experiment. In all panels except (E), error bars denote SD.

(*34*), although biases in formation of larger indels remain uncharacterized. Regardless, the relative rates of insertion and deletion mutations likely evolved too slowly to explain *C. briggsae*'s reduced genome size, given its recent divergence from *C. nigoni* (*27*). Gene loss can sometimes be adaptive (*35*, *36*) and has been proposed as a factor promoting genome shrinkage in selfing *Caenorhabditis* (*10*). Our results for the *C. nigoni*–*C. briggsae* pair support this hypothesis.

Genes encoding small proteins with male-biased expression are disproportionately lost in *C. briggsae*; here, *mss* provides an instance affecting reproduction. Unlike *comp-1*, which encodes a kinase required for male versus hermaphrodite sperm competition in *C. elegans* (*37*) and which is conserved regardless of mating system, we found *mss* orthologs only in outcrossing species. In interspecies matings, sperm from males of outcrossing species rapidly invade the ovaries and body cavities of selfing hermaphrodites, sterilizing or killing them (*9*). This cryptic toxicity of outcrossing sperm is likely due to ongoing sexual selection in outcrossing species. Given their pronounced role in sperm competition, MSS proteins may contribute to sperm invasiveness.

How MSS improves sperm competitiveness remains unclear, but mature MSS proteins are substantially glycosylated (fig. S5). Such post-translational modification may impose little constraint on MSS proteins, explaining how they can have weak sequence conservation yet strong functional conservation. Another poorly conserved O-glycosylated protein, the mucin PLG-1, forms a copulatory plug found in all male-female *Caenorhabditis* species but lost in many wild isolates of *C. elegans* (*4*). Glycoproteins form the glycocalyx coat of mammalian sperm and play important roles in fertility (*38*). *Caenorhabditis* provides a useful model for how the glycocalyx and female tissues interact and how these interactions affect sperm competition.

Independent loss of *mss* in the three known hermaphroditic *Caenorhabditis* species could reflect relaxed sexual selection coupled with mutation and drift, or it could reflect adaptive convergence. Other changes in selfing species—such as loss of *plg-1* and of *plep-1*, which mediates reliable male discrimination between the vulva and excretory pore (*4*, *6*)—are likely due to relaxed selection. However, restoring *mss to C. briggsae* enhances male fitness (Fig. 5, C and D), and mutations inactivating the *Cbr-mss-3-ps* pseudogene are not deletions that would be subject to loss via transmission ratio distortion (fig. S7). These findings suggest that loss of *mss* may instead reflect adaptive convergence, permitting protohermaphrodites to adapt to a selfing lifestyle and resolve emergent sexual conflicts related to mating (*39*–*41*). Selfing *Caenorhabditis* species lack inbreeding depression (*42*) and reproduce in spatially isolated habitats colonized by small numbers of founders (*3*). Reduced male mating success creates hermaphrodite-biased sex ratios (Fig. 5F), which may be adaptive under these conditions (*41*, *43*–*45*). Thus, evolutionary transitions in reproductive mode may produce conditions for selection to rapidly eliminate formerly constrained reproductive genes.

REFERENCES AND NOTES

1. A. M. Schurko, M. Neiman, J. M. Logsdon Jr., *Trends Ecol. Evol.* **24**, 208–217 (2009).
2. G. Bell, *The Masterpiece of Nature: The Evolution and Genetics of Sexuality* (Univ. of California Press, 1982).
3. K. C. Kiontke *et al*., *BMC Evol. Biol.* **11**, 339 (2011).
4. M. F. Palopoli *et al*., *Nature* **454**, 1019–1022 (2008).
5. L. R. Garcia, B. LeBoeuf, P. Koo, *Genetics* **175**, 1761–1771 (2007).
6. L. M. Noble *et al*., *Curr. Biol.* **25**, 2730–2737 (2015).
7. J. R. Chasnov, K. L. Chow, *Genetics* **160**, 983–994 (2002).
8. C. Shi, A. M. Runnels, C. T. Murphy, *eLife* **6**, e23493 (2017).
9. J. J. Ting *et al*., *PLOS Biol.* **12**, e1001915 (2014).
10. J. L. Fierst *et al*., *PLOS Genet.* **11**, e1005323 (2015).
11. C. G. Thomas *et al*., *Curr. Biol.* **22**, 2167–2172 (2012).
12. T. T. Hu *et al*., *Nat. Genet.* **43**, 476–481 (2011).
13. K. Kiontke *et al*., *Proc. Natl. Acad. Sci. U.S.A.* **101**, 9003–9008 (2004).
14. M. A. Félix, C. Braendle, A. D. Cutter, *PLOS ONE* **9**, e94723 (2014).
15. G. C. Woodruff, O. Eke, S. E. Baird, M. A. Félix, E. S. Haag, *Genetics* **186**, 997–1012 (2010).
16. A. D. Cutter, *BioEssays* **37**, 983–995 (2015).
17. Y. Bi *et al*., *PLOS Genet.* **11**, e1004993 (2015).
18. R. Li *et al*., *Genome Res.* **26**, 1219–1232 (2016).
19. J. D. Bundus, R. Alaei, A. D. Cutter, *Evolution* **69**, 2005–2017 (2015).
20. See supplementary materials.
21. G. Parra, K. Bradnam, Z. Ning, T. Keane, I. Korf, *Nucleic Acids Res.* **37**, 289–297 (2009).
22. S. I. Wright, N. Nano, J. P. Foxe, V. U. Dar, *Genet. Res.* **90**, 119–128 (2008).
23. A. Coghlan *et al*., *BMC Bioinformatics* **9**, 549 (2008).
24. D. M. Emms, S. Kelly, *Genome Biol.* **16**, 157 (2015).
25. L. D. Wilson *et al*., *BMC Dev. Biol.* **11**, 10 (2011).
26. B. J. Cassone, R. G. Kay, M. P. Daugherty, B. J. White, *G3* **7**, 1127–1136 (2017).
27. C. G. Thomas *et al*., *Genome Res.* **25**, 667–678 (2015).
28. S. Ward, E. Hogan, G. A. Nelson, *Dev. Biol.* **98**, 70–79 (1983).
29. S. Ward, Y. Argon, G. A. Nelson, *J. Cell Biol.* **91**, 26–44 (1981).
30. A. Barrière *et al*., *Genome Res.* **19**, 470–480 (2009).
31. A. D. Stewart, P. C. Phillips, *Genetics* **160**, 975–982 (2002).
32. J. Wang, P. J. Chen, G. J. Wang, L. Keller, *Science* **329**, 293 (2010).
33. T. S. Le *et al*., *Sci. Rep.* **7**, 12819 (2017).
34. D. R. Denver, K. Morris, M. Lynch, W. K. Thomas, *Nature* **430**, 679–682 (2004).
35. M. V. Olson, *Am. J. Hum. Genet.* **64**, 18–23 (1999).
36. A. D. Cutter, R. Jovelin, *BioEssays* **37**, 1169–1173 (2015).
37. J. M. Hansen, D. R. Chavez, G. M. Stanfield, *eLife* **4**, e05423 (2015).
38. E. Tecle, P. Gagneux, *Mol. Reprod. Dev.* **82**, 635–650 (2015).
39. S. Glémin, J. Ronfort, *Evolution* **67**, 225–240 (2013).
40. A. Sicard, M. Lenhard, *Ann. Bot.* **107**, 1433–1443 (2011).
41. J. R. Chasnov, *J. Evol. Biol.* **23**, 539–556 (2010).
42. E. S. Dolgin, B. Charlesworth, S. E. Baird, A. D. Cutter, *Evolution* **61**, 1339–1352 (2007).
43. W. D. Hamilton, *Science* **156**, 477–488 (1967).
44. C. M. Lively, D. G. Lloyd, *Am. Nat.* **135**, 489–500 (1990).
45. E. L. Charnov, *The Theory of Sex Allocation* (Princeton Univ. Press, 1982).

ACKNOWLEDGMENTS

We thank E. Antoniou, P. W. Sternberg, C. T. Brown, the Michigan State University High-Performance Computing Center (supported by USDA grant 2010-65205-20361 and NIFA-NSF grant IOS-0923812), and the UC Berkeley V. J. Coates Genomics Sequencing Laboratory (supported by NIHS10RR029668) for sequencing and computational support. We thank G. Williams and R. H. Waterston for transcriptome data, the *Caenorhabditis* Genomes Project for prepublication access to the genomes of *C. afra* and *C.* sp. 34, Z. Zhao and M. A. Félix for nematode and plasmid reagents, and S. Mount for helpful discussions. Supported by NSF award IOS-1355119 and NIH grant GM079414 (E.S.H.); NIH grant AI111173, Moore Foundation grant 4551, and Cornell University start-up funds (E.M.S.); and NIH grant GM030702 (B.J.M.). B.J.M. is an investigator of the Howard Hughes Medical Institute. Some strains were provided by the CGC, which is funded by the NIH Office of Research Infrastructure Programs (P40 OD010440). Data availability and accession codes: *C. nigoni* genomic and transcriptomic data have been archived as NCBI BioProject accessions PRJNA384657 and PRJNA384658, and the *C. nigoni* genome assembly as DDBJ/ENA/GenBank accession PDUG00000000. Genome assembly, gene prediction, and gene expression data for *C. nigoni*, with supplementary data sets for other species, have been archived at the OSF (*C. nigoni*, https://osf.io/dkbwt and doi:10.17605/osf.io/dkbwt; other species, https://osf.io/b47r8 and doi:10.17605/osf.io/b47r8).

SUPPLEMENTARY MATERIALS

www.sciencemag.org/content/359/6371/55/suppl/DC1
Materials and Methods
Figs. S1 to S9
Tables S1 to S9
Data S1 to S5
References (*46–119*)

13 June 2017; accepted 17 November 2017
10.1126/science.aao0827

REPORT

MATERIALS SCIENCE

Hydraulically amplified self-healing electrostatic actuators with muscle-like performance

E. Acome,[1] S. K. Mitchell,[1] T. G. Morrissey,[1] M. B. Emmett,[1] C. Benjamin,[1] M. King,[1] M. Radakovitz,[1] C. Keplinger[1,2]*

Existing soft actuators have persistent challenges that restrain the potential of soft robotics, highlighting a need for soft transducers that are powerful, high-speed, efficient, and robust. We describe a class of soft actuators, termed hydraulically amplified self-healing electrostatic (HASEL) actuators, which harness a mechanism that couples electrostatic and hydraulic forces to achieve a variety of actuation modes. We introduce prototypical designs of HASEL actuators and demonstrate their robust, muscle-like performance as well as their ability to repeatedly self-heal after dielectric breakdown—all using widely available materials and common fabrication techniques. A soft gripper handling delicate objects and a self-sensing artificial muscle powering a robotic arm illustrate the wide potential of HASEL actuators for next-generation soft robotic devices.

Human-made machines rely on rigid components and excel at repetitive tasks in a structured environment, whereas nature predominantly uses soft materials for creating versatile systems that conform to their environment. This discrepancy in mechanics has inspired the field of soft robotics (*1*–*4*), which promises to transform the way we interact with machines and to enable new technologies for biomedical devices, industrial automation, and other applications (*2*, *5*, *6*). For soft robotics to proliferate, there is a need for an artificial muscle technology that replicates the versatility, performance, and reliability of biological muscle (*2*).

Currently, soft robots predominantly rely on fluidic actuators (*7*), which can be designed to suit a variety of applications (*8*–*10*). However, fluidic actuators require a supply of pressurized gas or liquid, and fluid transport must occur through systems of channels and tubes, limiting speed and efficiency. Thermally activated artificial muscle actuators made from inexpensive polymer fibers can provide large actuation forces and work density, but these are difficult to control and have low efficiency (1.32%) (*11*). Electrically powered muscle-mimetic actuators, such as dielectric elastomer (DE) actuators, offer high actuation strain (>100%) and potentially high efficiency (80%) and are self-sensing (*12*–*14*). However, DE actuators are driven by high electric fields, making them prone to failure from dielectric breakdown and electrical aging (*15*). Fault-tolerant DE actuators have been demonstrated that rely on localized destruction of the electrodes or dielectric to isolate the location of breakdown (*16*, *17*). Dielectric materials made of silicone sponges swollen with silicone oil (*18*) continued operating after dielectric failure but demonstrated actuation strains only below 5%. More important, DE actuators are difficult to scale up to deliver high forces, as large areas of dielectric are required [e.g., in stacked actuators (*13*)], which are much more likely to experience premature electrical failure, following the Weibull distribution for dielectric breakdown (*19*).

Here, we develop a class of high-performance, versatile, muscle-mimetic soft transducers, termed HASEL (hydraulically amplified self-healing electrostatic) actuators. HASEL actuators harness an electrohydraulic mechanism to activate all–soft-matter hydraulic architectures, combining the versatility of soft fluidic actuators with the muscle-like performance and self-sensing abilities of DE actuators. In contrast to soft fluidic actuators, where inefficiencies and losses arise from fluid transport through systems of channels, HASEL actuators generate hydraulic pressure locally via electrostatic forces acting on liquid dielectrics distributed throughout a soft structure. The use of liquid dielectrics in HASEL actuators enables self-healing with immediate recovery of functionality after numerous dielectric breakdown events.

To discuss fundamental physical principles, we describe one design for HASEL actuators, where an elastomeric shell is partially covered by a pair of opposing electrodes and filled with a liquid dielectric (Fig. 1A). Applying voltage induces an electric field through the liquid and elastomeric dielectric. The resulting electrostatic Maxwell stress (*20*) pressurizes and displaces the liquid dielectric from between the electrodes to the surrounding volume. As voltage increases from V_1 to V_2, there is a small increase in actuation strain s. When voltage surpasses a threshold V_2, the increase in electrostatic force starts to exceed the increase in mechanical restoring force, causing the electrodes to abruptly pull together (Fig. 1B)—a characteristic feature of a so-called pull-in or snap-through transition. Pull-in transitions and other nonlinear behaviors are features of soft active systems that offer opportunities to improve actuation response or functionality (*21*) and have been used to amplify response of fluidic (*22*) and DE actuators (*23*). After the pull-in transition (Fig. 1A), actuation strain further increases with voltage (Fig. 1B). For this design, hydraulic pressure causes the soft structure to deform into a toroidal or donut shape (Fig. 1C).

Hydraulic pressure within the elastomeric shell is coupled to Maxwell pressure, $p \propto \varepsilon E^2$, where ε is the dielectric permittivity of the material system and E is the applied electric field (*20*). Because Maxwell pressure is independent of the electrode area, actuation force and strain can be scaled by adjusting the ratio of electrode area to total area of the elastomeric shell. We fabricated two donut HASEL actuators (fig. S1) (*24*) that were identical except for their respective electrode diameters. The donut HASEL actuators were made from polydimethylsiloxane (PDMS; Sylgard 184, Dow Corning) as the elastomeric shell, a vegetable-based transformer oil (Envirotemp FR3, Cargill) as the liquid dielectric, and ionically conductive polyacrylamide (PAM) hydrogels as the electrodes. The actuator with larger electrodes displaced more liquid dielectric, generating a larger strain but a smaller force, because the resulting hydraulic pressure acts over a smaller area (Fig. 1D and fig. S2). Conversely, the actuator with smaller electrodes displaced less liquid dielectric, generating less strain but more force, because the resulting hydraulic pressure acts across a larger area (Fig. 1E). We tested the cycle life of a donut HASEL actuator used in Fig. 1E for more than 1 million cycles while lifting 150 g (actuation stress ~0.75 kPa) at 15% strain and noticed no perceivable loss of performance (fig. S3). We performed a full-cycle analysis of actuator efficiency using force displacement and voltage charge work-conjugate planes (fig. S4) (*24*). Conversion efficiency was 21%, which is comparable to typical experimental values for DE actuators; whereas DE actuators have potentially high efficiencies (80%) (*12*), experimentally measured efficiency ranges from 10 to 30% (*25*–*27*).

The use of liquid dielectrics enables HASEL actuators to self-heal from dielectric breakdown. In contrast to solid dielectrics, which are permanently damaged from breakdown, liquid dielectrics immediately return to an insulating state (fig. S5 and movie S1). This characteristic allowed donut HASEL actuators to self-heal from 50 dielectric breakdown events (Fig. 1F and movie S2). Although breakdown through the liquid produced gas bubbles, which have low breakdown strength, the bubbles had a limited impact on self-healing performance because they were forced away from the region of highest electric field between the

[1]Department of Mechanical Engineering, University of Colorado, Boulder, CO 80309, USA. [2]Materials Science and Engineering Program, University of Colorado, Boulder, CO 80309, USA.
*Corresponding author. Email: christoph.keplinger@colorado.edu

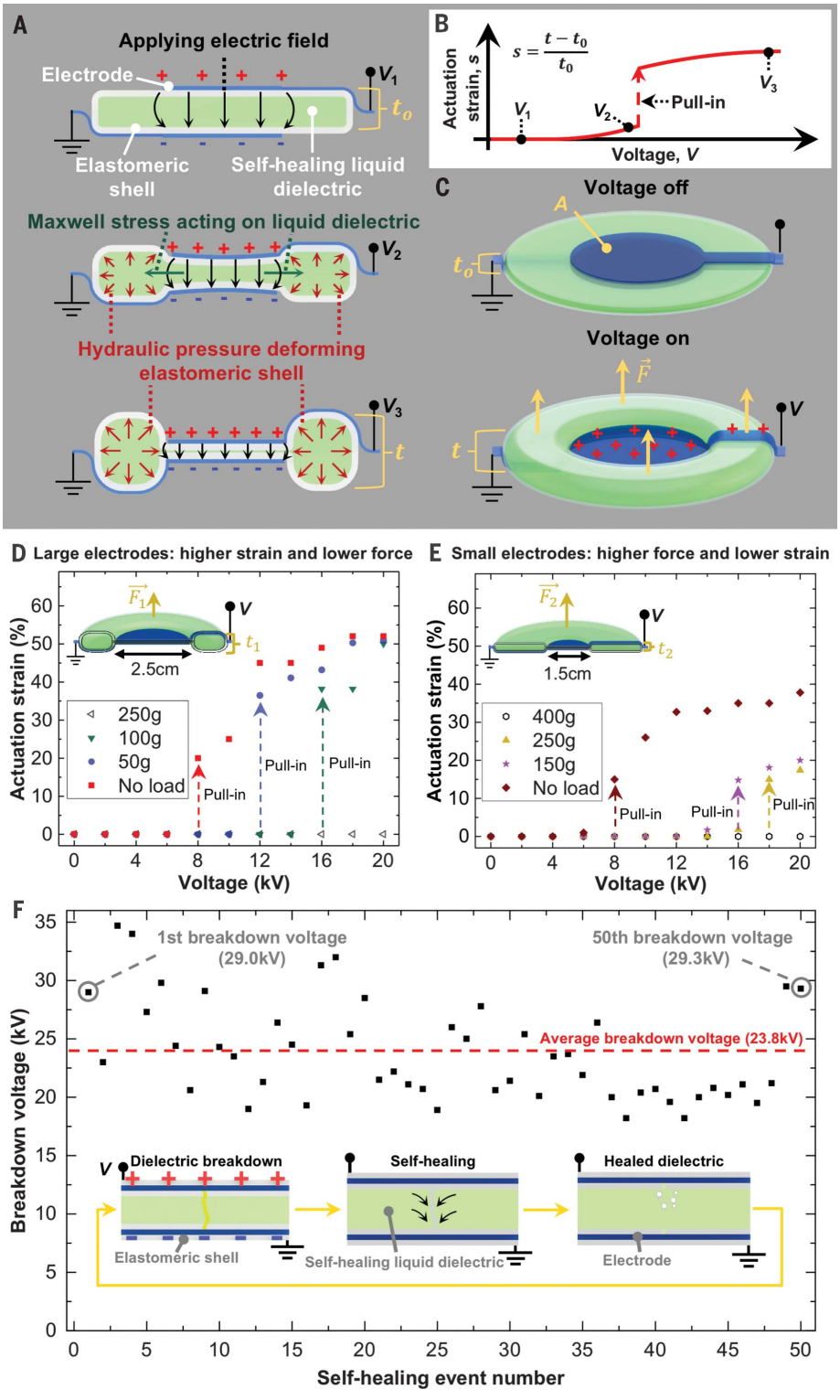

Fig. 1. Basic components and fundamental physical principles of HASEL actuators. (**A**) Schematic of a HASEL actuator shown at three different applied voltages, where $V_1 < V_2 < V_3$. (**B**) Typical actuation response of a HASEL actuator with geometry shown in (A). (**C**) The actuator deforms into a donut shape with application of voltage. This voltage-controlled deformation can be used to apply force F onto an external load. (**D** and **E**) Strain and force of actuation can be tuned by modifying the area of the electrode. The minimum electric field to trigger the pull-in transition was ~2.7 kV/mm; the maximum field applied was ~33 kV/mm. (**F**) The use of a liquid dielectric confers self-healing capabilities to HASEL actuators.

electrodes (movie S2). Dielectric breakdown is a statistical process (*19*), and voltage varied over 50 cycles, with several breakdown voltages exceeding the initial breakdown voltage (including the last one shown; Fig. 1F).

The ability of HASEL actuators to self-heal from electrical damage provides the means to scale up devices to produce a large actuation stroke by stacking multiple actuators (Fig. 2A). A stack of five donut HASEL actuators achieved 37% linear strain, which is comparable to linear strain achieved by biological muscle (*26*) and corresponds to an actuation stroke of 7 mm (Fig. 2B). Hydraulic pressure is generated locally in HASEL actuators, and liquid dielectrics are displaced over short distances, allowing for high-speed actuation. The stacked actuators readily showed large actuation response up to a frequency of 20 Hz (movie S3).

We modified two stacks of donut HASEL actuators to operate as a soft gripper, a common application for soft robotics (*8*, *28*). Actuators within the stacks were constrained on one side to produce a tilting motion (Fig. 2, C to G, and fig. S6). When a DC voltage was applied to the stacked HASEL actuators, the device grasped delicate objects such as a raspberry (Fig. 2, C to E, and movie S4) and a raw egg (Fig. 2, F and G, and movie S4).

The geometry of HASEL actuators, like that of soft fluidic actuators, can be adapted to react with a variety of different actuation modes. For planar HASEL actuators, the electric field is applied over almost the entire region of the actuator containing liquid dielectric. Planar HASEL actuators react to application of voltage with in-plane expansion, resembling a commonly used mode of operation for DE actuators, where an elastomeric dielectric contracts in thickness and expands in area under an applied electric field. To compare the actuation response of HASEL and DE actuators, we measured area strain as a function of voltage for two circular actuators with the same total dielectric thickness, t (Fig. 3A). Both were fabricated from Ecoflex 00-30 (Smooth-on); however, one-third of the thickness of the HASEL actuator was liquid dielectric, t_{liq} (*24*). At 11 kV, the area strain of the HASEL actuator exceeded the area strain of the DE actuator by a factor of ~4 (Fig. 3A and fig. S7). The higher actuation strain is attributed to the layer of liquid dielectric, which effectively reduces the modulus of the HASEL actuator while maintaining the high dielectric strength of the layered dielectric structure.

Linear actuation can be achieved with planar HASEL actuators by implementing a fixed prestretch in one planar direction and applying a load in the perpendicular planar direction (*29*). This lateral prestretch causes a preferential expansion in the direction of the load when voltage is applied (Fig. 3B). We fabricated single- and two-unit planar HASEL actuators, where a unit is defined as a discrete region of liquid dielectric (figs. S8 and S9) (*24*). Linear actuators were oriented vertically with the load applied in the direction of gravity, but they can be operated in any orientation as long as the liquid dielectric regions are sufficiently small to limit uneven distribution of liquid dielectric (fig. S10). A single-

unit planar HASEL actuator (Fig. 3C) was activated by increasing DC voltage in discrete steps and achieved a maximum of 79% linear actuation strain under a load of 250 g (actuation stress ~32 kPa), exceeding typical values of strain observed for biological muscle (*26*). Soft active devices such as HASEL actuators are elastic systems that can be used near resonances to improve performance and efficiency (*30*)—a characteristic that could find use in legged robots that move over long distances. We found that for planar HASEL actuators, linear actuation is amplified near a resonant frequency; a single-unit actuator achieved 107% linear strain under a load of 250 g (actuation stress ~32 kPa) and a two-unit actuator achieved 124% linear strain under a load of 700 g (actuation stress ~114 kPa) (fig. S11 and movie S5). Peak specific power during contraction of the two-unit actuator was 614 W/kg; specific work during contraction was 70 J/kg (fig. S12) (*24*). The measured peak specific power is double that of natural muscle and comparable to values for silicone DE actuators (*26*). Thermally activated coiled polymer fiber actuators (49.9 kW/kg) (*11*) and shape-memory alloys (50 kW/kg) (*11*, *26*) have higher peak specific power; however, their efficiency is low (<2%) (*11*, *26*) and thermomechanical actuators are more difficult to control than electromechanical actuators. Cycle life at high mechanical output power was demonstrated with a single-unit HASEL actuator, which provided 358 W/kg average (586 W/kg peak) specific power during contraction until mechanical rupture occurred at 158,061 cycles (fig. S12D). A single unit actuator was able to operate under a large applied load of 1.5 kg [corresponding to a stress of 0.3 MPa, near the maximum value for mammalian skeletal muscle (*26*)] and still achieved 16% strain (fig. S13).

Planar HASEL actuators were also able to self-heal from dielectric breakdown for at least 50 cycles, although, relative to donut HASEL actuators, gas bubbles were more easily trapped between the electrodes (fig. S14). Nonetheless, the ability of planar HASEL actuators to tolerate high electric fields applied over large areas enabled us to scale up actuation force by combining six planar HASEL actuators in parallel to lift a gallon of water (~4 kg, which corresponds to ~120 kPa) at 69% linear actuation strain (Fig. 3D and movie S6). The combination of high actuation strain and the ability to scale up for large actuation force is critical for developing high-performance soft robotic actuators for human scale devices.

Soft robotic actuators require feedback to sense and regulate position. The electrodes of a HASEL actuator form a hyperelastic capacitor with capacitance C, which is directly linked to geometry and actuation strain via $C \propto A/d$, where A is electrode area and d is the distance between electrodes. Consequently, HASEL actuators are able to self-sense deformation attributable to external forces or applied voltage. Because HASEL actuators are equivalent resistor-capacitor circuits, capacitance can be measured transiently by applying a low-amplitude AC voltage (*14*), then analyzing the phase and amplitude of voltage and current signals (fig. S15) (*24*). The low-amplitude AC signal can be superimposed onto a high-amplitude actuation voltage signal, so only one set of electrical connections is required for both actuation and sensing. To demonstrate self-sensing actuation, we powered a robotic arm with two planar HASEL actuators combined in parallel and simultaneously measured capacitance (Fig. 4, fig. S16, and movies S7 and S8). Here, we only measured capacitance and did not attempt to control position of the robotic arm; however, capacitive self-sensing has been used for closed-loop control of DE actuators (*31*).

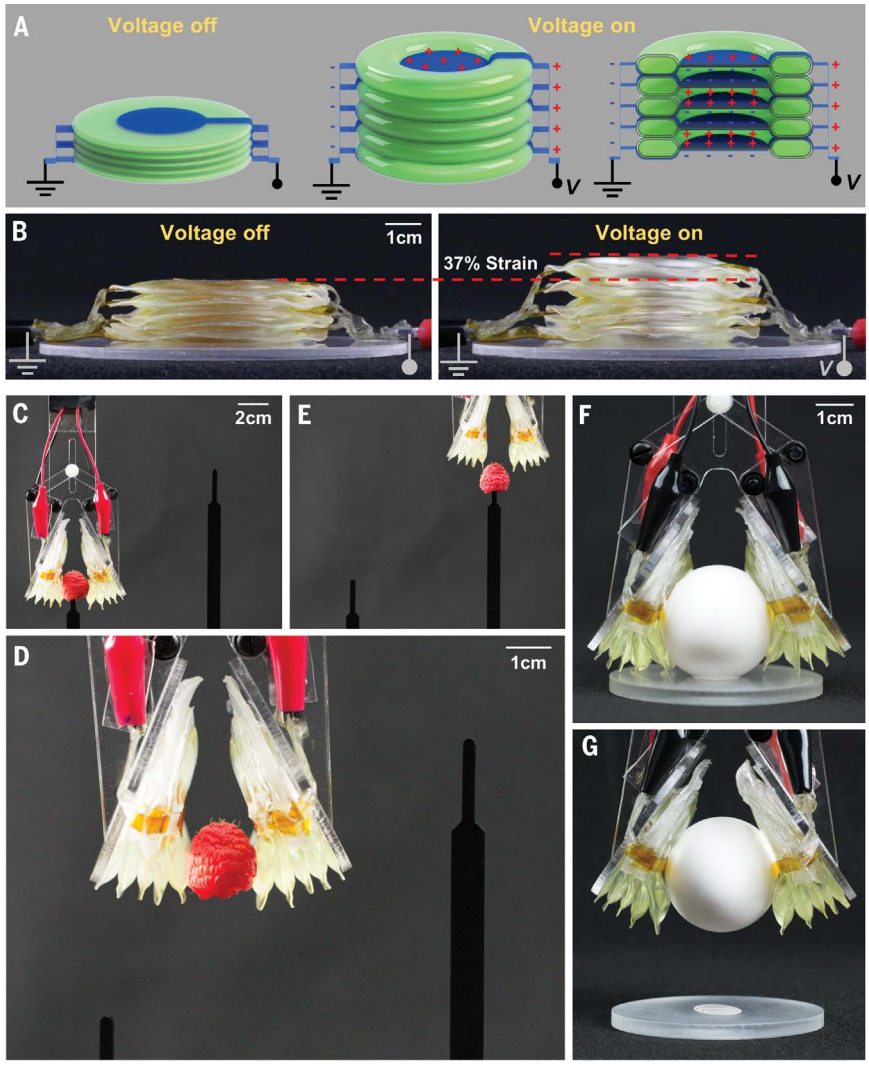

Fig. 2. Stacks of donut HASEL actuators operating as linear actuators and soft grippers. (**A**) Schematic depicting a stack of five donut HASEL actuators oriented such that adjacent electrodes are at the same electrical potential (cross-section view). (**B**) Demonstration of linear actuation with stacked-donut HASEL actuators. (**C** to **G**) A soft gripper fabricated from two modified stacks of donut HASEL actuators handled fragile objects such as a raspberry [(C) to (E)] and a raw egg [(F) and (G)].

HASEL actuators rely on all–soft-matter hydraulic architectures and local generation of hydraulic pressure via electrostatic forces acting on self-healing liquid dielectrics—a recipe that combines the strengths of soft fluidic and electrostatic actuators while addressing important problems of each. The use of hydraulic principles in HASEL actuators results in the capability to scale actuation force and strain—a feature also used in other device classes such as microhydraulic systems, which are constructed from thin films and rigid substrates (*32*), and in hydrostatically coupled DE actuators (*33*), where electric fields are applied across elastomeric layers, which do not self-heal after dielectric breakdown. We have demonstrated versatile, robust, muscle-like performance of HASEL actuators made from one set of inexpensive, widely available materials and using only basic fabrication techniques. However, the thick elastomer shells (>1 mm) used in this work required high voltages to reach electric fields large enough for actuation. This need for high voltage is an existing limitation that may be addressed by using dielectric layers with higher permittivity and by using advanced fabrication techniques to produce high-resolution dielectric structures with feature sizes on the order of 10 μm. With a plethora of geometries, materials, and advanced

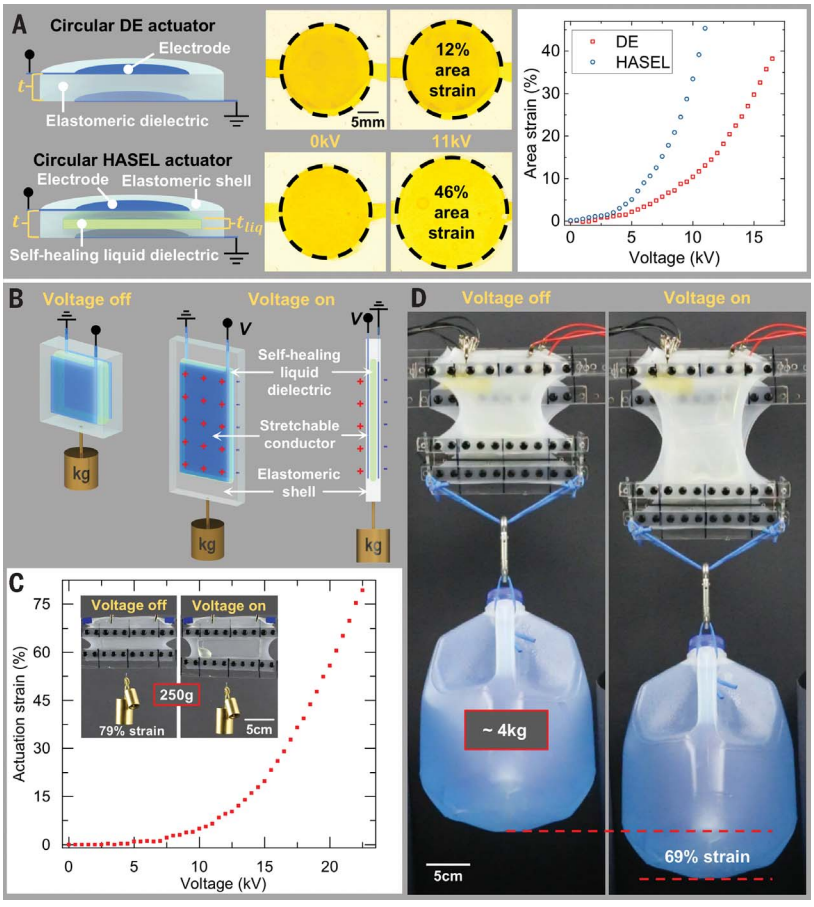

Fig. 3. Design and performance of planar HASEL actuators. (**A**) For a given voltage, a circular planar HASEL actuator achieves larger area strain in comparison to a circular DE actuator. (**B**) Schematic of a planar HASEL actuator that functions as a linear actuator. The actuator is prestretched laterally and a load is applied in the direction perpendicular to the prestretch. (**C**) Demonstration of linear actuation with a single-unit planar HASEL actuator. (**D**) HASEL actuators can be readily scaled up to exert large forces.

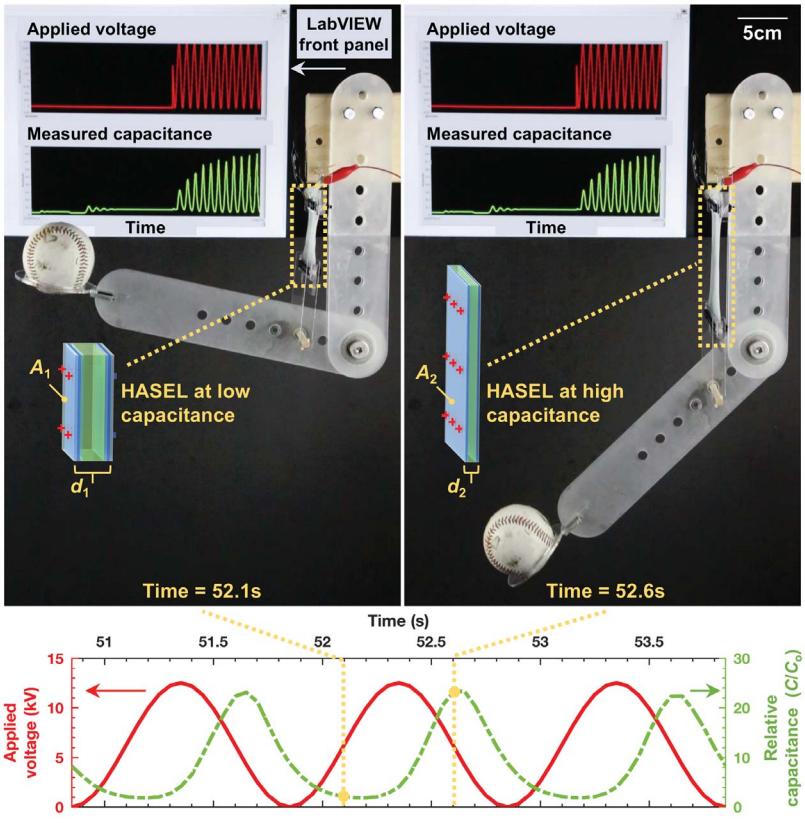

Fig. 4. A self-sensing planar HASEL actuator powering a robotic arm. HASEL actuators simultaneously serve as strain sensors; measured capacitance is low when the arm is fully flexed (left; screenshot of movie S7 at 52.1 s) and capacitance is high when the arm is extended (right; at 52.6 s). The bottom plot shows details of the applied voltage signal (red) and measured relative capacitance (green, dashed), C/C_o, where C is measured capacitance and C_o is the minimum value for capacitance. Voltage and capacitance are ~90° out of phase, which is typical for a driven damped oscillator.

fabrication strategies still unexplored, HASEL actuators offer a new platform for research and development of muscle-mimetic actuators with wide-ranging applications.

REFERENCES AND NOTES

1. S. Kim, C. Laschi, B. Trimmer, *Trends Biotechnol.* **31**, 287–294 (2013).
2. D. Trivedi, C. D. Rahn, W. M. Kier, I. D. Walker, *Appl. Bionics Biomech.* **5**, 99–117 (2008).
3. D. Rus, M. T. Tolley, *Nature* **521**, 467–475 (2015).
4. B. Mazzolai, L. Margheri, M. Cianchetti, P. Dario, C. Laschi, *Bioinspir. Biomim.* **7**, 025005 (2012).
5. S. Bauer *et al*., *Adv. Mater.* **26**, 149–161 (2014).
6. J.-Y. Sun, C. Keplinger, G. M. Whitesides, Z. Suo, *Adv. Mater.* **26**, 7608–7614 (2014).
7. B. Trimmer, *Soft Robot.* **4**, 1–2 (2017).
8. F. Ilievski, A. D. Mazzeo, R. F. Shepherd, X. Chen, G. M. Whitesides, *Angew. Chem. Int. Ed.* **50**, 1890–1895 (2011).
9. P. Polygerinos *et al*., *Adv. Eng. Mater.* **19**, 1700016 (2017).
10. R. F. Shepherd *et al*., *Proc. Natl. Acad. Sci. U.S.A.* **108**, 20400–20403 (2011).
11. C. S. Haines *et al*., *Science* **343**, 868–872 (2014).
12. R. Pelrine, R. Kornbluh, Q. Pei, J. Joseph, *Science* **287**, 836–839 (2000).
13. G. Kovacs, L. Düring, S. Michel, G. Terrasi, *Sens. Actuators Phys.* **155**, 299–307 (2009).
14. C. Keplinger, M. Kaltenbrunner, N. Arnold, S. Bauer, *Appl. Phys. Lett.* **92**, 192903 (2008).
15. P. Brochu, Q. Pei, *Macromol. Rapid Commun.* **31**, 10–36 (2010).
16. W. Yuan *et al*., *Adv. Mater.* **20**, 621–625 (2008).
17. S. J. Dünki, Y. S. Ko, F. A. Nüesch, D. M. Opris, *Adv. Funct. Mater.* **25**, 2467–2475 (2015).
18. S. Hunt, T. G. McKay, I. A. Anderson, *Appl. Phys. Lett.* **104**, 113701 (2014).
19. E. Y. Wu, R. P. Vollertsen, *IEEE Trans. Electron Dev.* **49**, 2131–2140 (2002).
20. Z. Suo, *Acta Mech. Solida Sin.* **23**, 549–578 (2010).
21. X. Zhao, Q. Wang, *Appl. Phys. Rev.* **1**, 021304 (2014).
22. J. T. B. Overvelde, T. Kloek, J. J. A. D'haen, K. Bertoldi, *Proc. Natl. Acad. Sci. U.S.A.* **112**, 10863–10868 (2015).
23. C. Keplinger, T. Li, R. Baumgartner, Z. Suo, S. Bauer, *Soft Matter* **8**, 285–288 (2012).
24. See supplementary materials.
25. F. Carpi, P. Chiarelli, A. Mazzoldi, D. De Rossi, *Sens. Actuators Phys.* **107**, 85–95 (2003).
26. J. D. W. Madden *et al*., *IEEE J. Oceanic Eng.* **29**, 706–728 (2004).
27. J.-S. Plante, S. Dubowsky, *Sens. Actuators Phys.* **137**, 96–109 (2007).
28. S. Song, D.-M. Drotlef, C. Majidi, M. Sitti, *Proc. Natl. Acad. Sci. U.S.A.* **114**, E4344–E4353 (2017).
29. S. J. A. Koh *et al*., *J. Mech. Phys. Solids* **105**, 81–94 (2017).
30. K. Zimmermann, I. Zeidis, C. Behn, in *Mechanics of Terrestrial Locomotion* (Springer, 2009), pp. 125–159.
31. S. Rosset *et al*., *Smart Mater. Struct.* **22**, 104018 (2013).
32. M. M. Sadeghi, H. S. Kim, R. L. B. Peterson, K. Najafi, *J. Microelectromech. Syst.* **25**, 557–569 (2016).
33. F. Carpi, G. Frediani, D. De Rossi, *IEEE/ASME Trans. Mechatron.* **15**, 308–315 (2010).

ACKNOWLEDGMENTS

This work was supported by startup funds from the University of Colorado, Boulder. M.B.E, M.K., and M.R. received financial support from the Undergraduate Research Opportunities Program at the University of Colorado, Boulder. E.A., S.K.M., M.B.E., and C.K. are listed as inventors on a provisional patent application (U.S. 62/474,814) submitted by the University of Colorado, Boulder, that covers fundamental principles and various designs of HASEL transducers.

SUPPLEMENTARY MATERIALS

www.sciencemag.org/content/359/6371/61/suppl/DC1
Materials and Methods
Figs. S1 to S16
References (*34*, *35*)
Movies S1 to S8

8 August 2017; resubmitted 28 September 2017
Accepted 4 December 2017
10.1126/science.aao6139

Cite as: J.-E. Wahlund *et al.*, *Science* 10.1126/science.aao4134 (2017).

In situ measurements of Saturn's ionosphere show that it is dynamic and interacts with the rings

J.-E. Wahlund,[1]* M. W. Morooka,[1] L. Z. Hadid,[1] A. M. Persoon,[2] W. M. Farrell,[3] D. A. Gurnett,[2] G. Hospodarsky,[2] W. S. Kurth,[2] S.-Y. Ye,[2] D. J. Andrews,[1] N. J. T. Edberg,[1] A. I. Eriksson,[1] E. Vigren[1]

[1]Swedish Institute of Space Physics, Box 537, SE-751 21 Uppsala, Sweden. [2]Department of Physics and Astronomy, University of Iowa, Iowa City, IA 52242, USA. [3]Solar System Exploration Division, NASA Goddard Space Flight Center, Greenbelt, MD, USA.

*Corresponding author. Email: jan-erik.wahlund@irfu.se

The ionized upper layer of Saturn's atmosphere, its ionosphere, provides a closure of currents mediated by the magnetic field to other electrically charged regions (e.g., rings) and hosts ion – molecule chemistry. In 2017, the Cassini spacecraft passed inside the planet's rings, allowing in situ measurements of the ionosphere. The Radio and Plasma Wave Science (RPWS) instrument detected a cold, dense and dynamic ionosphere at Saturn that interacts with the rings. Plasma densities reached up to 1000 cm^{-3} and electron temperatures were below 1160 K near closest approach. The density varied between orbits by up to 2 orders of magnitude. Saturn's A- and B-rings cast a shadow on the planet that reduced ionization in the upper atmosphere, causing a North-South asymmetry.

The gas giant planet Saturn is composed primarily of hydrogen and helium. The upper tenuous parts of its atmosphere are partially ionized (producing ions and electrons) foremost by the solar extreme ultraviolet (EUV) radiation, but also by energetic particle impacts originating from the planet's magnetosphere and cosmic rays. The result is an electrically charged layer, the ionosphere, situated approximately between 300 km to 5000 km altitude (*1*). By convention, the reference altitude of 0 km is at a pressure of 1 bar and is set to a distance of 60268 km from the center of Saturn. So far three methods of remote sensing observations have been used to infer the properties of Saturn's ionosphere: radio occultation (*2–5*), radio emission from Saturn's electrostatic discharges (*6*, *7*) and mm-band observations of protonated molecular hydrogen (H_3^+) (*8*). These measurement methods do not reveal small-scale variations (with scale sizes below 1000 km), only providing average constraints on the processes occurring in Saturn's ionosphere. In addition, the first two of those methods only derive the electron density which, in the presence of abundant organic or water cluster ions (positive and negatively charged), does not give a representative picture of the true ionospheric densities (*9*, *10*). Nevertheless, the radio occultation data set reveals a clear decrease in the plasma number densities toward lower latitudes and somewhat larger densities toward local dusk (*2–5*).

We present in situ measurements of Saturn's topside ionosphere from the Cassini spacecraft. The spacecraft first encountered the ionosphere around 09:00 UT on 2017 April 26 (Fig. 1), and continued to do so every ≈6.5 days during the subsequent orbits. Data from the first 11 orbits are considered in this paper. The closest approach during the first encounter occurred at an altitude of 2800 km, and varied from 2600 – 4000 km during the subsequent 10 crossings. Two types of data were collected using the Radio and Plasma Wave Science (RPWS) instrument package: Langmuir probe measurements and observations of whistler mode emissions, from which the electron plasma frequency (f_{pe}) is determined (*11*). Above 1500 km altitude, the hydrogen ions (H^+ and H_3^+) are expected to be the dominant ionospheric species, while methane and other heavier species become important for the ionospheric chemistry below this altitude (*12*). All the crossings we present occurred between 11-14 hours Saturn local time (LT, see also table S1).

Figure 2 displays the altitude profiles of the electron and ion number densities (Panel A) and the electron temperature (Panel B) derived from the RPWS measurements during the first Cassini ring/ionosphere crossing on 2017 April 26. By comparison with Fig. 1, it can be seen that the altitude profiles in Fig. 2 really are convolutions of latitude and altitude. During this initial flyby of the ionosphere the scale height varied between 1000 – 1500 km. The combination of a dense plasma (reaching 1000 cm^{-3} near closest approach) with a decreasing electron temperature (to below 0.1 eV or 1160 K) on approaching the planet indicate that the cold and dense ionosphere of Saturn is detected. Theoretical ionosphere modeling results indicate that electron temperatures near noon at 3000 km altitude could reach 500 K (*12*). However, the measured electron temperature data presented here is variable with altitudes up to 7000 km contrary to the theoretical predictions.

From the inbound ion density measurements in Fig. 2A, it is concluded that Saturn's ionosphere is dominated by H^+

ions during this flyby. This is a conclusion that holds in most of the data from all the 11 flybys. One exception is the flyby on 2017 June 4 (orbit 277, Fig. 3), where RPWS detected the signature of a heavier dominant ion species (>18 amu) near the equator, which is also related to differences in ion and electron densities indicative of negatively charged nm-sized grains or cluster ions being present. Orbit 277 is also one of the crossings closest to the D-ring (*13*), and the most distant of the orbit crossings with closest approach near 4000 km altitude. We interpret this observation, indicative of nm-sized grains and/or heavy ions near the equator, as a detection of ionized material from the nearby D-ring.

The rings cast shadows on Saturn. Based on data from the first 11 flybys, the A- and most of the B-ring must be opaque to solar EUV as very little plasma is detected in the regions within the geometric shadows cast by these rings (Fig. 2A and figs. S2 and S3). The drop-out of ionization corresponding to the shadow from the middle of the B-ring near 1.7 R_S (Fig. 1) is at a location where there are SOI (Saturn Orbit Injection) observations of a B-ring source of whistler mode emissions indicative of field-aligned currents (*14*) and a related plasma cavity (*15*). A plasma sink near the rings would lead to enhanced diffusion at magnetically connected higher latitudes (>35°), suppressing the plasma density at that point in the ionosphere. The Cassini division is somewhat less opaque to EUV, while no effects can be detected for the cases of the D- and C-rings (which thus must be EUV transparent). The enhanced ionization degree of the ionosphere illuminated by light passing through the Cassini division, compared to the opaque A- and B-rings (Fig. 2A), is clearly detectable in all 11 flybys (figs. S2 and S3). The low levels of ionospheric plasma observed by Cassini/RPWS in the shadowed regions (for latitudes between –20 and –40 degrees), indicate that no major transport occurs of plasma from nearby regions. The lack of measured emitted photoelectrons as detected by the Langmuir probe in this region confirms the low level of photoionization (figs. S2 and S3). Theoretical predictions of reduced ionization due to the ring shadows may explain why radio emissions from Saturn's electrostatic discharges leak out from lower atmospheric layers past the ionosphere peak (*16*).

The observations put constraints on possible transport of charged water products from the rings along conjugate magnetic field lines (also called ring rain), as indicated from remote infrared H_3^+ emissions (*8*, *17*). A steady influx of water ions would react quickly with atmospheric hydrogen, recombining to neutral species, thereby removing the ionized component much faster than if only H^+ recombines with electrons (*18*). An inflow of large quantities of heavy ions from the C-ring along connected magnetic flux tubes is not confirmed by the RPWS observations in the shadowed ionosphere region (Fig. 4). The question of ring rain at higher latitudes (>35°), on the other hand, is not constrained by the present data.

Figure 4 shows the large variability and fine structure of Saturn's ionosphere. Maximum electron densities are found in a wide range from 50 – 1300 cm^{-3}, which cannot be explained by a simple scale height model of a quiet ionosphere in photochemical equilibrium. One possibility is that a ring rain like mechanism operates here, where variable amounts of water group (or molecular) ions with origin from the D-ring material (near the equator or along connecting magnetic flux tubes) cause sporadic electron depletions. Electron depletions exist within ±10° latitude during orbits 272, 273, 275, 277, 278, 280 and 281 (Fig. 4). These suppressed electron density dips vary in the range 50 – 200 cm^{-3}. The equator crossings for Orbits 276 and 277 occurred furthest away from the planet around 4000 km altitude, which we expect to be inside the D-ring. An equatorial depletion of 50 cm^{-3} is detected during orbit 277, where the Langmuir probe also shows the presence of negatively charged cluster ions or nm-sized grains (Fig. 3). Orbit 276 does not show a clear depletion signature. It is however difficult to explain the full dynamic range of almost two orders of magnitude between each flyby with only this chemical process alone. There is no continuous evolution of plasma density from the first orbit to the last, and large variations can occur between adjacent orbits (e.g., orbits 277 and 278, Fig. 4).

The time constants for transport compete effectively with photo-chemistry and thus the plasmas sampled depend strongly on dynamics. We therefore suggest that an electrodynamic interaction occurs between the ionosphere and the electrically charged D ring via the strong magnetic field of Saturn. This would drive ionospheric ion outflows along magnetic flux tubes leading to plasma structuring, as is readily observed along magnetic flux tubes above the aurora at Earth (*19*). The strong magnetic field of Saturn makes the rate of plasma-neutral collisions much smaller than the gyration frequency along the Cassini spacecraft trajectory; the ionospheric dynamo region, with coupling to neutral winds, is at far lower altitude (*20*). The electrodynamics may instead be driven by the charged material in the D-ring (in Keplerian orbit) moving relative to the ionosphere (rotating with the planet), and a significant cross-magnetic field current density may arise from the $\Delta\mathbf{V}\mathrm{x}\mathbf{B}$ term (where $\Delta\mathbf{V}$ is the relative speed of the two components and $\mathbf{B}$ the magnetic field of Saturn). These ring currents then close via field-aligned currents to the conductive ionosphere below, with associated magnetic field-aligned ion flows along these flux tubes. Other possibilities for the variation in ionosphere dynamics involve strong longitudinal wind variations, coupled with variable EUV/X ionization levels, as is readily observed in the Earth's ionosphere at ±20° latitude (*21*).

REFERENCES AND NOTES

1. J. Moses, S. F. Bass, The effects of external material on the chemistry and structure of Saturn's ionosphere. *J. Geophys. Res.* **105**, 7013–7052 (2000). doi:10.1029/1999JE001172
2. A. J. Kliore, I. R. Patel, G. F. Lindal, D. N. Sweetnam, H. B. Hotz, J. H. Waite Jr., T. R.

McDonough, Structure of the ionosphere and atmosphere of Saturn from Pioneer 11 Saturn radio occultation. *J. Geophys. Res.* **85**, 5857 (1980). doi:10.1029/JA085iA11p05857
3. G. F. Lindal, D. N. Sweetnam, V. R. Eshleman, The atmosphere of Saturn – an analysis of the Voyager radio occultation measurements. *Astron. J.* **90**, 1136 (1985). doi:10.1086/113820
4. A. F. Nagy, A. J. Kliore, E. Marouf, R. French, M. Flasar, N. J. Rappaport, A. Anabtawi, S. W. Asmar, D. Johnston, E. Barbinis, G. Goltz, D. Fleischman, First results from the ionospheric radio occultations of Saturn by the Cassini spacecraft. *J. Geophys. Res.* **111**, A06310 (2006). doi:10.1029/2005JA011519
5. A. J. Kliore, A. F. Nagy, E. A. Marouf, A. Anabtawi, E. Barbinis, D. U. Fleischman, D. S. Kahan, Midlatitude and high-latitude electron density profiles in the ionosphere of Saturn obtained by Cassini radio occultation observations. *J. Geophys. Res.* **114**, A04315 (2009). doi:10.1029/2008JA013900
6. M. L. Kaiser, M. D. Desch, J. E. P. Connerney, Saturn's ionosphere: Inferred electron densities. *J. Geophys. Res.* **89**, 2371 (1984). doi:10.1029/JA089iA04p02371
7. G. Fischer, D. A. Gurnett, P. Zarka, L. Moore, U. A. Dyudina, Peak electron densities in Saturn's ionosphere derived from the low-frequency cutoff of Saturn lightning. *J. Geophys. Res.* **116**, A04315 (2011). doi:10.1029/2010JA016187
8. J. O'Donoghue, T. S. Stallard, H. Melin, G. H. Jones, S. W. H. Cowley, S. Miller, K. H. Baines, J. S. D. Blake, The domination of Saturn's low-latitude ionosphere by ring 'rain'. *Nature* **496**, 193–195 (2013). doi:10.1038/nature12049 Medline
9. M. W. Morooka, J.-E. Wahlund, A. I. Eriksson, W. M. Farrell, D. A. Gurnett, W. S. Kurth, A. M. Persoon, M. Shafiq, M. André, M. K. G. Holmberg, Dusty plasma in the vicinity of Enceladus. *J. Geophys. Res.* **116**, A12221 (2011). doi:10.1029/2011JA017038
10. O. Shebanits, J.-E. Wahlund, K. Mandt, K. Ågren, N. J. T. Edberg, J. H. Waite Jr., Negative ion densities in the ionosphere of Titan – Cassini RPWS/LP results. *Planet. Space Sci.* **84**, 153–162 (2013). doi:10.1016/j.pss.2013.05.021
11. Materials and methods are available as supplementary materials.
12. L. Moore, M. Galand, I. Müller-Wodarg, R. Yelle, M. Mendillo, Plasma temperatures in Saturn's ionosphere. *J. Geophys. Res.* **113**, A10306 (2008). doi:10.1029/2008JA013373
13. M. M. Hedman, M. R. Showalter, A new pattern in Saturn's D-ring created in late 2011. *Icarus* **279**, 155–165 (2016). doi:10.1016/j.icarus.2015.09.017
14. L. Xin, D. A. Gurnett, O. Santolik, W. S. Kurth, G. B. Hospodarsky, Whistler-mode auroral hiss emissions observed near Saturn's B ring. *J. Geophys. Res.* **111**, (2006). 10.1029/2005JA011432
15. W. M. Farrell, W. S. Kurth, D. A. Gurnett, A. M. Persoon, R. J. MacDowall, Saturn's rings and associated ring plasma cavity: Evidence for slow ring erosion. *Icarus* **292**, 48–53 (2017). doi:10.1016/j.icarus.2017.03.022
16. M. Mendillo, L. Moore, J. Clarke, I. Müller-Wodarg, W. S. Kurth, M. L. Kaiser, Effects of ring shadowing on the detection of electrostatic discharges at Saturn. *Geophys. Res. Lett.* **32**, (2004). 10.1029/2004GL021934
17. T. G. Northrop, J. R. Hill, Stability of negatively charged grains in Saturn's ring plane. *J. Geophys. Res.* **87**, 6045 (1982). doi:10.1029/JA087iA08p06045
18. L. Moore, A. F. Nagy, A. J. Kliore, I. Müller-Wodarg, J. D. Richardson, M. Mendillo, Cassini radio occultations of Saturn's ionosphere: Model comparisons using a constant water flux. *Geophys. Res. Lett.* **33**, L22202 (2006). doi:10.1029/2006GL027375
19. J.-E. Wahlund, H. J. Opgenoorth, I. Häggström, K.-J. Winser, G. O. L. Jones, EISCAT observations of topside ionospheric ion outflows during auroral activity: Revisited. *J. Geophys. Res.* **97**, 3019–3037 (1992). doi:10.1029/91JA02438
20. M. Galand, L. Moore, I. Mueller-Wodarg, M. Mendillo, S. Miller, Response of Saturn's auroral ionosphere to electron precipitation: Electron density, electron temperature, and electrical conductivity. *J. Geophys. Res.* **116**, 3019–3037 (2011). doi:10.1029/2010JA016412
21. H. Liu, C. Stolle, M. Förster, S. Watanabe, Solar activity dependence of the electron density in the equatorial anomaly region observed by CHAMP. *J. Geophys. Res.* **112**, A11311 (2007). doi:10.1029/2007JA012616
22. J.-E. Wahlund, M. André, A. I. E. Eriksson, M. Lundberg, M. W. Morooka, M. Shafiq, T. F. Averkamp, D. A. Gurnett, G. B. Hospodarsky, W. S. Kurth, K. S. Jacobsen, A. Pedersen, W. Farrell, S. Ratynskaia, N. Piskunov, Detection of dusty plasma near the E-ring of Saturn. *Planet. Space Sci.* **57**, 1795–1806 (2009). doi:10.1016/j.pss.2009.03.011

ACKNOWLEDGMENTS

The Swedish National Space Board (SNSB) supports the RPWS/LP instrument on board Cassini. W. M. Farrell gratefully acknowledges the Cassini project for internal NASA support. D. A. Gurnett, G. Hospodarsky, W. S. Kurth, A. M. Persoon, and S.-Y. Ye were supported by NASA through Contract 1415150 with the Jet Propulsion Laboratory. All Cassini RPWS data are archived in the Planetary Data System (PDS) Planetary Plasma Interaction (PPI) node at https://pds-ppi.igpp.ucla.edu/search/?t=Saturn&i=RPWS on a pre-arranged schedule.

SUPPLEMENTARY MATERIALS

www.sciencemag.org/cgi/content/full/science.aao4134/DC1
Materials and Methods
Figs. S1 to S4
Table S1
Reference (*22*)

18 July 2017; accepted 27 November 2017
Published online 11 December 2017
10.1126/science.aao4134

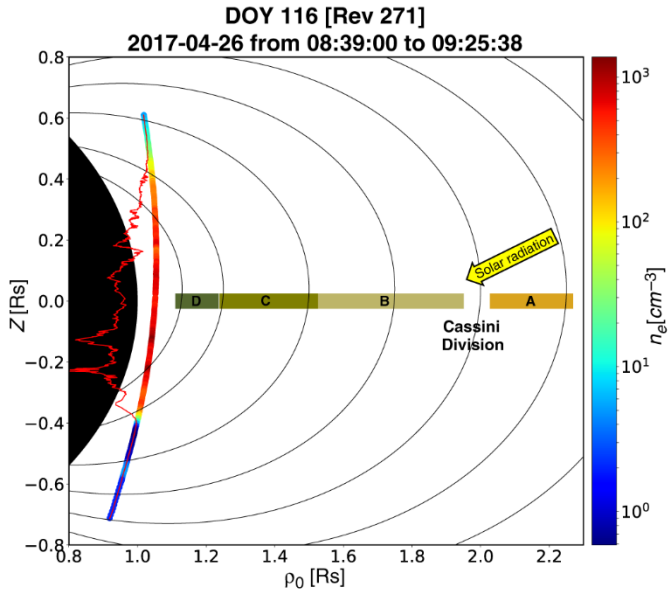

Fig. 1. Electron density (n_e, colored band) measured by the Cassini Langmuir probe on 2017 April 26. The spacecraft crossed through the gap between the planet Saturn (solid black) and its rings (denoted D, C, B, Cassini Division, A), passing from North to South. The color code signifies the measured electron number density, which is also shown as a red line (shown in linear scale, the density increases toward the left, with a maximum density of 1300 cm^{-3}). Four dominant electron density enhancements are mapped along Saturn's magnetic field to, or inside, the inner edge of the D-ring at the equator. The solar elevation angle was 26.7° during the event, and the shadows of the A ring and part of the B ring result in decreased ionization in the South (see text). [DOY = Day of Year, Rev = Orbit, R_s = Saturn Radius, ρ_0 = distance from Saturn.]

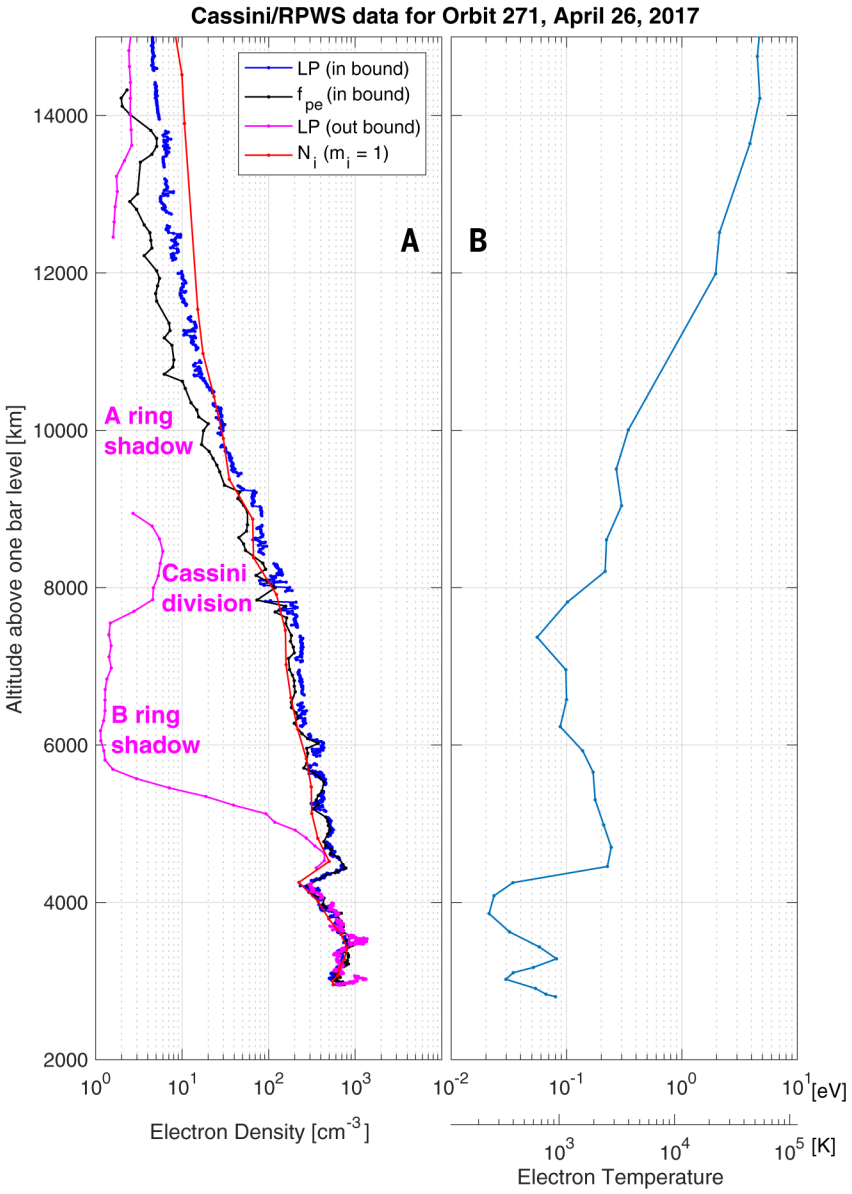

Fig. 2. Cassini/RPWS altitude profiles of the ionosphere number density (A) and inbound electron temperature (B) during the crossing on 2017 April 26. Two independent methods for estimating the inbound electron density (blue and black) gave almost identical results (see article text), confirming their validity. The Langmuir probe (LP) ion density (N_i, assuming H^+) also produces values in agreement with the estimated electron densities, confirming that hydrogen ions dominated during this flyby. The lower LP electron densities over the outbound sector (magenta) indicate that much of the A- and part of the B-ring are opaque to ionizing extreme ultraviolet radiation. No whistler emission mode cut-off data (black) exist for the outbound portion.

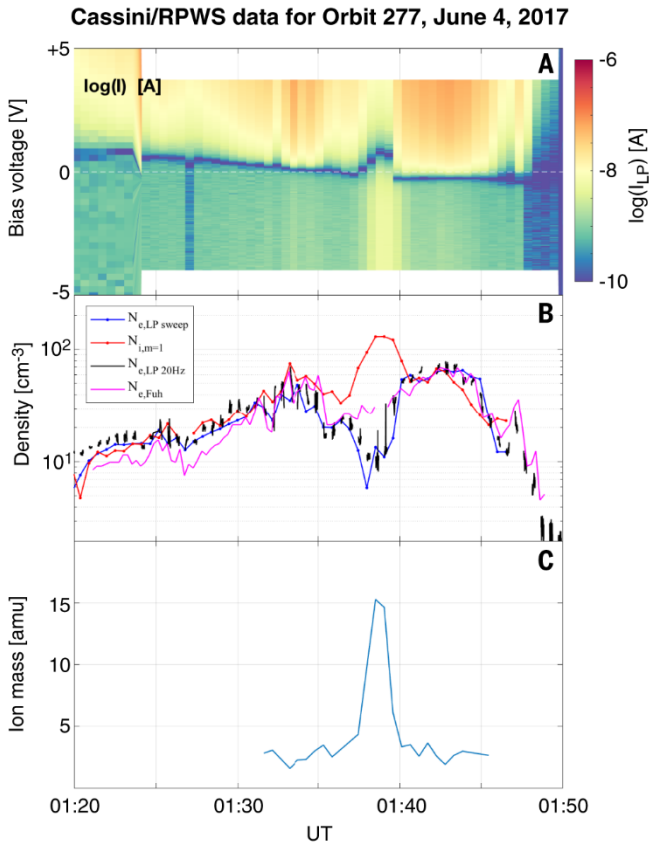

Fig. 3. RPWS data from an ionosphere crossings close to the D-ring of Saturn. The Langmuir probe (LP) measured current from voltage sweeps (**A**), RPWS densities (**B**), and inferred average ion mass (**C**) is displayed. The electron densities (N_e) from 3 measurement methods (*11*) are lower than the estimated ion density (N_i) when Cassini passed the D-ring edge at 01:38 UT. The inferred average ion mass rises above 1 amu at this time.

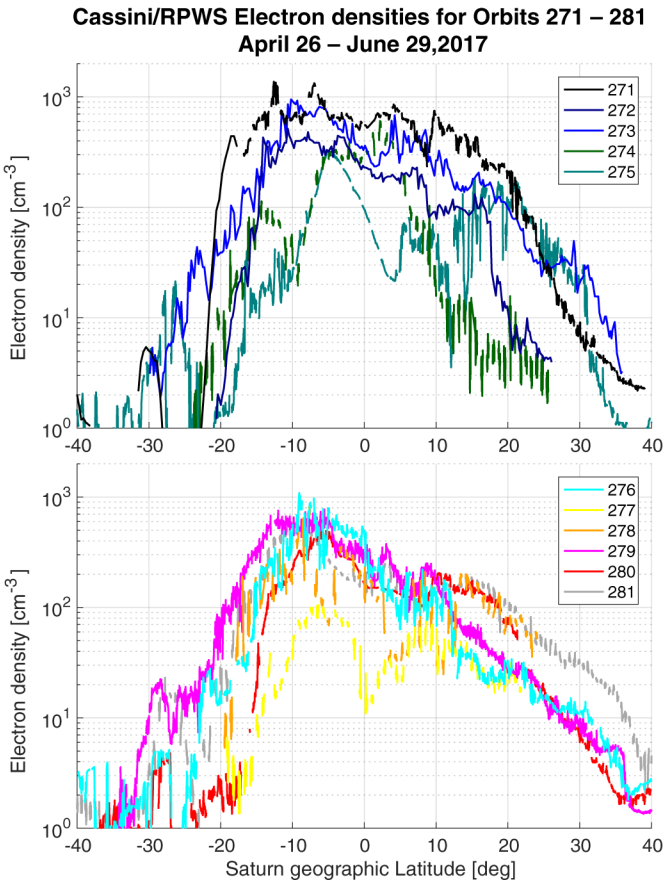

Fig. 4. Cassini/RPWS electron number densities from 11 ionosphere crossings near the equatorial plane of Saturn. The orbits 272 and 273 densities are based on whistler cut-off data, while the rest are from the Langmuir probe measurements (the Langmuir probe was in the wake of the spacecraft during orbits 272 and 273). There are about 6.5 days between each flyby from April 26 to June 29, all close to 11-14 hours Saturn LT. There is a large variability in the ionosphere, with fine structure over these latitudinal-altitude cuts of the ionosphere. The closest approach altitude occurs close to the geographic equator.

STELLAR ASTROPHYSICS

An excess of massive stars in the local 30 Doradus starburst

F. R. N. Schneider,[1]* H. Sana,[2] C. J. Evans,[3] J. M. Bestenlehner,[4,5] N. Castro,[6] L. Fossati,[7] G. Gräfener,[8] N. Langer,[8] O. H. Ramírez-Agudelo,[3] C. Sabín-Sanjulián,[9] S. Simón-Díaz,[10,11] F. Tramper,[12] P. A. Crowther,[5] A. de Koter,[13,2] S. E. de Mink,[13] P. L. Dufton,[14] M. Garcia,[15] M. Gieles,[16] V. Hénault-Brunet,[17,18] A. Herrero,[10,11] R. G. Izzard,[16,19] V. Kalari,[20] D. J. Lennon,[12] J. Maíz Apellániz,[21] N. Markova,[22] F. Najarro,[15] Ph. Podsiadlowski,[1,8] J. Puls,[23] W. D. Taylor,[3] J. Th. van Loon,[24] J. S. Vink,[25] C. Norman[26,27]

The 30 Doradus star-forming region in the Large Magellanic Cloud is a nearby analog of large star-formation events in the distant universe. We determined the recent formation history and the initial mass function (IMF) of massive stars in 30 Doradus on the basis of spectroscopic observations of 247 stars more massive than 15 solar masses ($M_\odot$). The main episode of massive star formation began about 8 million years (My) ago, and the star-formation rate seems to have declined in the last 1 My. The IMF is densely sampled up to 200 $M_\odot$ and contains 32 ± 12% more stars above 30 $M_\odot$ than predicted by a standard Salpeter IMF. In the mass range of 15 to 200 $M_\odot$, the IMF power-law exponent is $1.90^{+0.37}_{-0.26}$, shallower than the Salpeter value of 2.35.

Starbursts are large star-formation events whose feedback affects the dynamical and chemical evolution of star-forming galaxies throughout cosmic history (*1*–*3*). They are found at low and high redshift, with the earliest starburst galaxies contributing to the reionization of the universe (*2*, *4*). In such starbursts, massive stars [≥10 solar masses ($M_\odot$)] dominate the feedback through intense ionizing radiation, stellar outflows, and supernova explosions. Because of large distances to most starbursts, analyses have so far been restricted to either photometric observations or composite spectra of entire stellar populations. In the former case, the high surface temperature of massive stars precludes the determination of accurate physical parameters because their colors are too similar (*5*), and, in the latter case, physical parameters of individual stars cannot be determined (*6*). Greater understanding can be obtained by spectroscopically examining individual stars within star-forming regions.

The stellar initial mass function (IMF) influences many areas of astrophysics because it determines the relative fraction of massive stars; that is, those that undergo supernova explosions and drive the evolution of star-forming galaxies. Much effort has therefore gone into understanding whether the IMF is universal or varies with local environmental properties (*7*, *8*). Over the past few decades, evidence has accumulated that the IMF slope may be flatter than that of a Salpeter IMF (*9*)—in other words, there are more high-mass stars than expected—in regions of intense star formation (*10*–*12*). However, these studies are based on integrated properties of stellar populations, hampering the ability to infer IMFs.

The star-forming region 30 Doradus (30 Dor) lies within the Large Magellanic Cloud, a satellite galaxy of the Milky Way, and has a metallicity (total abundance of all elements heavier than helium) of ~40% of the solar value (*13*). At a distance of 50 kpc (*14*), 30 Dor is a nearby analog of distant starbursts and one of the brightest hydrogen-ionization (H II) regions in the local universe (*15*). With a diameter of ~200 pc, 30 Dor hosts several star clusters and associations and is similar in size to luminous H II complexes in more distant galaxies (*16*).

Through the use of the Fibre Large Array Multi Element Spectrograph (FLAMES) (*17*) on the Very Large Telescope (VLT), the VLT-FLAMES Tarantula Survey (VFTS) (*18*) has obtained optical spectra of ~800 massive stars in 30 Dor, avoiding the core region of the dense star cluster R136 because of difficulties with crowding (*18*). Repeated observations at multiple epochs allow determination of the orbital motion of potentially binary objects. For a sample of 452 apparently single stars, robust stellar parameters—such as effective temperatures, luminosities, surface gravities, and projected rotational velocities—are determined by modeling the observed spectra (*19*). Composite spectra of visual multiple systems and spectroscopic binaries are not considered here because their parameters cannot be reliably inferred from the VFTS data.

To match the derived atmospheric parameters of the apparently single VFTS stars to stellar evolutionary models, we use the Bayesian code Bonnsai, which has been successfully tested with high-precision observations of Galactic eclipsing binary stars (*20*). Bonnsai accounts for uncertainties in the atmospheric parameters and determines full posterior probability distributions of stellar properties, including the ages and initial masses of the VFTS stars (*19*). By summing these full posterior probability distributions of individual stars, we obtain the overall distributions of stellar ages and initial masses of massive stars currently present in 30 Dor (Fig. 1). These distributions are missing those stars that already ended their nuclear burning. However, given that we know both the present-day age and mass distributions, we can correct for these missing stars and derive the star-formation history (SFH) and IMF of massive stars in 30 Dor (*19*), allowing us to fully characterize this prototype starburst.

When determining the SFH and IMF, it is necessary to account for selection biases. The VFTS target selection implemented a magnitude cut, observing only stars brighter than the 17th magnitude in the V band (*18*). Compared with a full photometric census of massive stars in 30 Dor (*21*), the VFTS sample is ~73% complete. Although, owing to the magnitude limit, the VFTS is incomplete for stars $\lesssim 15\ M_\odot$, the completeness shows no correlation with the V-band magnitude of stars more massive than $15\ M_\odot$ (*19*). Of the 452 stars with robust stellar parameters, 247 are more massive than $15\ M_\odot$ and form the basis of our determination of the SFH and high-mass end of the IMF. Incompleteness corrections are applied to account for our selection process (*19*). We assume the high-mass IMF is a power-law function, $\xi(M) \propto M^{-\gamma}$, where M is the mass and γ the slope, and compute the SFH and corresponding prediction of the distribution of initial masses for different IMF slopes

[1]Department of Physics, University of Oxford, Keble Road, Oxford OX1 3RH, UK. [2]Institute of Astrophysics, KU Leuven, Celestijnenlaan 200D, 3001 Leuven, Belgium. [3]UK Astronomy Technology Centre, Royal Observatory Edinburgh, Blackford Hill, Edinburgh EH9 3HJ, UK. [4]Max-Planck-Institut für Astronomie, Königstuhl 17, 69117 Heidelberg, Germany. [5]Department of Physics and Astronomy, Hicks Building, Hounsfield Road, University of Sheffield, Sheffield S3 7RH, UK. [6]Department of Astronomy, University of Michigan, 1085 South University Avenue, Ann Arbor, MI 48109, USA. [7]Austrian Academy of Sciences, Space Research Institute, Schmiedlstraße 6, 8042 Graz, Austria. [8]Argelander-Institut für Astronomie der Universität Bonn, Auf dem Hügel 71, 53121 Bonn, Germany. [9]Departamento de Física y Astronomía, Universidad de La Serena, Avenida Juan Cisternas no. 1200 Norte, La Serena, Chile. [10]Instituto de Astrofísica de Canarias, E-38205 La Laguna, Tenerife, Spain. [11]Departamento de Astrofísica, Universidad de La Laguna, E-38206 La Laguna, Tenerife, Spain. [12]European Space Astronomy Centre, Mission Operations Division, P.O. Box 78, 28691 Villanueva de la Cañada, Madrid, Spain. [13]Astronomical Institute Anton Pannekoek, Amsterdam University, Science Park 904, 1098 XH Amsterdam, Netherlands. [14]Astrophysics Research Centre, School of Mathematics and Physics, Queen's University Belfast, Belfast BT7 1NN, Northern Ireland, UK. [15]Centro de Astrobiología, CSIC-INTA, Carretera de Torrejón a Ajalvir km-4, E-28850 Torrejón de Ardoz, Madrid, Spain. [16]Department of Physics, Faculty of Engineering and Physical Sciences, University of Surrey, Guildford, GU2 7XH, UK. [17]National Research Council, Herzberg Astronomy and Astrophysics, 5071 West Saanich Road, Victoria, British Columbia V9E 2E7, Canada. [18]Department of Astrophysics/Institute for Mathematics, Astrophysics and Particle Physics, Radboud University, P.O. Box 9010, NL-6500 GL Nijmegen, Netherlands. [19]Institute of Astronomy, The Observatories, Madingley Road, Cambridge CB3 0HA, UK. [20]Departamento de Astronomía, Universidad de Chile, Camino El Observatorio 1515, Las Condes, Santiago, Casilla 36-D, Chile. [21]Centro de Astrobiología, CSIC-INTA, European Space Astronomy Centre campus, camino bajo del castillo s/n, E-28 692 Villanueva de la Cañada, Spain. [22]Institute of Astronomy with National Astronomical Observatory, Bulgarian Academy of Sciences, P.O. Box 136, 4700 Smoljan, Bulgaria. [23]Ludwig-Maximilians-Universität München, Universitätssternwarte, Scheinerstrasse 1, 81679 München, Germany. [24]Lennard-Jones Laboratories, Keele University, Staffordshire ST5 5BG, UK. [25]Armagh Observatory, College Hill, Armagh BT61 9DG, Northern Ireland, UK. [26]Johns Hopkins University, Homewood Campus, Baltimore, MD 21218, USA. [27]Space Telescope Science Institute, 3700 San Martin Drive, Baltimore, MD 21218, USA.
*Corresponding author. Email: fabian.schneider@physics.ox.ac.uk

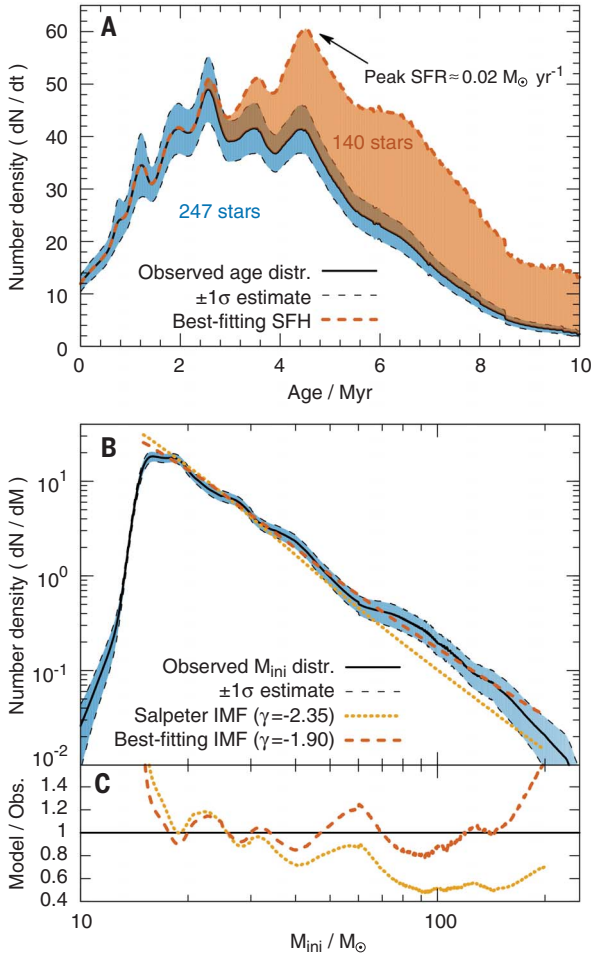

Fig. 1. Distributions of stellar ages and initial masses of massive stars in 30 Dor. (**A**) Age and (**B**) initial mass (M_{ini}) distribution of the VFTS sample stars more massive than 15 $M_\odot$ (black lines). Uncertainties are calculated by bootstrapping (*19*), and the 1σ regions are shaded blue. The best-fitting star-formation history (SFH) (A) and present-day distribution of initial masses (B) are plotted in red. For comparison, the expected present-day distribution of initial masses, assuming a Salpeter initial mass function (IMF), is also provided in (B) (note that these modeled mass distributions are no longer single power-law functions). About 140 stars above 15 $M_\odot$ are inferred to have ended their nuclear burning during the last ≈10 My, and their contribution to the SFH is shown by the red shaded region in (A). The peak star-formation rate (SFR) extrapolated to the entire 30 Dor region is ~0.02 $M_\odot$ year^{-1} (on the order of ≈1 $M_\odot$ year^{-1} kpc^{-2}, depending on the exact size of 30 Dor). The age and mass distributions are number density functions (dN/dt and dN/dM) with respect to age t and mass M. γ is the power-law slope of the IMF. (**C**) Ratio of modeled to observed present-day mass functions, illustrating that the Salpeter IMF model underpredicts the number of massive stars in our sample, particularly above 30 $M_\odot$.

until we best match (i) the number of stars above a given mass and (ii) the observed initial-mass distribution (*19*).

We find that the observed distribution of initial masses of stars in 30 Dor is densely sampled up to ~200 $M_\odot$. It is shallower than that predicted by a Salpeter IMF with γ = 2.35, and the discrepancy increases with mass (Fig. 1C). Relative to the Salpeter index, we find an excess of $18.2^{+6.8}_{-7.0}$ (32^{+12}_{-12}%) stars more massive than 30 $M_\odot$ and $9.4^{+4.0}_{-4.6}$ (73^{+31}_{-36}%) stars more massive than 60 $M_\odot$ (Fig. 2 and fig. S5; unless stated otherwise, uncertainties are 68.3% confidence intervals). The hypothesis that a Salpeter IMF can explain the large number of stars more massive than 30 $M_\odot$ in our sample can thus be rejected with >99% confidence (*19*). The number of stars more massive than 30 $M_\odot$ is best reproduced by an IMF slope of $\gamma = 1.84^{+0.18}_{-0.18}$ (Fig. 2). Using our second diagnostic, a least-squares fit to the observed distribution of initial masses over the full mass range of 15 to 200 $M_\odot$, our best fit is $\gamma = 1.90^{+0.37}_{-0.26}$ (Figs. 1 and 3), in agreement with our first estimate based on the number of massive stars ≥30 $M_\odot$. Our high-mass IMF slope is shallower than the slope inferred by other studies for stars below ≈20 $M_\odot$ in the vicinity of R136 (*22*, *23*).

The limitation of our sample to stars ≥15 $M_\odot$ means that we can reconstruct the SFH of 30 Dor over the past ≈12 million years (My). When also considering the 1- to 2-My-old stars in R136 that were not observed within VFTS (*24*), we find that the star-formation rate in 30 Dor sharply increased ~8 My ago and seems to have dropped ~1 My ago (Fig. 1A). If the currently observed drop continues for another million years, the duration of the main star-forming event will be shorter than ~10 My. This result complements a recent study (*23*) that found a similar time-dependence of star formation around the central R136 star cluster in 30 Dor on the basis of photometric data of low- and intermediate-mass stars. We therefore conclude that star formation in the 30 Dor starburst is synchronized across a wide mass range.

Our results challenge the suggested 150 $M_\odot$ limit (*25*) for the maximum birth mass of stars. The most massive star in our sample, VFTS 1025 (also known as R136c), has an initial mass of 203^{+40}_{-44} $M_\odot$ (*19*). From stochastic sampling experiments (*19*), we exclude maximum stellar birth masses of more than 500 $M_\odot$ in 30 Dor with 90% confidence because we would otherwise expect to find at least one star above 250 $M_\odot$ in our sample. Our observations are thus consistent with the claim that stars with initial masses of up to 300 $M_\odot$ exist in the core of R136 (*26*).

Approximately 15 to 40% of our sample stars are expected to be products of mass transfer in binary star systems (*27*). Binary mass transfer in a stellar population produces a net surplus of massive stars and rejuvenates stars such that they appear younger than they really are (*28*). Mass accretion alone biases the inferred IMF slope to flatter values, whereas rejuvenation steepens it. Taken together, we calculate that these two effects roughly cancel out in our case and, thus, binary mass transfer cannot explain the difference between our inferred IMF and that of Salpeter (*19*). Also, our final sample of stars contains unrecognized binaries, but they do not affect our conclusions (*19*).

The core of the R136 star cluster is excluded from the VFTS, but stars ejected from R136 (so-called runaway stars) may enter our sample. Runaway stars are biased toward high masses (*29*) and thus flatten the upper IMF. However, star clusters such as R136 typically eject about 5 to 10 stars above 15 $M_\odot$ (*30*, *31*), which is insufficient to explain the expected excess of 25 to 50 stars above 30 $M_\odot$ in 30 Dor, after correcting for the completeness of our sample and that of the VFTS (*19*).

We conclude that the 30 Dor starburst has produced stars up to very high masses (≳200 $M_\odot$), with a statistically significant excess of stars above 30 $M_\odot$ and an IMF shallower above 15 $M_\odot$ than a Salpeter IMF. Measuring the IMF slope above 30 to 60 $M_\odot$ has proven difficult (*7*), and, in general, large uncertainties in the high-mass IMF slope remain (*32*). This raises the question of whether star formation in 30 Dor proceeded differently. It has been suggested that starburst regions themselves provide conditions for forming relatively more massive stars by the heating of natal clouds from nearby and previous generations of stars (*33*). Alternatively, a lower metallicity may lead to the formation of more massive stars because of weaker gas cooling during star formation. An IMF slope shallower than the Salpeter value may then be expected at high redshift when the universe was hotter and the metallicity lower (*33*, *34*).

Because massive-star feedback increases steeply with stellar mass, it is strongly affected by the IMF slope. Comparing an IMF slope of $\gamma = 1.90^{+0.37}_{-0.26}$ to the Salpeter slope, we expect 70^{+10}_{-60}% more core-collapse supernovae and an increase of supernova metal-yields and hydrogen ionizing radiation by factors of $3.0^{+1.6}_{-1.8}$ and $3.7^{+2.4}_{-2.4}$, respectively (*19*). The formation rate of black holes increases by a factor of $2.8^{+1.0}_{-1.6}$ (*19*), directly affecting the expected rate of black hole mergers detected by their gravitational wave signals. We also expect an increase in the predicted number of exotic transients that are preferentially found in starbursting, metal-poor dwarf galaxies such as long-duration gamma-ray bursts (*35*) and hydrogen-poor superluminous supernovae (*36*). Many population synthesis models and large-scale cosmological simulations

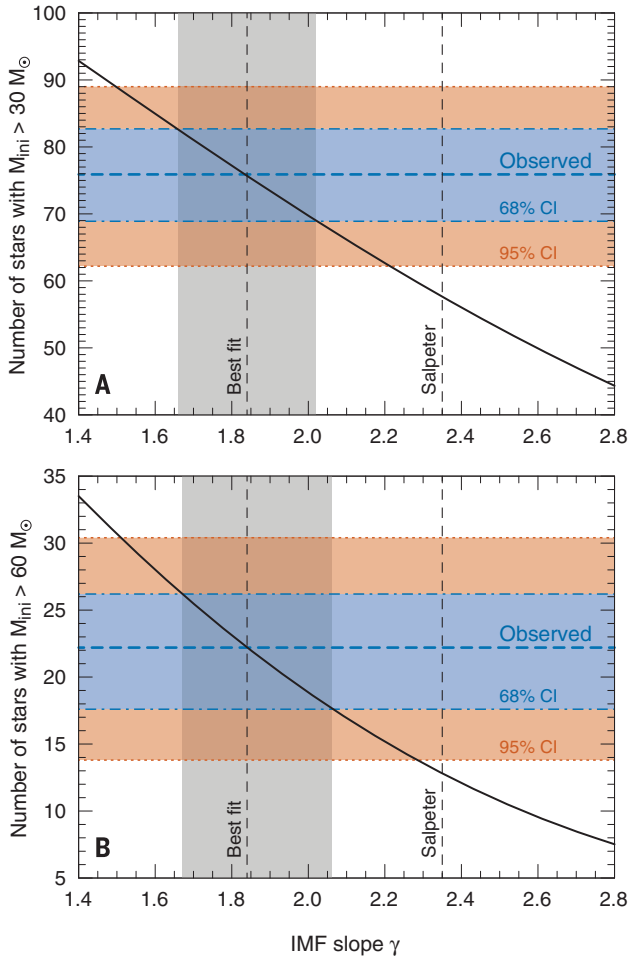

Fig. 2. Number of massive stars in our sample. Expected number of massive stars in our sample initially more massive than (**A**) 30 $M_\odot$ and (**B**) 60 $M_\odot$ as a function of the IMF slope γ (black solid lines). The blue and red shaded areas indicate the 68 and 95% confidence intervals (CIs), respectively, of the observed number of stars (see fig. S5). The IMF slopes best reproducing the observed number of stars and the associated 68% intervals are indicated by the vertical dashed lines and gray shaded regions and correspond to $\gamma = 1.84^{+0.18}_{-0.18}$ and $\gamma = 1.84^{+0.22}_{-0.17}$ for stars more massive than 30 $M_\odot$ and 60 $M_\odot$, respectively.

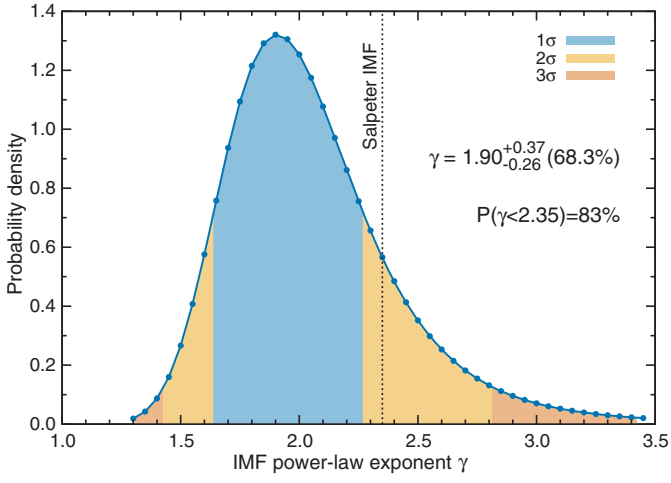

Fig. 3. Probability density function of the inferred IMF slope in 30 Dor. Results are based on a χ^2 power-law fitting over the mass range of 15 to 200 $M_\odot$. The shaded areas represent 1σ, 2σ, and 3σ confidence regions, and the slope of the Salpeter IMF is indicated by the vertical dashed line. Our inferred IMF is shallower than that of Salpeter (γ = 2.35), with 83% confidence.

assume an IMF that is truncated at 100 $M_\odot$. Compared with such models, the various factors estimated above are even larger (*19*).

REFERENCES AND NOTES

1. R. C. Kennicutt Jr., N. J. Evans II, *Annu. Rev. Astron. Astrophys.* **50**, 531–608 (2012).
2. P. Madau, M. Dickinson, *Annu. Rev. Astron. Astrophys.* **52**, 415–486 (2014).
3. D. Ceverino, A. Klypin, *Astrophys. J.* **695**, 292–309 (2009).
4. A. Loeb, R. Barkana, *Annu. Rev. Astron. Astrophys.* **39**, 19–66 (2001).
5. D. G. Hummer, D. C. Abbott, S. A. Voels, B. Bohannan, *Astrophys. J.* **328**, 704–708 (1988).
6. J. Maíz Apellániz, J. M. Mas-Hesse, C. Muñoz-Tuñón, J. M. Vílchez, H. O. Castañeda, *Astron. Astrophys.* **329**, 409–430 (1998).
7. N. Bastian, K. R. Covey, M. R. Meyer, *Annu. Rev. Astron. Astrophys.* **48**, 339–389 (2010).
8. S. Dib, S. Schmeja, S. Hony, *Mon. Not. R. Astron. Soc.* **464**, 1738–1752 (2017).
9. E. E. Salpeter, *Astrophys. J.* **121**, 161 (1955).
10. C. M. Baugh *et al.*, *Mon. Not. R. Astron. Soc.* **356**, 1191–1200 (2005).
11. M. L. P. Gunawardhana *et al.*, *Mon. Not. R. Astron. Soc.* **415**, 1647–1662 (2011).
12. M. Marks, P. Kroupa, J. Dabringhausen, M. S. Pawlowski, *Mon. Not. R. Astron. Soc.* **422**, 2246–2254 (2012).
13. B. Davies *et al.*, *Astrophys. J.* **806**, 21 (2015).
14. G. Pietrzyński *et al.*, *Nature* **495**, 76–79 (2013).
15. R. C. Kennicutt Jr., Y.-H. Chu, *Astron. J.* **95**, 720–730 (1988).
16. M. S. Oey, J. S. Parker, V. J. Mikles, X. Zhang, *Astron. J.* **126**, 2317–2329 (2003).
17. L. Pasquini *et al.*, *Messenger* **110**, 1–9 (2002).
18. C. J. Evans *et al.*, *Astron. Astrophys.* **530**, A108 (2011).
19. Materials and methods are available as supplementary materials.
20. F. R. N. Schneider *et al.*, *Astron. Astrophys.* **570**, A66 (2014).
21. E. I. Doran *et al.*, *Astron. Astrophys.* **558**, A134 (2013).
22. M. Andersen *et al.*, *Astrophys. J.* **707**, 1347–1360 (2009).
23. M. Cignoni *et al.*, *Astrophys. J.* **811**, 76 (2015).
24. P. A. Crowther *et al.*, *Mon. Not. R. Astron. Soc.* **458**, 624–659 (2016).
25. D. F. Figer, *Nature* **434**, 192–194 (2005).
26. P. A. Crowther *et al.*, *Mon. Not. R. Astron. Soc.* **408**, 731–751 (2010).
27. S. E. de Mink, H. Sana, N. Langer, R. G. Izzard, F. R. N. Schneider, *Astrophys. J.* **782**, 7 (2014).
28. F. R. N. Schneider *et al.*, *Astrophys. J.* **780**, 117 (2014).
29. A. Blaauw, *Bull. Astron. Inst. Neth.* **15**, 265–290 (1961).
30. M. S. Fujii, S. Portegies Zwart, *Science* **334**, 1380–1383 (2011).
31. S. Oh, P. Kroupa, J. Pflamm-Altenburg, *Astrophys. J.* **805**, 92 (2015).
32. D. R. Weisz *et al.*, *Astrophys. J.* **762**, 123 (2013).
33. R. B. Larson, *Mon. Not. R. Astron. Soc.* **359**, 211–222 (2005).
34. V. Bromm, P. S. Coppi, R. B. Larson, *Astrophys. J.* **527**, L5–L8 (1999).
35. J. F. Graham, A. S. Fruchter, *Astrophys. J.* **834**, 170 (2017).
36. J. Japelj, S. D. Vergani, R. Salvaterra, L. K. Hunt, F. Mannucci, *Astron. Astrophys.* **593**, A115 (2016).

ACKNOWLEDGMENTS

We thank the referees for constructive feedback that helped to improve this work. Our findings are based on observations collected at the European Southern Observatory (ESO) under program ID 182.D-0222. This work was supported by the Oxford Hintze Centre for Astrophysical Surveys, which is funded through generous support from the Hintze Family Charitable Foundation. H.S. acknowledges support from the FWO-Odysseus program under project G0F8H6N. G.G. acknowledges financial support from Deutsche Forschungsgemeinschaft grant GR 1717/5. O.H.R.-A. acknowledges funding from the European Union's Horizon 2020 research and innovation program under a Marie Skłodowska-Curie grant agreement (665593) awarded to the Science and Technology Facilities Council (STFC). C.S.-S. acknowledges support from CONICYT-Chile through the FONDECYT Postdoctoral Project (grant 3170778). S.S.-D. and A.H. thank the Spanish Ministry of Economy and Competitiveness (MINECO) for grants AYA2015-68012-C2-1 and SEV2015-0548. S.E.d.M. has received funding under the European Union's Horizon 2020 research and innovation program from the European Commission under a Marie Skłodowska-Curie grant agreement (661502) and the European Research Council (ERC) (grant agreement 715063). M.Ga. and F.N. acknowledge Spanish MINECO grants FIS2012-39162-C06-01 and ESP2015-65597-C4-1-R. M.Gi. acknowledges financial support from the Royal Society (University Research Fellowship) and the European Research Council (ERC StG-335936, CLUSTERS). R.G.I. thanks the STFC for funding his Rutherford fellowship under grant ST/L003910/1 and Churchill College, Cambridge, for his fellowship and access to their library. V.K. acknowledges funding from FONDECYT-Chile fellowship grant 3160117. J.M.A. acknowledges support from the Spanish government Ministerio de Economía y Competitividad (MINECO) through grant AYA2016-75 931-C2-2-P. N.M. acknowledges the financial support of the Bulgarian National Science Fund under grant DN08/1/13.12.2016. The Space Telescope Science Institute is operated by the Association of Universities for Research in Astronomy under NASA contract NAS5-26555. C.J.E. is also a visiting professor at the University of Edinburgh. The raw VFTS observations are available from ESO's Science Archive Facility at http://archive.eso.org under project ID 182.D-0222. A web interface for the Bonnsai software is available at www.astro.uni-bonn.de/stars/bonnsai. Input and derived stellar parameters for all stars used in this study are provided in table S3 and in machine-readable form in data S1, the best-fitting SFH can be found in data S2, and our Python code for determining the stellar maximum birth masses is available in data S3.

SUPPLEMENTARY MATERIALS

www.sciencemag.org/content/359/6371/69/suppl/DC1
Materials and Methods
Supplementary Text
Figs. S1 to S10
Tables S1 to S3
References (*37*–*116*)
Data S1 to S3

21 February 2017; accepted 30 November 2017
10.1126/science.aan0106

Cite as: Y. Yanagisawa *et al.*, *Science* 10.1126/science.aam7588 (2017).

Mechanically robust, readily repairable polymers via tailored noncovalent cross-linking

Yu Yanagisawa,[1,2] Yiling Nan,[1] Kou Okuro,[1] Takuzo Aida[1,2]*

[1]Department of Chemistry and Biotechnology, School of Engineering, The University of Tokyo, 7-3-1 Hongo, Bunkyo-ku, Tokyo 113-8656, Japan. [2]RIKEN Center for Emergent Matter Science, 2-1 Hirosawa, Wako, Saitama 351-0198, Japan.

*Corresponding author. Email: aida@macro.t.u-tokyo.ac.jp

Expanding the range of healable materials is an important challenge for sustainable societies. Noncrystalline, high molecular weight polymers generally form mechanically robust materials, which, however, are difficult to repair once they are fractured. This is because their polymer chains are heavily entangled and diffuse too sluggishly to unite fractured surfaces within reasonable timescales. Here, we report that low molecular weight polymers, when cross-linked by dense hydrogen bonds, give mechanically robust yet readily repairable materials, despite their extremely slow diffusion dynamics. A key was to utilize thiourea, which anomalously forms a zigzag hydrogen-bonded array that does not induce unfavorable crystallization. Another key was to incorporate a structural element for activating the exchange of hydrogen-bonded pairs, which enables the fractured portions to rejoin readily upon compression.

Healable polymers with enhanced longevity and reliability are particularly attractive as next-generation materials for the realization of a sustainable society (*1*–*3*). On the basis of their healing mechanisms, such materials are classified as exhibiting extrinsic (*1*, *2*) or intrinsic (*1*, *3*) healing behavior. Extrinsic healing depends on the presence of finely dispersed small capsules or vascular networks that separately entrap monomers and initiators that are mixed when the containers are broken, resulting in the formation of new polymer chains that connect the fractured parts (*4*, *5*). This approach is reliable, but it allows the material to heal only a limited number of times. In contrast, intrinsic mechanisms enable polymeric materials to heal multiple times, in some cases at ambient temperatures, through the reorganization of dynamic covalent bonds (*6*–*10*) or through noncovalent interactions, mostly involving hydrogen bonds (H-bonds) (*11*–*15*). These healable materials are usually soft and deformable. Some healable materials with high mechanical properties have also been developed by cross-linking with dynamic covalent bonds. However, in most cases, heating to high temperatures, on the order of 120°C or more, to reorganize their cross-linked networks, is necessary for the fractured portions to repair (*6*–*8*).

In general, noncrystalline, high molecular weight polymers form mechanically robust materials due to the entanglement of long polymer chains. However, once the materials are fractured, they are difficult to repair unless they are heated to melt, because the entangled polymer chains diffuse too sluggishly to unite fractured portions within reasonable timescales (*2*). Meanwhile, low molecular weight polymers, when they are non-covalently cross-linked by H-bonds, may be elaborated into mechanically robust yet healable polymer materials, because their dynamic properties are modulable by changing the cross-linking density. So far, rubber-like soft materials (*11*) and thermoplastic elastomers (*14*) with H-bonding motifs have been designed to heal upon gentle compression. However, the presence of a large number of H-bonds often leads to crystallization or clustering of polymer materials, thereby making them brittle (*16*–*18*). In other words, high mechanical robustness and healing ability tend to be mutually exclusive. Here, we report that poly(ether–thioureas) such as $TUEG_2$ and $TUEG_3$ (Fig. 1A) anomalously form amorphous materials, despite carrying dense H-bonding thiourea units. More interestingly, these materials are highly robust mechanically yet can readily be repaired by compression at fractured surfaces. Why are they amorphous despite carrying a large number of H-bonded thiourea units? We found that their H-bonded thiourea arrays are geometrically nonlinear (less ordered), so that they do not induce crystallization. Originally, we prepared $TUEG_3$ as a synthetic intermediate for guanidinium ion-appended polymers that strongly bind to oxyanionic groups in biomacromolecules (*19*–*21*). During the isolation of $TUEG_3$, we noticed that cut surfaces of this polymer are self-adhesive despite their rigid and nontacky nature. In fact, cut pieces of a 2-mm-thick rectangular sheet of $TUEG_3$ (10 × 20 mm) formed a merged sheet that withstood a 300-g load, when their fractured surfaces were manually compressed for 30 s at an ambient temperature of 21°C (fig. S1).

$TUEG_3$ (Fig. 1A) can be prepared by a one-pot polycondensation of commercially available monomers (see supplementary materials; page S4). It was characterized by means of ^1H and ^{13}C NMR spectroscopy and elemental analysis. ^1H NMR end-group analysis and multiangle light-scattering studies showed that its number- and weight-average molecular weights (M_n and M_w) were 9,500 and 22,300, respectively (Fig. 1C). $TUEG_3$ is amorphous, as shown by its differential scanning calorimetry (DSC) profile on the second heating (Fig. 1B). No sharp peaks due to crystallization appeared in the temperature range from −20 to 200°C at any scan rate from 1 to 10°C/min, whereas a broad peak corresponding to a glass transition appeared at 27°C (T_g, fig. S8B). Furthermore, in its X-ray diffraction (XRD) profile recorded at 22°C, $TUEG_3$ exhibited a broad diffraction peak centered at $2\theta = 23°$, typical of an amorphous material (fig. S10B). The thiourea group is unique as a H-bonding motif (*22*), because UEG_3, the urea analog of $TUEG_3$, is semicrystalline (Fig. 1, A and B, and fig. S10E). According to a thorough crystallographic study on the geometries of H-bonded thiourea and urea derivatives (*23*), the former mostly form nonlinear zigzag arrays of H-bonded thiourea units adopting cis/trans and strained trans/trans conformations ([I] in Fig. 2A), whereas the latter form linear arrays of H-bonded urea units adopting only a trans/trans conformation ([II] in Fig. 2A). We consider that the amorphous nature of $TUEG_3$ originates from such less ordered, nonlinear geometries of its H-bonded thiourea units. Fourier-transform infrared (FTIR) spectroscopy of $TUEG_3$ at 22°C showed broad vibrational bands at around 3,290 and 3,060 cm^{-1} (Fig. 2B), the former of which can be assigned to the NH stretching vibration, while the latter is characteristic of a NH deformation vibration of nonlinearly H-bonded thiourea units (*24*). Because the estimated energy gap between the cis/trans and trans/trans conformations is 2.9–4.2 kJ/mol (*25*), these two conformers likely coexist in the polymer matrix of $TUEG_3$. Meanwhile, semicrystalline UEG_3, the urea analog of $TUEG_3$, did not display an IR absorption at around 3,060 cm^{-1} (Fig. 2B). This is in accord with a previous report that H-bonded urea units adopt only a trans/trans conformation (Fig. 2, A and B) (*23*). The contrasting FTIR spectral features observed for amorphous $TUEG_3$ and semicrystalline UEG_3 highlight an important principle that densely located thiourea units, like urea units, tightly cross-link the polymer main chains through H-bonding interactions but do not induce crystallization because the resultant H-bonded arrays are nonlinear and less ordered.

To follow up on our preliminary healing test of $TUEG_3$ described above (fig. S1), we fabricated tensile bars by a method analogous to that used for the preparation of the polymer sheet, and then subjected the bars to tensile tests (test rate: 10 mm/min) at an ambient temperature of 21°C. The stress–strain curve, shown in Fig. 1D (red solid curve), displayed an abrupt increase in stress of as much as 45 ± 8 MPa, and the sample yielded at an applied strain of 6 ± 2%. After this yielding stage, the specimen elongated by up to 393 ± 5% before fracture (fig. S11). The elastic modulus of $TUEG_3$, as estimated from the initial slope of the stress–strain curve (Fig. 1D), was 1.4 GPa. Since dynamic mechanical properties are important for understanding the healing events at fractured portions, we performed temperature-dispersion tests for $TUEG_3$ at 200–0°C (5°C/min) at a constant frequency (ω) of 10 rad/s. The storage modulus (G') and loss modulus (G'') curves of $TUEG_3$ allowed for confirming the glass transition at around 30°C (fig. S12B). Noteworthy, $TUEG_3$ displayed a rubber plateau region, typical of long polymer chains upon being entangled, at around 50–70°C, despite the fact that its molecular weight is less than 10 kDa.

We then tested the healing of $TUEG_3$ by a method analogous to that reported by Corté and co-workers (*26*). Thus, a 0.1-mm-thick sheet of Teflon (10 × 10 mm) with a 1-mm-diameter hole at its center (Fig. 3A) was sandwiched between two discs of $TUEG_3$ (diameter: 8 mm; thickness: 1.0 mm). This assembled specimen was set on a rheometer stage, gently pressed with a jig, and then annealed for 20 min at 90°C (hot melt), so that the touching parts of the upper and lower discs merged inside the hole area of the Teflon sheet. The resultant specimen was cooled to 24°C at a rate of 5°C/min, and then the stage and jig in the rheometer were rapidly separated from one another at a rate of 100 mm/min to cause brittle fracture in the merged part of the specimen. After 3 min, the fractured surfaces were mechanically brought back into contact and compressed at the designated temperature under a constant applied stress. The compressed specimen was then subjected to tensile testing (tensile rate: 2 mm/min) to determine the stress at fracture. Although the contact area between the upper and lower discs was only 0.79 mm^2, the tensile tests were highly reproducible (fig. S13). Even when the contact area was enlarged from 0.79 to 1.76, 3.14, or 19.6 mm^2 (figs. S14 and S15), the results obtained were consistent (fig. S16). Meanwhile, when the applied compression stress was increased from 0.12 to 1.0 MPa, the recovery levelled off at 0.4 MPa after the initial abrupt increase (fig. S17). On the basis of these results, we carried out systematic healing tests by setting the contact area and applied compression stress at 0.79 mm^2 and 1.0 MPa, respectively. Figure 3B shows the stresses at break (black circles) observed for the assembled specimens of $TUEG_3$ prepared by compression for 1 hour at various temperatures (T_{comp} = 10–36°C). Note that the elastic moduli (red circles) of the compressed specimens at ≤ 32°C were rather high (≥ 0.9 GPa). Figure 3D shows the percentage recoveries of the stresses at break ($\sigma/\sigma_{pristine} \times 100$) of $TUEG_3$, where the specimen compressed at 24°C completely recovered its original mechanical strength ($\sigma_{pristine}$) in 6 hours. Accordingly, the interfacial adhesion energy was estimated to

be ~0.9 J/m^2 (supplementary materials; page S4). When T_{comp} was raised from 24°C to the higher range of 28–36°C, the specimen completely recovered within 1 hour (Fig. 3B), and the healing could be repeated multiple times without noticeable deterioration (fig. S18). Notably, even at T_{comp} = 12°C, the specimen recovered partially. On the basis of the frequency-dispersion properties of the G' and G'' values at 20–100°C with ω = 628 to 6.28 × 10^{-3} rad/s (figs. S19 and S20), we estimated the relaxation times (τ) for the flow transition of $TUEG_3$ by using their master curves (*27*) at 24–32°C (Fig. 3E and fig. S21). The τ values were in the range 10^7 seconds (~months) to 10^5 seconds (~days) (Fig. 3F), which are far longer than the compression times required for $TUEG_3$ to heal completely at T_{comp} = 24–32°C (≤ 6 hours). This contrast suggests that the rapid healing behavior of $TUEG_3$ is not a consequence of the flow of polymer chains (*11*, *14*), but is certainly dominated by a much more rapid process.

Other polymeric thiourea derivatives $TUEG_2$, $TUEG_4$, TUC_8, and TUC_{12} (Fig. 1A), in which diethylene glycol, tetraethylene glycol, octamethylene, and dodecamethylene spacer units, respectively, connect the thiourea units, were synthesized. Just like $TUEG_3$, $TUEG_2$ and $TUEG_4$ were both amorphous and displayed only single broad glass-transition peaks at 58 and 5°C, respectively (Fig. 1B and figs. S8 and S10). TUC_8 was also amorphous (T_g = 39°C), whereas TUC_{12} was semicrystalline (Fig. 1B and figs. S8 and S10). As in the case of $TUEG_3$, the FTIR spectra (Fig. 2B) of these reference polymers exhibited NH stretching and deformation vibrations in a range of 3,250–3,300 cm^{-1} and at around 3,060 cm^{-1}, respectively, the latter of which is typical of nonlinear H-bonded arrays of thiourea units (*23*). We investigated the tensile behaviors of these polymers and that of UEG_3 at an ambient temperature of 21°C with a tensile rate of 10 mm/min (Fig. 1D). In contrast to $TUEG_3$, all of these polymers were highly brittle, except $TUEG_4$ that was too fluid-like to be tested. However, in the tensile tests just below their glass transition temperatures, $TUEG_2$ did not fracture in a brittle manner, but yielded like $TUEG_3$, whereas TUC_8 again showed brittle fracture (fig. S23). We then conducted healing tests on amorphous $TUEG_2$ and TUC_8 at T_{comp} = 58 and 44°C, respectively. These temperatures were employed in order to properly compare the healing behaviors of these polymers with those of $TUEG_3$ at 24°C (Fig. 3D), since their viscosities, as determined by shear creep tests, were in the same level as one another (2.5 × 10^9 Pa·s for $TUEG_2$ at 58°C, 2.2 × 10^9 Pa·s for TUC_8 at 44°C, and 3.3 × 10^9 Pa·s for $TUEG_3$ at 24°C) (fig. S25). Figure 3D shows that $TUEG_2$ at T_{comp} = 58°C displayed an 85% recovery of its mechanical strength ($\sigma_{pristine}$) upon compression for 6 hours. Even when T_{comp} was lowered to 48°C (Fig. 3C, black circles), compressed $TUEG_2$ showed a partial recovery (22%) in 1 hour, although the elastic modulus of $TUEG_2$, at temperatures up to 70°C, remained high (≥ 1 GPa) (Fig. 3C, red circles). In contrast, TUC_8 barely healed, even upon compression at 44°C over a long period of 24 hours. Analogous to the case of $TUEG_3$, we evaluated the relaxation times (τ) of $TUEG_2$ and TUC_8 for the flow transition (fig. S22) from their temperature-dispersion (fig. S12) and frequency-dispersion properties (figs. S19 and S20). As shown in fig. S22, $TUEG_2$ and TUC_8 displayed a rubber plateau region similar to that of $TUEG_3$. Furthermore, both of these polymers showed extremely slow relaxation properties at T_{comp} [τ = 10^7 s (~months) to 10^6 s (~weeks)]. Why can $TUEG_2$ as well as $TUEG_3$ readily heal despite such slow diffusion dynamics? We consider that their healing properties are dominated by a segmental motion such as the exchange of H-bonded thiourea pairs, leading to the interpenetration of polymer chains at the fractured portions upon compression (*28*). The H-bond exchange of thiourea pairs should occur far more rapidly than the flow relaxation of these polymers (Fig. 3E and figs. S21 and S22). Consequently, virtually frozen $TUEG_2$ and $TUEG_3$ can heal only in a few hours. Then, why does TUC_8 hardly heal? This question prompted us to consider a special role of the spacer units that connect the thiourea units. Arrhenius plots of the intersection frequencies for the storage modulus (G') and loss modulus (G'') curves (fig. S20) allowed us to estimate the apparent activation energies (E_a) for the slippage of polymer chains (Fig. 4A). As shown in Fig. 4B, the E_a values for $TUEG_2$, $TUEG_3$, and TUC_8 were 171, 149, and 203 kJ/mol, respectively. In H-bonded polymer materials, polymer chains presumably slip and interpenetrate by exchanging their H-bonded pairs. According to the Flory–Huggins interaction parameters (χ) of the model structures in Fig. 4C, thiourea is much more miscible with ethers than with hydrocarbons. In ethereal media, the ether oxygen atoms might facilitate the exchange of H-bonded thiourea pairs by serving as temporal H-bond acceptors (Fig. 4D); in other words, the ether-containing $TUEG_2$ and $TUEG_3$ utilize this mechanism to lower the energy barrier for the slippage of their polymer chains. Obviously, this is not the case in TUC_8, since the thiourea group is incompatible with hydrocarbons (Fig. 4C). It is therefore reasonable that the E_a value for TUC_8 is larger than those for ether-containing $TUEG_2$ and $TUEG_3$, and the same might hold true even in a lower temperature range.

The present work provides the essential structural elements listed below for the design of mechanically robust yet healable polymer materials: (1) relatively short polymer chains that permit greater segmental motions, (2) tight cross-links by a large number of H-bonds for better mechanical properties, (3) nonlinear (less ordered) H-bond arrays that do not induce crystallization, and (4) implemented mechanisms to facilitate the exchange of H-bonded pairs. The triethylene glycol spacer that connects the thiourea units in $TUEG_3$ optimally modulates the activation energy for the exchange of H-

bonded thiourea pairs; consequently, the polymer material, although highly cross-linked noncovalently, can heal by only compression without heating.

REFERENCES AND NOTES

1. C. E. Diesendruck, N. R. Sottos, J. S. Moore, S. R. White, Biomimetic self-healing. *Angew. Chem. Int. Ed.* **54**, 10428–10447 (2015). doi:10.1002/anie.201500484 Medline
2. R. P. Wool, Self-healing materials: A review. *Soft Matter* **4**, 400–418 (2008). doi:10.1039/b711716g
3. Y. Yang, M. W. Urban, Self-healing polymeric materials. *Chem. Soc. Rev.* **42**, 7446–7467 (2013). doi:10.1039/c3cs60109a Medline
4. S. R. White, N. R. Sottos, P. H. Geubelle, J. S. Moore, M. R. Kessler, S. R. Sriram, E. N. Brown, S. Viswanathan, Autonomic healing of polymer composites. *Nature* **409**, 794–797 (2001). doi:10.1038/35057232 Medline
5. K. S. Toohey, N. R. Sottos, J. A. Lewis, J. S. Moore, S. R. White, Self-healing materials with microvascular networks. *Nat. Mater.* **6**, 581–585 (2007). doi:10.1038/nmat1934 Medline
6. X. Chen, M. A. Dam, K. Ono, A. Mal, H. Shen, S. R. Nutt, K. Sheran, F. Wudl, A thermally re-mendable cross-linked polymeric material. *Science* **295**, 1698–1702 (2002). doi:10.1126/science.1065879 Medline
7. D. Montarnal, M. Capelot, F. Tournilhac, L. Leibler, Silica-like malleable materials from permanent organic networks. *Science* **334**, 965–968 (2011). doi:10.1126/science.1212648 Medline
8. J. P. Brutman, P. A. Delgado, M. A. Hillmyer, Polylactide vitrimers. *ACS Macro Lett.* **3**, 607–610 (2014). doi:10.1021/mz500269w
9. M. Capelot, D. Montarnal, F. Tournilhac, L. Leibler, Metal-catalyzed transesterification for healing and assembling of thermosets. *J. Am. Chem. Soc.* **134**, 7664–7667 (2012). doi:10.1021/ja302894k Medline
10. Y. Yang, Z. Pei, X. Zhang, L. Tao, Y. Wei, Y. Ji, Carbon nanotube–vitrimer composite for facile and efficient photo-welding of epoxy. *Chem. Sci.* **5**, 3486–3492 (2014). doi:10.1039/C4SC00543K
11. P. Cordier, F. Tournilhac, C. Soulié-Ziakovic, L. Leibler, Self-healing and thermoreversible rubber from supramolecular assembly. *Nature* **451**, 977–980 (2008). doi:10.1038/nature06669 Medline
12. A. M. Kushner, J. D. Vossler, G. A. Williams, Z. Guan, A biomimetic modular polymer with tough and adaptive properties. *J. Am. Chem. Soc.* **131**, 8766–8768 (2009). doi:10.1021/ja9009666 Medline
13. J. Fox, J. J. Wie, B. W. Greenland, S. Burattini, W. Hayes, H. M. Colquhoun, M. E. Mackay, S. J. Rowan, High-strength, healable, supramolecular polymer nanocomposites. *J. Am. Chem. Soc.* **134**, 5362–5368 (2012). doi:10.1021/ja300050x Medline
14. Y. Chen, A. M. Kushner, G. A. Williams, Z. Guan, Multiphase design of autonomic self-healing thermoplastic elastomers. *Nat. Chem.* **4**, 467–472 (2012). doi:10.1038/nchem.1314 Medline
15. T. L. Sun, T. Kurokawa, S. Kuroda, A. B. Ihsan, T. Akasaki, K. Sato, M. A. Haque, T. Nakajima, J. P. Gong, Physical hydrogels composed of polyampholytes demonstrate high toughness and viscoelasticity. *Nat. Mater.* **12**, 932–937 (2013). doi:10.1038/nmat3713 Medline
16. D. Boils, M.-È. Perron, F. Monchamp, H. Duval, T. Maris, J. D. Wuest, Molecular tectonics. Disruption of self-association in melts derived from hydrogen-bonded solids. *Macromolecules* **37**, 7351–7357 (2004). doi:10.1021/ma035977d
17. O. Lebel, T. Maris, M.-È. Perron, E. Demers, J. D. Wuest, The dark side of crystal engineering: Creating glasses from small symmetric molecules that form multiple hydrogen bonds. *J. Am. Chem. Soc.* **128**, 10372–10373 (2006). doi:10.1021/ja063353s Medline
18. C. B. St.Pourcain, A. C. Griffin, Thermoreversible supramolecular networks with polymeric properties. *Macromolecules* **28**, 4116–4121 (1995). doi:10.1021/ma00116a010
19. R. Mogaki, K. Okuro, T. Aida, Molecular glues for manipulating enzymes: Trypsin inhibition by benzamidine-conjugated molecular glues. *Chem. Sci.* **6**, 2802–2805 (2015). doi:10.1039/C5SC00524H Medline
20. P. K. Hashim, K. Okuro, S. Sasaki, Y. Hoashi, T. Aida, Reductively cleavable nanocaplets for siRNA delivery by template-assisted oxidative polymerization. *J. Am. Chem. Soc.* **137**, 15608–15611 (2015). doi:10.1021/jacs.5b08948 Medline
21. R. Mogaki, P. K. Hashim, K. Okuro, T. Aida, Guanidinium-based "molecular glues" for modulation of biomolecular functions. *Chem. Soc. Rev.* **46**, 6480–6491 (2017). doi:10.1039/C7CS00647K Medline
22. C. Stefaniu, P.-L. Zaffalon, A. Carmine, Q. Verolet, S. Fernandez, T. A. Wesolowski, G. Brezesinski, A. Zumbuehl, Rigid urea and self-healing thiourea ethanolamine monolayers. *Langmuir* **31**, 1296–1302 (2015). doi:10.1021/la5039987 Medline
23. R. Custelcean, Crystal engineering with urea and thiourea hydrogen-bonding groups. *Chem. Commun.* **2008**, 295–307 (2008). doi:10.1039/B708921J Medline
24. R. Custelcean, M. G. Gorbunova, P. V. Bonnesen, Steric control over hydrogen bonding in crystalline organic solids: A structural study of *N,N'*-dialkylthioureas. *Chemistry* **11**, 1459–1466 (2005). doi:10.1002/chem.200400973 Medline
25. M. Obrzud, M. Rospenk, A. Koll, Self-association of N,N'-dialkylthiourea derivatives in non-polar solvents. *J. Mol. Struct.* **1018**, 54–63 (2012). doi:10.1016/j.molstruc.2012.01.042
26. F. Maes, D. Montarnal, S. Cantournet, F. Tournilhac, L. Corté, L. Leibler, Activation and deactivation of self-healing in supramolecular rubbers. *Soft Matter* **8**, 1681–1687 (2012). doi:10.1039/C2SM06715C
27. M. Rubinstein, R. H. Colby, *Polymer Physics* (Oxford Univ. Press, 2003).
28. S. Seiffert, J. Sprakel, Physical chemistry of supramolecular polymer networks. *Chem. Soc. Rev.* **41**, 909–930 (2012). doi:10.1039/C1CS15191F Medline
29. R. F. Fedors, A method for estimating both the solubility parameters and molar volumes of liquids. *Polym. Eng. Sci.* **14**, 147–154 (1974). doi:10.1002/pen.760140211
30. J. Brandrup, E. H. Immergut, E. A. Grulke (Eds.), *Polymer Handbook* (Wiley, ed. 4, 2003).
31. P. G. de Gennes, Soft adhesives. *Langmuir* **12**, 4497–4500 (1996). doi:10.1021/la950886y

ACKNOWLEDGMENTS

We appreciate the valuable discussion provided by Professors Z. Guan (University of California, Irvine), K. Mayumi, and K. Ito (The University of Tokyo), and Dr. H. Sasaki (Toagosei Co. Ltd.) and Dr. E. Silver and Mr. K. Morishita (The University of Tokyo). We also thank Professors H. Ejima and N. Yoshie (The University of Tokyo), and Messrs. Y. Kamei, H. Ochiai, and A. Masumoto (Shimadzu Corporation) for performing the mechanical tests, and Ms. M. Ishikawa (Tokyo Institute of Technology), Messrs. M. Nakamura, K. Kurono, and Dr. T. Tokai (Shoko Science Co. Ltd.) for the MALS analysis. This work was financially supported by a Grant-in-Aid for Specially Promoted Research (25000005) on 'Physically Perturbed Assembly for Tailoring High-Performance Soft Materials with Controlled Macroscopic Structural Anisotropy'. We also acknowledge assistance from the ImPACT Program of the Council for Science, Technology and Innovation (Cabinet Office, Government of Japan). Y.Y. thanks the Fellowship of Japan Society for the Promotion of Science (JSPS) for Young Scientists and the Program for Leading Graduate Schools (MERIT).

SUPPLEMENTARY MATERIALS

www.sciencemag.org/cgi/content/full/science.aam7588/DC1
Materials and Methods
Figs. S1 to S25
Reference (*31*)
Movie S1

12 January 2017; accepted 4 December 2017
Published online 14 December 2017
10.1126/science.aam7588

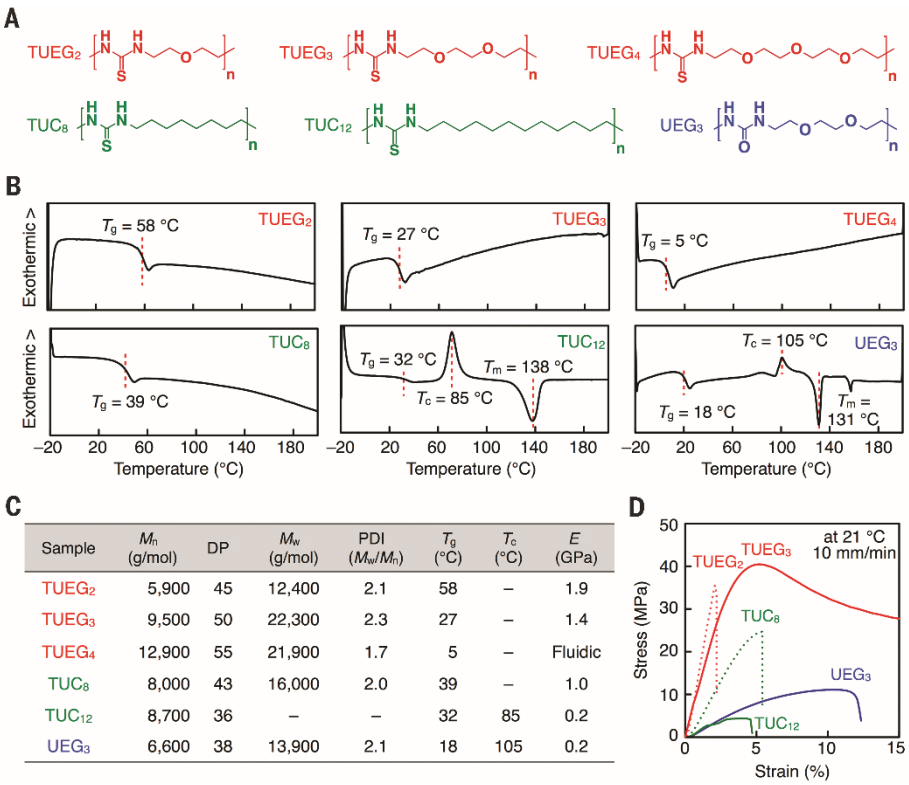

Sample	M_n (g/mol)	DP	M_w (g/mol)	PDI (M_w/M_n)	T_g (°C)	T_c (°C)	E (GPa)
$TUEG_2$	5,900	45	12,400	2.1	58	–	1.9
$TUEG_3$	9,500	50	22,300	2.3	27	–	1.4
$TUEG_4$	12,900	55	21,900	1.7	5	–	Fluidic
TUC_8	8,000	43	16,000	2.0	39	–	1.0
TUC_{12}	8,700	36	–	–	32	85	0.2
UEG_3	6,600	38	13,900	2.1	18	105	0.2

Fig. 1. Molecular structures and characterization of poly(ether-thiourea) $TUEG_3$ and its reference polymers. (A) Schematic structures of poly(ether-thioureas) with diethylene glycol ($TUEG_2$), triethylene glycol ($TUEG_3$), and tetraethylene glycol ($TUEG_4$) as spacers; schematic structures of poly(alkylene-thioureas) with octamethylene (TUC_8) and dodecamethylene chains (TUC_{12}) as spacers, and schematic structure of a poly(ether-urea) with triethylene glycol (UEG_3) as a spacer. (B) Differential scanning calorimetry (DSC) thermograms for $TUEG_2$, $TUEG_3$, $TUEG_4$, TUC_8, TUC_{12}, and UEG_3 on the second heating from −20°C to 200°C at a rate of 10°C/min. T_g, T_c, and T_m denote the glass-transition temperature, crystallization temperature, and melting temperature, respectively. (C) Characterization of polymers. M_n is the number-average molecular weight and DP is the degree of polymerization as estimated by ^{1}H NMR end-group analysis, M_w is the weight-average molecular weight, obtained by multiangle light scattering, and PDI is the polydispersity index (M_w/M_n); E is the elastic modulus, evaluated from the stress–strain curve in tensile testing (Fig. 1D); (D) Stress–strain curves of $TUEG_2$, $TUEG_3$, TUC_8, TUC_{12}, and UEG_3 at 21°C.

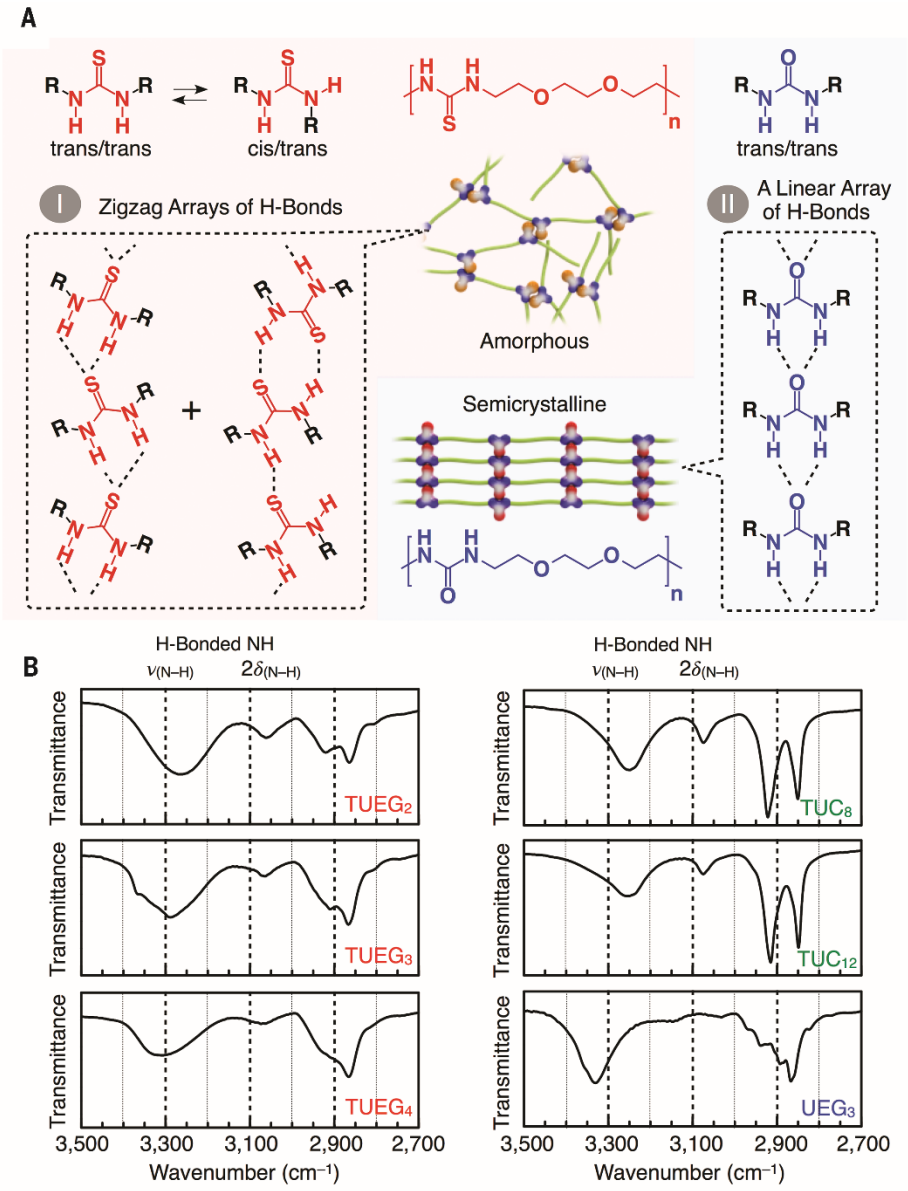

Fig. 2. Hydrogen-bonding interactions of thiourea and urea moieties in polymer matrices. (A) Schematic representations of the hydrogen-bonding modes of thiourea and urea. (B) FTIR spectra (bulk) at 22°C of poly(ether-thioureas) $TUEG_2$, $TUEG_3$, and $TUEG_4$; poly(alkylene-thioureas) TUC_8 and TUC_{12}; and poly(ether-urea) UEG_3.

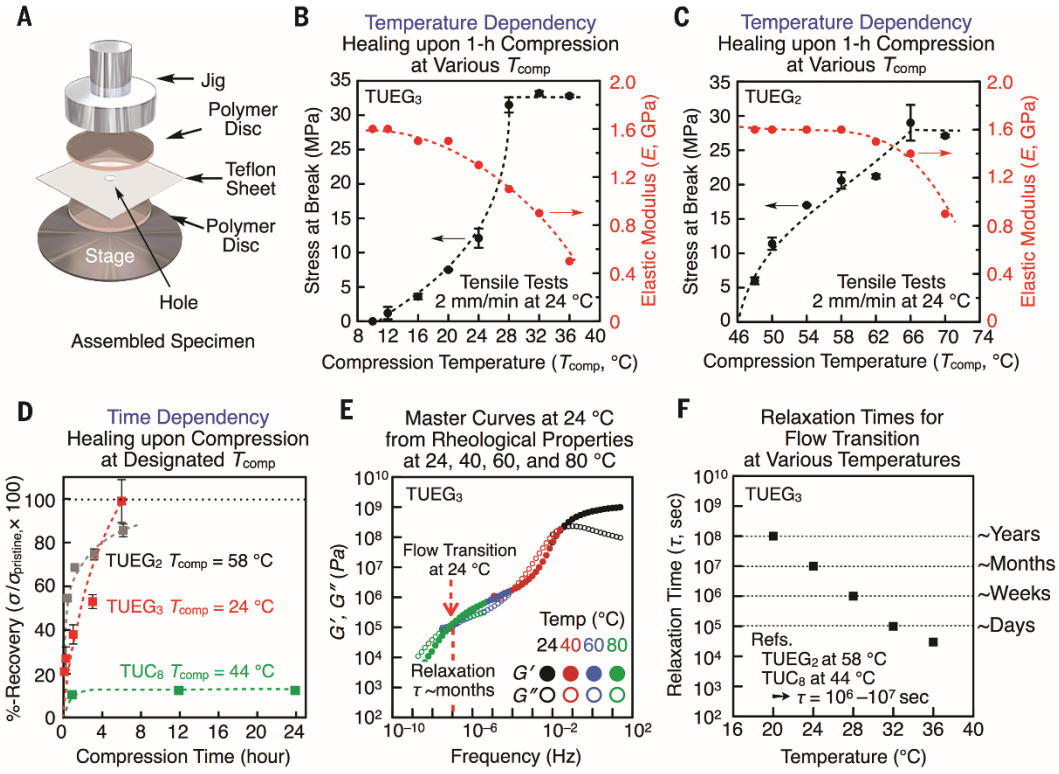

Fig. 3. Healing behaviors of polymeric thiourea derivatives upon compression. (A to D) Healing tests using a rheometer (*26*): (A) Schematic representation of the assembled specimen. (B and C) Elastic moduli (*E*, red circles) of poly(ether-thioureas) (B) $TUEG_3$ and (C) $TUEG_2$ at various temperatures, as estimated by compression testing (10 mm/min; red circles), and stresses at break for the assembled specimens (black circles) prepared by compression for 1 hour at various temperatures under a constant applied stress of 1.0 MPa. (D) Percentage recoveries of the stress at break for assembled specimens of $TUEG_2$, $TUEG_3$, and TUC_8 ($\sigma_{pristine}$; 26.5 ± 0.3, 31.7 ± 0.5, 39.1 ± 1.6 MPa, respectively), prepared by compression for various periods of time at T_{comp} of 58, 24, and 44°C, respectively, under a constant applied stress of 1.0 MPa. (E) Master curves for $TUEG_3$ at a reference temperature of 24°C, prepared by the time–temperature superposition treatment of *G′* and *G″* values obtained at 24, 40, 60, and 80°C in frequency (ω)-dispersion tests at ω = 628 to 6.28 × 10^{-3} rad/s at an applied strain of 0.05 or 0.1%. (F) Relaxation times (τ) of $TUEG_3$ for the flow transition, estimated from the crossover points of *G′* and *G″* at various temperatures (20–36°C) (fig. S21).

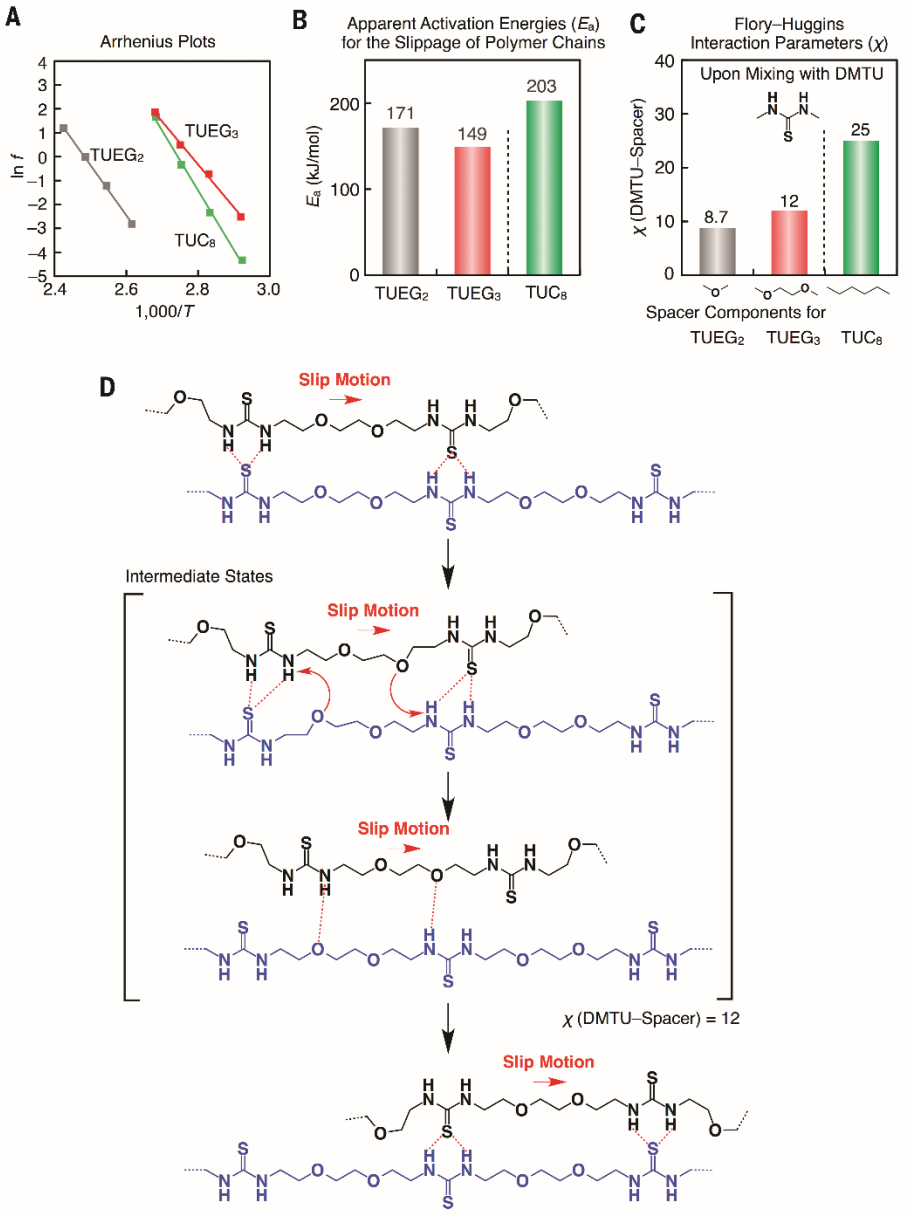

Fig. 4. Slip motions of polymer chains in poly(ether-thiourea) and poly(alkylene-thiourea) through exchange of hydrogen-bonded pairs. (**A**) Arrhenius plots of the intersection frequencies for the storage-modulus (G') and 1oss-modulus (G'') curves of poly(ether-thioureas) $TUEG_2$ and $TUEG_3$ and poly(alkylene-thiourea) TUC_8, estimated from a frequency (ω) sweep tests at ω = 100–0.05 rad/s at a constant applied strain of 0.1% in the temperature range for the flow transition (fig. S20). (**B**) Apparent activation energies (E_a) of $TUEG_2$, $TUEG_3$, and TUC_8 for the slippage of polymer chains, estimated from the Arrhenius plots. (**C**) Flory–Huggins interaction parameters χ (DMTU–Spacer) for *N,N'*-dimethylthiourea (DMTU) in combination with dimethyl ether (a model mixture for $TUEG_2$), ethylene glycol dimethyl ether (a model mixture for $TUEG_3$), or hexane (a model mixture for TUC_8). These values were estimated from the corresponding Hildebrand solubility parameters, determined by the Fedors method (*29*, *30*). (**D**) Proposed mechanism of how the exchange of H-bonded thiourea pairs in $TUEG_3$ is enhanced.

TOPOLOGICAL MATTER

Observation of the quantum spin Hall effect up to 100 kelvin in a monolayer crystal

Sanfeng Wu,[1]*† Valla Fatemi,[1]*† Quinn D. Gibson,[2] Kenji Watanabe,[3] Takashi Taniguchi,[3] Robert J. Cava,[2] Pablo Jarillo-Herrero[1]†

A variety of monolayer crystals have been proposed to be two-dimensional topological insulators exhibiting the quantum spin Hall effect (QSHE), possibly even at high temperatures. Here we report the observation of the QSHE in monolayer tungsten ditelluride (WTe_2) at temperatures up to 100 kelvin. In the short-edge limit, the monolayer exhibits the hallmark transport conductance, ~e^2/h per edge, where e is the electron charge and h is Planck's constant. Moreover, a magnetic field suppresses the conductance, and the observed Zeeman-type gap indicates the existence of a Kramers degenerate point and the importance of time-reversal symmetry for protection from elastic backscattering. Our results establish the QSHE at temperatures much higher than in semiconductor heterostructures and allow for exploring topological phases in atomically thin crystals.

A time-reversal (TR) invariant topological insulator (TI) in two dimensions, also known as a quantum spin Hall (QSH) insulator, can be identified by its helical edge modes (*1*–*4*). So far, evidence for the helical edge mode in two-dimensional (2D) TIs, particularly quantized transport, has been limited to very low temperatures (i.e., near liquid helium temperature) in HgTe and InAs/GaSb quantum wells (*5*, *6*). In the search for high-temperature TIs, substantial efforts have focused on a variety of atomically thin materials (*7*–*14*), which hold the promise of advancing the field of topological physics using the tools developed for 2D crystals. However, experimental observation of the quantum spin Hall effect (QSHE) in monolayer systems is challenging, often owing to structural or chemical instabilities (*9*, *15*–*17*). Indications of a high-temperature QSH phase in bulk-attached bismuth bilayers have been reported (*7*, *18*, *19*), but a conclusive demonstration is still lacking.

Among the proposals for atomically thin TIs are monolayer transition metal dichalcogenides (TMDs), materials that are either 2D semiconductors or semimetals depending on their structural phase (*9*). Calculations suggest that an inverted band gap can develop in 1T′ TMD monolayers, resulting in a nontrivial Z_2 topological phase (*9*, *20*). Recent experiments have shown promising results (*12*–*14*), including that monolayer WTe_2 exhibits a ground state with an insulating interior and conducting edges associated with a zero-bias anomaly (*12*), distinct from its multilayer counterparts (*12*, *21*). Here we observe the QSHE in WTe_2 monolayers and identify this 2D material as an atomically layered TI with conductance ~e^2/h per edge at high temperatures, where e is the electron charge and h is Planck's constant.

QSH transport through a 2D TR-invariant TI should exhibit the following characteristics: (i) helical edge modes, characterized by an edge conductance that is approximately the quantum value of e^2/h per edge (*5*); (ii) saturation to the conductance quantum in the short-edge limit (*22*); and (iii) suppression of conductance quantization upon application of a magnetic field, owing to the loss of protection by TR symmetry (*5*, *23*, *24*). Signatures of a Zeeman gap should be seen if the Kramers degeneracy (Dirac point) is located inside the bulk band gap. To date, simultaneous observation of the above criteria in existing 2D TI systems is still lacking (*5*, *6*, *22*, *23*, *25*), prompting the search for new QSH materials.

To check the above criteria in monolayer WTe_2, we fabricated devices with the structure depicted in Fig. 1A [see (*26*) and figs. S1 and S2]. The goal of the design was threefold: to ensure an atomically flat, chemically protected channel (no flake bending or exposure) by fully encapsulating the flake with hexagonal boron nitride (*15*, *21*); to minimize the effect of contact resistance; and to enable a length-dependence study on a single device. Our devices generally contain eight contact electrodes, a top graphite gate, and a series of in-channel local bottom gates with length L_c varying from 50 to 900 nm. The monolayer flakes are carefully selected to have a long strip shape, typically a few μm wide and about 10 μm long (table S1). Figure 1B shows a typical measurement of the four-probe conductance (in device 1) across all the local gates (~8 μm long) as a function of top-gate voltage, V_{tg}. A finite conductance plateau develops around V_{tg} = 0 V. This characteristic feature for monolayer WTe_2 stems from conduction along the edges (*12*). The measured value is highly sensitive to contact properties (*12*), which prevents observation of the intrinsic edge conductance. We overcome this obstacle in our devices through selective doping of the flake using a combination of global top and local bottom gates. A short transport channel with length L_c can be selectively defined by a local gate voltage V_c, whereas the rest of the flake is highly doped by V_{tg} to secure good contact to the electrodes (see fig. S3 for dI/dV characteristics, where dI ~ 1 nA is the applied ac current). Figure 1C maps out the resistance R in the same device as a function of V_{tg} and V_c (for a local gate with L_c = 100 nm). The step structure indicates a transition from a bulk-metallic state (doped) to a bulk-insulating state (undoped) within the locally gated region. We define the offset resistance, $\Delta R = R(V_c) - R(V_c = -1V)$, as the resistance change from the value in the highly doped limit (V_c = –1V, in this case). Figure 1D shows a ΔR trace (red curve) extracted from Fig. 1C (dashed white line in Fig. 1C), where V_{tg} is fixed at 3.5 V. The average value of ΔR at the plateau, which measures the step height, saturates when V_{tg} is high enough (Fig. 1D, inset, and figs. S4 to S7).

This saturated value, ΔR_s, thus measures the resistance of the undoped channel, which can only originate from the edges because the monolayer interior is insulating (*12*–*14*). Notably, ΔR_s is approximately equal to $h/2e^2$ for both this 100-nm channel and the 60- and 70-nm channels on device 2 (Fig. 1D). Fluctuations in the range of a few kilohm, which may originate from residual disorder or correlation effects (*12*, *27*, *28*), are visible, but decrease substantially above 4 K. Given that the sample has two edges, the observed conductance per edge is therefore ~e^2/h, pointing to helical edge modes as the source of the conductance (*5*, *6*). To confirm this scenario, one must rule out the possibility of trivial diffusive edge modes that happen to exhibit the quantized conductance value for some particular length (*22*). We thus performed a length-dependence study using a series of local gates with different L_c. Detailed analysis of measurements from representative devices and gates at ~4 K can be found in figs. S3 to S5. In Fig. 2, we summarize the data by plotting the undoped-channel resistance, ΔR_s, as a function of L_c. For long edges, the resistance generally decreases with decreasing length, which is arguably captured by a linear trend. The behavior, however, clearly deviates from the trend when L_c is reduced to 100 nm or less, where the resistance saturates to a value close to $h/2e^2$. Such behavior is present in all three devices that enter this short-length regime, independent of the width of the monolayer flake (varying from 1 to 4 μm). These observations reveal the intrinsic conductance as e^2/h per edge, as per the abovementioned criteria (i) and (ii) for the QSHE.

To check criterion (iii), regarding TR symmetry protection from elastic scattering, we performed magnetoconductance measurements. The data

[1]Department of Physics, Massachusetts Institute of Technology (MIT), Cambridge, MA 02139, USA. [2]Department of Chemistry, Princeton University, Princeton, NJ 08544, USA. [3]Advanced Materials Laboratory, National Institute for Materials Science, 1-1 Namiki, Tsukuba 305-0044, Japan.
*These authors contributed equally to this work.
†Corresponding author. Email: swu02@mit.edu (S.W.); vfatemi@mit.edu (V.F.); pjarillo@mit.edu (P.J.-H.)

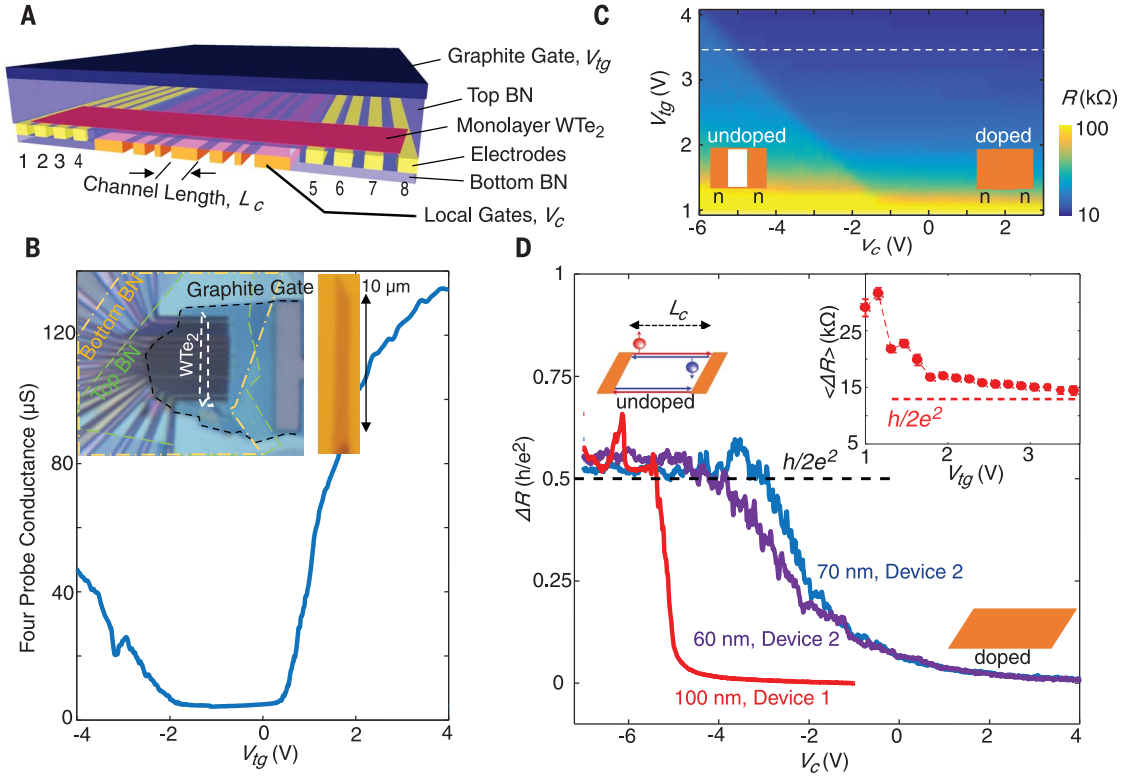

Fig. 1. Device structure and resistance near $h/2e^2$. (**A**) Schematic of the device structure. BN, boron nitride. (**B**) Four-probe conductance measurement at 4 K of device 1 as a function of V_{tg} across all the local gates, which are floating. Inset shows the optical image of device 1 (left) and the corresponding monolayer WTe_2 flake before fabrication (right). (**C**) Color map of the flake resistance tuned by V_{tg} and the 100-nm-wide local gate V_c at 4 K. Two regions are separated by a step in the resistance, which distinguishes the doped and undoped local channels, as depicted by the inset schematics. Ω, ohm. (**D**) ΔR versus V_c for the 100-nm-wide gate on device 1 at V_{tg} = 3.5 V [white dashed line in (C)] and the 60- and 70-nm-wide gates on device 2 at V_{tg} = 4.1V (taken at 5 K). For clarity, the two curves from device 2 are offset by +3 V along the *x* axis. Inset shows the average step height <Δ*R*>, extracted from (C), as a function of V_{tg}, showing a clear saturation toward $h/2e^2$ for large V_{tg}.

taken from the 100-nm-long channel in device 1 in the QSHE regime (i.e., gate range of the plateau) are shown in Fig. 3. We define G_s as $1/\Delta R_s$, which measures the conductance of the edges in the short channel limit. G_s is plotted as a function of V_c in Fig. 3A for a series of magnetic fields B applied perpendicular to the monolayer at 1.6 K. G_s decreases substantially once B is turned on, in contrast to the bulk state, which is hardly affected (fig. S8). For all V_c, G_s decreases rapidly for low magnetic fields (B < 2 T). After this initial stage, two types of behavior are observed, depending on V_c, as shown in Fig. 3B. When V_c is near −6.44 V, G_s decreases exponentially without saturation, up to 8 T. For other values of V_c, G_s saturates at high B. These behaviors are notably different from the previous observations for resistive channels (*12*).

Both types of behavior can be understood in the context of the QSHE. The 1D edge state of the QSH phase consists of two species: left and right movers associated with opposite spin polarization. The two linearly dispersing bands cross at the Kramers degeneracy point (Fig. 3B, inset I). Magnetic fields applied nonparallel to the spin polarization are expected to open an energy gap at the Kramers point owing to the Zeeman effect (*29*). For a homogeneous chemical potential close to the degeneracy point (Fig. 3B, inset II), one would expect an exponential decay of the conductance without saturation. To reveal the existence of the gap, we performed temperature-dependence measurements of the magnetoconductance at V_c = −6.44 V. The exponential decay of G_s persists up to high temperatures (measured up to 34 K, inset of Fig. 3C). Moreover, all the curves collapse onto a single universal trend when renormalized by plotting the dimensionless values $-\log(G_s/G_0)$ versus $\mu_B B/k_B T$ (Fig. 3C), where G_0 is the zero-field conductance, μ_B is the Bohr magneton, k_B is the Boltzmann constant, and T is the temperature. The slope of the trend

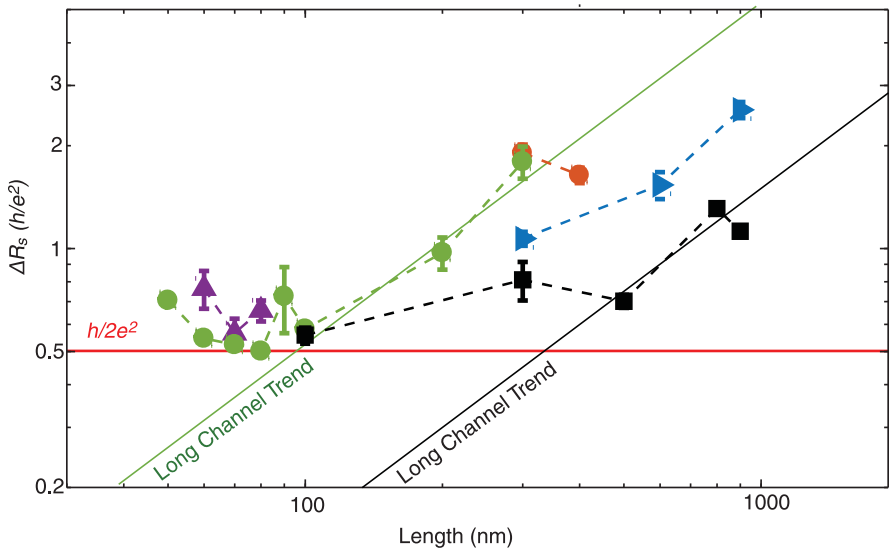

Fig. 2. Length dependence of the undoped-channel resistance. Data taken at 4 K from five different devices (table S1), each denoted by a different color and symbol. The device numbers and associated colors are: 1, black; 2, green; 3, purple; 4, red; and 5, blue. The ΔR_s values approach a minimum of $h/2e^2$ in the short-channel limit, confirming a total conductance of $2e^2/h$ for the undoped channel, i.e., a conductance of e^2/h per edge in the device, in agreement with QSHE. Detailed analysis of raw data can be found in figs. S4 to S7.

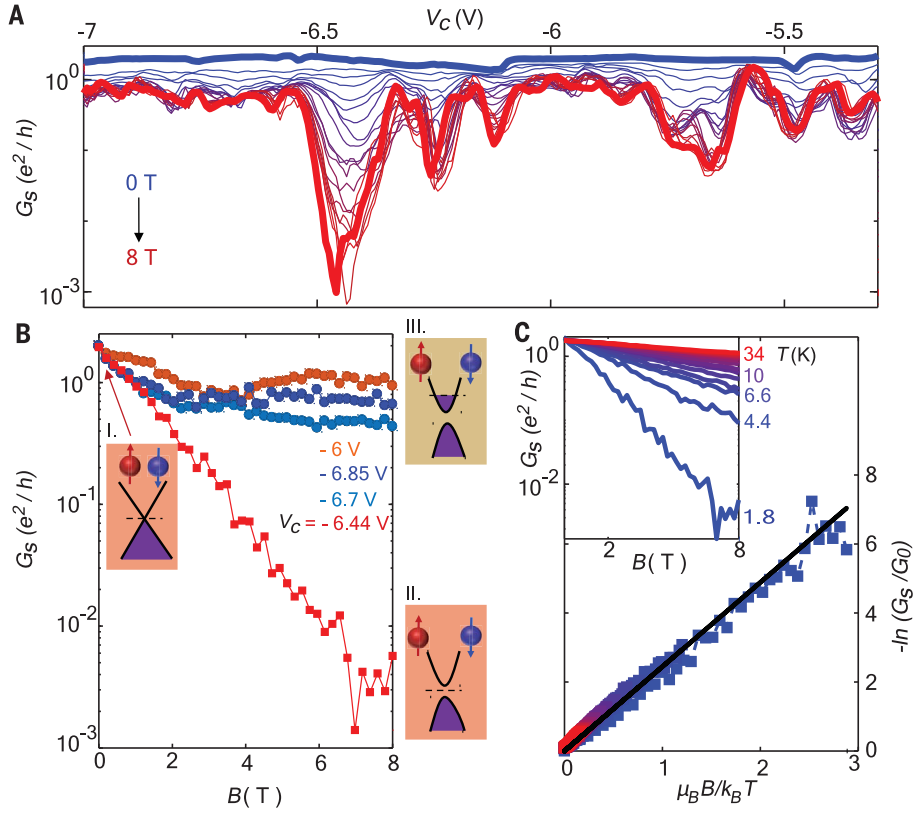

Fig. 3. Magnetoconductance and Zeeman-like gap at the Dirac point. (**A**) The evolution of the edge conductance G_s versus local gate voltage V_c under the application of a perpendicular magnetic field, B (from 0 T, thick blue curve, to 8 T, thick red curve, in 0.2-T steps) at 1.8 K, for device 1, 100-nm channel. (**B**) Traces of G_s versus B for a few selected V_c, showing two types of behavior, saturation and nonsaturation, associated with whether the Fermi energy (E_F) is in the Zeeman gap, as depicted in the band schematics inset I (linear bands at zero B, E_F at Dirac point), II (gapped bands at finite B, E_F at Dirac point), and III (gapped bands at finite B, E_F away from Dirac point). Red and blue spheres illustrate the opposite spin polarization of the edge bands, respectively. Purple areas indicate the filled bands. (**C**) Inset shows temperature dependence of G_s versus B for the nonsaturating curves (V_c = −6.44 V). All the curves in the inset collapse to a single trend in the normalized plot of $-\log(G_s/G_0)$ versus $\mu_B B/k_B T$. The black line is a linear fit. Additional temperature and magnetic field dependence is shown in figs. S9 to S11.

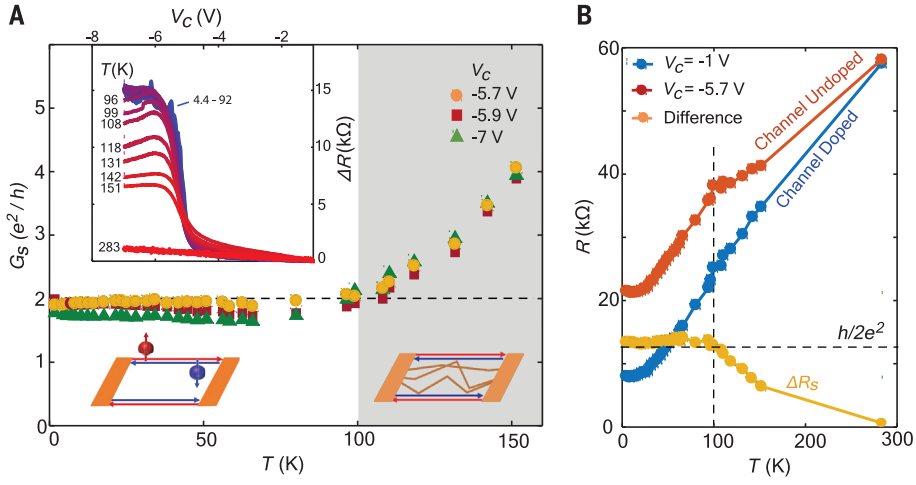

Fig. 4. Quantum spin Hall effect up to 100 K. (**A**) Temperature dependence of the edge conductance at a few representative gate voltages for the 100-nm channel in device 1. The conductance is dominated by the QSHE up to about 100 K. The right schematic depicts the onset of bulk-state contribution to the conductance. Inset shows gate dependence of ΔR at various temperatures. (**B**) Temperature dependence of the resistance of the whole flake (full length) when the Fermi energy in the local channel is in the doped (V_c = −1 V, red) and undoped (V_c = −5.7 V, blue) regimes, at V_{tg} = 3.5 V. The difference between the curves yields the temperature-dependent channel resistance ΔR_s (yellow). The vertical dashed line highlights the kink in the undoped regime at 100 K, indicating the transition to the QSHE edge-dominated regime.

yields an effective g-factor ~4.8 for the out-of-plane field in this device [i.e., the device conductance obeys $G_s = G_0 \exp(-g\mu_B B/2k_B T)$]. This observation confirms a Zeeman-type gap opening in the edge bands.

If the Fermi energy at the edge is gated away from the Kramers degeneracy point (Fig. 3B, inset III), the Zeeman gap will not be directly observed, and the magnetoconductance should be determined by the scattering mechanisms at the edge allowed by the TR symmetry breaking. For example, in our devices, the presence of local charge puddles can be natural. According to theoretical calculations, the edge conductance will be reduced to $\alpha e^2/h$, where α is a field-dependent coefficient determined by the microscopic details of the edge (*24*, *30*). Calculations show that, at high magnetic fields, an individual puddle can reduce transmission along an edge by 50% (*24*, *31*), leading to a saturated α determined by the distribution of the puddles along the edges. We find the conductance saturation is consistent with this picture (fig. S9). In addition to vertical magnetic fields, we have also found considerably reduced edge conductance when in-plane magnetic field is applied (fig. S10). We expect that both in- and out-of-plane magnetic fields will suppress the conductance: TR symmetry removes protection of the edge conduction, and the edge-mode spin-polarization axis is not necessarily normal or parallel to the layer because the monolayer lacks out-of-plane mirror symmetry. The exact spin-polarization axis may be influenced by multiple factors, such as the direction of the crystallographic edge and the existence of displacement electric fields. The irregular edge of the exfoliated monolayer makes the situation more complex. Overall, the magnetoconductance behavior is consistent with criterion (iii). Therefore, the QSHE is indeed observed in monolayer WTe_2.

Notably, the distinctive zero-field conductance value survives up to high temperatures. Figure 4A plots the temperature dependence of G_s at different V_c in the QSHE regime; G_s stays

approximately constant and close to $2e^2/h$ up to 100 K, indicating that the conductance is dominated by the QSHE up to this temperature. In terms of ΔR, the resistance plateau starts to drop at around 100 K (Fig. 4A, inset). We note that it is not obvious a priori what the temperature dependence of the QSH edge conductance should be, and some proposed mechanisms indicate weak (*32*) or even negative temperature dependence (*27*). Above 100 K, the channel conductance increases rapidly with temperature, indicating the activation of bulk-conduction channels. To reveal the transition more clearly, in Fig. 4B we plot the temperature dependence of the resistance R of the whole flake (i.e., the entire length, which consists of the locally gated region in series with the rest of the flake) when the chemical potential in the local channel is placed in the metallic regime (V_c = −1 V) and the QSH regime (V_c < −5.3 V). A clear kink at 100 K can be seen in the QSH regime. The difference between the two curves yields the channel resistance, which drops above the transition temperature.

This high-temperature QSHE is consistent with the prediction of a large inverted band gap (~100 meV) in monolayer WTe_2 (*20*) as well as recent experiments that observe a ~45-meV bulk band gap in spectroscopy (*13*, *14*) and a similar onset temperature for bulk conduction (*12*). We suspect the 100 K transition temperature may not be an intrinsic limit. Improvements in device quality may enable observation of the QSHE at even higher temperatures and for longer edges.

Our observations have confirmed the nontrivial TR invariant topological phase in monolayer WTe_2 and demonstrated the QSHE at high temperatures in an isolated 2D monolayer device. The exploration of 2D topological physics and device performance above liquid nitrogen temperatures has therefore become possible. Distinct from quantum well systems, the exposed nature of isolated monolayers may allow for engineering topological phases in unprecedented ways. In particular, WTe_2 can be readily combined with other 2D materials to form van der Waals heterostructures, a promising platform for studying the proximity effect between a QSH system and superconductors or magnets (*3*, *4*) at the atomic scale.

REFERENCES AND NOTES

1. C. L. Kane, E. J. Mele, *Phys. Rev. Lett.* **95**, 226801 (2005).
2. B. A. Bernevig, S.-C. Zhang, *Phys. Rev. Lett.* **96**, 106802 (2006).
3. M. Z. Hasan, C. L. Kane, *Rev. Mod. Phys.* **82**, 3045–3067 (2010).
4. X.-L. Qi, S.-C. Zhang, *Rev. Mod. Phys.* **83**, 1057–1110 (2011).
5. M. König *et al.*, *Science* **318**, 766–770 (2007).
6. I. Knez, R.-R. Du, G. Sullivan, *Phys. Rev. Lett.* **107**, 136603 (2011).
7. S. Murakami, *Phys. Rev. Lett.* **97**, 236805 (2006).
8. Y. Xu *et al.*, *Phys. Rev. Lett.* **111**, 136804 (2013).
9. X. Qian, J. Liu, L. Fu, J. Li, *Science* **346**, 1344–1347 (2014).
10. J.-J. Zhou, W. Feng, C.-C. Liu, S. Guan, Y. Yao, *Nano Lett.* **14**, 4767–4771 (2014).
11. S. S. Li *et al.*, *Sci. Rep.* **6**, 23242 (2016).
12. Z. Fei *et al.*, *Nat. Phys.* **13**, 677–682 (2017).
13. S. Tang *et al.*, *Nat. Phys.* **13**, 683–687 (2017).
14. Z.-Y. Jia *et al.*, *Phys. Rev. B* **96**, 041108 (2017).
15. Y. Cao *et al.*, *Nano Lett.* **15**, 4914–4921 (2015).
16. L. Wang *et al.*, *Nat. Commun.* **6**, 8892 (2015).
17. F. Ye *et al.*, *Small* **12**, 5802–5808 (2016).
18. C. Sabater *et al.*, *Phys. Rev. Lett.* **110**, 176802 (2013).
19. I. K. Drozdov *et al.*, *Nat. Phys.* **10**, 664–669 (2014).
20. F. Zheng *et al.*, *Adv. Mater.* **28**, 4845–4851 (2016).
21. V. Fatemi *et al.*, *Phys. Rev. B* **95**, 041410 (2017).
22. F. Nichele *et al.*, *New J. Phys.* **18**, 083005 (2016).
23. E. Y. Ma *et al.*, *Nat. Commun.* **6**, 7252 (2015).
24. S. Essert, K. Richter, *2D Mater* **2**, 024005 (2015).
25. L. Du, I. Knez, G. Sullivan, R.-R. Du, *Phys. Rev. Lett.* **114**, 096802 (2015).
26. See supplementary materials.
27. J. Maciejko *et al.*, *Phys. Rev. Lett.* **102**, 256803 (2009).
28. T. Li *et al.*, *Phys. Rev. Lett.* **115**, 136804 (2015).
29. M. König *et al.*, *J. Phys. Soc. Jpn.* **77**, 031007 (2008).
30. J. Maciejko, X.-L. Qi, S.-C. Zhang, *Phys. Rev. B* **82**, 155310 (2010).
31. A. Roth *et al.*, *Science* **325**, 294–297 (2009).
32. J. I. Väyrynen, M. Goldstein, Y. Gefen, L. I. Glazman, *Phys. Rev. B* **90**, 115309 (2014).

ACKNOWLEDGMENTS

We thank L. Fu and X. Qian for helpful discussions. This work was partly supported through Air Force Research Laboratory grant no. FA9550-16-1-0382 as well as the Gordon and Betty Moore Foundation's Emergent Phenomena in Quantum Systems (EPiQS) Initiative through grant no. GBMF4541 to P.J.-H. Device nanofabrication was partly supported by the Center for Excitonics, an Energy Frontier Research Center funded by the U.S. Department of Energy, Basic Energy Sciences Office, under award no. DE-SC0001088. This work made use of the Materials Research Science and Engineering Center's shared experimental facilities supported by the NSF under award no. DMR-0819762. Sample fabrication was performed in part at the Harvard Center for Nanoscale Science supported by the NSF under grant no. ECS-0335765. S.W. acknowledges the support of the MIT Pappalardo Fellowship in Physics. The WTe_2 crystal growth performed at Princeton University was supported by the NSF Materials Research Science and Engineering Center (MRSEC) grant DMR-1420541. Growth of hexagonal boron nitride crystals was supported by the Elemental Strategy Initiative conducted by the Ministry of Education, Culture, Sports, Science and Technology (MEXT), Japan; and the Japan Society for the Promotion of Science (JSPS) Grants-in-Aid for Scientific Research (KAKENHI) through grant nos. JP15K21722 and JP25106006. The data presented in this paper are available from the corresponding authors upon reasonable request.

SUPPLEMENTARY MATERIALS

www.sciencemag.org/content/359/6371/76/suppl/DC1
Materials and Methods
Supplementary Text
Figs. S1 to S11
Table S1
References (*33*, *34*)

7 May 2017; accepted 17 November 2017
10.1126/science.aan6003

CORAL REEFS

Spatial and temporal patterns of mass bleaching of corals in the Anthropocene

Terry P. Hughes,[1]* Kristen D. Anderson,[1] Sean R. Connolly,[1,2] Scott F. Heron,[3,4] James T. Kerry,[1] Janice M. Lough,[1,5] Andrew H. Baird,[1] Julia K. Baum,[6] Michael L. Berumen,[7] Tom C. Bridge,[1,8] Danielle C. Claar,[6] C. Mark Eakin,[3] James P. Gilmour,[9] Nicholas A. J. Graham,[1,10] Hugo Harrison,[1] Jean-Paul A. Hobbs,[11] Andrew S. Hoey,[1] Mia Hoogenboom,[1,2] Ryan J. Lowe,[12] Malcolm T. McCulloch,[12] John M. Pandolfi,[13] Morgan Pratchett,[1] Verena Schoepf,[12] Gergely Torda,[1,5] Shaun K. Wilson[14]

Tropical reef systems are transitioning to a new era in which the interval between recurrent bouts of coral bleaching is too short for a full recovery of mature assemblages. We analyzed bleaching records at 100 globally distributed reef locations from 1980 to 2016. The median return time between pairs of severe bleaching events has diminished steadily since 1980 and is now only 6 years. As global warming has progressed, tropical sea surface temperatures are warmer now during current La Niña conditions than they were during El Niño events three decades ago. Consequently, as we transition to the Anthropocene, coral bleaching is occurring more frequently in all El Niño–Southern Oscillation phases, increasing the likelihood of annual bleaching in the coming decades.

The average surface temperature of Earth has risen by close to 1°C as of the 1880s (*1*), and global temperatures in 2015 and 2016 were the warmest since instrumental record keeping began in the 19th century (*2*). Recurrent regional-scale (>1000 km) bleaching and mortality of corals is a modern phenomenon caused by anthropogenic global warming (*3*–*10*). Bleaching before the 1980s was recorded only at a local scale of a few tens of kilometers because of small-scale stressors such as freshwater inundation, sedimentation, or unusually cold or hot weather (*3*–*5*). The modern emergence of regional-scale bleaching is also evident from the growth bands of old Caribbean corals: synchronous distortions of skeletal deposition (stress bands) along a 400-km stretch of the Mesoamerican Reef have only been found after recent hot conditions, confirming that regional-scale heat stress is a modern phenomenon caused by anthropogenic global warming (*10*). Bleaching occurs when the density of algal symbionts, or zooxanthellae (*Symbiodinium* spp.), in the tissues of a coral host diminishes as a result of environmental stress, revealing the underlying white skeleton of the coral (*8*). Bleached corals are physiologically and nutritionally compromised, and prolonged bleaching over several months leads to high levels of coral mortality (*11*, *12*). Global climate modeling and satellite observations also indicate that the thermal conditions for coral bleaching are becoming more prevalent (*13*, *14*), leading to predictions that localities now considered to be thermal refugia could disappear by midcentury (*15*).

Although several global databases of bleaching records are available (notably ReefBase, reefbase.org), they suffer from intermittent or lapsed maintenance and from uneven sampling effort across both years and locations (*7*). The time spans of five earlier global studies of coral bleaching range from 1870 to 1990 (*3*), 1960 to 2002 (*4*), 1973 to 2006 (*5*), 1980 to 2005 (*6*), and 1985 to 2010 (*7*). Here we compiled de novo the history of recurrent bleaching from 1980 to 2016 for 100 globally distributed coral reef locations in 54 countries using a standardized protocol to examine patterns in the timing, recurrence, and intensity of bleaching episodes, including the latest global bleaching event from 2015 to 2016 (table S1). This approach avoids the bias of the continuous addition of new sites in open-access databases and retains the same range of spatial scales through time (fig. S1). A bleaching record in our analysis consists of three elements: the location, from 1 to 100; the year; and the binary presence or absence of bleaching. Our findings reveal that coral reefs have entered the distinctive human-dominated era characterized as the Anthropocene (*16*–*18*), in which the frequency and intensity of bleaching events is rapidly approaching unsustainable levels. At the spatial scale we examined (fig. S1), the

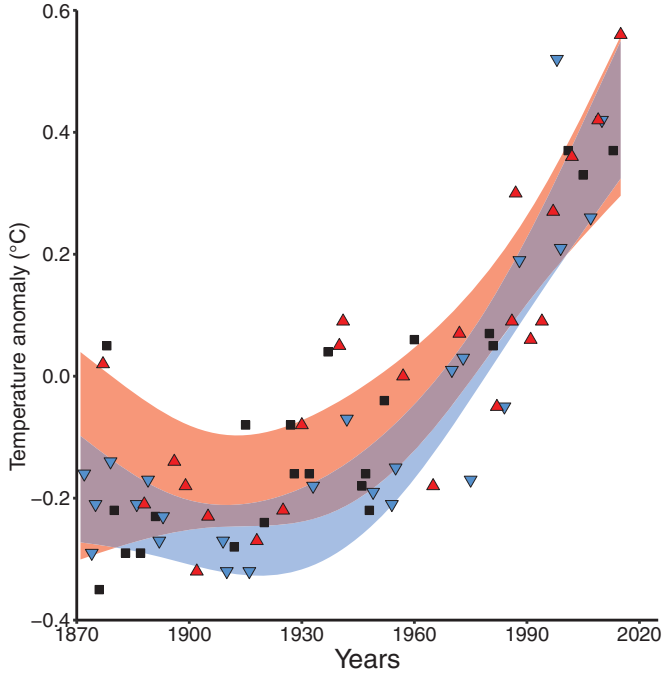

Fig. 1. Global warming throughout ENSO cycles. Sea surface temperature anomalies from 1871 to 2016, relative to a 1961–1990 baseline, averaged across 1670 1° latitude–by–1° longitude boxes containing coral reefs between latitudes of 31°N and 31°S. Data points differentiate El Niño (red triangles), La Niña (blue triangles), and ENSO neutral periods (black squares). Ninety-five percent confidence intervals are shown for nonlinear regression fits for years with El Niño and La Niña conditions (red and blue shading, respectively; overlap is shown in purple).

[1]Australian Research Council (ARC) Centre of Excellence for Coral Reef Studies, James Cook University, Townsville, QLD 4811, Australia. [2]College of Marine and Environmental Sciences, James Cook University, Townsville, QLD 4811, Australia. [3]Coral Reef Watch, U.S. National Oceanic and Atmospheric Administration, College Park, MD 20740, USA. [4]Marine Geophysical Laboratory, Physics Department, College of Science, Technology, and Engineering, James Cook University, Townsville, QLD 4811, Australia. [5]Australian Institute of Marine Science, PMB 3, Townsville, QLD 4810, Australia. [6]Department of Biology, University of Victoria, Victoria, BC V8W 2Y2, Canada. [7]Red Sea Research Center, King Abdullah University of Science and Technology, Thuwal 23599-6900, Saudi Arabia. [8]Queensland Museum, 70-102 Flinders Street, Townsville, QLD 4810, Australia. [9]Australian Institute of Marine Science, Indian Ocean Marine Science Centre, University of Western Australia (UWA), WA 6009, Australia. [10]Lancaster Environment Centre, Lancaster University, Lancaster LA1 4YQ, UK. [11]Department of Environment and Agriculture, Curtin University, Perth, WA 6845, Australia. [12]ARC Centre of Excellence in Coral Reef Studies, UWA Oceans Institute, and School of Earth Sciences, University of Western Australia, Crawley, WA 6009, Australia. [13]ARC Centre of Excellence for Coral Reef Studies, School of Biological Sciences, University of Queensland, Brisbane, QLD 4072, Australia. [14]Department of Biodiversity, Conservation and Attractions, Kensington, Perth, WA 6151, Australia.
*Corresponding author. Email: terry.hughes@jcu.edu.au

number of years between recurrent severe bleaching events has diminished fivefold in the past four decades, from once every 25 to 30 years in the early 1980s to once every 5.9 years in 2016. Across the 100 locations, we scored 300 bleaching episodes as severe, i.e., >30% of corals bleached at a scale of tens to hundreds of kilometers, and a further 312 as moderate (<30% of corals bleached). Our analysis indicates that coral reefs have moved from a period before 1980 when regional-scale bleaching was exceedingly rare or absent (*3*–*5*) to an intermediary phase beginning in the 1980s when global warming increased the thermal stress of strong El Niño events, leading to global bleaching events. Finally, in the past two decades, many additional regional-scale bleaching events have also occurred outside of El Niño conditions, affecting more and more former spatial refuges and threatening the future viability of coral reefs.

Increasingly, climate-driven bleaching is occurring in all El Niño–Southern Oscillation (ENSO) phases, because as global warming progresses, average tropical sea surface temperatures are warmer today under La Niña conditions than they were during El Niño events only three decades ago (Fig. 1). Since 1980, 58% of severe bleaching events have been recorded during four strong El Niño periods (1982–1983, 1997–1998, 2009–2010, and 2015–2016) (Fig. 2A), with the remaining 42% occurring during hot summers in other ENSO phases. Inevitably, the link between El Niño as the predominant trigger of mass bleaching (*3*–*5*) is diminishing as global warming continues (Fig. 1) and as summer temperature thresholds for bleaching are increasingly exceeded throughout all ENSO phases.

The 2015–2016 bleaching event affected 75% of the globally distributed locations we examined (Figs. 2A and *3*) and is therefore comparable in scale to the then-unprecedented 1997–1998 event, when 74% of the same 100 locations bleached. In both periods, sea surface temperatures were the warmest on record in all major coral reef regions (*2*, *19*). As the geographic footprint of recurrent bleaching spreads, fewer and fewer potential refuges from global warming remain untouched (Fig. 2B), and only 6 of the 100 locations we examined have escaped severe bleaching so far (Fig. 2B and table S1). This result is conservative because of type 2 errors (false negatives) in our analyses, where bleaching could have occurred but was not recorded.

After the extreme bleaching recorded from 2015 to 2016, the median number of severe bleaching events experienced across our study locations since 1980 is now three (Fig. 2C). Eighty-eight percent of the locations that bleached from 1997 to 1998 have bleached severely at least once again. As of 1980, 31% of reef locations have experienced four or more (up to nine) severe bleaching events (Fig. 2C), as well as many moderate episodes (table S1). Globally, the annual risk

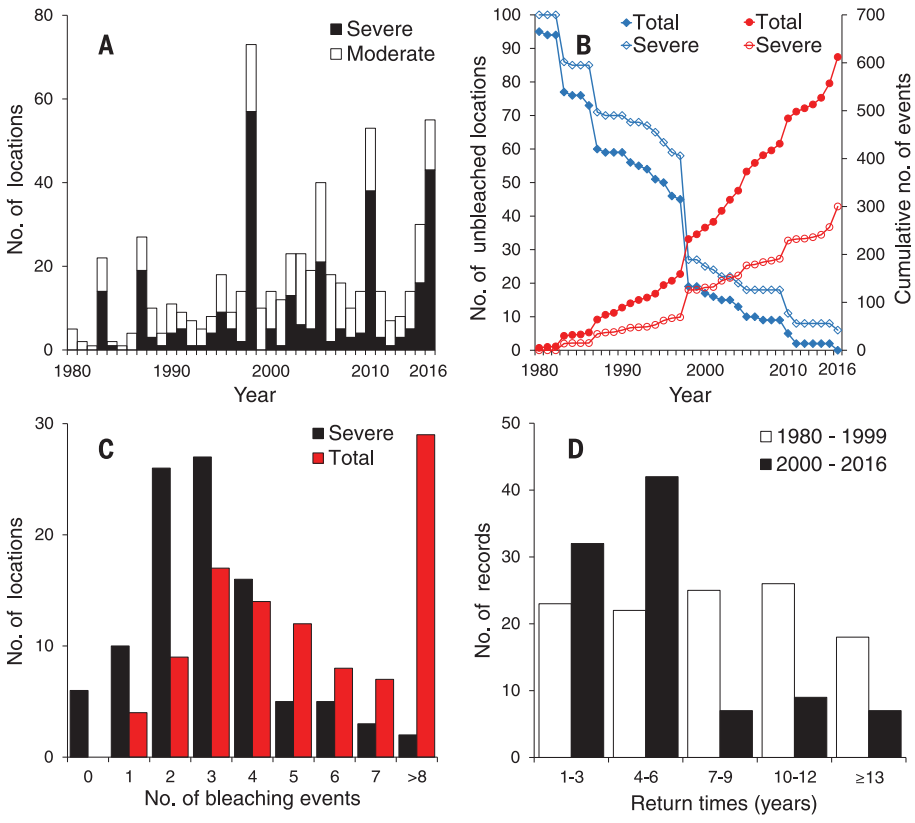

Fig. 2. Temporal patterns of recurrent coral bleaching. (**A**) Number of 100 pantropical locations that have bleached each year from 1980 to 2016. Black bars indicate severe bleaching affecting >30% of corals, and white bars depict moderate bleaching of <30% of corals. (**B**) Cumulative number of severe and total bleaching events since 1980 (red; right axis) and the depletion of locations that remain free of any bleaching or severe bleaching over time (blue; left axis). (**C**) Frequency distribution of the number of severe (black) and total bleaching events (red) per location. (**D**) Frequency distribution of return times (number of years) between successive severe bleaching events from 1980 to 1999 (white bars) and 2000 to 2016 (black bars).

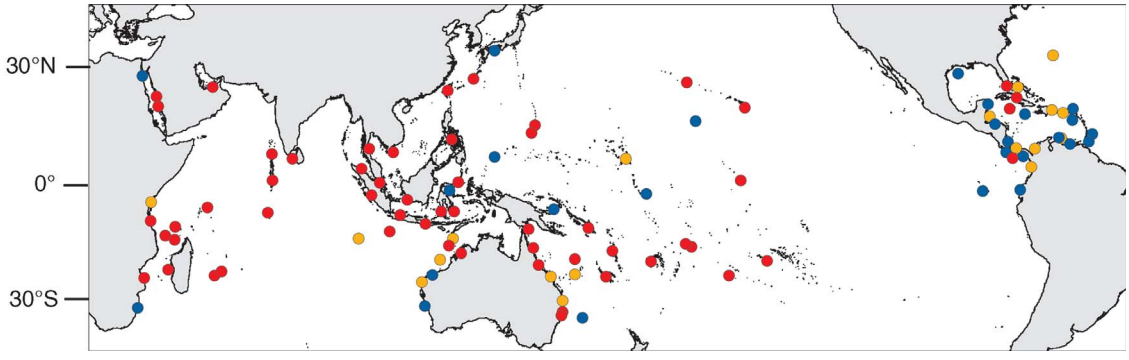

Fig. 3. The global extent of mass bleaching of corals in 2015 and 2016. Symbols show 100 reef locations that were assessed: red circles, severe bleaching affecting >30% of corals; orange circles, moderate bleaching affecting <30% of corals; and blue circles, no substantial bleaching recorded. See table S1 for further details.

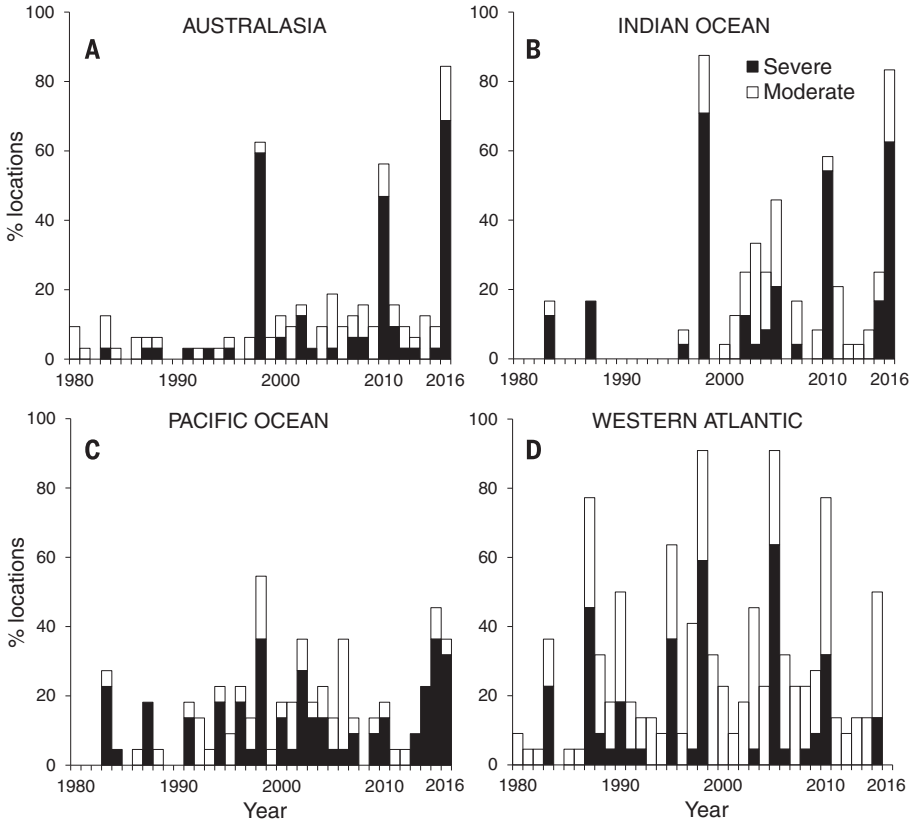

Fig. 4. Geographic variation in the timing and intensity of coral bleaching from 1980 to 2016. (**A**) Australasia (32 locations). (**B**) Indian Ocean (24 locations). (**C**) Pacific Ocean (22 locations). (**D**) Western Atlantic (22 locations). For each region, black bars indicate the percentage of locations that experienced severe bleaching, affecting >30% of corals. White bars indicate the percentage of locations per region with additional moderate bleaching affecting <30% of corals.

of bleaching (both severe and more moderate events) has increased by a rate of approximately 3.9% per annum (fig. S2), from an expected 8% of locations in the early 1980s to 31% in 2016. Similarly, the annual risk of severe bleaching has also increased, at a slightly faster rate of 4.3% per annum, from an expected 4% of locations in the early 1980s to 17% in 2016 (fig. S2). This trend corresponds to a 4.6-fold reduction in estimated return times of severe events, from once every 27 years in the early 1980s to once every 5.9 years in 2016. Thirty-three percent of return times between recurrent severe bleaching events since 2000 have been just 1, 2, or 3 years (Fig. 2D).

Our analysis also reveals strong geographic patterns in the timing, severity, and return times of mass bleaching (Fig. 4). The Western Atlantic, which has warmed earlier than elsewhere (*13*, *19*), began to experience regular bleaching sooner, with an average of 4.1 events per location before 1998, compared with 0.4 to 1.6 in other regions (Fig. 4 and fig. S2). Furthermore, widespread bleaching (affecting >50% of locations) has now occurred seven times since 1980 in the Western Atlantic, compared to three times for both Australasia and the Indian Ocean, and only twice in the Pacific. Over the entire period, the number of bleaching events has been highest in the Western Atlantic, with an average of 10 events per location, two to three times more than in other regions (Fig. 4).

In the 1980s, bleaching risk was highest in the Western Atlantic followed by the Pacific, with the Indian Ocean and Australasia having the lowest bleaching risk. However, bleaching risk increased most strongly over time in Australasia and the Middle East, at an intermediate rate in the Pacific, and slowly in the Western Atlantic (Fig. 4, fig. S3B, and tables S2 and S3). The return times between pairs of severe bleaching events are declining in all regions (fig. S3C), with the exception of the Western Atlantic, where most locations have escaped a major bleaching event from 2010 to 2016 (Fig. 2D).

We tested the hypothesis that the number of bleaching events that have occurred so far at each location is positively related to the level of postindustrial warming of sea surface temperatures that has been experienced there (fig. S4). However, we found no significant relationship for any of the four geographic regions, consistent with each bleaching event being caused by a short-lived episode of extreme heat (*12*, *19*, *20*) that is superimposed on much smaller long-term warming trends. Hence, the long-term predictions of future average warming of sea surface temperatures (*13*) are also unlikely to provide an accurate projection of bleaching risk or the location of spatial refuges over the next century.

In the coming years and decades, climate change will inevitably continue to increase the number of extreme heating events on coral reefs and further drive down the return times between them. Our analysis indicates that we are already approaching a scenario in which every hot summer, with or without an El Niño event, has the potential to cause bleaching and mortality at a regional scale. The time between recurrent events is increasingly too short to allow a full recovery of mature coral assemblages, which generally takes from 10 to 15 years for the fastest growing species and far longer for the full complement of life histories and morphologies of older assemblages (*21*–*24*). Areas that have so far escaped severe bleaching are likely to decline further in number (Fig. 2B), and the size of spatial refuges will diminish. These impacts are already underway, with an increase in average global temperature of close to 1°C. Hence, 1.5° or 2°C of warming above preindustrial conditions will inevitably contribute to further degradation of the world's coral reefs (*14*). The future condition of reefs, and the ecosystem services they provide to people, will depend critically on the trajectory of global emissions and on our diminishing capacity to build resilience to recurrent high-frequency bleaching through management of local stressors (*18*) before the next bleaching event occurs.

REFERENCES AND NOTES

1. D. L. Hartmann *et al.*, in *Climate Change 2013: The Physical Science Basis. Contribution of Working Group I to the Fifth Assessment Report of the Intergovernmental Panel on Climate Change*, T. F. Stocker, Ed. (Cambridge Univ. Press, 2013).
2. National Aeronautics and Space Administration (NASA), Global Analysis—2016 year-to-date temperatures versus previous years (2016); www.ncdc.noaa.gov/sotc/global/2016/11/supplemental/page-2.
3. P. W. Glynn, *Coral Reefs* **12**, 1–17 (1993).
4. G. M. Wellington, P. W. Glynn, in *Geological Approaches to Coral Reef Ecology*, R. B. Aronson, Ed. (Springer, 2007).
5. J. K. Oliver, R. Berkelmans, C. M. Eakin, in *Ecological Studies: Analysis and Synthesis*, M. J. H. van Oppen, J. M. Lough, Eds. (Springer, 2009).
6. J. A. Kleypas, G. Danabasoglu, J. M. Lough, *Geophys. Res. Lett.* **35**, L03613 (2008).
7. S. D. Donner, G. J. M. Rickbeil, S. F. Heron, *PLOS ONE* **12**, e0175490 (2017).
8. A. C. Baker, P. W. Glynn, B. Riegl, *Estuar. Coast. Shelf Sci.* **80**, 435–471 (2008).
9. T. P. Hughes *et al.*, *Science* **301**, 929–933 (2003).
10. J. E. Carilli, R. D. Norris, B. Black, S. M. Walsh, M. McField, *Glob. Change Biol.* **16**, 1247–1257 (2010).
11. A. H. Baird, P. A. Marshall, *Mar. Ecol. Prog. Ser.* **237**, 133–141 (2002).
12. M. D. Spalding, B. E. Brown, *Science* **350**, 769–771 (2015).
13. O. Hoegh-Guldberg *et al.*, in *Climate Change 2014: Impacts, Adaptation and Vulnerability. Part B: Regional Aspects: Contribution of Working Group II to the Fifth Assessment Report of the Intergovernmental Panel on Climate Change*, T. F. Stocker, Ed. (Cambridge Univ. Press, 2013).

14. S. F. Heron, J. A. Maynard, R. van Hooidonk, C. M. Eakin, *Sci. Rep.* **6**, 38402 (2016).
15. R. van Hooidonk, J. A. Maynard, S. Planes, *Nat. Clim. Chang.* **3**, 508–511 (2013).
16. P. J. Crutzen, in *Earth System Science in the Anthropocene*, E. Ehlers, T. Krafft, Eds. (Springer, 2006).
17. J. Rockström *et al.*, *Nature* **461**, 472–475 (2009).
18. T. P. Hughes *et al.*, *Nature* **546**, 82–90 (2017).
19. J. M. Lough, *Geophys. Res. Lett.* **27**, 3901–3904 (2000).
20. T. P. Hughes *et al.*, *Nature* **543**, 373–377 (2017).
21. H. Kayanne, S. Harii, Y. Ide, F. Akimoto, *Mar. Ecol. Prog. Ser.* **239**, 93–103 (2002).
22. J. P. Gilmour, L. D. Smith, A. J. Heyward, A. H. Baird, M. S. Pratchett, *Science* **340**, 69–71 (2013).
23. P. W. Glynn, B. Riegl, S. Purkis, J. M. Kerr, T. B. Smith, *Coral Reefs* **34**, 421–436 (2015).
24. T. R. McClanahan, *Coral Reefs* **33**, 939–950 (2014).

ACKNOWLEDGMENTS

Major funding for this research was provided by the Australian Research Council's Centre of Excellence Program (CE140100020). The contents of this manuscript are solely the opinions of the authors and do not constitute a statement of policy, decision, or position on behalf of the National Oceanic and Atmospheric Administration or the U.S. government. Data reported in this paper are tabulated in the supplementary materials.

SUPPLEMENTARY MATERIALS

www.sciencemag.org/content/359/6371/80/suppl/DC1
Materials and Methods
Figs. S1 to S4
Tables S1 to S3
References (*25*–*29*)

26 May 2017; accepted 5 December 2017
10.1126/science.aan8048

ECOLOGICAL GENOMICS

Genomic signals of selection predict climate-driven population declines in a migratory bird

Rachael A. Bay,[1,2]* Ryan J. Harrigan,[1] Vinh Le Underwood,[1] H. Lisle Gibbs,[3] Thomas B. Smith,[1,4] Kristen Ruegg[1,5]

The ongoing loss of biodiversity caused by rapid climatic shifts requires accurate models for predicting species' responses. Despite evidence that evolutionary adaptation could mitigate climate change impacts, evolution is rarely integrated into predictive models. Integrating population genomics and environmental data, we identified genomic variation associated with climate across the breeding range of the migratory songbird, yellow warbler (*Setophaga petechia*). Populations requiring the greatest shifts in allele frequencies to keep pace with future climate change have experienced the largest population declines, suggesting that failure to adapt may have already negatively affected populations. Broadly, our study suggests that the integration of genomic adaptation can increase the accuracy of future species distribution models and ultimately guide more effective mitigation efforts.

Anthropogenic climate change is having a marked impact on Earth's biodiversity (*1*). Rapid fluctuations in temperature and precipitation can alter the suitability of particular regions and in some cases, exceed the physiological limits of organisms (*2*, *3*). The mismatch between environment and physiology can lead to shifts in species ranges, population declines, or even extinction (*4*–*6*). The difference between these evolutionary outcomes can in part be determined by the adaptive capacity of a species; those that possess standing genetic variation for climate-related traits are most likely to have the ability to adapt to rapidly changing environments (*7*, *8*). Understanding the effects and distributions of potentially adaptive alleles associated with climate can therefore aid efforts to accurately predict species responses to future conditions (*9*), and aid in mitigation efforts.

Although migratory birds are highly sensitive to climate change (*10*–*12*), little is understood about how populations differ in adaptive capacity. Breeding ranges of North American migrants have shifted northward (*13*), but microevolutionary responses associated with these shifts remain poorly documented. Although genome-wide associations with climate variables have been shown to affect many groups across the tree of life (*14*–*16*), in migratory species it is less clear to what extent genomic variation is shaped by environmental variables. Here, we examined the genomic basis of climate adaptation in a North American migratory bird, the yellow warbler (*Setophaga petechia*). Yellow warblers have a broad breeding range across the United States and Canada and are common throughout their range, though they have experienced local population declines and, in some regions, are listed as a species of concern (*17*). Because of their broad distribution, yellow warblers inhabit a large range of environmental conditions, making them an ideal system for investigating variation in local climate adaptation.

We used restriction site–associated DNA sequencing (RAD-Seq) to test for signals of selection across the breeding range. We examined 104,711 single-nucleotide polymorphisms (SNPs) in 229 individuals from 21 locations (table S1 and fig. S1), using our assembly of the first yellow warbler genome (*18*). Pairwise genetic distance between locations ($F_{ST}/1 - F_{ST}$) was highly correlated with geographic distance, suggesting a strong signal of isolation by distance (Fig. 1A: Mantel's $r = 0.85$, $P = 1 \times 10^{-5}$), consistent with previous findings using microsatellite loci (*19*). Analysis of population structure using ADMIXTURE found little evidence of substructure, consistent with strong isolation by distance (fig. S2). Genetic distance was also significantly associated with environmental distance, based on climate variables, vegetation indices, and elevation, downloaded from public environmental databases (Fig. 1B: Mantel's $r = 0.36$; $P = 0.0006$). In a multiple regression of distance matrices, only geographic distance was significant (MRM: $R^2 = 0.73$; geography $P = 1 \times 10^{-5}$; environment $P = 0.12$), suggesting that isolation by distance is the strongest force structuring genome-wide variation. This result is not unexpected, however, because environmental adaptation likely affects a small fraction of the genome (*9*). We used gradient forest (*20*), a machine-learning regression tree-based approach, to test whether a subset of genomic variation can be explained by environment and to visualize climate-associated genetic variation across the breeding range (Fig. 1, C and D). Strong differences in environmentally associated genetic variation are apparent across longitude and latitude, and unique genotype-environment associations are present in the Rocky Mountains and Coastal British Columbia. Our results suggest that despite high dispersal capacity and vagility via annual migration, yellow warblers exhibit standing genetic variation associated with the environment among populations and are likely subject to environmentally mediated selection during the breeding season.

To investigate which populations might be most vulnerable to future climate change, we defined the metric "genomic vulnerability" as the mismatch between current and predicted future genomic variation based on genotype-environment relationships modeled across contemporary populations. We followed the method presented in Fitzpatrick and Keller (*21*) to calculate genomic vulnerability using an extension of the gradient forest analysis. Populations with the greatest mismatch are least likely to adapt quickly enough to track future climate shifts, potentially resulting in population declines or extirpations. Under future climate change scenarios [representative concentration pathways—RCPs—defined by the Intergovernmental Panel on Climate Change (*22*)], the regions with highest genomic vulnerability stretch from the southern Rocky Mountains to Alaska, along with patchy regions in the Eastern United States (Fig. 2A). As expected, genomic vulnerability increases under more severe climate change scenarios; under the most extreme scenario (RCP8.0), nearly the entire range is estimated to have high genomic vulnerability (fig. S4).

If future climate change is correlated with recent shifts (for example, if regional drying over the last century in some regions will continue and become more severe), we expect that recent climate change will have already negatively affected populations with high genomic vulnerability. We tested this idea by comparing genomic vulnerability scores (using 2050 RCP2.6, though the results were robust to different scenarios; fig. S4) to population trends estimated from North American Breeding Bird Surveys (*23*) (Fig. 2B). Regions that had higher genomic vulnerability scores experienced the largest population declines over the past half century [generalized additive model (GAM): adjusted $R^2 = 0.101$; $P < 0.001$; Fig. 2C], showing that populations already in decline are most vulnerable to future climate change and suggesting that a mismatch between genomic variation and climate may have already resulted in negative impacts. We believe that genomic vulnerability can therefore be used alongside other known causes of population decline, such as habitat degradation and avian disease, to understand and predict population dynamics.

Understanding which environmental variables are most closely associated with local adaptation to particular climate conditions and vulnerability

[1]Center for Tropical Research, Institute for the Environment and Sustainability, University of California–Los Angeles, Los Angeles, CA 90095, USA. [2]Department of Evolution and Ecology, University of California, Davis, CA 95616, USA. [3]Department of Evolution, Ecology, and Organismal Biology and Ohio Biodiversity Conservation Partnership, Ohio State University, Columbus, OH 43210, USA. [4]Department of Ecology and Evolutionary Biology, University of California, 621 Charles E. Young Drive South, Los Angeles, CA 90095, USA. [5]Department of Ecology and Evolutionary Biology, University of California, Santa Cruz, CA 95064, USA.
*Corresponding author. Email: rachaelbay@gmail.com

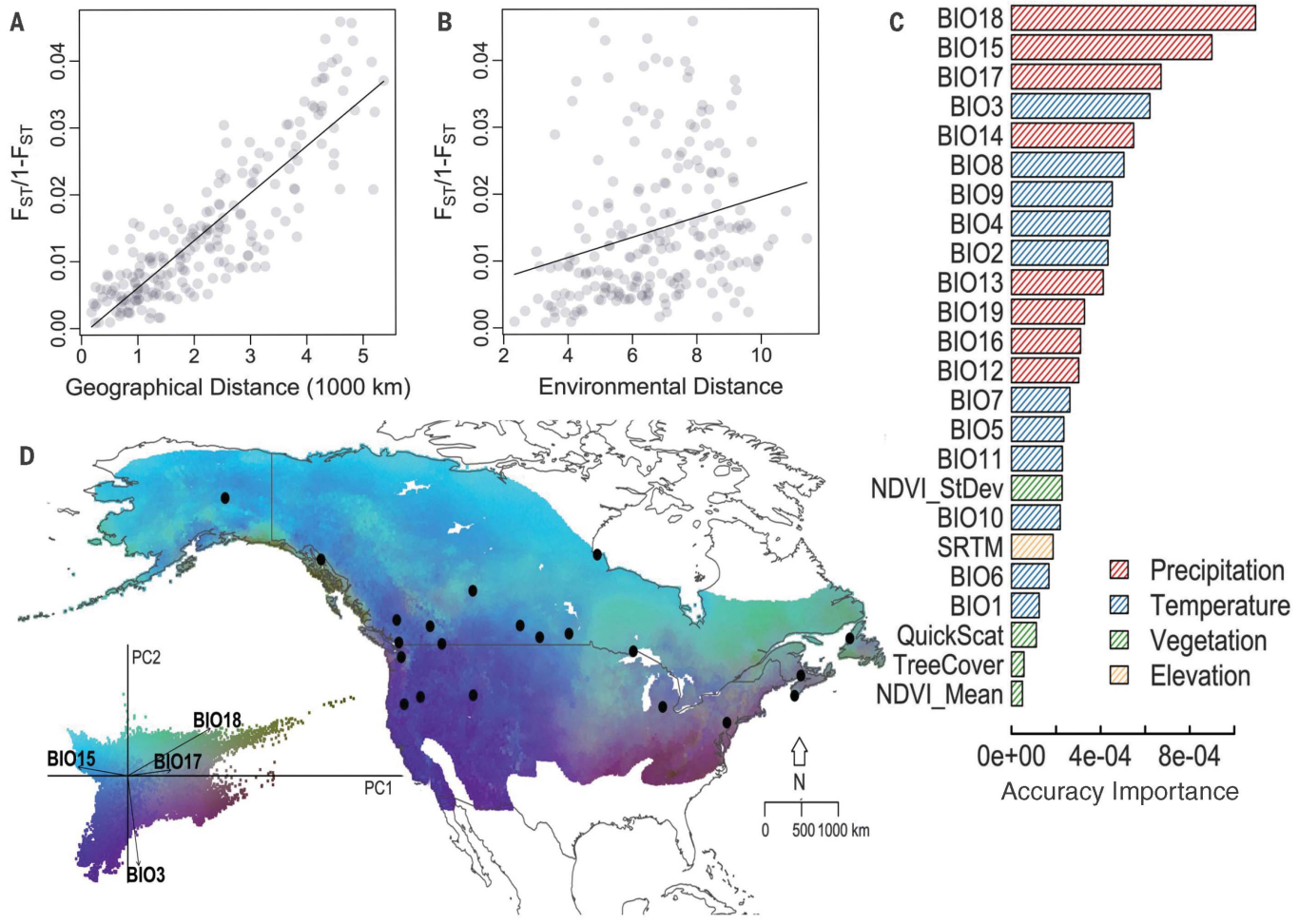

Fig. 1. Geography and environment explain genomic variation in yellow warblers. (**A**) Pairwise genetic distance ($F_{ST}/1 - F_{ST}$) is associated with geographical distance and (**B**) environmental distance. (**C**) Ranked importance of environmental variables based on gradient forest analysis shows that climate, especially precipitation, strongly explains genomic variation. (**D**) Gradient forest-transformed climate variables show climate adaptation across the breeding range. Colors are based on principal components analysis (PCA) of transformed climate variables [(D) inset: loadings of all variables are shown in fig. S3]. Points on map reflect sampled locations, and arrows on PCA show the loadings of top climate variables on PCA.

can prove useful in determining the biological mechanisms involved in population declines. Climate variables, especially precipitation measures, were most strongly associated with genomic variation across the breeding range of yellow warblers (Fig. 1C). Of the 25 environmental variables tested in the gradient forest analysis, the top three explanatory variables were precipitation related: (i) precipitation of the warmest quarter (BIO18), (ii) seasonality of precipitation (BIO15), and (iii) precipitation of the driest quarter (BIO17). Overall, precipitation variables were most important, followed by temperature variables and to a lesser extent, vegetation and elevation variables, suggesting that adaptation to precipitation is important on the breeding grounds.

To investigate the genomic basis of adaptation across contemporary climate gradients, we identified genomic regions associated with the top precipitation-related variables using latent factor mixed models (LFMMs) (*24*), which test for associations between genotypes and environments while accounting for background population structure (Fig. 3A and fig. S5). We found 85, 67, and 35 SNPs associated with climate variables BIO18, BIO15, and BIO17 (described above), respectively [false discovery rate (FDR)–corrected $P < 0.05$]. These SNPs were broadly distributed across the genome, on 27 chromosomes (table S2). For the 13 SNPs associated with all three variables, we identified 12 adjacent genes with a range of functions including zinc finger genes (*ZNF397* and *ZKscan1*), peptide secretion (*SCT* and *MUC4*), and transmembrane proteins (CDHR5, SLC25A33, and TEMEM201). Targeted genotyping using Fluidigm assays for 17 SNPs associated with climate in the LFMM analysis in an additional 309 birds at 29 locations independently validated climate associations in 8 out of 17 SNPs (FDR-corrected $P < 0.05$; table S3) with marginal associations in an additional two SNPs (FDR-corrected $P < 0.1$).

One of the strongest associations between genotype and climate was upstream of genes with known function in avian behavior and migration. A SNP on chromosome 5 was very strongly associated with all three top environmental variables (LFMM $P < 0.001$; Fig. 3), and these associations were validated with Fluidigm assays ($P < 0.001$; Fig. 3, C and D). The highest allele frequencies at this SNP occurred in the Maritime provinces of Canada (Nova Scotia and Newfoundland), areas of high rainfall and low seasonality. This SNP is upstream of two genes, *DRD4* and *DEAF1* (Fig. 3B), that have known associations with migration in birds (*25*, *26*). The *DRD4* gene in particular, a dopamine receptor, has been extensively studied for its involvement in novelty-seeking behavior in primates, fish, and birds (*26*). Polymorphisms in this gene are linked to novelty-seeking or exploratory behavior in a number of bird species (*27*, *28*), and linkage blocks extend into the neighboring *DEAF1* gene, a transcription factor involved in serotonergenic signaling. The exploratory phenotype has been linked to dispersal, which is thought to allow species to occupy new environments (*25*), but experimental studies linking behavior, genotype, and environment are needed to fully understand how these variants might

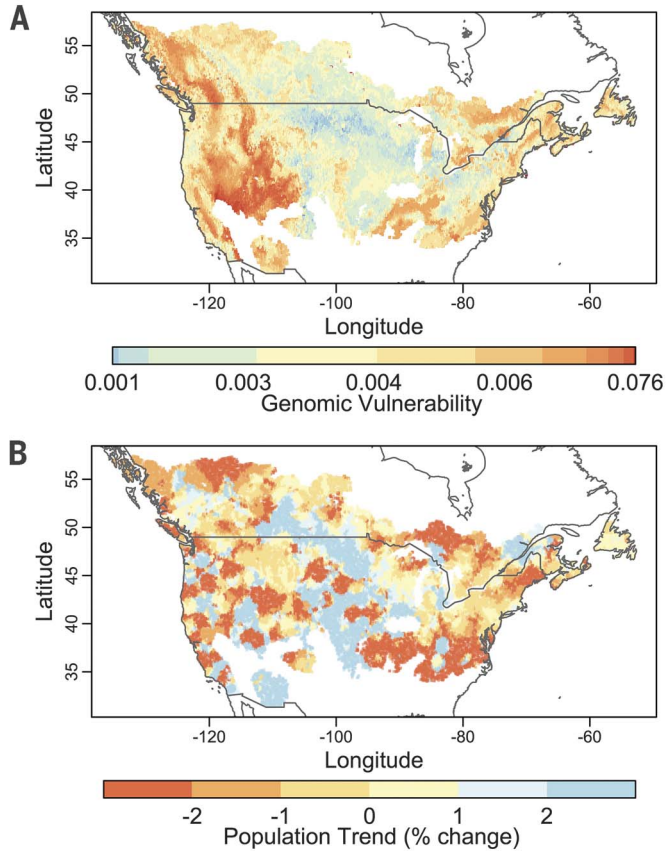

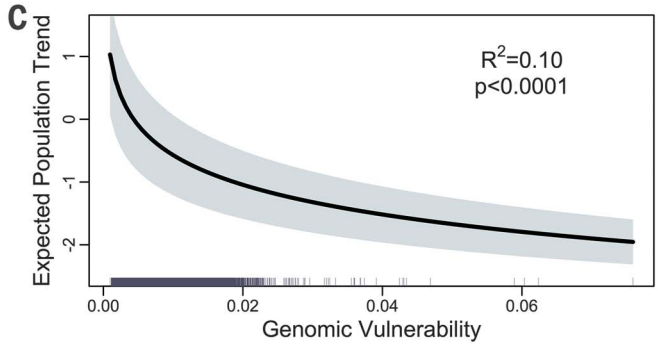

Fig. 2. Genomic vulnerability to future climate change is associated with a higher probability of population decline. (**A**) Genomic vulnerability based on 2050 RCP2.6 projections. (**B**) Population trend estimates (percent change per year) for yellow warblers based on North American Breeding Bird Survey analysis (*23*). (**C**) Generalized additive model (GAM) showing the relationship between population trend and predicted genomic vulnerability. The black line represents the model fit, and the shaded area is the 95% confidence interval.

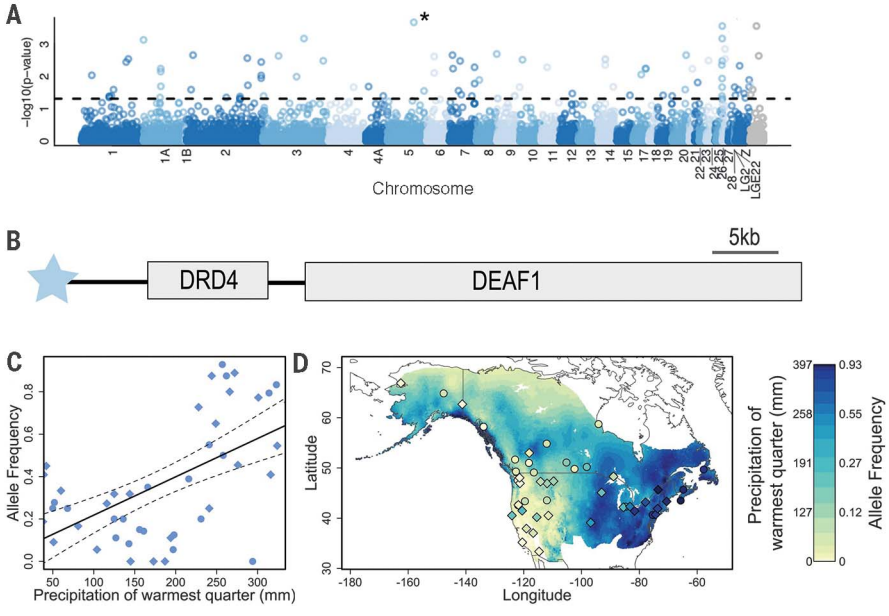

Fig. 3. Genome-wide variation associated with climate variables. (**A**) Manhattan plots show the significance level (FDR-corrected) for SNP associations with precipitation of the warmest month (BIO18). Dashed line represents $P = 0.05$. Colors distinguish different chromosomes, and gray points are SNPs on scaffolds not anchored to a chromosome. (**B**) The most significant SNP association, marked with an asterisk (*) in (A), is upstream from the *DRD4* and *DEAF1* genes. (**C** and **D**) Correlations between allele frequency and BIO18 for this SNP. Samples genotyped by RAD-Seq are represented as circles, and samples genotyped with Fluidigm assays are shown as diamonds.

be involved in climate adaptation. However, this SNP represents a single locus with significant associations between genotype and environment, but many other highly significant candidates exist (table S2), highlighting the complex and polygenic nature of climate adaptation.

Expected patterns of environmentally mediated evolution in migratory animals are complex but could drastically alter predictions of species response to climate change. We showed that standing variation for adaptation to different climate regimes exists and that natural selection during breeding months is driving evolutionary shifts in the genome. High genomic vulnerability, or mismatch between current allelic variation and future environmental conditions, was correlated with a higher likelihood of population decline, suggesting that yellow warbler populations may have already experienced some negative impacts of climate change over the past 50 years.

Our results show how the integration of genomic, environmental, and demographic data can provide a more thorough understanding of future climate change impacts on a migratory bird species. More broadly, we illustrate a new approach for understanding climate-associated causes of current and future declines and an important tool for making more-informed conservation decisions.

REFERENCES AND NOTES

1. B. R. Scheffers *et al*., *Science* **354**, aaf7671 (2016).
2. G. N. Somero, *J. Exp. Biol.* **213**, 912–920 (2010).
3. C. Parmesan, *Annu. Rev. Ecol. Evol. Syst.* **37**, 637–669 (2006).
4. M. L. Pinsky, B. Worm, M. J. Fogarty, J. L. Sarmiento, S. A. Levin, *Science* **341**, 1239–1242 (2013).
5. M. C. Urban, *Science* **348**, 571–573 (2015).
6. C. Parmesan, G. Yohe, *Nature* **421**, 37–42 (2003).
7. R. D. Barrett, D. Schluter, *Trends Ecol. Evol.* **23**, 38–44 (2008).
8. S. N. Aitken, S. Yeaman, J. A. Holliday, T. Wang, S. Curtis-McLane, *Evol. Appl.* **1**, 95–111 (2008).
9. R. A. Bay *et al*., *Am. Nat.* **189**, 463–473 (2017).
10. M. E. Visser *et al*., *PLOS Biol.* **13**, e1002120–e17 (2015).
11. N. Jonzén *et al*., *Science* **312**, 1959–1961 (2006).
12. C. Both, S. Bouwhuis, C. M. Lessells, M. E. Visser, *Nature* **441**, 81–83 (2006).
13. A. T. Hitch, P. L. Leberg, *Conserv. Biol.* **21**, 534–539 (2007).
14. A. M. Hancock *et al*., *Science* **334**, 83–86 (2011).
15. R. A. Bay, S. R. Palumbi, *Curr. Biol.* **24**, 2952–2956 (2014).
16. J. R. Lasky *et al*., *Sci. Adv.* **1**, e1400218–e1400218 (2015).
17. W. D. Shuford, T. Gardali, Eds., "California Bird Species of Special Concern: A ranked assessment of species, subspecies, and distinct populations of birds of immediate conservation concern in California" (2008), pp. 332–339.
18. Materials and methods are available as supplementary materials.
19. H. L. Gibbs, R. J. G. Dawson, K. A. Hobson, *Mol. Ecol.* **9**, 2137–2147 (2000).
20. N. Ellis, S. J. Smith, C. R. Pitcher, *Ecology* **93**, 156–168 (2012).
21. M. C. Fitzpatrick, S. R. Keller, *Ecol. Lett.* **18**, 1–16 (2015).
22. Intergovernmental Panel on Climate Change, *Climate Change 2014: Synthesis Report* (IPCC, Geneva, Switzerland, 2014), pp. 151–206.
23. J. R. Sauer, J. E. Hines, J. E. Fallon, K. L. Pardieck, *The North American Breeding Bird Survey, Results and Analysis 1966-2012, Version 02.19. 2014* (U.S. Geological Survey, 2014).
24. E. Frichot, S. D. Schoville, G. Bouchard, O. François, *Mol. Biol. Evol.* **30**, 1687–1699 (2013).
25. M. Liedvogel, S. Åkesson, S. Bensch, *Trends Ecol. Evol.* **26**, 561–569 (2011).
26. A. Fidler, in *From Genes to Animal Behavior* (Springer Japan, Tokyo, 2011), *Primatology Monographs*, pp. 275–294.
27. L. Z. Garamszegi *et al*., *Ecol. Evol.* **4**, 1466–1479 (2014).
28. J. C. Mueller *et al*., *Mol. Ecol.* **22**, 2797–2809 (2013).

ACKNOWLEDGMENTS

The yellow warbler genome and annotations are available through DRYAD (doi:10.5061/dryad.dm540) and population-level RAD-Seq data are available through the National Center for Biotechnology Information's Sequence Read Archive. We thank many people who assisted in sample collection, especially M. Boulet, R. Dawson, E. Milot, K. Hobson, B. Keith, the University of Washington Burke Museum, S. Albert, and T. Kita, and many Institute for Bird Populations and MAPS (Monitoring Avian Productivity and Survivorship) volunteers for providing or assisting with collection of samples. We thank L. Frishkoff for advice on statistical analysis and N. Rose and D. Karp for helpful comments on the manuscript. This work used the Extreme Science and Engineering Discovery Environment (XSEDE), which is supported by National Science Foundation grant ACI-1548562. This work was made possible by a generous gift from J. Ellis as well as funding from an NSF Postdoctoral Fellowship (to R.A.B.), NSF grant PD-08-1269 (to R.J.H.), and NSF grant IIA PIRE 1243524 (to T.B.S.), and support from M. Nicholson, the California Energy Commission grant EPC-15-043, and First Solar Incorporated.

SUPPLEMENTARY MATERIALS

www.sciencemag.org/content/359/6371/83/suppl/DC1
Materials and Methods
Figs. S1 to S7
Tables S1 to S3
References (*29*–*48*)

19 April 2017; accepted 16 November 2017
10.1126/science.aan4380

HIV SUSCEPTIBILITY

Elevated *HLA-A* expression impairs HIV control through inhibition of NKG2A-expressing cells

Veron Ramsuran,[1,2,3,4]* Vivek Naranbhai,[1,2,4,5]* Amir Horowitz,[6] Ying Qi,[1] Maureen P. Martin,[1] Yuko Yuki,[1] Xiaojiang Gao,[1] Victoria Walker-Sperling,[7] Gregory Q. Del Prete,[8] Douglas K. Schneider,[8] Jeffrey D. Lifson,[8] Jacques Fellay,[9] Steven G. Deeks,[10] Jeffrey N. Martin,[11] James J. Goedert,[12] Steven M. Wolinsky,[13] Nelson L. Michael,[14] Gregory D. Kirk,[15] Susan Buchbinder,[10,11,16] David Haas,[17] Thumbi Ndung'u,[2,18,19,20] Philip Goulder,[18,21] Peter Parham,[22] Bruce D. Walker,[2,18,23] Jonathan M. Carlson,[24] Mary Carrington[1,2]†

The highly polymorphic human leukocyte antigen (*HLA*) locus encodes cell surface proteins that are critical for immunity. *HLA-A* expression levels vary in an allele-dependent manner, diversifying allele-specific effects beyond peptide-binding preference. Analysis of 9763 HIV-infected individuals from 21 cohorts shows that higher *HLA-A* levels confer poorer control of HIV. Elevated *HLA-A* expression provides enhanced levels of an HLA-A–derived signal peptide that specifically binds and determines expression levels of HLA-E, the ligand for the inhibitory NKG2A natural killer (NK) cell receptor. *HLA-B* haplotypes that favor NKG2A-mediated NK cell licensing (i.e., education) exacerbate the deleterious effect of high *HLA-A* on HIV control, consistent with NKG2A-mediated inhibition impairing NK cell clearance of HIV-infected targets. Therapeutic blockade of HLA-E:NKG2A interaction may yield benefit in HIV disease.

Diversity within regions of human leukocyte antigen (HLA) class I molecules that determine peptide-binding specificity has a major impact on human disease pathogenesis. Variation in expression levels across alleles of certain *HLA* genes has also been shown to associate with disease outcome (*1*–*6*), emphasizing the importance of *HLA* polymorphism that determines characteristics other than peptide specificity alone. Elevated expression levels of HLA-C associates with reduced HIV viral load (VL) (*1*), resulting, in part, from a greater frequency of cytotoxic T lymphocyte (CTL) responses to HLA-C–restricted peptides with increasing HLA-C. Like *HLA-C*, *HLA-A* alleles vary in expression levels in an allotype-specific manner (*7*), but these two class I loci have many distinguishing characteristics. Compared with HLA-C, HLA-A is expressed at a 13- to 18-fold higher level on the cell surface (*8*) and is about twofold more polymorphic. Mechanisms of transcriptional regulation for these two loci are also distinct under healthy conditions (*7*, *9*, *10*). These and other differences may affect how these two loci affect human disease.

We verified that the pattern of allele-specific variation in *HLA-A* expression levels was not modified by HIV infection by comparing *HLA-A* expression in 243 HIV-uninfected and 162 HIV-infected ethnicity-matched individuals (fig. S1). Being HIV infected did not associate with a change in the overall level of *HLA-A* mRNA expression ($Effect_{unadjusted}$ = 0.00, SE = 0.07, P =1), nor did HIV status modify expression estimates for any single *HLA-A* allele (interaction P-values were 0.226 to 0.987 for each of the alleles tested). Therefore, in HIV infection, the gradient in *HLA-A* expression level attributable to each allele is similar to that in healthy individuals.

To test whether *HLA-A* expression levels are associated with HIV control, we examined a pooled data set of 2298 HIV-infected (clade C) individuals recruited at 11 sites in sub-Saharan Africa, in which the estimated effect of each *HLA* allele on HIV VL measured cross-sectionally has been reported (*11*). The *HLA-A* expression level of each allele, estimated for black African individuals, was positively correlated with the estimate of effect of that allele on HIV VL (correlation coefficient R = 0.54, P = 0.007, Fig. 1A and Table 1).

Next, we sought to validate the discovery of a deleterious effect of elevated *HLA-A* expression level in independent cohorts with prospective follow-up and of broader demographic background. We included 62,843 VL measurements obtained longitudinally over a total of 32,804 person years of antiretroviral therapy–free observation time (median 2.86 years per individual) in 5818 individuals enrolled in one of six studies in the USA or one study in Switzerland (see online methods). We modeled *HLA-A* expression as z-scores (equivalent to one standard deviation change in expression level), using mRNA levels measured in 436 white and black healthy donors (table S1). Consistent with the discovery analysis among sub-Saharan Africans, elevated *HLA-A* expression levels were significantly associated with higher HIV viremia, even after accounting for the individual allelic effects of *HLA-A*, *-B*, and *-C*. For every one z-score increase in *HLA-A* expression level, the VL increase over time was 0.06 $\log_{10}$ copies/ml higher ($P = 4.4 \times 10^{-19}$; Table 1). Grouping individuals by estimated *HLA-A* expression level demonstrates the effect of increasing *HLA-A* expression on unadjusted HIV VL (Fig. 1B).

The association between *HLA-A* expression level and HIV viremia was independently significant in each ethnicity stratum ($P_{whites} = 6.1 \times 10^{-6}$; $P_{Africans/African\text{-}Americans} = 1.1 \times 10^{-18}$; and $P_{Hispanic/other} = 2.3 \times 10^{-10}$), notwithstanding distinct *HLA-A* allelic frequencies in each ethnic group. Among 2019 donors enrolled during acute, early HIV infection with known dates of seroconversion, elevated *HLA-A* expression was similarly associated with higher VL ($P = 2.5 \times 10^{-9}$), confirming that this finding is unlikely to be confounded by frailty bias. *HLA-A* expression level was associated with a spectrum of alternative HIV outcomes, including elevated mean VL ($P = 9.3 \times 10^{-12}$) and odds of being an HIV noncontroller (HIV VL >10,000 copies/ml) relative to being a controller (HIV VL <2000 copies/ml) ($P = 9.2 \times 10^{-11}$). Furthermore, among 2100 individuals for whom longitudinal $CD4^+$ T cell count measures

[1]Cancer and Inflammation Program, Leidos Biomedical Research, Inc., Frederick National Laboratory for Cancer Research, Frederick, MD 21702, USA. [2]Ragon Institute of Massachusetts General Hospital, Massachusetts Institute of Technology and Harvard University, Cambridge, MA 02139, USA. [3]KwaZulu-Natal Research Innovation and Sequencing Platform (KRISP), School of Laboratory Medicine and Medical Sciences, University of KwaZulu-Natal, Durban, South Africa. [4]Centre for the AIDS Programme of Research in South Africa (CAPRISA), Durban, South Africa. [5]Wellcome Trust Centre for Human Genetics, Nuffield Department of Medicine, University of Oxford, Oxford, UK. [6]Department of Oncological Sciences, Precision Immunology Institute, Icahn School of Medicine at Mount Sinai, New York, NY 10029, USA. [7]Cancer and Inflammation Program, Center for Cancer Research, National Cancer Institute, National Institutes of Health, Frederick, MD 21702, USA. [8]AIDS and Cancer Virus Program, Leidos Biomedical Research, Inc., Frederick National Laboratory for Cancer Research, Frederick, MD 21702, USA. [9]School of Life Sciences, École Polytechnique Fédérale de Lausanne, and Swiss Institute of Bioinformatics, Lausanne, Switzerland. [10]Department of Medicine University of California, San Francisco, CA 94143, USA. [11]Department of Epidemiology and Biostatistics, University of California, San Francisco, CA 94143, USA. [12]Infections and Immunoepidemiology Branch, Division of Cancer Epidemiology and Genetics, National Cancer Institute, National Institutes of Health, Rockville, MD 20850, USA. [13]Division of Infectious Diseases, The Feinberg School of Medicine, Northwestern University, Chicago, IL 60611, USA. [14]U.S. Military HIV Research Program, Walter Reed Army Institute of Research, Silver Spring, MD 20910, USA. [15]Department of Epidemiology, Johns Hopkins University Bloomberg School of Public Health, Baltimore, MD 21205, USA. [16]San Francisco Department of Public Health, HIV Research Section, San Francisco, CA 94102, USA. [17]Vanderbilt University School of Medicine, Nashville, TN 37232, USA. [18]African Health Research Institute, Durban, South Africa. [19]HIV Pathogenesis Programme, Doris Duke Medical Research Institute, Nelson R. Mandela School of Medicine, University of KwaZulu-Natal, Durban, South Africa. [20]Max Planck Institute for Infection Biology, Berlin, Germany. [21]Department of Paediatrics, University of Oxford, Oxford, UK. [22]Departments of Structural Biology and Microbiology and Immunology, Stanford University, Stanford, CA 94305, USA. [23]Institute for Medical and Engineering Sciences, Massachusetts Institute of Technology, Cambridge, MA 02139, USA. [24]Microsoft Research, Redmond, WA 98052, USA.
*These authors contributed equally to this work.
†Corresponding author. Email: carringm@mail.nih.gov

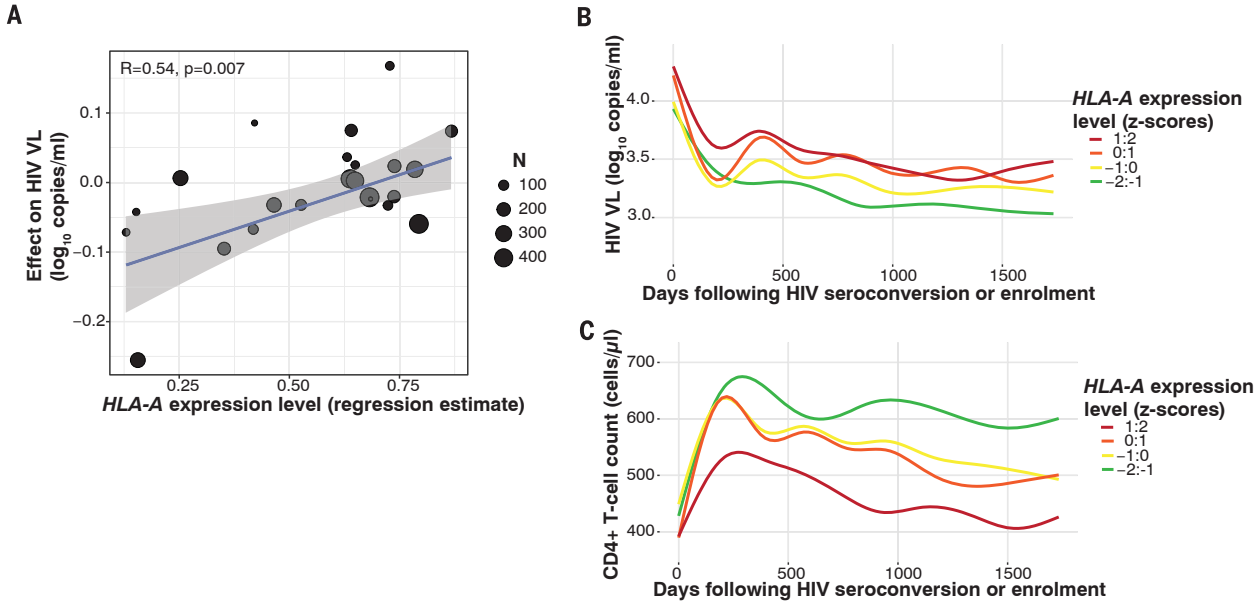

Fig. 1. Elevated *HLA-A* expression levels are associated with increased HIV viremia and reduced CD4$^+$ T cell counts. (**A**) Data represent 2298 HIV-infected individuals from South Africa, Botswana, and Zambia, enrolled at 11 sites with cross-sectionally measured VLs. Each dot represents the average estimated expression level for a specific *HLA-A* allele by that allele's reported effect on cross-sectional VL (*11*). A linear regression line is shown in blue with 95% confidence interval in gray. The size of each point is scaled by the number of contributing alleles; however, the correlation estimate is not weighted. (**B**) HIV viremia among 5818 HIV-infected adults and (**C**) CD4$^+$ T cell counts among 2100 HIV-infected adults followed prospectively and grouped according to one-unit *z*-score change in *HLA-A* expression. VLs are plotted against time following seroconversion or date of enrollment (censored at ~5 years). In (B) and (C), lines are best fit (LOWESS lines) to unadjusted VL or CD4 counts.

were available, higher *HLA-A* expression was strongly, and substantially, associated with reduced CD4$^+$ T cell counts (Table 1). The effects of *HLA-A* expression levels on VL and CD4 count were stable over time (Fig. 1, B and C), consistent with a temporally sustained mechanism. Finally, we examined a partially nonoverlapping (39.1% of donors were not included in the VL analyses) collection of five natural-history cohorts, including 1159 antiretroviral-naïve individuals followed prospectively after HIV infection. Even in this limited sample, elevated *HLA-A* expression was associated with accelerated progression to $AIDS_{1987}$ ($P = 0.04$) and progression to CD4$^+$ T cell count of <200 cells/μl ($P = 0.02$), again after adjusting for all individual HLA alleles.

HLA-A expression levels vary across alleles in a continuous manner, indicating multiple polymorphic regulatory sites that together determine the expression level of any given allele. As no single variant controls *HLA-A* expression levels, genome-wide association studies (GWAS) are not expected to detect such effects. Using formal *HLA-A* typing results, we inferred expression level for 3057 white, Hispanic, and black individuals included in the International HIV Controllers GWAS (*12*) (40% of whom were not included in any of the analyses described above). *HLA-A* expression was significantly associated with HIV elite controller or noncontroller status even after adjusting for population structure ($P = 2.7 \times 10^{-5}$). This observation emphasizes a limitation of GWAS when the combined effects of multiple genetic variants determine a phenotype.

Next, we sought to determine the likely mechanism(s) for the finding that elevated *HLA-A* expression associates with impaired HIV control. HLA-E serves as a ligand for the strongly inhibitory receptor CD94/NKG2A expressed on both natural killer (NK) cells and T cells. Expression of HLA-E is dependent on stable binding of a signal peptide derived from the leader sequence of HLA-A, -B and -C molecules (residues −22 to −14 relative to the mature protein) (*13*, *14*). Methionine at position 2 of the signal peptide (residue −21) stabilizes and promotes HLA-E expression, and all HLA-A and -C allotypes are fixed for methionine, whereas *HLA-B* contains a polymorphism that encodes either methionine (−21M) or threonine (−21T) at this position (*15*, *16*). Unlike *HLA-A*, there is minimal variance in *HLA-B* transcriptional levels across alleles and individuals (*17*), so HLA-E expression is expected to vary not as a consequence of differences in *HLA-B* expression levels, but rather as a result of HLA-B −21M/T variation. Accordingly, HLA-B −21M enhances HLA-E expression level in a copy-dependent manner (*15*). We tested whether *HLA-A* expression levels may similarly be associated with HLA-E expression levels. Among 58 healthy donors, higher predicted *HLA-A* expression levels, and therefore higher HLA-A–derived signal peptide, was significantly correlated with higher HLA-E expression levels on the cell surface, independently of the reported effects of HLA-B −21 (Fig. 2A and table S2).

HLA-E has two common allelic variants denoted *E*01:01* and *E*01:03*, reportedly varying in peptide affinities, peptide repertoires, and surface expression levels (*18*). Although *HLA-E*01:03* associates with higher surface expression in univariate analyses, this association was not significant after adjusting for *HLA-B −21* and *HLA-A* genotypes (table S2). As *HLA-E*01:03* and *HLA-B −21M* alleles are in significant linkage disequilibrium ($D' = 0.52$), the increased peptide supply attributable to HLA-B −21M and HLA-A expression level likely account for higher expression of HLA-E*01:03, rather than the variant distinguishing *HLA-E*01:03* from − *E*01:01*. Accordingly, *HLA-E* variants did not show independent association with HIV outcomes (table S3). Similarly, addition of *HLA-E* genotype to a model fitting *HLA-A* expression and *HLA-B −21M* (and their interaction) was inferior to a model excluding *HLA-E* genotype in explaining HIV viremia.

The responsiveness of NK cells varies according to the presence of inhibitory-receptor/HLA pairs because of a process termed NK cell education or licensing (*19*). Accordingly, quantitative variation in HLA expression may influence target cell recognition through both ligand density variation and licensing modulation. The *HLA-B −21 M/T* variant distinguishes between two sets of *HLA* haplotypes that have differential effects on NK cell education, where *−21M* marks haplotypes that bias toward NKG2A-mediated education and *−21T* marks alternative haplotypes that bias toward KIR (killer cell immunoglobulin-like receptor)–mediated education (*15*). The reported linkage disequilibrium between *HLA-B −21M* and *HLA-B Bw6/HLA-C* group1 alleles that interact

Table 1. *HLA-A* expression level is associated with impaired HIV control and is robust to multiple outcome definitions, and subset analyses across 9763 independent individuals of varying geographic and ethnic background. Effect estimates denote the effect of one z-score (i.e. one standard deviation) increase in *HLA-A* expression on the outcome denoted.

Study	Outcome measure	Modeling approach	*n*	Effect estimate per *HLA-A z*-score increase	95% CI	*P*-value
Cross-sectional discovery studies						
Pooled analysis of 2298 individuals from 11 African sites (*11*). Black individuals only.	Viral load (log_{10} copies/ml)	Spearman correlation of VL effect and expression level for 23 *HLA-A* alleles	2298 volunteers	Spearman R = 0.54	NA‡	0.007
Prospective validation studies with longitudinal follow-up						
Pooled analysis of 5818 individuals from six U.S. cohorts (ACTG, ALIVE, MACS, MHRP, Ragon, SCOPE) and one Swiss cohort (SWISS). Pooled data from 3442 white, 1497 black, 233 Hispanic, 60 Asian, 14 other, and 572 of mixed or other ancestry.	Longitudinal viral load (VL)	Mixed effects-linear*				
	All individuals		62,843 VL in 5,818 volunteers	0.06 log_{10} copies/ml	0.05:0.08	4.4×10^{-19}
	Known date of seroconversion		21,817 VL in 2,019 volunteers	0.06 log_{10} copies/ml	0.04:0.08	2.5×10^{-9}
Mean viral load (mVL)	Mixed effects-linear*	5,818 mVL in 5,818 volunteers	0.14 log_{10} copies/ml	0.10:0.18	9.3×10^{-12}	
Controller/non-controller	Mixed effects-binomial*	2011 controller/ 2997 noncontroller	OR§ = 1.30	1.20:1.42	9.2×10^{-11}	
$CD4^+$ T cell count (cells/μl)	Mixed effects-linear*	56,415 CD4 counts in 2,100 volunteers	−37.8 cells/μl	−41.3:34.2	5.9×10^{-94}	
Prospective natural history validation studies						
Pooled analysis of 1159 individuals from five U.S. sites (ALIVE, MACS, MHCS, SFCCC and DCGCS). Pooled data from white, black, Hispanic or other ethnicities.	Time to AIDS (CDC 1987)	Mixed effects-Cox*	1159 at-risk individuals, 433 events	HR‖ = 1.25	1.01:1.55	0.04
Time to CD4 <200 cells/μl	Mixed effects-Cox*	1159 at-risk individuals, 537 events	HR = 1.24	1.03:1.49	0.02	
Reanalysis of broad HIV case-control genome-wide association study						
Pooled analysis of 3057 white, Hispanic, and black ethnicities.	Controller/ non-controller	Logistic-regression†	737 controller/ 2300 noncontroller	OR = 1.29	1.14:1.45	2.7×10^{-5}

**HLA-A*, *-B*, and *-C* alleles, and timing of viral load measurements (for prospective studies) were taken into account by being coded as random effects. †For GWAS analysis, population structure was adjusted for using the top five principal components. ‡NA, not applicable. §OR, odds ratio. ||HR, hazard ratio.

poorly with KIR is evident in our cohort (fig. S2). Using a ligand-independent activation assay designed to measure NK cell licensing, $NKG2A^+/KIR^-$ NK cells from *HLA-B –21MM*+ donors were more responsive than $NKG2A^-/KIR^+$ NK cells from the same donors ($P_{wilcoxon} = 1.5 \times 10^{-6}$), and notably, the strength of licensing among $NKG2A^+/KIR^-$ NK cells correlated with *HLA-A* expression level ($R = 0.69$, $P = 0.03$; Fig. 2B). Conversely, $KIR^+/NKG2A^-$ NK cells were more strongly licensed in HLA-B –21TT donors ($P = 1.1 \times 10^{-5}$), and this was not correlated with *HLA-A* expression. Thus, *HLA* haplotypes characterized by both *HLA-B –21M* and high *HLA-A* genotypes, which provide highest levels of HLA-E epitope, strongly bias toward NKG2A-mediated education.

We next tested whether variation in *HLA-A* expression alters NK cell responses toward HIV-infected target cells, and whether this varies according to *HLA-B –21* genotype. Increasing *HLA-A* expression was significantly correlated with greater inhibition of NK cell degranulation exclusively among HLA-B –21MM donors, when target cells were HIV infected and the autologous effector NK cells necessarily expressed NKG2A ($R = -0.77$, $P = 0.016$, Fig. 2C). These data extend previous observations (*20*).

We reasoned that the genetic epidemiological effect of *HLA-A* expression level on impairing HIV control may vary according to *HLA-B –21* genotype. We examined the two extremes in variation of NK cell education demarcated by *HLA-B –21* MM versus TT, although education varies across a continuum (*21*). Haplotypes tagged by *HLA-B –21M* exacerbate the deleterious effect of *HLA-A* expression on HIV viremia (interaction $P = 5.3 \times 10^{-9}$), regardless of ethnicity (Fig. 3). The effect of *HLA-A* expression level on HIV viremia is of greater magnitude in individuals with two *HLA-B* methionine-encoding alleles [$VL_{effect\text{-}MM}$ = 0.22, 95% confidence interval (CI) 0.17–0.26 log_{10} copies/ml per one *z*-score, $P = 1.5 \times 10^{-21}$] than in donors with two threonine-encoding *HLA-B* alleles ($VL_{effect\text{-}TT} = 0.06$, 95% CI 0.04–0.08 log_{10} copies/ml per one *z*-score, $P = 1.8 \times 10^{-9}$). The independent effect of *HLA-B –21M* varied across Caucasians and Africans/African Americans (fig. S4), perhaps owing to substantial differences in *HLA* haplotypes in Africans. In an *HLA-B* –21M/M individual, decrease in *HLA-A* expression by two *z*-scores (0.44log_{10} copies/ml lower VL) is comparable in magnitude to the effect of the presence of HLA-*B**57 (0.41 log_{10} copies/ml lower VL in the same data set).

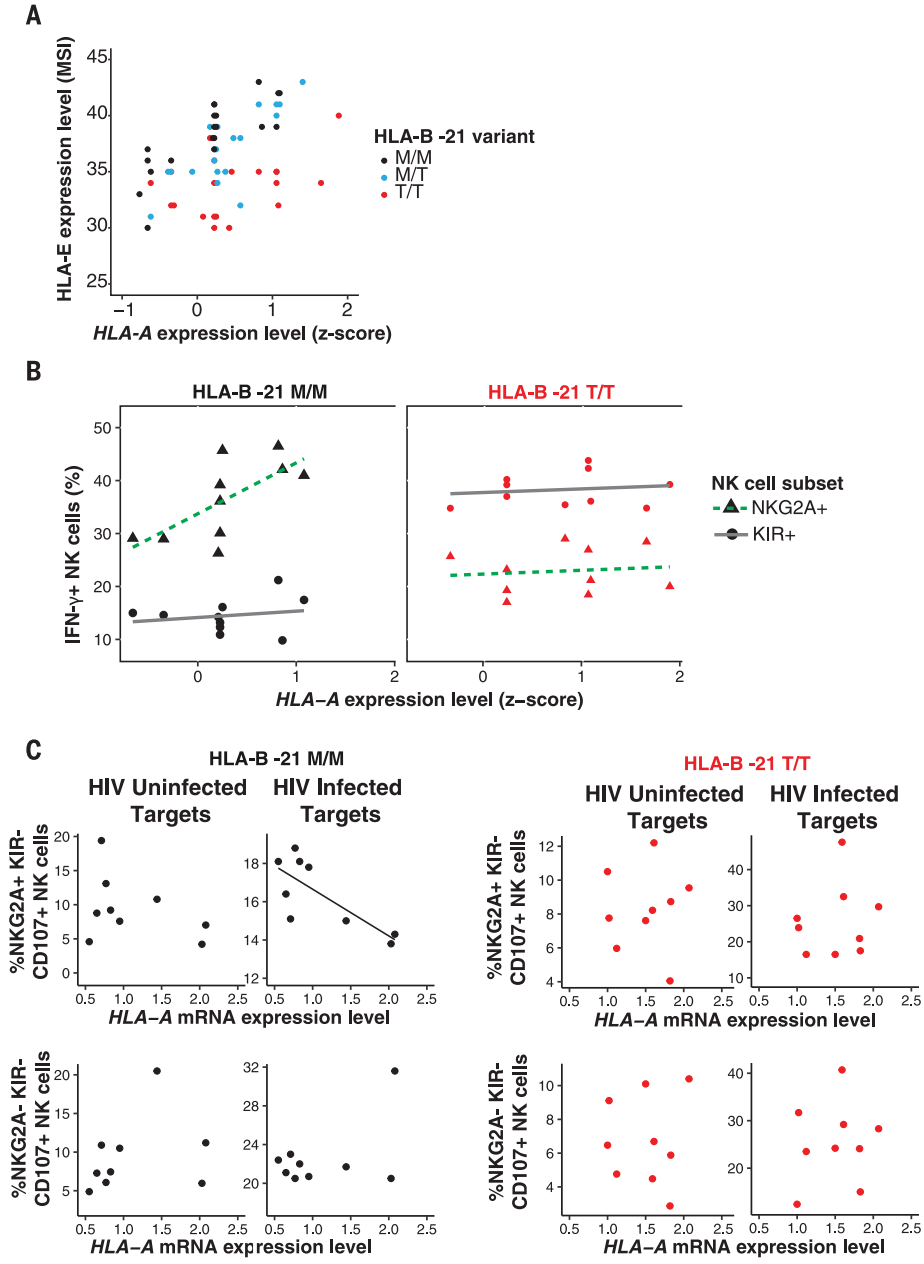

Fig. 2. *HLA-A* expression and HLA-B −21M regulate HLA-E expression, resulting in biased licensing of NKG2A-expressing NK cells that are impaired in their killing of HIV-infected target cells. (A) HLA-E expression according to *HLA-A* expression and HLA-B −21M in 58 HIV-uninfected donors. Each dot represents HLA-E expression levels (expressed as median signal intensity on a linear scale), as determined by CyTOF (*15*), and imputed *HLA-A* expression (*z*-score) ($R_{pearson}$ = 0.43; 95% CI 0.20–0.62; $P = 5 \times 10^{-4}$). **(B)** $NKG2A^+$ NK cell licensing varies by HLA-A expression and HLA-B −21M. Peripheral blood mononuclear cells (PBMCs) from 10 HLA-B −21M/M and 10 HLA-B −21T/T donors were coincubated with Raji cells pretreated with mouse antibody (2.5 μg/ml) against human CD20 for 6 hours to probe NK cell licensing and education. Each point represents the proportion of IFN-γ^+ NK cells from each individual that are $NKG2A^{+/}KIR^-$ (triangles) or $KIR^+/NKG2A^-$ (circles) as a function of *HLA-A* expression. Dotted and solid lines show best fit lines for $NKG2A^+$ and KIR^+ subsets, respectively. The association between NK cell responsiveness and *HLA-A* expression for $NKG2A^+$ NK cells in HLA-B −21M/M donors was $R_{pearson}$ = 0.69 (95% CI 0.10–0.92), P = 0.03; all other correlations were not significant. **(C)** PBMCs from 9 HLA-B −21M/M and 9 HLA-B −21T/T donors were cocultured for 6 hours with autologous T cell blasts that were left uninfected or were infected with HIV [vesicular stomatitis virus G glycoprotein (VSV-G) pseudotyped NL4-3] and stained for CD107A, a marker of NK cell degranulation (see fig. S3 for gating strategy). *HLA-A* expression was formally measured in these T cell blasts by quantitative polymerase chain reaction and is expressed relative to β*2M* expression levels. Plots show individual proportions of NK cells expressing CD107a among $NKG2A^+KIR^-$ and $NKG2A^-KIR^-$ subsets. A best fit line is shown for significantly correlated observations. Red and black lines and dots denote TT and MM donors, respectively. The association between $NKG2A^+KIR^-$ NK cell response to HIV-infected target cells, and *HLA-A* expression in HLA-B −21M/M donors was $R_{pearson}$ = −0.77 (95% CI −0.21 to −0.95), P = 0.02; all other correlations were not significant.

Taken together, these data support a model of increased *HLA-A* expression having a deleterious effect on HIV control through enhanced HLA-E expression that results in increased NKG2A-mediated NK (and/or T cell) inhibition, and impaired elimination of HIV-infected target cells.

HIV is capable of avoiding both T cell and NK cell recognition of infected host cells. HIV Nef-mediated reduction of HLA-A and -B (*22*) surface expression and Vpu-mediated reduction of HLA-C (*23*) likely serve to reduce antigen presentation and T cell killing of infected targets. These viral mechanisms occur posttranslationally (*22*, *23*) and should not affect the contribution of HLA class I signal peptides to enhancing HLA-E expression. This in turn may serve to allow continued evasion of NK cell responses through enhanced NKG2A inhibition among those individuals with *HLA* haplotypes that provide ample signal peptide to bind HLA-E. HIV encodes a peptide (AISPRTLNA, AA9) that may further exploit the inhibitory effects of HLA-E, but discrepancies regarding the effects of this peptide on HLA-E expression, NKG2A binding, and NK cell killing have been reported (*24*, *25*). NKG2A-expressing CD8 T cells are involved in antiviral responses (*26*), but the functional assays that we used are not appropriate for evaluating $CD8^+$ T cell responses, and thus, we cannot rule out a role for CD8 T cells in the genetic data presented herein. Although NKG2C, an activating receptor that also binds HLA-E (*27*), may play some role in the pathway that we delineate, signaling through NKG2A dominates and overrides NKG2C signaling (*28*).

These data show that expression level variation participates in the complex patterns of *HLA* associations in HIV disease, a pattern recognized for class I in other species (*29*). Blockade of HLA-E:NKG2A–mediated inhibition in vivo is a therapeutic strategy being explored through clinical trials of an antibody against NKG2A (monalizumab) for treatment of rheumatoid arthritis (NCT02331875), cancer (NCT 02557516, NCT02643550, NCT02459301, NCT02671435), and stem-cell transplantation (NCT02921685), because a role for HLA-E–mediated immunosuppression is recognized in these disorders (*30*, *31*). Our data suggest that antagonizing HLA-E/NKG2A

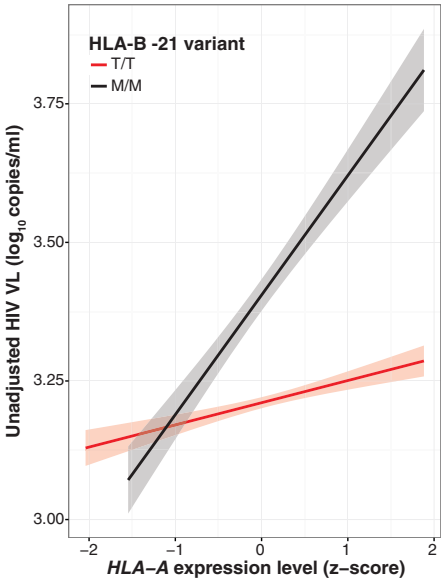

Fig. 3. The effect of *HLA-A* expression on HIV VL is modified by *HLA-B* alleles encoding methionine at position −21 in the signal peptide. The magnitude of effect (slope) of *HLA-A* expression on HIV viral load is stronger among individuals with *HLA-B* −21 MM (VL from 428 individuals, black line, $VL_{effect\text{-}MM} = 0.22$ log_{10} copies/ml, $P = 1.5 \times 10^{-21}$ adjusted for *HLA-A*, *-B*, and *-C*) compared with HLA-B TT (VL from 3071 individuals, red line, $VL_{effect\text{-}TT} = 0.06$ log_{10} copies/ml, $P = 1.8 \times 10^{-9}$ adjusted for *HLA-A*, *-B*, and *-C*). Interaction $P = 5.3 \times 10^{-9}$. Gray shading represents 95% CI of the linear estimate.

interactions, perhaps in combination with other therapies, may provide benefit in HIV disease. This might be an attractive approach in HIV cure strategies. Genetic validation of NKG2A as a therapeutic target in additional diseases by testing for effects of *HLA-A* and *HLA-B −21* genotypes may rationalize the use of anti-NKG2A therapy in other disorders.

REFERENCES AND NOTES

1. R. Apps *et al.*, *Science* **340**, 87–91 (2013).
2. E. C. Ibrahim *et al.*, *Am. J. Pathol.* **162**, 501–508 (2003).
3. E. W. Petersdorf *et al.*, *Blood* **124**, 3996–4003 (2014).
4. E. W. Petersdorf *et al.*, *N. Engl. J. Med.* **373**, 599–609 (2015).
5. P. Raj *et al.*, *eLife* **5**, e12089 (2016).
6. W. T. Wissemann *et al.*, *Am. J. Hum. Genet.* **93**, 984–993 (2013).
7. V. Ramsuran *et al.*, *Hum. Mol. Genet.* **24**, 4268–4275 (2015).
8. R. Apps *et al.*, *J. Immunol.* **194**, 3594–3600 (2015).
9. S. Kulkarni *et al.*, *Nature* **472**, 495–498 (2011).
10. N. Vince *et al.*, *Am. J. Hum. Genet.* **99**, 1353–1358 (2016).
11. J. M. Carlson *et al.*, *Nat. Med.* **22**, 606–613 (2016).
12. International HIV Controllers Study, *Science* **330**, 1551–1557 (2010).
13. V. M. Braud *et al.*, *Nature* **391**, 795–799 (1998).
14. N. Lee *et al.*, *Proc. Natl. Acad. Sci. U.S.A.* **95**, 5199–5204 (1998).
15. A. Horowitz *et al.*, *Sci. Immunol.* **1**, eaag1672 (2016).
16. N. Lee, D. R. Goodlett, A. Ishitani, H. Marquardt, D. E. Geraghty, *J. Immunol.* **160**, 4951–4960 (1998).
17. V. Ramsuran *et al.*, *J. Immunol.* **198**, 2320–2329 (2017).
18. R. K. Strong *et al.*, *J. Biol. Chem.* **278**, 5082–5090 (2003).
19. M. T. Orr, L. L. Lanier, *Cell* **142**, 847–856 (2010).
20. A. M. Merino *et al.*, *Clin. Exp. Immunol.* **174**, 414–423 (2013).
21. P. Brodin, K. Kärre, P. Höglund, *Trends Immunol.* **30**, 143–149 (2009).
22. G. B. Cohen *et al.*, *Immunity* **10**, 661–671 (1999).
23. R. Apps *et al.*, *Cell Host Microbe* **19**, 686–695 (2016).
24. Z. B. Davis *et al.*, *PLOS Pathog.* **12**, e1005421 (2016).
25. J. Nattermann *et al.*, *Antivir. Ther.* **10**, 95–107 (2005).
26. J. M. Moser, J. Gibbs, P. E. Jensen, A. E. Lukacher, *Nat. Immunol.* **3**, 189–195 (2002).
27. H. Wada, N. Matsumoto, K. Maenaka, K. Suzuki, K. Yamamoto, *Eur. J. Immunol.* **34**, 81–90 (2004).
28. V. Béziat *et al.*, *Blood* **117**, 4394–4396 (2011).
29. J. Kaufman, H. Völk, H. J. Wallny, *Immunol. Rev.* **143**, 63–88 (1995).
30. L. Wieten, N. M. Mahaweni, C. E. Voorter, G. M. Bos, M. G. Tilanus, *Tissue Antigens* **84**, 523–535 (2014).
31. R. T. Manguso *et al.*, *Nature* **547**, 413–418 (2017).

ACKNOWLEDGMENTS

We thank the volunteers in the contributing cohorts, their health-care providers, and the investigators involved in data collection. This work was supported by the National Cancer Institute, National Institutes of Health, and the Collaboration for AIDS Vaccine Discovery of the Bill and Melinda Gates Foundation. Additional funding was provided by the Howard Hughes Medical Institute (T.N.), International AIDS Vaccine Initiative, and South Africa National Research Foundation. See the extended acknowledgments in the supplementary materials for full details. Data and code to understand and assess the conclusions of this research are available in the main text, supplementary materials, or upon request of the authors. Genotyping of samples was subject to materials transfer agreements and institutional review board approved protocols, full details of which have been supplied to *Science*. V.N., V.R., A.H., J.M.C, and M.C. conceived and designed the study. All authors contributed to the generation, acquisition, analysis, and/or interpretation of data. V.N., V.R., and M.C. drafted the manuscript. All authors critically reviewed the manuscript for important intellectual content and approved the final version of the manuscript. This work is licensed under a Creative Commons Attribution 4.0 International (CC BY 4.0) license, which permits unrestricted use, distribution, and reproduction in any medium, provided the original work is properly cited. To view a copy of this license, visit http://creativecommons.org/licenses/by/4.0/. This license does not apply to figures/photos/artwork or other content included in the article that is credited to a third party; obtain authorization from the rights holder before using such material.

SUPPLEMENTARY MATERIALS

www.sciencemag.org/content/359/6371/86/suppl/DC1
Materials and Methods
Table S1 to S3
Figs. S1 to S3
References (*32–49*)

30 January 2017; resubmitted 16 October 2017
Accepted 4 December 2017
10.1126/science.aam8825

Cite as: B. Routy *et al.*, *Science* 10.1126/science.aan3706 (2017).

Gut microbiome influences efficacy of PD-1–based immunotherapy against epithelial tumors

Bertrand Routy,[1,2,3] Emmanuelle Le Chatelier,[4] Lisa Derosa,[1,2,3] Connie P. M. Duong,[1,2,5] Maryam Tidjani Alou,[1,2,3] Romain Daillère,[1,2,3] Aurélie Fluckiger,[1,2,5] Meriem Messaoudene,[1,2] Conrad Rauber,[1,2,3] Maria P. Roberti,[1,2,5] Marine Fidelle,[1,3,5] Caroline Flament,[1,2,5] Vichnou Poirier-Colame,[1,2,5] Paule Opolon,[6] Christophe Klein,[7] Kristina Iribarren,[8,9,10,11,12] Laura Mondragón,[8,9,10,11,12] Nicolas Jacquelot,[1,2,3] Bo Qu,[1,2,3] Gladys Ferrere,[1,2,3] Céline Clémenson,[1,13] Laura Mezquita,[1,14] Jordi Remon Masip,[1,14] Charles Naltet,[15] Solenn Brosseau,[15] Coureche Kaderbhai,[16] Corentin Richard,[16] Hira Rizvi,[17] Florence Levenez,[4] Nathalie Galleron,[4] Benoit Quinquis,[4] Nicolas Pons,[4] Bernhard Ryffel,[18] Véronique Minard-Colin,[1,19] Patrick Gonin,[1,20] Jean-Charles Soria,[1,14] Eric Deutsch,[1,13] Yohann Loriot,[1,3,14] François Ghiringhelli,[16] Gérard Zalcman,[15] François Goldwasser,[9,21,22] Bernard Escudier,[1,14,23] Matthew D. Hellmann,[24,25] Alexander Eggermont,[1,2,14] Didier Raoult,[26] Laurence Albiges,[1,3,14] Guido Kroemer,[8,9,10,11,12,27,28]* Laurence Zitvogel[1,2,3,5]*

[1]Gustave Roussy Cancer Campus (GRCC), Villejuif, France. [2]Institut National de la Santé et de la Recherche Medicale (INSERM) U1015 and Equipe Labellisée–Ligue Nationale contre le Cancer, Villejuif, France. [3]Univ. Paris-Sud, Université Paris-Saclay, Gustave Roussy, Villejuif, France. [4]MGP MetaGénoPolis, INRA, Université Paris-Saclay, Jouy-en-Josas, France. [5]Center of Clinical Investigations in Biotherapies of Cancer (CICBT) 1428, Villejuif, France. [6]Gustave Roussy, Laboratoire de Pathologie Expérimentale, 94800 Villejuif, France. [7]Centre de Recherche des Cordeliers, INSERM, Université Paris Descartes, Sorbonne Paris Cité, UMRS 1138, Université Pierre et Marie Curie Université Paris 06, Sorbonne Universités, Paris, France. [8]Metabolomics and Cell Biology Platforms, GRCC, Villejuif, France. [9]Paris Descartes University, Sorbonne Paris Cité, Paris, France. [10]Equipe 11 Labellisée–Ligue Nationale contre le Cancer, Centre de Recherche des Cordeliers, Paris, France. [11]INSERM U1138, Paris, France. [12]Université Pierre et Marie Curie, Paris, France. [13]Department of Radiation Oncology, INSERM U1030, and Molecular Radiotherapy, Gustave Roussy, Université Paris-Saclay, F-94805 Villejuif, France. [14]Department of Medical Oncology, Gustave Roussy, Villejuif, France. [15]Thoracic Oncology Department–CIC1425/CLIP2 Paris-Nord, Hospital Bichat-Claude Bernard, AP-HP, Université Paris-Diderot, Paris, France. [16]Department of medical oncology, Center GF Leclerc, Dijon, France. [17]Druckenmiller Center for Lung Cancer Research, Memorial Sloan Kettering Cancer Center, New York, NY, USA. [18]Molecular Immunology and Embryology, UMR 7355, CNRS, University of Orleans, Orléans, France. [19]Department of Pediatric Oncology, GRCC, Villejuif, France. [20]Preclinical Research Platform, GRCC, Villejuif, France. [21]Department of Medical Oncology, Cochin Hospital, Assistance Publique—Hôpitaux de Paris, Paris, France. [22]Immunomodulatory Therapies Multidisciplinary Study Group (CERTIM), Paris, France. [23]INSERM U981, GRCC, Villejuif, France. [24]Department of Medicine, Thoracic Oncology Service, Memorial Sloan Kettering Cancer Center, New York, NY, USA. [25]Department of Medicine, Weill Cornell Medical College, New York, NY, USA. [26]URMITE, Aix Marseille Université, UM63, CNRS 7278, IRD 198, INSERM 1095, IHU–Méditerranée Infection, 13005 Marseille, France. [27]Pôle de Biologie, Hôpital Européen Georges Pompidou, Assistance Publique–Hôpitaux de Paris, Paris, France. [28]Department of Women's and Children's Health, Karolinska University Hospital, 17176 Stockholm, Sweden.

***Corresponding author. Email: laurence.zitvogel@gustaveroussy.fr (L.Z.); kroemer@orange.fr (G.K.)**

Immune checkpoint inhibitors (ICI) targeting the PD-1/PD-L1 axis induce sustained clinical responses in a sizeable minority of cancer patients. Here, we show that primary resistance to ICI can be due to abnormal gut microbiome composition. Antibiotics (ATB) inhibited the clinical benefit of ICI in patients with advanced cancer. Fecal microbiota transplantation (FMT) from cancer patients who responded to ICI (but not from non-responding patients) into germ-free or ATB-treated mice ameliorated the antitumor effects of PD-1 blockade. Metagenomics of patient stools at diagnosis revealed correlations between clinical responses to ICI and the relative abundance of *Akkermansia muciniphila*. Oral supplementation with *A. muciniphila* post-FMT with non-responder feces restored the efficacy of PD-1 blockade in an IL-12–dependent manner, by increasing the recruitment of $CCR9^+CXCR3^+CD4^+$ T lymphocytes into tumor beds.

Cancer immunotherapy has become highly successful against an array of distinct hematological and solid metastatic malignancies (*1*–*6*). Administration of immune checkpoint inhibitors (ICI) unleash T lymphocyte-mediated immune responses by suppressing the interaction of T cell inhibitory receptors with their cognate ligands on tumor or stromal cells (*7*). The most widely used ICI are monoclonal antibodies (mAb) targeting programmed cell death protein 1 (PD-1) and its ligand PD-L1 (*7*). PD-1 blockade is highly efficacious against advanced melanoma, non-small-cell-lung cancer (NSCLC) and renal cell carcinoma (RCC). Primary resistance, observed in 60-70% of cases (*3*, *5*, *8*), has been attributed to low mutational burden, poor intrinsic antigenicity of tumor cells (*9*, *10*), absent priming by potentially immunogenic pretreatment with chemo- or radiotherapy (*11*), defective antigen presentation during the priming phase (*12*), local immunosuppression by extracellular metabolites (*13*) and functional exhaustion of tumor-infiltrating lymphocytes (*13*–*15*).

Recent work in mice has highlighted the key role of the

gut microbiota in mediating tumor responses to chemotherapeutic agents and immunotherapies targeting PD-L1 or cytotoxic T-lymphocyte-associated protein 4 (CTLA-4) (*16*–*21*). Therefore, we explored the possibility that dysbiosis associated with malignant disease or concomitant ATB use could influence primary resistance to PD-1 blockade in tumor bearing mice and cancer patients.

Initially, we compared the therapeutic efficacy of anti-PD-1 mAb alone or combined with anti-CTLA-4 mAb in mice with established MCA-205 sarcoma and RET melanoma. Mice were reared in specific pathogen-free (SPF) conditions and either left untreated, or treated for 14 days with broad-spectrum combination ATB (ampicillin + colistin + streptomycin). ATB treatment significantly compromised the anti-tumor effects and survival of mice treated with anti-PD-1 mAb alone or in combination with anti-CTLA-4 mAb (Fig. 1, A and B).

We next addressed the impact of ATB on patients with advanced NSCLC (n = 140), RCC (n = 67) or urothelial carcinoma (UC) (n = 42) who received anti-PD-1/PD-L1 mAb after one or several prior therapies. Out of all 249 patients, 69 (28%) were prescribed ATB (β-lactam+/– inhibitors, fluoroquinolones or macrolides) within 2 months before, or 1 month after, the first administration of anti-PD-1/PD-L1 mAb. ATB were generally taken orally for common indications (dental, urinary and pulmonary infections). There were no major statistical differences in baseline clinical characteristics between ATB-treated and untreated patients (tables S1 to S6). Progression-free survival (PFS) and overall survival (OS) were significantly shorter in the ATB-treated group when all patients were combined (Fig. 1C). Similarly, PFS and/or OS were shorter in ATB-treated groups when individual tumor types were considered (Fig. 1, D and E, and fig. S1, A to C). In univariate and multivariate Cox regression analyses, ATB represented a predictor of resistance to PD-1 blockade, independent from classical prognostic markers in NSCLC and RCC (tables S7 to S9). A validation cohort of 239 advanced NSCLC patients confirmed the negative role of ATB uptake on OS during PD-1/PD-L1 inhibition (fig. S1D). In contrast, proton pump inhibitors, a medication that can also alter the microbiota composition, failed to affect the PFS or OS in these patients (fig. S2) (*22*). Based on previous observations that ATB can transiently change the composition of the gut microbiome (*23*), we hypothesized that dysbiosis might affect the therapeutic efficacy of ICI.

We explored the composition of the gut microbiota using quantitative metagenomics by shotgun sequencing, reaching >20 million short DNA sequence reads per sample followed by analysis of the results in a 9.9 million-gene reference catalog (*24*). Total DNA was extracted from 100 patients diagnosed with NSCLC (n = 60) and RCC (n = 40) prior to starting therapy and serially after PD-1 blockade (tables S10 to S13). The higher richness of the samples evaluated at the gene count (GC) or metagenomic species (MGS) levels correlated with the clinical response defined by the absence of progression of disease, 6 months after initiation of ICI based on RECIST 1.1 criteria (Fig. 2A) (*25*). Stool richness increased at the MGS level over the course of therapy, more in RCC than NSCLC patients (fig. S3). MGS occurrence was visualized for each sample using 'barcodes', i.e., heat maps reflecting the abundance of 50 marker genes for each MGS (fig. S4). The taxonomical annotation of each MGS was performed based on gene homology to previously sequenced organisms (using blastN against the nt and WGS databanks). When segregating responders (R) from non-responders (NR) (according to the best clinical response as assessed by RECIST1.1), we observed an overrepresentation of unclassified and classified Firmicutes, as well as distinct bacterial genera (such as *Akkermansia* and *Alistipes*) (Fig. 2B and fig. S4). The commensal that was most significantly associated with favorable clinical outcome (in both NSCLC and RCC) was *A. muciniphila* (p = 0.004 considering all patients and p = 0.003 excluding ATB-treated patients) (Fig. 2B, fig. S4, A and B, and tables S10 to S13). When analyzing PFS according to RECIST 1.1, *A. muciniphila* was also enriched in patients with a PFS superior than 3 months compared to those with a PFS shorter than 3 months, both in the whole cohort (p = 0.028, fig. S5A) and when excluding patients on ATB (p = 0.007, Fig. 2C and fig. S5B). *A. muciniphila* was also enriched when analyzing the NSCLC cohort alone (p = 0.045 with or without ATB, fig. S6A; p = 0.026 excluding ATB, fig. S6B) along with other commensals such as *Ruminococcus spp., Alistipes spp.* and *Eubacterium spp.* with a relative underrepresentation of *Bifidobacterium adolescentis, B. longum* and *Parabacteroides distasonis.* More precisely, the fecal presence of *A. muciniphila* was detectable in 69% (11/16) and 58% (23/40) of patients exhibiting a partial response or stable disease respectively, while it could only be detectable in 34% (15/44) of patients who progressed or died (p = 0.007, Fig. 2D). A validation cohort of 53 patients (27 NSCLC and 26 RCC) confirmed that *A. muciniphila* was enriched in patients with the best clinical response and PFS > 3 months (fig. S7 and table S14). Altogether, *A. muciniphila* was overrepresented at diagnosis in feces of patients prone to benefit from PD-1 inhibition.

In an attempt to link the gut microbial content to the systemic immune tone, we analyzed memory T cell responses from peripheral blood, elicited against microbiota after the initiation of PD-1 blockade. The recall response of circulating $CD4^+$ and $CD8^+$ T cells harvested from 27 NSCLC and 28 RCC patients under PD-1 blockade was measured upon co-culture with autologous monocytes preincubated with distinct commensals (Fig. 2E and tables S15 and S16). In this setting, the secretion of cytokines by MHC class II-restricted

$CD4^+$ T cells (Th1, Th22 or Tr1) was quantified (figs. S8 and S9). The only immune responses that correlated with the clinical outcome during anti-PD-1 mAb targeted ICI were the Th1 (Fig. 2F) and Tc1 (fig. S10A) cell reactivity against *A. muciniphila*, IFN-γ release above the median being associated with prolonged PFS. In contrast, no association was found between clinical outcome and IFN-γ, IL-10 or IL-22 secretion stimulated by non-specific cross-linking of the T cell receptor (fig. S10B) or memory T cell responses to 10 other commensals with the exception of *Enterococcus hirae* 13144 (*E. hirae*) for the Tc1 response (Fig. 2F), as previously reported (*19*). We also observed a higher incidence of cultivatable *E. hirae* in R than in NR NSCLC patients among 32 stools tested at diagnosis (Fig. 2G), further supporting the relevance of *E. hirae* to predict best clinical outcome.

To establish a cause-effect relationship between the anticancer efficacy of PD-1 blockade and the dominance of distinct commensal species in clinical responses, we recolonized ATB-treated mice reared in SPF conditions (or alternatively germ-free [GF] animals) by fecal microbiota transplantation (FMT) using patient stool. Such 'avatar mice' were prepared by oral gavage of feces harvested at diagnosis from 8 different NSCLC patients, 4 R and 4 NR (defined using best clinical outcome). Two weeks later, C57BL/6 avatar mice were inoculated with MCA-205 tumor cells and treated 5 days after with anti-PD-1 mAb (Fig. 3A). Stools from clinical R conferred sensitivity, while those from NR patients conveyed resistance to PD-1 blockade with a similar efficiency in ATB-treated or GF avatar mice (Fig. 3B and table S17). While stool composition failed to influence the natural progression of MCA-205 sarcomas, it did so following PD-1 blockade (Fig. 3C). FMT from R patients (but not from NR) into avatar mice caused tumor growth delay (Fig. 3C, middle and right panels), the accumulation of $CXCR3^+CD4^+$ T cells in the tumor microenvironment (Fig. 3D) and the upregulation of PD-L1 in splenic T cells (Fig. 3E) following PD-1 blockade. Importantly, these findings could be corroborated by FMT from 7 RCC patients into ATB-treated BALB/c mice that were then orthotopically implanted with luciferase expressing-renal cancer (RENCA) cells resistant to PD-1 monotherapy and treated with a combination of anti-CTLA-4 and anti-PD-1 mAb (fig. S11 and table S18). Bioluminescence monitoring revealed that stools from R patients restored the antitumor activity of simultaneous CTLA-4 and PD-1 blockade unlike those from NR (Fig. 3F). Taken together, these results suggest that the intestinal microbiota from patients influences the outcome of ICI in avatar mice.

To validate the biological significance of the microbiota identified in the metagenomic analysis of patients with a favorable clinical outcome, we mono- or bi-colonized intestines from mice with *A. muciniphila* alone or combined with other commensals in several conditions of gut dysbiosis. First, ATB-mediated sterilization of the microbiome was followed by natural recolonization supplemented with 5 oral gavages of *A. muciniphila,* alone or together with the goblet cell-stimulating *E. hirae* (*17*, *19*), in an attempt to restore responsiveness to PD-1 blockade in RET melanoma-bearing hosts reared in SPF conditions. *A. muciniphila* alone or combined with *E. hirae* reinstated the anticancer effects of PD-1 blockade that were previously inhibited by ATB (Fig. 1A, Fig. 4A, and fig. S12A). Secondly, we utilized an orthotopic luciferase expressing Lewis lung carcinoma (LLC) model amenable to combination treatment by local radiotherapy and PD-1 blockade (*26*). Again, oral gavages with *A. muciniphila* and *E. hirae* increased the efficacy of PD-1 blockade with respect to tumor growth, measured by whole body imaging (Fig. 4B). Finally, we confirmed that monocolonization with *A. muciniphila* or bicolonization of *A. muciniphila* plus *E. hirae* reversed the compromised efficacy of PD-1 blockade observed after the recolonization of GF or ATB-treated SPF mice with FMT from NR patients (Fig. 4C and fig. S12B). In addition to this, *Alistipes indistinctus*, which was found to be overrepresented among NSCLC responders, was efficient in restoring the efficacy of this ICI in avatar mice (Fig. 4C and fig. S12) while other unrelated commensals failed to do so (fig. S13).

Next, we analyzed the immunological changes elicited by oral gavage with a combination of *A. muciniphila* and *E. hirae* in mesenteric lymph nodes (mLN), tumor draining LN (dLN) and tumor beds. Central memory (TCM) $CD4^+$ T cells expressing the small intestine associated chemokine receptor CCR9 and/or the Th1 associated chemokine receptor CXCR3 accumulated 48h after the 1^{st} injection in mLN (Fig. 4D) and were observed in dLN (fig. S14A) and tumor beds at sacrifice (Fig. 4E and fig. S14, B and C). Immunohistochemical studies revealed the formation of intratumoral granulomas (fig. S15) and increased CD4/Foxp3 ratios in tumors from animals cotreated with anti-PD-1 mAb and *A. muciniphila* (Fig. 4, F and G). Moreover, *A. muciniphila* and *E. hirae* (*19*) induced dendritic cells to secrete IL-12 (fig. S16A), a Th1 cytokine involved in the immunogenicity of PD-1 blockade in eubiotic conditions (Fig. 4H, left panel, and fig. S16B) as well as in the adjuvant effects of *A. muciniphila* in dysbiotic settings (Fig. 4H, right panel), as previously shown for *B. fragilis* in the context of CTLA-4 blockade (*20*).

We conclude from this study that the gut microbiome markedly influences the outcome of PD-1 blockade in mice and patients. Several issues remain unresolved. The mechanisms accounting for the immunomodulatory effects of *A. muciniphila,* one of the most abundant bacterium in the ileum microbiota, remain unclear (*27*). Cancer patients face stresses that can cause gut barrier dysfunction and systemic endotoxemia. By reinforcing intestinal barrier integrity and

reducing systemic inflammation, *A. muciniphila, Clostridiales* and *Ruminococcaceae* might generate 'homeostatic' consortia of commensals that prevent leaky colon and systemic immunosuppression (*28*–*30*). In parallel, unleashing T cells by PD-1 blockade alleviated small intestinal tolerance, eliciting local and systemic recall Th1 immune responses against *A. muciniphila* that might improve cancer immunosurveillance. Finally, a comprehensive analysis of the stool composition after a chronic shift of the microbiome enforced by commensals endowed with anticancer effects, might unveil further functional links between the microbial ecosystem and anticancer immunosurveillance (*28*). Irrespective of these remaining questions, our findings suggest that the microbiome governs the cancer-immune set point of cancer bearing individuals (*30*) and offer novel avenues for manipulating the gut ecosystem to circumvent primary resistance to ICI.

REFERENCES AND NOTES

1. C. Robert, L. Thomas, I. Bondarenko, S. O'Day, J. Weber, C. Garbe, C. Lebbe, J.-F. Baurain, A. Testori, J.-J. Grob, N. Davidson, J. Richards, M. Maio, A. Hauschild, W. H. Miller Jr., P. Gascon, M. Lotem, K. Harmankaya, R. Ibrahim, S. Francis, T.-T. Chen, R. Humphrey, A. Hoos, J. D. Wolchok, Ipilimumab plus dacarbazine for previously untreated metastatic melanoma. *N. Engl. J. Med.* **364**, 2517–2526 (2011). doi:10.1056/NEJMoa1104621 Medline

2. N. P. Restifo, M. E. Dudley, S. A. Rosenberg, Adoptive immunotherapy for cancer: Harnessing the T cell response. *Nat. Rev. Immunol.* **12**, 269–281 (2012). doi:10.1038/nri3191 Medline

3. H. Borghaei, L. Paz-Ares, L. Horn, D. R. Spigel, M. Steins, N. E. Ready, L. Q. Chow, E. E. Vokes, E. Felip, E. Holgado, F. Barlesi, M. Kohlhäufl, O. Arrieta, M. A. Burgio, J. Fayette, H. Lena, E. Poddubskaya, D. E. Gerber, S. N. Gettinger, C. M. Rudin, N. Rizvi, L. Crinò, G. R. Blumenschein Jr., S. J. Antonia, C. Dorange, C. T. Harbison, F. Graf Finckenstein, J. R. Brahmer, Nivolumab versus docetaxel in advanced nonsquamous non-small-cell lung cancer. *N. Engl. J. Med.* **373**, 1627–1639 (2015). doi:10.1056/NEJMoa1507643 Medline

4. S. M. Ansell, A. M. Lesokhin, I. Borrello, A. Halwani, E. C. Scott, M. Gutierrez, S. J. Schuster, M. M. Millenson, D. Cattry, G. J. Freeman, S. J. Rodig, B. Chapuy, A. H. Ligon, L. Zhu, J. F. Grosso, S. Y. Kim, J. M. Timmerman, M. A. Shipp, P. Armand, PD-1 blockade with nivolumab in relapsed or refractory Hodgkin's lymphoma. *N. Engl. J. Med.* **372**, 311–319 (2015). doi:10.1056/NEJMoa1411087 Medline

5. S. L. Topalian, F. S. Hodi, J. R. Brahmer, S. N. Gettinger, D. C. Smith, D. F. McDermott, J. D. Powderly, R. D. Carvajal, J. A. Sosman, M. B. Atkins, P. D. Leming, D. R. Spigel, S. J. Antonia, L. Horn, C. G. Drake, D. M. Pardoll, L. Chen, W. H. Sharfman, R. A. Anders, J. M. Taube, T. L. McMiller, H. Xu, A. J. Korman, M. Jure-Kunkel, S. Agrawal, D. McDonald, G. D. Kollia, A. Gupta, J. M. Wigginton, M. Sznol, Safety, activity, and immune correlates of anti-PD-1 antibody in cancer. *N. Engl. J. Med.* **366**, 2443–2454 (2012). doi:10.1056/NEJMoa1200690 Medline

6. A. Ribas, O. Hamid, A. Daud, F. S. Hodi, J. D. Wolchok, R. Kefford, A. M. Joshua, A. Patnaik, W.-J. Hwu, J. S. Weber, T. C. Gangadhar, P. Hersey, R. Dronca, R. W. Joseph, H. Zarour, B. Chmielowski, D. P. Lawrence, A. Algazi, N. A. Rizvi, B. Hoffner, C. Mateus, K. Gergich, J. A. Lindia, M. Giannotti, X. N. Li, S. Ebbinghaus, S. P. Kang, C. Robert, Association of pembrolizumab with tumor response and survival among patients with advanced melanoma. *J. Am. Med. Assoc.* **315**, 1600–1609 (2016). doi:10.1001/jama.2016.4059 Medline

7. D. Pardoll, Cancer and the immune system: Basic concepts and targets for intervention. *Semin. Oncol.* **42**, 523–538 (2015). doi:10.1053/j.seminoncol.2015.05.003 Medline

8. R. J. Motzer, B. Escudier, D. F. McDermott, S. George, H. J. Hammers, S. Srinivas, S. S. Tykodi, J. A. Sosman, G. Procopio, E. R. Plimack, D. Castellano, T. K. Choueiri, H. Gurney, F. Donskov, P. Bono, J. Wagstaff, T. C. Gauler, T. Ueda, Y. Tomita, F. A. Schutz, C. Kollmannsberger, J. Larkin, A. Ravaud, J. S. Simon, L.-A. Xu, I. M. Waxman, P. Sharma, Nivolumab versus everolimus in advanced renal-cell carcinoma. *N. Engl. J. Med.* **373**, 1803–1813 (2015). doi:10.1056/NEJMoa1510665 Medline

9. N. A. Rizvi, M. D. Hellmann, A. Snyder, P. Kvistborg, V. Makarov, J. J. Havel, W. Lee, J. Yuan, P. Wong, T. S. Ho, M. L. Miller, N. Rekhtman, A. L. Moreira, F. Ibrahim, C. Bruggeman, B. Gasmi, R. Zappasodi, Y. Maeda, C. Sander, E. B. Garon, T. Merghoub, J. D. Wolchok, T. N. Schumacher, T. A. Chan, Mutational landscape determines sensitivity to PD-1 blockade in non–small cell lung cancer. *Science* **348**, 124–128 (2015). doi:10.1126/science.aaa1348 Medline

10. N. Riaz, J. J. Havel, S. M. Kendall, V. Makarov, L. A. Walsh, A. Desrichard, N. Weinhold, T. A. Chan, Recurrent SERPINB3 and SERPINB4 mutations in patients who respond to anti-CTLA4 immunotherapy. *Nat. Genet.* **48**, 1327–1329 (2016). doi:10.1038/ng.3677 Medline

11. D. P. Carbone, M. Reck, L. Paz-Ares, B. Creelan, L. Horn, M. Steins, E. Felip, M. M. van den Heuvel, T.-E. Ciuleanu, F. Badin, N. Ready, T. J. N. Hiltermann, S. Nair, R. Juergens, S. Peters, E. Minenza, J. M. Wrangle, D. Rodriguez-Abreu, H. Borghaei, G. R. Blumenschein Jr., L. C. Villaruz, L. Havel, J. Krejci, J. Corral Jaime, H. Chang, W. J. Geese, P. Bhagavatheeswaran, A. C. Chen, M. A. Socinski, First-line nivolumab in stage IV or recurrent non-small-cell lung cancer. *N. Engl. J. Med.* **376**, 2415–2426 (2017). doi:10.1056/NEJMoa1613493 Medline

12. T. N. Schumacher, R. D. Schreiber, Neoantigens in cancer immunotherapy. *Science* **348**, 69–74 (2015). doi:10.1126/science.aaa4971 Medline

13. S. Spranger, R. Bao, T. F. Gajewski, Melanoma-intrinsic β-catenin signalling prevents anti-tumour immunity. *Nature* **523**, 231–235 (2015). doi:10.1038/nature14404 Medline

14. M. J. Smyth, S. F. Ngiow, A. Ribas, M. W. L. Teng, Combination cancer immunotherapies tailored to the tumour microenvironment. *Nat. Rev. Clin. Oncol.* **13**, 143–158 (2016). doi:10.1038/nrclinonc.2015.209 Medline

15. S. Koyama, E. A. Akbay, Y. Y. Li, G. S. Herter-Sprie, K. A. Buczkowski, W. G. Richards, L. Gandhi, A. J. Redig, S. J. Rodig, H. Asahina, R. E. Jones, M. M. Kulkarni, M. Kuraguchi, S. Palakurthi, P. E. Fecci, B. E. Johnson, P. A. Janne, J. A. Engelman, S. P. Gangadharan, D. B. Costa, G. J. Freeman, R. Bueno, F. S. Hodi, G. Dranoff, K.-K. Wong, P. S. Hammerman, Adaptive resistance to therapeutic PD-1 blockade is associated with upregulation of alternative immune checkpoints. *Nat. Commun.* **7**, 10501 (2016). doi:10.1038/ncomms10501 Medline

16. . J. U. Peled, S. M. Devlin, A. Staffas, M. Lumish, R. Khanin, E. R. Littmann, L. Ling, S. Kosuri, M. Maloy, J. B. Slingerland, K. F. Ahr, K. A. Porosnicu Rodriguez, Y. Shono, A. E. Slingerland, M. D. Docampo, A. D. Sung, D. Weber, A. M. Alousi, B. Gyurkocza, D. M. Ponce, J. N. Barker, M.-A. Perales, S. A. Giralt, Y. Taur, E. G. Pamer, R. R. Jenq, M. R. M. van den Brink, Intestinal microbiota and relapse after hematopoietic-cell transplantation. *J. Clin. Oncol.* **35**, 1650–1659 (2017). doi:10.1200/JCO.2016.70.3348

17. S. Viaud, F. Saccheri, G. Mignot, T. Yamazaki, R. Daillère, D. Hannani, D. P. Enot, C. Pfirschke, C. Engblom, M. J. Pittet, A. Schlitzer, F. Ginhoux, L. Apetoh, E. Chachaty, P.-L. Woerther, G. Eberl, M. Bérard, C. Ecobichon, D. Clermont, C. Bizet, V. Gaboriau-Routhiau, N. Cerf-Bensussan, P. Opolon, N. Yessaad, E. Vivier, B. Ryffel, C. O. Elson, J. Doré, G. Kroemer, P. Lepage, I. G. Boneca, F. Ghiringhelli, L. Zitvogel, The intestinal microbiota modulates the anticancer immune effects of cyclophosphamide. *Science* **342**, 971–976 (2013). doi:10.1126/science.1240537 Medline

18. N. Iida, A. Dzutsev, C. A. Stewart, L. Smith, N. Bouladoux, R. A. Weingarten, D. A. Molina, R. Salcedo, T. Back, S. Cramer, R.-M. Dai, H. Kiu, M. Cardone, S. Naik, A. K. Patri, E. Wang, F. M. Marincola, K. M. Frank, Y. Belkaid, G. Trinchieri, R. S.

Goldszmid, Commensal bacteria control cancer response to therapy by modulating the tumor microenvironment. *Science* **342**, 967–970 (2013). doi:10.1126/science.1240527 Medline

19. R. Daillère, M. Vétizou, N. Waldschmitt, T. Yamazaki, C. Isnard, V. Poirier-Colame, C. P. M. Duong, C. Flament, P. Lepage, M. P. Roberti, B. Routy, N. Jacquelot, L. Apetoh, S. Becharef, S. Rusakiewicz, P. Langella, H. Sokol, G. Kroemer, D. Enot, A. Roux, A. Eggermont, E. Tartour, L. Johannes, P.-L. Woerther, E. Chachaty, J.-C. Soria, E. Golden, S. Formenti, M. Plebanski, M. Madondo, P. Rosenstiel, D. Raoult, V. Cattoir, I. G. Boneca, M. Chamaillard, L. Zitvogel, *Enterococcus hirae* and *Barnesiella intestinihominis* facilitate cyclophosphamide-induced therapeutic immunomodulatory effects. *Immunity* **45**, 931–943 (2016). doi:10.1016/j.immuni.2016.09.009 Medline

20. M. Vétizou, J. M. Pitt, R. Daillère, P. Lepage, N. Waldschmitt, C. Flament, S. Rusakiewicz, B. Routy, M. P. Roberti, C. P. M. Duong, V. Poirier-Colame, A. Roux, S. Becharef, S. Formenti, E. Golden, S. Cording, G. Eberl, A. Schlitzer, F. Ginhoux, S. Mani, T. Yamazaki, N. Jacquelot, D. P. Enot, M. Bérard, J. Nigou, P. Opolon, A. Eggermont, P.-L. Woerther, E. Chachaty, N. Chaput, C. Robert, C. Mateus, G. Kroemer, D. Raoult, I. G. Boneca, F. Carbonnel, M. Chamaillard, L. Zitvogel, Anticancer immunotherapy by CTLA-4 blockade relies on the gut microbiota. *Science* **350**, 1079–1084 (2015). doi:10.1126/science.aad1329 Medline

21. A. Sivan, L. Corrales, N. Hubert, J. B. Williams, K. Aquino-Michaels, Z. M. Earley, F. W. Benyamin, Y. M. Lei, B. Jabri, M.-L. Alegre, E. B. Chang, T. F. Gajewski, Commensal *Bifidobacterium* promotes antitumor immunity and facilitates anti-PD-L1 efficacy. *Science* **350**, 1084–1089 (2015). doi:10.1126/science.aac4255 Medline

22. M. A. Jackson, J. K. Goodrich, M.-E. Maxan, D. E. Freedberg, J. A. Abrams, A. C. Poole, J. L. Sutter, D. Welter, R. E. Ley, J. T. Bell, T. D. Spector, C. J. Steves, Proton pump inhibitors alter the composition of the gut microbiota. *Gut* **65**, 749–756 (2016). doi:10.1136/gutjnl-2015-310861 Medline

23. M. J. Blaser, Antibiotic use and its consequences for the normal microbiome. *Science* **352**, 544–545 (2016). doi:10.1126/science.aad9358 Medline

24. J. Li, H. Jia, X. Cai, H. Zhong, Q. Feng, S. Sunagawa, M. Arumugam, J. R. Kultima, E. Prifti, T. Nielsen, A. S. Juncker, C. Manichanh, B. Chen, W. Zhang, F. Levenez, J. Wang, X. Xu, L. Xiao, S. Liang, D. Zhang, Z. Zhang, W. Chen, H. Zhao, J. Y. Al-Aama, S. Edris, H. Yang, J. Wang, T. Hansen, H. B. Nielsen, S. Brunak, K. Kristiansen, F. Guarner, O. Pedersen, J. Doré, S. D. Ehrlich, P. Bork, J. Wang, J.-M. Batto, S. Kennedy, F. Haimet, Y. Winogradski, E. Pelletier, D. LePaslier, F. Artiguenave, T. Bruls, J. Weissenbach, K. Turner, J. Parkhill, M. Antolin, F. Casellas, N. Borruel, E. Varela, A. Torrejon, G. Denariaz, M. Derrien, J. E. T. van Hylckama Vlieg, P. Viega, R. Oozeer, J. Knoll, M. Rescigno, C. Brechot, C. M'Rini, A. Mérieux, T. Yamada, S. Tims, E. G. Zoetendal, M. Kleerebezem, W. M. de Vos, A. Cultrone, M. Leclerc, C. Juste, E. Guedon, C. Delorme, S. Layec, G. Khaci, M. van de Guchte, G. Vandemeulebrouck, A. Jamet, R. Dervyn, N. Sanchez, H. Blottière, E. Maguin, P. Renault, J. Tap, D. R. Mende, An integrated catalog of reference genes in the human gut microbiome. *Nat. Biotechnol.* **32**, 834–841 (2014). doi:10.1038/nbt.2942 Medline

25. E. A. Eisenhauer, P. Therasse, J. Bogaerts, L. H. Schwartz, D. Sargent, R. Ford, J. Dancey, S. Arbuck, S. Gwyther, M. Mooney, L. Rubinstein, L. Shankar, L. Dodd, R. Kaplan, D. Lacombe, J. Verweij, New response evaluation criteria in solid tumours: Revised RECIST guideline (version 1.1). *Eur. J. Cancer* **45**, 228–247 (2009). doi:10.1016/j.ejca.2008.10.026 Medline

26. X. Wang, J. E. Schoenhals, A. Li, D. R. Valdecanas, H. Ye, F. Zang, C. Tang, M. Tang, C.-G. Liu, X. Liu, S. Krishnan, J. P. Allison, P. Sharma, P. Hwu, R. Komaki, W. W. Overwijk, D. R. Gomez, J. Y. Chang, S. M. Hahn, M. A. Cortez, J. W. Welsh, Suppression of type I IFN signaling in tumors mediates resistance to anti-PD-1 treatment that can be overcome by radiotherapy. *Cancer Res.* **77**, 839–850 (2017). doi:10.1158/0008-5472.CAN-15-3142 Medline

27. M. C. Collado, M. Derrien, E. Isolauri, W. M. de Vos, S. Salminen, Intestinal integrity and *Akkermansia muciniphila*, a mucin-degrading member of the intestinal microbiota present in infants, adults, and the elderly. *Appl. Environ. Microbiol.* **73**, 7767–7770 (2007). doi:10.1128/AEM.01477-07 Medline

28. N. Geva-Zatorsky, E. Sefik, L. Kua, L. Pasman, T. G. Tan, A. Ortiz-Lopez, T. B. Yanortsang, L. Yang, R. Jupp, D. Mathis, C. Benoist, D. L. Kasper, Mining the human gut microbiota for immunomodulatory organisms. *Cell* **168**, 928–943.e11 (2017). doi:10.1016/j.cell.2017.01.022 Medline

29. A. Suau, R. Bonnet, M. Sutren, J. J. Godon, G. R. Gibson, M. D. Collins, J. Doré, Direct analysis of genes encoding 16S rRNA from complex communities reveals many novel molecular species within the human gut. *Appl. Environ. Microbiol.* **65**, 4799–4807 (1999). Medline

30. D. S. Chen, I. Mellman, Elements of cancer immunity and the cancer-immune set point. *Nature* **541**, 321–330 (2017). doi:10.1038/nature21349 Medline

31. A. Criscuolo, S. Brisse, AlienTrimmer: A tool to quickly and accurately trim off multiple short contaminant sequences from high-throughput sequencing reads. *Genomics* **102**, 500–506 (2013). doi:10.1016/j.ygeno.2013.07.011 Medline

32. B. Langmead, S. L. Salzberg, Fast gapped-read alignment with Bowtie 2. *Nat. Methods* **9**, 357–359 (2012). doi:10.1038/nmeth.1923 Medline

33. A. Cotillard, S. P. Kennedy, L. C. Kong, E. Prifti, N. Pons, E. Le Chatelier, M. Almeida, B. Quinquis, F. Levenez, N. Galleron, S. Gougis, S. Rizkalla, J.-M. Batto, P. Renault, J. Doré, J. D. Zucker, K. Clément, S. D. Ehrlich, S. D. Ehrlich, H. Blottière, M. Leclerc, C. Juste, T. de Wouters, P. Lepage, C. Fouqueray, A. Basdevant, C. Henegar, C. Godard, M. Fondacci, A. Rohia, F. Hajduch, J. Weissenbach, E. Pelletier, D. Le Paslier, J.-P. Gauchi, J.-F. Gibrat, V. Loux, W. Carré, E. Maguin, M. van de Guchte, A. Jamet, F. Boumezbeur, S. Layec, Dietary intervention impact on gut microbial gene richness. *Nature* **500**, 585–588 (2013). doi:10.1038/nature12480 Medline

34. E. Le Chatelier, T. Nielsen, J. Qin, E. Prifti, F. Hildebrand, G. Falony, M. Almeida, M. Arumugam, J.-M. Batto, S. Kennedy, P. Leonard, J. Li, K. Burgdorf, N. Grarup, T. Jørgensen, I. Brandslund, H. B. Nielsen, A. S. Juncker, M. Bertalan, F. Levenez, N. Pons, S. Rasmussen, S. Sunagawa, J. Tap, S. Tims, E. G. Zoetendal, S. Brunak, K. Clément, J. Doré, M. Kleerebezem, K. Kristiansen, P. Renault, T. Sicheritz-Ponten, W. M. de Vos, J.-D. Zucker, J. Raes, T. Hansen, P. Bork, J. Wang, S. D. Ehrlich, O. Pedersen, E. Guedon, C. Delorme, S. Layec, G. Khaci, M. van de Guchte, G. Vandemeulebrouck, A. Jamet, R. Dervyn, N. Sanchez, E. Maguin, F. Haimet, Y. Winogradski, A. Cultrone, M. Leclerc, C. Juste, H. Blottière, E. Pelletier, D. LePaslier, F. Artiguenave, T. Bruls, J. Weissenbach, K. Turner, J. Parkhill, M. Antolin, C. Manichanh, F. Casellas, N. Boruel, E. Varela, A. Torrejon, F. Guarner, G. Denariaz, M. Derrien, J. E. T. van Hylckama Vlieg, P. Veiga, R. Oozeer, J. Knol, M. Rescigno, C. Brechot, C. M'Rini, A. Mérieux, T. Yamada, Richness of human gut microbiome correlates with metabolic markers. *Nature* **500**, 541–546 (2013). doi:10.1038/nature12506 Medline

35. H. B. Nielsen, M. Almeida, A. S. Juncker, S. Rasmussen, J. Li, S. Sunagawa, D. R. Plichta, L. Gautier, A. G. Pedersen, E. Le Chatelier, E. Pelletier, I. Bonde, T. Nielsen, C. Manichanh, M. Arumugam, J.-M. Batto, M. B. Quintanilha Dos Santos, N. Blom, N. Borruel, K. S. Burgdorf, F. Boumezbeur, F. Casellas, J. Doré, P. Dworzynski, F. Guarner, T. Hansen, F. Hildebrand, R. S. Kaas, S. Kennedy, K. Kristiansen, J. R. Kultima, P. Léonard, F. Levenez, O. Lund, B. Moumen, D. Le Paslier, N. Pons, O. Pedersen, E. Prifti, J. Qin, J. Raes, S. Sørensen, J. Tap, S. Tims, D. W. Ussery, T. Yamada, P. Renault, T. Sicheritz-Ponten, P. Bork, J. Wang, S. Brunak, S. D. Ehrlich, A. Jamet, A. Mérieux, A. Cultrone, A. Torrejon, B. Quinquis, C. Brechot, C. Delorme, C. M'Rini, W. M. de Vos, E. Maguin, E. Varela, E. Guedon, F. Gwen, F. Haimet, F. Artiguenave, G. Vandemeulebrouck, G. Denariaz, G. Khaci, H. Blottière, J. Knol, J. Weissenbach, J. E. T. van Hylckama Vlieg, J. Torben, J. Parkhill, K. Turner, M. van de Guchte, M. Antolin, M. Rescigno, M. Kleerebezem, M. Derrien, N. Galleron, N. Sanchez, N. Grarup, P. Veiga, R. Oozeer, R. Dervyn, S. Layec, T. Bruls, Y. Winogradski, E. G. Zoetendal, Identification and assembly of genomes and genetic elements in complex metagenomic samples without using reference genomes. *Nat. Biotechnol.* **32**, 822–828 (2014). doi:10.1038/nbt.2939 Medline

ACKNOWLEDGMENTS
We are thankful to the animal facility team and V. Rouffiac from the imaging platform of G. Roussy, as well as S. Jabs for her technical help. The data reported in this manuscript are tabulated in the main paper and in the supplementary materials. The metagenomic shotgun sequencing data are available from the European Nucleotide Archive (EMBL-EBI) under the accession number PRJEB22863. BR was supported by Gustave Roussy Course of Excellence in Oncology- Fondation Philanthropia and the McGill University Townsend hematology research fellowship award. LZ and GK were supported by the Ligue contre le Cancer (équipe labelisée); Agence Nationale de la Recherche (ANR) – Projets blancs; ANR under the frame of E-Rare-2, the ERA-Net for Research on Rare Diseases; Association pour la recherche sur le cancer (ARC); Cancéropôle Ile-de-France; Institut National du Cancer (INCa); Institut Universitaire de France; Fondation pour la Recherche Médicale (FRM); the European Commission (ArtForce); the European Research Council (ERC); the LeDucq Foundation; the LabEx Immuno-Oncology; the SIRIC Stratified Oncology Cell DNA Repair and Tumor Immune Elimination (SOCRATE); the SIRIC Cancer Research and Personalized Medicine (CARPEM); the Paris Alliance of Cancer Research Institutes (PACRI) and by philanthropia (Mrs E. Badinter and Mrs N. Meyer). L. Z, E. LC and B.R are inventors on patent EP17305206 and European license 16306779.6 held by Institut Gusave Roussy that covers use of microbial modulators for anti-PD1/PD-L1/PD-L2 Ab-based treatments. LZ and GK are cofounders of EverImmune, a biotech company focused on the use of commensal bacteria for cancer treatment.

SUPPLEMENTARY MATERIALS
www.sciencemag.org/cgi/content/full/science.aan3706/DC1
Materials and Methods
Figs. S1 to S16
Tables S1 to S18
References (*31*–*35*)

5 April 2017; accepted 20 September 2017
Published online 2 November 2017
10.1126/science.aan3706

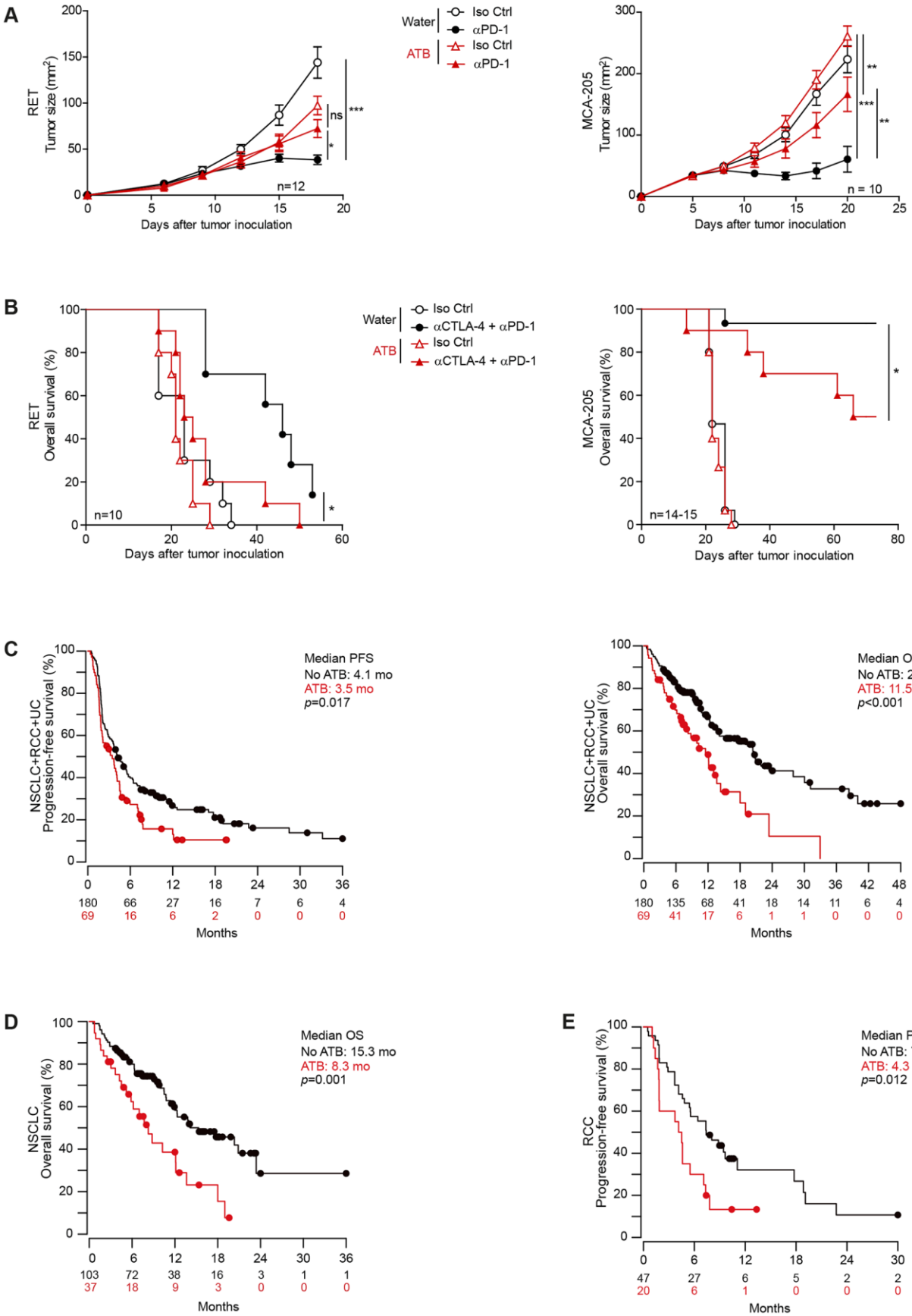

Fig. 1 (preceding page). Antibiotics compromise the efficacy of PD-1 blockade in mouse tumor models and cancer patients. (**A**) Tumor growth kinetics of RET melanoma (left panel) and MCA-205 sarcoma in mice (right panel) treated with four injections of anti-PD-1 (clone RMP1-14) or isotype control (Iso Ctrl) mAb in the presence or absence of broad-spectrum antibiotics (ATB). Means ± SEM of tumor sizes are depicted for 10-12 mice/group. (**B**) Survival curves of RET and MCA-205 bearing mice treated with anti-PD-1 mAb combined with anti-CTLA-4 mAbs (left and right, respectively). Each line represents one survival curve for each group of 5 mice from 2-3 independent experiments. Anova & Log-rank (Mantel-Cox) statistical analyses: $*p < 0.05$, $**p < 0.01$, $***p < 0.001$, ns: not significant. (**C** to **E**) Kaplan-Meier estimates for progression-free survival (PFS) or overall survival (OS) of cancer patients. All cancer patients (n = 249) (C) including patients with advanced non-small cell lung cancer (NSCLC, n = 140, fig. S1A; fig. S1D for the validation cohort) (D), renal cell carcinoma (RCC, n = 67, fig. S1B) (E) and urothelial carcinoma (UC, n = 42), (fig. S1C) treated with anti-PD-1/PD-L1 mAb who did or did not receive ATB were monitored (tables S1 to S6). The points represent data censored at the last time the patient was known to be alive and without progression. Log-rank (Mantel-Cox) analysis with indicated *p*-value.

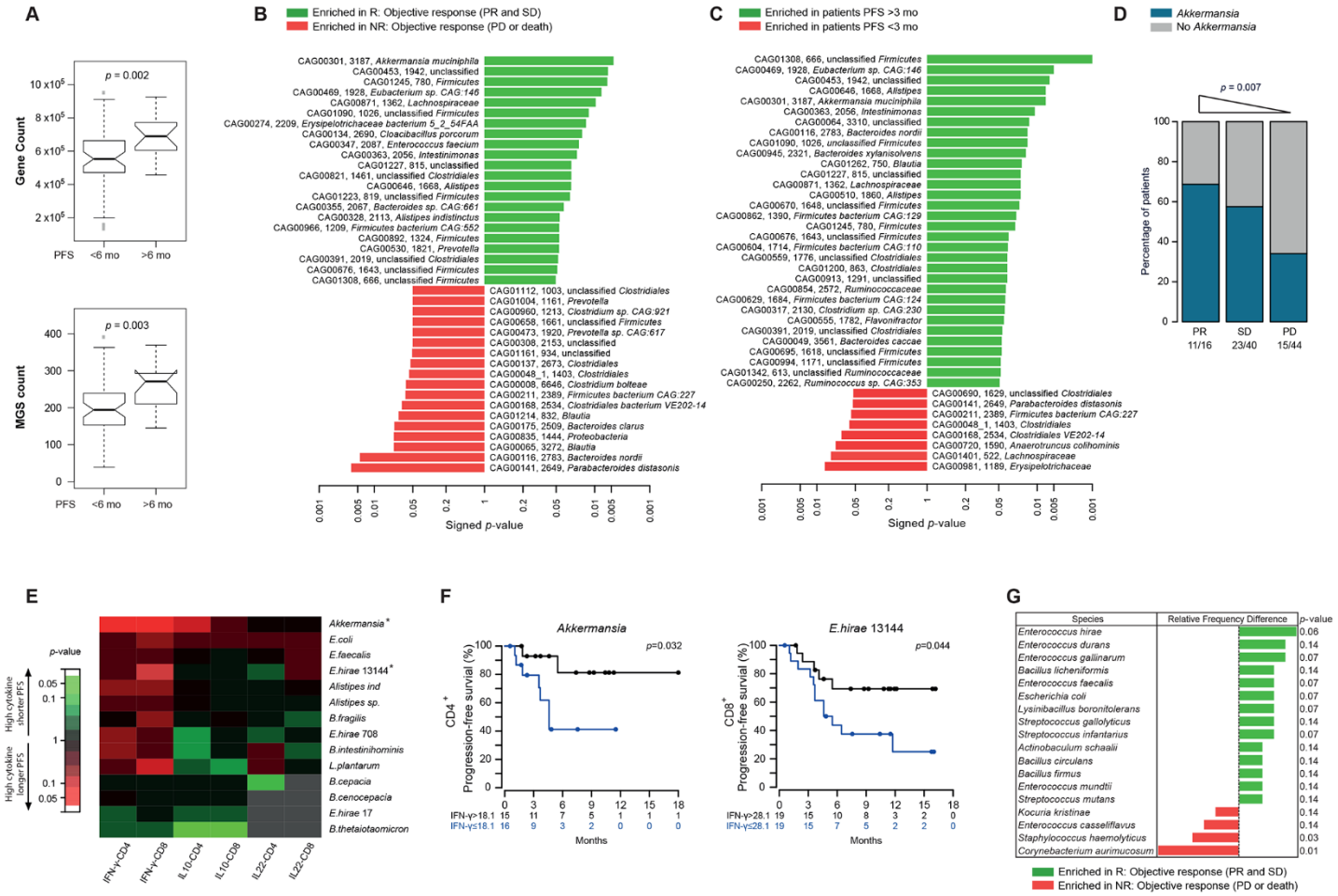

Fig. 2. Metagenomic analyses of fecal samples predicts response at 3 months of anti-PD-1 mAb in cancer patients. (**A**) Shot gun sequencing of fecal samples at diagnosis with representation of gene and MGS counts for all cancer patients according to clinical outcome (PFS at 6 months). Mean ± SEM of counts are depicted for patients experiencing PFS > or < 6 months. Of note, gene or MGS richness did not predict PFS at 3 months. (**B** and **C**) Shot gun sequencing of fecal samples at diagnosis with representation of the relative abundance of each MGS in responders (R) (partial response or stable disease) over non-responders (NR) (progression or death) patients defined using the best clinical response according to RECIST1.1 criteria (B) or PFS at 3 months (C) and the corresponding *p*-value on the entire cohort of n = 100 (60 NSCLC and 40 RCC) patients (B) and excluding those who took ATB (C) (fig. S5B), n = 78, 42R, 36 NR, also refer to fig. S5A for all patients. T0 samples were analyzed, and when not available, T1 specimens were used, as there was no statistical difference between T0 and T1 (fig. S3A). (**D**) Frequency of patients with detectable *A. muciniphila* in their feces according to the PR, SD and PD clinical status, as assessed by MG and analyzed by Cochran-Armitage test. (**E** and **F**) Circulating memory T cell immune responses directed against commensals detected during PD-1 blockade and evaluation of the time to progression. Heat map of the *p*-values for each cytokine and each commensal, segregating NSCLC+RCC patients' PFS according to the median value of cytokine production of the whole cohort. Significant *p* values <0.05 are indicated with a star for the relevant commensal (E). The univariate analysis and Kaplan-Meier curves showing PFS for peripheral blood memory Th1 and Tc1 immune responses directed against *A. muciniphila and E. hirae* 13144 respectively (F). PFS curves for the non-specific TCR-driven cytokine release are depicted in fig. S9. (**G**) Culturomics-based analyses of feces in 16 R and 16 NR NSCLC (defined as the best clinical outcome) prior to therapy, each commensal colony being identified by mass-spectrometry. The relative frequencies of each commensal in all fecal cultures in R over NR is represented and the *p*-value of the difference is annotated in the right column. Student *t* test: *<0.05.

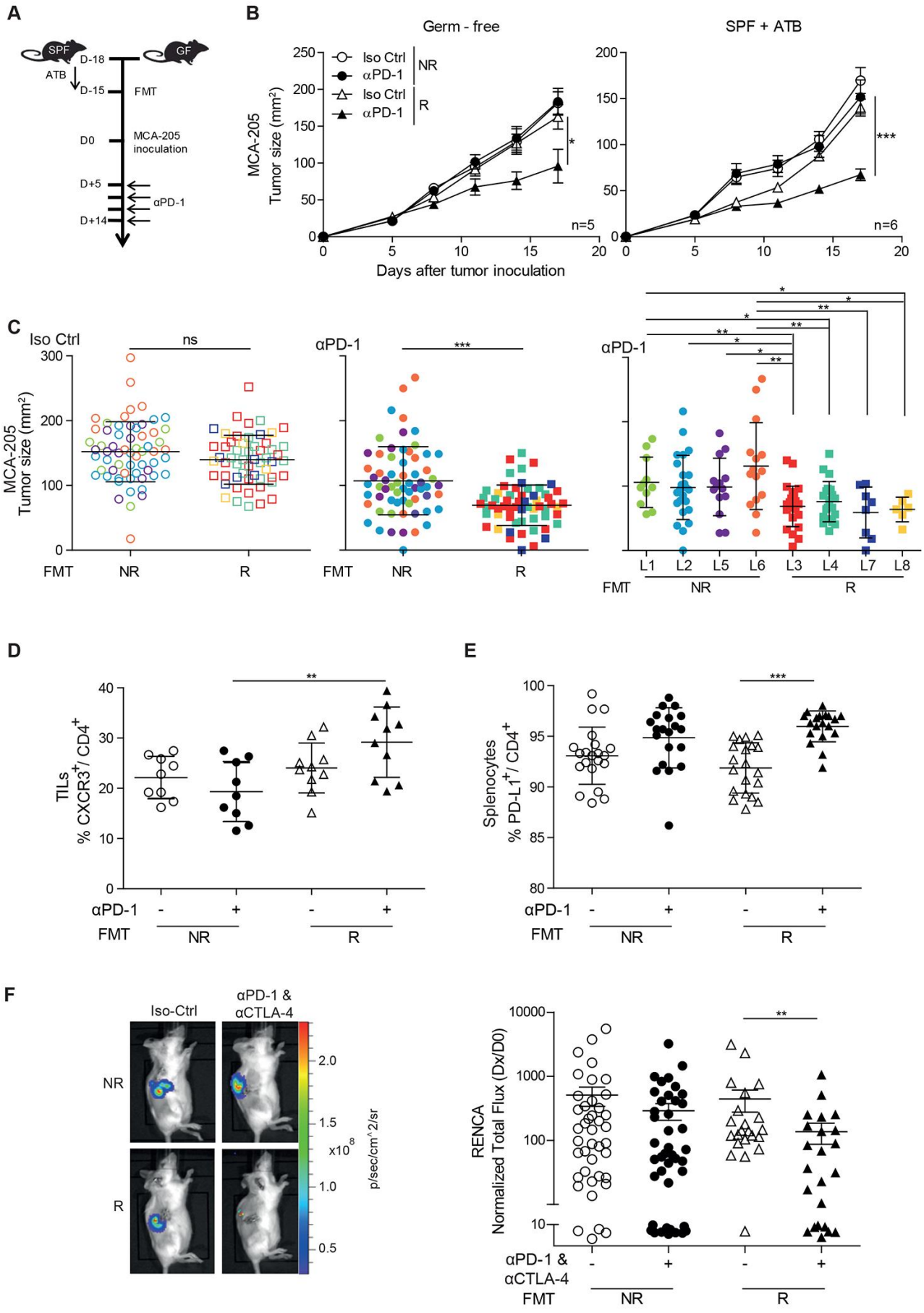

Fig. 3 (preceding page). Fecal microbiota transplantation (FMT) of stool samples from NSCLC and RCC patients into mice dictates outcome following PD-1 blockade. (**A**) Experimental setting: FMT was performed in germ-free (GF) recipients or following 3 days of ATB in SPF mice. Two weeks later, MCA-205 sarcoma cells were inoculated and anti-PD-1 mAb were injected intraperitoneally every 3 days starting on D+5. (**B**) Representative MCA-205 tumor growth curves post-FMT from NSCLC patients into GF (left panel) or ATB-treated mice (right panel) during therapy with anti-PD-1 mAb. (**C**) Means ± SEM of tumor sizes following Iso Ctrl (left), anti-PD1 mAb (middle and right), in MCA-205 bearing SPF reared mice treated with ATB and then receiving FMT from 8 NSCLC patients (n = 4 NR, n = 4 R) prior to anti-PD1 mAb. Pooled data from all patients (left and middle) or individual patients (right), each feces being transferred into 5 mice/group. (**D** and **E**) Flow cytometry analysis of CXCR3 (D) or PD-L1 (E) expression on TILs (D) or $CD3^+CD4^+$ splenocytes (E) in 38 and 80 animals, respectively, analyzed at sacrifice corresponding to Fig. 3C. (**F**) Monitoring of RENCA progression using bioluminescence imaging of luciferase activity in n = 133 ATB-treated mice post-FMT with feces from 3 R vs 4 NR RCC patients and treated with the combination of anti-PD-1 and anti-CTLA-4 mAb. All experiments were composed of 5-7 mice/group and were performed at least twice in similar conditions yielding similar results. Anova & Student *t* test statistical analyses of means±SEM: $*p < 0.05$, $**p < 0.01$, $***p < 0.001$, Dx: Last IVIS measurement, D0: Day of randomization.

Fig. 4 (next page). Biological significance of *A. muciniphila* during anticancer PD-1 blockade treatment. (**A** and **B**) ATB-induced dysbiosis were restored by oral administration of *A. muciniphila* (*Akkermansia*) alone or combined with *Enterococcus hirae* 13144 (*E. hirae*) to recipient mice receiving anti-PD-1 mAb. Commensals and anti-PD-1 mAb regimens were administered 5 times every 3 days against RET melanomas (A), and 4 times in luciferase-expressing orthotopic LLC non-small-cell lung cancers (B). (**C**) Means ± SEM of tumor sizes at sacrifice in mice exhibiting NR FMT- induced dysbiosis and compensated with *A. muciniphila* alone or combined with *E. hirae* (also refer to fig. S12) or control bacteria (fig. S13) during anti-PD-1 mAb-based therapy. Each color represents one NR donor of feces transferred into 5 mice/group. (**D** and **E**) Flow cytometry analysis of CCR9 and CXCR3 expression in mesenteric lymph nodes (mLN) residing $CD4^+$ TCM at 48h (D) and at D+17 in the tumor (E) after the 1^{st} injection of anti-PD-1 mAb in ATB-treated animals compensated with a mixture of *A. muciniphila* & *E. hirae*. Pooled data from two independent experiments composed of 5-7 mice/group, each dot representing one mouse. (**F** and **G**) Immunohistochemical determination of CD4 and FoxP3 infiltrates in D+10-treated tumor beds [representative micrograph in (F)] calculated by image analyzer for the experimental setting described in Fig. 3C and calculation of the ratios between these two values on the whole tumor sample [(G), left]. Spearman correlation between CD4/FoxP3 ratios and tumor size at sacrifice [(G), right]. (**H**) Effects of neutralizing anti-IL-12p40 mAb on the anticancer efficacy of PD-1 inhibition alone (left) or combined with *Akkermansia* (right). Means ± SEM of tumor sizes at sacrifice, each dot representing one tumor, each group comprising 5 mice. One representative experiment out of four is shown. Anova & Student *t* test statistical analyses: $*p < 0.05$, $**p < 0.01$, $***p < 0.001$. Dx: Last IVIS measurement, D0: Day of randomization.

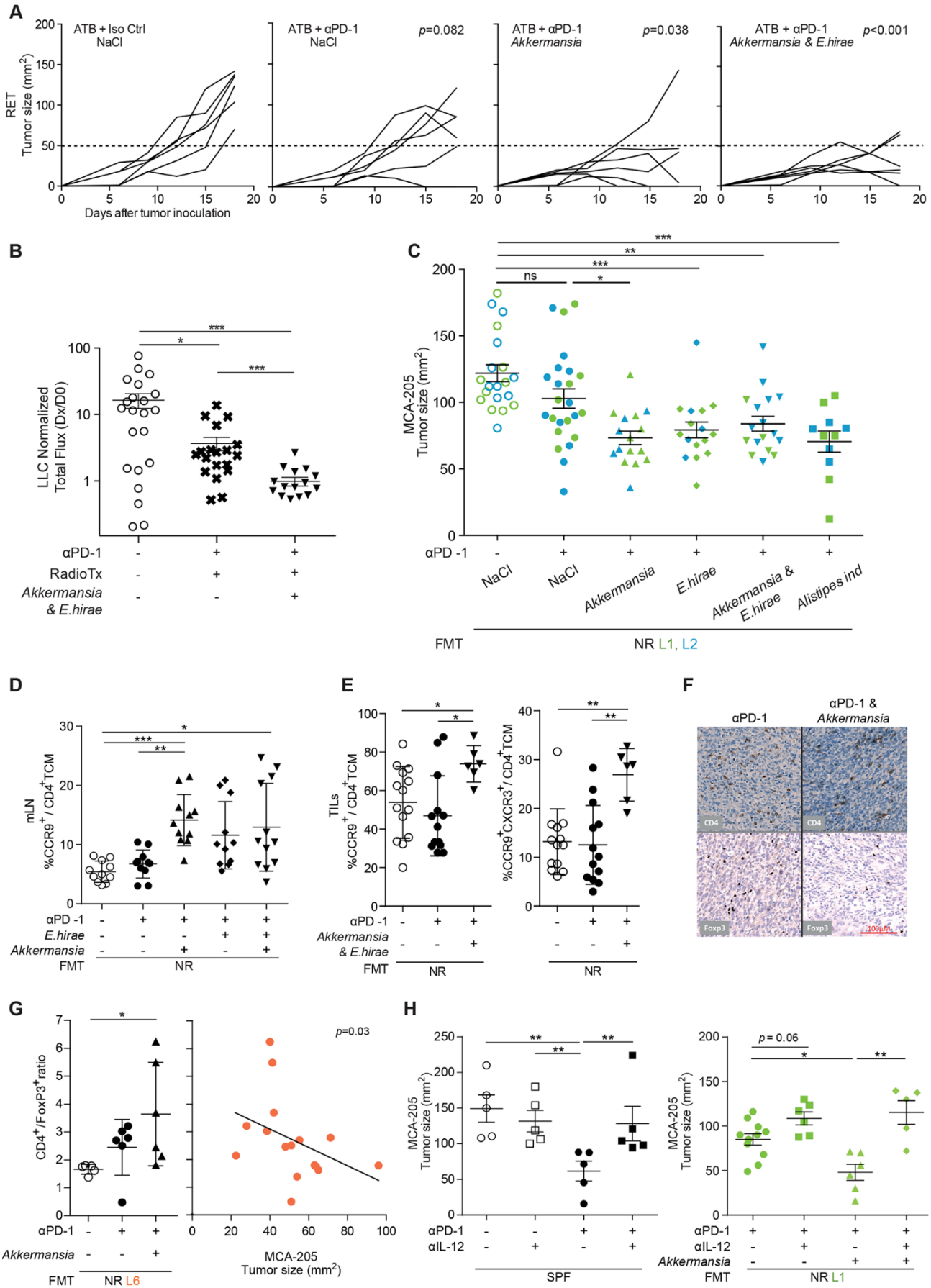

Cite as: V. Gopalakrishnan *et al.*,
Science 10.1126/science.aan4236 (2017).

Gut microbiome modulates response to anti–PD-1 immunotherapy in melanoma patients

V. Gopalakrishnan,[1,2*] C. N. Spencer,[2,3*] L. Nezi,[3*] A. Reuben,[1] M. C. Andrews,[1] T. V. Karpinets,[3] P. A. Prieto,[1†] D. Vicente,[1] K. Hoffman,[4] S. C. Wei,[5] A. P. Cogdill,[1,5] L. Zhao,[3] C. W. Hudgens,[6] D. S. Hutchinson,[7] T. Manzo,[3] M. Petaccia de Macedo,[6‡] T. Cotechini,[8] T. Kumar,[3] W. S. Chen,[9] S. M. Reddy,[10] R. Szczepaniak Sloane,[1] J. Galloway-Pena,[11] H. Jiang,[1] P. L. Chen,[9§] E. J. Shpall,[12] K. Rezvani,[12] A. M. Alousi,[12] R. F. Chemaly,[11] S. Shelburne,[3,11] L. M. Vence,[5] P. C. Okhuysen,[11] V. B. Jensen,[13] A. G. Swennes,[7] F. McAllister,[14] E. Marcelo Riquelme Sanchez,[14] Y. Zhang,[14] E. Le Chatelier,[15] L. Zitvogel,[16] N. Pons,[15] J. L. Austin-Breneman,[1||] L. E. Haydu,[1] E. M. Burton,[1] J. M. Gardner,[1] E. Sirmans,[17] J. Hu,[18] A. J. Lazar,[6,9] T. Tsujikawa,[8] A. Diab,[17] H. Tawbi,[17] I. C. Glitza,[17] W. J. Hwu,[17] S. P. Patel,[17] S. E. Woodman,[17] R. N. Amaria,[17] M. A. Davies,[17] J. E. Gershenwald,[1] P. Hwu,[17] J. E. Lee,[1] J. Zhang,[3] L. M. Coussens,[8] Z. A. Cooper,[1,3¶] P. A. Futreal,[3] C. R. Daniel,[4,2] N. J. Ajami,[7] J. F. Petrosino,[7] M. T. Tetzlaff[6,9] P. Sharma,[5,19] J. P. Allison,[5] R. R. Jenq,[3#] J. A. Wargo,[1,3#]**

[1]Department of Surgical Oncology, The University of Texas MD Anderson Cancer Center, Houston, TX 77030, USA. [2]Department of Epidemiology, Human Genetics and Environmental Sciences, University of Texas School of Public Health, Houston, TX 77030, USA. [3]Department of Genomic Medicine, The University of Texas MD Anderson Cancer Center, Houston, TX 77030, USA. [4]Department of Epidemiology, The University of Texas MD Anderson Cancer Center, Houston, TX 77030, USA. [5]Department of Immunology, The University of Texas MD Anderson Cancer Center, Houston, TX 77030, USA. [6]Department of Translational Molecular Pathology, The University of Texas MD Anderson Cancer Center, Houston, TX 77030, USA. [7]Department of Molecular Virology and Microbiology, Baylor College of Medicine, Houston, TX 77030, USA. [8]Department of Cell, Developmental and Cell Biology, Oregon Health and Sciences University, Portland, OR 97239, USA. [9]Department of Pathology, The University of Texas MD Anderson Cancer Center, Houston, TX 77030, USA. [10]Department of Breast Medical Oncology, The University of Texas MD Anderson Cancer Center, Houston, TX 77030, USA. [11]Department of Infectious Diseases, The University of Texas MD Anderson Cancer Center, Houston, TX 77030, USA. [12]Department of Stem Cell Transplantation, The University of Texas MD Anderson Cancer Center, Houston, TX 77030, USA. [13]Department of Veterinary Medicine and Surgery, The University of Texas MD Anderson Cancer Center, Houston, TX 77030, USA. [14]Department of Clinical Cancer Prevention, The University of Texas MD Anderson Cancer Center, Houston, TX 77030, USA. [15]Centre de Recherche de Jouy-en-Josas, Institut National de la Recherche Agronomique, 78352 Jouy-en-Josas, France. [16]Centre d'Investigation Clinique Biothérapie, Institut Gustave-Roussy, 94805 Villejuif Cedex, France. [17]Department of Melanoma Medical Oncology, The University of Texas MD Anderson Cancer Center, Houston, TX 77030, USA. [18]Department of Biostatistics, The University of Texas MD Anderson Cancer Center, Houston, TX 77030, USA. [19]Department of Genitourinary Medical Oncology, The University of Texas MD Anderson Cancer Center, Houston, TX 77030, USA.

*These authors contributed equally to this work. †Present address: University of Rochester James P. Wilmot Cancer Center, Rochester, NY 14642, USA. ‡Present address: A.C.Camargo Cancer Center, São Paolo, Brazil. §Present address: Moffitt Cancer Center, Tampa, FL 33612, USA. ||Present address: Harvard University, Cambridge, MA 02138, USA. ¶Present address: MedImmune, Gaithersburg, MD 20878, USA. #These authors contributed equally to this work.

**Corresponding author. Email: jwargo@mdanderson.org

Pre-clinical mouse models suggest that the gut microbiome modulates tumor response to checkpoint blockade immunotherapy; however, this has not been well-characterized in human cancer patients. Here we examined the oral and gut microbiome of melanoma patients undergoing anti-PD-1 immunotherapy (n=112). Significant differences were observed in the diversity and composition of the patient gut microbiome of responders (R) versus non-responders (NR). Analysis of patient fecal microbiome samples (n=43, 30R, 13NR) showed significantly higher alpha diversity (p<0.01) and relative abundance of Ruminococcaceae bacteria (p<0.01) in responding patients. Metagenomic studies revealed functional differences in gut bacteria in R including enrichment of anabolic pathways. Immune profiling suggested enhanced systemic and anti-tumor immunity in responding patients with a favorable gut microbiome, as well as in germ-free mice receiving fecal transplants from responding patients. Together, these data have important implications for the treatment of melanoma patients with immune checkpoint inhibitors.

Tremendous advances have been made in the treatment of melanoma and other cancers using immune checkpoint inhibitors targeting the cytotoxic T-lymphocyte-associated antigen (CTLA-4) and the programmed death 1 (PD-1) protein, however responses to these therapies are often heterogeneous and not durable (*1–3*). It has recently emerged that factors beyond tumor genomics influence cancer development and therapeutic responses (*4–7*), including host factors such as the gastrointestinal (gut) microbiome (*8–10*). A number of studies have shown that the gut microbiome may influence anti-tumor immune responses via innate and adaptive immunity (*11, 12*), and that therapeutic responses may be improved via its modulation (*13, 14*), however this has not been extensively studied in cancer patients.

To better understand the role of the microbiome in response to immune checkpoint blockade, we prospectively collected microbiome samples from patients with metastatic melanoma starting treatment with anti-PD-1 therapy (n=112 patients) (fig. S1 and table S1). Oral (buccal) and gut (fecal) microbiome samples were collected at treatment initiation, and tumor biopsies and blood samples were collected at matched pre-treatment time points when possible to assess for genomic alterations, as well as the density and phenotype of tumor-infiltrating and circulating immune cell subsets (Fig. 1A and fig. S2). Taxonomic profiling via 16S rRNA gene sequencing was performed on all available oral and gut samples, with metagenomic whole genome shotgun (WGS) sequencing on a subset (n=25). Eligible patients (n=89) were classified as responders (R; n=54) versus non-responders (NR; n=35) based on radiographic assessment using the Response Evaluation Criteria in Solid Tumors (RECIST 1.1) criteria (*15*) at 6 months after treatment initiation. Patients were classified as R if they achieved an objective response (complete or partial response or stable disease lasting at least 6 months), versus NR if they progressed on therapy or had stable disease lasting less than 6 months. This classification accounts for the subset of patients who may derive long-term disease benefit despite not achieving a bona fide RECIST response, and has been employed in numerous published studies of patients on checkpoint blockade (*16–19*). Of note, patients in R versus NR groups were similar with respect to age, gender, primary type, prior therapy, concurrent systemic therapy and serum lactate dehydrogenase (LDH) (table S2). Prior genomic analyses have demonstrated that patients with tumors having a higher mutational load are more likely to respond to anti-CTLA-4 (*16*, *20*, *21*) or anti-PD-1 therapy (*21–24*), however a high mutational load alone appears neither sufficient nor essential for response. In this cohort, the total number and specific melanoma driver mutations were within comparable parameters between R and NR following anti-PD-1 therapy (fig. S3), though the number of tumors available for sequencing (n=10, R=7, NR=3) was limited and may have reduced our ability to detect a significant association between mutational burden and response.

We first assessed the landscape of the oral and gut microbiome in all available samples in patients (n=112) with metastatic melanoma via 16S sequencing, noting that both communities were relatively diverse, with a high abundance of Lactobacillales in the oral microbiome and Bacteroidales in the fecal microbiome (Fig. 1B). Bipartite network analysis (*25*) demonstrated a clear separation of community structure between the oral and fecal microbiomes in terms of both matched and aggregate samples (fig. S4), suggesting that these communities are distinct. Loss of microbial diversity (dysbiosis) is associated with chronic health conditions (*26–28*) and cancer (*8–10*), and is also associated with poor outcomes to certain forms of cancer therapy including allogeneic stem cell transplant (*29*). Based on these data, we examined the diversity of the oral and gut microbiomes in eligible patients on anti-PD1 therapy, and found that alpha diversity of the gut microbiome was significantly higher in R (n=30) compared to NR (n=13) using several indices ($p<0.01$, Fig. 1C and fig. S5). No significant differences were observed in the oral microbiome (R=54, NR=32, $p=0.11$, fig. S6). We then tested the relationship of diversity and progression-free survival (PFS) in our cohort by stratifying patients based on tertiles of Inverse Simpson scores, demonstrating that patients with a high diversity in the fecal microbiome had significantly prolonged PFS compared to those with intermediate or low diversity ($p=0.02$ and 0.04, respectively; Fig. 1, D and E, and fig. S7). No differences in PFS were noted when comparing diversity of the oral microbiome (fig. S8). Importantly, upon visualizing beta diversity weighted UniFrac distances (*30*) by principal coordinate analysis, we found a notable clustering effect by response status in the gut microbiome of these patients, which was not observed in the oral microbiome (Fig. 1F and fig. S8E).

Since compositional differences in the microbiome may also influence cancer development and response to therapy (*12*, *14*, *15*, *23*), we sought to determine if differences existed in the oral or gut microbiomes of R and NR to anti-PD-1 therapy. To test this, we first compared an enrichment of operational taxonomic units (OTUs) in R versus NR, demonstrating that distinct sets of rare low abundance OTUs were associated with response to anti-PD-1 therapy, with enrichment of Clostridiales in R and Bacteroidales in NR in the gut microbiome ($p<0.01$, Fig. 2, A and B, and fig. S9, A and C). No significant differences in enrichment were noted in the oral microbiome of R versus NR (fig. S9, B and D, and fig. S10). To further explore these findings, we performed high dimensional class comparisons via linear discriminant analysis of effect size (LEfSe) (*31*), which again demonstrated differentially abundant bacteria in the fecal microbiome of R versus NR to anti-PD-1 therapy, with Clostridiales/Ruminococcaceae enriched in R and Bacteroidales enriched in NR (Fig. 2, C and D). No major differences were observed in the oral microbiome between R and NR, with the exception of higher Bacteroidales in NR to anti-PD-1 therapy (fig. S11). Pairwise comparisons were then performed for bacterial taxa at all levels by response. In addition to confirming the previous taxonomic differences, these analyses identified the *Faecalibacterium* genus as significantly enriched in R (Fig. 2E and table S3). Metagenomic WGS further confirmed enrichment of *Faecalibacterium* species in addition to others in R, while *Bacteroides thetaiotaomicron*, *Escherichia coli*, and *Anaerotruncus colihominis* were enriched in NR (Fig. 2F and

table S4). Importantly, the gut microbiome was shown to be relatively stable over time in a limited number of longitudinal samples tested (fig. S12).

We next asked whether bacterial composition and abundances within the gut and/or oral microbiomes of patients were associated with a specific treatment outcome to anti-PD-1 therapy. We grouped all identified OTUs into clusters of related OTUs (crOTUs) via construction of a phylogenetic tree from sequence alignment data (*32*). This technique involves comparison of abundances of different potential groupings of bacteria based on 16S sequence similarity and helps address the sparse distribution of OTU abundances observed in the absence of this approach (fig. S13). Unsupervised hierarchical clustering of crOTU abundances within the gut and oral microbiomes was then performed without input of response data. We found that patients segregated into 2 distinct community types. Type 1 comprised entirely of R and was enriched for Clostridiales, whereas Type 2 comprised a mixture of R and NR (p=0.02) and was enriched for Bacteroidales (Fig. 3A). To better understand compositional differences between these crOTU community types, we again performed pairwise comparisons of the gut microbiota, and identified a pattern very similar to that seen when clustering by response, with Clostridiales/Ruminococcaceae enriched in Type 1, and Bacteroidales enriched in Type 2 (fig. S14A and table S5). Further, these communities clustered distinctly using principal coordinate analysis of weighted Unifrac distances (fig. S14B). Analysis of crOTUs in the oral microbiome revealed no apparent relationship to treatment response (fig. S15, A and B).

To explore how specific bacterial taxa impact patient treatment response, we compared PFS following anti-PD-1 therapy as it related to the "top hits" consistently observed across our analyses. From the Ruminococcaceae family of the Clostridiales order, we focused on the *Faecalibacterium* genus in R, and Bacteroidales order in NR, and stratified patients into high versus low categories based on the median relative abundance of these taxa in the gut microbiome. Patients with high *Faecalibacterium* abundance had a significantly prolonged PFS versus those with a low abundance (p=0.03). Conversely, patients with a high abundance of Bacteroidales had a shortened PFS compared to those with a low abundance (p=0.05, Fig. 3D). This is in line with recently published data in a small cohort of patients on CTLA-4 blockade, where patients with a higher abundance of *Faecalibacterium* had a prolonged PFS compared to those with a higher abundance of Bacteroidales in the gut microbiome (*33*). In addition, univariate Cox proportional hazards analyses demonstrated that the strongest microbial predictors of response to anti-PD-1 therapy were alpha diversity [Intermediate hazard ratio (HR)=3.60, 95% C.I.=1.02-12.74; Low HR=3.57, 95% confidence interval (C.I.)=1.02-12.52], and abundance of *Faecalibacterium* (HR=2.92, 95% C.I.=1.08-7.89) and Bacteroidales (HR= 0.39, 95% CI=0.15-1.03) in the fecal microbiome. There was no association found between PFS and stage in our cohort. Our final multivariate model was selected by forward stepwise selection and included *Faecalibacterium* abundance (HR=2.95, 95% C.I.=1.31-7.29, p=0.03) and prior immunotherapy (HR=2.87, 95% C.I.=1.10-7.89, p=0.03) (table S6). Abundance of *Faecalibacterium* and Bacteroidales also outperformed relevant clinical variables in receiver operating characteristic curve (ROC) analysis (fig. S16).

Next, we sought to gain insight into the mechanism through which the gut microbiome may influence response to anti-PD-1 therapy, and first conducted functional genomic profiling of gut microbiome samples via metagenomic WGS sequencing (n=25) in R (n=14) vs NR (n=11). Organism-specific gene hits were assigned to the Kyoto Encyclopedia of Genes and Genomes (KEGG) orthology (KO), and based on these annotations, metagenomes for each sample were reconstructed into metabolic pathways using the MetaCyc hierarchy of pathway classifications (*34*, *35*). Unsupervised hierarchical clustering of predicted pathway enrichment identified two groups of patient samples, with response rates of 69.2% and 41.7% (Fig. 3E). A similar pattern was also noted for KO-abundances with 70.6% and 37.5% response rates (fig. S17). Comparisons of pathway enrichment across these groups showed changes in metabolic functions, with anabolic functions predominating in R including amino acid biosynthesis (Fig. 3E), which may promote host immunity (*36*), whereas catabolic functions predominated in NR (Fig. 3E, fig. S16, and table S7).

There is clear evidence in pre-clinical models that differential composition of the gut microbiome may influence therapeutic responses to anti-PD-1 therapy at the level of the tumor microenvironment (*12*), thus we next examined the relationship between the gut microbiota and systemic and anti-tumor immune responses in our cohort of patients on anti-PD-1 therapy. We compared the tumor-associated immune infiltrates via multi-parameter immunohistochemistry (IHC) and observed a higher density of CD8+ T cells in baseline samples of R versus NR (p=0.04), consistent with prior reports (Fig. 4A and fig. S18) (*18*, *37*). Pairwise comparisons using Spearman rank correlations were then performed between specific bacterial taxa enriched in the gut microbiome of R and NR and immune markers in the tumor microenvironment, demonstrating a statistically significant positive correlation between the CD8+ T cell infiltrate in the tumor and abundance of the *Faecalibacterium* genus, the Ruminococcaceae family and the Clostridiales order in the gut and a non-significant but negative correlation with Bacteroidales (Fig. 4, B and C, and figs. S19 and S20). No associations were seen between CD8+ T cell density and diversity or crOTU community type membership (fig. S21). Analysis of

systemic immune responses via flow cytometry and cytokine assays revealed that patients with a high abundance of Clostridiales, Ruminococcaceae or *Faecalibacterium* in the gut had higher levels of effector CD4+ and CD8+ T cells in the systemic circulation with a preserved cytokine response to anti-PD-1 therapy, whereas patients with a higher abundance of Bacteroidales in the gut microbiome had higher levels of regulatory T cells (Treg) and myeloid derived suppressor cells (MDSC) in the systemic circulation, with a blunted cytokine response (Fig. 4D and figs. S22 and S23). To better understand the influence of compositional differences in the gut microbiome on antigen processing and presentation within the tumor microenvironment, we next performed multiplex IHC targeting the myeloid compartment (*38*). In these studies, patients with a high abundance of *Faecalibacterium* in the gut microbiome had a higher density of immune cells and markers of antigen processing and presentation compared to those with a high abundance of Bacteroidales (Fig. 4, E and F, and figs. S24 and S25), suggesting a possible mechanism through which the gut microbiome may modulate anti-tumor immune responses (*12*), though this must be validated in a larger cohort.

To investigate a causal link between a "favorable" gut microbiome and response to immune checkpoint blockade, we performed Fecal Microbiome Transplantation (FMT) experiments in germ-free recipient mice (Fig. 4G). In these studies, mice that were transplanted with stool from R to anti-PD-1 therapy (R-FMT) had significantly reduced tumor growth ($p=0.04$, Fig. 4H and fig. S26A) by day 14 compared to those transplanted with stool from NR (NR-FMT). Importantly, mice transplanted with R-FMT also exhibited improved responses to anti-PD-L1 therapy (Fig. 4I) in contrast to mice that were transplanted with stool from NR (NR-FMT). Next we performed 16S sequencing on fecal samples collected from mice treated with FMT, demonstrating that R-FMT mice also had significantly higher abundance of *Faecalibacterium* in their gut microbiome ($p<0.01$) (fig. S27). We also wanted to better understand the mechanism through which the gut microbiome may influence systemic and anti-tumor immune responses, and performed correlative studies on tumors, peripheral blood and spleens from these mice. These studies demonstrated that tumors of mice receiving R-FMT had a higher density of CD8+ T cells than mice receiving NR-FMT, consistent with human data (Fig. 4J and fig. S26B, top series). Analysis of CD45+ myeloid and lymphoid tumor infiltrating cells by flow cytometry confirmed this result (fig. S26C). Moreover, FMT from R locally increased the number of CD45+ immune and CD8+ T cells in the gut compared to NR-FMT (Fig. 4K and fig. S26B, bottom series). Mass cytometry analysis using t-SNE dimension reduction was performed on tumors from mice, and demonstrated up-regulation of PD-L1 in the tumor microenvironment of mice receiving R-FMT versus NR-FMT (fig. S26D), suggesting the development of a "hot" tumor microenvironment. Further phenotypic studies of tumor immune infiltrates revealed a significant enrichment of innate effector cells (expressing CD45+CD11b+Ly6G+) in mice receiving R-FMT (fig. S26E). A lower frequency of suppressive myeloid cells (expressing CD11b+CD11c+) was observed in mice receiving R-FMT compared to mice receiving NR-FMT (fig. S26F). Finally, an increase in the frequency of RORγT+ Th17 cells in the tumor was also detected in NR-FMT mice (fig. S26G), in line with what we observed in tumors from patients who failed to respond to anti-PD-1 therapy. Mice receiving NR-FMT also had higher levels of regulatory CD4+ FoxP3+ T cells (fig. S26H) and CD4+ IL-17+ (fig. S26I) cells in the spleen, suggesting impaired host immune responses.

Our results indicate that the gut microbiome may modulate responses to anti PD-1 immunotherapy in melanoma patients. We propose that patients with a "favorable" gut microbiome (e.g., high diversity and abundance of Ruminococcaceae/*Faecalibacterium*) have enhanced systemic and anti-tumor immune responses mediated by increased antigen presentation, and improved effector T cell function in the periphery and the tumor microenvironment. In contrast, patients with an "unfavorable" gut microbiome (e.g., low diversity and high relative abundance of Bacteroidales) have impaired systemic and anti-tumor immune responses mediated by limited intratumoral lymphoid and myeloid infiltration and weakened antigen presentation capacity. These findings highlight the therapeutic potential of modulating the gut microbiome in patients receiving checkpoint blockade immunotherapy, and warrant prompt evaluation in cancer patients through clinicaltrials.

REFERENCES AND NOTES

1. D. Schadendorf, F. S. Hodi, C. Robert, J. S. Weber, K. Margolin, O. Hamid, D. Patt, T.-T. Chen, D. M. Berman, J. D. Wolchok, Pooled analysis of long-term survival data from phase II and phase III trials of ipilimumab in unresectable or metastatic melanoma. *J. Clin. Oncol.* **33**, 1889–1894 (2015). doi:10.1200/JCO.2014.56.2736 Medline
2. C. Robert *et al.*, KEYNOTE-006 investigators, Pembrolizumab versus ipilimumab in advanced melanoma. *N. Engl. J. Med.* **372**, 2521–2532 (2015). doi:10.1056/NEJMoa1503093 Medline
3. C. Robert, G. V. Long, B. Brady, C. Dutriaux, M. Maio, L. Mortier, J. C. Hassel, P. Rutkowski, C. McNeil, E. Kalinka-Warzocha, K. J. Savage, M. M. Hernberg, C. Lebbé, J. Charles, C. Mihalcioiu, V. Chiarion-Sileni, C. Mauch, F. Cognetti, A. Arance, H. Schmidt, D. Schadendorf, H. Gogas, L. Lundgren-Eriksson, C. Horak, B. Sharkey, I. M. Waxman, V. Atkinson, P. A. Ascierto, Nivolumab in previously untreated melanoma without *BRAF* mutation. *N. Engl. J. Med.* **372**, 320–330 (2015). doi:10.1056/NEJMoa1412082 Medline
4. M. D. Vesely, R. D. Schreiber, Cancer immunoediting: Antigens, mechanisms, and implications to cancer immunotherapy. *Ann. N. Y. Acad. Sci.* **1284**, 1–5 (2013). doi:10.1111/nyas.12105 Medline
5. S. L. Topalian, C. G. Drake, D. M. Pardoll, Immune checkpoint blockade: A common denominator approach to cancer therapy. *Cancer Cell* **27**, 450–461 (2015). doi:10.1016/j.ccell.2015.03.001 Medline

6. E. Tran, P. F. Robbins, S. A. Rosenberg, 'Final common pathway' of human cancer immunotherapy: Targeting random somatic mutations. *Nat. Immunol.* **18**, 255–262 (2017). doi:10.1038/ni.3682 Medline
7. P. Bachireddy, U. E. Burkhardt, M. Rajasagi, C. J. Wu, Haematological malignancies: At the forefront of immunotherapeutic innovation. *Nat. Rev. Cancer* **15**, 201–215 (2015). doi:10.1038/nrc3907 Medline
8. W. S. Garrett, Cancer and the microbiota. *Science* **348**, 80–86 (2015). doi:10.1126/science.aaa4972 Medline
9. J. A. Segre, Microbial growth dynamics and human disease. *Science* **349**, 1058–1059 (2015). doi:10.1126/science.aad0781 Medline
10. J. L. Drewes, F. Housseau, C. L. Sears, Sporadic colorectal cancer: Microbial contributors to disease prevention, development and therapy. *Br. J. Cancer* **115**, 273–280 (2016). doi:10.1038/bjc.2016.189 Medline
11. C. M. Paulos, C. Wrzesinski, A. Kaiser, C. S. Hinrichs, M. Chieppa, L. Cassard, D. C. Palmer, A. Boni, P. Muranski, Z. Yu, L. Gattinoni, P. A. Antony, S. A. Rosenberg, N. P. Restifo, Microbial translocation augments the function of adoptively transferred self/tumor-specific $CD8^+$ T cells via TLR4 signaling. *J. Clin. Invest.* **117**, 2197–2204 (2007). doi:10.1172/JCI32205 Medline
12. A. Sivan, L. Corrales, N. Hubert, J. B. Williams, K. Aquino-Michaels, Z. M. Earley, F. W. Benyamin, Y. M. Lei, B. Jabri, M.-L. Alegre, E. B. Chang, T. F. Gajewski, Commensal Bifidobacterium promotes antitumor immunity and facilitates anti–PD-L1 efficacy. *Science* **350**, 1084–1089 (2015). doi:10.1126/science.aac4255 Medline
13. N. Iida, A. Dzutsev, C. A. Stewart, L. Smith, N. Bouladoux, R. A. Weingarten, D. A. Molina, R. Salcedo, T. Back, S. Cramer, R.-M. Dai, H. Kiu, M. Cardone, S. Naik, A. K. Patri, E. Wang, F. M. Marincola, K. M. Frank, Y. Belkaid, G. Trinchieri, R. S. Goldszmid, Commensal bacteria control cancer response to therapy by modulating the tumor microenvironment. *Science* **342**, 967–970 (2013). doi:10.1126/science.1240527 Medline
14. S. Viaud, F. Saccheri, G. Mignot, T. Yamazaki, R. Daillère, D. Hannani, D. P. Enot, C. Pfirschke, C. Engblom, M. J. Pittet, A. Schlitzer, F. Ginhoux, L. Apetoh, E. Chachaty, P.-L. Woerther, G. Eberl, M. Bérard, C. Ecobichon, D. Clermont, C. Bizet, V. Gaboriau-Routhiau, N. Cerf-Bensussan, P. Opolon, N. Yessaad, E. Vivier, B. Ryffel, C. O. Elson, J. Doré, G. Kroemer, P. Lepage, I. G. Boneca, F. Ghiringhelli, L. Zitvogel, The intestinal microbiota modulates the anticancer immune effects of cyclophosphamide. *Science* **342**, 971–976 (2013). doi:10.1126/science.1240537 Medline
15. L. H. Schwartz, S. Litière, E. de Vries, R. Ford, S. Gwyther, S. Mandrekar, L. Shankar, J. Bogaerts, A. Chen, J. Dancey, W. Hayes, F. S. Hodi, O. S. Hoekstra, E. P. Huang, N. Lin, Y. Liu, P. Therasse, J. D. Wolchok, L. Seymour, RECIST 1.1–Update and clarification: From the RECIST committee. *Eur. J. Cancer* **62**, 132–137 (2016). doi:10.1016/j.ejca.2016.03.081 Medline
16. A. Snyder, V. Makarov, T. Merghoub, J. Yuan, J. M. Zaretsky, A. Desrichard, L. A. Walsh, M. A. Postow, P. Wong, T. S. Ho, T. J. Hollmann, C. Bruggeman, K. Kannan, Y. Li, C. Elipenahli, C. Liu, C. T. Harbison, L. Wang, A. Ribas, J. D. Wolchok, T. A. Chan, Genetic basis for clinical response to CTLA-4 blockade in melanoma. *N. Engl. J. Med.* **371**, 2189–2199 (2014). doi:10.1056/NEJMoa1406498 Medline
17. P. Sharma, M. Retz, A. Siefker-Radtke, A. Baron, A. Necchi, J. Bedke, E. R. Plimack, D. Vaena, M.-O. Grimm, S. Bracarda, J. Á. Arranz, S. Pal, C. Ohyama, A. Saci, X. Qu, A. Lambert, S. Krishnan, A. Azrilevich, M. D. Galsky, Nivolumab in metastatic urothelial carcinoma after platinum therapy (CheckMate 275): A multicentre, single-arm, phase 2 trial. *Lancet Oncol.* **18**, 312–322 (2017). doi:10.1016/S1470-2045(17)30065-7 Medline
18. P. L. Chen, W. Roh, A. Reuben, Z. A. Cooper, C. N. Spencer, P. A. Prieto, J. P. Miller, R. L. Bassett, V. Gopalakrishnan, K. Wani, M. P. De Macedo, J. L. Austin-Breneman, H. Jiang, Q. Chang, S. M. Reddy, W.-S. Chen, M. T. Tetzlaff, R. J. Broaddus, M. A. Davies, J. E. Gershenwald, L. Haydu, A. J. Lazar, S. P. Patel, P. Hwu, W.-J. Hwu, A. Diab, I. C. Glitza, S. E. Woodman, L. M. Vence, I. I. Wistuba, R. N. Amaria, L. N. Kwong, V. Prieto, R. E. Davis, W. Ma, W. W. Overwijk, A. H. Sharpe, J. Hu, P. A. Futreal, J. Blando, P. Sharma, J. P. Allison, L. Chin, J. A. Wargo, Analysis of immune signatures in longitudinal tumor samples yields insight into biomarkers of response and mechanisms of resistance to immune checkpoint blockade. *Cancer Discov.* **6**, 827–837 (2016). doi:10.1158/2159-8290.CD-15-1545 Medline
19. W. Roh, P.-L. Chen, A. Reuben, C. N. Spencer, P. A. Prieto, J. P. Miller, V. Gopalakrishnan, F. Wang, Z. A. Cooper, S. M. Reddy, C. Gumbs, L. Little, Q. Chang, W.-S. Chen, K. Wani, M. P. De Macedo, E. Chen, J. L. Austin-Breneman, H. Jiang, J. Roszik, M. T. Tetzlaff, M. A. Davies, J. E. Gershenwald, H. Tawbi, A. J. Lazar, P. Hwu, W.-J. Hwu, A. Diab, I. C. Glitza, S. P. Patel, S. E. Woodman, R. N. Amaria, V. G. Prieto, J. Hu, P. Sharma, J. P. Allison, L. Chin, J. Zhang, J. A. Wargo, P. A. Futreal, Integrated molecular analysis of tumor biopsies on sequential CTLA-4 and PD-1 blockade reveals markers of response and resistance. *Sci. Transl. Med.* **9**, eaah3560 (2017). doi:10.1126/scitranslmed.aah3560 Medline
20. E. M. Van Allen, D. Miao, B. Schilling, S. A. Shukla, C. Blank, L. Zimmer, A. Sucker, U. Hillen, M. H. G. Foppen, S. M. Goldinger, J. Utikal, J. C. Hassel, B. Weide, K. C. Kaehler, C. Loquai, P. Mohr, R. Gutzmer, R. Dummer, S. Gabriel, C. J. Wu, D. Schadendorf, L. A. Garraway, Genomic correlates of response to CTLA-4 blockade in metastatic melanoma. *Science* **350**, 207–211 (2015). doi:10.1126/science.aad0095 Medline
21. N. McGranahan, A. J. S. Furness, R. Rosenthal, S. Ramskov, R. Lyngaa, S. K. Saini, M. Jamal-Hanjani, G. A. Wilson, N. J. Birkbak, C. T. Hiley, T. B. K. Watkins, S. Shafi, N. Murugaesu, R. Mitter, A. U. Akarca, J. Linares, T. Marafioti, J. Y. Henry, E. M. Van Allen, D. Miao, B. Schilling, D. Schadendorf, L. A. Garraway, V. Makarov, N. A. Rizvi, A. Snyder, M. D. Hellmann, T. Merghoub, J. D. Wolchok, S. A. Shukla, C. J. Wu, K. S. Peggs, T. A. Chan, S. R. Hadrup, S. A. Quezada, C. Swanton, Clonal neoantigens elicit T cell immunoreactivity and sensitivity to immune checkpoint blockade. *Science* **351**, 1463–1469 (2016). doi:10.1126/science.aaf1490 Medline
22. W. Hugo, J. M. Zaretsky, L. Sun, C. Song, B. H. Moreno, S. Hu-Lieskovan, B. Berent-Maoz, J. Pang, B. Chmielowski, G. Cherry, E. Seja, S. Lomeli, X. Kong, M. C. Kelley, J. A. Sosman, D. B. Johnson, A. Ribas, R. S. Lo, Genomic and transcriptomic features of response to anti-PD-1 therapy in metastatic melanoma. *Cell* **165**, 35–44 (2016). doi:10.1016/j.cell.2016.02.065 Medline
23. D. B. Johnson, G. M. Frampton, M. J. Rioth, E. Yusko, Y. Xu, X. Guo, R. C. Ennis, D. Fabrizio, Z. R. Chalmers, J. Greenbowe, S. M. Ali, S. Balasubramanian, J. X. Sun, Y. He, D. T. Frederick, I. Puzanov, J. M. Balko, J. M. Cates, J. S. Ross, C. Sanders, H. Robins, Y. Shyr, V. A. Miller, P. J. Stephens, R. J. Sullivan, J. A. Sosman, C. M. Lovly, Targeted next generation sequencing identifies markers of response to PD-1 blockade. *Cancer Immunol. Res.* **4**, 959–967 (2016). doi:10.1158/2326-6066.CIR-16-0143 Medline
24. N. A. Rizvi, M. D. Hellmann, A. Snyder, P. Kvistborg, V. Makarov, J. J. Havel, W. Lee, J. Yuan, P. Wong, T. S. Ho, M. L. Miller, N. Rekhtman, A. L. Moreira, F. Ibrahim, C. Bruggeman, B. Gasmi, R. Zappasodi, Y. Maeda, C. Sander, E. B. Garon, T. Merghoub, J. D. Wolchok, T. N. Schumacher, T. A. Chan, Mutational landscape determines sensitivity to PD-1 blockade in non-small cell lung cancer. *Science* **348**, 124–128 (2015). doi:10.1126/science.aaa1348 Medline
25. B. D. Muegge, J. Kuczynski, D. Knights, J. C. Clemente, A. González, L. Fontana, B. Henrissat, R. Knight, J. I. Gordon, Diet drives convergence in gut microbiome functions across mammalian phylogeny and within humans. *Science* **332**, 970–974 (2011). doi:10.1126/science.1198719 Medline
26. Human Microbiome Project Consortium, Structure, function and diversity of the healthy human microbiome. *Nature* **486**, 207–214 (2012). doi:10.1038/nature11234 Medline
27. P. J. Turnbaugh, F. Bäckhed, L. Fulton, J. I. Gordon, Diet-induced obesity is linked to marked but reversible alterations in the mouse distal gut microbiome. *Cell Host Microbe* **3**, 213–223 (2008). doi:10.1016/j.chom.2008.02.015 Medline
28. J. Qin *et al.*, MetaHIT Consortium, A human gut microbial gene catalogue established by metagenomic sequencing. *Nature* **464**, 59–65 (2010). doi:10.1038/nature08821 Medline
29. Y. Taur, R. R. Jenq, M.-A. Perales, E. R. Littmann, S. Morjaria, L. Ling, D. No, A. Gobourne, A. Viale, P. B. Dahi, D. M. Ponce, J. N. Barker, S. Giralt, M. van den Brink, E. G. Pamer, The effects of intestinal tract bacterial diversity on mortality following allogeneic hematopoietic stem cell transplantation. *Blood* **124**, 1174–1182 (2014). doi:10.1182/blood-2014-02-554725 Medline
30. C. Lozupone, M. E. Lladser, D. Knights, J. Stombaugh, R. Knight, UniFrac: An effective distance metric for microbial community comparison. *ISME J.* **5**, 169–172 (2011). doi:10.1038/ismej.2010.133 Medline
31. N. Segata, J. Izard, L. Waldron, D. Gevers, L. Miropolsky, W. S. Garrett, C. Huttenhower, Metagenomic biomarker discovery and explanation. *Genome Biol.* **12**, R60 (2011). doi:10.1186/gb-2011-12-6-r60 Medline
32. J. U. Peled, S. M. Devlin, A. Staffas, M. Lumish, R. Khanin, E. R. Littmann, L. Ling, S. Kosuri, M. Maloy, J. B. Slingerland, K. F. Ahr, K. A. Porosnicu Rodriguez, Y.

Shono, A. E. Slingerland, M. D. Docampo, A. D. Sung, D. Weber, A. M. Alousi, B. Gyurkocza, D. M. Ponce, J. N. Barker, M.-A. Perales, S. A. Giralt, Y. Taur, E. G. Pamer, R. R. Jenq, M. R. M. van den Brink, Intestinal microbiota and relapse after hematopoietic-cell transplantation. *J. Clin. Oncol.* **35**, 1650–1659 (2017). doi:10.1200/JCO.2016.70.3348 Medline

33. N. Chaput, P. Lepage, C. Coutzac, E. Soularue, K. Le Roux, C. Monot, L. Boselli, E. Routier, L. Cassard, M. Collins, T. Vaysse, L. Marthey, A. Eggermont, V. Asvatourian, E. Lanoy, C. Mateus, C. Robert, F. Carbonnel, Baseline gut microbiota predicts clinical response and colitis in metastatic melanoma patients treated with ipilimumab. *Ann. Oncol.* **28**, 1368–1379 (2017). doi:10.1093/annonc/mdx108 Medline
34. R. Caspi, H. Foerster, C. A. Fulcher, P. Kaipa, M. Krummenacker, M. Latendresse, S. Paley, S. Y. Rhee, A. G. Shearer, C. Tissier, T. C. Walk, P. Zhang, P. D. Karp, The MetaCyc Database of metabolic pathways and enzymes and the BioCyc collection of Pathway/Genome Databases. *Nucleic Acids Res.* **36**, D623–D631 (2008). doi:10.1093/nar/gkm900 Medline
35. M. Kanehisa, S. Goto, KEGG: Kyoto encyclopedia of genes and genomes. *Nucleic Acids Res.* **28**, 27–30 (2000). doi:10.1093/nar/28.1.27 Medline
36. E. Blacher, M. Levy, E. Tatirovsky, E. Elinav, Microbiome-modulated metabolites at the interface of host immunity. *J. Immunol.* **198**, 572–580 (2017). doi:10.4049/jimmunol.1601247 Medline
37. P. C. Tumeh, C. L. Harview, J. H. Yearley, I. P. Shintaku, E. J. M. Taylor, L. Robert, B. Chmielowski, M. Spasic, G. Henry, V. Ciobanu, A. N. West, M. Carmona, C. Kivork, E. Seja, G. Cherry, A. J. Gutierrez, T. R. Grogan, C. Mateus, G. Tomasic, J. A. Glaspy, R. O. Emerson, H. Robins, R. H. Pierce, D. A. Elashoff, C. Robert, A. Ribas, PD-1 blockade induces responses by inhibiting adaptive immune resistance. *Nature* **515**, 568–571 (2014). doi:10.1038/nature13954 Medline
38. T. Tsujikawa, S. Kumar, R. N. Borkar, V. Azimi, G. Thibault, Y. H. Chang, A. Balter, R. Kawashima, G. Choe, D. Sauer, E. El Rassi, D. R. Clayburgh, M. F. Kulesz-Martin, E. R. Lutz, L. Zheng, E. M. Jaffee, P. Leyshock, A. A. Margolin, M. Mori, J. W. Gray, P. W. Flint, L. M. Coussens, Quantitative multiplex immunohistochemistry reveals myeloid-inflamed tumor-immune complexity associated with poor prognosis. *Cell Reports* **19**, 203–217 (2017). doi:10.1016/j.celrep.2017.03.037 Medline
39. Human Microbiome Project Consortium, A framework for human microbiome research. *Nature* **486**, 215–221 (2012). doi:10.1038/nature11209 Medline
40. J. G. Caporaso, C. L. Lauber, W. A. Walters, D. Berg-Lyons, J. Huntley, N. Fierer, S. M. Owens, J. Betley, L. Fraser, M. Bauer, N. Gormley, J. A. Gilbert, G. Smith, R. Knight, Ultra-high-throughput microbial community analysis on the Illumina HiSeq and MiSeq platforms. *ISME J.* **6**, 1621–1624 (2012). doi:10.1038/ismej.2012.8 Medline
41. T. Rognes, T. Flouri, B. Nichols, C. Quince, F. Mahé, VSEARCH: A versatile open source tool for metagenomics. *PeerJ* **4**, e2584 (2016). doi:10.7717/peerj.2584 Medline
42. R. C. Edgar, Search and clustering orders of magnitude faster than BLAST. *Bioinformatics* **26**, 2460–2461 (2010). doi:10.1093/bioinformatics/btq461 Medline
43. R. C. Edgar, UPARSE: Highly accurate OTU sequences from microbial amplicon reads. *Nat. Methods* **10**, 996–998 (2013). doi:10.1038/nmeth.2604 Medline
44. T. Z. DeSantis, P. Hugenholtz, N. Larsen, M. Rojas, E. L. Brodie, K. Keller, T. Huber, D. Dalevi, P. Hu, G. L. Andersen, Greengenes, a chimera-checked 16S rRNA gene database and workbench compatible with ARB. *Appl. Environ. Microbiol.* **72**, 5069–5072 (2006). doi:10.1128/AEM.03006-05 Medline
45. J. R. Cole, Q. Wang, J. A. Fish, B. Chai, D. M. McGarrell, Y. Sun, C. T. Brown, A. Porras-Alfaro, C. R. Kuske, J. M. Tiedje, Ribosomal Database Project: Data and tools for high throughput rRNA analysis. *Nucleic Acids Res.* **42**, D633–D642 (2014). doi:10.1093/nar/gkt1244 Medline
46. C. Quast, E. Pruesse, P. Yilmaz, J. Gerken, T. Schweer, P. Yarza, J. Peplies, F. O. Glöckner, The SILVA ribosomal RNA gene database project: Improved data processing and web-based tools. *Nucleic Acids Res.* **41**, D590–D596 (2013). doi:10.1093/nar/gks1219 Medline
47. J. G. Caporaso, K. Bittinger, F. D. Bushman, T. Z. DeSantis, G. L. Andersen, R. Knight, PyNAST: A flexible tool for aligning sequences to a template alignment. *Bioinformatics* **26**, 266–267 (2010). doi:10.1093/bioinformatics/btp636 Medline
48. P. D. Schloss, S. L. Westcott, T. Ryabin, J. R. Hall, M. Hartmann, E. B. Hollister, R. A. Lesniewski, B. B. Oakley, D. H. Parks, C. J. Robinson, J. W. Sahl, B. Stres, G. G. Thallinger, D. J. Van Horn, C. F. Weber, Introducing mothur: Open-source, platform-independent, community-supported software for describing and comparing microbial communities. *Appl. Environ. Microbiol.* **75**, 7537–7541 (2009). doi:10.1128/AEM.01541-09 Medline
49. M. N. Price, P. S. Dehal, A. P. Arkin, FastTree 2—approximately maximum-likelihood trees for large alignments. *PLOS ONE* **5**, e9490 (2010). doi:10.1371/journal.pone.0009490 Medline
50. J. G. Caporaso, J. Kuczynski, J. Stombaugh, K. Bittinger, F. D. Bushman, E. K. Costello, N. Fierer, A. G. Peña, J. K. Goodrich, J. I. Gordon, G. A. Huttley, S. T. Kelley, D. Knights, J. E. Koenig, R. E. Ley, C. A. Lozupone, D. McDonald, B. D. Muegge, M. Pirrung, J. Reeder, J. R. Sevinsky, P. J. Turnbaugh, W. A. Walters, J. Widmann, T. Yatsunenko, J. Zaneveld, R. Knight, QIIME allows analysis of high-throughput community sequencing data. *Nat. Methods* **7**, 335–336 (2010). doi:10.1038/nmeth.f.303 Medline
51. N. Yutin, M. Y. Galperin, A genomic update on clostridial phylogeny: Gram-negative spore formers and other misplaced clostridia. *Environ. Microbiol.* **15**, 2631–2641 (2013). Medline
52. C. Lozupone, R. Knight, UniFrac: A new phylogenetic method for comparing microbial communities. *Appl. Environ. Microbiol.* **71**, 8228–8235 (2005). doi:10.1128/AEM.71.12.8228-8235.2005 Medline
53. X. C. Morgan, C. Huttenhower, Chapter 12: Human microbiome analysis. *PLOS Comput. Biol.* **8**, e1002808 (2012). doi:10.1371/journal.pcbi.1002808 Medline
54. A. Chao, Nonparametric estimation of the number of classes in a population. *Scand. J. Stat.* **11**, 265–270 (1984).
55. E. H. Simpson, Measurement of diversity. *Nature* **163**, 688–688 (1949). doi:10.1038/163688a0
56. C. E. Shannon, A mathematical theory of communication. *Mob. Comput. Commun. Rev.* **5**, 3–55 (2001). doi:10.1145/584091.584093
57. C. E. Shannon, W. Weaver, A mathematical theory of communication. *Bell Syst. Tech. J.* **27**, 623–656 (1948). doi:10.1002/j.1538-7305.1948.tb00917.x
58. P. T. Shannon, M. Grimes, B. Kutlu, J. J. Bot, D. J. Galas, RCytoscape: Tools for exploratory network analysis. *BMC Bioinformatics* **14**, 217 (2013). doi:10.1186/1471-2105-14-217 Medline
59. J. Li *et al.*, MetaHIT Consortium, An integrated catalog of reference genes in the human gut microbiome. *Nat. Biotechnol.* **32**, 834–841 (2014). doi:10.1038/nbt.2942 Medline
60. B. Langmead, S. L. Salzberg, Fast gapped-read alignment with Bowtie 2. *Nat. Methods* **9**, 357–359 (2012). doi:10.1038/nmeth.1923 Medline
61. A. Cotillard *et al.*, ANR MicroObes Consortium, Dietary intervention impact on gut microbial gene richness. *Nature* **500**, 585–588 (2013). doi:10.1038/nature12480 Medline
62. N. Pons, J.-M. Batto, S. Kennedy, M. Almeida, F. Boumezbeur, paper presented at the Annual Conference of the JOBIM (Journées Ouvertes en Biologie, Informatique et Mathématique), Montpellier, France, 7 to 9 September 2010.
63. H. B. Nielsen *et al.*, MetaHIT Consortium, Identification and assembly of genomes and genetic elements in complex metagenomic samples without using reference genomes. *Nat. Biotechnol.* **32**, 822–828 (2014). doi:10.1038/nbt.2939 Medline
64. H. Li, R. Durbin, Fast and accurate short read alignment with Burrows-Wheeler transform. *Bioinformatics* **25**, 1754–1760 (2009). doi:10.1093/bioinformatics/btp324 Medline
65. A. McKenna, M. Hanna, E. Banks, A. Sivachenko, K. Cibulskis, A. Kernytsky, K. Garimella, D. Altshuler, S. Gabriel, M. Daly, M. A. DePristo, The Genome Analysis Toolkit: A MapReduce framework for analyzing next-generation DNA sequencing data. *Genome Res.* **20**, 1297–1303 (2010). doi:10.1101/gr.107524.110 Medline
66. K. Cibulskis, M. S. Lawrence, S. L. Carter, A. Sivachenko, D. Jaffe, C. Sougnez, S. Gabriel, M. Meyerson, E. S. Lander, G. Getz, Sensitive detection of somatic point mutations in impure and heterogeneous cancer samples. *Nat. Biotechnol.* **31**, 213–219 (2013). doi:10.1038/nbt.2514 Medline
67. K. Ye, M. H. Schulz, Q. Long, R. Apweiler, Z. Ning, Pindel: A pattern growth approach to detect break points of large deletions and medium sized insertions from paired-end short reads. *Bioinformatics* **25**, 2865–2871 (2009). doi:10.1093/bioinformatics/btp394 Medline
68. R. Sachidanandam *et al.*, International SNP Map Working Group, A map of human genome sequence variation containing 1.42 million single nucleotide polymorphisms. *Nature* **409**, 928–933 (2001). doi:10.1038/35057149 Medline

69. 1000 Genomes Project Consortium, An integrated map of genetic variation from 1,092 human genomes. *Nature* **491**, 56–65 (2012). doi:10.1038/nature11632 Medline
70. M. Lek *et al.*, Exome Aggregation Consortium, Analysis of protein-coding genetic variation in 60,706 humans. *Nature* **536**, 285–291 (2016). doi:10.1038/nature19057 Medline
71. W. Fu, T. D. O'Connor, G. Jun, H. M. Kang, G. Abecasis, S. M. Leal, S. Gabriel, M. J. Rieder, D. Altshuler, J. Shendure, D. A. Nickerson, M. J. Bamshad, J. M. Akey, NHLBI Exome Sequencing Project, Analysis of 6,515 exomes reveals the recent origin of most human protein-coding variants. *Nature* **493**, 216–220 (2013). doi:10.1038/nature11690 Medline
72. T. Zhang, K. Dutton-Regester, K. M. Brown, N. K. Hayward, The genomic landscape of cutaneous melanoma. *Pigment Cell Melanoma Res.* **29**, 266–283 (2016). doi:10.1111/pcmr.12459 Medline
73. Z. A. Cooper, A. Reuben, C. N. Spencer, P. A. Prieto, J. L. Austin-Breneman, H. Jiang, C. Haymaker, V. Gopalakrishnan, M. T. Tetzlaff, D. T. Frederick, R. J. Sullivan, R. N. Amaria, S. P. Patel, P. Hwu, S. E. Woodman, I. C. Glitza, A. Diab, L. M. Vence, J. Rodriguez-Canales, E. R. Parra, I. I. Wistuba, L. M. Coussens, A. H. Sharpe, K. T. Flaherty, J. E. Gershenwald, L. Chin, M. A. Davies, K. Clise-Dwyer, J. P. Allison, P. Sharma, J. A. Wargo, Distinct clinical patterns and immune infiltrates are observed at time of progression on targeted therapy versus immune checkpoint blockade for melanoma. *Oncoimmunology* **5**, e1136044 (2016). Medline
74. P. Blanche, J. F. Dartigues, H. Jacqmin-Gadda, Estimating and comparing time-dependent areas under receiver operating characteristic curves for censored event times with competing risks. *Stat. Med.* **32**, 5381–5397 (2013). doi:10.1002/sim.5958 Medline
75. C. O. Fritz, P. E. Morris, J. J. Richler, Effect size estimates: Current use, calculations, and interpretation. *J. Exp. Psychol. Gen.* **141**, 2–18 (2012). doi:10.1037/a0024338 Medline
76. R Development Core Team, (R Foundation for Statistical Computing, Vienna, Austria, 2017).
77. National Research Council, *Guide for the Care and Use of Laboratory Animals* (National Academies Press, ed. 8, 2011), pp. 1–220.
78. Z. A. Cooper, V. R. Juneja, P. T. Sage, D. T. Frederick, A. Piris, D. Mitra, J. A. Lo, F. S. Hodi, G. J. Freeman, M. W. Bosenberg, M. McMahon, K. T. Flaherty, D. E. Fisher, A. H. Sharpe, J. A. Wargo, Response to BRAF inhibition in melanoma is enhanced when combined with immune checkpoint blockade. *Cancer Immunol. Res.* **2**, 643–654 (2014). doi:10.1158/2326-6066.CIR-13-0215 Medline
79. E. D. Amir, K. L. Davis, M. D. Tadmor, E. F. Simonds, J. H. Levine, S. C. Bendall, D. K. Shenfeld, S. Krishnaswamy, G. P. Nolan, D. Pe'er, viSNE enables visualization of high dimensional single-cell data and reveals phenotypic heterogeneity of leukemia. *Nat. Biotechnol.* **31**, 545–552 (2013). doi:10.1038/nbt.2594 Medline

ACKNOWLEDGMENTS

The data reported in this paper are tabulated in the main text and Supplementary Materials. The authors wish to acknowledge all patients and families affected by melanoma. J.A.W. is supported by the Binational Science Foundation, the Melanoma Research Alliance, Stand Up To Cancer, an Institutional Research Grant, a Multidisciplinary Research Program Grant, and MD Anderson's Melanoma Moon Shot Program. This project was supported by the generous philanthropic contributions to The University of Texas MD Anderson Melanoma Moon Shots program. J.A.W, P.S and J.P.A are members of the Parker Institute for Cancer Immunotherapy at M. D. Anderson Cancer Center. A.R. is supported by the Kimberley Clarke Foundation Award for Scientific Achievement provided by the Odyssey Fellowship program at The University of Texas MD Anderson Cancer Center. K.L.H. is supported by the NCI/NIH under Award Numbers CA016672 (PI: Ronald DePinho, M.D.) and R25CA057730 (PI: Shine Chang, Ph.D.). J.E.L. is supported by philanthropic contributions to the University of Texas MD Anderson Cancer Center Moon Shots Program, The University of Texas MD Anderson Cancer Center Various Donors Melanoma and Skin Cancers Priority Program Fund, the Miriam and Jim Mulva Research Fund, the McCarthy Skin Cancer Research Fund and the Marit Peterson Fund for Melanoma Research. The authors acknowledge the Miriam and Sheldon G. Adelson Medical Research Foundation for their support of MD Anderson's Biospecimen Collection team. L.M.C acknowledges a Stand Up To Cancer – Lustgarten Foundation Pancreatic Cancer Convergence Dream Team Translational Research Grant, support from the NIH/NCI, and the Brenden-Colson Center for Pancreatic Health. T.T. acknowledges the Oregon Clinical and Translational Research Institute (OCTRI) from the National Center for Advancing Translational Sciences (NCATS) at the NIH (NIH, #UL1TR000128). J.A.W. acknowledges Christine Diaz for administrative support. Fecal, oral and murine 16S, and fecal WGS data are available from the European Nucelotide Archive under accession numbers PRJEB22894, PRJEB22874, PRJEB22895 and PRJEB22893 respectively. Human WES data are available from the European Genome-phenome Archive under accession number EGAS00001002698. J.A.W and V.G. are inventors on a patent application (PCT/US17/53717) submitted by The University of Texas MD Anderson Cancer Center that covers methods to enhance checkpoint blockade therapy by the microbiome. T.T. and L.M.C are inventors on a patent (WO 2017/087847) held by Oregon Health and Science University that covers the multiplex technology. M.A.D. is an advisory board member for Bristol-Myers Squibb, Novartis, GlaxoSmithKline, Roche/Genentech, Sanofi-Aventis, and Vaccinex and has received funding from GlaxoSmithKline, Roche/Genentech, Merck, AstraZeneca, and Sanofi-Aventis. A.J.L. is a consultant for MedImmune, Bristol-Myers Squibb, Novartis, and Merck, and has received research support from AstraZeneca/MedImmune. Z.A.C. is an employee of MedImmune and owns stock or options in AstraZeneca. J.E.G. is on the advisory board of Merck, and receives royalties from Mercator Therapeutics. S.P.P. has honoraria from Speaker's bureau of Dava Oncology, Merck, and Bristol-Myers Squibb, and is an advisory board member for Amgen and Roche/Genentech. P.H. serves on the advisory board of Lion Biotechnologies and Immatics US. R.N.A. has received research support from Merck, Novartis and Bristol-Myers Squibb. P.S. is a consultant for Bristol-Myers Squibb, Jounce Therapeutics, Helsinn, and GlaxoSmithKline as well as a stockholder from Jounce Therapeutics. J.P.A. is a consultant and stockholder for Jounce Therapeutics, receives royalties from Bristol-Myers Squibb, and has intellectual property with Bristol-Myers Squibb and Merck. J.A.W. has received honoraria from Speakers' bureau of Dava Oncology, Bristol-Myers Squibb, Illumina, and is an advisory board member for GlaxoSmithKline, Novartis, and Roche/Genentech. The other authors declare no competing interests.

SUPPLEMENTARY MATERIALS

www.sciencemag.org/cgi/content/full/science.aan4236/DC1
Materials and Methods
Figs. S1 to S28
Tables S1 to S9
References (*39*–*79*)

12 April 2017; accepted 17 October 2017
Published online 2 November 2017
10.1126/science.aan4236

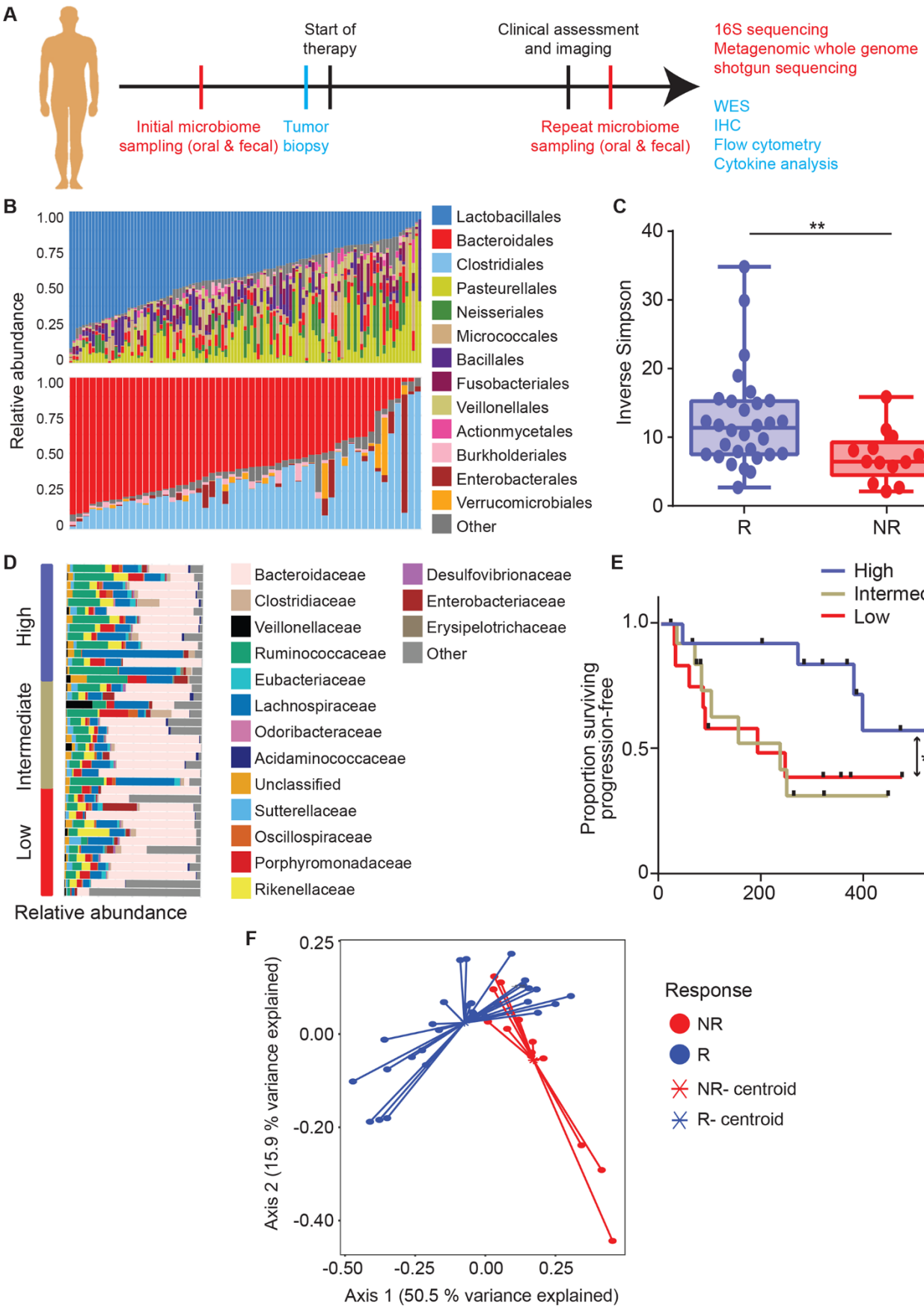

Fig. 1. Enhanced gut microbiome diversity is associated with improved response to anti-PD-1 immunotherapy in patients with metastatic melanoma. (**A**) Schema of sample collection and analyses. (**B**) Stacked bar plot of phylogenetic composition of common bacterial taxa (>0.1% abundance) at the order level in oral (n=109, top) and fecal (n=53, bottom) samples by 16S rRNA sequencing. (**C**) Inverse Simpson diversity scores of the gut microbiome in R (n=30) and NR (n=13) to anti PD-1 immunotherapy by Mann-Whitney (MW) test. Error bars represent the distribution of diversity scores. (**D**) Phylogenetic composition of fecal samples (n=39) at the family level (>0.1% abundance) at baseline. High (blue) (>11.63, n=13), intermediate (gold) (7.46-11.63, n=13) and low (red) (<7.46, n=13) diversity groups were determined using tertiles of Inverse Simpson scores. (**E**) Kaplan-Meier (KM) plot of progression-free survival (PFS) by fecal diversity; high (median PFS undefined), intermediate (median PFS=232 days), and low (median PFS=188 days). High vs intermediate diversity (HR 3.60, 95% C.I. 1.02-12.74) and high vs low (HR 3.57, 95% C.I. 1.02-12.52) by univariate Cox model. **p*<0.05, ***p*<0.01. (**F**) Principal coordinate analysis of fecal samples (n=43) by response using Weighted UniFrac distances.

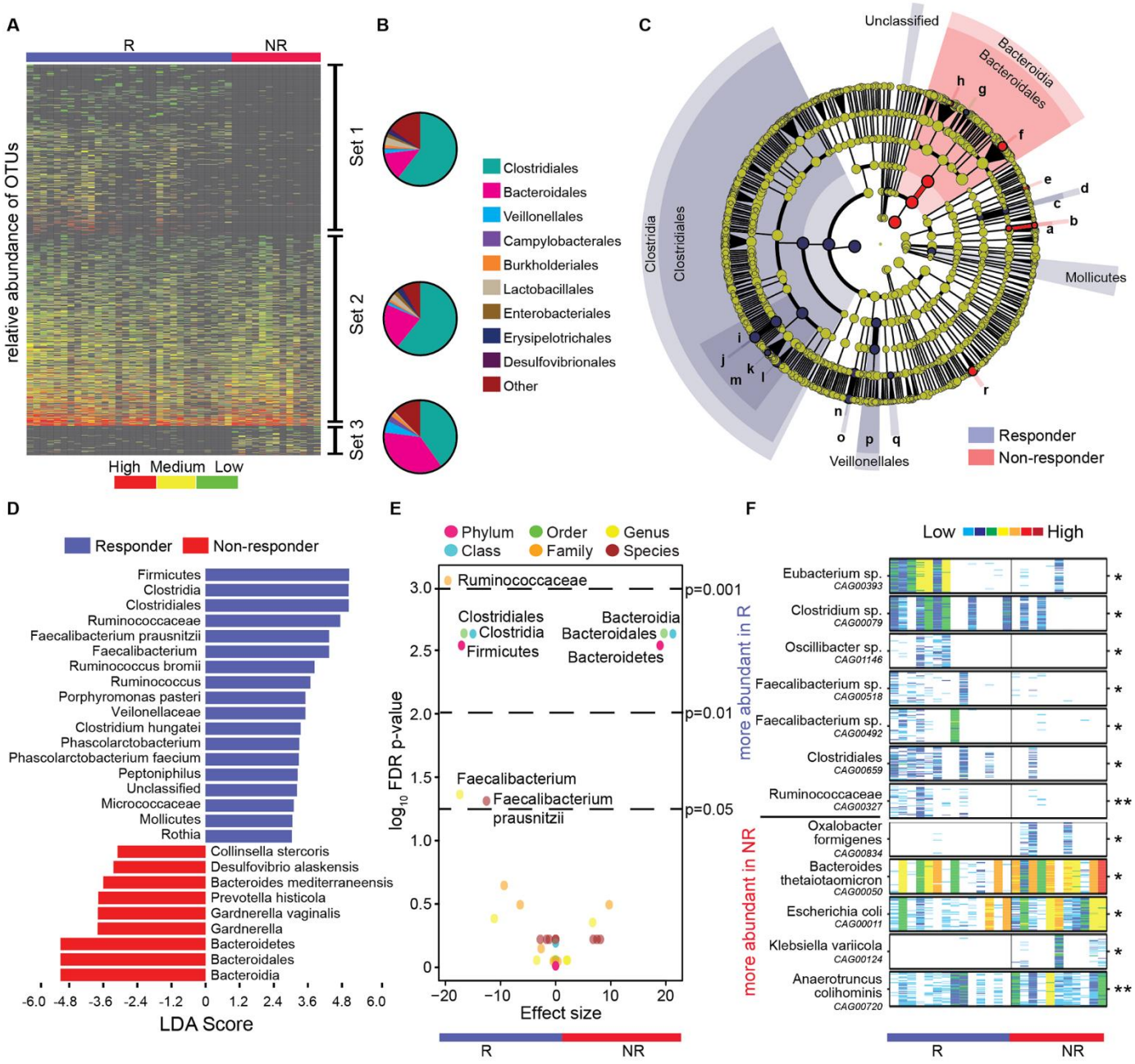

Fig. 2. Compositional differences in the gut microbiome are associated with responses to anti-PD-1 immunotherapy (**A**) Heatmap of OTU abundances in R (n=30) and NR (n=13). Columns denote patients grouped by response and sorted by diversity within R and NR groups; rows denote bacterial OTUs grouped into 3 sets according to their enrichment/depletion in R versus NR: Set 1 (enriched in R), Set 2 (unenriched), and Set 3 (enriched in NR), and then sorted by mean abundance within each set. (**B**) Phylogenetic composition of OTUs within each set at the order level. Set 1 (enriched in R); Set 2 (unenriched); Set 3 (enriched in NR). (**C**) Taxonomic cladogram from LEfSe showing differences in fecal taxa. Dot size is proportional to the abundance of the taxon. Letters correspond to the following taxa: (a) *Gardnerella vaginalis*, (b) Gardnerella, (c) *Rothia*, (d) *Micrococcaceae*, (e) *Collinsella stercoris*, (f) *Bacteroides mediterraneensis*, (g) *Porphyromonas pasteri*, (h) *Prevotella histicola*, (i) *Faecalibacterium prausnitzii*, (j) *Faecalibacterium*, (k) *Clostridium hungatei*, (l) *Ruminococcus bromii*, (m) Ruminococcaceae, (n) *Phascolarctobacterium faecium*, (o) *Phascolarctobacterium*, (p) *Veilonellaceae*, (q) *Peptoniphilus*, (r) *Desulfovbrio alaskensis.* (**D**) LDA scores computed for differentially-abundant taxa in the fecal microbiomes of R (blue) and NR (red). Length indicates effect size associated with a taxon. p=0.05 for the Kruskal-Wallis test; LDA score > 3. (**E**) Differentially-abundant gut bacteria in R (blue) vs NR (red) by MW test (FDR-adjusted) within all taxonomic levels. (**F**) Pairwise comparisons by MW test of abundances of metagenomic species (MGS) identified by metagenomic WGS in fecal samples (n=25): R (n=14, blue), NR (n=11, red). *p<0.05, **p<0.01. Colors reflect gene abundances visualized using "barcodes" with the following order of intensity: white(0)<light blue<blue<green<yellow<orange<red for increasing abundance and each color change corresponds to a 4x fold abundance change. In these barcodes, MGS appear as vertical lines (co-abundant genes in a sample) colored according to the gene abundance.blue<blue<green<yellow<orange<red for increasing abundance and each color change corresponds to a 4x fold abundance change. In these barcodes, MGS appear as vertical lines (co-abundant genes in a sample) colored according to the gene abundance.

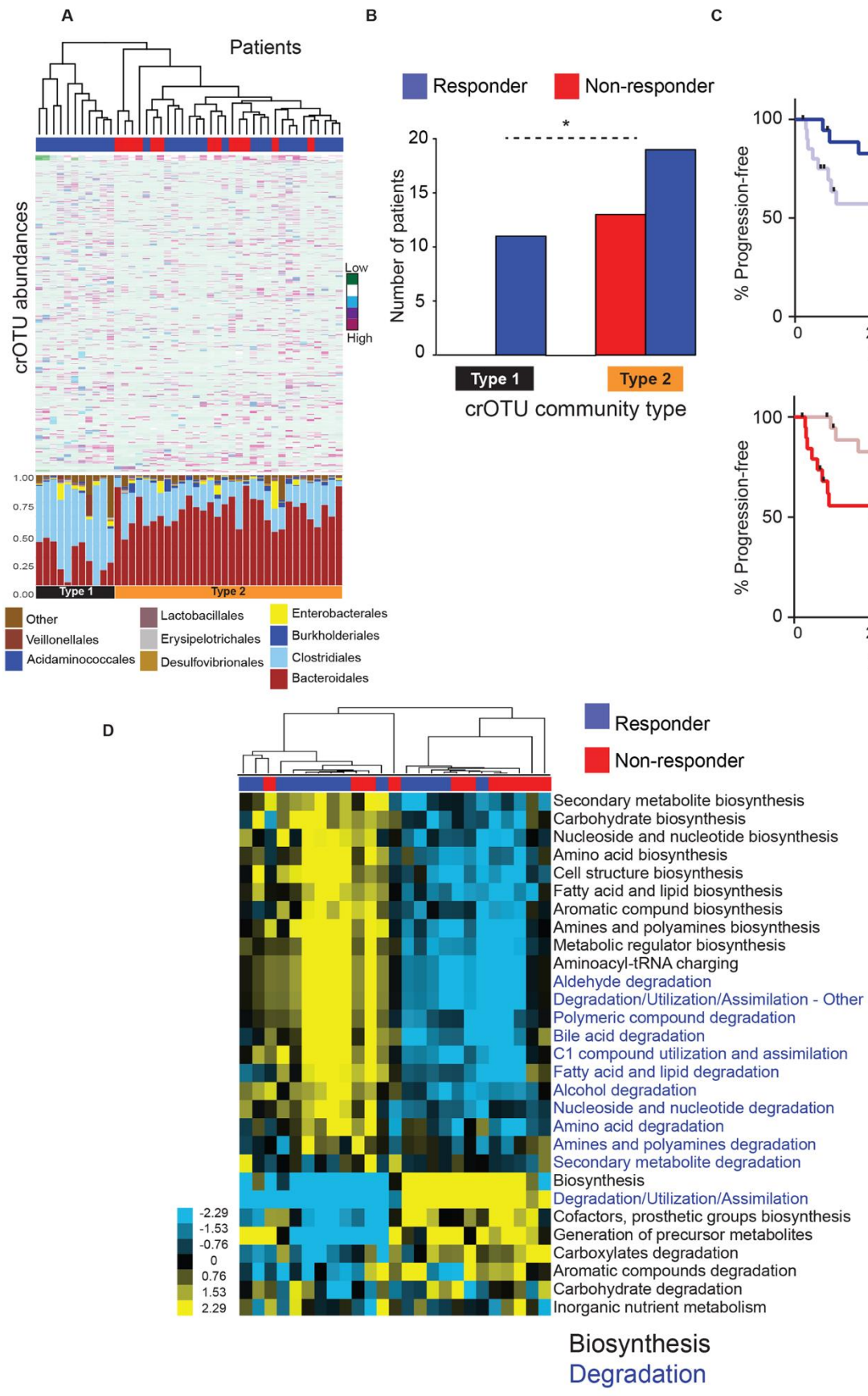

Fig. 3. Abundance of crOTUs within the gut microbiome is predictive of response to anti-PD-1 immunotherapy (**A**) Top: Unsupervised hierarchical clustering by complete linkage of Euclidean distances of crOTU abundances in 43 fecal samples. Bottom: Stacked bar plot of relative abundances at the order level by crOTU community-type. (**B**) Association of crOTU community types with response to anti-PD-1 by Fisher's exact test. crOTU community type 1 (black, n=11: R=11, NR=0); crOTU community type 2 (orange, n=32: R=19, NR=13). Blue bars indicate responders, whereas red bars indicate non-responders. (**C**) Comparison KM PFS curves by long-rank test in patients with high abundance (dark blue, n=19, median PFS=undefined) or low abundance (light blue, n=20, median PFS=242 days) of *Faecalibacterium* (top PFS curve). High abundance (dark red, n=20, median PFS=188 days) or low abundance (light red, n=19, median PFS=393 days) of Bacteroidales (bottom PFS curve). (**D**) Unsupervised hierarchical clustering of pathway class enrichment calculated as the number of MetaCyc pathways predicted in the metagenomes of fecal samples from 25 patients (R=14, NR=11). Columns represent patient samples (blue=R, red=NR) and rows represent enrichment of predicted MetaCyc pathways (blue=low enrichment, black=medium enrichment, yellow= high enrichment). Black text: biosynthetic pathways, blue text: degradative pathways. *$p<0.05$.

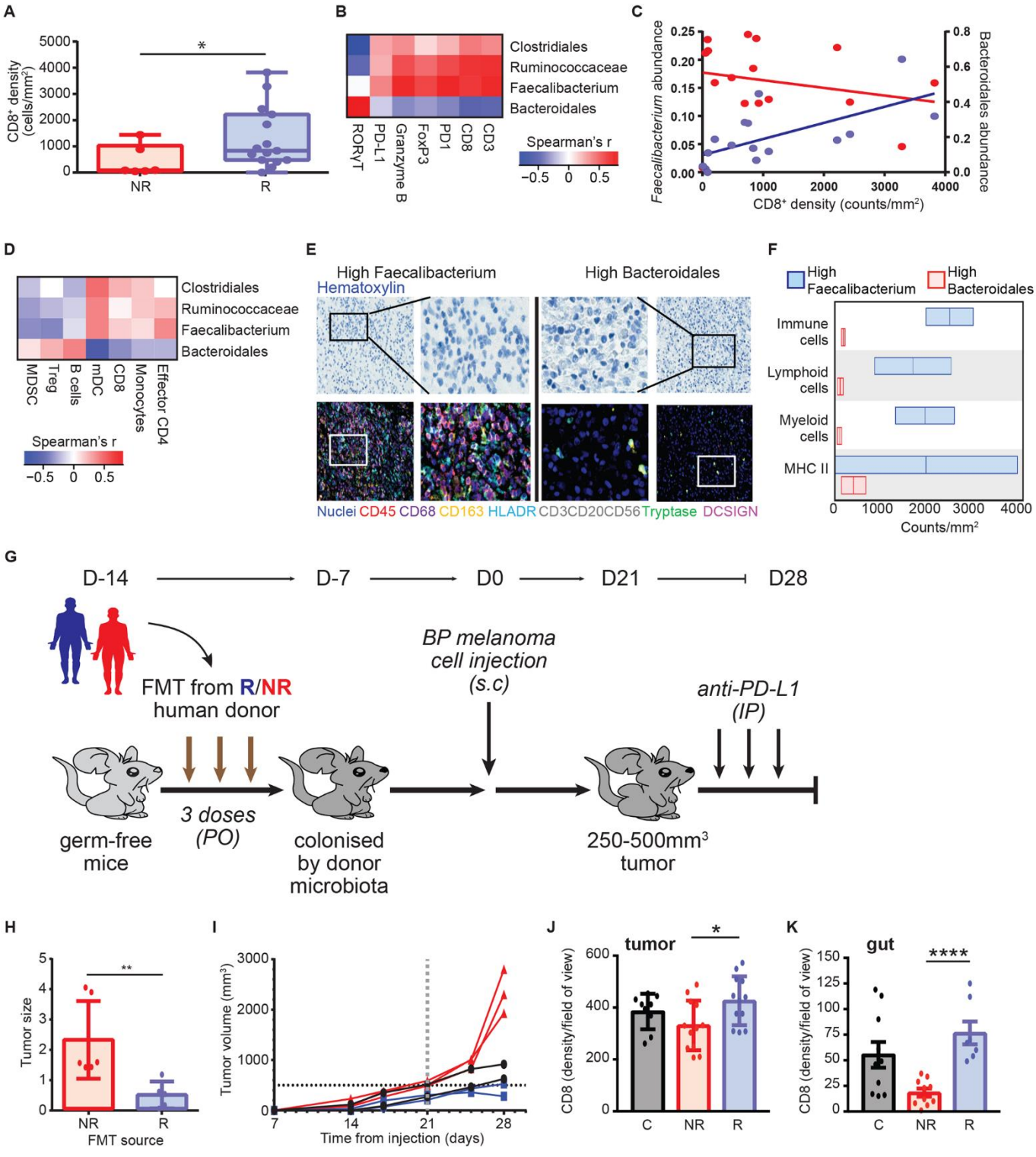

Fig. 4. A favorable gut microbiome is associated with enhanced systemic and anti-tumor immunity. (**A**) Quantification by IHC of the CD8+ T cell infiltrate at pre-treatment in tumors in R (n=15, blue) and NR (n=6, red) by one-sided MW test. Error bars represent the distribution of CD8+ T cell densities. (**B**) Pairwise Spearman rank correlation heatmap of significantly different taxa in fecal samples (n=15) at baseline and CD3, CD8, PD-1, FoxP3, Granzyme B, PD-L1 and RORγT density by H-score in matched tumors. (**C**) Univariate linear regression between CD8+ counts/mm2 in the tumor versus *Faecalibacterium* (blue, r^2=0.42, p<0.01) and Bacteroidales (red, r^2=0.06, p=0.38) abundance in the gut. (**D**) Pairwise Spearman rank correlation heatmap between significantly different fecal taxa and frequency of indicated cell types by flow cytometry in peripheral blood at baseline. (**E**) Representative multiplex IHC images and (**F**) Frequency of various immune cell types in patients having high *Faecalibacterium* (n=2) or Bacteroidales (n=2) in the gut. (**G**) Experimental design of studies in germ-free (GF) mice. Time in days (indicated as D) relative to tumor injection (2.5-8x10^5 tumor cells). (**H**) Difference in size by MW test of tumors at day 14, implanted in R-FMT (blue) and NR-FMT mice (red) expressed as fold change (FC) relative to average tumor volume of Control GF mice. Data from 2 independent FMT experiments (R-FMT, n=5, median FC=0.18; NR-FMT, n=6, median FC=1.52). (**I**) Representative tumor growth curves for each GF mouse from α-PD-L1 treated R-FMT (blue n=2, median tumor volume=403.7 mm^3), NR-FMT (red n=3, median tumor volume=2301 mm^3), and Control (black, n=2, median tumor volume=771.35 mm^3) mice. Statistics are as follows: p=0.20 (R-FMT vs NR-FMT), p=0.33 (NR-FMT vs Control) by MW test. Dotted black line marks tumor size cutoff for α-PD-L1 treatment (500mm^3). (**J**) Quantification of CD8+ density in tumor of R-FMT (n=2, median=433.5 cells/HPF across 12 regions), NR-FMT (NR-FMT n=2, median=325 cells/HPF across 12 regions) and Control mice (n=2, median=412 cells/HPF across 9 regions). MW test p=0.30 (R-FMT vs Control). (**K**) Quantification of CD8+ density in gut (R-FMT n=2, median=67 cells/HPF across 7 regions), NR-FMT (n=2, median=24 cells/HPF across in 5 regions), Control n=2 (median=47 cells/HPF across 10 regions). MW test p=0.17 (R-FMT vs Control). **p*<0.05, ***p*<0.01, *****p*<0.0001.

CANCER IMMUNOTHERAPY

The commensal microbiome is associated with anti–PD-1 efficacy in metastatic melanoma patients

Vyara Matson,[1]* Jessica Fessler,[1]* Riyue Bao,[2,3]* Tara Chongsuwat,[4] Yuanyuan Zha,[4] Maria-Luisa Alegre,[4] Jason J. Luke,[4] Thomas F. Gajewski[1,4]†

Anti–PD-1–based immunotherapy has had a major impact on cancer treatment but has only benefited a subset of patients. Among the variables that could contribute to interpatient heterogeneity is differential composition of the patients' microbiome, which has been shown to affect antitumor immunity and immunotherapy efficacy in preclinical mouse models. We analyzed baseline stool samples from metastatic melanoma patients before immunotherapy treatment, through an integration of 16S ribosomal RNA gene sequencing, metagenomic shotgun sequencing, and quantitative polymerase chain reaction for selected bacteria. A significant association was observed between commensal microbial composition and clinical response. Bacterial species more abundant in responders included *Bifidobacterium longum*, *Collinsella aerofaciens*, and *Enterococcus faecium*. Reconstitution of germ-free mice with fecal material from responding patients could lead to improved tumor control, augmented T cell responses, and greater efficacy of anti–PD-L1 therapy. Our results suggest that the commensal microbiome may have a mechanistic impact on antitumor immunity in human cancer patients.

The therapeutic efficacy of immunotherapies targeting the PD-1/PD-L1 interaction is favored in patients who show evidence of a T cell–inflamed tumor microenvironment at baseline (*1*, *2*). Therefore, host and tumor factors that regulate the magnitude of endogenous immune priming and T cell infiltration into the tumor microenvironment are being sought as an opportunity to further expand therapeutic efficacy (*3*). Preclinical studies have indicated that the composition of the commensal microbiome could exert a major influence; mice with favorable microbiota showed far greater therapeutic activity of anti–PD-L1 treatment than did mice with an unfavorable microbiome, and this benefit could be transferred by cohousing or fecal transplant (*4*). These observations prompted an analogous analysis of the human microbiome with respect to therapeutic efficacy of anti–PD-1 in cancer patients.

To evaluate whether commensal bacterial composition might be associated with clinical efficacy of PD-1 blockade immunotherapy, stool samples were collected from 42 patients before treatment as part of a multidimensional biomarker analysis in metastatic melanoma. The majority of patients received an anti–PD-1 regimen; four patients received anti–CTLA-4 treatment, but the downstream data conclusions did not change with the removal of these subjects, so they were retained in the analysis. Clinical response rate was determined in a blinded manner from biomarker results by using Response Evaluation Criteria In Solid Tumors (RECIST) version 1.1. There were 16 responders (from here on, referred to as R) and 26 nonresponders (NR), yielding a response rate of 38%, which is in line with published clinical data of anti–PD-1 therapy in metastatic melanoma patients (*5*, *6*). No major differences in patient characteristics were observed in R versus NR, except a borderline difference in prior (but not current) smoking history (table S1).

To determine whether the composition of the commensal microbiota is associated with clinical response, we integrated three methods for DNA sequence–based bacterial identification (fig. S1A). First, using 16*S* ribosomal RNA (rRNA) gene amplicon sequencing, we identified operational taxonomic units (OTUs) with taxonomic assignment present at different abundance in R versus NR (table S2). We used a Basic Local Alignment Search Tool (BLAST) search of the 16*S* sequences against the National Center for Biotechnology Information (NCBI) database to reveal potential species-level identities (table S3). Further level of confidence in species identification was gained by matching the OTUs from the 16*S* data set to species-level identities revealed through metagenomic shotgun sequencing (table S4). We used species-specific quantitative polymerase chain reaction (PCR) for those candidate species having previously validated primers (table S5). Compared with the 16*S* analysis, the metagenomic sequencing yielded a smaller number of species differentially represented in R versus NR, which overlapped with the 16*S* results (table S6). Treating these assays as a screen for maximizing the number of candidate species, we used the 16*S* sequencing method as a starting point in our analysis.

After removing OTUs present in less than 10% of the samples, the 16*S* sequencing revealed 62 OTUs of different abundance in R versus NR [$P < 0.05$, unadjusted, permutation test with Quantitative Insights Into Microbial Ecology (QIIME)] (table S2). Hierarchical clustering of samples based on relative abundance of these OTUs revealed that most patients were accurately grouped according to clinical response (fig. S2). Clustering of patients within each clinical group is depicted in Fig. 1A. Thirty-nine OTUs were more abundant in R, and 23 were more abundant in NR. One *Bifidobacteriaceae* OTU was significantly more abundant in R, and a second *Bifidobacteriaceae* OTU (559527) had borderline significance ($P = 0.058$, unadjusted) and was included in the analyses (total = 63 OTUs). This observation recapitulates our previous findings that associated *Bifidobacteriaceae* family members with improved immune-mediated tumor control and efficacy of anti–PD-L1 therapy in mice (*4*). A principal component analysis (PCA) of the 63 OTUs revealed separation of R from NR (Fig. 1B).

A BLAST search of the 63 OTUs against the NCBI database of bacterial sequences returned for most OTUs multiple species with ≥98% identity (table S3). To gain more accurate species-level characterization, the same samples were subjected to metagenomic shotgun sequencing (available for 39 of the 42 samples). Illumina paired-end reads were assigned to microbial clades and analyzed for closest matches to the 63 OTUs identified with 16*S* sequencing. Potential species matches were identified for 43 of the original 63 OTUs (table S4). Species-specific quantitative PCR assays were performed as an additional approach to assess the identity of species, for which sufficiently validated quantitative PCR primers were available (table S5). Thus, integration of the three methods led to the selection of 10 species differentially enriched in R versus NR. Eight of these were more abundant in R—*Enterococcus faecium*, *Collinsella aerofaciens*, *Bifidobacterium adolescentis*, *Klebsiella pneumoniae*, *Veillonella parvula*, *Parabacteroides merdae*, *Lactobacillus* sp., and *Bifidobacterium longum*—whereas two were more abundant in NR: *Ruminococcus obeum* and *Roseburia intestinalis*. As an example, the integrative analysis for *B. longum* (OTU 559627) is depicted in Fig. 2, A to C. Similar correlation analyses for the remaining nine species are depicted in figs. S3 and S4. Quantitative PCR results for these 10 species were integrated into a summation quantitative PCR score for each patient, which was significantly higher in responders ($P = 0.004$) (Fig. 2D).

This list of species is likely an underestimate of the total number of entities showing differential abundance in R versus NR because of the stringency of this composite analysis. For example, *Akkermansia muciniphila* OTU (185186), in line with the study of anti–PD-1 efficacy in epithelial cancers by Routy *et al.* (*7*), was detected by means of 16*S* sequencing in four patients, and all were responders, but statistical analysis of the entire cohort is limited by the number of samples above the detection threshold. As an alternative way to

[1]Department of Pathology, University of Chicago, Chicago, IL 60637, USA. [2]Center for Research Informatics, University of Chicago, IL 60637, USA. [3]Department of Pediatrics, University of Chicago, IL 60637, USA. [4]Department of Medicine, University of Chicago, Chicago, IL 60637, USA.
*These authors contributed equally to this work.
†Corresponding author. Email: tgajewsk@medicine.bsd.uchicago.edu

represent the aggregate data toward development of a candidate predictive biomarker, the total numbers of potentially "beneficial" and "non-beneficial" OTUs were scored for each patient (fig. S5), and a ratio was calculated. When plotted against the absolute change in tumor size as assessed with RECIST, a clean correlation was observed so that patients with a ratio over 1.5 all showed clinical response (Fig. 2E). These results suggest that the commensal microbiota composition might be useful as a biomarker to predict response to checkpoint blockade therapy, which motivated comparison with other candidate predictive biomarkers. Archived pretreatment tumor specimens that passed quality control were available for 15 patients (5 R, 10 NR). Microbial composition remained significantly different in R versus NR for this subset ($P < 0.01$) (fig. S6, A and B). Exome sequencing followed by enumeration of nonsynonymous somatic mutations showed a trend of higher frequency in R, as did levels of PD-L1 and PD-1 mRNA (fig. S6, C to E) and enumeration of baseline $CD8^+$ T cells by means of immunohistochemistry (fig. S6F). Although these trends not reaching statistical significance level of 0.05 were likely limited by sample size, the microbiota parameters still markedly separated responders and nonresponders.

The strong correlation between commensal bacteria and clinical response to immunotherapy suggested a potential causal effect, in light of data demonstrating an immune-potentiating impact of the microbiome in mouse tumor models (*4*, *8*–*10*). To investigate the capability of human commensal microbes to potentiate antitumor T cell responses, we used germ-free (GF) mice as recipients. We had previously reported that spontaneous immune-mediated tumor control in Taconic mice could be improved by means of fecal microbiota transfer from mice obtained from a different vendor, the Jackson Laboratories (*4*). In setting up the current model, we found that B16.SIY melanoma tumor growth in GF mice was similar to that in specific pathogen–free (SPF) mice (both from Taconic), and colonization of GF mice with feces from Taconic SPF mice did not affect this baseline growth rate (fig. S8). These results suggest a reduced spontaneous immune-mediated tumor control inherent to GF mice, which makes them suitable recipients for human-derived microbiota, with an opportunity to detect improved antitumor immunity depending on microbial composition. Fecal material was transferred from three R and three NR into cohorts of GF mice (Fig. 1A and figs. S2, S5, and S7), followed by implantation of B16.SIY melanoma cells 2 weeks later. The human microbiota–colonized mouse groups segregated into two phenotypes with respect to tumor growth rate: (i) a faster growing group and (ii) a slower growing group (Fig. 3A). Two of three mouse cohorts reconstituted with R fecal material had slower baseline tumor growth, and two of the three cohorts reconstituted from NR showed faster baseline tumor growth. Thus, the ability of the human microbiota to support improved tumor control in mice usually, but not always, paralleled the clinical response to anti–PD-1 seen in the donor patient. Achieving slower tumor growth with fecal transplant alone is similar to previous mouse studies, in which transfer of feces from Jackson into Taconic mice was sufficient for a partial therapeutic effect owing to a more favorable microbiome (*4*).

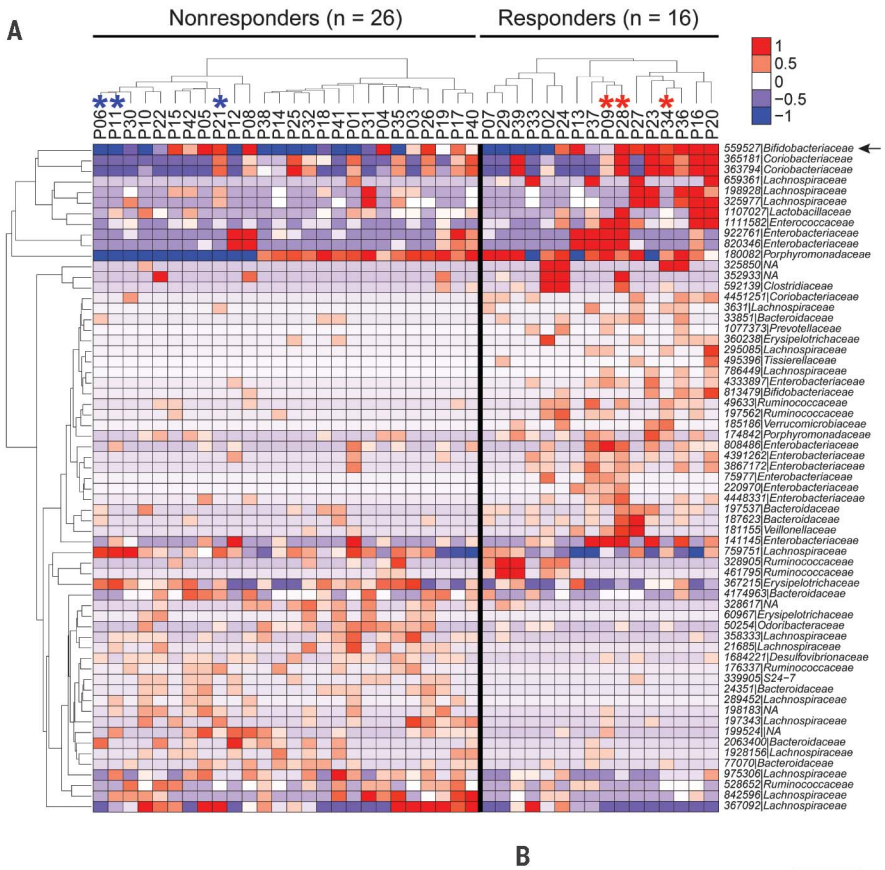

Fig. 1. Distinct commensal microbial communities in anti–PD-1 responding patients and nonresponding patients as assessed with 16*S* rRNA gene amplicon sequencing. (**A**) Relative abundance of differentially abundant taxa in responders versus nonresponders; 62 OTUs were identified as different with $P < 0.05$ (unadjusted, permutation test). An additional OTU 559527 (arrow) identified as *Bifidobacteriaceae* approached significance ($P = 0.058$). Hierarchical clustering of the samples was performed within each clinical group. Individual samples are organized in columns, labeled with patient identification number. Asterisks indicate samples used in further in vivo experiments. The ID of de novo assembled OTUs (new clean-up reference OTUs picked with QIIME) were abbreviated to show only the individual identifier digits, and the full OTU IDs are provided in table S4. (**B**) PCA of relative abundance of the 63 OTUs shown in Fig. 1A.

Composition of bacterial taxa that successfully reconstituted mice and fidelity to the original human donor were assessed with 16*S* rRNA gene amplicon sequencing. Groups C and D, which did not show the same pattern of tumor control as the therapeutic outcome in the original human donors, showed a large degree of difference of microbiota composition from the original human donors (fig. S9). In agreement, a binary Bray-Curtis dissimilarity index for each donor/recipient pair was highest, at 0.7, for cohorts C and D versus 0.5 to 0.6 for the rest of the groups. We conclude that whereas reconstitution of GF mice with human fecal material often recapitulates the microbial composition and the phenotype of the human donor, in some cases there is a high degree of drift so that some bacteria expand and others contract to a degree that is sufficient to change phenotype. Nonetheless, for the reconstituted GF mice that do recapitulate the clinical outcome of the original donor, this model system may be useful for the ultimate isolation of specific bacteria that regulate antitumor immunity in vivo.

We focused on mouse groups A and B for further mechanistic studies. There was a high level of consistency between repeated experiments,

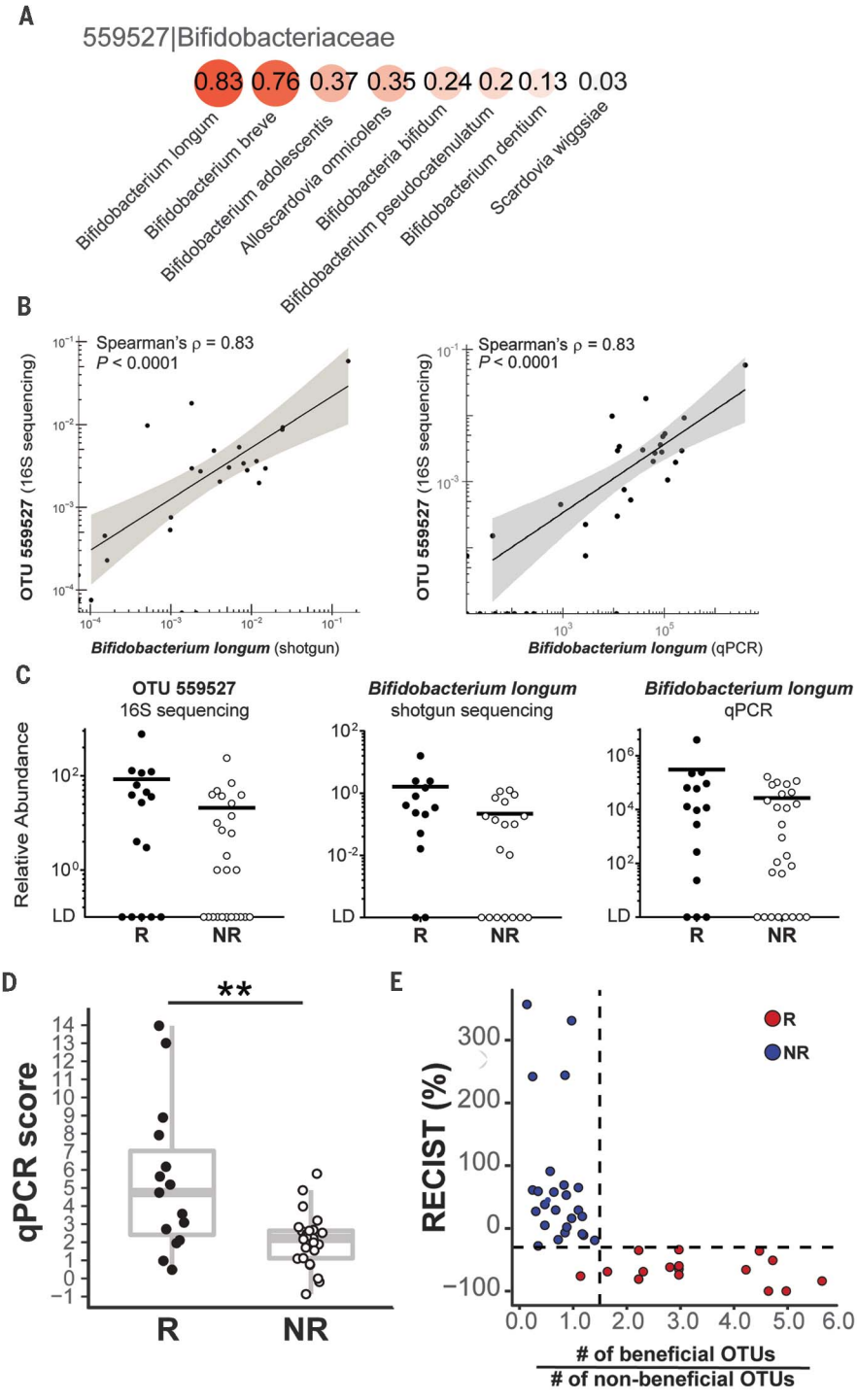

Fig. 2. Identification of commensal bacterial species associated with patient clinical response to anti–PD-1 therapy. (**A**) Spearman's correlation coefficients between the relative abundances of *Bifidobacteriaceae* OTU 559527 from the 16*S* data set and species-level identities suggested by shotgun sequencing. The species profiled with shotgun sequencing were compared with the taxonomy of OTUs generated from 16*S* sequencing at the family level. (**B**) Spearman's correlation between abundance of OTU 559527 from the 16*S* data set and *B. longum* identified by means of metagenomics shotgun sequencing analysis (left) and quantitative PCR (right). Shaded band indicates 95% confidence interval (CI) of the values fitted by linear regression. (**C**) Relative abundance in responders (R) versus nonresponders (NR) of OTU 559527 (16*S* sequencing; left), *B. longum* (shotgun sequencing; middle), and *B. longum* (quantitative PCR; right). LD, limit of detection. (**D**) Quantitative PCR score representing aggregate data for the relative abundances of 10 species correlated to OTUs with differential abundance in R versus NR. Wilcoxon-Mann-Whitney test (nonparametric) was used to compare quantitative PCR score between R and NR groups. (**E**) Ratio of beneficial to nonbeneficial OTU numbers for each patient versus the patient's RECIST aggregate tumor measurement change. Dashed lines label RECIST% = −30 and ratio = 1.5. Only the 43 16*S* OTUs confirmed with shotgun metagenomic sequencing were included. $P < 0.05$ was considered statistically significant; $^{*}P < 0.05$, $^{**}P < 0.01$, $^{***}P < 0.001$, $^{****}P < 0.0001$.

both with respect to tumor growth rate and microbial colonization (Fig. 3B, group A1 versus A2 and B1 versus B2 comparisons). To determine whether the difference in tumor control could be attributed to host immunity, interferon-γ (IFN-γ) enzyme-linked immunosorbent spot (ELISPOT) of ex vivo SIY-stimulated splenocytes was performed and indicated an increased frequency of activated T cells from R microbiota-reconstituted mice 3 weeks after inoculation with B16.SIY melanoma cells (Fig. 3C). Analysis of the tumor microenvironment also showed a significantly greater number of SIY-specific $CD8^+$ T cells, but not of $FoxP3^+CD4^+$ regulatory T cells, in these mice (Fig. 3, D and E), which is consistent with increased priming of tumor antigen–specific $CD8^+$ T cells. Anti–PD-L1 was markedly efficacious in mice colonized with R microbiota yet completely ineffective in NR-derived mice (Fig. 3F), demonstrating a profound impact of the commensal microbiota on immunotherapy efficacy in vivo. Interrogation of fecal DNA from these mice by means of quantitative PCR recapitulated the results from our analysis of patients. Of the PCR reactions validated in patients, six were observed in reconstituted mice, with the same pattern of enrichment as was seen in patients (Fig. 2G).

Together, our data suggest that the composition of the commensal microbiota in patients is associated with therapeutic efficacy of anti–PD-1 monoclonal antibody (mAb). Although *B. longum* was one commensal identified in the current study that had also been found in mouse

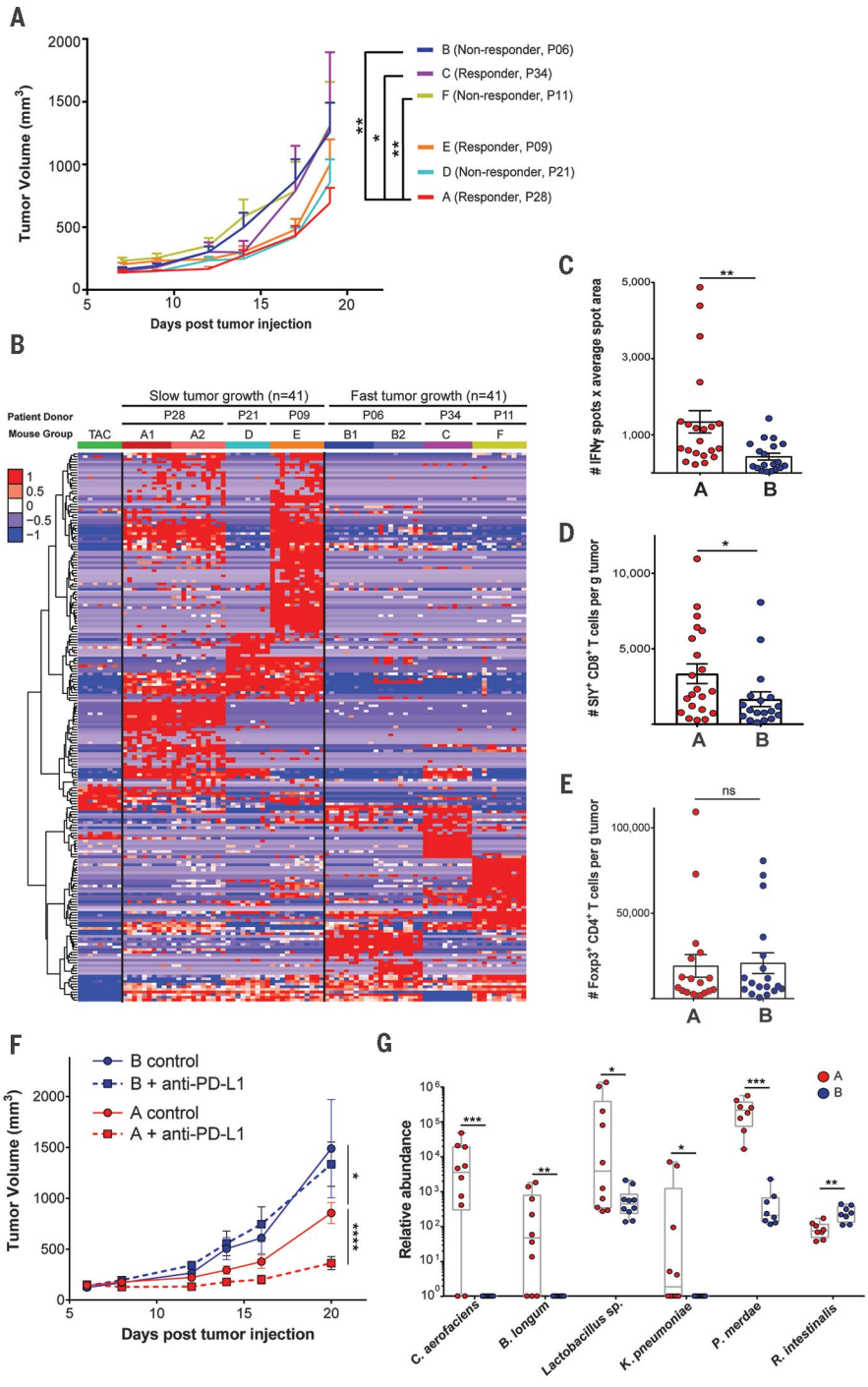

Fig. 3. Human commensal communities modulate antitumor immunity in a mouse melanoma model. GF mice were gavaged with fecal material from three responder (P28, P34, and P09) and three nonresponder (P06, P21, and P11) patient donors. (**A**) B16.SIY melanoma was injected subcutaneously 2 weeks after gavage; tumor growth data are from one (groups C, D, E, and F) or two experiments (groups A and B) with 7 to 11 mice per group per experiment. Error bars represent mean + SEM. (**B**) Relative abundance of 207 OTUs from patient donors that colonized in mice and were differentially abundant between slow- and fast-tumor-growth groups. Columns depict individual mice arranged in groups A through F. Groups A1, B1, A2, and B2 are from two independent duplicate experiments. Rows indicate individual OTUs with exact reference ID match between human and mouse 16S rRNA data sets. (**C**) In groups A and B, ex vivo activation of splenocytes by SIY peptide was measured with IFN-γ ELISPOT 3 weeks after tumor injection. (**D** and **E**) Tumor-infiltrating SIY-specific $CD8^+$ T cells (D) and $FoxP3^+$ regulatory T cells (E) were enumerated with flow cytometry. (**F**) Efficacy of anti–PD-L1 therapy was determined in groups A and B. Data are from one experiment with 7 or 8 mice per group. (**G**) Relative abundance in mouse groups A and B of key species validated for quantitative PCR scoring. Six out of the 10 species are shown that gave positive PCR signals. The remaining four species were absent from these particular recipient groups. Tumor growth curves were analyzed with two-way analysis of variance by Tukey's multiple comparisons post-test; flow cytometry and quantitative PCR data were analyzed by Wilcoxon-Mann-Whitney test (nonparametric). $P < 0.05$ was considered statistically significant; $^*P < 0.05$, $^{**}P < 0.01$, $^{***}P < 0.001$, $^{****}P < 0.0001$.

models to be associated with improved immune-mediated tumor control (*4*), it seems likely that multiple specific bacteria may contribute to improved antitumor immunity in patients. In addition to the panel of bacteria overrepresented in responders, several OTUs were overrepresented in nonresponders, and prior work in mice has indicated that some commensals have the potential to be immune-inhibitory—for example, through the induction of $FoxP3^+$ regulatory T cells (*11*, *12*). In addition, our current cohort suggested that a ratio of "beneficial" OTUs to "nonbeneficial" OTUs was the strongest predictor of clinical response. This may indicate that a higher frequency of beneficial bacteria, together with a lower frequency of bacteria with negative impact, may combine for the most favorable clinical outcome.

Several of the bacterial species that were identified in the current study to be differentially abundant in responding versus nonresponding patients have been examined previously for mechanistic impact on host immune responses in GF mice in vivo (*13*). Monocolonization with several species found to be at increased frequency in our responders—including *E. faecium*, *C. aerofaciens*, *B. adolescentis*, and *P. merdae*—were reported to result in a decreased frequency of peripherally derived colonic regulatory T cells as compared with that of other bacterial species. An increased frequency of the Batf3-lineage dendritic cells (DCs) and greater T helper cell 1 (T_H1) responses were also found with bacteria currently identified to be more abundant in responders (*13*). Decreased regulatory T cells, increased Batf3 DCs, and augmented $T_H1$responses would all be expected to improve immune-mediated tumor control. Although

care should be taken extrapolating these results in the setting of a complex microbiota, the data suggest that patient responder–associated bacteria may have a distinct effect on innate and adaptive immunity both locally and systemically.

Two additional studies have identified an association of the commensal microbiome with anti–PD-1 mAb efficacy in different solid cancers (*7*, *14*). Our approaches differ in the method of segregation of patients between R and NR groups and in some methods of analysis. Therefore, direct comparison of the differentially enriched commensal microbiota in R and NR patients across publications should be addressed with caution. Nonetheless, there is agreement with respect to a mechanistic impact of the microbiome on efficacy of anti–PD-1 immunotherapy because fecal transfer from R versus NR patients to GF mice was also able to recapitulate the patient phenotype.

In addition to the microbiome, it is apparent that additional tumor and host factors can affect the efficacy of antitumor immunity and cancer immunotherapy. Tumor-intrinsic activation of the Wnt/β-catenin pathway (*15*) and deletion or mutation of *Pten* (*16*) have been shown to lead to deficient T cell infiltration into the tumor microenvironment and resistance to checkpoint blockade immunotherapy. Germline polymorphisms in immune regulatory genes also have the potential to influence the magnitude of spontaneous antitumor T cell responses (*17*). Our results described here open the avenue for integrating commensal microbial composition, along with tumor genomics and germline genetics, into a multiparameter model with which to maximize the ability of predicting which patients are likely to respond to immunotherapies such as anti–PD-1.

REFERENCES AND NOTES

1. P. C. Tumeh *et al.*, *Nature* **515**, 568–571 (2014).
2. M. Ayers *et al.*, *J. Clin. Invest.* **127**, 2930–2940 (2017).
3. L. Corrales, V. Matson, B. Flood, S. Spranger, T. F. Gajewski, *Cell Res.* **27**, 96–108 (2017).
4. A. Sivan *et al.*, *Science* **350**, 1084–1089 (2015).
5. S. L. Topalian *et al.*, *N. Engl. J. Med.* **366**, 2443–2454 (2012).
6. C. Robert *et al.*, *N. Engl. J. Med.* **372**, 2521–2532 (2015).
7. B. Routy *et al.*, *Science* **359**, 91–97 (2018).
8. R. Daillère *et al.*, *Immunity* **45**, 931–943 (2016).
9. N. Iida *et al.*, *Science* **342**, 967–970 (2013).
10. M. Vétizou *et al.*, *Science* **350**, 1079–1084 (2015).
11. K. Atarashi *et al.*, *Science* **331**, 337–341 (2011).
12. J. L. Round, S. K. Mazmanian, *Proc. Natl. Acad. Sci. U.S.A.* **107**, 12204–12209 (2010).
13. N. Geva-Zatorsky *et al.*, *Cell* **168**, 928–943.e11 (2017).
14. V. Gopalakrishnan *et al.*, *Science* eaan4236 (2017).
15. S. Spranger, R. Bao, T. F. Gajewski, *Nature* **523**, 231–235 (2015).
16. W. Peng *et al.*, *Cancer Discov.* **6**, 202–216 (2016).
17. S. Ugurel *et al.*, *Cancer Immunol. Immunother.* **57**, 685–691 (2008).

ACKNOWLEDGMENTS

We thank E. Chang, A. Sivan, C. Nagler, L. Huang, P. Bleda-Ferre, N. Hubert, Z. Early, and B. Theriault for helpful discussions and M. Jarsulic, B. Choy, N. Martinez, S. Owens, S. Greenwald, H. Morrison, and J. Polinski for technical assistance. This work was supported by NIH grant R35 CA210098, a Team Science Award from the Melanoma Research Alliance, the American Cancer Society–Jules L. Plangere Jr. Family Foundation Professorship in Cancer Immunotherapy, funds from the University of Chicago Medicine Comprehensive Cancer Center, the University of Chicago Cancer Biology Training program (T32 CA009594), and The Center for Research Informatics of The University of Chicago Biological Science Division. The bioinformatics analysis was performed on Gardner High-Performance Computing clusters at Center for Research Informatics, Biological Sciences Division. Data reported in this study are tabulated in the main text and supplementary materials. The 16S and shotgun sequencing were performed at the Argonne National Laboratory and the University of Chicago-affiliated Marine Biological Laboratory, respectively; data files were deposited into The NCBI Sequence Read Archive (SRA) and are available under the accession no. SRP116709. Custom code and additional processed data used in this study are publicly available on GitHub at https://github.com/cribioinfo/sci2017_analysis. T.F.G. is an advisory board member for Roche-Genentech, Merck, Abbvie, Bayer, Aduro, and Fog Pharma. T.F.G. receives research support from Roche-Genentech, BMS, Merck, Incyte, Seattle Genetics, and Ono. T.F.G. is a shareholder/cofounder of Jounce Therapeutics. The University of Chicago holds a licensing arrangement with Evelo. T.F.G is an inventor on U.S. patent US20160354416 A1 submitted by the University of Chicago that covers the use the microbiota to improve cancer immunotherapy. J.J.L. is a consultant to and receives research funding from Bristol-Myers Squibb and Merck.

SUPPLEMENTARY MATERIALS

www.sciencemag.org/content/359/6371/104/suppl/DC1
Materials and Methods
Figs. S1 to S9
Tables S1 to S6
References (*18*–*53*)

9 July 2017; accepted 13 November 2017
10.1126/science.aao3290

Cite as: L. Kabeche *et al.*, *Science* 10.1126/science.aan6490 (2017).

A mitosis-specific and R loop–driven ATR pathway promotes faithful chromosome segregation

Lilian Kabeche,[1] Hai Dang Nguyen,[1] Remi Buisson,[1] Lee Zou[1,2]*

[1]Massachusetts General Hospital Cancer Center, Harvard Medical School, Charlestown, MA 02129, USA. [2]Department of Pathology, Massachusetts General Hospital, Harvard Medical School Boston, MA 02114, USA.

*Corresponding author. E-mail: zou.lee@mgh.harvard.edu

The ATR kinase is crucial for DNA damage and replication stress responses. Here, we describe a surprising role of ATR in mitosis. Acute inhibition or degradation of ATR in mitosis induces whole-chromosome missegregation. The effect of ATR ablation is not due to altered CDK1 activity, DNA damage responses, or unscheduled DNA synthesis, but to loss of an ATR function at centromeres. In mitosis, ATR localizes to centromeres through Aurora A–regulated association with CENP-F, allowing ATR to engage RPA-coated centromeric R loops. As ATR is activated at centromeres, it stimulates Aurora B through Chk1, preventing formation of lagging chromosomes. Thus, a mitosis-specific and R loop–driven ATR pathway acts at centromeres to promote faithful chromosome segregation, revealing functions of R loops and ATR in suppressing chromosome instability.

ATR is a master checkpoint kinase safeguarding the genome (*1*). Loss of ATR during DNA replication increases genomic instability in S phase and subsequent mitosis (*2*–*4*). While analyzing the localization of ATR in diploid RPE1 cells across the cell cycle, we surprisingly found that ATR localized to all centromeres detected by ACA (anti-centromere antibody) on mitotic chromosomes (Fig. 1, A and B, and fig. S1A). Autophosphorylated ATR (p-ATR T1989) also colocalized with ACA (Fig. 1A and fig. S1B), suggesting that ATR is active at centromeres. The staining of ATR and p-ATR was eliminated by ATR siRNA (fig. S1, C and D), confirming the specificity of the antibodies. Colocalization of ATR and CENP-B was detected by the proximity ligation assay in unperturbed mitotic cells, but not in interphase cells (fig. S2, A and B). Chromatin immunoprecipitation (ChIP) of ATR confirmed that ATR was enriched at the centromere of chromosome 1 compared to a non-centromere locus in mitotic RPE1 and U2OS cells (Fig. 1C and fig. S2C). In contrast to ATR, another master checkpoint kinase ATM was not detected at centromeres (Fig. 1A).

The presence of ATR at centromeres during mitosis prompted us to investigate if ATR functions in chromosome segregation. Short (1 h) treatments of asynchronously growing RPE1 and U2OS cells with two structurally distinct ATR inhibitors (ATRi), VE-821 and AZ20, increased the rate of lagging chromosomes in anaphase (Fig. 1, D and E), indicating a defect in whole-chromosome segregation (*5*, *6*). Rapid degradation of AID degron-tagged ATR in mitotic *ATR*$^{-/-}$, *AID-ATR* DT40 cells also increased lagging chromosomes (Fig. 1F and fig. S3A) (*7*). In contrast to lagging chromosomes, anaphase bridges typically arise from S-phase problems persisting into mitosis but not whole-chromosome missegregation (*8*). Short ATRi treatments did not induce anaphase bridges (fig. S3B), suggesting that the S-phase cells affected by ATRi had not entered mitosis. As ATRi-treated mitotic cells progressed into the next cell cycle, an increased rate of aneuploidy was observed (fig. S3C). These results suggest that ATR has a previously uncharacterized role in chromosome segregation distinct from its functions in S phase.

Replication interference in S phase may affect mitosis indirectly by inducing persistent DNA synthesis in mitotic cells (fig. S4, A and B) (*9*). To investigate if ATR has a replication-independent role in mitosis, we arrested RPE1 and U2OS cells in G2 with CDK1 inhibitor and then released them into mitosis in the absence or presence of ATRi (fig. S4, A and B). Post-replication ATRi treatment did not induce DNA synthesis or anaphase bridges, but increased lagging chromosomes (fig. S4, B to D). To unequivocally separate the functions of ATR in S phase and mitosis, we treated live prometaphase cells with ATRi and followed chromosome segregation. ATRi treatment of cells already in mitosis increased the rate of lagging chromosomes in anaphase (Fig. 1G), demonstrating that ATR acts in mitosis to ensure faithful chromosome segregation.

In mitotic cells, ATRi did not affect baseline levels of DNA synthesis and γH2AX, and the canonical ATR pathway was not activated by replication inhibitor hydorxyurea (fig. S5, A to C). ATRi did not significantly alter mitotic progression or affect the inhibitory phosphorylation of CDK1 at Y15 (fig. S6, A to C). Furthermore, ATRi did not increase the rate of multipolar spindles in prometaphase or lead to premature mitotic exit (fig. S6, D and E). However, ATRi reduced the autophosphorylation of Aurora B at T232 (p-Aurora B) in prometaphase (Fig. 2, A and B, and fig. S7A) (*10*). ATRi did

not affect Aurora B activity in vitro (fig. S7B), ruling out off-target effects on Aurora B. In contrast to ATRi, ATM inhibitor (ATMi) did not affect p-Aurora B (Fig. 2B). While ATRi reduced p-Aurora B, it did not affect the centromeric localization of Aurora B and other components of the chromosome passenger complex (fig. S7C). Moreover, the activation of Aurora A and PLK1 was not affected by ATRi (fig. S7D). The Aurora B-dependent phosphorylation of histone H3 at S10 and S28 was reduced by ATRi (Fig. 2C and fig. S8, A and B). When AID-ATR was rapidly degraded in mitotic *ATR*$^{-/-}$, *AID-ATR* DT40 cells, p-H3 S10 and p-H3 S28 was also reduced (Fig. 2D and fig. S8C). Nonetheless, ATRi did not significantly affect the localization of BubR1 to kinetochores (fig. S8D), suggesting that Aurora B retains some of its functions (*11*). Partial inhibition of Aurora B by AurBi increased the rate of lagging chromosomes (fig. S9, A and B) (*12*), recapitulating the effects of ATRi. Combination of ATRi with low concentrations of AurBi further decreased p-Aurora B and increased lagging chromosomes (fig. S9, A and B). Thus, ATR is required for the full activation of Aurora B at centromeres, which is critical for correction of erroneous microtubule attachments at kinetochores (Fig. 2H) (*12*, *13*).

To determine how ATR regulates Aurora B in mitosis, we analyzed the ATR effector kinase Chk1, which is implicated in Aurora B activation (*14*). Like ATR, Chk1 and its ATR- and auto-phosphorylated forms (p-Chk1 S317, S345, S296) were detected at all centromeres in mitotic cells (Fig. 2, E and F, and fig. S10, A and B). ATRi reduced p-Chk1 at centromeres (Fig. 2F), suggesting that Chk1 is phosphorylated by ATR. Similar to ATRi, Chk1 inhibitor (Chk1i) did not affect Aurora B activity in vitro, but reduced p-Aurora B, p-H3 S10, and p-H3 S28 in mitotic cells (Fig. 2, C and G, and figs. S8B and S10C). Furthermore, the combination of ATRi and Chk1i did not further reduce p-Aurora B compared to ATRi or Chk1i alone (Fig. 2G), suggesting that ATR promotes Aurora B activation through Chk1 (Fig. 2H).

The unexpected role of ATR at centromeres begs the question as to how ATR is activated. To distinguish whether ATR is activated in or prior to mitosis, we tested if ATR can be reactivated in mitotic cells after transient inhibition. At 2 μM, the ATRi VE-821 inhibited ATR in a reversible manner in interphase cells (fig. S11A). On mitotic chromosomes, the p-Chk1 at centromeres was reduced by 2 μM ATRi but quickly recovered after ATRi washout (Fig. 3A and fig. S11B), showing that ATR is reactivated. Similarly, in mitotic cells p-Aurora B and p-H3 S10 also recovered after ATRi washout (fig. S11, C and D), confirming de novo activation of ATR in mitosis.

To understand how ATR localizes to centromeres in mitosis, we tested if ATR interacts with mitotic regulators and centromere proteins. Immunoprecipitations of ATR and its regulatory partner ATRIP from mitotic cell extracts, but not interphase cell extracts, captured Aurora A, TPX2 and CENP-F (Fig. 3B and fig. S12A). ATR-ATRIP did not capture several other mitotic regulators (fig. S12B), suggesting that ATR transiently but specifically interacts with the Aurora A-TPX2 complex and CENP-F in mitosis. The levels of ATR at centromeres were reduced by AurAi and CENP-F siRNA (Fig. 3, C and D, and fig. S12C). The p-ATR at centromeres was diminished by two independent AurAi, but not by inhibitors of ATM, Chk1, Aurora B, MPS1 and the proteasome (MG132) (fig. S12D). Importantly, AurAi disrupted the interaction between ATR-ATRIP and CENP-F without altering the levels and localization of CENP-F (Fig. 3E and fig. S12E), suggesting that Aurora A promotes the localization of ATR to centromeres by enabling ATR-ATRIP to bind CENP-F (Fig. 3G). Consistent with the role for CENP-F in ATR localization, a CENP-F fragment that binds to kinetochores exerted dominant negative effects on ATR and p-H3 S10 at centromeres (Fig. 3F and fig. S13) (*15*). Thus, Aurora A and CENP-F likely bring ATR-ATRIP to the vicinity of centromeres in mitosis, facilitating its activation at centromeres (Fig. 3G).

We next investigated how ATR is activated at centromeres in mitosis. The single-stranded DNA (ssDNA) binding protein RPA directly interacts with ATRIP and plays a key role in ATR activation at sites of DNA damage and stalled replication forks (*16*). Surprisingly, although DNA damage and DNA synthesis were undetectable at centromeres in mitosis (*9*), p-RPA staining was detected at all centromeres in synchronized and unsynchronized mitotic cells (Fig. 4A and fig. S14, A and B). The RPA at centromeres was phosphorylated at S33, a substrate site of ATR. Like ATR, RPA was detected at the centromere of chromosome 1 but not a non-centromere locus by ChIP (Fig. 4B and fig. S14C). ssDNA is not only generated by DNA repair and DNA replication, but also by R loops, which contain DNA-RNA hybrids and displaced ssDNA (*17*, *18*). In yeast R loops are found at centromeres and linked to H3 S10 phosphorylation and chromatin compaction (*19*). We recently showed that RPA is a sensor of R loops (*20*), raising the possibility that RPA is recruited to centromeres by the ssDNA in R loops.

To test if R loops are present at centromeres in human cells, we analyzed mitotic chromosomes in RPE1 cells with the monoclonal antibody S9.6, which specifically recognizes DNA-RNA hybrids (*18*). Indeed, S9.6 staining was detected at all centromeres in synchronized and unsynchronized mitotic cells (Fig. 4A and fig. S15, A and B). S9.6 staining was enriched at centromeres compared to telomeres and chromosome arms (fig. S15C). To confirm that centromeric S9.6 signals arise from DNA-RNA hybrids, we conditionally expressed RNaseH1, an enzyme that cleaves the RNA in DNA-RNA hybrids, in HeLa cells. The centromeric S9.6 staining was reduced by induction of wild-type RNaseH1 (RNaseH1^{WT}) (Fig. 4C). In contrast, the catalytically inactive RNaseH1

D210N mutant (RNaseH1^{MUT}) (*21*), which is dominant negative over endogenous RNaseH1, increased S9.6 staining at centromeres (Fig. 4C). RNaseA, which cleaves single- and double-stranded RNA, did not affect S9.6 staining at centromeres (fig. S15D). Consistent with S9.6 staining, R loops were detected at the centromere of chromosome 1 but not a non-centromere locus by DNA-RNA immunoprecipitation (DRIP) (Fig. 4D). The DRIP signal at the centromere was abolished by RNaseH1. Thus, like ATR, R loops are specifically enriched at centromeres in mitosis.

Next, we tested if R loops regulate RPA and ATR at centromeres in mitosis. The ChIP signals of RPA and ATR at the centromere of chromosome 1 were reduced by RNaseH1^{WT} but enhanced by RNaseH1^{MUT} (Fig. 4B). Furthermore, the ATR staining at centromeres was decreased by RNaseH1^{WT} but increased by RNaseH1^{MUT} (Fig. 4E). The centromeric p-ATR and p-RPA staining was also diminished by RNaseH1^{WT} but enhanced by the RNaseH1^{MUT} (Fig. 4F and fig. S16A), suggesting that R loops are important for ATR activation at centromeres (Fig. 4I). The levels of CENP-F at kinetochores were only slightly affected by RNaseH1 (fig. S16B), suggesting that R loops largely act downstream of CENP-F to promote ATR activation. RNA polymerase II (RNAPII)–mediated transcription occurs at centromeres in mitosis and is required for accurate chromosome segregation (*22*, *23*). Inhibition of RNAPII but not RNA polymerase III in mitotic cells reduced the ATR and p-RPA at centromeres (fig. S16C), suggesting that centromeric R loops are generated through RNAPII-mediated transcription during mitosis.

The role of R loops in ATR activation at centromeres predicts that R loops are important for Aurora B activation and suppression of lagging chromosomes. Indeed, p-Aurora B was reduced by RNaseH1^{WT} but increased by RNaseH1^{MUT} (Fig. 4G). Furthermore, the rate of lagging chromosomes was increased by RNaseH1^{WT} but reduced by RNaseH1^{MUT} (Fig. 4H). Notably, RNaseH1^{MUT} increased p-H3 S10 and reduced lagging chromosomes, and both of these effects were reversed by ATRi (fig. S17, A and B), suggesting that stabilization of R loops facilitates Aurora B activation and chromosome segregation through ATR. Together these results strongly suggest that the R loop-ATR circuitry is important for accurate chromosome segregation.

Our results revealed a mitosis-specific ATR pathway that is distinct from the canonical ATR pathway operating in S phase and the DNA damage response. The activation of the mitotic ATR pathway is independent of DNA damage and DNA replication, but dependent on the key mitotic regulator Aurora A and R loops at centromeres (fig. S18). In an Aurora A-dependent manner, ATR interacts with CENP-F in mitosis and is brought to the vicinity of centromeres. The R loops at centromeres may present RPA-coated ssDNA, a key platform for ATR activation. Unlike the canonical ATR pathway, the mitotic ATR pathway avoids the suppression by centromeric DNA loops behind replication forks (*24*). The requirement of both the Aurora A-CENP-F axis and the R loop-RPA axis for ATR activation may ensure that ATR is specifically activated in prometaphase at centromeres. The local activation of ATR at centromeres does not appear to affect CDK1 in mitosis, possibly due to the restriction of p-Chk1 to centromeres and the stabilization of CDC25A by CDK1 (*25*, *26*). Instead, ATR activates Chk1 locally at centromeres to promote Aurora B activation, ensuring accurate chromosome segregation in mitosis.

This study uncovers an R loop–driven signaling pathway that promotes accurate cell division. While R loops cause genomic instability in S phase, they are necessary for faithful mitosis. The opposite effects of R loops on genomic stability during S phase and mitosis create a demand for cell cycle–regulated ATR responses. Through two distinct ATR pathways, ATR suppresses R loop-associated genomic instability in S phase, but mediates the centromeric function of R loops in mitosis (fig. S18). The activation and function of ATR at DNA breaks and replication forks are regulated by DNA repair and replication proteins. The unique ability of the ATR circuitry to rewire in a context-dependent manner may allow it to play an integral role at centromeres in mitosis distinct from its other functions. Both the genomic instability in S phase (replication stress) and the chromosome instability in mitosis (CIN) are hallmarks of cancer and vulnerabilities of cancer cells (*27*–*29*). The dual functions of ATR in countering replication stress and CIN may make ATR a particularly attractive therapeutic target in cancers with both vulnerabilities.

REFERENCES AND NOTES

1. S. A. Yazinski, L. Zou, Functions, regulation, and therapeutic implications of the ATR checkpoint pathway. *Annu. Rev. Genet.* 50, 155–173 (2016). doi:10.1146/annurev-genet-121415-121658 Medline
2. E. J. Brown, D. Baltimore, ATR disruption leads to chromosomal fragmentation and early embryonic lethality. *Genes Dev.* **14**, 397–402 (2000). Medline
3. A. M. Casper, P. Nghiem, M. F. Arlt, T. W. Glover, ATR regulates fragile site stability. *Cell* **111**, 779–789 (2002). doi:10.1016/S0092-8674(02)01113-3 Medline
4. R. Buisson, J. L. Boisvert, C. H. Benes, L. Zou, Distinct but concerted roles of ATR, DNA-PK, and Chk1 in countering replication stress during S phase. *Mol. Cell* **59**, 1011–1024 (2015). doi:10.1016/j.molcel.2015.07.029 Medline
5. A. J. Holland, D. W. Cleveland, Boveri revisited: Chromosomal instability, aneuploidy and tumorigenesis. *Nat. Rev. Mol. Cell Biol.* **10**, 478–487 (2009). doi:10.1038/nrm2718 Medline
6. S. L. Thompson, S. F. Bakhoum, D. A. Compton, Mechanisms of chromosomal instability. *Curr. Biol.* **20**, R285–R295 (2010). doi:10.1016/j.cub.2010.01.034 Medline
7. J. K. Eykelenboom, E. C. Harte, L. Canavan, A. Pastor-Peidro, I. Calvo-Asensio, M. Llorens-Agost, N. F. Lowndes, ATR activates the S-M checkpoint during unperturbed growth to ensure sufficient replication prior to mitotic onset. *Cell Reports* **5**, 1095–1107 (2013). doi:10.1016/j.celrep.2013.10.027 Medline
8. Y. Liu, C. F. Nielsen, Q. Yao, I. D. Hickson, The origins and processing of ultra fine anaphase DNA bridges. *Curr. Opin. Genet. Dev.* **26**, 1–5 (2014). doi:10.1016/j.gde.2014.03.003 Medline
9. S. Minocherhomji, S. Ying, V. A. Bjerregaard, S. Bursomanno, A. Aleliunaite, W. Wu, H. W. Mankouri, H. Shen, Y. Liu, I. D. Hickson, Replication stress activates DNA

repair synthesis in mitosis. *Nature* **528**, 286–290 (2015). doi:10.1038/nature16139 Medline
10. Y. Yasui, T. Urano, A. Kawajiri, K. Nagata, M. Tatsuka, H. Saya, K. Furukawa, T. Takahashi, I. Izawa, M. Inagaki, Autophosphorylation of a newly identified site of Aurora-B is indispensable for cytokinesis. *J. Biol. Chem.* **279**, 12997–13003 (2004). doi:10.1074/jbc.M311128200 Medline
11. C. Ditchfield, V. L. Johnson, A. Tighe, R. Ellston, C. Haworth, T. Johnson, A. Mortlock, N. Keen, S. S. Taylor, Aurora B couples chromosome alignment with anaphase by targeting BubR1, Mad2, and Cenp-E to kinetochores. *J. Cell Biol.* **161**, 267–280 (2003). doi:10.1083/jcb.200208091 Medline
12. D. Cimini, X. Wan, C. B. Hirel, E. D. Salmon, Aurora kinase promotes turnover of kinetochore microtubules to reduce chromosome segregation errors. *Curr. Biol.* **16**, 1711–1718 (2006). doi:10.1016/j.cub.2006.07.022 Medline
13. M. A. Lampson, I. M. Cheeseman, Sensing centromere tension: Aurora B and the regulation of kinetochore function. *Trends Cell Biol.* **21**, 133–140 (2011). doi:10.1016/j.tcb.2010.10.007 Medline
14. E. Petsalaki, T. Akoumianaki, E. J. Black, D. A. Gillespie, G. Zachos, Phosphorylation at serine 331 is required for Aurora B activation. *J. Cell Biol.* **195**, 449–466 (2011). doi:10.1083/jcb.201104023 Medline
15. D. Hussein, S. S. Taylor, Farnesylation of Cenp-F is required for G2/M progression and degradation after mitosis. *J. Cell Sci.* **115**, 3403–3414 (2002). Medline
16. L. Zou, S. J. Elledge, Sensing DNA damage through ATRIP recognition of RPA-ssDNA complexes. *Science* **300**, 1542–1548 (2003). doi:10.1126/science.1083430 Medline
17. S. Hamperl, K. A. Cimprich, Conflict resolution in the genome: How transcription and replication make it work. *Cell* **167**, 1455–1467 (2016). doi:10.1016/j.cell.2016.09.053 Medline
18. J. M. Santos-Pereira, A. Aguilera, R loops: New modulators of genome dynamics and function. *Nat. Rev. Genet.* **16**, 583–597 (2015). doi:10.1038/nrg3961 Medline
19. M. Castellano-Pozo, J. M. Santos-Pereira, A. G. Rondón, S. Barroso, E. Andújar, M. Pérez-Alegre, T. García-Muse, A. Aguilera, R loops are linked to histone H3 S10 phosphorylation and chromatin condensation. *Mol. Cell* **52**, 583–590 (2013). doi:10.1016/j.molcel.2013.10.006 Medline
20. H. D. Nguyen, T. Yadav, S. Giri, B. Saez, T. A. Graubert, L. Zou, Functions of replication protein A as a sensor of R loops and a regulator of RNaseH1. *Mol. Cell* **65**, 832–847.e4 (2017). doi:10.1016/j.molcel.2017.01.029 Medline
21. H. Wu, W. F. Lima, S. T. Crooke, Investigating the structure of human RNase H1 by site-directed mutagenesis. *J. Biol. Chem.* **276**, 23547–23553 (2001). doi:10.1074/jbc.M009676200 Medline
22. F. L. Chan, O. J. Marshall, R. Saffery, B. W. Kim, E. Earle, K. H. A. Choo, L. H. Wong, Active transcription and essential role of RNA polymerase II at the centromere during mitosis. *Proc. Natl. Acad. Sci. U.S.A.* **109**, 1979–1984 (2012). doi:10.1073/pnas.1108705109 Medline
23. J. I. Gent, R. K. Dawe, RNA as a structural and regulatory component of the centromere. *Annu. Rev. Genet.* **46**, 443–453 (2012). doi:10.1146/annurev-genet-110711-155419 Medline
24. A. Aze, V. Sannino, P. Soffientini, A. Bachi, V. Costanzo, Centromeric DNA replication reconstitution reveals DNA loops and ATR checkpoint suppression. *Nat. Cell Biol.* **18**, 684–691 (2016). doi:10.1038/ncb3344 Medline
25. N. Mailand, A. V. Podtelejnikov, A. Groth, M. Mann, J. Bartek, J. Lukas, Regulation of G(2)/M events by Cdc25A through phosphorylation-dependent modulation of its stability. *EMBO J.* **21**, 5911–5920 (2002). doi:10.1093/emboj/cdf567 Medline
26. G. Zachos, E. J. Black, M. Walker, M. T. Scott, P. Vagnarelli, W. C. Earnshaw, D. A. F. Gillespie, Chk1 is required for spindle checkpoint function. *Dev. Cell* **12**, 247–260 (2007). doi:10.1016/j.devcel.2007.01.003 Medline
27. M. K. Zeman, K. A. Cimprich, Causes and consequences of replication stress. *Nat. Cell Biol.* **16**, 2–9 (2014). doi:10.1038/ncb2897 Medline
28. S. F. Bakhoum, D. A. Compton, Chromosomal instability and cancer: A complex relationship with therapeutic potential. *J. Clin. Invest.* **122**, 1138–1143 (2012). doi:10.1172/JCI59954 Medline
29. H. Gaillard, T. García-Muse, A. Aguilera, Replication stress and cancer. *Nat. Rev. Cancer* **15**, 276–289 (2015). doi:10.1038/nrc3916 Medline
30. P. A. Ginno, P. L. Lott, H. C. Christensen, I. Korf, F. Chédin, R-loop formation is a distinctive characteristic of unmethylated human CpG island promoters. *Mol. Cell* **45**, 814–825 (2012). doi:10.1016/j.molcel.2012.01.017 Medline

ACKNOWLEDGMENTS

We thank D. Compton for H2B-GFP–expressing RPE1 cells, N. Lowndes for the *ATR*$^{-/-}$, *AID-ATR* DT40 cell line expressing degron-ATR, S. Taylor for the CENP-F C630 expression plasmid, and N. Dyson and members of the Zou and Dyson laboratories for discussions. L.K., H.D.N., and R.B. are supported by NIH fellowships 5T32CA009216-35, T32DK007540, and 1K99CA212154, respectively. L.Z. is the James and Patricia Poitras Endowed Chair in Cancer Research and supported by the Jim and Ann Orr Massachusetts General Hospital Research Scholar Award. This work is supported by NIH grants (GM076388 and CA197779) to L.Z.

SUPPLEMENTARY MATERIALS

www.sciencemag.org/cgi/content/full/science.aan6490/DC1
Materials and Methods
Fig. S1 to S18
Reference (*30*)

12 May 2017; resubmitted 22 September 2017
Accepted 9 November 2017
Published online 23 November 2017
10.1126/science.aan6490

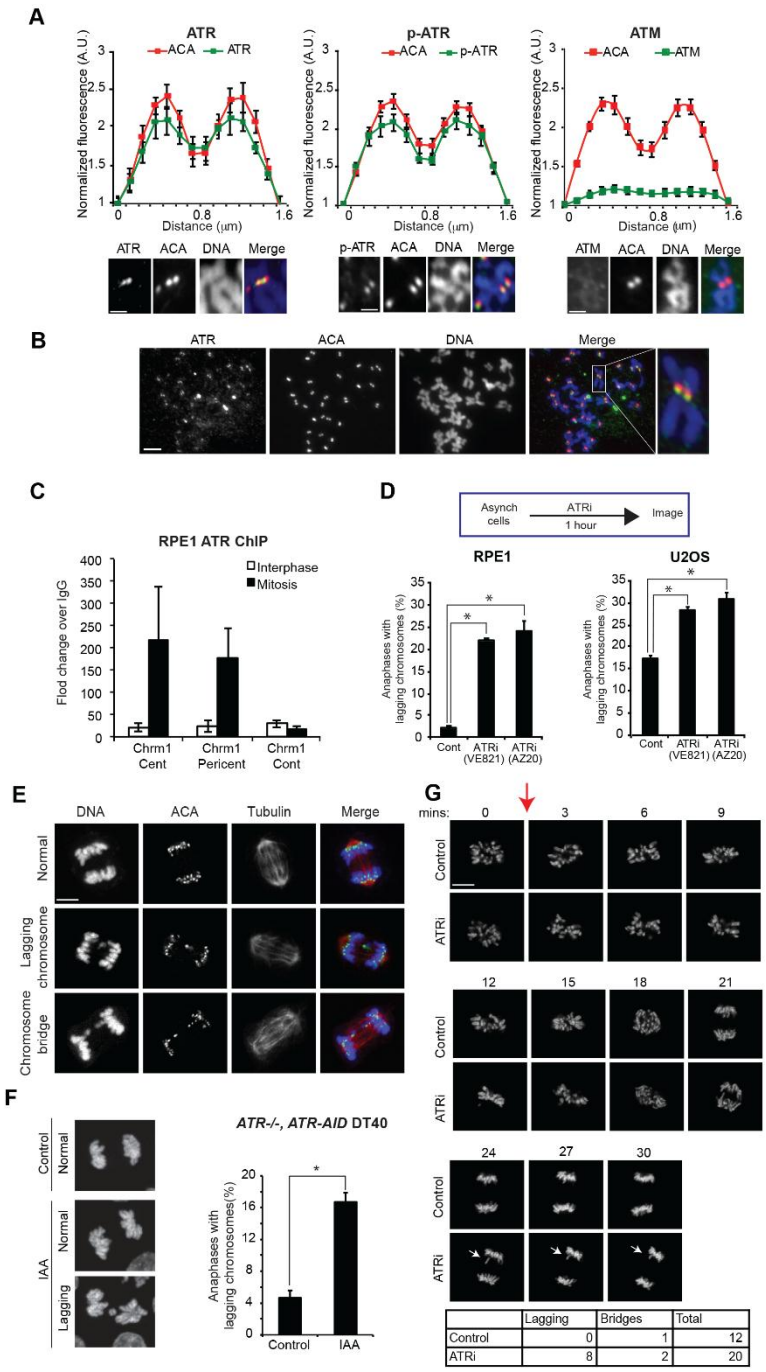

Fig. 1. ATR localizes to centromeres in mitosis and promotes accurate whole-chromosome segregation. (**A**) Line scan analysis (top) and representative images (bottom) of fluorescence of ATR, phospho-ATR S1989 (p-ATR), ATM, and ACA at centromeres in chromosome spreads of RPE1 cells. Cells were arrested with nocodazole for 5 hours. Centromeric fluorescence intensities of the indicated proteins are normalized to the background fluorescence near centromeres (see Methods). Scale bar, 2 μm. (**B**) Chromosome spreads of unsynchronized mitotic RPE1 cells were stained for ATR and ACA. Asynchronously growing cells were treated with nocodazole for 15 min to facilitate spreading of chromosomes. Scale bar, 10 μm. (**C**) Quantitative PCR of ATR ChIP in mitotic and interphase RPE1 cells. (**D**) Percentage of anaphase RPE1 and U2OS cells (>300 anaphases analyzed per condition) with lagging chromosomes after mock or ATRi (10 μM VE-821, 1 hour) treatments. (**E**) Representative images of anaphase RPE1 cells in (D). Scale bar, 5 μm. (**F**) *ATR*$^{-/-}$, *AID-ATR* DT40 cells were untreated or treated with 0.5 mM indole-3-acetic acid (IAA) for 30 min to induce AID-ATR degradation. Representative maximum projection images of anaphase cells (left) and quantification of cells with lagging chromosomes (right) are shown (>300 anaphases analyzed per condition). Scale bar, 5 μm. (**G**) Time-lapse imaging of H2B-GFP expressing RPE1 cells untreated or treated with ATRi. Red arrow signifies time of treatment. A lagging chromosome is demarcated by white arrows. Scale bar, 5 μm. Error bars in all panels represent SEM. *$P \leq 0.01$, two-tailed *t* test.

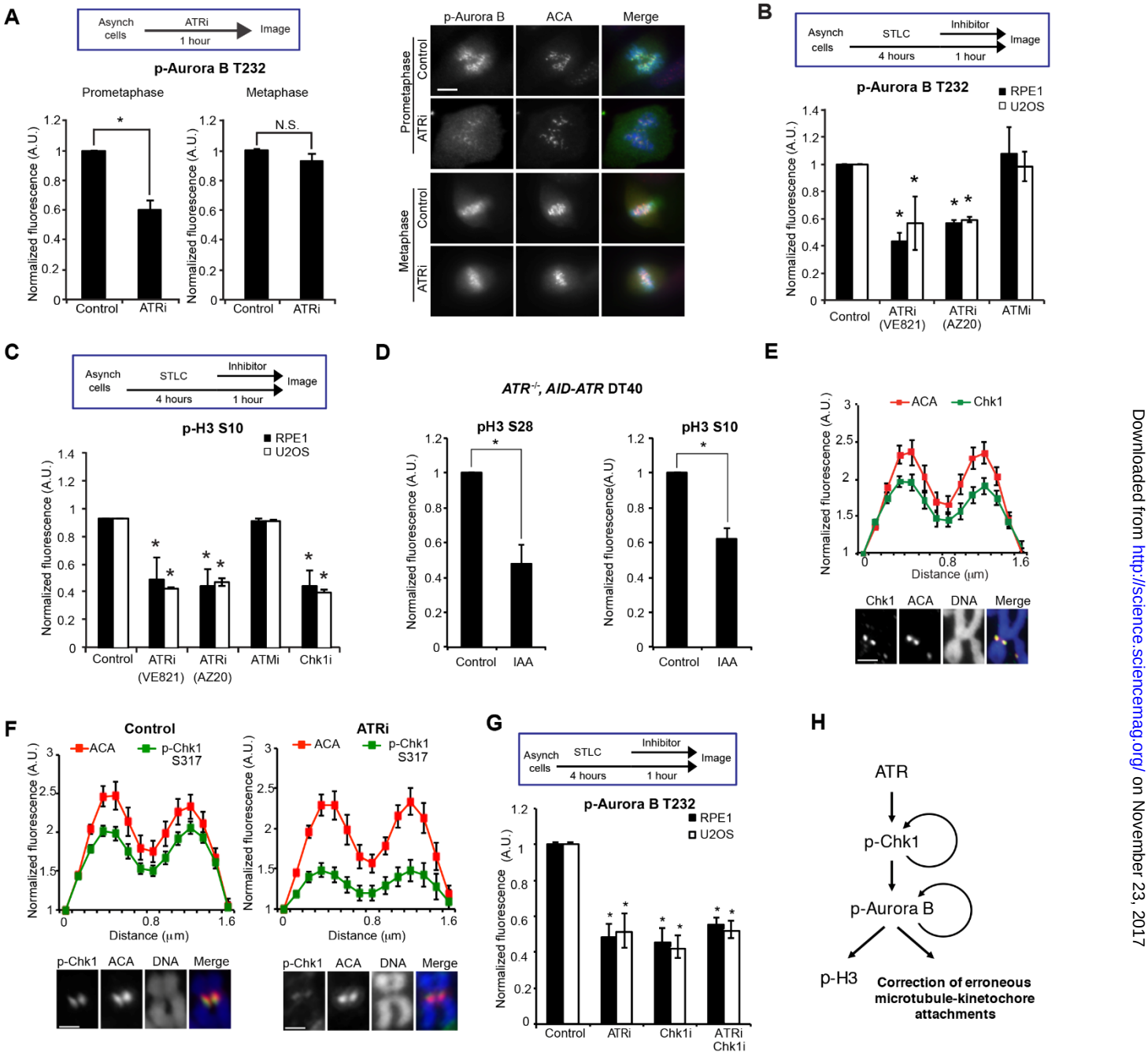

Fig. 2. ATR promotes Aurora B activation at centromeres. (A) Fluorescence intensity of phospho-Aurora B T232 (p-Aurora B) at centromeres in prometaphase or metaphase RPE1 cells untreated or treated with ATRi for 1 hour (left). Representative images of untreated and ATRi-treated cells (right). Scale bar, 5 μm. (B and C) Fluorescence intensities of centromeric p-Aurora B (B) and overall p-H3 S10 (C) in S-Trityl L-cysteine (STLC)-arrested prometaphase cells after mock treatments or treatments with the indicated inhibitors for 1 hour. (D) Fluorescence intensities of p-H3 S28 and p-H3 S10 in *ATR*$^{-/-}$, *AID-ATR* DT40 cells untreated or treated with IAA for 30 min. (E) Line scan analysis of Chk1 and ACA at centromeres in chromosome spreads of RPE1 cells. Cells were arrested with nocodazole for 5 hours. Scale bar, 2 μm. (F) Line scan analysis of p-Chk1 and ACA at centromeres in chromosome spreads of RPE1 cells. Cell were arrested with nocodazole for 4 hours and then mock or ATRi treated for 1 hour. Scale bar, 2 μm. (G) Fluorescence intensity of centromeric p-Aurora B in STLC-arrested prometaphase cells after mock treatments or treatments with the indicated inhibitors. Error bars in all panels represent SEM. *$P \leq 0.01$, two-tailed *t* test. (H) A schema of the ATR-Chk1-Aurora B pathway in mitosis. This pathway is required for full Aurora B activation, which is necessary for H3 phosphorylation and proper kinetochore-microtubule attachment.

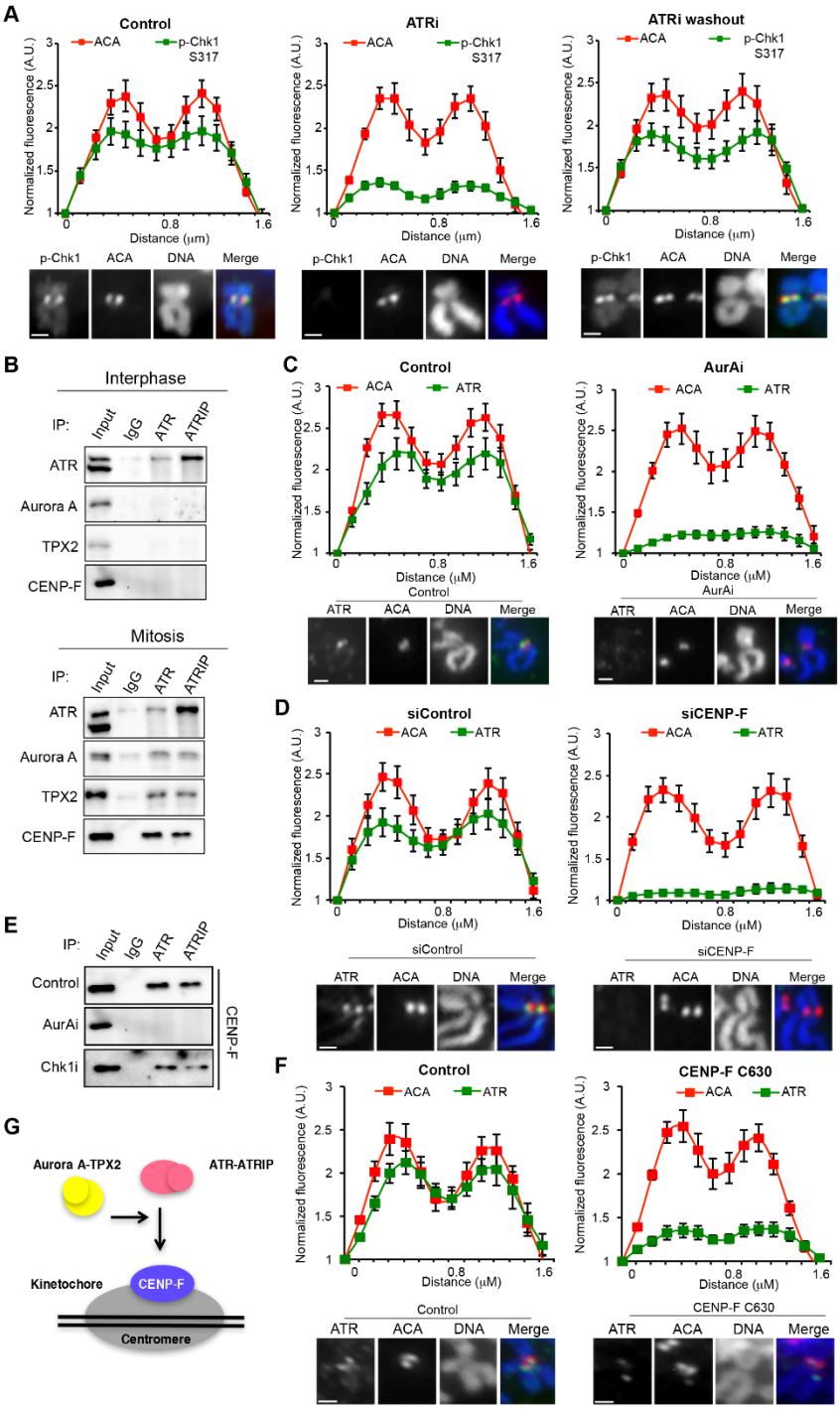

Fig. 3. ATR localizes to centromeres in an Aurora A and CENP-F-dependent manner. (**A**) Line scan analysis (top) and representative images (bottom) of centromeric p-Chk1 and ACA in chromosome spreads of RPE1 cells. Mitotic cells were isolated by shake off after 4 h of nocodazole treatment. Cells were then mock treated (control) or treated with 2 μM VE-821 (ATRi) for 1 hour in the presence of nocodazole. The ATRi washout sample was released from VE-821 for 1 hour in the presence of nocodazole. (**B**) Immunoprecipitates of endogenous ATR and ATRIP from interphase (top) or mitotic (bottom) RPE1 cell extracts. Input = 5%. (**C**) Line scan analysis (top) and representative images (bottom) of centromeric ATR in chromosome spreads of RPE1 cells. Cells were arrested with nocodazole for 4 h and then mock or AurAi treated for 1 hour. (**D**) Line scan analysis of centromeric ATR and ACA in chromosome spreads of RPE1 cells. Cells were treated with control or CENP-F siRNA and arrested with nocodazole for 5 hours. (**E**) CENP-F in the immunoprecipitates of endogenous ATR and ATRIP from mitotic RPE1 cell extracts. Cells were treated with AurAi and Chk1i as indicated. Input = 5%. (**F**) Line scan analysis (top) and representative images (bottom) of centromeric ATR and ACA in U2OS cells uninfected or infected with CENP-F C630 expressing retrovirus. Scale bar in all panels, 2 μm. Error bars in all panels represent SEM. *$P \leq 0.01$, two-tailed t test. (**G**) A model in which ATR is recruited to the vicinity of centromeres through an interaction with CENP-F. This interaction is dependent on Aurora A activity and occurs specifically in mitosis.

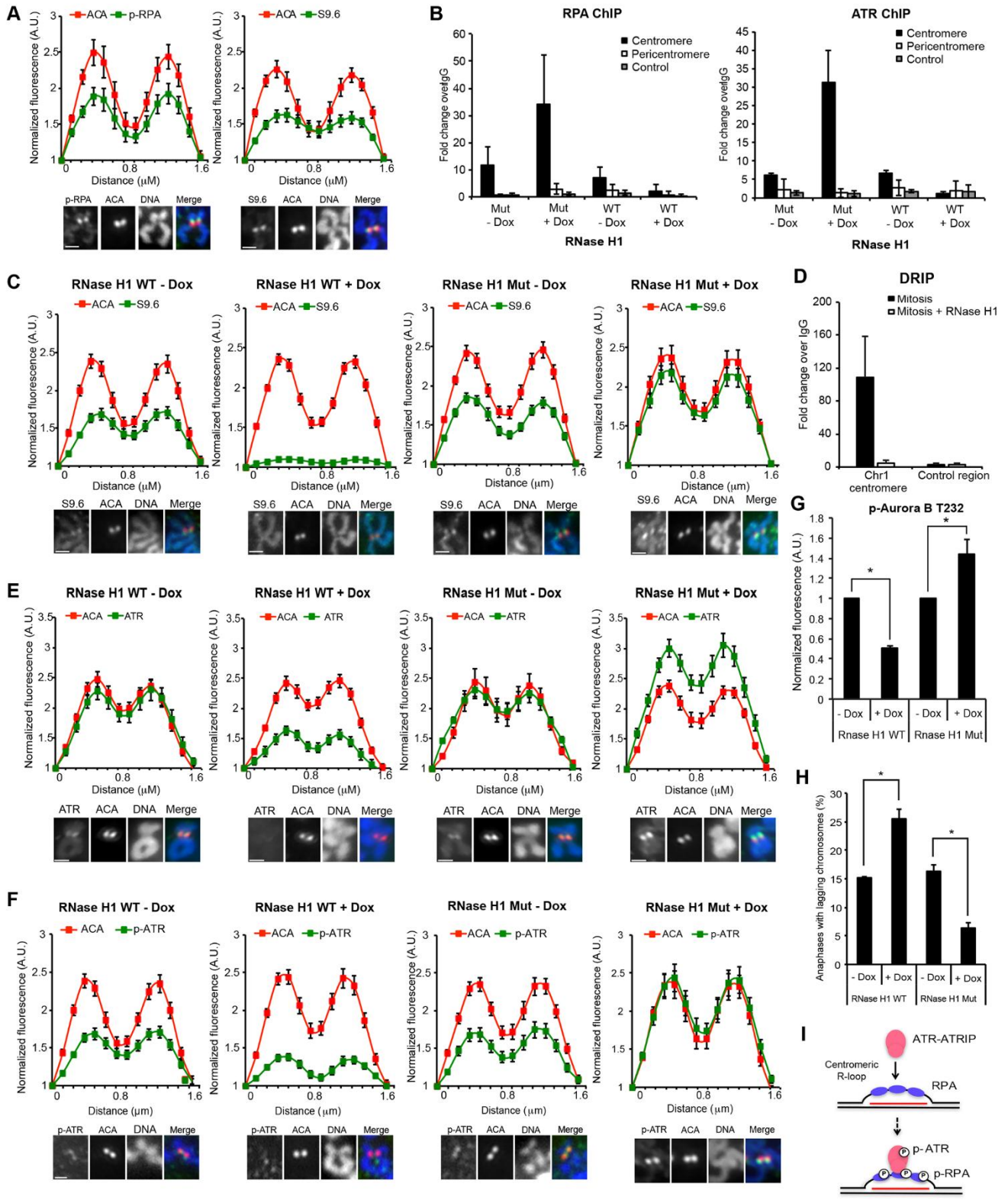

Fig. 4. ATR activation at centromeres is driven by R loops. (**A**) Line scan analysis (top) and representative images (bottom) of centromeric phospho-RPA32 S33 (p-RPA), S9.6, and ACA in chromosome spreads of RPE1 cells. Scale bar, 2 μm. (**B**) Quantitative PCR of RPA (right) or ATR (left) ChIP in HeLa-derived RNaseH1 WT/MUT inducible cell lines. Cells were synchronized in G2 with CDK1i, uninduced or induced with Dox for 4 hours, and released into mitosis in the presence of nocodazole for 1 hour (see Methods). (**C**, **E**, and **F**) Line scan analysis (top) and representative images (bottom) of centromeric S9.6 (C), ATR (E), p-ATR (F), and ACA in RNaseH1 WT/MUT inducible cell lines. Cells were treated as in (B). Scale bar, 2 μm. (**D**) Quantitative PCR of DRIP in mitotic RPE1 cells. (**G**) Relative fluorescence intensity of p-Aurora B in RNaseH1 WT/MUT inducible cell lines. Cells were treated as in (B). (**H**) Percentage of anaphase cells with lagging chromosomes. Cells were treated as in (B). Scale bar for all panels, 2 μm. Error bars in all panels represent SEM. $*P \leq 0.01$, two-tailed *t* test. (**I**) A model in which ATR-ATRIP is recruited to and activated by RPA-coated centromeric R loops in mitosis. The red line depicts centromeric RNA hybridized with DNA.

IMMUNOLOGY

S1P-dependent interorgan trafficking of group 2 innate lymphoid cells supports host defense

Yuefeng Huang,[1]*† Kairui Mao,[2]* Xi Chen,[1] Ming-an Sun,[3] Takeshi Kawabe,[1] Weizhe Li,[2] Nicholas Usher,[1,4] Jinfang Zhu,[1] Joseph F. Urban Jr.,[5] William E. Paul,[1]‡ Ronald N. Germain[1,2]†

Innate lymphoid cells (ILCs) are innate counterparts of adaptive T lymphocytes, contributing to host defense, tissue repair, metabolic homeostasis, and inflammatory diseases. ILCs have been considered to be tissue-resident cells, but whether ILCs move between tissue sites during infection has been unclear. We show here that interleukin-25– or helminth-induced inflammatory ILC2s are circulating cells that arise from resting ILC2s residing in intestinal lamina propria. They migrate to diverse tissues based on sphingosine 1-phosphate (S1P)–mediated chemotaxis that promotes lymphatic entry, blood circulation, and accumulation in peripheral sites, including the lung, where they contribute to anti-helminth defense and tissue repair. This ILC2 expansion and migration is a behavioral parallel to the antigen-driven proliferation and migration of adaptive lymphocytes to effector sites and indicates that ILCs complement adaptive immunity by providing both local and distant tissue protection during infection.

Innate lymphoid cells (ILCs) (*1*, *2*) lack antigen-specific receptors but, upon suitable stimulation, produce effector cytokines that parallel those made by antigen-induced T helper subsets (*3*). Various ILC progenitors have been identified in fetal liver and bone marrow (*4*), whereas mature ILCs are abundant in mucosal tissues and provide immune protection against pathogens early in infection (*5*–*8*). ILCs are also found in nonmucosal sites, such as secondary lymphoid tissues, and can mediate the transition from innate to adaptive immune responses (*9*, *10*) while also playing important roles in epithelial tissue repair (*11*), fat metabolism (*12*, *13*), and tumor immune surveillance (*14*). One issue that remains incompletely explored involves the specific origin(s) of ILCs present in diverse tissue sites and whether mature ILCs move between sites when infection demands. This is of special importance in the case of ILC2s and helminthic infections, because the latter typically involve different tissues such as the intestinal tract and lungs. Here we show that inflammatory ILC2s (iILC2s) (*15*) induced by helminths or the cytokine interleukin-25 (IL-25) migrate between tissues in response to activating signals. We also show how this migration is mediated and demonstrate the important role of such interorgan trafficking in host defense.

To probe the origin of tissue-resident ILCs, we monitored their numbers in the lung and small intestine of mice from postnatal day 1 through adulthood. On day 1, a few hundred GATA-3^{hi} ILC2s and RORγt^+ ILC3s each were detected in the lungs (fig. S1A) and small intestine (fig. S1B). ILC2s, but not ILC3s, dramatically increased in number in the lung in the first week after birth and became the dominant ILC population, expanding further over the subsequent 3 weeks (fig. S1A). The greatest increase in ILCs in the small intestine occurred 2 to 4 weeks after birth (fig. S1B), the same time period that gut microbiota diversity increases. The percentage of Ki-67$^+$ ILCs was ~80% on day 1 after birth, then decreased to a stable 5 to 10% in adults. This represents a lower proliferation rate relative to CD4 T cells, of which 20 to 30% were Ki-67$^+$ in adults (fig. S1, C and D).

ILCs are generally considered to be tissue-resident cells (*16*, *17*). To further study ILC localization in the steady state and during infection, parabiotic mice were used. Given the substantial effects of commensal bacteria on the host immune system, antibiotics were administered for only 2 weeks after surgery. A 50:50 exchange rate in blood leukocytes was observed 1 week after surgery (fig. S2A), and lung and intestinal CD4 T cells showed exchange rates of 50:50 and 30:70 to 40:60, respectively, 2 months after surgery (fig. S2B). In contrast, lung ILC2s and intestinal ILC3s did not appreciably exchange between the two partners even 6 to 8 months after surgery (Fig. 1, A and B), suggesting that these ILC subsets are largely self-maintained and that progenitors in bone marrow contribute little to their numbers in the steady state. Although intestinal ILC2 exchange was barely detected at 2 months, a modest but significant increase to a ~10% exchange rate was observed at 6 to 8 months after surgery (Fig. 1B). ILC2s in mesenteric lymph nodes (MLNs) showed a 20% exchange rate, whereas ILC3s in the MLNs did not exchange (Fig. 1C). Thus, although other ILC2 or ILC3 subsets appear to be self-maintained, intestinal ILC2s are refreshed at a low rate in the steady state.

We recently reported the existence of a lineage-negative (Lin$^-$), KLRG1^{hi} ILC2 population that is induced in the lung, liver, MLNs, and spleen after treatment with IL-25 or inoculation with infective third-stage *Nippostrongylus brasiliensis* larvae (L3) (*15*). These iILC2s are distinct from the ILC2s that naturally reside in the lung (nILC2s) (*18*). However, the source of iILC2s in various organs remained undetermined. Thus, we investigated ILC2 activation and migration in response to IL-25 treatment. Intranasal administration of IL-25 did not elicit iILC2s in the lung, whereas intraperitoneal (i.p.) injection of IL-25 induced the appearance of KLRG1^{hi} ST2$^-$ iILC2s (Fig. 1D), suggesting the absence of iILC2 precursors in the lungs. In vivo antibody labeling was performed in CD45.1$^+$ CD45.2$^+$ mice treated with IL-25. nILC2s were not labeled acutely by injected antibodies, indicating that they reside in parenchymal lung tissue. In contrast, like CD4 T cells, a large number of iILC2s were labeled, suggesting that they exist in the vascular space and circulate in the blood stream (Fig. 1E).

A parabiotic mouse model was used to further address the issue of iILC2 recirculation. After IL-25 i.p. injection into the CD45.1$^+$ mouse of a parabiotic pair, KLRG1^{hi} iILC2s were found in the lungs of both the CD45.1$^+$ mouse and its CD45.2$^+$ partner (Fig. 1F). Notably, the majority of iILC2s in the lung and liver, 50% of iILC2s in the spleen, and 25% of iILC2s in MLNs in the CD45.2$^+$ mouse were derived from its CD45.1$^+$ partner (Fig. 1F and fig. S3, A to C), indicating that they are circulating cells. In contrast, Thy1^{hi} nILC2s in the lung were endogenously derived (Fig. 1F), suggesting that they did not circulate upon IL-25 treatment. Very few CD45.2$^+$ iILC2s were found in the lung and liver (Fig. 1F and fig. S3A), possibly owing to the short half-life of exogenous IL-25 circulating via the blood to the partner mouse. Although IL-33 treatment induced lung nILC2 proliferation in both animals (Fig. 1G), based on increased Ki-67 expression (fig. S1C), nILC2 transfer between the parabiotic animals did not occur, indicating that these cells do not enter the circulation. Consistent with the IL-25 treatment data, 5 days after the inoculation of both parabiotic partners with *N. brasiliensis* L3, 35% of iILC2s in the lung were derived from the partner mouse, whereas the majority of nILC2s were endogenous (Fig. 1H). Thus, IL-25– or *N. brasiliensis*–induced iILC2s are circulating cells, distinct from tissue-resident ILC subsets.

To identify the source of circulating iILC2s, total leukocytes were isolated from different CD45.1$^+$ *Rag1*$^{-/-}$ mouse tissues and then transferred into CD45.2$^+$ *Rag1*$^{-/-}$ mice; this was followed by IL-25 treatment. Unexpectedly, cells

[1]Laboratory of Immunology, National Institute of Allergy and Infectious Diseases (NIAID), National Institutes of Health, Bethesda, MD 20892, USA. [2]Laboratory of Systems Biology, NIAID, National Institutes of Health, Bethesda, MD 20892, USA. [3]Eunice Kennedy Shriver National Institute of Child Health and Human Development, National Institutes of Health, Bethesda, MD 20892, USA. [4]Department of Undergraduate Biology, Cornell University, Ithaca, NY 14853, USA. [5]Diet, Genomics, and Immunology Laboratory, Beltsville Human Nutrition Research Center, Agricultural Research Service, U.S. Department of Agriculture (USDA), Beltsville, MD 20705, USA.
*These authors contributed equally to this work.
†Corresponding author. Email: yuefeng.huang@nih.gov (Y.H.); rgermain@niaid.nih.gov (R.N.G.) ‡Deceased.

from small intestine lamina propria (siLP) gave rise to high numbers of rapidly proliferating iILC2s in the lungs of the recipients, whereas transferred bone marrow cells gave rise to few iILC2s, and lung cells gave rise to none (Fig. 2A). This suggested that the intestine contains an enriched source of "pre-iILC2s." siLP leukocytes were then divided into three groups, and similar cell transfer experiments were performed. Only KLRG1$^+$ ILC2s from the siLP could give rise to iILC2s in the lung of recipients—neither Lin$^+$ cells nor KLRG1$^-$ ILCs could do so (Fig. 2B)—suggesting that IL-25–induced iILC2s in peripheral sites are derived from intestinal ILC2s. In addition, we purified lung nILC2s, bone marrow (BM) ILC2 progenitors, and siLP ILC2s and transferred equal numbers of these populations to recipients; we then administered IL-25 treatment. Intestinal ILC2s were much more efficient in giving rise to iILC2s than were BM ILC2 progenitors. Most iILC2s in the recipients were Ki-67$^+$, indicating that they were proliferating rather than just phenotypically converted from donor cells (Fig. 2C). Although BM ILC2 progenitors may contribute to peripheral responses in chronic conditions, they are unlikely to be the major source of iILC2s during acute helminthic infections, owing to the lack of local IL-25 producers such as the tuft cells of the gastrointestinal tract (*19*–*21*).

Flow cytometry revealed that IL-25–induced iILC2s and siLP ILC2s possess similar surface-marker phenotypes (Fig. 2D). To further characterize ILC2 populations, we examined the transcriptomes of BM ILC2 progenitors, lung nILC2s, IL-33–activated lung nILC2s, intestinal ILC2s, IL-25–induced lung iILC2s, and MLN iILC2s by RNA sequencing (RNA-seq). Despite the difference in location, lung and MLN iILC2s have very similar transcriptome profiles (Fig. 2E). Intestinal ILC2s showed the closest resemblance in gene expression pattern to iILC2s, providing additional evidence that the source of IL-25–induced iILC2s is intestinal ILC2s. Activated lung nILC2s and lung iILC2s showed highly distinct gene expression patterns, although they were in the same tissue (Fig. 2F). iILC2s produce more IL-13, whereas nILC2s produce more IL-9. We also found that iILC2s express high levels of CCR9 and some inhibitory receptors such as KLRG1 and TIGIT. In addition, we found that iILC2s produce IL-17A, which is consistent with our previous findings (*15*), whereas nILC2s express a higher level of the receptor (IL-18R1) and receptor-associated protein (IL-1RAcP) involved in responses to IL-18 and IL-1 (Fig. 2F), cytokines that are important for the conversion of lung ILC2s into ILC1s (*22*–*24*).

iILC2s appear in the lungs during the early stage of pulmonary *N. brasiliensis* larval migration and disappear after the expulsion of adult worms from the intestine (*15*). In parabiotic mouse experiments, KLRG1^{hi} iILC2s were no longer detected in the lungs 12 days after a 3-day IL-25 treatment. However, among lung nILC2s in the untreated CD45.2$^+$ mouse partner, ~10% were CD45.1$^+$ (fig. S4A). Among lung nILC2s, ~16% were derived from the parabiotic donor 20 days after inoculation of *N. brasiliensis* into both partners (fig. S4B), suggesting that iILC2s can contribute to the lung nILC2 pool late in infection. Notably, among siLP ILC2s of the CD45.2$^+$ mouse, ~40% were CD45.1$^+$ (fig. S4A). iILC2s were found to express high levels of integrin $\alpha4\beta7$ (*25*) and

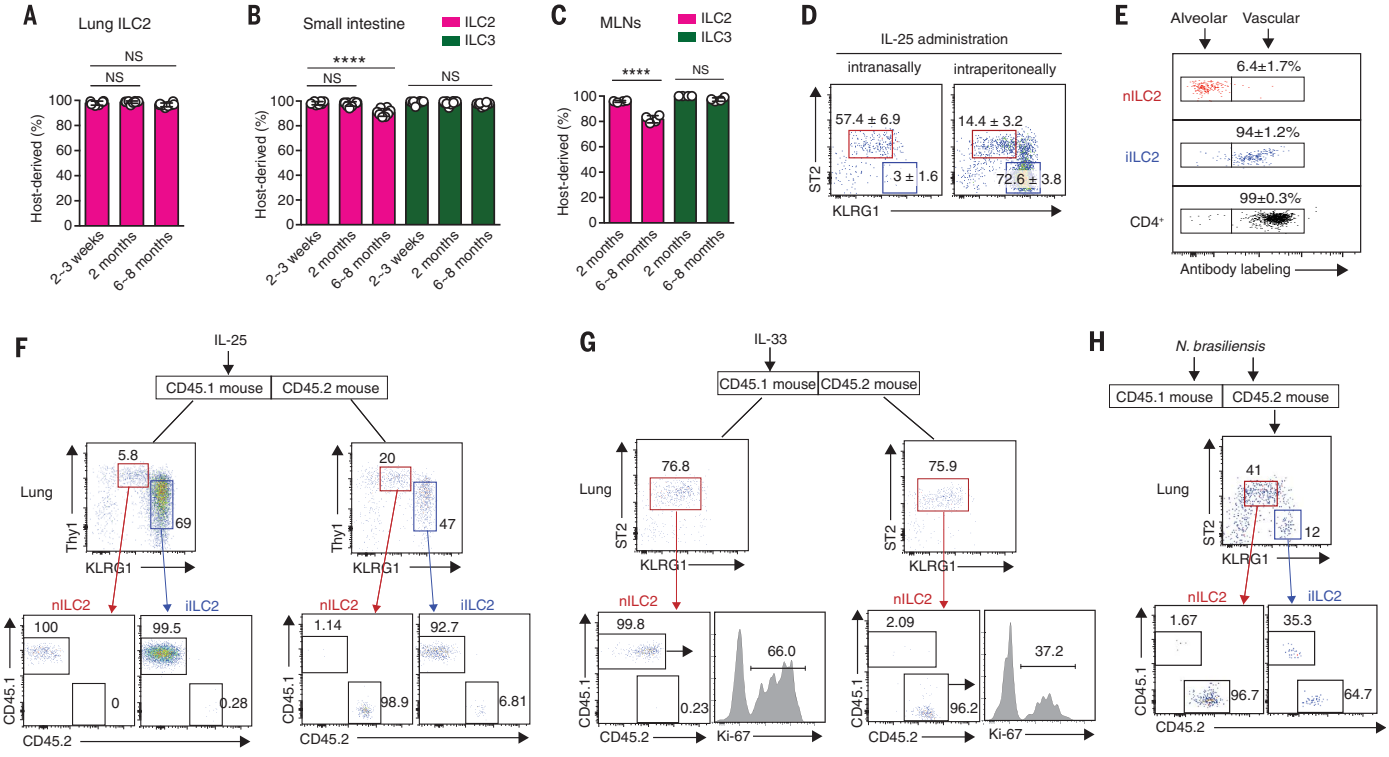

Fig. 1. IL-25– or helminthic infection–induced inflammatory ILC2s are circulating cells that differ from tissue-resident ILCs. (**A** to **C**) CD45.1$^+$ and CD45.2$^+$ mice were surgically connected to generate parabiotic partners. Percentages of host-derived cells were analyzed among ILC2s and ILC3s 2 to 3 weeks, 2 months, and 6 to 8 months after surgery. ILC2s were gated as lineage-negative (Lin$^-$) CD127$^+$ GATA-3^{hi}, and ILC3s were gated as Lin$^-$ CD127$^+$ RORγt$^+$. MLNs, mesenteric lymph nodes. (**D**) B6 mice were treated with IL-25 intranasally or intraperitoneally (i.p.) daily for 3 days. Lung leukocytes were then analyzed by flow cytometry. Cells were gated on CD45.2$^+$ Lin$^-$ CD127$^+$. (**E**) CD45.1$^+$ CD45.2$^+$ mice were treated with IL-25 i.p. daily for 3 days. Mice were intravenously injected with phycoerythrin-labeled antibodies against CD45.1 and euthanized 5 minutes later for analysis of CD45.2 on Lin$^-$ CD127$^+$ ST2$^+$ KLRG1^{int} naturally lung-residing ILC2s (nILC2s), Lin$^-$ CD127$^+$ ST2$^-$ KLRG1^{hi} inflammatory ILC2s (iILC2s), and CD4$^+$ T cells in the lungs without perfusion. (**F** and **G**) Two months after surgery, the CD45.1$^+$ partner of each parabiotic pair was treated i.p. with IL-25 (F) or IL-33 (G) daily for 3 days. Cells in the lungs were then analyzed. nILC2s were gated as Lin$^-$ CD127$^+$ Thy1^{hi} KLRG1^{int}, and iILC2s were gated as Lin$^-$ CD127$^+$ Thy1^{lo} KLRG1^{hi}. (**H**) Two months after surgery, both mice in each parabiotic pair were inoculated with ~200 infective *N. brasiliensis* larvae (L3). Cells in the lungs were analyzed on day 5 postinoculation. Means ± SEM from six to eight mice at each time point in (A) to (C) and from three mice in (D). ****$P \leq 0.0001$; NS, not significant; unpaired two-tailed *t* test. Results are representative of at least two independent experiments.

gut-homing receptor CCR9 (*26*) (fig. S4C), suggesting that iILC2s also have the potential to return to the gut after infection. CD62L expression was detected on iILC2s in the MLNs, but not in the lung. Thus, iILC2s present in peripheral sites are a transient cell population, converting into nILC2s in tissues such as the lung and/or migrating back to the gut.

To gain mechanistic insight into the effects of IL-25 on siLP pre-iILC2s and the control of their exit into the circulation, we used confocal imaging. The coexpression of GATA-3 and KLRG1 confirmed that KLRG1 is a reliable marker for intestinal ILC2s (fig. S5). In the steady state, $CD3^-$ $KLRG1^+$ ILC2s predominantly resided in the lamina propria, and only a small fraction were $Ki\text{-}67^+$ (Fig. 3A, left). Thirty-six hours after IL-25 treatment, more than 50% of ILC2s were $Ki\text{-}67^+$. Sixty hours after IL-25 treatment, ILC2 numbers dramatically increased, and the majority were $Ki\text{-}67^+$ (Fig. 3, A and B). Intestinal ILC2s expressed substantial levels of cell-surface CD69, whereas levels in circulating iILC2s were lower (Fig. 3C). CD69 has an important role in the control of T cell migration between tissues. It is highly expressed on tissue-resident memory T cells, prolonging their residency, and on activated T cells in lymph nodes during the sequestration phase shortly after the initiation of an immune response. In contrast, its expression on trafficking T cells is low (*27*). Given that $KLRG1^{hi}$ ILC2s were present in many peripheral sites 60 hours after IL-25 administration (fig. S3C), we hypothesized that activated intestinal ILC2s behave like activated T cells in lymph nodes, crossing the lymphatic endothelium, entering lymphatics, and entering the blood circulation. When Lyve-1 staining was used to delineate lymphatic vessels (*28*), $KLRG1^+$ ILC2s were observed within these vessels in the villi of IL-25–treated mice but not of naïve mice (Fig. 3D). Three-dimensional image reconstruction confirmed the localization of ILC2s within, rather than adjacent to, the lymphatic vessels (movie S1). iILC2s were also detected in peripheral blood 60 hours after IL-25 treatment (Fig. 3E). Thus, intestinal ILC2s rapidly proliferate after IL-25 stimulation and enter lymphatic vessels and then the blood, accumulating as iILC2s in many peripheral sites.

G protein–coupled sphingosine 1-phosphate (S1P) receptors are required for T lymphocyte egress from lymphoid organs across lymphatic endothelial barriers (*29*, *30*). Thus, we examined the possible role of this chemotactic pathway in ILC migration. ILC2s or ILC3s in naïve mice did not express S1P receptors, but IL-25–induced iILC2s in the lung and MLNs, like CD4 T cells, expressed S1PR1 and S1PR4 (Fig. 4A). iILC2s in MLNs also expressed S1PR5 (Fig. 4A), which has been reported to be expressed on natural killer cells (*31*). FTY720, which antagonizes the S1P-signaling pathway, did not affect IL-25–induced intestinal ILC2 proliferation (Fig. 4, B and C) but blocked iILC2 accumulation in the lung, liver, and spleen and partially blocked iILC2 accumulation in MLNs (Fig. 4D). This is consistent with

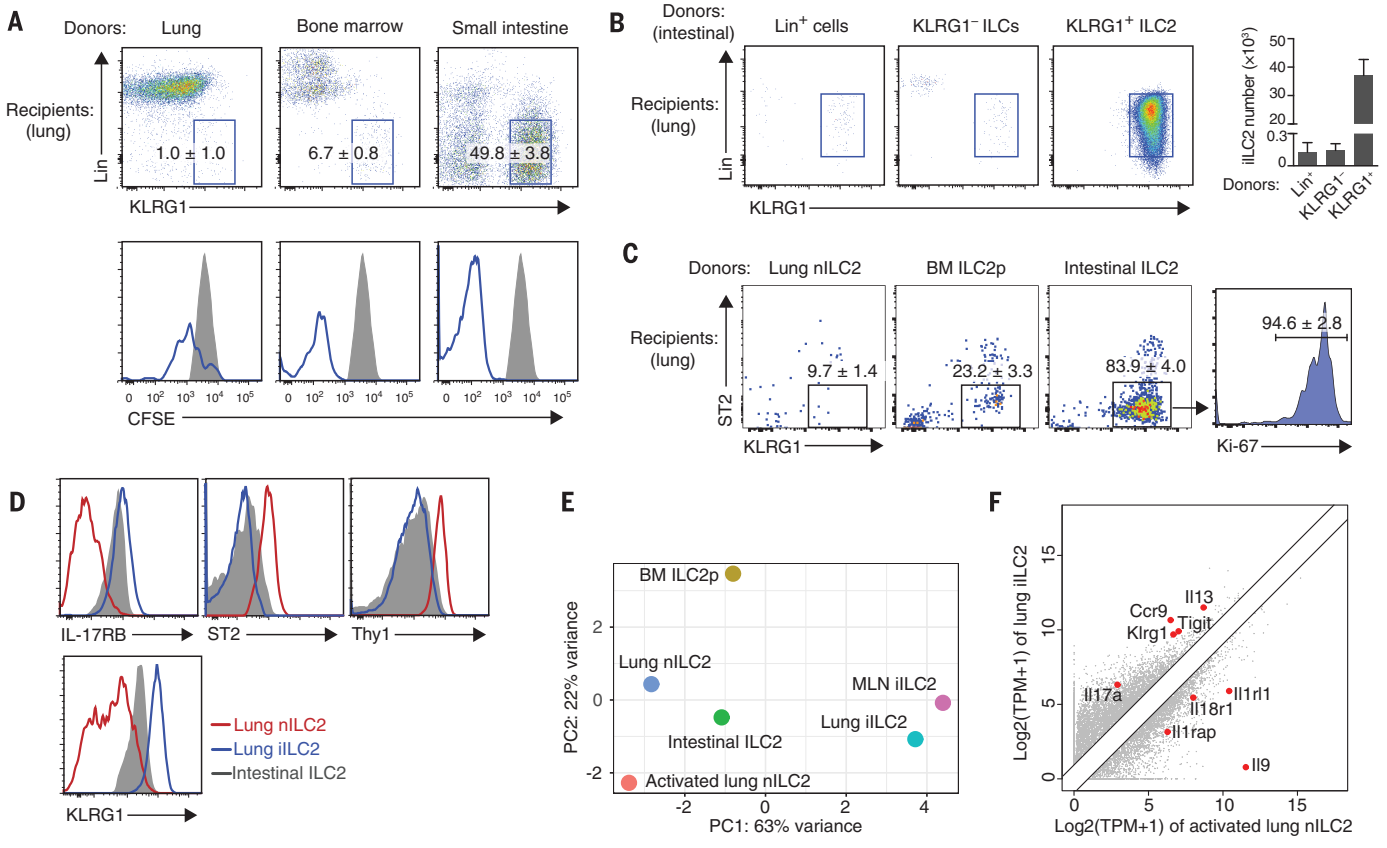

Fig. 2. Intestinal ILC2s are the immediate source of iILC2s. (**A**) Total leukocytes from lung, bone marrow, or siLP of CD45.1$^+$ *Rag1*$^{-/-}$ mice were labeled with carboxyfluorescein succinimidyl ester (CFSE) and transferred into CD45.2$^+$ *Rag1*$^{-/-}$ mice; this was followed by a 3-day treatment with IL-25 injected i.p. Cells in the lungs were analyzed for CD45.1$^+$ donor cells. Blue line, Lin^- $KLRG1^{hi}$ iILC2s; gray shaded area, CD45.1$^+$ cells labeled with CFSE before transfer. (**B**) siLP leukocytes were divided into the three indicated groups by cell sorting and subjected to a similar transfer experiment to that described in (A). Left, cells were gated on CD45.1$^+$ Lin^-; right, CD45.1$^+$ iILC2 numbers in the lungs. (**C**) Equal numbers of lung nILC2, siLP ILC2, and bone marrow (BM) ILC2 progenitors were sorted and subjected to a similar transfer experiment to that described in (A). (**D**) Comparison of surface markers on lung iILC2s in IL-25–treated mice and lung nILC2s and intestinal ILC2s in naïve mice by flow cytometry. (**E**) Principal component analysis of the transcriptomes of different ILC2 populations identified by RNA-seq. The analysis is based on $\log_{10}$[transcripts per million (TPM) + 1] of 53 immune-related genes. (**F**) Scatter plot comparing the gene expression patterns from RNA-seq between activated lung nILC2s and lung iILC2s. The *x* and *y* axes show the $\log_{10}$(TPM + 1) values for each sample. Only genes with at least a twofold difference were plotted. Means ± SEM from three mice in (A) to (C). Data are representative of two independent experiments in (A) to (D).

the tissue-specific differences in CD69 expression (Fig. 3C) (*27*, *32*). Together, these results indicate that iILC2 cells use a similar molecular mechanism to that of conventional $CD4^+$ and $CD8^+$ T cells, which regulates their exit from tissues into the lymph as they move to a distant site of effector activity.

$IL\text{-}25R^+$ ILC2 progenitors were recently identified in bone marrow (*33*). Thus, we addressed the relationship between BM ILC2 progenitors and iILC2s. $IL\text{-}25R^+$ progenitors expressed ST2 but not KLRG1 in naïve mice (fig. S6, A and B). IL-25 treatment not only expanded the progenitor population, but also induced $ST2^-$ $KLRG1^{hi}$ iILC2s in the bone marrow (fig. S6B). FTY720 did not affect the expansion of ILC2 progenitors but abolished the presence of iILC2s in bone marrow (fig. S6, B and C). These results indicate that intestinally derived iILC2s can infiltrate the bone marrow and highlight the distinction between iILC2 and BM ILC2 progenitors.

Last, we investigated the physiological implications of ILC2 migratory responses during antihelminth immunity. Inoculation of conventional $Rag1^{-/-}$ mice with *N. brasiliensis* established a chronic adult worm infection in the intestine, which was cleared by the administration of IL-25 (Fig. 4E), suggesting that an increase in iILC2 numbers is sufficient to expel the worms even in the absence of adaptive lymphocytes. Parasitic *N. brasiliensis* L3 pass through the lungs early in the infection and cause inflammation and tissue damage. FTY720 treatment of $Rag1^{-/-}$ mice inoculated with a dose of 500 L3 resulted in the death of 80% of the mice at early stages of infection (Fig. 4F). This mortality was largely prevented by the transfer of iILC2s into the circulating pool before FTY720 treatment, which compensated for the drug-induced blockade of endogenous iILC2s in the lung. Larvae were observed in the lungs (arrows) on day 5, and severe epithelial destruction was noted (asterisks) on day 8 postinoculation in FTY720-treated mice not given adoptive cell therapy (Fig. 4G). Prolonged worm residency and tissue damage could be prevented by iILC2 transfer. Furthermore, iILC2s were found to express higher levels of amphiregulin—a key contributor to epithelial tissue repair during infection—compared with nILC2s (Fig. 4H). Thus, intestinally derived iILC2s accumulate in the lung in a S1P-dependent manner and provide crucial protection at the early stage of infection, contributing to worm clearance, tissue repair, and host survival.

Here we have characterized in detail a distinct cell population that resides in the gut but can migrate to the lung and other distal sites and make substantial contributions to host defense. Tissue-resident ILC2s undergo interorgan migration, a property essential to their protective role in infection. This study also shows that epithelium-resident ILC2s move into lymphatics in a S1P-dependent manner by the same mechanism previously described for adaptive lymphocytes

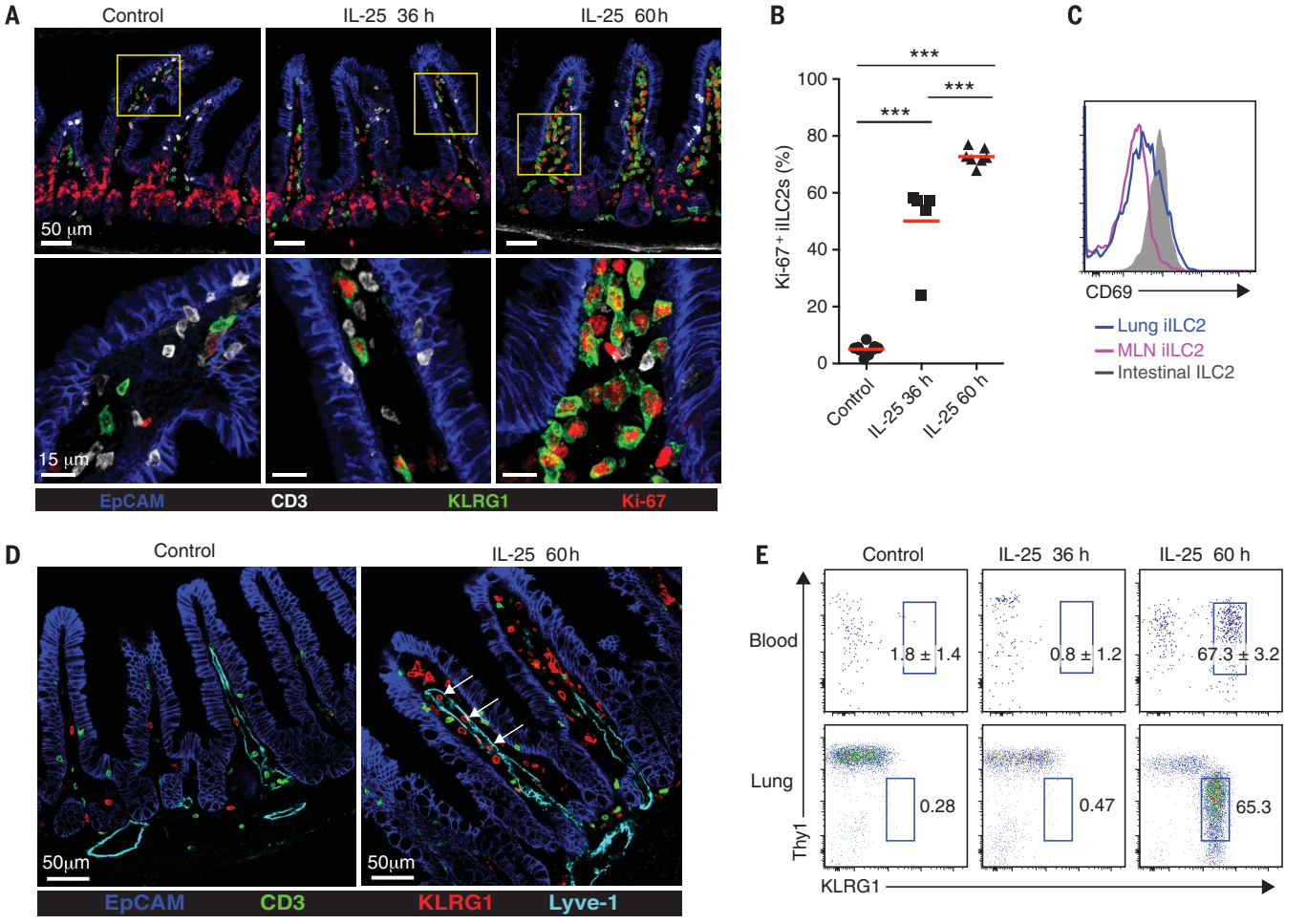

Fig. 3. Intestinal ILC2s proliferate and enter lymphatics in response to IL-25. (**A**) Immunofluorescence staining of ilea from B6 mice 0, 36, and 60 hours (h) after treatment with IL-25. The lower panels are magnified views of the boxed areas in the upper panels. (**B**) Quantification of $Ki\text{-}67^+$ ILC2s in the small intestine. (**C**) Comparison of CD69 expression on siLP ILC2s, lung iILC2s, and MLN iILC2s by flow cytometry. (**D**) Immunofluorescence staining of ilea from mice 0 and 60 hours after treatment with IL-25. Arrows, $KLRG1^+$ ILC2s within a lymphatic vessel. (**E**) iILC2s in peripheral blood or lungs were analyzed from B6 mice 0, 36, and 60 hours after treatment with IL-25. Images are representative of three gut sections from two mice in each group. Data are representative of two independent experiments in (C) and (E). Means ± SEM; n = 6 to 9 and 3 for each group in (B) and (E), respectively. ***$P \leq 0.001$; unpaired two-tailed t test.

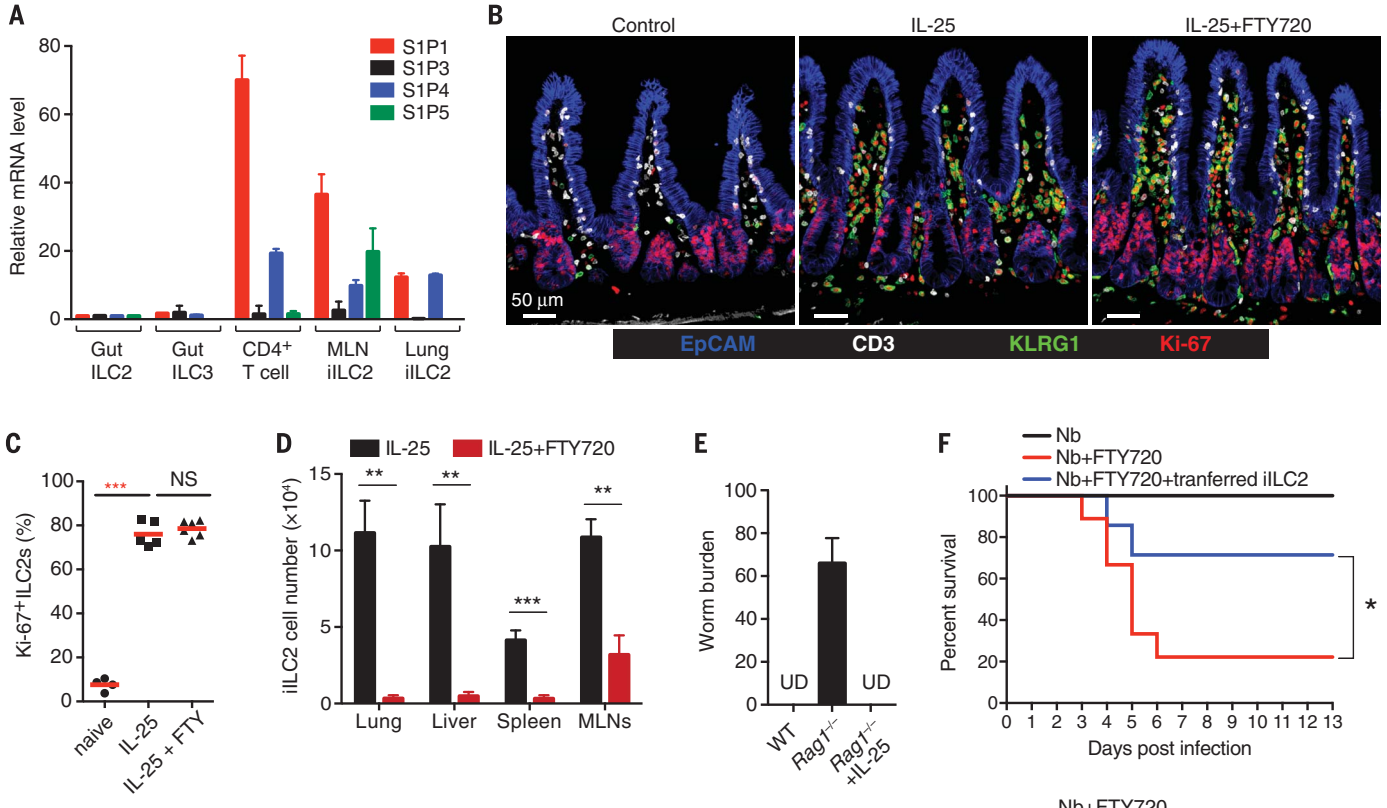

Fig. 4. Intestinally derived iILC2s migrate and provide protection to the lung in a S1P-dependent manner. (**A**) S1P receptor expression by the indicated cell populations was assessed by real-time polymerase chain reaction. Intestinal ILC2s and ILC3s and MLN CD4 T cells were obtained from naïve mice, whereas iILC2s in the lung or MLNs were from IL-25–treated mice. (**B**) Immunofluorescence staining of ilea from mice that were untreated, treated with IL-25, or treated with IL-25 plus FTY720 for 3 days. (**C**) Quantification of Ki-67$^+$ ILC2s in (B). (**D**) B6 mice were treated with IL-25 or with IL-25 plus FTY720 i.p. for 3 days, and the iILC2s in indicated tissues were analyzed by flow cytometry. (**E**) Worm burden on day 14 in the small intestine of the mice infected with ~300 *N. brasiliensis* L3. IL-25 treatment was given every other day in the third group. UD, undetected. (**F**) *Rag1*$^{-/-}$ mice were inoculated with ~500 *N. brasiliensis* L3 (Nb), and FTY720 treatment started on day 3 and continued daily until day 10, in two groups. In the transfer group, ~3 × 10^6 iILC2s sorted from IL-25–treated mice were transferred intravenously into each animal on the same day as worm inoculation. Death and survival were monitored until day 13, and the difference between two groups was determined by the log-rank (Mantel-Cox) test. (**G**) Histology of lung sections from *Rag1*$^{-/-}$ mice inoculated with ~300 *N. brasiliensis* L3. Arrows, worm larvae; asterisk, tissue destruction. (**H**) Amphiregulin mRNA levels in nILC2s and iILC2s, which were sorted from lungs on day 5 postinoculation with *N. brasiliensis*. Means ± SEM; $n = 3$ in (A), (D), (E), and (H) and 4 to 6 in (C). *$P \le 0.05$; **$P \le 0.01$; ***$P \le 0.001$; unpaired two-tailed t test. Data in (A), (D), and (E) are representative of three experiments; data in (F) are the summary of two experiments ($n = 10$). Images are representative of three sections from two mice of each group in (B) and (G).

egressing from secondary lymphoid tissues. We hypothesize that S1P-dependent dissemination of activated effectors from one tissue through the lymphatics and blood to a distant site of infection evolved as a mechanism within the innate lymphoid system, which was later grafted onto the emerging adaptive system, rather than being a late development of the T cell adaptive immune system. Last, the ability of FTY720 to block ILC2 dissemination suggests that the immunosuppressive effects of this drug that have been attributed solely to the blockade of adaptive T cell migration from lymph nodes and the spleen need to be reassessed.

REFERENCES AND NOTES

1. D. Artis, H. Spits, *Nature* **517**, 293–301 (2015).
2. C. S. Klose, D. Artis, *Nat. Immunol.* **17**, 765–774 (2016).
3. G. Eberl, M. Colonna, J. P. Di Santo, A. N. McKenzie, *Science* **348**, aaa6566 (2015).
4. E. C. Zook, B. L. Kee, *Nat. Immunol.* **17**, 775–782 (2016).
5. K. Moro *et al.*, *Nature* **463**, 540–544 (2010).
6. D. R. Neill *et al.*, *Nature* **464**, 1367–1370 (2010).
7. A. E. Price *et al.*, *Proc. Natl. Acad. Sci. U.S.A.* **107**, 11489–11494 (2010).
8. G. F. Sonnenberg, D. Artis, *Nat. Med.* **21**, 698–708 (2015).
9. C. J. Oliphant *et al.*, *Immunity* **41**, 283–295 (2014).
10. A. S. Mirchandani *et al.*, *J. Immunol.* **192**, 2442–2448 (2014).
11. L. A. Monticelli *et al.*, *Nat. Immunol.* **12**, 1045–1054 (2011).
12. M. W. Lee *et al.*, *Cell* **160**, 74–87 (2015).
13. J. R. Brestoff *et al.*, *Nature* **519**, 242–246 (2015).
14. S. Dadi *et al.*, *Cell* **164**, 365–377 (2016).
15. Y. Huang *et al.*, *Nat. Immunol.* **16**, 161–169 (2015).
16. G. Gasteiger, X. Fan, S. Dikiy, S. Y. Lee, A. Y. Rudensky, *Science* **350**, 981–985 (2015).

17. K. Moro *et al*., *Nat. Immunol.* **17**, 76–86 (2016).
18. Y. Huang, W. E. Paul, *Int. Immunol.* **28**, 23–28 (2016).
19. J. von Moltke, M. Ji, H. E. Liang, R. M. Locksley, *Nature* **529**, 221–225 (2016).
20. M. R. Howitt *et al*., *Science* **351**, 1329–1333 (2016).
21. F. Gerbe *et al*., *Nature* **529**, 226–230 (2016).
22. J. S. Silver *et al*., *Nat. Immunol.* **17**, 626–635 (2016).
23. Y. Ohne *et al*., *Nat. Immunol.* **17**, 646–655 (2016).
24. S. M. Bal *et al*., *Nat. Immunol.* **17**, 636–645 (2016).
25. A. Hamann, D. P. Andrew, D. Jablonski-Westrich, B. Holzmann, E. C. Butcher, *J. Immunol.* **152**, 3282–3293 (1994).
26. M. Svensson *et al*., *J. Clin. Invest.* **110**, 1113–1121 (2002).
27. C. O. Park, T. S. Kupper, *Nat. Med.* **21**, 688–697 (2015).
28. S. Banerji *et al*., *J. Cell Biol.* **144**, 789–801 (1999).
29. M. L. Allende, J. L. Dreier, S. Mandala, R. L. Proia, *J. Biol. Chem.* **279**, 15396–15401 (2004).
30. M. Matloubian *et al*., *Nature* **427**, 355–360 (2004).
31. T. Walzer *et al*., *Nat. Immunol.* **8**, 1337–1344 (2007).
32. L. R. Shiow *et al*., *Nature* **440**, 540–544 (2006).
33. Y. Yu *et al*., *Nature* **539**, 102–106 (2016).

ACKNOWLEDGMENTS

We thank K. Weng, T. Moyer, and C. Henry for cell sorting; A. Moseman for technical assistance with parabiosis surgery; M. Wong for assistance with library preparation; J. M. Ward for analyzing histological sections; and the staff of the NIAID animal facility for the postoperative care of parabiotic mice. We thank E. Shevach and members of the Laboratories of Immunology and Systems Biology, NIAID, for discussions. This work was supported by the Intramural Research Program of NIAID, NIH, and by the USDA (8040-51000-058-00D). Y. Huang was also supported by a NIAID K99 award (1K99AI123350-01A1). RNA-seq data are available in the Gene Expression Omnibus database (accession number GSE104708). Y.F. designed, performed, and interpreted the majority of the experiments and drafted the manuscript. K.M. designed, performed, and interpreted confocal imaging experiments. X.C., T.K., and N.U. assisted with experiments. M.S. performed RNA-seq data analysis. W.L. assisted with image data analysis. J.Z. helped to design and interpret the experiments. J.F.U. provided *N. brasiliensis* and helped to design and interpret worm experiments. W.E.P. designed the experiments. R.N.G. designed the experiments, interpreted the data, and finalized the manuscript. All authors (with exception of W.E.P.) contributed to the discussion of experimental findings and preparation of the manuscript.

SUPPLEMENTARY MATERIALS

www.sciencemag.org/content/359/6371/114/suppl/DC1
Materials and Methods
Figs. S1 to S6
References (*34*–*36*)
Movie S1

22 December 2016; resubmitted 5 September 2017
Accepted 10 November 2017
10.1126/science.aam5809

Collaboration across the Pacific: China-U.S. partnership seeks to improve Earth system predictions at high resolution

There is a pressing need to develop a new advanced modeling framework for high-resolution multiscale Earth system predictions. We have already seen that climate variations impact the likelihood and intensity of extreme weather, including tropical cyclones, heat waves, winter storms, droughts, floods, and coastal sea-level rise. Such events have profound effects on human well-being, particularly as it relates to agriculture, energy use, industrial activity, marine ecosystems, and coastal sustainability, with economic impacts in the billions of dollars.

In order to address this need, Qingdao National Laboratory for Marine Science and Technology (QNLM), Texas A&M University (TAMU), and the U.S. National Center for Atmospheric Research (NCAR) are collaborating to establish the International Laboratory for High-Resolution Earth System Prediction (iHESP). This international collaboration has the potential to yield enormous social, economic, and environmental benefits, making it an extremely valuable effort for policymakers and stakeholders. The new laboratory will play a fundamental role in moving Earth System science and prediction forward by combining the expertise of these three renowned research institutions to pursue transformational efforts in the development of high resolution Earth System models.

The new modeling framework and products that iHESP intends to develop will be critical to formulating solutions for risks associated with rapidly changing environmental conditions across the planet, including those associated with climate variability on subseasonal to decadal timescales. iHESP seeks to provide reliable information at both global and regional levels, thereby helping decision makers around the world to implement more effective policies.

QNLM, a hitherto unique national laboratory, was launched in 2015 with Professor, Lixin Wu, Fellow of the Chinese Academy of Sciences, as its director. A comprehensive, world-class marine science institution, QNLM pools innovative resources and teams for original research, to boost the nation's capacity for innovation and to take the lead in marine science and technology. Jointly supported by national and local government, QNLM focuses

Lixin Wu,
Director of QNLM

on basic and applied research, and especially the development of cutting-edge technology. The research areas cover ocean dynamics and climate change, marine life processes and bioresource utilization, benthic processes and mineral resources, evolution and protection of marine ecological environments, extreme environments and resources in deep sea and polar oceans, and marine technologies and equipment. QNLM has launched one of the world's fastest marine research computers, and created a research vessel sharing system, including the manned submersible Jiaolong. Sticking to the principles of "openness, mobility, collaboration, sharing," and as part of its internationalization strategy, QNLM vigorously advances the construction of a global collaborative innovation network. In cooperation with Australia's Commonwealth Scientific and Industrial Research Organization (CSIRO), QNLM has established the Centre for Southern Hemisphere Oceans Research (CSHOR), to collaborate on the southern hemisphere oceans and Antarctic observation and research. To respond to the many challenges facing ocean science today, QNLM actively participates in building the international network for cooperation and exchange, holding the Global Ocean Summit to promote the sharing of knowledge, experience, and infrastructure.

TAMU, located in College Station, Texas, and established in 1876, is the flagship school of the Texas A&M system. The fourth-largest university in the U.S. and the largest in Texas, it is one of 17 U.S. universities to be designated a land-grant, sea-grant, and space-grant university. TAMU is also one of the few universities in the United States to have a college of geosciences that encompasses a broad range of disciplines in Earth system science, including oceanography, atmospheric sciences, geology and geophysics, and geography, as well as the International Ocean Discovery Program (IODP)—a U.S. National Science Foundation–funded international marine research collaboration dedicated to advancing scientific understanding of the Earth through drilling, coring, and monitoring the subsea floor. Together, these academic departments and research centers have brought TAMU a wide range of talents and capabilities in Earth system science, positioning it extremely well to deal with challenges in integrated research.

NCAR, which is the U.S. National Science Foundation's oldest and largest federally funded research and development center, is one of world's premiere centers in atmospheric and Earth system science. Established in 1960, NCAR's mission is to understand the behavior of the atmosphere and related Earth and geospace systems; to support, enhance, and extend the capabilities of the university community and the broader scientific community, nationally and internationally; and to foster the transfer of knowledge and technology for the betterment of human life. NCAR is committed to the continued advancement of Earth system modeling, improved predictive capabilities, and more effective applications of these advances to societal needs. Through this new international laboratory, and in collaboration with the broader research community, NCAR will be able to accelerate its progress on these strategic objectives, thereby enhancing its ability to bring relevant and objective information to national and international decisions on mitigation, adaptation, resiliency, and sustainability.

QNLM, TAMU, and NCAR representatives signing the iHESP memorandum of agreement.

iHESP is anticipated to begin operations in January 2018. Its overarching objective is to accelerate efforts in: (1) high-resolution ocean and Earth system model development; (2) high-resolution ocean and Earth system simulation and prediction; and (3) advancing scientific understanding of interactions among different Earth System components across different space and timescales.

The specific science goals of iHESP for the next five years are as follows:

1) Assess and quantify the role of mesoscale ocean eddies and their interactions with the atmosphere and sea-ice in climate variability, predictability, and prediction by carrying out an unprecedented ensemble of present and future climate simulations at high resolution;

2) Develop a new advanced modeling framework for high-resolution regional and global Earth system predictions at subseasonal to decadal timescales by focusing on:

- Advancing ocean component of Earth system models with improved upper-ocean mixing processes, including surface wave and tidal effects, as well as other unresolved small-scale dynamics;

- Developing a new online coupled data assimilation capability for high-resolution regional and global Earth system models; and

- Enhancing the Community Earth System Model (CESM) coupling software framework by developing a set of online nesting tools for dynamical downscaling through nesting of a regional CESM version within the global CESM.

Today, as innovative resources are actively exchanged among the global marine science community at an unprecedented rate, open science and collaboration have become an important mode for international science and technology innovation and development. It is believed that iHESP will quickly develop into a world-class research center for Earth system modeling and prediction, greatly benefiting the global marine science community and all humanity, through gathering high-caliber talent, pooling complementary resources, and carrying out innovative research. It is also expected that iHESP will work with such international programs and initiatives as Future Earth, the International Geosphere Biosphere Program (IGBP), and the World Climate Research Program (WCRP) to provide scientific guidance and management strategies for climate prediction.

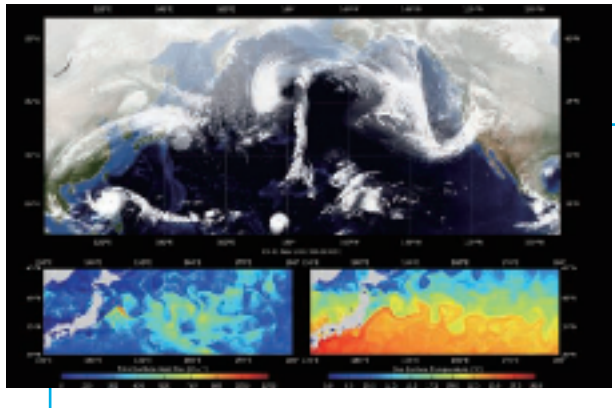

A snapshot taken from a 9-km coupled regional climate model simulation of North Pacific storm systems interacting with the Kuroshio Current and its eddies, conducted as a collaboration between TAMU and QNLM scientists. The top panel shows simulated outgoing longwave radiation (OLR) (Wm-2); lower-left and lower-right panels show the net surface heat flux (SHF)(Wm-2) and sea-surface temperature (SST)(C) over the Kuroshio Extension region. Ocean mesoscale eddies are clearly visible in the SHF, indicative of strong feedbacks between ocean mesoscale eddies and atmosphere. Wm-2, watts per square meter; C, centigrade.

Millipore®
Filtration, Separation
& Preparation

REFINED WITH YOU IN MIND

Stericup® Quick Release Filtration Systems

Work With Ease. Filter With Confidence.

Stericup® Quick Release Filtration Systems streamline your workflow with ergonomic design updates and safeguard your results with the proven performance of Millipore® membranes.

1. Quarter-Turn Quick Release Funnel Removal
2. Frosted Writing Surface
3. Lighter Color for Legibility
4. Click-Seal Confidence Cap

Explore New Features
SigmaAldrich.com/stericupquickrelease

The life science business of Merck KGaA, Darmstadt, Germany operates as MilliporeSigma in the U.S. and Canada.

Bottletop Dispensers

The Varispenser 2 and Varispenser 2x from Eppendorf are universally applicable bottletop dispensers. Bottletop dispensers are needed in any lab where aggressive solutions like lyes, acids, bases, or solvents are dispensed from large supply bottles. Thanks to the proven positive displacement principle, loss of residue is almost completely avoided. This technology, combined with the high chemical resistance of all components that might encounter aggressive liquids, allows the use of Varispenser 2 and Varispenser 2x with nearly all liquids commonly found in labs. Accessories including an easily assembled drying tube, a filter, and a flexible discharge tube enable a broad range of dispensing options. All devices are equipped with standard GL 45 threads and are compatible with almost all thread types used in labs, thanks to the additional adapters included in the scope of delivery.

Eppendorf
For info: 800-645-3050
www.eppendorf.com

Filter Plugs

Universal Pipette Filter Plugs from iNLABTEC are designed to provide a final barrier to protect the internal components of your pipettes against contamination from accidental splashes during pipetting, foaming samples, or aerosolized vapors. As well as offering a cost-effective alternative to filter tips, the versatile and flexible foam design of iNLABTEC pipette filter plugs allows them to fit into any brand of pipette with a cone opening of 3 mm–4.5 mm. Plugs are autoclavable and come in 50 filters/sachet.

iNLABTEC
For info: +41-(0)-71-222-48-65
www.inlabtec.com

Evaporator

An optimized EZ-2 evaporator is available to suit your solvent removal needs for many applications. The EZ-Envi is created specifically for concentration of volatile solvents prior to analysis, the EZ-Standard for drying water and volatile solvents, the EZ-2 Plus for working with solvents with higher boiling points—up to 165°C—and the EZ-2 Elite for more difficult solutions such as dimethyl sulfoxide (DMSO) and N-Methyl-2-pyrrolidone (NMP), or fast freeze-drying. EZ-2 evaporators can be further modified for the most difficult and hazardous solvents, and a special model exists for those working with potentially explosive solvents such as diethyl ether. Each EZ-2 evaporator enables evaporation from sample container formats including round-bottom flasks up to 500 mL, tubes up to 150 mm long, vials, and custom reaction blocks as well as shallow and deep-well microplates. Running an EZ-2 evaporator is easier than running a rotary evaporator. Just load your samples, select maximum safe temperature for samples, select solvent type, and hit start.

Genevac
For info: 845-687-5000
www.genevac.com

Multi-Tube Vortex Mixer

The TT-2500-VM Multi-Tube Vortex Mixer is a high-capacity vortex mixer designed to provide gentle to vigorous mixing of reagents at an adjustable speed of 500 rpm–2,500 rpm for up to 50 test tubes simultaneously. Packed with a range of features, the microprocessor-controlled unit has an easy-to-read LED display, a variety of available tube frames to hold different test tube sizes, and two built-in-operation modes that can be run by either short mixing or time mixing. The vortexing action is created by holding the top of the vessel securely in place and moving the bottom tray freely in a defined orbit. A DC brushless motor creates quiet, rattle-free mixing. The TT-2500-VM is ideal for use in high-throughput testing labs such as clinical, environmental, and chemistry labs.

Hercuvan Lab Systems
For info: 858-335-8871
www.hercuvan.com

Volumetric Glassware

BrandTech is introducing a line of BLAUBRAND Class A, USP-certified volumetric glassware from Brand GmbH. The line includes clear and amber volumetric flasks, graduated cylinders, bulb pipettes, and volumetric pipettes. USP volumetric instruments comply with Class A error limits required by the United States Pharmacopeia (USP). They make an excellent choice for companies that are audited by the U.S. Food and Drug Administration or any other U.S. authority. BLAUBRAND is also well suited for companies that are not audited but demand high-quality glassware that meets Class A error limits. Volumetric instruments are individually calibrated on computer-controlled, automated production lines for maximum precision. High-quality inks combined with carefully controlled annealing processes provide durable graduations and long service life. Thermal stress in the glass blanks is eliminated prior to adjustment so there are no permanent volume changes after heating (up to 250°C).

BrandTech Scientific
For info: 888-522-2726
www.brandtech.com

Chilling/Heating Dry Bath

The two-position EchoTherm Model IC22 Digital Chilling/Heating Dry Bath can be used in chilling or heating biological samples from –10°C to 100°C. The unit is two dry baths in one, saving valuable bench space. It can run two separate or identical temperatures and two different sample blocks simultaneously. It has a built-in data logger, 30-day countdown timer with alarm, and RS232 interface, making it ideal for use with robotic systems. IC22 can be used with standard accessory sample blocks for 0.5-mL, 1.5-mL, and 2.0-mL centrifuge tubes, PCR tubes and plates, 96-well and 384-well assay plates of all kinds, vials, and most test tube sizes. Custom blocks are available on special order. IC22 is perfect for enzyme reactions and deactivations, hybridizations, ligations, storing enzymes or DNA libraries, maintaining 17°C for storing oocytes, storing samples at ice bucket temperatures, incubating samples at, above, or below room temperature, and much more.

Torrey Pines Scientific
For info: 866-573-9104
www.torreypinesscientific.com

Electronically submit your new product description or product literature information! Go to www.sciencemag.org/about/new-products-section for more information.

Newly offered instrumentation, apparatus, and laboratory materials of interest to researchers in all disciplines in academic, industrial, and governmental organizations are featured in this space. Emphasis is given to purpose, chief characteristics, and availability of products and materials. Endorsement by *Science* or AAAS of any products or materials mentioned is not implied. Additional information may be obtained from the manufacturer or supplier.

Science Robotics | AAAS

The First Journal of Interdisciplinary Robotics Research.

NEW AND UPCOMING SPECIAL ISSUES

NEW **MARINE AND SPACE ROBOTICS**

HUMANOIDS

NEW MATERIALS AND ACTUATORS

Submit Your Article for Publication in *Science Robotics*:

- Rapid review, scoop protection and no article page limits.
- Exposure to an international audience.
- Supportive and knowledgeable editorial staff.
- Promotion on the *Science Robotics* website and the potential for accompanying commentary or podcasts.
- AAAS social media and media relations support.

Learn more at **robotics.sciencemag.org**.

Send pre-submission inquiries to **sciroboteditors@aaas.org**.

want new technologies?

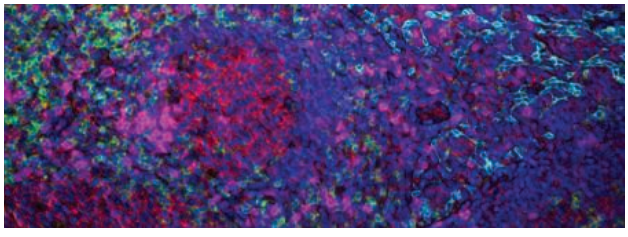

antibodies
apoptosis
biomarkers
cancer
cytometry
data
diseases
DNA
epigenetics
genomics
immunotherapies
medicine
microbiomics
microfluidics
microscopy
neuroscience
proteomics
sequencing
toxicology
transcriptomics

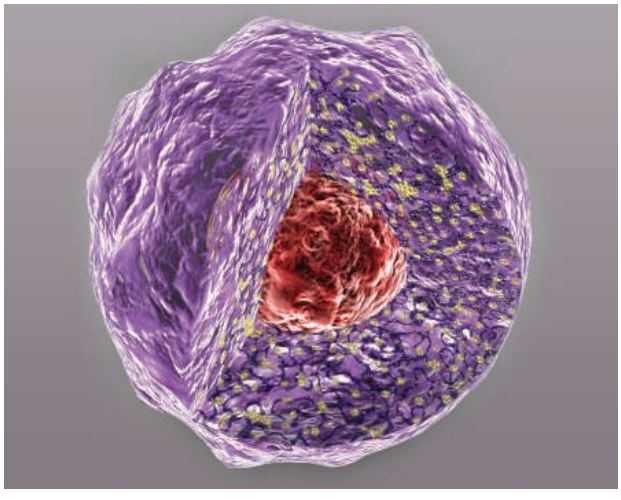

watch our webinars

Learn about the latest break-throughs, new technologies, and ground-breaking research in a variety of fields. Our expert speakers explain their quality research to you and answer questions submitted by live viewers.

VIEW NOW!
webinar.sciencemag.org

Science
AAAS

Brought to you by the *Science*/AAAS Custom Publishing Office

@SciMagWebinars

GE Healthcare

Focus on discovery with the DeltaVision™ Ultra

An easy-to-use, automated widefield microscope, DeltaVision Ultra enhances data quality so you can see the structures that matter in time-lapse live cell imaging, multi-point cell tracking, and multi-well plate scanning.

Learn about the microscope that supports all your research needs at **gelifesciences.com/deltavisionultra**

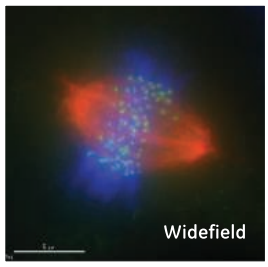

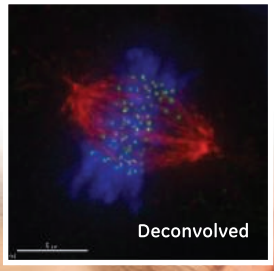

GE Healthcare

Experience counts.

It takes vision to invent ECL imaging and continue to improve it. Let our experience work for you with the Amersham™ Imager 680, a sensitive, robust, and easy-to-use CCD imager for publication quality digital images of DNA and protein gels and blots.

Results you can trust. Images you can count on.

To request a demo or for more information, visit **gelifesciences.com/AI680demo**

New no-binning feature allows you to confidently detect small changes in protein levels and low-abundance proteins.

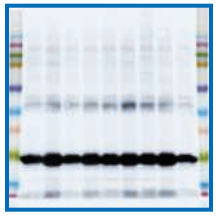

Determine molecular weights quickly by confirming the real colors of the marker right on the display.

新潟大學腦研究所
BRAIN RESEARCH INSTITUTE, NIIGATA UNIVERSITY

Job Opening

Professor in Cellular Neuropathology
Brain Research Institute, Niigata University, Japan

Brain Research Institute, Niigata University is currently seeking a full professor who explores system neuropathology and neurobiology for brain diseases, applying molecular biology, cellular biology, mouse engineering and/or neurophysiology. Candidates who have a potential to lead the given neuroscience field are desirable.

1. JOB DETAILS

1. Position
   A full professor (Tenured. Salary will be commensurate with experience)
2. Employment starting date
   Anticipated starting date is April 2018, or as soon as possible thereafter.

2. APPLICATION PROCEDURE

Interested candidates are encouraged to apply by email and should submit as PDF documents:

1. A Curriculum Vitae
2. List of achievements
3. Reprints of main research publications (5 papers)
4. Research interests and accomplishments, teaching experience, and a research plan
5. References (at least 2)

3. CLOSING DATE

January 31, 2018 at 5:00 pm (JST)

To apply or make inquiries, please email Brain Research Institute, Niigata University, at **noukenshomu@adm.niigata-u.ac.jp**

Please refer to the following webpages for more information:
http://www.bri.niigata-u.ac.jp/en/info/officialannounce/000960.html

INDIANA UNIVERSITY
SCHOOL OF MEDICINE

SEEKING NOMINATIONS FOR TRANSLATIONAL RESEARCH PRIZE

Indiana University School of Medicine is accepting nominations for the 2018 August M. Watanabe Prize in Translational Research, awarded to an investigator who has made a significant contribution to the field of translational science.

The Watanabe Prize is one of the nation's largest and most prestigious awards recognizing individuals focused on shepherding scientific discoveries into new therapies for patients. It is named in honor of the late August Watanabe, a titan in the field of translational research in both academia and industry, who impacted the health of people around the world as a leader at IU and Eli Lilly and Company.

Nominees for the Watanabe Prize should be members of the scientific or medical community who have achieved outstanding accomplishments in translational research. This award is conferred upon senior investigators whose influential research deserves major recognition.

The winner of the 2018 Watanabe Prize will receive a $100,000 award and spend time in Indianapolis as a visiting dignitary to share knowledge with audiences at IU and partner institutions. Over the next two years, the honoree also will serve as a long-distance mentor to two exceptional young investigators named concurrently as Watanabe Translational Scholars. Note: This year's prize nominees must be available to travel to Indianapolis from September 12-14, 2018.

To submit a nomination, email **amwprize@iu.edu** with: 1) a letter of nomination including a detailed description of the nominee's major translational research accomplishments and their impact, and 2) a copy of the nominee's current curriculum vitae (CV) by January 31, 2018. Questions? Contact **amwprize@iu.edu** or 317-278-2874.

Indiana University is an equal opportunity employer committed to building a culturally diverse intellectual community and strongly encourages applications from women and minorities.

UW Medicine
UW SCHOOL OF MEDICINE

Professor and Chair, Department of Microbiology, University of Washington

The University of Washington, School of Medicine seeks a Professor and Chair of the Department of Microbiology. Candidates for this full time position should have a PhD and/or an MD (or foreign equivalent) in Microbiology or a related biomedical discipline, an internationally recognized research program in Microbiology and demonstrated academic leadership skills. The Department of Microbiology has outstanding research and training programs, including an undergraduate major and participation in both departmental and interdisciplinary graduate programs (https://microbiology.washington.edu). The Department is ranked #3 worldwide in microbiology by *U.S. News and World Reports* and is an integral part of a broad, vigorous research community. The UW School of Medicine is #2 in the nation and #1 among public universities in NIH funding. UW faculty engage in teaching, research and service while training the next generation of scientists through undergraduate, graduate and medical student education.

Please submit an application (including a cover letter addressed to Dr. Joan Goverman, Chair, Microbiology Chair Search Committee and your curriculum vitae) at **http://apply.interfolio.com/47603**.

Applications will be considered until the position is filled.

University of Washington is an Affirmative Action and Equal Opportunity Employer. All qualified applicants will receive consideration for employment without regard to race, color, religion, sex, sexual orientation, gender identity, gender expression, national origin, age, protected veteran or disabled status, or genetic information.

Head and Professor
Department of Biological Sciences
Purdue University

Purdue University invites applications for the position of Head of the Department of Biological Sciences to start August 2018. The department seeks a dynamic leader with creative vision and an outstanding record of research, administration, and teaching.

The department is undergoing a period of exciting development. Departmental strengths include Biology Education; Cell & Molecular Biology; Ecology and Evolutionary Biology; Microbiology & Infectious Disease; Neuroscience & Physiology; and Structural Biology. Many departmental faculty are involved in university-wide multidisciplinary research through Discovery Park (www.discoverypark.purdue.edu) and the Purdue Center for Cancer Research (www.cancerresearch.purdue.edu). In addition, members of the department play leading roles in the recently launched Purdue Institute for Integrative Neuroscience http://www.purdue.edu/discoverypark/pillars/integrative-neuroscience-center/ and Purdue Institute of Inflammation, Immunology and Infectious Disease https://www.purdue.edu/discoverypark/pillars/pi4d/. As of Fall 2017, the Biological Sciences Department is comprised of 55 faculty members, 27 post-doctoral researchers, 118 graduate students, and 899 undergraduate biology majors. Further information about the department is available at www.bio.purdue.edu.

Qualifications: The successful candidate will have: a Ph.D. in Biology or a related discipline; an outstanding record of scholarly achievement and a history of extramurally funded research commensurate with the rank of full professor at Purdue; dedication to building a diverse, inclusive, and vibrant scientific community, exceptional and proven leadership abilities; an effective vision for the department in the university, state, and nation; commitment to excellence in undergraduate and graduate education; and an enthusiasm for engagement.

Applications: We encourage qualified candidates to apply online at **http://hiring.science.purdue.edu**. Inquiries should be directed to **Biology Head Search Committee, Department of Biological Sciences, Purdue University, 915 W. State St., West Lafayette, IN 47907-2054** or **search@bio.purdue.edu**. Purdue University's Department of Biological Sciences is committed to advancing diversity in all areas of faculty effort, including scholarship, instruction and engagement. Candidates should address at least one of these in their cover letter, indicating their past experiences, current interests or activities, and/or future goals to promote a climate that values diversity and inclusion. Review of applications will begin **January 8, 2018** and will continue until the position is filled.

A background check is required for employment in this position. Purdue University is an EEO/AA Employer. All individuals, including minorities, women, individuals with disabilities, and veterans are encouraged to apply.

THE UNIVERSITY OF TEXAS AT DALLAS
School of Natural Sciences and Mathematics

DEPARTMENT OF BIOLOGICAL SCIENCES
ASSISTANT PROFESSOR

The Department of Biological Sciences in the School of Natural Sciences and Mathematics at the University of Texas at Dallas (**http://www.utdallas.edu/biology/**) invites applications for a faculty position at the rank of Assistant Professor. We seek to hire an outstanding scientist with research interests that complement and build on existing departmental strengths in biochemistry, cell and molecular biology, computational and systems biology, genomics, microbiology, and pathobiology (cancer, neurodegenerative disorders, and infectious disease). Since the department has the goal of expanding its research and teaching into new directions, we will also consider applications from excellent candidates in other areas of the biological sciences. The University has recently made a major investment in new laboratory space, and in core facilities (genomics, imaging and histology, flow cytometry, and protein analysis) that will be available to support the research of new recruits.

Applicants should be prepared to establish a vigorous and independent research program and should have enthusiasm for teaching at both graduate and undergraduate levels.

Review of applications will begin immediately and will continue until the position is filled. Indication of sex and ethnicity for affirmative action statistical purposes is requested as part of the application but is not required.

Application materials: cover letter, curriculum vitae, short descriptions of research plans and teaching interests and the full contact information for at least three references should be submitted at:
http://jobs.utdallas.edu/postings/9165.

The University of Texas at Dallas is an Equal Opportunity/ Affirmative Action employer and strongly encourages applications from candidates who would enhance the diversity of the University's faculty and administration.

Systems, Molecular, and Cellular Mechanisms of Alzheimer's Disease and Dementia

THE OHIO STATE UNIVERSITY

The Ohio State University is launching a major initiative focused on the systems, molecular, and cellular mechanisms of Alzheimer's disease and adult-onset dementia. To this end, the University is recruiting 15 faculty to multiple departments at all ranks to study injury-induced dementia and Alzheimer's disease. As part the initiative, The **Department of Neuroscience** in the College of Medicine is currently recruiting four or more tenure-track faculty at all ranks, in association with the OSU Discovery Theme in Chronic Brain Injury. Candidates must hold a PhD or MD (or equivalent) with research expertise in areas directly related to mechanisms of Alzheimer's Disease or related disorders. This recruitment is part of an ongoing commitment to develop distinguished research and clinical care centers at The Ohio State University focused on adult-onset dementias.

Successful candidates are expected to contribute to the missions of the University, Department, and Centers via active participation in research and teaching programs, mentoring of trainees and serving on departmental or college-level committees. Salary will be competitive and commensurate with experience.

Prospective candidates should send a statement of research interests, vitae and a list of three references to Melissa Stenger (**Melissa.stenger@osumc.edu**). Consideration of candidates will begin on **1 January 2018**.

Unless confidentiality is requested in writing, information regarding the applicants must be released upon request. For more information about career opportunities, please visit www.Discovery.osu.edu or https://wexnermedical.osu.edu/neurological-institute/departments-and-centers/departments/department-of-neuroscience

The Ohio State University is an Equal Opportunity, Affirmative Action Employer and as such, women and underrepresented individuals in science are encouraged to apply.

By **Lydia Zepeda**

The harassment tax

A senior faculty member asked me into his office. I assumed it was to talk about agricultural data. It was the fall of 1991 and I was untenured, 32 years old, and 7 months pregnant. He was in his 60s and one of many men who were going to vote on my tenure. He showed me the recent issue of *Vanity Fair* with Demi Moore on the cover, pregnant and nude. "She reminds me of you," he said as he tried to catch my eye. I looked at the floor, stunned. I mumbled something and backed out of his office, wondering whether I would ever feel clean again.

This was just one example of the sexual harassment I experienced during my career as a professor. It happened to me; it happens to other female faculty members; and it happens to female staff, graduate students, and undergraduates. It wasn't all men and it didn't happen all the time, but it happened, and it was part of my life in academia: grant writing, teaching, publishing in peer-reviewed journals—oh, and dealing with creeps and the messes they made.

Sexual harassment is draining. It takes up time and energy, and it does not result in anything for one's CV or annual review. It is a productivity tax on women. In my case, it meant I avoided co-authoring or having joint grants with male colleagues, things that would likely have increased my funding and publications.

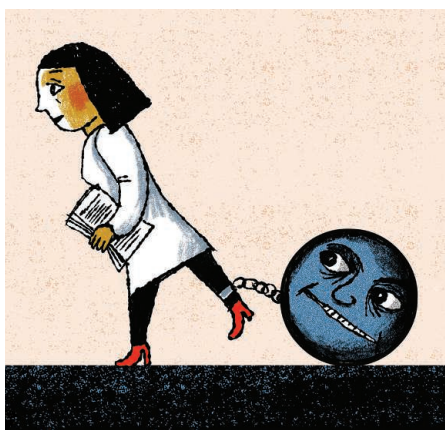

"Sexual harassment is ... a productivity tax on women."

The costs also spill over to others. By taking up women's energy and lowering productivity, harassment wastes valuable grant money and taxpayer funding. It is also a key reason women leave academia, which ultimately hurts the entire scientific enterprise in the form of lost investment, potential, and diversity of ideas. In my case, even though I was productive and loved research, teaching, and advising students, ubiquitous harassment was one of the reasons why I retired early.

Here are just a few examples of the sexual harassment I experienced that affected my productivity. A married colleague bragged to me about his sexual conquests. A junior colleague told me he wanted to date me. (I am married!) While I was interviewing for a full professor job, a department head in his 40s inquired how many children I had and, staring at my body, insisted that I "should get pregnant many more times." After I got tenure, the burden of harassment only increased. That's because I experienced it not just directly, but also secondhand, as other victims—students, staff members, colleagues, mentees—sought my help and time.

Recently, a graduate student confided in me that a renowned researcher had hit on her and touched her inappropriately during a postdoc interview. I advised her not to take the job because if he did that during the interview, in all likelihood it would escalate later. She would not be dissuaded. "It is just too good a job," she said. She decided to take a calculated risk because, she said, "what else are you going to do? It's everywhere." So, along with doing first-class research, she has to figure out how to keep her boss's hands off her.

Sexual harassment even affected my free time, interfering with my efforts to recharge and sustain my productivity. Earlier in my career, I played basketball with faculty and staff members on campus. I was usually the only woman. One day, a man guarding me couldn't get the ball from me and punched me in the breast. It was hard enough to knock me to the floor and leave a bruise. When I demanded to know why he punched me, he yelled, "Women have no business here!" I wondered, did he mean playing basketball or being at the university?

I stopped playing basketball; dealing with harassment at work took enough energy and time. While I was angry at the man who assaulted me, I was angrier at the eight other men on the court. They all saw and heard what happened, yet they said and did nothing. They literally looked away. They may not have meant it, but to me their silence spoke volumes: approval.

It is time to speak up. We can start by having meaningful and transparent Title IX investigations that support, not attack or shame, victims. Speak up every time harassment happens. Men, call out other men. Every time. Show that you do not condone sexual harassment. Enough is enough. ■

Lydia Zepeda is a professor emeritus at the University of Wisconsin in Madison and a AAAS fellow. Send your career story to SciCareerEditor@aaas.org.

ILLUSTRATION: ROBERT NEUBECKER